The evolution of antievolution *p. 28*

Epigenetic control of scouting in ants *p. 42*

Printing complex 3D patterned ceramics *p. 58*

Science

$15
1 JANUARY 2016
sciencemag.org

AAAS

Vaccines on ice

Needed shots stuck in R&D *p. 16*

CONTENTS

1 JANUARY 2016 • VOLUME 351 • ISSUE 6268

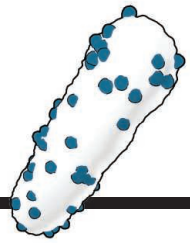

34 Light-harvesting dots on microbes

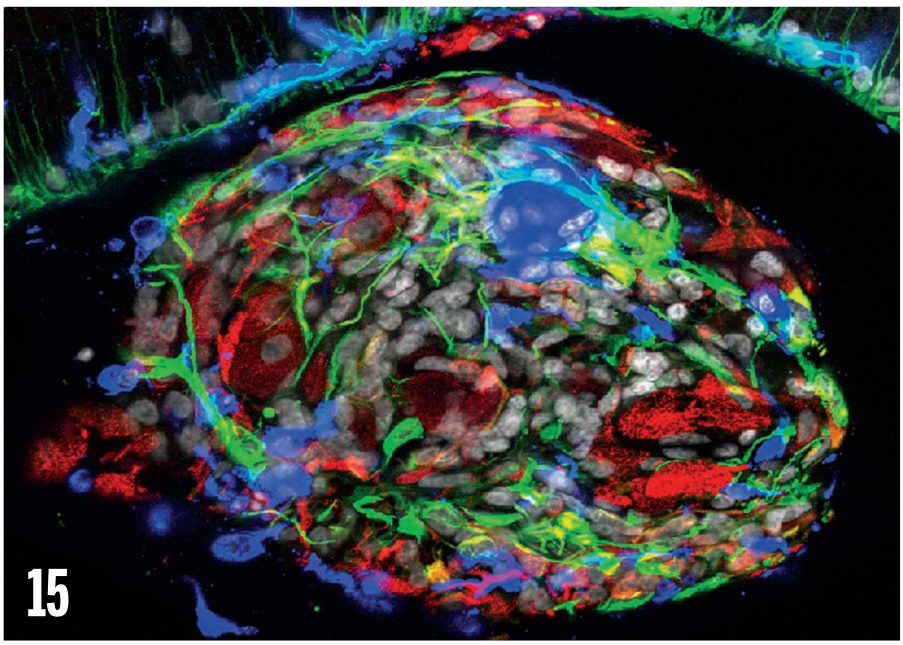

15

NEWS

IN BRIEF

8 News at a glance

IN DEPTH

10 RESEARCH AGENCIES REVEL IN FINAL 2016 BUDGET
NIH gets $2 billion hike, NASA and DOE science grow, NSF avoids restrictive language *By J. Mervis*

12 AS EBOLA EPIDEMIC DRAWS TO A CLOSE, A THIN SCIENTIFIC HARVEST
Thirteen clinical trials in West Africa have yielded only one unequivocally positive result *By J. Cohen and M. Enserink*

13 SPERM RNA FRAGMENTS MODIFY OFFSPRING METABOLISM
Molecules transfer mouse paternal parental traits to progeny *By M. Leslie*

14 FUNDING FOR KEY DATA RESOURCES IN JEOPARDY
NIH genome institute wants to scale back support of human and model organism databases *By J. Kaiser*

15 CALIFORNIA STEM CELL AGENCY PLOTS A RACE TO THE CLINIC
CIRM lays out endgame and prospects for new money *By K. Servick*

FEATURE

16 UNFILLED VIALS
Scientifically feasible vaccines against major diseases are stalled for lack of funds. *Science* names 10 top candidates that need a boost *By J. Cohen*

INSIGHTS

LETTERS

20 NEXTGEN VOICES: POLITICAL PRIORITIES

PERSPECTIVES

24 ILLUMINATING ANHEDONIA
Optogenetics and fMRI reveal the brain circuitry of anhedonia *By T. W. Robbins*
▸ REPORT P. 41

25 SEEING mTORC1 SPECIFICITY
Structural information reveals how a multiprotein complex responds to amino acid abundance *By G. R. Buel and J. Blenis*
▸ RESEARCH ARTICLES PP. 43, 48, & 53

26 WHEN TWO REACTIONS BECOME ONE
Merging two fundamental reactions of organoboron compounds provides a new platform for catalysis
By J. W. B. Fyfe and A. J. B. Watson
▸ REPORT P. 70

28 THE EVOLUTION OF ANTIEVOLUTION POLICIES AFTER *KITZMILLER* V. *DOVER*
A phylogeny identifies ancestors of modern creationist legislation
By N. J. Matzke

30 THE SCREAMS OF A STAR BEING RIPPED APART
A star being devoured by a black hole provides a route to study accretion and jet formation *By G. C. Bower*
▸ REPORT P. 62

32 THE POWER OF CROWDS
Combining humans and machines can help tackle increasingly hard problems
By P. Michelucci and J. L. Dickinson

34 MICROBES IN A KNIGHT'S ARMOR
Bacteria studded with nanoparticles produce acetate from carbon dioxide and sunlight *By V. Müller*
▸ REPORT P. 74

BOOKS *ET AL.*

35 NEWTON'S APPLE AND OTHER MYTHS ABOUT SCIENCE
R. L. Numbers and K. Kampourakis, Eds.
reviewed by J. Endersby

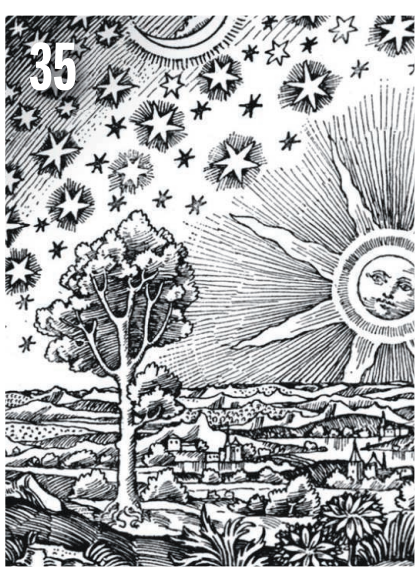

35

Published by AAAS

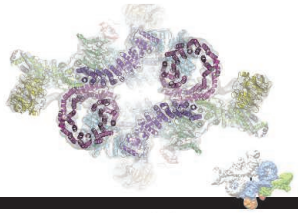

48
A complex key to growth and metabolism

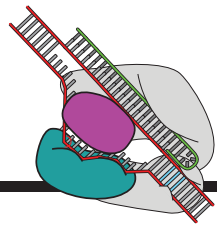

84
More precise genome editing

36 THE DEATH OF CANCER
By V. T. DeVita Jr. and E. DeVita-Raeburn, reviewed by A. Woolfson

36 PATTERNS OF THE UNIVERSE
By A. Bellos and E. Harriss

RESEARCH

IN BRIEF

37 From *Science* and other journals

REVIEW

40 ANTIBIOTIC RESISTANCE
Multidrug evolutionary strategies to reverse antibiotic resistance *M. Baym* et al.
REVIEW SUMMARY; FOR FULL TEXT: dx.doi.org/10.1126/science.aad3292

RESEARCH ARTICLES

41 NEURAL CIRCUITS
Prefrontal cortical regulation of brainwide circuit dynamics and reward-related behavior *E. A. Ferenczi* et al.
RESEARCH ARTICLE SUMMARY; FOR FULL TEXT: dx.doi.org/10.1126/science.aac9698
▸ PERSPECTIVE P. 24

42 BEHAVIORAL GENETICS
Epigenetic (re)programming of caste-specific behavior in the ant *Camponotus floridanus D. F. Simola* et al.
RESEARCH ARTICLE SUMMARY; FOR FULL TEXT: dx.doi.org/10.1126/science.aac6633
▸ VIDEO

METABOLISM

43 Sestrin2 is a leucine sensor for the mTORC1 pathway *R. L. Wolfson* et al.

48 Architecture of human mTOR complex 1 *C. H. S. Aylett* et al.

53 Structural basis for leucine sensing by the Sestrin2-mTORC1 pathway *R. A. Saxton* et al.
▸ PERSPECTIVE P. 25

REPORTS

58 3D PRINTING
Additive manufacturing of polymer-derived ceramics *Z. C. Eckel* et al.
▸ VIDEO

62 BLACK HOLE PHYSICS
A radio jet from the optical and x-ray bright stellar tidal disruption flare ASASSN-14li *S. van Velzen* et al.
▸ PERSPECTIVE P. 30

65 ASTROCHEMISTRY
Statistical ortho-to-para ratio of water desorbed from ice at 10 kelvin *T. Hama* et al.

68 MEMBRANES
Sieving hydrogen isotopes through two-dimensional crystals *M. Lozada-Hidalgo* et al.

70 ORGANIC CHEMISTRY
Catalytic conjunctive cross-coupling enabled by metal-induced metallate rearrangement *L. Zhang* et al.
▸ PERSPECTIVE P. 26

74 MICROBIAL ENGINEERING
Self-photosensitization of nonphotosynthetic bacteria for solar-to-chemical production *K. K. Sakimoto* et al.
▸ PERSPECTIVE P. 34

VIROLOGY

77 An orthopoxvirus-based vaccine reduces virus excretion after MERS-CoV infection in dromedary camels *B. L. Haagmans* et al.

81 Co-circulation of three camel coronavirus species and recombination of MERS-CoVs in Saudi Arabia *J. S. M. Sabir* et al.

84 GENOME EDITING
Rationally engineered Cas9 nucleases with improved specificity *I. M. Slaymaker* et al.

88 PROTEIN TRANSLOCATION
Structure of the Sec61 channel opened by a signal sequence *R. M. Voorheees and R. S. Hegde*

DEPARTMENTS

7 EDITORIAL
New members of the family
By Marcia McNutt

98 WORKING LIFE
Beyond the tick boxes
By Artaza Gilani

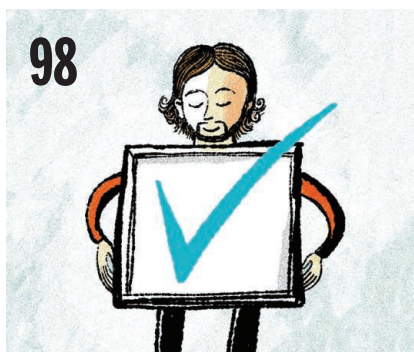

ON THE COVER

Vials of experimental vaccines against severe acute respiratory syndrome, Marburg virus, and chikungunya sit on ice at the Vaccine Pilot Plant run by the U.S. National Institutes of Health in Frederick, Maryland. In the wake of the Ebola epidemic in West Africa, a growing number of researchers and public health advocates are arguing that more should be done to aggressively advance vaccines that have weak commercial markets but appear feasible. See page 16. *Photo: © Ken Garrett*

Science Staff 6
New Products 92
Science Careers 93

SCIENCE (ISSN 0036-8075) is published weekly on Friday, except the last week in December, by the American Association for the Advancement of Science, 1200 New York Avenue, NW, Washington, DC 20005. Periodicals mail postage (publication No. 484460) paid at Washington, DC, and additional mailing offices. Copyright © 2016 by the American Association for the Advancement of Science. The title SCIENCE is a registered trademark of the AAAS. Domestic individual membership and subscription (51 issues): $165 ($74 allocated to subscription). Domestic institutional subscription (51 issues): $1522; Foreign postage extra: Mexico, Caribbean (surface mail) $55; other countries (air assist delivery) $89. First class, airmail, student, and emeritus rates on request. Canadian rates with GST available upon request, GST #1254 88122. Publications Mail Agreement Number 1069624. **Printed in the U.S.A.**
Change of address: Allow 4 weeks, giving old and new addresses and 8-digit account number. **Postmaster:** Send change of address to AAAS, P.O. Box 96178, Washington, DC 20090–6178. **Single-copy sales:** $15.00 current issue, $20.00 back issue prepaid includes surface postage; bulk rates on request. **Authorization to photocopy** material for internal or personal use under circumstances not falling within the fair use provisions of the Copyright Act is granted by AAAS to libraries and other users registered with the Copyright Clearance Center (CCC) Transactional Reporting Service, provided that $35.00 per article is paid directly to CCC, 222 Rosewood Drive, Danvers, MA 01923. The identification code for *Science* is 0036-8075. *Science* is indexed in the *Reader's Guide to Periodical Literature* and in several specialized indexes.

Published by AAAS

Science
AAAS
1200 New York Avenue, NW, Washington, DC 20005
Bateman House, 82-88 Hills Road, Cambridge, UK CB2 1LQ

Editor-in-Chief Marcia McNutt
Executive Editor Monica M. Bradford **News Editor** Tim Appenzeller
Managing Editor, Research Journals Katrina L. Kelner
Deputy Editors Barbara R. Jasny, Andrew M. Sugden(UK), Valda J. Vinson, Jake S. Yeston

Research and Insights

SR. EDITORS Caroline Ash(UK), Gilbert J. Chin, Lisa D. Chong, Julia Fahrenkamp-Uppenbrink(UK), Pamela J. Hines, Stella M. Hurtley(UK), Paula A. Kiberstis, Marc S. Lavine(Canada), Kristen L. Mueller, Ian S. Osborne(UK), Beverly A. Purnell, L. Bryan Ray, Guy Riddihough, H. Jesse Smith, Jelena Stajic, Peter Stern(UK), Phillip D. Szuromi, Brad Wible, Nicholas S. Wigginton, Laura M. Zahn **ASSOCIATE EDITORS** Brent Grocholski, Keith T. Smith, Sacha Vignieri **ASSOCIATE BOOK REVIEW EDITOR** Valerie B. Thompson **ASSOCIATE LETTERS EDITOR** Jennifer Sills **CHIEF CONTENT PRODUCTION EDITOR** Cara Tate **SR. CONTENT PRODUCTION EDITORS** Harry Jach, Lauren Kmec **CONTENT PRODUCTION EDITORS** Jeffrey E. Cook, Chris Filiatreau, Cynthia Howe, Barbara P. Ordway, Catherine Wolner **SR. EDITORIAL COORDINATORS** Carolyn Kyle, Beverly Shields **EDITORIAL COORDINATORS** Ramatoulaye Diop, Joi S. Granger, Lisa Johnson, Anita Wynn **PUBLICATIONS ASSISTANTS** Aneera Dobbins, Jeffrey Hearn, Dona Mathieu, Le-Toya Mayne Flood, Shannon McMahon, Scott Miller, Jerry Richardson, Rachel Roberts(UK), Alice Whaley(UK), Brian White **EXECUTIVE ASSISTANT** Anna Bashkirova **ADMINISTRATIVE SUPPORT** Janet Clements(UK), Lizanne Newton(UK), Maryrose Madrid, Laura-Nadine Schuhmacher (UK, Intern), Alix Welch (Intern), John Wood(UK)

News

NEWS MANAGING EDITOR John Travis **INTERNATIONAL EDITOR** Richard Stone **DEPUTY NEWS EDITORS** Daniel Clery(UK), Robert Coontz, Elizabeth Culotta, David Grimm, David Malakoff, Leslie Roberts **CONTRIBUING EDITOR** Martin Enserink(Europe) **SR. CORRESPONDENTS** Jeffrey Mervis, Elizabeth Pennisi **NEWS WRITERS** Adrian Cho, Jon Cohen, Jennifer Couzin-Frankel, Carolyn Gramling, Eric Hand, Jocelyn Kaiser, Catherine Matacic, Kelly Servick, Robert F. Service, Erik Stokstad(Cambridge, UK), Emily Underwood **INTERNS** Hanae Armitage, Nala Rogers **CONTRIBUTING CORRESPONDENTS** Michael Balter(Paris), John Bohannon, Ann Gibbons, Mara Hvistendahl, Sam Kean, Eli Kintisch, Kai Kupferschmidt(Berlin), Andrew Lawler, Christina Larson(Beijing), Mitch Leslie, Charles C. Mann, Eliot Marshall, Virginia Morell, Dennis Normile(Shanghai), Heather Pringle, Tania Rabesandratana(London), Gretchen Vogel(Berlin), Lizzie Wade(Mexico City) **CAREERS** Donisha Adams, Rachel Bernstein(Editor) **COPY EDITORS** Julia Cole, Dorie Chevlen, Jennifer Levin (Chief) **ADMINISTRATIVE SUPPORT** Jessica Williams

Executive Publisher Rush D. Holt
Publisher Kent R. Anderson **Chief Digital Media Officer** Rob Covey

BUSINESS OPERATIONS AND PORTFOLIO MANAGEMENT DIRECTOR Sarah Whalen **BUSINESS SYSTEMS AND FINANCIAL ANALYSIS DIRECTOR** Randy Yi **MANAGER OF FULFILLMENT SYSTEMS** Neal Hawkins **SYSTEMS ANALYST** Nicole Mehmedovich **ASSISTANT DIRECTOR, BUSINESS OPERATIONS** Eric Knott **MANAGER, BUSINESS OPERATIONS** Jessica Tierney **BUSINESS ANALYSTS** Cory Lipman **FINANCIAL ANALYST** Robert Clark **RIGHTS AND PERMISSIONS ASSISTANT DIRECTOR** Emilie David **PERMISSIONS ASSOCIATE** Elizabeth Sandler **RIGHTS, CONTRACTS, AND LICENSING ASSOCIATE** Lili Kiser

MARKETING DIRECTOR Elise Swinehart **ASSOCIATE DIRECTOR OF ACQUISITION AND RETENTION** Julianne Wielga **MARKETING ASSOCIATE** Elizabeth Sattler **SR. MARKETING EXECUTIVE** Jennifer Reeves **ASSOCIATE DIRECTOR, CREATIVE SERVICES** Tzeitel Sorrosa **ART ASSOCIATE** Seil Lee **JR. ART ASSOCIATE** Kim Huynh **ASSISTANT COMMERCIAL EDITOR** Selby Frame **MARKETING PROJECT MANAGER** Angelissa McArthur **PROGRAM DIRECTOR, AAAS MEMBER CENTRAL** Peggy Mihelich **FULFILLMENT SYSTEMS AND OPERATIONS** membership@aaas.org **MANAGER, MEMBER SERVICES** Pat Butler **SPECIALISTS** Terrance Morrison, Latasha Russell **MANAGER, DATA ENTRY** Mickie Napoleoni **DATA ENTRY SPECIALISTS** Brenden Aquilino, Fiona Giblin

DIRECTOR, SITE LICENSING Tom Ryan **DIRECTOR, CORPORATE RELATIONS** Eileen Bernadette Moran **SR. PUBLISHER RELATIONS SPECIALIST** Kiki Forsythe **PUBLISHER RELATIONS MANAGER** Catherine Holland **PUBLISHER RELATIONS, EASTERN REGION** Keith Layson **PUBLISHER RELATIONS, WESTERN REGION** Ryan Rexroth **SALES RESEARCH COORDINATOR** Aiesha Marshall **MANAGER, SITE LICENSE OPERATIONS** Iquo Edim **SENIOR PRODUCTION SPECIALIST** Robert Koepke **SENIOR OPERATIONS ANALYST** Lana Guz **FULFILLMENT ANALYST** Judy Lillibridge **ASSOCIATE DIRECTOR, MARKETING** Christina Schlecht **MARKETING ASSOCIATES** Thomas Landreth, Isa Sesay-Bah

WEB TECHNOLOGIES SR. DEVELOPER Chris Coleman **DEVELOPERS** Dan Berger, Jimmy Marks, Ryan Jensen **SR. PROJECT MANAGER** Trista Smith

MULTIMEDIA DIRECTOR OF ANALYTICS Enrique Gonzales **SR. WEB PRODUCER** Sarah Crespi **WEB PRODUCER** Alison Crawford **VIDEO PRODUCER** Nguyen Nguyen **SOCIAL MEDIA PRODUCER** Brice Russ

DIRECTOR OF OPERATIONS PRINT AND ONLINE Lizabeth Harman **DIGITAL/PRINT STRATEGY MANAGER** Jason Hillman **QUALITY TECHNICAL MANAGER** Marcus Spiegler **PROJECT ACCOUNT MANAGER** Tara Kelly **DIGITAL PRODUCTION MANAGER** Lisa Stanford **ASSISTANT MANAGER DIGITAL/PRINT** Rebecca Doshi **SENIOR CONTENT SPECIALISTS** Steve Forrester, Antoinette Hodal, Lori Murphy, Anthony Rosen **CONTENT SPECIALISTS** Jacob Hedrick, Kimberley Oster

DESIGN DIRECTOR Beth Rakouskas **DESIGN EDITOR** Marcy Atarod **SENIOR DESIGNER** Garvin Grullón **DESIGNER** Chrystal Smith **GRAPHICS MANAGING EDITOR** Alberto Cuadra **SENIOR SCIENTIFIC ILLUSTRATORS** Chris Bickel, Katharine Sutliff **SCIENTIFIC ILLUSTRATOR** Valerie Altounian **SENIOR ART ASSOCIATES** Holly Bishop, Nathalie Cary, Preston Huey **SENIOR PHOTO EDITOR** William Douthitt **PHOTO EDITORS** Leslie Blizard, Christy Steele

DIRECTOR, GLOBAL COLLABORATION, CUSTOM PUBLICATIONS, ADVERTISING Bill Moran **EDITOR, CUSTOM PUBLISHING** Sean Sanders: 202-326-6430 **ASSISTANT EDITOR, CUSTOM PUBLISHING** Tianna Hicklin: 202-326-6463 **ADVERTISING MARKETING MANAGER** Justin Sawyers: 202-326-7061 science_advertising@aaas.org **ADVERTISING MARKETING ASSOCIATE** Javia Flemmings **ADVERTISING SUPPORT MANAGER** Karen Foote: 202-326-6740 **ADVERTISING PRODUCTION OPERATIONS MANAGER** Deborah Tompkins **SR. PRODUCTION SPECIALIST/GRAPHIC DESIGNER** Amy Hardcastle **SR. TRAFFIC ASSOCIATE** Christine Hall **SALES COORDINATOR** Shirley Young **ASSOCIATE DIRECTOR, COLLABORATION, CUSTOM PUBLICATIONS/CHINA/TAIWAN/KOREA/SINGAPORE** Ruolei Wu: +86-186 0082 9345, rwu@aaas.org **COLLABORATION/CUSTOM PUBLICATIONS/JAPAN** Adarsh Sandhu + 81532-81-5142 asandhu@aaas.org **EAST COAST/E. CANADA** Laurie Faraday: 508-747-9395, FAX 617-507-8189 **WEST COAST/W. CANADA** Lynne Stickrod: 415-931-9782, FAX 415-520-6940 **MIDWEST** Jeffrey Dembksi: 847-498-4520 x3005, Steven Loerch: 847-498-4520 x3006 **UK EUROPE/ASIA** Roger Goncalves: TEL/FAX +41 43 243 1358 **JAPAN** Katsuyoshi Fukamizu(Tokyo): +81-3-3219-5777 kfukamizu@aaas.org **CHINA/TAIWAN** Ruolei Wu: +86-186 0082 9345, rwu@aaas.org

WORLDWIDE ASSOCIATE DIRECTOR OF SCIENCE CAREERS Tracy Holmes: +44 (0) 1223 326525, FAX +44 (0) 1223 326532 tholmes@science-int.co.uk **CLASSIFIED** advertise@sciencecareers.org **U.S. SALES** Tina Burks: 202-326-6577, Nancy Toema: 202-326-6578 **EUROPE/ROW SALES** Sarah Lelarge **SALES ASSISTANT** Kelly Grace **JAPAN** Hiroyuki Mashiki(Kyoto): +81-75-823-1109 hmashiki@aaas.org **CHINA/TAIWAN** Ruolei Wu: +86-186 0082 9345 rwu@aaas.org **MARKETING MANAGER** Allison Pritchard **MARKETING ASSOCIATE** Aimee Aponte

AAAS BOARD OF DIRECTORS RETIRING PRESIDENT, CHAIR Gerald R. Fink **PRESIDENT** Geraldine (Geri) Richmond **PRESIDENT-ELECT** Barbara A. Schaal **TREASURER** David Evans Shaw **CHIEF EXECUTIVE OFFICER** Rush D. Holt **BOARD** Bonnie L. Bassler, May R. Berenbaum, Carlos J. Bustamante, Stephen P.A. Fodor, Claire M. Fraser, Michael S. Gazzaniga, Laura H. Greene, Elizabeth Loftus, Mercedes Pascual

SUBSCRIPTION SERVICES For change of address, missing issues, new orders and renewals, and payment questions: 866-434-AAAS (2227) or 202-326-6417, FAX 202-842-1065. Mailing addresses: AAAS, P.O. Box 96178, Washington, DC 20090-6178 or AAAS Member Services, 1200 New York Avenue, NW, Washington, DC 20005

INSTITUTIONAL SITE LICENSES 202-326-6730 **REPRINTS:** Author Inquiries 800-635-7181 **COMMERCIAL INQUIRIES** 803-359-4578 **PERMISSIONS** 202-326-6765, permissions@aaas.org **AAAS Member Services** 202-326-6417 or http://membercentral.aaas.org/discounts

Science serves as a forum for discussion of important issues related to the advancement of science by publishing material on which a consensus has been reached as well as including the presentation of minority of conflicting points of view. Accordingly, all articles published in *Science*—including editorials, news and comment, and books reviews—are signed and reflect the individual views of the authors and not official points of view adopted by AAAS or the institutions with which the authors are affiliated.

INFORMATION FOR AUTHORS See pages 678 and 679 of the 6 February 2015 issue or access www.sciencemag.org/about/authors

SENIOR EDITORIAL BOARD

Robert H. Grubbs, *California Institute of Technology,* **Gary King,** *Harvard University*
Susan M. Rosenberg, *Baylor College of Medicine,* **Ali Shilatifard,** *Northwestern University Feinberg School of Medicine,* **Michael S. Turner,** *U. of Chicago*

BOARD OF REVIEWING EDITORS (Statistics board members indicated with **(S)**)

Adriano Aguzzi, *U. Hospital Zürich*
Takuzo Aida, *U. of Tokyo*
Leslie Aiello, *Wenner-Gren Foundation*
Judith Allen, *U. of Edinburgh*
Sonia Altizer, *U. of Georgia*
Sebastian Amigorena, *Institut Curie*
Kathryn Anderson, *Memorial Sloan-Kettering Cancer Center*
Meinrat O. Andreae, *Max-Planck Inst. Mainz*
Paola Arlotta, *Harvard U.*
Johan Auwerx, *EPFL*
David Awschalom, *U. of Chicago*
Clare Baker, *University of Cambridge*
Jordi Bascompte, *University of Zurich*
Facundo Batista, *London Research Inst.*
Ray H. Baughman, *U. of Texas, Dallas*
David Baum, *U. of Wisconsin*
Carlo Beenakker, *Leiden U.*
Kamran Behnia, *ESPCI-ParisTech*
Yasmine Belkaid, *NIAID, NIH*
Philip Benfey, *Duke U.*
May Berenbaum, *U. of Illinois*
Gabriele Bergers, *U. of California, San Francisco*
Bradley Bernstein, *Massachusettes General Hospital*
Peer Bork, *EMBL*
Bernard Bourdon, *Ecole Normale Supérieure de Lyon*
Chris Bowler, *École Normale Supérieure*
Ian Boyd, *U. of St. Andrews*
Emily Brodsky, *U. of California, Santa Cruz*
Ron Brookmeyer, *U. of California Los Angeles* **(S)**
Christian Büchel, *U. Hamburg-Eppendorf*
Joseph A. Burns, *Cornell U.*
Carter Tribley Butts, *U. of California, Irvine*
Gyorgy Buzsaki, *New York U. School of Medicine*
Blanche Capel, *Duke U.*
Mats Carlsson, *U. of Oslo*
Ib Chorkendorff, *U. of Denmark*
David Clapham, *Children's Hospital Boston*
Joel Cohen, *Rockefeller U., Columbia U.*
James J. Collins, *MIT*
Robert Cook-Deegan, *Duke U.*
Lisa Coussens, *Oregon Health & Science U.*
Alan Cowman, *Walter & Eliza Hall Inst.*
Robert H. Crabtree, *Yale U.*
Roberta Croce, *Vrije Universiteit*
Janet Currie, *Princeton U.*
Jeff L. Dangl, *U. of North Carolina*
Tom Daniel, *U. of Washington*
Frans de Waal, *Emory U.*
Stanislas Dehaene, *Collège de France*
Robert Desimone, *MIT*
Claude Desplan, *New York U.*
Dennis Discher, *U. of Pennsylvania*
Gerald W. Dorn II, *Washington U. School of Medicine*
Jennifer A. Doudna, *U. of California, Berkeley*
Bruce Dunn, *U. of California, Los Angeles*
William Dunphy, *Caltech*
Christopher Dye, *WHO*
Todd Ehlers, *U. of Tuebingen*
David Ehrhardt, *Carnegie Inst. of Washington*
Tim Elston, *U. of North Carolina at Chapel Hill*
Gerhard Ertl, *Fritz-Haber-Institut, Berlin*
Barry Everitt, *U. of Cambridge*
Ernst Fehr, *U. of Zurich*
Anne C. Ferguson-Smith, *U. of Cambridge*
Michael Feuer, *The George Washington U.*
Toren Finkel, *NHLBI, NIH*
Kate Fitzgerald, *U. of Massachusetts*
Peter Fratzl, *Max-Planck Inst.*
Elaine Fuchs, *Rockefeller U.*
Daniel Geschwind, *UCLA*
Karl-Heinz Glassmeier, *TU Braunschweig*
Ramon Gonzalez, *Rice U.*
Julia R. Greer, *Caltech*
Elizabeth Grove, *U. of Chicago*
Nicolas Gruber, *ETH Zurich*
Kip Guy, *St. Jude's Children's Research Hospital*
Taekjip Ha, *U. of Illinois at Urbana-Champaign*
Christian Haass, *Ludwig Maximilians U.*
Michael Hasselmo, *Boston U.*
Martin Heimann, *Max-Planck Inst. Jena*
Yka Helariutta, *U. of Cambridge*
James A. Hendler, *Rensselaer Polytechnic Inst.*
Janet G. Hering, *Swiss Fed. Inst. of Aquatic Science & Technology*
Kai-Uwe Hinrichs, *U. of Bremen*
David Hodell, *U. of Cambridge*
David Holden, *Imperial College*
Lora Hooper, *UT Southwestern Medical Ctr. at Dallas*
Tamas Horvath, *Yale University*
Raymond Huey, *U. of Washington*
Auke Ijspeert, *EPFL Lausanne*
Steven Jacobsen, *U. of California, Los Angeles*
Stephen Jackson, *U. of Arizona*
Kai Johnsson, *EPFL Lausanne*
Peter Jonas, *Inst. of Science & Technology (IST) Austria*
Matt Kaeberlein, *U. of Washington*
William Kaelin Jr., *Dana-Farber Cancer Inst.*
Daniel Kahne, *Harvard U.*
Daniel Kammen, *U. of California, Berkeley*
Masashi Kawasaki, *U. of Tokyo*
V. Narry Kim, *Seoul National U.*
Joel Kingsolver, *U. of North Carolina at Chapel Hill*
Robert Kingston, *Harvard Medical School*
Etienne Koechlin, *Ecole Normale Supérieure*
Alexander Kolodkin, *Johns Hopkins U.*
Thomas Langer, *U. of Cologne*
Mitchell A. Lazar, *U. of Pennsylvania*
David Lazer, *Harvard U.*
Thomas Lecuit, *IBDM*
Virginia Lee, *U. of Pennsylvania*
Stanley Lemon, *U. of North Carolina at Chapel Hill*
Ottoline Leyser, *Cambridge U.*
Wendell Lim, *U.C. San Francisco*
Marcia C. Linn, *U. of California, Berkeley*
Jianguo Liu, *Michigan State U.*
Luis Liz-Marzan, *CIC biomaGUNE*
Jonathan Losos, *Harvard U.*
Ke Lu, *Chinese Acad. of Sciences*
Christian Lüscher, *U. of Geneva*
Laura Machesky, *CRUK Beatson Inst. for Cancer Research*
Anne Magurran, *U. of St. Andrews*
Oscar Marin, *CSIC & U. Miguel Hernández*
Charles Marshall, *U. of California, Berkeley*
C. Robertson McClung, *Dartmouth College*
Graham Medley, *U. of Warwick*
Tom Misteli, *NCI*
Yasushi Miyashita, *U. of Tokyo*
Mary Ann Moran, *U. of Georgia*
Richard Morris, *U. of Edinburgh*
Alison Motsinger-Reif, *NC State U.* **(S)**
Thomas Murray, *The Hastings Center*
Daniel Neumark, *U. of California, Berkeley*
Kitty Nijmeijer, *U. of Twente*
Pär Nordlund, *Karolinska Inst.*
Helga Nowotny, *European Research Advisory Board*
Ben Olken, *MIT*
Joe Orenstein, *U. of California Berkeley & Lawrence Berkeley National Lab*
Harry Orr, *U. of Minnesota*
Andrew Oswald, *U. of Warwick*
Steve Palumbi, *Stanford U.*
Jane Parker, *Max-Planck Inst. of Plant Breeding Research*
Giovanni Parmigiani, *Dana-Farber Cancer Inst.* **(S)**
John H. J. Petrini, *Memorial Sloan-Kettering Cancer Center*
Samuel Pfaff, *Salk Institute for Biological Studies*
Joshua Plotkin, *U. of Pennsylvania*
Albert Polman, *FOM Institute AMOLF*
Philippe Poulin, *CNRS*
Jonathan Pritchard, *Stanford U.*
David Randall, *Colorado State U.*
Felix Rey, *Institut Pasteur*
Trevor Robbins, *U. of Cambridge*
Jim Roberts, *Fred Hutchinson Cancer Research Ctr.*
Barbara A. Romanowicz, *U. of California,Berkeley*
Amy Rosenzweig, *Northwestern University*
Mike Ryan, *U. of Texas, Austin*
Mitinori Saitou, *Kyoto U.*
Shimon Sakaguchi, *Kyoto U.*
Miquel Salmeron, *Lawrence Berkeley National Lab*
Jürgen Sandkühler, *Medical U. of Vienna*
Alexander Schier, *Harvard U.*
Vladimir Shalaev, *Purdue U.*
Robert Siliciano, *Johns Hopkins School of Medicine*
Denis Simon, *Arizona State U.*
Uri Simonsohn, *U. of Pennsylvania*
Alison Smith, *John Innes Centre*
Richard Smith, *U. of North Carolina* **(S)**
John Speakman, *U. of Aberdeen*
Allan C. Spradling, *Carnegie Institution of Washington*
Jonathan Sprent, *Garvan Inst. of Medical Research*
Eric Steig, *U. of Washington*
Paula Stephan, *Georgia State U. and National Bureau of Economic Research*
Molly Stevens, *Imperial College London*
V. S. Subrahmanian, *U. of Maryland*
Ira Tabas, *Columbia U.*
Sarah Teichmann, *Cambridge U.*
John Thomas, *North Carolina State U.*
Shubha Tole, *Tata Institute of Fundamental Research*
Christopher Tyler-Smith, *The Wellcome Trust Sanger Inst.*
Herbert Virgin, *Washington U.*
Bert Vogelstein, *Johns Hopkins U.*
Cynthia Volkert, *U. of Göttingen*
Douglas Wallace, *Dalhousie U.*
David Wallach, *Weizmann Inst. of Science*
Ian Walmsley, *U. of Oxford*
Jane-Ling Wang, *U. of California, Davis*
David A. Wardle, *Swedish U. of Agric. Sciences*
David Waxman, *Fudan U.*
Jonathan Weissman, *U. of California, San Francisco*
Chris Wikle, *U. of Missouri* **(S)**
Ian A. Wilson, *The Scripps Res. Inst.* **(S)**
Timothy D. Wilson, *U. of Virginia*
Rosemary Wyse, *Johns Hopkins U.*
Jan Zaanen, *Leiden U.*
Kenneth Zaret, *U. of Pennsylvania School of Medicine*
Jonathan Zehr, *U. of California, Santa Cruz*
Len Zon, *Children's Hospital Boston*
Maria Zuber, *MIT*

BOOK REVIEW BOARD

David Bloom, *Harvard U.,* **Samuel Bowring,** *MIT,* **Angela Creager,** *Princeton U.,* **Richard Shweder,** *U. of Chicago,* **Ed Wasserman,** *DuPont*

Published by AAAS

EDITORIAL

New members of the family

Marcia McNutt
Editor-in-Chief
Science *Journals*

Some publishers add new journal titles more often than I buy new shoes. The American Association for the Advancement of Science (AAAS), the publisher of *Science*, certainly cannot be accused of that, having grown to only four journal titles in 136 years. Yet many members of the scientific community have encouraged AAAS to expand its repertoire, arguing that the *Science* family of journals is high quality, well curated and edited, and worth supporting because they enable the mission of a nonprofit scientific society that is governed by scientists working to further the best interests of the scientific community. It is thus with some pride that I describe the launch in 2016 of two new journals: *Science Robotics* and *Science Immunology*.

"Editors can launch journals, but it takes excellent authors to make them successful."

Science Robotics will welcome cutting-edge advances from researchers working in human health, space, ocean, land, atmosphere, industrial, and service environments. These advances could arise from breakthroughs in artificial intelligence, systems design, materials science, new sensors, power systems, propulsion systems, advanced actuators, enhanced reliability and durability, or even in the science of human-robotic interfaces and interactions. I am pleased to announce that Professor Guang-Zhong Yang from Imperial College London has agreed to serve as Editor for this new journal.

Immunology is in a period of unprecedented evolution and expansion, and *Science Immunology* will showcase new trends in this exciting field. Previously underappreciated, the influence of the immune system is vast, touching aspects of health and disease that are just beginning to be understood. The immune system is mobile and pervasive, and integrates with all bodily systems and organs. New tools are revealing the extent of this influence with exceptional precision and reach. *Science Immunology* will welcome articles that explore these exciting developments, in any organism—particularly humans.

The *Science* family of journals also seeks to become "author-centric" publications, moving toward a process that gives authors maximum flexibility in deciding which journal is most suitable for their paper. A robotics paper could be submitted to *Science Robotics* if the target audience is the robotics community or to *Science* or *Science Advances* if it is important that the paper reach an audience broader than the robotics community. To target the medical research community, a medical robotics manuscript might be best presented in *Science Translational Medicine*. While *Science* will remain our highest-impact journal, *Science Advances*, an open access title launched in February 2015, may be the best venue for results that are of immediate interest to broad audiences in and beyond the academic community. An immunology paper will have a number of suitable options within the *Science* family—*Science, Science Immunology*, *Science Advances, Science Signaling,* or *Science Translational Medicine*—depending on the topic and the intended audience. We will make it easy to submit a paper to multiple *Science* journals by allowing authors to indicate their priority order of journals at the time of initial submission, with reviews being transferred between *Science* journals if the authors so desire.

What value do two more journals bring to the already crowded scientific publishing landscape? Although the number of publications is growing, what isn't increasing is the researcher's time. By expanding the *Science* journal family, authors will have more opportunities to publish under the *Science* umbrella, where their papers benefit from careful peer review and editing, broad dissemination, and high visibility. Carefully curated content published in *Science* journals helps busy researchers find which papers to prioritize from the flood of information available. Editors can launch journals, but it takes excellent authors to make them successful. If your research might fit with *Science Robotics* or *Science Immunology*, please watch for the first calls for papers, coming soon!

–Marcia McNutt

10.1126/science.aaf1338

PHOTOS: (RIGHT) STACEY PENTLAND PHOTOGRAPHY; IPOPBA/ISTOCKPHOTO.COM

Published by AAAS

NEWS

> “It will be important to make sure the world is still watching.”
>
> **U.S. Special Envoy for Climate Change Todd Stern** to the Center for American Progress, acknowledging concerns that the COP21 climate agreement reached in Paris last month lacks an enforcement mechanism.

IN BRIEF

2016: A LOOK AHEAD

What's hot—and what's not

At the end of 2015, *Science* looked back at some of the biggest science stories of the year. Now we're looking forward, pondering which research trends and ideas are poised to create buzz in 2016—the scientific equivalent of the recent *Star Wars* movie—and which ones may be losing some steam. Here, we offer our best guesses, in no particular order, of the new themes that will take hold in 2016, shoving aside some previously sizzling topics. Got your own ideas about what should be on this list? Share your thoughts on Twitter with #SciHotNot.

▲ Commercial weather data
▼ Government weather data

Government agencies such as the U.S. National Oceanic and Atmospheric Administration (NOAA) generally own and operate the massive, billion-dollar satellites that gather data crucial for weather forecasting. But Congress wants NOAA to forge a pilot commercial data agreement with fledgling space companies; taking data from their constellations of microsatellites, which measure temperature, pressure, and humidity by intercepting GPS signals skimming through the atmosphere.

▲ India emissions
▼ China emissions

China's emergence as the world's top emitter of greenhouse gases has been one of the biggest climate stories of the past decade. But the spotlight may now shift to India, which is rapidly rising into the ranks of the emissions superpowers.

▲ Zika
▼ Chikungunya

Two years ago, the chikungunya virus began taking Latin America by storm. Now, another virus called Zika, transmitted by the same *Aedes* mosquitoes, is spreading—and has been tentatively linked to a rise in microcephaly, a serious birth defect.

▲ Reusable rockets
▼ Disposable rockets

What if you had to destroy your jumbo jet after every transcontinental trip? Until recently, expensive rockets always went kerplunk in the ocean after delivering satellites to orbit. Now, two companies, SpaceX and Blue Origin, have reverse-landed the first stages of their rockets, demonstrating the possibility of reuse—and of a dramatic reduction in the cost of space science.

Last month, SpaceX's Falcon 9 rocket landed intact after deploying its payload.

PHOTO: SPACEX

▲ Ending AIDS
▼ Treatment upon immune damage

Evidence suggests that treating all HIV-infected people as soon as they're diagnosed is good for both the individual and communities, by both thwarting AIDS and reducing transmission risks. When coupled with a push to use antiretrovirals as prophylaxis in uninfected people, this "treat-all" dictum has led to increasing optimism that communities can bring their AIDS epidemics to a halt.

▲ Gene editing
▼ Gene therapy

Although U.S. regulators could approve the first gene therapy this year—for blindness—this strategy has been eclipsed in the lab by gene editing, which fixes a cell's defective DNA instead of pasting in a new gene. The first gene-repair clinical trials, for hemophilia and cancer, are already getting underway.

▲ Ethical no-go zones
▼ 'Cowboy science'

Unfettered experimentation driven by pure curiosity is giving way to a debate over whether to establish "no-go" areas of science—such as using new gene-editing technologies to produce engineered babies, giving flu viruses and other pathogens new capabilities, and engineering microbes to produce illegal drugs.

▲ Higgs partners
▼ Natural supersymmetry

For decades, supersymmetry has been particle physicists' best guess at what lies beyond the current Standard Model. Supersymmetry posits a partner particle for every Standard Model particle—but Europe's Large Hadron Collider (LHC) has seen no sign of those partners. Some physicists now speculate that a sidekick to the Higgs boson (discovered by the LHC in 2012) will be the next step beyond.

Published by AAAS

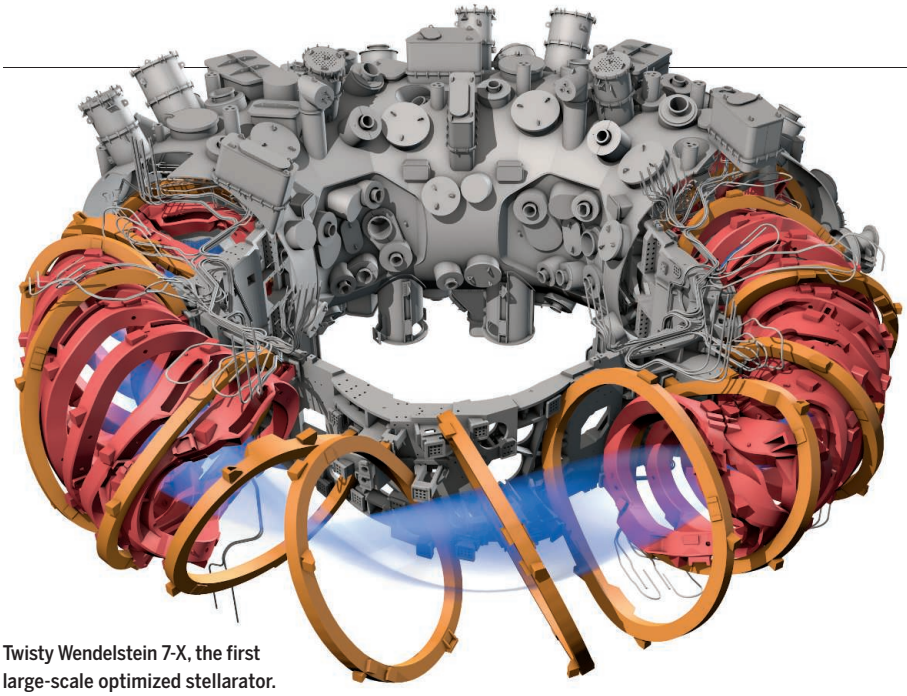

Twisty Wendelstein 7-X, the first large-scale optimized stellarator.

▲ Alternative fusion technology
▼ Tokamaks

The ITER project, which aims to build the world's largest tokamak fusion reactor, is growing more unwieldy and expensive. Meanwhile, startup companies with alternative fusion technologies are forging ahead while stellarators and spherical tokamaks are just launching or upgrading.

▲ Ancient genomes
▼ Ancient mitochondrial DNA

In the past 2 years, researchers began sequencing entire nuclear genomes of ancient humans, from Neandertals to Bronze Age Europeans and Asians. These genomes offer far more information about identity, migrations, and evolution than maternally inherited mitochondrial DNA.

▲ Brexit
▼ Grexit

A potential U.K. referendum about a British exit from the European Union could threaten academic collaborations and €1 billion of Horizon 2020 funds for U.K. science. Meanwhile, Greek scientists are relieved that their country's financial crisis did not force them out of the European Union or its single currency.

▲ Flexible electronics
▼ Rigid electronics

Old-fashioned rigid electronics brought us phones, tablets, and Fitbits. But research buzz has shifted to flexible electronics and the promise of gizmos such as artificial skin for prosthetics or implantable health monitors.

▲ DOE national labs
▼ Hubs

From 2009 to 2013, then-Secretary of Energy Steven Chu tried to reinvent how the Department of Energy (DOE) addresses energy science by developing "hubs," Bell Labs–like centers designed to tackle specific problems. Current Secretary of Energy Ernest Moniz has kept existing hubs but has focused on optimizing the performance of DOE's 16 national labs.

▲ Voluntary conservation
▼ Endangered species regulation

Some U.S. conservationists worry that listing certain endangered species—such as the greater sage grouse—under the Endangered Species Act will fuel efforts to gut the law. Instead, they are offering incentives to states and private landowners to preserve habitat in exchange for avoiding regulation.

The greater sage grouse, subject of fierce conservation debate.

▲ FDA-approved lab tests
▼ Rogue diagnostics

The Food and Drug Administration is finalizing guidance to require approval for lab-developed tests—a move that it says will crack down on unreliable and potentially risky diagnostics, but that has the industry (and supporters in Congress) uneasy.

▲ 'Democratizing' ocean research
▼ Large research vessels

Expensive, scarce ship time in the standard research fleet has long been a limiting factor in ocean research. But private ventures are lifting that constraint, whether through ship time offered by the Schmidt Ocean Institute or X Prizes offered for new robotic submersibles and sensors.

▲ Human chimera research
▼ Human embryo genome editing

Plans to put human cells into animal embryos may get a green light from the United States, but negative reaction to a Chinese team's attempted edits of human embryo DNA may curtail follow-ups.

▲ Perovskite solar cells
▼ Dye-sensitized solar cells

Hybrid solar cells—made from both organic and inorganic materials—are still the rage. Efficiency improvements have largely stalled for the dye-sensitized variety of these cells, but efficiencies for perovskite solar cells are reaching new heights.

▲ The 45th president
▼ Obama administration

It's the last hurrah for White House chief science adviser John Holdren, National Institutes of Health Director Francis Collins, and NASA Administrator Charles Bolden, who have each stayed for the 44th U.S. president's full two terms.

▲ Climate monitoring
▼ Climate commitment

Nearly 200 nations have vowed to curb their emissions of greenhouse gases—and the next question will be how to monitor and verify that they are following through on their pledges. New carbon measuring satellites should help provide a global picture.

CREDITS: (IMAGE) C. BICKEL/*SCIENCE*; (PHOTO) © DANITA DELIMONT/ALAMY STOCK PHOTO

Published by AAAS

IN DEPTH

U.S. FUNDING

Research agencies revel in final 2016 budget

NIH gets $2 billion hike, NASA and DOE science grow, NSF avoids restrictive language

By **Jeffrey Mervis**

Congress rejected a proposed squeeze on NSF-funded geoscience research like this early-Earth study of zircon crystals in Iceland (above).

Money matters, of course. But so does having the freedom to support the best research. This year advocates for U.S. science succeeded not just in winning more dollars for major federal research agencies, but also in dissuading Congress from imposing policies that they believe would have harmed the scientific enterprise.

On 18 December, President Barack Obama signed into law a $1.1 trillion spending bill covering the entire federal government for the last 9 months of the 2016 fiscal year. The budgetary increases contained in the so-called omnibus bill were greased by a late-October agreement between the Republican-led Congress and the Obama administration that added $50 billion to an existing 2016 cap on overall discretionary spending.

At the National Institutes of Health (NIH), backers of biomedical research achieved their ambitious goal of winning a $2 billion increase for the king of the research hill; the 6.6% boost over its 2015 budget was the largest NIH has received since 2003. Science at NASA and the Department of Energy did much better than expected, with hikes of 6.6% and 5.5%, respectively. The National Science Foundation (NSF) ended up with a more modest bump of 1.6% that nevertheless exceeded the amounts approved earlier in the budget process by congressional spending panels. Research funded by grant competitions will expand at the U.S. Department of Agriculture and the National Oceanic and Atmospheric Administration as well.

Research lobbyists also prevailed on important nonpocketbook issues. In particular, Republican lawmakers dropped bill language approved last June by the House of Representatives that would have required NSF to favor other disciplines over geoscience. They also modified instructions seen as impinging on NSF's grantsmaking process.

Representative John Culberson (R–TX), chairman of the House Commerce, Justice, and Science (CJS) spending panel that funds NSF and NASA, proposed earlier this year that NSF spend 70% of its research dollars on just four of its six research directorates and place a lower priority on directorates that fund the earth and social sciences. The requirement would have meant double-digit budget cuts at those two directorates.

Culberson and Representative Lamar Smith (R–TX), chairman of the House science committee that oversees those agencies, also wanted space exploration to take priority over the earth sciences at NASA. The two Texans have argued repeatedly that the physical sciences, computing, biology, and engineering should get the most federal research dollars, although many believe the real driver is their skepticism of climate change research and social sciences in general.

The final spending measure removes the 70% mandate for NSF. But it still prevents the social, behavioral, and economic sciences directorate from receiving any part of the $99 million increase given to NSF's overall research account.

The omnibus also frees NSF from controversial language in a bill written by the science committee and passed earlier this year by the House that has not been taken up by the Senate. The 2015 America Creating Opportunities to Meaningfully Promote Excellence in Technology, Education, and Science (COMPETES) Act would reauthorize various NSF programs, requiring NSF to certify that every one of its grants is in the "national interest" based on several criteria in the bill. Smith and others say the provision is simply intended to promote "transparency and accountability."

But to most U.S. researchers, the checklist represents an unprecedented—and unwise—intrusion into how grants are awarded. And they found allies in Congress, particularly among Democrats. Smith's national interest provisions are part of a broader attempt by Republicans "to impose their own will and micromanage science," argues Representative Mike Honda (D–CA), the top Democrat on the CJS spending panel. "And you just can't do that."

Lawmakers jettisoned the reference to the certification process in the COMPETES bill during the closed-door meetings that shaped the final spending measure. Instead, the omnibus reminds NSF to enforce its own recent directive that abstracts for each award must "articulate how the project serves the national interest." Researchers hope that the Senate bill, still being drafted, will also conform to current NSF practices.

Culberson says "strong opposition from other parts of Congress" led to that change and to the deletion of the 70% language that would have cut funding for the geosciences. Geoscientists credit Honda with leading that opposition by lobbying colleagues and sponsoring a September forum on Capitol Hill that featured geoscience research in such key sectors as national security, economic development, and climate resilience.

In making the case for the geosciences within the CJS panel, Honda had to perform a delicate balancing act. Culberson is a self-professed superfan of planetary sci-

PHOTO: ABRAHAM PADILLA, EARTH AND ENVIRONMENTAL STUDIES, VANDERBILT UNIVERSITY

Published by AAAS

ence but takes a much chillier view of the earth sciences. Honda's solution was to accentuate the positive.

"My relationship with chairman Culberson is pretty good, and he understands the value of research," explains Honda, whose 30-year career in education included 3 years teaching high school science. "But I also realize that he's a member of a party that holds a different view of science. So he has to be adroit in helping us out."

Rank-and-file scientists also got engaged. Sharon Mosher, geosciences dean at the University of Texas, Austin, made repeated trips to Washington, D.C., this year to meet with congressional staff to discuss the value of federal research across all disciplines. And she noticed a big turnaround in the last few months. "We started late in the spring," says Mosher, a former president of both the American Geosciences Institute and the Geological Society of America, who has met personally with Culberson and with aides to Smith. "In October I could sense attitudes were starting to change. And by early December there was definitely something in the air."

Honda praises scientists such as Mosher for their ability to use simple language to explain research. The stories the scientists told at the September event "were very effective … in moving members to stand up for the geosciences," Honda says. "It helped us move the ball down the field."

At NASA, meanwhile, Culberson made his mark by adding money and bill language, not by subtracting it. The omnibus gives the agency's planetary science program a 13.4% boost, to $1.63 billion, and directs the agency to apply $175 million—nearly six times the amount NASA requested—to a robotic mission that would not only travel to Jupiter's moon Europa, but also drop a lander on it.

Culberson is "passionate" about the Europa mission, which he believes could find life in a liquid ocean beneath the moon's icy crust. Such a discovery would help "return NASA to the glory of the Apollo era," he predicts, "by galvanizing public opinion and transforming our view of the universe."

The omnibus also contains compromise language for a third agency within the CJS bill, the Census Bureau. The House had stripped away much of the bureau's requested 45% increase, most of it to help prepare for the 2020 census, after some Republicans complained that some questions on its monthly American Community Survey, a key data source for social scientists, violated respondents' privacy. The final omnibus restores most of those cuts. It also removes restrictions on how the bureau can spend its money and substitutes a simple directive to invest in "activities that have the greatest potential to reduce cost and risk for the 2020 Census, as well as activities to reduce survey respondent burden."

Even as researchers revel in this year's success, some are already bracing for a tighter future. That's because the current budget deal provides just $3 billion in additional discretionary cash for 2017. That negligible rise could mean flat budgets for most agencies. Asked whether 2016 represents a high-water mark, Culberson would only say that "I'll do whatever it takes to make sure America stays No. 1" in science and space exploration. ■

With reporting from Science*'s news staff.*

Good news for U.S. federal research

New agreement hikes 2016 budgets of most science agencies (in billions of dollars).

INSTITUTION	2015	2016 REQUEST	HOUSE	SENATE	2016 FINAL	% CHANGE 16 VS 15
NIH	30.1	31.1	31.2	32.1	32.1	+6.65%
NSF	7.344	7.724	7.394	7.344	7.463	+1.62%
Research	5.934	6.186	5.984	5.934	6.033	+1.67%
Education	0.866	0.963	0.866	0.866	0.880	+1.62%
DOE Office of Science	5.068	5.340	5.100	5.144	5.347	+5.51%
Basic energy	1.733	1.849	1.770	1.844	1.849	+6.69%
Bio/environmental	0.592	0.612	0.538	0.610	0.609	+2.87%
Fusion	0.468	0.420	0.468	0.270	0.438	–6.41%
High energy physics	0.766	0.788	0.776	0.788	0.795	+3.79%
Nuclear physics	0.595	0.625	0.616	0.592	0.617	+3.70%
Advanced computing	0.541	0.621	0.538	0.610	0.621	+14.79%
ARPA-E	0.275	0.325	0.280	0.291	0.291	+5.82%
NIST	0.864	1.120	0.855	0.893	0.964	+11.57%
Research	0.676	0.755	0.675	0.685	0.69	+2.07%
USGS	1.045	1.104	1.045	1.059	1.062	+1.63%
NASA	18.01	18.53	18.53	18.29	19.29	+7.08%
Science office	5.245	5.289	5.238	5.295	5.589	+6.56%
Earth science	1.773	1.947	1.683	1.932	1.921	+8.35%
Planetary science	1.438	1.361	1.557	1.321	1.631	+13.42%
Astrophysics	0.685	0.709	0.736	0.731	0.731	+6.72%
Heliophysics	0.662	0.651	0.642	0.650	0.650	–1.81%
USDA Research	1.133	1.192	1.223	1.137	1.144	+0.97%
AFRI competitive grants	0.325	0.450	0.335	0.325	0.350	+7.69%
NOAA	5.441	5.975	5.169	5.382	5.766	+5.97%
Oceanic/atmospheric research	0.446	0.507	0.431	0.456	0.462	+8.07%
DOD Basic Research	2.278	2.089	2.100	2.317	2.310	+1.40%
DHS S&T	1.104	0.779	0.787	0.765	0.787	–28.71%
EPA S&T	0.735	0.769	0.705	0.704	0.735	+0.00%
FDA	2.599	2.746	2.627	2.637	2.720	+4.66%
Census periodic programs	0.840	1.222	0.731	0.862	1.100	+30.95%
DARPA	2.916	2.972	2.872	2.865	2.87	–1.0%

DATA: U.S. CONGRESS; OMB

Published by AAAS

An Ebola survivor in Monrovia donated plasma in December 2014 to be tested as a treatment.

INFECTIOUS DISEASE

As Ebola epidemic draws to a close, a thin scientific harvest

Thirteen clinical trials in West Africa have yielded only one unequivocally positive result

By **Jon Cohen** *and* **Martin Enserink**

For all of the suffering that the West African Ebola epidemic has caused, it offered a unique opportunity to develop weapons against the next outbreak. As the epidemic exploded in the summer of 2014, a frenzied effort began to test vaccines and drugs in the three most affected countries: Liberia, Sierra Leone, and Guinea. Investigators hoped to harvest a bumper crop of clinical findings that would be rapidly shared in high-profile medical journals, help stop the epidemic, and guide future interventions.

That hasn't happened.

To date, results from just one clinical trial have appeared in a peer-reviewed journal: a study of Merck's Ebola vaccine, organized by the World Health Organization (WHO) in Guinea. An interim analysis published by *The Lancet* last summer suggested that the vaccine is remarkably successful; it may well be enlisted to control future outbreaks (*Science*, 7 August 2015, p. 569). But an anticlimactic silence has set in around a dozen other Ebola studies.

Many trials didn't deliver a clear answer because they failed to enroll the planned number of participants. Some did recruit enough patients but didn't use a randomized controlled trial (RCT) design, which weakened results and helps explain why those researchers have had trouble publishing their data in top-tier journals. Still others were halted early. (Details about all of the studies can be found online in "Thin harvest," published this week at http://scim.ag/ThinHarvest.)

The epidemic now appears to be in its last throes; Liberia reported three new cases in late November but had not seen additional ones as *Science* went to press on 28 December. Sierra Leone and Guinea reported their last cases in September and October, respectively. As the window for research closes, relief is mixing with soul-searching by scientists about why they have come away almost empty-handed.

ONLINE

Comprehensive coverage is at http://scim.ag/ThinHarvest

Some say WHO should have played a stronger role coordinating the many disparate efforts. But part of the problem was simply that the world was ill prepared. Ebola vaccine candidates, for instance, had to be rushed through phase I safety studies before efficacy tests could begin; designing trials, getting regulatory approval, and organizing logistics all cost valuable time.

As a result, most Ebola trials did not start until the first quarter of 2015, when intensified containment efforts already had led to a sharp decline in cases. Studies that sought to test plasma from Ebola survivors as a therapy succeeded in enrolling only six patients in Liberia and three in Sierra Leone. A trial in Guinea of interferon-β as a treatment enrolled a mere nine people. A study of a second Ebola vaccine, produced by GlaxoSmithKline, aimed to give the shot to 9000 people in Liberia but managed to inject only 500 volunteers.

Two treatment studies carried out in Guinea recruited enough patients to potentially yield scientifically robust answers, but both had designs that make it difficult to interpret the data. One enrolled more than 200 people at four Ebola treatment centers to evaluate favipiravir, a Japanese influenza drug; the other tested plasma from people who had survived the disease in about 100 patients in the country's capital, Conakry. Neither study, however, had a conventional, untreated control group; instead, scientists used "historical controls," those who passed through treatment centers before the trials began. But Ebola survival rates varied widely over time and from one place to the other, making such comparisons tricky. Although the favipiravir team reported hints of efficacy at a meeting in February (http://scim.ag/FavipiravirStudy), neither of the two trials has produced definitive results.

Such uncontrolled studies caused more harm than good, contends Luciana Borio, the acting chief scientist at the U.S. Food and Drug Administration in Silver Spring, Maryland. "It resulted in that nebulous data zone that we were so fearful about," Borio says. "We're left with not knowing whether the products help, hurt, or do nothing."

But Denis Malvy of France's Institute of Health and Medical Research in Paris, who led the favipiravir trial, says an RCT—which requires withholding a potential treatment—was unacceptable to Guinean regulators and the local population. "It's easy to criticize a study," Malvy says. "We set out to look for a signal, not formal proof of efficacy." The lack of an RCT design led *The New England of Journal of Medicine* (*NEJM*) to reject a paper about the study, Malvy says—although the journal did offer to publish a 300-word letter to the editor, which he says is laughable. The paper is now under review at *PLOS Medicine*, he says.

Inconclusive results also led *NEJM* to reject a paper about a Sierra Leonean trial of TKM-Ebola, says its leader, Peter Horby of the University of Oxford in the United Kingdom. The study of the drug, which inhibits

PHOTO: DANIEL BEREHULAK/GETTY IMAGES REPORTAGE

Published by AAAS

Ebola virus RNA, was started in March 2015 and stopped 3 months later when an interim analysis of 14 patients showed the compound was unlikely to work. "We're struggling to publish informative, but not definitive data from trials," Horby says. But Johan van Griensven of the Institute of Tropical Medicine Antwerp in Belgium, who led the plasma study in Guinea, says his results, although far from iron-clad, will be published in a "top journal" on 7 January.

Questions surround the fate of several other studies. A trial of brincidofovir, an antiviral drug that had test tube activity against the Ebola virus, began in January 2015 and was stopped after enrolling just four patients because Chimerix, the company that produces the compound, pulled the plug. Horby, who led that study, too, says he never heard the full story. "We invested a huge amount of resources, time, effort, in very difficult circumstances," Horby says. "It should not have been stopped unless it was for a very good reason." A company spokesperson declined to answer detailed questions from *Science*.

Nor is it clear what happened to the very first clinical study, set up by Sierra Leonean scientists in the fall of 2014, which transfused Ebola patients with whole blood from survivors. Wiltshire Johnson of Sierra Leone's Pharmacy Board, charged with overseeing clinical trials in the country, told *Science* in May 2015 that 33 out of 44 transfused patients survived. The results have not been published, however, and its lead investigator, hematologist Sahr Gevao of the University of Sierra Leone in Freetown, did not respond to emails from *Science*. Even WHO isn't sure what became of the trial.

One last hope for an uplifting result remains: an ongoing study of ZMapp, an antibody cocktail that worked well in monkey experiments and famously was used to treat Kent Brantly and Nancy Writebol, two Americans who contracted Ebola in Liberia and recovered. Coordinated by the U.S. National Institutes of Health, the study began in Liberia in February 2015. After Ebola faded in that country, researchers began enrolling patients in Sierra Leone and Guinea and added one patient in the United States.

The study now includes about 70 patients, and because it has an RCT design, only half have received the antibodies. An independent panel has done several analyses of the trial, but Clifford Lane of the National Institute of Allergy and Infectious Diseases in Bethesda, Maryland, says it's hard to conclude anything based on these interim assessments. "I'm hopeful that even if the data don't reach statistical significance, there might be at least a trend for efficacy," he says. Given the high hopes just 15 months ago, that's a most modest aspiration indeed. ■

EPIGENETICS

Sperm RNA fragments modify offspring metabolism

Molecules transfer mouse paternal traits to progeny

By **Mitch Leslie**

Male mice bequeath an unexpected legacy to their progeny. Two studies published online this week in *Science* reveal that sperm from the rodents carry pieces of RNAs that alter the metabolism of their offspring. The RNAs spotlighted by the studies normally help synthesize proteins, so the findings point to an unconventional form of inheritance. The results are "exciting and surprising, but not impossible," says geneticist Joseph Nadeau of the Pacific Northwest Diabetes Research Institute in Seattle, Washington.

"Impossible" is exactly how biologists once described so-called epigenetic inheritance, in which something other than a DNA sequence passes a trait between generations. In recent years, however, researchers have found many examples. A male mouse's diet and stress level, for instance, can tweak offspring metabolism. Researchers are still trying to determine how offspring inherit a father's metabolic attributes and physiological condition. Some evidence implicates chemical modification of DNA. Other work by neuroscientist Tracy Bale of the University of Pennsylvania Perelman School of Medicine in Philadelphia and colleagues has found that mammalian sperm pack gene-regulating molecules called microRNAs.

> ***"We've found another link that can connect the father and offspring."***
>
> **Qi Chen**, University of Nevada School of Medicine

The new work highlights a different class of RNAs, transfer RNAs (tRNAs). In one study, genomicist Oliver Rando of the University of Massachusetts Medical School in Worcester and colleagues delved into a case of epigenetic inheritance in which the progeny of mice fed a low-protein diet show elevated activity of genes involved in cholesterol and lipid metabolism. When Rando's group analyzed sperm from the protein-deprived males, they uncovered an increased abundance of fragments from several kinds of tRNAs. The researchers concluded the sperm acquired most of these fragments while passing through the epididymis, a duct from the testicle where the cells mature.

In the second study, a team from the Chinese Academy of Sciences in Beijing and other institutions also homed in on tRNA fragments. After feeding male mice either a high-fat or low-fat diet, the scientists injected the animals' sperm into unfertilized eggs. They then tracked the metabolic performance of the offspring, which ate a normal diet. Although progeny of the fat-eating fathers remained lean, they showed two abnormalities often found in their dads and in people who are obese or diabetic: abnormal absorption of glucose and insensitivity to insulin. To determine whether tRNA fragments were responsible for the traits, the researchers inserted the fragments into eggs fertilized with other sperm. Fragments that came from fathers that ate the high-fat diet resulted in offspring that also showed impaired glucose absorption. "We've found another link that can connect the father and offspring," says reproductive biologist Qi Chen, a study coauthor, now at the University of Nevada School of Medicine in Reno.

Although tRNAs are best known for roles in protein synthesis, their fragments are turning up in other cellular situations. "Pieces of functional units that are pretty well understood can have interesting moonlighting functions," Rando says. Both studies suggest that the RNA bits alter gene activity. Rando and colleagues blocked one of the tRNA fragments inside embryonic stem cells and increased the activity of about 70 genes.

Bale says "both papers are really impressive" for digging deep into epigenetic mechanisms. And Nadeau says they should help overcome the challenge of identifying "the molecules that are responsible for inheritance outside of DNA sequences."

Researchers now need to ask "how permanent these changes are and how quickly they can be reversed by changing diet," says developmental endocrinologist Susan Ozanne of the University of Cambridge in the United Kingdom. The effects of the RNA fragments don't have to be harmful, Chen notes. "If a bad diet can influence us, I think a healthy diet can do it in the same way," he predicts. ■

Published by AAAS

BIOMEDICAL RESOURCES

Funding for key data resources in jeopardy

NIH genome institute wants to scale back support of human and model organism databases

By **Jocelyn Kaiser**

As the world's most authoritative catalog of human disease-related genes approaches its 50th birthday, it faces unsettling change. Over the next few years, the National Human Genome Research Institute (NHGRI) expects to bow out as sole funder for the granddaddy of genomic databases, known as Online Mendelian Inheritance in Man (OMIM). Who will pick up the tab is not yet clear. Other, newer databases supported by NHGRI are facing a similar threat as the National Institutes of Health (NIH) takes stock of all its data resources.

Users are concerned. These free-to-use resources, which cover everything from yeast genomics to proteins, are "critical for our daily life as geneticists and biomedical researchers," says University of California, Berkeley, geneticist Jasper Rine, president of the Genetics Society of America. Ada Hamosh of Johns Hopkins University in Baltimore, Maryland, who oversees OMIM, adds: "If NIH is going to develop new funding models, they need to make sure they don't compromise the integrity of existing, heavily used resources."

NHGRI Director Eric Green says that nothing has been decided and that rumors that his institute plans to phase out all of its funding are incorrect. But he and other NIH leaders are searching for ways to make the databases more efficient, and are urging databases to consider charging for use.

Biology databases have long had funding woes. Science agencies often complain that database support diverts resources from their mission of funding research. Philip Bourne, NIH's first associate director for data science, estimates that the 50 largest NIH-supported resources—not counting GenBank and other databases at the National Library of Medicine (NLM)—require $110 million of the agency's $30 billion annual budget. An explosion in data is making them ever more costly to run. "There is a sustainability issue. We need to do something," Bourne says.

In addition to OMIM, NHGRI supports five databases for model organisms and others such as UniProt, which holds data on protein function. All are troves of molecular data annotated with information that curators have gleaned from the literature. OMIM, which began 50 years ago as a paper resource and moved to the Web in 1995, draws more than 23 million page views a year. Clinicians use it to diagnose patients with rare diseases, while basic researchers rely on OMIM and model organism databases as go-to references for genes and their protein products.

Last May, Green called together leaders of these databases to tell them that by 2020 they need to find new options for funding. Grantees across many NIH institutes use the NHGRI databases, he said, and the nearly $30 million a year NHGRI now provides isn't enough as the databases expand beyond genomes to biological data. "We're not a good long-term home," Green says. "We need to think about new ways to do business."

Bourne's office plans to compile data on database usage across NIH, although he notes this can't be the only measure of value: "You can have a relatively small number of users, but it's absolutely critical for those users," he says. He and Green wonder whether some databases could be combined to lower costs. Further automating curation might also help. But humans still need to read papers and pull out data, in part because formats and nomenclatures vary.

Shifting some databases to other institutes could cut NHGRI's costs, as could adopting a subscription model. The Arabidopsis Information Resource (TAIR), the central database for a model organism in plant science, started charging fees in 2013 after the National Science Foundation phased out funding. "We resisted very strongly," says TAIR Director Eva Huala in San Francisco, California, but in the end, "we were converted."

TAIR tailors its prices to how much individuals, institutions, and companies use the database. "It's a great way to ensure that those who benefit the most from a resource also contribute the most," Huala says. As a bonus, she adds, because TAIR doesn't rely on federal grants, it no longer has to please peer reviewers and can focus instead on what users want, mainly up-to-date data.

The shift required some major changes, however. Huala and her staff left the Carnegie Institution for Science, which had hosted TAIR, to start a nonprofit, Phoenix Bioinformatics, to run it. They also had to set up accounting and business systems.

Several of the NHGRI-funded databases are wary of this model. "It isn't practical for many reasons," says Janan Eppig of the Jackson Laboratory in Bar Harbor, Maine, principal investigator for the Mouse Genome Database. One problem is that paywalls may prevent researchers from linking to genetic data in other databases. And researchers would need to use their grant money to subscribe. "NIH ultimately pays the bill anyway," says Monte Westerfield of the University of Oregon in Eugene, who heads the Zebrafish Model Organism Database.

Bourne says an NIH-wide committee hopes to begin considering new funding schemes later this year. The fate of these data troves may not be clear, however, until the agency has hired a new director for NLM—a possible new home for the beleaguered databases. ■

Data troves in transition

These databases supported by the National Human Genome Research Institute have 4 years to develop new funding models.

DATABASE	ORGANISM	UNIQUE USERS PER MONTH	2015 NHGRI FUNDING
FlyBase	*Drosophila*	51,300	$4.2 million
Gene Ontology Consortium	Multiple	36,000	$3.7 million
Mouse Genome Database	Mouse	53,100	$4.7 million
Online Mendelian Inheritance in Man	Human	300,000	$2.1 million (2014)
Reactome (biological pathways)	Human	19,400	$1.2 million
Saccharomyces Genome Database	Yeast	65,000	$2.7 million
UniProt (protein function)	Multiple	433,100	$4.9 million
WormBase	*Caenorhabditis elegans*	15,500	$2.9 million
Zebrafish Model Organism Database	Zebrafish	23,300	$3.1 million

DATA: FLYBASE/GO CONSORTIUM/MGD/OMIM/REACTOME/SGD/UNIPROT/WORMBASE/ZFIN

Published by AAAS

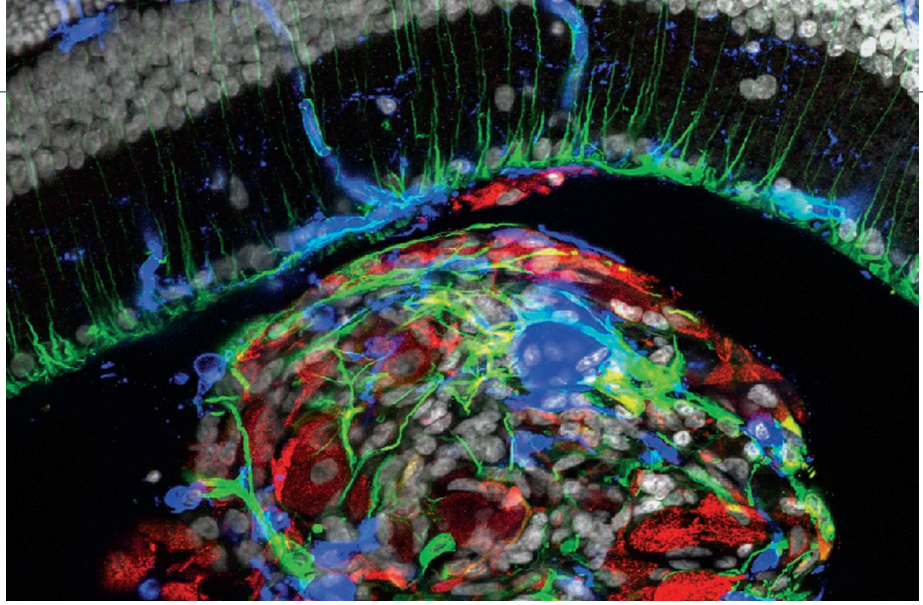

The CIRM-funded firm jCyte has found that when injected into a rat eye, human retinal progenitor cells (red) can differentiate into different cell types and protect photoreceptors.

IMAGE: COURTESY OF DR. GEOFF LEWIS, UCSB

REGENERATIVE MEDICINE

California stem cell agency plots a race to the clinic

CIRM lays out endgame and prospects for new money

By **Kelly Servick**

Born out of discontent with the federal restrictions on research with cells from human embryos, California's stem cell agency is at a key juncture: Over the past decade, it's spent a large portion of its $3 billion budget nurturing fledgling disease therapies, but that state money may run out before most of the treatments are ready for the clinic.

The California Institute for Regenerative Medicine (CIRM), created in 2004 through a state ballot initiative, is down to its last $759 million in grant funding. CIRM has so far propelled 23 stem cell projects into clinical trials, and made California a magnet for research in regenerative medicine. But none of its efforts have yet produced an approved treatment, and only 8% of the academic projects it funds have found industry partners to help commercialize discoveries. "CIRM has built an infrastructure," says Rocky Tuan, a stem cell biologist at the University of Pittsburgh School of Medicine in Pennsylvania, "but substantive delivery still is to come."

Although CIRM's leadership is already pursuing new sources of cash to keep the agency alive after 2020, for now the agency intends to spend its remaining dollars as though they'll be the last. Last month, its independent governing board signed off on an ambitious 5-year plan to award its final funds by 2020 and to push more potential treatments toward the clinic.

The new plan focuses on making CIRM-funded projects attractive to pharmaceutical companies and investors who could bankroll large clinical trials. These players have historically become interested in a stem cell treatment only after it has demonstrated proof of concept, typically at the end of a phase II trial, says CIRM's board chairman, investment banker Jonathan Thomas in Oakland, California. So the agency hopes to create two new resources for its grantees: a "translating center" that would develop manufacturing processes and run basic safety studies to prepare for a clinical trial; and an "accelerating center," which would manage clinical trials and coordinate filings with the Food and Drug Administration. The two centers would be selected from existing organizations that submit applications to CIRM. Each would receive $12 million to $15 million over the next 5 years to provide their services to CIRM-funded investigators.

The plan also creates a program, called Accelerating Therapies through Public-Private Partnership (ATP^3), which allows industry applicants—pharma companies, venture capital firms, or individual investors, for example—to compete for a licensing agreement that bundles multiple CIRM projects of their choosing. The winner would commit up to $75 million in upfront capital, which CIRM would match, likely in the form of a loan, to further develop the therapies. And the license winner would continue to benefit from CIRM funding flowing into the projects.

Both the new centers and the partnership are unusual models for a state agency, said Stephen Juelsgaard, a former Genentech executive and CIRM board member, at a 17 December board meeting in Los Angeles, California. "This plan is full of experiments—things that I've never seen done before. … We'll have to see how they play out." The board unanimously approved the proposal, with other members describing it in terms such as "inspiring" and "seismic."

Even if all goes according to plan, however, most CIRM-funded projects will not finish phase II trials in the next 5 years, and may not be ready for an industry partner, Thomas told the board. "If [CIRM doesn't] have additional funding at that point, we will have only partially met our obligation to develop therapies and cures."

The agency has a number of options to survive past 2020. Partnerships catalyzed by ATP^3 and other CIRM programs could, if they pan out, generate large royalty payments. CIRM can also seek private gifts—a strategy Thomas says he has begun to discuss with potential donors. Finally, it could ask California voters to approve more funding.

Real estate developer Robert Klein in Palo Alto, California, who led the campaign to create CIRM in 2004 and served as the first chair of the governing board, hopes to spearhead a new ballot effort. The medical research advocacy group Klein founded and directs, Americans for Cures, intends to use polling in 2017 to gauge voter interest. If the polling finds support, Klein says his "goal would be in 2018 to have a major new initiative."

CIRM, as a public agency, couldn't help gather signatures to place the measure on the ballot. Its leaders could directly ask state lawmakers to sponsor the measure. But one member of the CIRM board, vice chair and former state senator Art Torres in San Francisco, California, is uneasy about that idea. At the December meeting, he noted that this past summer some members of the California legislature proposed an audit of Planned Parenthood to investigate its distribution of tissue from aborted fetuses—a source of stem cells for various disease research, including some funded by CIRM. There are "people that don't believe in what we do, who are members of the legislature," Torres warned, and they "could invariably impact any [CIRM funding] proposal."

Democratic lawmakers ultimately blocked the tissue investigation. And whether there will be enough believers in CIRM to keep the agency afloat may depend on how well it can build—and publicize—a track record for moving stem cell discoveries to the clinic. ■

Published by AAAS

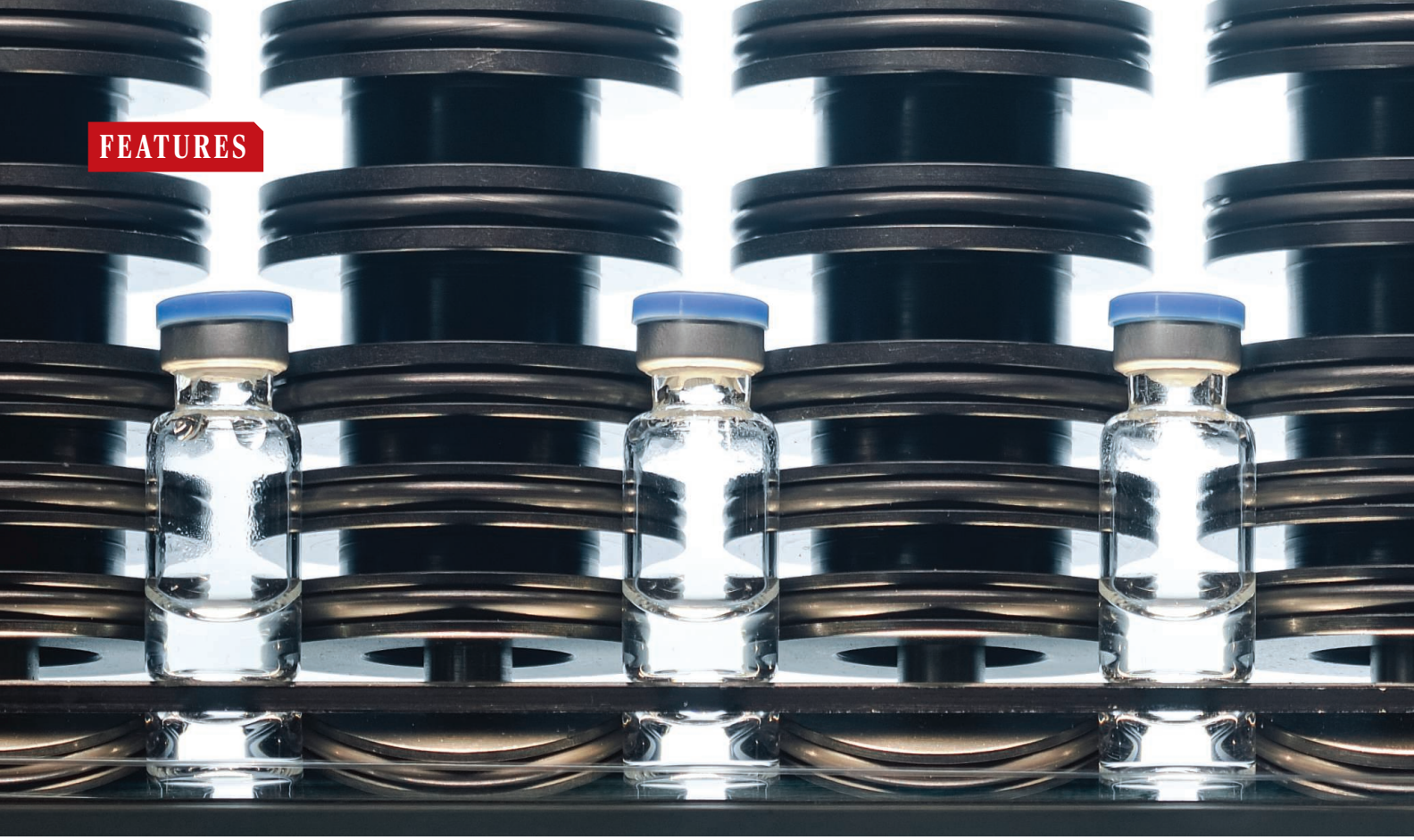

UNFILLED VIALS

Scientifically feasible vaccines against major diseases are stalled for lack of funds. *Science* names 10 top candidates that need a boost

By **Jon Cohen**

When the Ebola epidemic exploded in 2014, a vaccine could have been on hand. During the preceding 14 years, several vaccines had proven themselves capable of protecting monkeys from a high-dose "challenge" of the virus. Yet neither of the two most promising candidates had even gone through preliminary tests in humans that assess their safety and ability to trigger relevant immune responses. Instead, they sat in laboratory freezers in the United States, Canada, and Germany until the crisis erupted.

Once its magnitude became clear, both vaccines were rushed through additional testing and into human trials in record time. One, which the pharmaceutical giant Merck agreed to manufacture at the eleventh hour, worked: A trial in some 4000 people was halted early in July 2015 because of the vaccine's remarkable success, and it may even have helped stop the outbreak in Guinea. But a vaccine ready for clinical use when the outbreak began could have saved many more lives.

Several other potential vaccines are similarly languishing in freezers, says infectious disease specialist Jeremy Farrar, who heads the Wellcome Trust research charity in London. Developed in university, government, or industry labs, they have proven effective in animals and even been tested in small human trials. But because the diseases they target, like Ebola, are not seen as important threats in the developed world, they have not attracted the industry investment needed to prove efficacy in people. "The Ebola outbreak has woken everyone up," Farrar says. "We were all slow." In the 23 July 2015 issue of *The New England Journal of Medicine,* Farrar and two veteran vaccine developers, Stanley Plotkin of the University of Pennsylvania and Adel Mahmoud of Princeton University, declared the situation a crisis and called for a new $2 billion global fund to bankroll development of commercially unattractive vaccines that are "badly needed and feasible."

It's of course foolish to suggest that money

PHOTO: © KEN GARRETT

Published by AAAS

Rotating pillars spin vials for inspection at a manufacturing plant run by the U.S. National Institutes of Health.

and willpower alone will bring a vaccine to the clinic. Vaccine history is littered with promising products that flamed out because they did not work, were too difficult to manufacture, or even caused harm. "I don't know of any vaccines that are chip shots," says Tachi Yamada, a former executive at GlaxoSmithKline (GSK) and head of global health at the Bill & Melinda Gates Foundation who is now a venture capitalist in Seattle, Washington.

Little headway has been made for vaccines against some high-profile diseases, including HIV/AIDS, malaria, tuberculosis, and hepatitis C, despite decades of scientific research and billions of dollars. But many diseases are easier targets, especially those for which infection leads to long-term immunity—think smallpox, measles, polio, and Ebola. "When the body tells you it can make a pretty good immune response that clears the virus and leaves you with lasting protection, there really should not be any scientific obstacles to making a vaccine," says Anthony Fauci, who heads the U.S. National Institute of Allergy and Infectious Diseases (NIAID) in Bethesda, Maryland. Another good sign is the ability of a candidate vaccine to thwart an intentional attempt to infect, or challenge, an animal with a pathogen—particularly when the species is closely related to humans. Advances in vaccine development have also made it easier to find the most promising products; stitching a few innocuous genes from an otherwise dangerous organism into a harmless "vector" rather than using the pathogen itself, for example, makes it simpler to compare and contrast various vaccine candidates.

Yet scientific feasibility isn't the only factor determining which vaccine R&D efforts most deserve extra help. A disease's fatality rate, geographic reach, ease of spread, and potential to cause economic and social chaos are key factors determining which candidate vaccines to take off the ice and develop further.

In the past few weeks, the World Health Organization (WHO) and the nonprofit Foundation for Vaccine Research that Plotkin and Mahmoud helped start have taken a stab at identifying what those vaccines are, and they've zeroed in on the exact same targets. With the help of a dozen vaccine experts, *Science* compiled its own list—including seven of the vaccines already listed and three others—that do not present obvious scientific hurdles, would fill a pressing public health need, and have attracted scant attention from the pharmaceutical industry. In an email survey, 50 people from around the world involved with vaccine R&D and advocacy ranked their relative importance (see list, below).

Descriptions of the vaccines on *Science*'s list are on p. 18, including evidence—from animal models and small human trials—that they have a good chance of working. Now, it is up to global funders to move them methodically from lab freezers to the field, avoiding the slapdash, haphazard, panicky development process that ultimately paid off with Ebola.

A NUMBER OF GLOBAL health leaders have begun floating ideas about how to accelerate R&D for these vaccines. "The public sector has to have a better discussion with industry about the vaccines we need and a much better mechanism for sharing the risks early," the Wellcome Trust's Farrar says.

Merck, GSK, and just two other large-scale vaccine-makers exist today, and to move a new vaccine from concept to product, they must invest on the order of $500 million or more. Not surprisingly, these companies devote their resources to diseases that have large commercial markets, leaving the development of many feasible vaccines to academia, governments, and smaller biotech companies, which often cannot afford to move candidates through clinical trials.

Farrar, Plotkin, and Mahmoud's proposed Global Vaccine-Development Fund aims to create a public-private partnership that would bankroll the first two phases of testing for safety and immune responses in, say, a few hundred people. It would also support limited phase III efficacy trials and the manufacturing needed to produce doses for the trials. The vaccines would be selected by an independent panel, which would consider factors like public health need and likelihood of success. Industry, with government support if required, would have to pay for larger efficacy studies that would lead to licensure and sale of a product. The trio hopes to raise money from pharmaceutical companies, government, philanthropies, and multilateral banks, and their proposal is on the agenda to be discussed 21 January at the World Economic Forum in Davos, Switzerland.

GSK has a plan for overcoming a chief hurdle to manufacturing commercially unattractive vaccines. Like Merck, GSK was asked at the last minute to produce hundreds of thousands of doses of an Ebola vaccine for trials in West Africa and possible wide-scale use. Manufacturing candidate vaccines in small batches for phase I and II studies is far different from scaling up to hundreds of thousands of doses—leading to surprises that can bring production to a halt. "One of the biggest challenges in vaccine development is having the availability of—plus maintaining and investing in—industrial-quality R&D," says Moncef Slaoui, GSK's head of global vaccines in Philadelphia, Pennsylvania.

The company has a new state-of-the-art manufacturing plant in Rockville, Maryland, for commercial vaccines and Slaoui says its expert staff could help develop products for global health, ideally becoming involved at the phase I stage. "That requirement for production-at-scale should be built into the design of vaccines at the earliest stages or we will lose critical time dur-

Top shots

At *Science*'s request, 50 experts ranked these vaccines in order of R&D priority based on feasibility and need.

#	DISEASE
1	Ebola Sudan
2	Chikungunya
3	MERS
4	Lassa fever
5	Marburg
6	Paratyphoid fever
7	Schistosomiasis
8	Rift Valley fever
9	SARS
10	Hookworm

Published by AAAS

The NIH plant manufactures small batches of experimental vaccines, but producing large lots often requires a different process.

ing 'crisis' moments of an outbreak," Slaoui says. To proceed, though, he says the company needs predictable funding—GSK invested $80 million in an Ebola vaccine that has an uncertain fate—from partners who agree to share the risks.

Others are exploring new ways to test vaccines during disease outbreaks that would speed development and lower the cost. One model is the successful trial of Merck's Ebola vaccine, which jumped from small phase I studies into a large phase III trial to quickly test efficacy. The vaccine subsequently was used to help quell a new outbreak in Sierra Leone, and it remains "investigational" while, for licensure purposes, researchers glean additional safety and immunologic data from ongoing phase II tests in several countries.

At the vaccine-centric Jenner Institute in Oxford, U.K., director Adrian Hill and his team have a systematic plan for making and testing six vaccines for diseases that cause serious outbreaks but have attracted little commercial interest: Ebola Sudan, Marburg, Rift Valley fever, Lassa, Middle East respiratory syndrome (MERS), and Crimean-Congo hemorrhagic fever. For each of these vaccines, the Jenner Institute is inserting genes from the viruses into chimpanzee adenovirus vectors it developed. By using standard vectors, the team should be able to crank out the vaccines in quantity without significantly altering procedures for each one. "We need to take a generic platform where the manufacturing costs are minimized that allows us to change the genes and plug along in making stockpiles of these outbreak pathogen vaccines," Hill says.

If phase I trials don't raise any red flags, the stockpiles of these vaccines would be ready for phase III trials the moment an outbreak surfaced. GSK's Slaoui, who says the world needs to "rethink the entire approach" to vaccines needed for public health, shares this vision. "We need more ideas like this from all corners," he says.

Hill notes that the world spent billions of dollars to contain the Ebola epidemic. In comparison, the investments needed to develop vaccines against outbreak and endemic diseases that have little direct effect on wealthy countries are modest, he says. "It's undoubtedly cost-effective to do something about these diseases and just stop them," he says. "It's kind of difficult to explain to the minister of health in Uganda that, yeah, we know how to make a Marburg vaccine, but we're doing more exciting things with our medical research budget," Hill says. "If we can do this and we're not doing it, clearly there's something wrong." ■

ONLINE

More results from *Science*'s survey are at http://scim.ag/VaccinesRanking

SARS

Causative agent: Coronavirus

Symptoms: High fever, dry cough, pneumonia, and hypoxia

Geographic range: Global

Burden: One major outbreak of 8096 cases

Mortality: 9.5%

On 12 March 2003, WHO issued a global alert about the emergence of SARS in Vietnam, Hong Kong, and mainland China. Two weeks later, scientists nailed the causative agent as a new coronavirus,and vaccine R&D began in earnest as the virus raced around the world. By that July, containment efforts had controlled the outbreak, and save for nine cases in China in 2004, SARS has not surfaced again—but it could. After several vaccine constructs protected mice, hamsters, and monkeys, NIAID in December 2004 launched a clinical trial of a SARS vaccine in 10 people. The vaccine appeared safe and capable of triggering an immune response, but because there was no more SARS, NIAID put it in a freezer. "It just sort of sits there," says Anthony Fauci, NIAID's director, in Bethesda, Maryland.

MERS

Causative agent: Coronavirus

Symptoms: fever, shortness of breath, cough, diarrhea, nausea, pneumonia, and kidney failure

Geographic range: Arabian Peninsula and South Korea

Burden: Fewer than 1700 confirmed cases

Mortality: 53%

Unlike its viral cousin SARS, MERS has had a limited reach since it appeared in 2012, but it continues to cause deadly outbreaks. Camels naturally become infected with the MERS coronavirus, and experimental MERS vaccines appear to work in dromedaries. But no one knows whether they would also work in humans, who suffer a different pathology.

A workshop of leading MERS vaccine developers, held in Riyadh in November, concluded that the field needs to better coordinate efforts. "It is challenging to

PHOTO: © KEN GARRETT

Published by AAAS

select the best candidate vaccines based on the available information given our poor understanding of disease," a meeting report concluded.

Ebola Sudan

Causative agent: Filovirus

Symptoms: Fever, headache, diarrhea, vomiting, and hemorrhaging

Geographic range: Sudan and Uganda

Burden: Seven outbreaks since 1976 with fewer than 800 cases

Mortality: 53%

Before the 2014–15 West Africa Ebola epidemic,which was caused by the Zaire strain, another strain of the virus, Ebola Sudan, was responsible for the largest outbreak on record: 425 people, 224 of whom died, in Uganda in 2000–01. Government and academic labs have developed several Ebola Sudan vaccines. One, which used the same strategy behind the successful Ebola Zaire vaccine tested in Guinea—vesicular stomatitis virus (VSV) with an Ebola surface protein stitched in—provided 100% protection in a monkey study. Ebola Sudan vaccines have also been tested in phase I human trials.

Marburg

Causative agent: Filovirus

Symptoms: Same as Ebola

Geographic range: Zimbabwe, Kenya, Democratic Republic of the Congo, Uganda, and Angola

Burden: 12 outbreaks since 1967 with fewer than 500 total cases

Mortality: 80%

Ebola vaccine candidates are strain specific,offering spotty cross-protection in monkey studies, but experimental Marburg vaccines have been able to defeat every Marburg strain thrown at them. One monkey experiment with a VSV vector that contained a blend of Marburg, Ebola Sudan,and Ebola Zaire showed that a single injection could protect against all three viruses—and that may be the vaccine of the future. One Marburg vaccine has been tested in a phase I clinical trial.

Rift Valley fever

Causative agent: Bunyavirus

Symptoms: Flulike disease, retinal lesions, and brain inflammation, and hemorrhaging

Geographic range: Africa, Arabian Peninsula, and Indian Ocean islands

Burden: Outbreaks affect 200,000+

Mortality: <1%

Rift Valley fever, a devastating livestock disease, spreads through herds via mosquitoes,and outbreaks occur with heavy rainfalls. People can catch it from mosquito most become infected by slaughtering and caring for animals. Veterinary vaccines have protected livestock since the 1940s. Two investigational vaccines have been given to humans—primarily laboratory workers—since 1962; both appear safe and capable of triggering relevant immune responses. Outside of the U.S. Army, which worries that Rift Valley fever could be used as a bioweapon, few efforts are underway to develop human candidate vaccines. (Crimean-Congo hemorrhagic fever, a tick-borne bunyavirus that spreads between livestock and humans, is less common but deadlier, and a top vaccine priority for many.)

Lassa fever

Causative agent: Arenavirus

Symptoms: Fever, malaise, vomiting, diarrhea, and hemorrhaging

Geographic range: West Africa

Burden: 100,000 to 300,000 cases per year, endemic

Mortality: 1%

Ebola and Marburg are rare, but another hemorrhagic fever, Lassa, accounts for 10% or more of hospital admissions in some locales in West Africa. It is milder than its cousins, causing no symptoms in an estimated 80% of people infected, but 25% of those who get sick and survive become deaf. Two different vaccine strategies have proven their worth in monkey challenge studies: One uses VSV as a vector for Lassa proteins and the other weakens the virus itself by blending its RNA together with RNA from a nonpathogenic arenavirus called Mopeia.

Hookworm

Causative agent: Helminth

Symptoms: Itching, rash, abdominal pain, and anemia

Geographic range: Global

Burden: ~600 million chronic infections

Mortality: <0.01%

Children chronically infected with this worm, which hooks itself into the gut and sucks blood, become exhausted and listless and often do poorly at school. A vaccine for dogs was marketed in the 1970s, but today no vaccine exists for animals or humans. In 2000, the Sabin Vaccine Institute, a Washington, D.C.–based nonprofit, formed a private-public partnership to develop a vaccine for hookworm, and it is conducting clinical trials of two candidates. (Three candidate vaccines are in clinical trials for schistosomiasis, a helminthic infection that causes similar symptoms and afflicts 250 million.)

Chikungunya

Causative agent: Alphavirus

Symptoms: Acute fever and severe joint pain

Geographic range: Global

Burden: Outbreaks quickly infect tens of thousands

Mortality: 0.001%

Spread by *Aedes* mosquitoes, chikungunya first surfaced in Africa in 1952. In 2006, India suffered the largest outbreak to date with 1.25 million suspected cases. More recently the virus has been hopscotching around the Caribbean. NIAID's Vaccine Research Center has just begun a phase II trial at six sites in the Caribbean that will involve 600 people. VRC's Barney Graham says even though the disease is widespread, they've had trouble attracting industry interest.

Paratyphoid fever

Causative agent: *Salmonella paratyphi* bacterium

Symptoms: Fever, malaise, abdominal pain, and rash

Geographic range: Global

Burden: ~6 million cases annually

Mortality: <1% (if treated)

Paratyphoid fever is less common but almost as severe as its famous cousin, typhoid fever: Untreated, *S. paratyphi* kills about 25% of the people it infects. At least three paratyphoid vaccines have been tested in small human trials, and a group at the University of Oxford in the United Kingdom hopes to vaccinate humans and then, in an unusual experiment, challenge their protection by giving them *S. paratyphi*. (Typhoid fever vaccines exist, but they only have limited effect and do not work against paratyphoid. An experimental typhoid fever vaccine that had 91.5% efficacy in a 2001 trial of 11,000 children in Vietnam was stagnated.)

West Nile

Causative agent: Flavivirus

Symptoms: Fever, joint pain, and fatigue

Geographic range: Global

Burden: Outbreaks cause thousands of cases annually

Mortality: <0.1%

Although 80% of people infected with the West Nile virus will not experience any symptoms, in rare instances it can cause coma and paralysis. Spread by mosquitoes and birds, it has made serious inroads in the United States since 1999, and that has spurred vaccine development. Licensed vaccines exist for horses, and a human vaccine is on the market for yellow fever, a related flavivirus. Several West Nile vaccines have been tested in early phase human trials. "Everybody knows it's easy to make a West Nile vaccine," says Princeton University's Adel Mahmoud, the former president of vaccines at Merck. ■

Published by AAAS

INSIGHTS

Bringing boron reactions together *p. 26*

The computing power of crowds *p. 32* ▸

LETTERS

Edited by **Jennifer Sills**

Political priorities

In October, we asked young scientists how political priorities affect their ability to do and communicate science. We received a range of answers, some frustrated by political interference, others optimistic about the ability of political attention to effect change. Although many submissions focused on pleas for more science funding, we have focused our selection below on more specific examples. Because of the potentially sensitive nature of the question, we agreed to withhold the names of respondents upon request, after verifying their identities, to allow them to speak freely. In some cases we have printed excerpts of longer submissions (indicated by ellipses) and lightly copyedited original text for clarity. To read the complete versions, as well as many more, go to http://scim.ag/NG17R. Follow *Science*'s NextGen VOICES survey on Twitter with the hashtag #NextGenSci.

NEXTGEN VOICES

NEW ZEALAND IS known for its unique biodiversity and the efforts that are put into conserving it. We cherish and protect our native species and we are merciless in our fight against introduced species. However, political sensitivity toward hunting and fishing groups in New Zealand can interfere with conservation efforts. Whitebaits are the juveniles of five native species of Galaxiid fish that migrate from the sea upstream in spring. Three of them are considered as declining, and a fourth species is classified as threatened. Unfortunately, they are also delicious and a traditional spring meal. Because of the pressure to maintain the seasonal fishing activity and the associated market for this highly praised fish, conservation laws fail to protect them. At the other end of the spectrum, millions of dollars are spent every year to eradicate or control introduced mammalian species in New Zealand. But when mammals are big, tasty, and fun to shoot, as is the case for

ILLUSTRATION: JOHN HOLCROFT

Published by AAAS

feral pigs and deer, then there are no plans to eradicate them. The fact that these species can disrupt native ecosystems and facilitate the spread of other invasive species seems trivial compared to the value of the hunting industry.

Stéphane Boyer

Department of Natural Sciences, Faculty of Social and Health Sciences, Unitec Institute of Technology, Auckland, 1025, New Zealand and The Bio-Protection Research Centre, Lincoln University, Lincoln, 7647, New Zealand. E-mail: sboyer@unitec.ac.nz

...THERE IS A story in Argentina that illustrates the attitude of the government toward science: Twenty years ago, the Minister of Economy sent a researcher to "wash the dishes" because she was studying the effect of their policies on society (and because she was a woman). Until recently, many scientists left the country for better conditions. Luckily, science has now become a political priority; the number of Ph.D. students and researchers has increased, more than 1000 researchers have returned to the country, and we have seen an extraordinary investment in infrastructure and scientific projects. Argentina's political priorities are essential for encouraging science.

Lilen Yema

Laboratory of Limnology, Institute of Ecology, Genetics, and Evolution, and Faculty of Exact and Natural Sciences, University of Buenos Aires, C1428EHA, Argentina. E-mail: lilen.y@ege.fcen.uba.ar

IN THE FIELD of microbiology...funding priority is given to projects that research the small subset of microbes that cause disease. This narrow mindset has impeded the search for industrially relevant microbes. Nonpathogenic microbes have revolutionized disease theory and treatment. For example, the discovery of restriction enzymes in the humble bacteriophage spawned the recombinant technology revolution and has allowed us to affordably produce drugs such as insulin in *E. coli*. Another example lies in the unicellular pond critter Tetrahymena, in which telomeres—the age-monitoring caps on DNA—were discovered. The regeneration of telomeres is a hurdle all cancer cells must overcome. By studying this microbe, we are unlocking the mysteries of aging and oncogenesis. I would implore others to see the importance of discovering what understudied microbes have to offer us....

M. Clayton Speed

Department of Biochemistry, Colorado State University, Fort Collins, CO 80523, USA. E-mail: cspeed@rams.colostate.edu

SUBMIT NOW:
MEASURES OF SUCCESS

Add your voice to *Science*! Our new NextGen VOICES survey is now open:

Do publications (number and impact) convey the true value of an early career scientist? If so, how should these numbers be used? If not, how should young scientists be evaluated?

To submit, go to http://scim.ag/NG_18

Deadline for submissions is 12 February. A selection of the best responses will be published in the 1 April issue of *Science*. Submissions should be 100 words or less. Anonymous submissions will not be considered.

IN MEXICO, RESOURCES are biased toward "renowned" universities. For renowned universities, rules and regulations are more relaxed. Favored universities cover the costs of research and attendance for researchers and students, whereas those universities that do not receive enough resources prioritize certain areas or departments, neglecting many others....

Rigoberto Medina Andrés

Instituto de Investigación en Ciencias Básicas y Aplicadas, Universidad Autónoma del Estado de Morelos, Cuernavaca, Morelos, 62209, México. E-mail: rigoberto.medinaa@uaem.edu.mx

...THE POLITICAL LEADERS of the local government of Chongqing, China, vigorously promote a low-carbon economy and sustainable development to mitigate environmental pollution. Accordingly, research grants focused on this issue were supported by the government, and our group obtained a grant for a project about industrial park planning and design....In my view, political priorities based on correct decision-making and market requirements are beneficial for researchers.

Jingzheng Ren

Department of Technology and Innovation, Centre for Sustainable Engineering Operations Management, University of Southern Denmark, 5230, Odense M, Denmark. E-mail: jire@iti.sdu.dk

...PHARMACISTS POSSESS the scientific background and training to educate the public on health-related scientific matters....However, American pharmacists are ineligible for reimbursement for these services under Medicare Part B. Legally, pharmacists are not recognized as providers under Section 1861 of the Social Security Act. Instead, the majority of their compensation is tied to drug sales and their traditional dispensing role. This political issue, unknown to many, limits patient access to these services. As a pharmacy student, I believe that we could do more, given our extensive clinical and scientific training, and that our patients would see that benefit through fewer unnecessary hospitalizations, better quality of care, and decreased health care costs.

Joseph M. Cusimano

College of Pharmacy, The Ohio State University, Columbus, OH 43210, USA. E-mail: cusimano.6@osu.edu

I BECAME AN expatriate to learn to do science. Simply, the Dominican Republic does not offer graduate studies in my field. The crude reality is that, to do science, I might have to remain abroad after finishing my studies. "We have neither conditions nor support for doing research here," the director of a national research institute once told me. I want to believe that things are changing, albeit slowly. For example, a few years ago, the Ministry of Education was split into two institutions. The new ministry specializes in higher education, science, and technology, and it funds small scientific projects. Still, there is much to do, starting with having good education in science just as we have for baseball....

Luis B. Gómez Luciano

Biodiversity Research Center, Academia Sinica, Taipei, 11529, Taiwan. E-mail: lbien@sinica.edu.tw

...IT IS NO SECRET that Canada's previous government was blatantly accused of "muzzling" government scientists, reducing and reallocating funding to research institutions, and directly limiting and dictating how much research was conducted and in what areas research funds would be allocated. The previous regime's attitude toward research led to scientists who had less money to work with, research that was disproportionately skewed toward certain sectors of the economy, and most troubling of all, restrictions on communication....I don't think that prioritizing research to drive political agendas is what science is all about....

Abraham Munene

Department of Ecosystem and Public Health, Faculty of Veterinary Medicine, University of Calgary, Calgary, AB, T2N 4Z6, Canada. E-mail: abraham.munene2@ucalgary.ca

...THE TOXIC ENVIRONMENT of political brinksmanship that has grasped U.S. federal politics has caused anxiety for countless scientists, regardless of funding source.... Yet when I read of Syrian scientists forced to withdraw seeds from the Svalbard Global

Published by AAAS

Seed Vault or Iranian scientists juggling a web of political and budgetary hurdles, I cannot help but be grateful. Although we may have a politically volatile climate here in the United States, the amazing consistency and reliability of resources and personnel is something to be treasured.

Keith C. Heyde

Department of Engineering Science and Mechanics, Virginia Polytechnic Institute and State University, Blacksburg, VA 24061, USA. E-mail: kch2118@vt.edu

AS A PH.D. student in genetics, I am concerned about the political decisions being made in response to public sensitivity that extends beyond a layperson's awareness of science. For example, a national debate about genetically modified food (GMF) has arisen in my home country, China. At the beginning, it was simply about safety. However, due to inefficient communication between scientists and the public, many people began to be firmly convinced that GMFs are potentially hazardous to health. Shortly, it became a public crisis of trust in scientists, especially agriculturists and geneticists....The consequences are so serious that funding from various sources has been cut, many laboratories have been closed, and many scientists are obliged to change their research focuses....

Fan Wu

Department of Cardiac Development and Remodelling, Max Planck Institute for Heart and Lung Research, Bad Nauheim, 61231, Germany. E-mail: fan.wu@mpi-bn.mpg.de

I HAVE TWO choices when doing my research. I can do a plant sciences project in which the final product is a transgenic. I cannot use it as a technology because the government policies are against genetically modified organisms, so all my funding and hard work will be wasted from an applicability standpoint. However, I will publish a high-impact research paper that will be lauded and I will be promoted with merit. On the other hand, I could use institutional funds to develop a technology as mandated by the organization and government policies. The work may have low international publication impact, and my promotion will be delayed, but it will be highly applicable to a marginal population. Which option would you take?

Name Withheld

India

IN MAINLAND CHINA, the use of the Internet is limited in the name of "maintaining stability" or "cyberspace purification."... Quite a lot of academic information on the Internet is free to access abroad but inaccessible in mainland China. Even Google is disabled. The country's largest search engine, Baidu, which is extensively used by the Chinese, fails to find much foreign information. Internet regulation supposedly contributes to the unified leadership in politics, ideology, and cognition. However, such a situation can harm academia, resulting in a decrease of pluralism and screening potentially valuable information that could foster creative and critical thinking....

Xin Miao

School of Management, Harbin Institute of Technology, Harbin, 150001, China. E-mail: xin.miao@aliyun.com

THE CONSTRUCTION AND operation of dams is often politically charged, and related controversies have fueled important scientific inquiries. What are the ecological effects of dam removal? How do dams affect fish populations? Policy-makers and managers can help scientists ask nuanced, management-relevant questions that work toward addressing these controversies. For example, studies that quantify ecological responses to different dam management regimes are more meaningful when the dam operations tested are feasible in a larger policy context. Cooperation and collaborative exchange between scientists and policy-makers can be mutually beneficial in this way; scientists formulate policy-relevant questions, and policy-makers get policy-relevant scientific information. I have experienced this type of exchange, and I believe that my research is better for it...

Bridget R. Deemer

School of the Environment, Washington State University, Vancouver, WA 98686, USA. E-mail: bdeemer@wsu.edu

AS A CLIMATE ADVOCATE working for a political organization, all of my communication has to be carefully constructed to work with political messaging priorities. Although we, as scientists, would hope that a sufficiently well-supported and clearly communicated argument would regularly convince policy-makers, this is simply not the case. In order to effect change, we have to work with the system we have, not the system we want, and that means communicating politically. Results that would be objectionable to certain groups need to be minimized through careful framing of studies, and we select only projects that are very likely to produce a politically beneficial result.

Name Withheld

United States

FOR VARIOUS HISTORICAL reasons, the Southeast region of Brazil is privileged in terms of financial resources and therefore responsible for most scientific publications, led by the University of São Paulo. However, for the past 10 years, the National Council for Scientific and Technological Development requested that at least 30% of the total amount granted for science projects should go to institutions placed in less privileged regions. This political priority made a huge impact in expanding science production and graduate programs, giving opportunity to younger and talented scientists to make high-quality science in an environment of more equality, and decreasing the educational deficits in less advantaged areas. Northeastern institutions are now listed among the best national institutions, publishing in the most prestigious journals, filling a growing number of patents, and receiving international awards of excellence.

João Ricardo Oliveira

Keiso Asami Laboratory and Department of Neuropsychiatry, Federal University of Pernambuco, 50670-901, Recife, Brazil. E-mail: joao.ricardo@ufpe.br

ILLUSTRATION: JOHN HOLCROFT

Published by AAAS

PERSPECTIVES

NEUROSCIENCE

Illuminating anhedonia

Optogenetics and fMRI reveal the brain circuitry of anhedonia

By **Trevor W. Robbins**

The mesolimbic dopamine (DA) system is part of the brain's reward circuitry (see the figure). It controls an individual's responses to rewards such as food, social interactions, and money, and is therefore an important determinant of motivation. Midbrain DA neurons projecting to the striatum are causally involved in reward-like processes. Less clear is how another apparent target of midbrain DA neurons, the ventromedial prefrontal cortex (vmPFC), may contribute to the reward system. On page 41 of this issue, Ferenczi *et al.* (*1*) report using a unique combination of optogenetic tools and functional magnetic resonance brain imaging (fMRI) in conscious rats to investigate the underlying mechanisms of the competitive relationships of these two brain regions over striatal function and reward-like behavior. The findings have implications for understanding and treating affective symptoms in disorders such as depression, schizophrenia, and addiction.

Evidence of a reward system was derived from experiments in rats some 40 years ago and has been confirmed by recent studies showing that rodents will choose to receive optogenetic stimulation of midbrain DA neurons [which were engineered to be activated by light (*2*)]. The findings have been paralleled in humans by fMRI; thus, the anticipation of reward evokes increased activity in the human ventral striatum. This correlated with indirect measures (from positron emission tomography) of DA release in the striatum (*3*). Exposure to both primary rewards (e.g., pleasant tastes and sights) and conditioned or symbolic rewards (such as money) leads to increased activity in the vmPFC (*4*). It is therefore paradoxical that hyperactivity of this region has also been linked in humans to anhedonia, the inability to feel pleasure (*5*, *6*). Removing this hyperactivity has been a target for various antidepressant treatments, including pharmacotherapy, cognitive therapy, and deep brain stimulation. Ferenczi *et al.* asked whether the effect of enhancing midbrain DA neuron activity is blunted by influences from the rat medial PFC.

DA-containing midbrain neurons in the rat were exposed to laser light (via implanted optic fibers) to activate ion channels (opsins) that were either inhibitory or excitatory. Stimulation via excitation acted as a reward, as rats chose to turn on such stimulation. Stimulation also produced an increased blood oxygen level–dependent (BOLD) fMRI response in the striatum, just as would have been predicted from prior human studies. Moreover, this activation of the striatum was DA-dependent, as exposure to DA receptor antagonists blocked both the rewarding effects and the BOLD signature.

A key question is the precise physiological nature of this potent rewarding effect; there are at least two reasons for thinking it may not always be equivalent to other forms of reward. Stimulant drugs such as cocaine are presumed to produce their rewarding effects, at least partly, by increasing tonic (background) levels of striatal DA rather than by increasing phasic DA release in the striatum as a consequence of mesolimbic DA neuron activity. In the study of Ferenczi *et al.*, phasic stimulation of midbrain DA neurons not only activated regions of the dorsal and ventral striatum, but also activated regions of the cerebral cortex (the retrosplenial cortex), although surprisingly not the vmPFC itself, as has been shown in studies of natural reward anticipation and feedback in humans (*4*).

Ferenczi *et al.* used a clever optogenetic stimulation method to drive an asynchronous enhancement of medial PFC hyperexcitability in awake rats, thereby mimicking states in human patients with depression; increased BOLD responses in the vmPFC to happy (but not sad) stimuli have been correlated with anhedonia ratings (*5*, *6*). Hyperexcitability of the medial PFC suppressed sucrose preference in the rat, but not drinking per se, and curtailed social interaction without affecting general locomotor activity, suggestive of a specific inhibitory effect of medial PFC on reward-motivated behavior. The same medial PFC hyperexcitability also suppressed the striatal responses to optically stimulated DA neurons in the midbrain, and abolished a behavioral preference for the place associated with midbrain DA neuron stimulation.

More generally, the state of medial PFC hyperexcitability elicited greater connectivity between the medial PFC, lateral orbitofrontal cortex (OFC), and ventral striatum by enhancing synchronous firing. This greater synchronous connectivity correlated with reduced sucrose preference (through mechanisms that are still obscure). This is reminiscent of the discovery of greater connectivity of the subgenual cingulate cortex with nodes of the "default network," including the OFC, the thalamus, and the precuneus in depressed patients (*5*) and of the association of vmPFC activity with anhedonia during the processing of positive emotional information in nonclinical individuals (*6*). Whether this

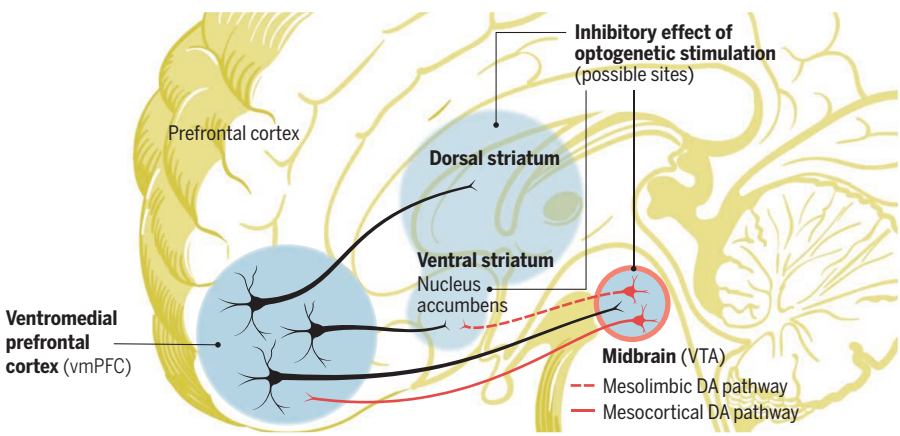

Reward circuitry. Shown are approximate anatomical relationships in the human brain between the midbrain dopamine (DA) pathways from the ventral tegmental area (VTA) to the nucleus accumbens (part of the ventral striatum) and the vmPFC, and reciprocal influences (mediated by glutamate) of the vmPFC. The vmPFC includes the medial orbitofrontal cortex and parts of the ventral cingulate cortex, including the subgenual cingulate cortex. Ferenzi *et al*. show that the rewarding effects of optogenetic stimulation of the VTA were counteracted by optogenetically-induced hyperexcitability of the vmPFC to mimic behavioral anhedonia-like symptoms in rats, presumably via descending pathways to the subcortical regions including the striatum and VTA.

ILLUSTRATION: K. SUTLIFF/*SCIENCE*

Department of Psychology and Behavioural and Clinical Neuroscience Institute, University of Cambridge, Cambridge CB2 3EB, UK. E-mail: twr2@cam.ac.uk

Published by AAAS

is true of other patient groups exhibiting anhedonia, including schizophrenia (*7*), is, however, less clear.

The findings of Ferenczi *et al.* highlight PFC hyperactivity as a causal inhibitory influence on reward-related behavior in the rodent mediated via the striatum. This contrasts with a more traditional view of the importance of PFC hypoactivity in human and experimental animal models, in which hypoactivity may cause a lack of control over subcortical structures such as the striatum and amygdala. It would be interesting to use optogenetics to compare the effects of medial PFC hyperexcitability with those of medial PFC silencing on measures of reward-related behavior in the rodent model. Other PFC-subcortical interactions potentially mediate a broader range of symptom dimensions, including anxiety and impulse control. It may be overly simplistic to relate only symptoms of anhedonia to depression; other motivational symptoms such as apathy and reward prediction, as well as negative affective bias, may also contribute to this phenotype (*8*).

Some explanation is still required for the origin of the vmPFC hyperexcitability in depression, as well as the striking paradox that although a hyperactive vmPFC is correlated with the mood state of anhedonia, this structure actually mediates responses to reward in humans (*5*–*7*). An initial step may be to determine whether such BOLD-related reward signals also occur in the rat vmPFC. A recent study, however, using amperometric O_2 measures as a proxy BOLD response, reported that transient signals in the medial PFC were more related to negative than to positive reward signals (*9*), so this question may represent another important translational focus.

Future work may contrast the effects of hypo- and hyper-PFC function and distinguish whether both of these influences can occur concurrently in parallel PFC-striatal circuitry involving distinct PFC sectors with potentially different, even opposing (*10*), functions. This research cannot proceed until controversies regarding evolutionary relationships of the PFC in rodent and primate brains are fully resolved, which in turn may have to await the development of optogenetic tools that can be deployed more readily in nonhuman primates. ■

REFERENCES

1. E. A. Ferenczi *et al.*, *Science* **351**, aac9698 (2016).
2. H.-C. Tsai *et al.*, *Science* **324**, 1080 (2009).
3. B. H. Schott *et al.*, *J. Neurosci.* **28**, 14311 (2008).
4. S. N. Haber, B. Knutson, *Neuropsychopharmacol. Rev.* **35**, 4 (2010).
5. P. A. Keedwell *et al.*, *Biol. Psychiatr.* **58**, 843 (2005).
6. P.-O. Harvey *et al.*, *Mol. Psychiatr.* **12**, 767 (2007).
7. P.-O. Harvey *et al.*, *J. Psychiatr. Res.* **44**, 707 (2010).
8. J. Roiser *et al.*, *Neuropsychopharmacol. Rev.* **37**, 117 (2012).
9. J. Francois *et al.*, *J. Neurosci.* **34**, 596 (2015).
10. I. Vidal-Gonzalez *et al.*, *Learn. Mem.* **13**, 728 (2006).

10.1126/science.aad9698

CELL SIGNALING

Seeing mTORC1 specificity

Structural information reveals how a multiprotein complex responds to amino acid abundance

By **Gwen R. Buel** *and* **John Blenis**

Cells must sense their environment to determine whether conditions are suitable for growth. Despite the physiological importance of a multiprotein complex called mammalian/mechanistic target of rapamycin complex 1 (mTORC1) in this process, a detailed molecular understanding of its assemblage and regulation of its serine-threonine kinase function have proven difficult to elucidate. On page 48 of this issue, Aylett *et al.* (*1*) help uncover the molecular underpinnings of mTORC1, while on pages 43 and 53, Wolfson *et al.* (*2*) and Saxton *et al.* (*3*), respectively, make strides in determining how mTORC1 is regulated by the amino acid leucine.

> ***"The studies...help to clarify an important aspect of mTORC1 regulation."***

mTORC1 exists as a dimer of two mTOR molecules along with its accessory proteins, but it has been unclear how the mTORC1 component called regulatory-associated protein of mTOR (Raptor) fits into the structure and promotes substrate specificity (*4*). Aylett *et al.* used cryo–electron microscopy to resolve the structure of mTORC1, and combined this with crystallographic studies of Raptor to better understand the function of mTORC1 components. They found, as shown before (*4*), that mTORC1 exhibits the shape of a bumpy doughnut, with twofold rotational symmetry. Additionally, Aylett *et al.* show that the backbone is continuous from one mTOR subunit to the next, and that Raptor binds at the junctions of the two mTOR molecules, appearing to stabilize the dimer as a piece of tape would hold together two pieces of overlapping wrapping paper.

Another partial structure of mTOR previously revealed that the catalytic site of mTOR is found deep in a cleft, which is thought to allow access to selected substrates (*5*). The structure determined by Aylett *et al.* shows that Raptor makes this cleft even smaller, suggesting that Raptor may play an important role in limiting access to substrates. Additionally, the authors provide a model as to how Raptor may select substrates containing a TOR signaling (TOS) motif (*6*). Raptor has homology to cysteine-aspartic proteases (CASPases), including a domain that these enzymes use to bind a conserved aspartate-containing motif on substrates. It is known that TOS motifs are important for recruitment of some substrates to mTORC1 *(6),* and the authors hypothesized which region of Raptor may bind TOS motifs based on the homology to CASPases. They found that this region in Raptor is located at the base of the active-site cleft, likely allowing for Raptor to position substrates.

Given the importance of the structural support and substrate specificity that Raptor provides for mTORC1, it would be interesting to see if rapamycin-insensitive companion of mTOR (Rictor) has the same role in mTORC2 or if the complex achieves these feats by other means. mTORC2 promotes cell growth and survival partially through activation of mTORC1, and Rictor is an accessory component comparable to Raptor. Another question is how the new structural information might explain how mTORC1 recognizes targets that do not contain a TOS motif. Additionally, the mechanisms by which the protein called Ras homology enriched in brain (Rheb) binds to and activates mTORC1 are still unclear. Rheb is a member of the Ras superfamily of guanosine triphosphatases (GTPases) and is tethered to endomembranes by a lipid anchor. The higher-resolution structure of mTORC1 might enable future studies to better answer these questions.

Although much can be learned about the function and regulation of mTORC1 from the structure of mTORC1 itself, a plethora of signaling molecules come into contact with mTORC1 directly or indirectly to regulate its activity, and focusing on those proteins can help elucidate mTORC1 function as well. Wolfson *et al.* and Saxton *et al.* looked at a family of proteins called Sestrins, which the authors show can sense leucine and correspondingly regulate mTORC1. Sestrins were initially implicated in regulating oxidative stress, cell metabolism, and life span (*7*). Sestrins 1 and 2 were first connected to mTORC1 signaling through their ability to activate

[1]*Department of Pharmacology, Meyer Cancer Center, Weill Cornell Medical College, New York, NY 10065, USA. E-mail: job2064@med.cornell.edu*

Published by AAAS

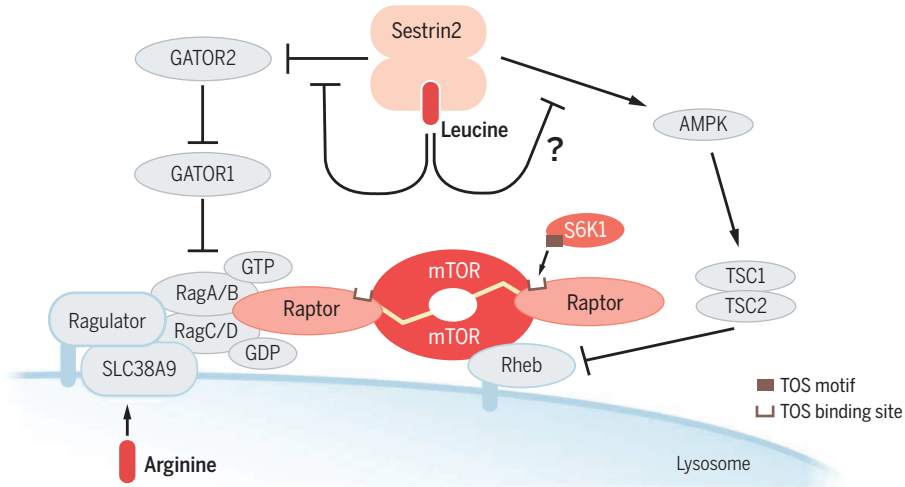

Regulation by Sestrins. Sestrin2 binds to leucine, triggering its dissociation from GATOR2. This activates mTORC1, promoting protein synthesis, metabolism, and cell growth. Sestrins also inhibit mTORC1 by activating the AMPK pathway. Whether leucine interaction with Sestrins blocks this pathway and activates mTORC1 is not known. Arginine activates mTORC1 through a distinct mechanism. S6K1, ribosomal protein S6 kinase 1; SLC38A9, solute carrier family 38 member 9.

adenosine monophosphate–activated protein kinase (AMPK) (*8*). AMPK phosphorylates and activates a negative regulator of mTORC1, the tuberous sclerosis complex (TSC) complex (TSC complex), and in this way, Sestrins have a negative role in mTORC1 signaling. An AMPK-independent mechanism is also responsible for Sestrin inhibition of mTORC1, in which the Sestrins negatively regulate a component of the amino acid sensing pathway, the Rag GTPases (*9*–*12*). Wolfson *et al.* show that leucine, which binds to Sestrin 1 and 2 with affinity greater than other amino acids, disrupts the interaction between Sestrins and the protein complex called GTPase-activating protein (GAP) activity toward Rags 2 (GATOR2). GATOR2 is a positive regulator of the mTORC1 pathway, via the Rag proteins. Disruption of Sestrin-GATOR2 interaction frees GATOR2 to block downstream events that would normally prevent mTORC1 activation (see the figure).

To better understand the mechanism by which Sestrins bind to leucine, Saxton *et al.* crystallized Sestrin2 in complex with leucine. The authors found that Sestrin2 consists of two structurally similar domains, of which leucine is bound only to the carboxyl-terminal domain. The size and hydrophobicity of the leucine-binding pocket favor binding to the side chain of leucine ideally over other amino acids, and mutation of this pocket affects the sensitivity of mTORC1 to leucine. It is unclear from the structure, however, how leucine binding causes dissociation of Sestrin2 from GATOR2. Wolfson *et al.* identified a residue in the amino terminus of Sestrin2 that is required for binding to GATOR2, and Saxton *et al.*, identified additional residues in the carboxyl terminus, suggesting the possibility of a large interaction surface. Curiously, a model (*9*) was proposed in which Sestrin2 acts as a guanine nucleotide dissociation inhibitor (GDI) for RagA/B. This study identified an arginine residue whose mutation hinders the ability of Sestrin2 to inhibit mTORC1, and mutation of two additional lysine residues nearby seemed to have an additive effect on inhibition of Sestrin2 function as a GDI. Saxton *et al.* found that the two lysine residues are buried in the structure, calling into question the GDI hypothesis. However, Saxton *et al.* were unable to crystallize Sestrin2 in the absence of leucine, so it is unclear whether these residues, which are close to the surface of the structure, could be revealed in the absence of leucine.

The studies of Aylett *et al.*, Wolfson *et al.*, and Saxton *et al.* advance our understanding of mTORC1 in terms of its molecular architecture, and help to clarify an important aspect of its regulation. Future work should elucidate how leucine binding to Sestrin2 causes dissociation from GATOR2, and determine if the proposed activation of AMPK by Sestrins can be similarly inhibited by leucine binding. Additionally, although a putative arginine sensor has been proposed (*13*), the mechanisms by which mTORC1 senses other amino acids still need to be worked out. ■

REFERENCES

1. C. H. S. Aylett *et al.*, *Science* **351**, 48 (2016).
2. R. L. Wolfson *et al.*, *Science* **351**, 43 (2016).
3. R. A. Saxton *et al.*, *Science* **351**, 53 (2016).
4. C. K. Yip *et al.*, *Mol. Cell* **38**, 768 (2010).
5. H. Yang *et al.*, *Nature* **497**, 217 (2013).
6. S. S. Schalm, J. Blenis, *Curr. Biol.* **12**, 632 (2002).
7. J. H. Lee *et al.*, *Cell Metab.* **18**, 792 (2013).
8. A. V. Budanov, M. Karin, *Cell* **134**, 451 (2008).
9. M. Peng *et al.*, *Cell* **159**, 122 (2014).
10. L. Chantranupong *et al.*, *Cell Rep.* **9**, 1 (2014).
11. A. Parmigiani *et al.*, *Cell Rep.* **9**, 1281 (2014).
12. J. S. Kim *et al.*, *Sci. Rep.* **5**, 10.1038/srep09502 (2015).
13. S. Wang *et al.*, *Science* **347**, 188 (2015).

10.1126/science.aad9696

ORGANIC CHEMISTRY

When two reactions become one

Merging two fundamental reactions of organoboron compounds provides a new platform for catalysis

By **James W. B. Fyfe** *and* **Allan J. B. Watson**

Organoboron compounds are among the most widely used reagents in organic synthesis and underpin many of the most frequently practiced and important reactions in synthetic organic chemistry (*1*). These reactions are based on specific mechanistic events that are distinctive to the reaction class. Catalytic processes are usually driven by transmetallation to transition metal complexes (passing a ligand from boron to the metal), whereas stoichiometric processes are based on metallate rearrangement mechanisms—ligands undergoing redistribution around a boron center—initiated by an incoming nucleophile. On page 70 of this issue, Zhang *et al.* (*2*) report an alternative transmetallation process that harmoniously merges these usually independent mechanisms, and they demonstrate its application within a multicomponent catalytic reaction that generates specific chiral products.

The new reaction is built upon the union of two key areas of organoboron chemistry: the Suzuki-Miyaura (S-M) reaction, a Pd-catalyzed reaction between an organoboron compound and an organic electrophile (*3*), and the 1,2-metallate rearrangement, a stoichiometric reaction between an organoboron compound and a nucleophilic organometallic reagent such as an organolithium (*4*). The S-M reaction proceeds through three key mechanistic events (see the figure, panel A). Oxidative addition involves the insertion of the Pd(0) catalyst into the carbon-halogen (C–X) bond of the aryl halide (Ar–X) electrophile. This step is followed by transmetallation, where the organoboron compound transfers its associated carbon ligand (R) to the Pd center. Finally, reductive elimination forms a new C–C bond between

Department of Pure and Applied Chemistry, WestCHEM, University of Strathclyde, Glasgow G1 1XL, UK. E-mail: allan.watson.100@strath.ac.uk

ILLUSTRATION: N. CARY/*SCIENCE*

Published by AAAS

Ar and R, giving the desired product while simultaneously regenerating the Pd(0) catalyst and allowing it to reenter the catalytic cycle. This Nobel Prize–winning reaction is frequently used by synthetic chemists in both academia and industry and remains widely investigated, with aspects of its utility and mechanism still the focus of investigation several decades after its discovery (*5*, *6*).

In contrast to the small quantities of Pd catalyst used in the S-M reaction, metallate rearrangements require the addition of stoichiometric amounts of an organometallic reagent. For example, the electrophile-induced 1,2-metallate rearrangement operates by addition of an organometallic reagent to an organoboron, forming a charged "boronate" (negatively charged boron) complex (see the figure, panel B). Addition of an electrophile (E) promotes migration of the R group, forming a new C–R bond and C–E bond simultaneously. Similar to the S-M reaction, this process continues to be explored by many chemists (*4*).

Until now, the key mechanistic features that drive these fundamental reactions of organoboron compounds usually remained isolated to their respective reactions, with transmetallation belonging to the S-M reaction and rearrangement events belonging to metallate chemistry. Building on work from the Murakami group (*7*), the report by Zhang *et al.* cleverly merges these mechanistic events (see the figure, panel C). Instead of using an electrophile to promote the metallate rearrangement, the authors find that Pd(II) species—the same intermediate generated in the first step of the S-M reaction—can drive this rearrangement. This enables the merging of the S-M catalytic cycle with the metallate process to generate a catalytic reaction based on an unprecedented transmetallation process.

The overall reaction fuses three starting materials together in a "conjunctive cross-coupling" reaction. An organolithium generates a boronate from an organoboron compound in the same way that the 1,2-metallate rearrangement begins. This boronate is intercepted by the electrophilic Pd(II) complex resulting from the oxidative addition step of the S-M catalytic cycle. The addition of E promotes a metal-induced metallate rearrangement, generating a new alkyl-Pd(II) species. Reductive elimination can then take place to deliver a new product, creating two new C–C bonds and a new C–B stereocenter. The configuration of this stereocenter can be readily controlled using a chiral ligand on the Pd catalyst, giving products with high enantioselectivity. Crucially, the reaction avoids the typical transmetallation step of the S-M pathway; otherwise, mixtures of products might result.

This new catalytic reaction was shown to be general, with the reaction tolerating substantial variation of the three starting materials. In addition, the products of this reaction are themselves synthetically versatile organoboron compounds and can be readily manipulated in a variety of ways with established synthetic methods (*1*). Zhang *et al.* developed a remarkably efficient two-step synthesis of the natural product combretastatin from readily available starting materials. However, the true importance of this work is not the utility of the products generated, but rather the revelation of the new transmetallation pathway. In the nearly 40 years since the discovery of the S-M reaction, there has been very little advance in our understanding of the basic mechanistic events associated with Pd catalysis with organoboron compounds (*6*). The introduction of an alternative transmetallation pathway is therefore of enormous potential value in terms of the development of new catalytic transformations, paving the way for a new generation of exciting research in the field of catalysis using organoboron compounds. ■

REFERENCES

1. D. G. Hall, Ed., *Boronic Acids: Preparation and Applications in Organic Synthesis, Medicine and Materials* (Wiley-VCH, Weinheim, Germany, 2011).
2. L. Zhang *et al.*, *Science* **351**, 70 (2016).
3. N. Miyaura, K. Yamada, A. Suzuki, *Tetrahedron Lett.* **20**, 3437 (1979).
4. S. P. Thomas *et al.*, *Chem. Rec.* **9**, 24 (2009).
5. A. Suzuki, *J. Organomet. Chem.* **653**, 83 (2002).
6. A. J. J. Lennox, G. C. Lloyd-Jones, *Angew. Chem. Int. Ed.* **52**, 7362 (2013).
7. N. Ishida, Y. Shimamoto, M. Murakami, *Org. Lett.* **11**, 5434 (2009).

10.1126/science.aad8698

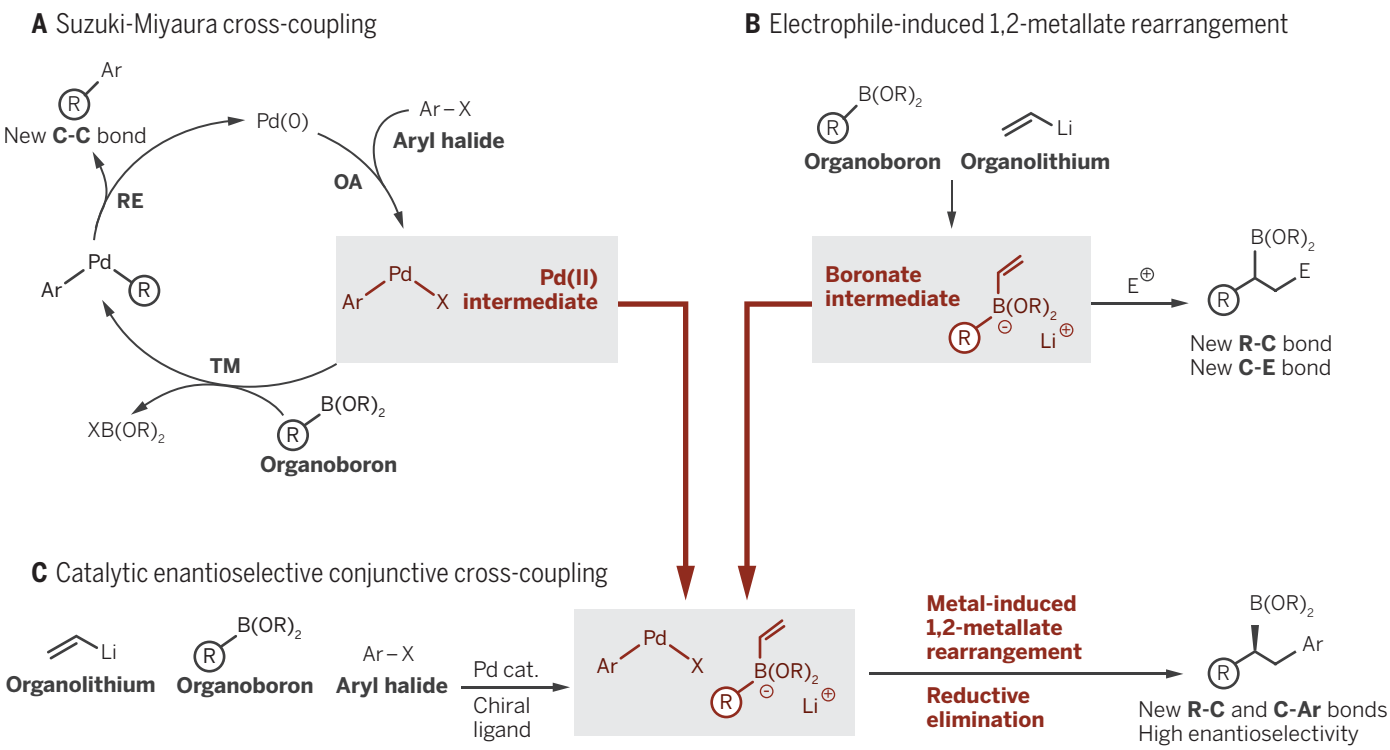

ILLUSTRATION: K. SUTLIFF/*SCIENCE*

Bringing it all together. (**A**) The three key steps of the Suzuki-Miyaura reaction catalytic cycle. OA, oxidative addition; TM, transmetallation; RE, reductive elimination. (**B**) The main steps in the electrophile-induced 1,2-metallate rearrangement. (**C**) Combining key mechanistic events to enable conjunctive cross-coupling via metal-induced 1,2-metallate rearrangement.

Published by AAAS

SCIENCE EDUCATION

The evolution of antievolution policies *after* Kitzmiller *v.* Dover

A phylogeny identifies ancestors of modern creationist legislation

By **Nicholas J. Matzke**[1,2]*

Political attempts to denigrate and dilute the teaching of evolution in science classrooms have been a feature of the U.S. educational scene for 90 years (*1*). These may be classified into three major waves (*2*). Bans on teaching evolution were enacted in the 1920s (and unsuccessfully challenged in the 1925 Scopes Monkey Trial) and persisted until ruled unconstitutional in 1968. When bans were rescinded, creationists (*3*) began to lobby for "balanced treatment" for creationism whenever evolution was taught, first trying biblical creationism, then "creation science," and finally "intelligent design" (ID). Each strategy was ruled unconstitutional (table S1), in part due to court attention to creationist origins. Creationists did not give up with the defeat of ID in *Kitzmiller* v. *Dover*, decided in U.S. District Court on 20 December 2005, but instead shifted political efforts to the third wave of antievolutionism, "stealth creationism" (*2*): legislation that avoids mentioning creationism in any of its varieties but advances creationist antievolutionism with an evolving collection of strategies (table S1). I use a phylogenetic tree to show how antievolution legislation has evolved, and at times succeeded, in the 10 years since *Kitzmiller*.

EDUCATION

After *Kitzmiller*, even the Discovery Institute (DI), the institutional home of ID, claimed it had never encouraged teaching ID in public schools [incorrectly: (*4*)] and heavily promoted "Academic Freedom Acts" (AFAs), aimed at encouraging teachers to promote antievolutionism. At least 71 bills have been proposed in 16 states (table S1). Stealth creationist bills have been signed into law in three states [Louisiana, Tennessee, and Mississippi (*5*)]. Legal challenges seem to have been dissuaded by strategic vagueness in avoiding mention of the bills' religious motivations and by only permitting, rather than requiring, disparagement of evolution. Previous court rulings against teaching creationism remain in effect and are not trumped by state legislation, but acts by individual teachers can only be challenged if students and parents complain, and complaints can be discouraged by local social pressures.

Phylomemetic analysis (*6*), using the tools of statistical phylogenetics to study cultural transmission, is useful for estimating the detailed evolutionary history of policies by considering which passages from which bills were copied and modified into other bills. Phylogenetic comparative methods can illuminate which key events produced the array of antievolution bills in circulation, assessing the influence of legislative success on the evolving antievolution tradition and the strategies likely to be used in the future.

EVOLUTION OF LEGISLATION. Texts of 65 bills archived by the National Center for Science Education (NCSE) (*7*) were studied, along with the DI model bill and an obscure but crucial policy from Ouachita Parish, Louisiana [full details of all analyses provided in supplementary material (SM)]. Maximum parsimony searches provide strong evidence of bill-to-bill copying and "descent with modification" (see the chart). In addition to this lineal (parent-to-offspring) transmission, it has been noted (*2*) that the 2008 Louisiana bill [originally an AFA but renamed a "science education act" (SEA)] and later antievolution bills have a composite history, combining text from the AFA tradition and from the Ouachita policy.

> ***"The creationist origins of modern antievolution strategies are clear...."***

Scientific targets of antievolution bills. Most strategies used in the AFA and SEA bills have precedents in pre–third-wave antievolutionism (table S1). However, mapping the strategies on the phylogeny (see the chart) shows a major innovation in the SEA tradition that originated from the Ouachita policy: targeting for "critical analysis" not only evolution and origin-of-life studies but also global warming and human cloning. The tactic appears to be an attempt to circumvent earlier legal decisions suggesting that targeting evolution alone is prima facie evidence of religious motivation and, thus, unconstitutional; an additional motivation may be dislike of climate change research by economic and religious conservatives (*2*). The addition of human cloning and global warming was copied in over a dozen subsequent bills, two of which passed (the 2008 Louisiana SEA and the 2011 Tennessee bill).

Direct ancestors. It may be useful in educational and legal contexts to identify the exact sources of now-prominent antievolution policies. Traditional phylogenetic analyses do not infer direct ancestry (i.e., bill Y copied directly from bill X, rather than X and Y from a common ancestor), but a new Bayesian method (*8*, *9*) can search phylogenies where some tip branches have 0 time length (and are thus direct ancestors rather than side branches). Here, the method identifies seven bills as having greater than 90% probability of being direct ancestors of the dominant subsequent tradition (see the chart). Direct ancestors of the AFAs include four Alabama bills from 2004 to 2005 (HB391c and SB336c are identical copies) and a 2006 Oklahoma bill. Two Tennessee bills (SB893 and HB368a) introduced before passage of a modified bill (HB368b) served as direct ancestors of the nine SEA bills proposed from 2012 to 2015. All post-2008 SEA bills are clearly members of a clade beginning in Louisiana, although no published Louisiana bill can be identified as the direct ancestor, perhaps because of extensive legislative modifications.

The phylomemetic tree exhibits strong asymmetry (SM), which indicates bias in which policies have been selected for new antievolution efforts. This suggests that antievolutionists tend to select particular bills and/or strategies for promotion. Heavy promotion in one state may spread to others, or perhaps, simply, "success sells."

The Discovery Institute model bill. The DI supported key changes to Alabama bills in 2004 (www.discovery.org/a/2037). Thus, there is some chance that the model bill was distributed before being posted online in Fall 2007 and might be ancestral to AFAs. Leaving the date free to vary and estimating it (fig. S10) along with the phylogeny indicates an earlier date, closest to the 2006 Alabama bills but suggests that the 2005 AL HB352 was directly ancestral to later legislative proposals. The DI's "brand" may have been suf-

[1]The Australian National University, Canberra, ACT 2601, Australia. [2]Work began at: National Institute for Mathematical and Biological Synthesis, University of Tennessee, Knoxville, TN 37996 USA. E-mail: nick.matzke@anu.edu.au.

Published by AAAS

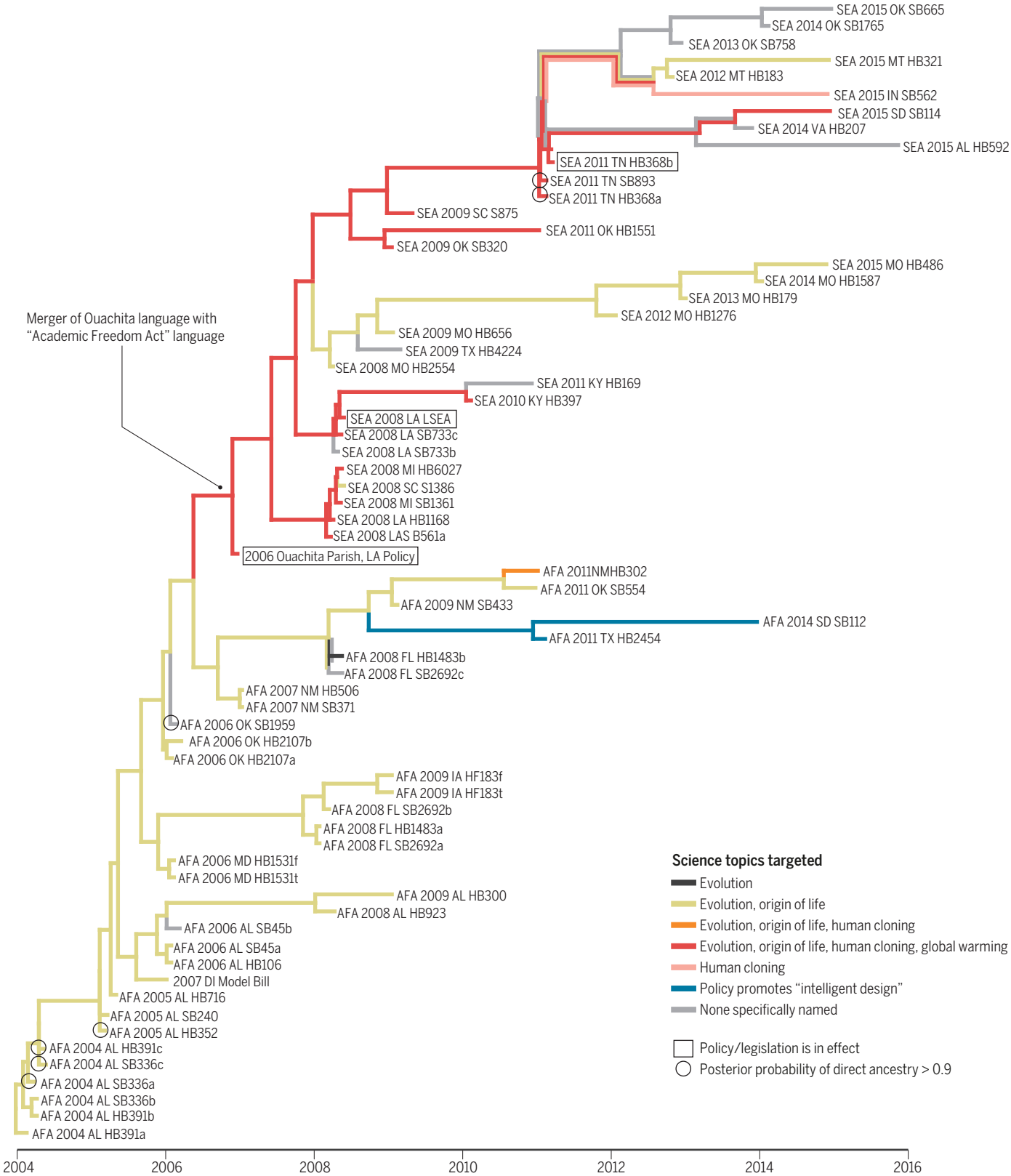

ILLUSTRATION: P. HUEY/*SCIENCE*

Tracing the evolution of antievolution legislation. Maximum clade credibility tree from Bayesian tip-dating analysis of 67 policies. The SEAs originated by combining text from the AFAs with Ouachita Parish, Louisiana, policy text from 2006. Seven bills have a high posterior probability of being direct ancestors of the rest of the tradition (circles). The tips of branches reflect the bills' publication dates [except for the DI model bill (see text)]. The nodes (splitting events) represent copying events. The distance between a tip and a node is an inference about how much change occurred and how much time this took. When the node-to-tip distance is effectively zero, this indicates a high probability of direct ancestry. Tip labels indicate AFA or SEA, year, state, bill number (SB, senate bill; HB, house bill), and versions (a, b, or c, for legislative revisions; t or f, teachers or faculty targeted). Branch colors indicate the sciences targeted; mixed colors on a branch indicate uncertainty in the reconstruction. See SM for full details of analyses.

Published by AAAS

ficiently damaged by the *Kitzmiller* case that politicians shied away from direct use of DI resources, and found inspiration elsewhere, such as previous legislation. This may help explain the strong signal of descent with modification in the AFA-SEA tradition.

The creationist antievolution movement has reinvented itself not once but twice in the decade since *Kitzmiller*. The first guise was "academic freedom," but after the success of the Louisiana SEA, AFA proposals were almost completely replaced with SEAs. The inclusion of global warming in the SEAs indicates that societal debate over evolution education has the potential to leak into other societal debates where high-quality science education is inconvenient to certain established interests. The passage of SEAs in Louisiana and Tennessee have spread language devised in Ouachita Parish, population ~150,000, to negatively affect science education in two states with ~11.2 million people. Additional policies on the books in other states (table S1) indicate that science educators have substantial work to do to ensure that science classes teach the best science available, rather than false critiques and controversies promoted by creationists. Advocates for science education should not be dissuaded by the strategic vagueness of SEAs: The creationist origins of modern antievolution strategies are clear (table S1), and at least 63 of 65 antievolution bills considered here can be tied directly to creationism through statements in the legislation or by sponsors (SM). ■

REFERENCES AND NOTES

1. C. A. Bleckmann, *Bioscience* **56**, 151 (2006).
2. G. Branch, E. C. Scott, J. Rosenau, *Annu. Rev. Genomics Hum. Genet.* **11**, 317 (2010).
3. N. J. Matzke, in *But Is It Science? The Philosophical Question in the Creation/Evolution Controversy*, M. Ruse, R. T. Pennock, Eds. (Prometheus Books, Amherst, NY, 2009), chap. 20.
4. K. Padian, N. J. Matzke, *Biochemist* **31**, 8 (2009).
5. Mississippi HB214, signed into law in 2006, includes an academic-freedom–style amendment added to an unrelated bill, but the language is too short (just one sentence) to include in the phylogeny.
6. C. J. Howe, H. F. Windram, *PLOS Biol.* **9**, e1001069 (2011).
7. National Center for Science Education, "Academic Freedom" Bills by State & Year (2015); http://ncse.com/creationism/general/academic-freedom-bills-by-state-year.
8. A. Gavryushkina, D. Welch, T. Stadler, A. J. Drummond, *PLOS Comput. Biol.* **10**, e1003919 (2014).
9. A. Gavryushkina *et al.*, arXiv.org:1506.04797 (2015).

ACKNOWLEDGMENTS

Helpful comments were provided by E. Scott, G. Branch, J. Rosenau, E. Meikle, C. Knight, J. Felsenstein, S. Kawano, J. Louys, M. Lawing, and N. Jackson. N.J.M. was supported by NSF awards 0919124, and DBI1300426, and Australian Research Council award DE150101773.

SUPPLEMENTARY MATERIALS

www.sciencemag.org/content/351/6268/28/suppl/DC1

Published online 17 December 2015

10.1126/science.aad4057

ASTROPHYSICS

The screams of a star being ripped apart

A star being devoured by a black hole provides a route to study accretion and jet formation

By **Geoffrey C. Bower**

Closely coupled, ubiquitous, and complex, accretion and outflow are the yin and yang of astrophysics (*1*). The processes occur on all length and time scales, from the formation of the first galaxies in the early universe to the formation of stars in our Milky Way. Compact objects such as white dwarfs, neutron stars, and black holes provide some of the most spectacular examples of these entangled phenomena. Quasars, for instance, are supermassive black holes with masses as large as 10 billion times that of the Sun that lurk in the centers of galaxies and are extraordinarily efficient accretors as revealed through luminous x-ray emission as well as producers of narrowly collimated relativistic jets that can extend millions of light years away from the black hole (see the figure). On page 62 of this issue, van Velzen *et al.* (*2*) report the discovery of a transient relativistic jet flowing from a supermassive black hole system that captured and destroyed a passing star. The discovery further confirms the coupled nature of accretion and outflow. Most important, the discovery shows that these events short-circuit the extraordinarily long evolutionary time scale of quasars, creating a laboratory for the study of accretion and outflow physics.

Since their discovery more than 50 years ago, quasars have provided deep insights into accretion and outflow processes. Accretion appears to occur in a wide variety of states, from highly efficient near the theoretical maximum accretion rate to very inefficient at low accretion rates (*3*, *4*). Outflows appear as both wide-angle winds and narrowly collimated jets. A central phenomenological fact has been the discovery that ~10% of all quasars produce so-called radio-loud jets, in which the radio emission from the relativistic outflow is a substantial fraction of the total accretion energy budget. The spin of the black hole may be a hidden parameter that determines whether accreting systems will launch a relativistic jet. Other evidence points to jets in some systems switching on and off, presumably as the result of changes in the accretion flow.

Unfortunately, much of what is known about accretion and outflow in quasars is circumstantial and derives from studies of the entire population. Evolutionary time scales are typically much, much longer than human lifetimes. For instance, one can't simply study the evolution of a quasar from radio-loud to radio-quiet. Einstein's theory of general relativity shows that all black holes have a minimum time scale determined by the size of a black hole, that is, the Schwarzschild radius, which is linearly proportional to the black hole mass. The minimum time scale is the period of the last stable circular orbit for accreting gas, which is 30 min for the 4×10^6 solar mass black hole in the center of the Milky Way (*5*) and tens of days for the most massive quasars. Quasars, however, have structures that can be millions of times larger than the Schwarzschild radius. Evolutionary time scales are primarily set by the size and dynamics of the gas reservoir supplying the black hole, which can extend to millions of years, as evidenced by the sizes of radio jets (*6*).

Stellar mass black holes have time scales that are millions of times faster than those

Academia Sinica Institute of Astronomy and Astrophysics, Hilo, HI 96720, USA. E-mail: gbower@asiaa.sinica.edu.tw

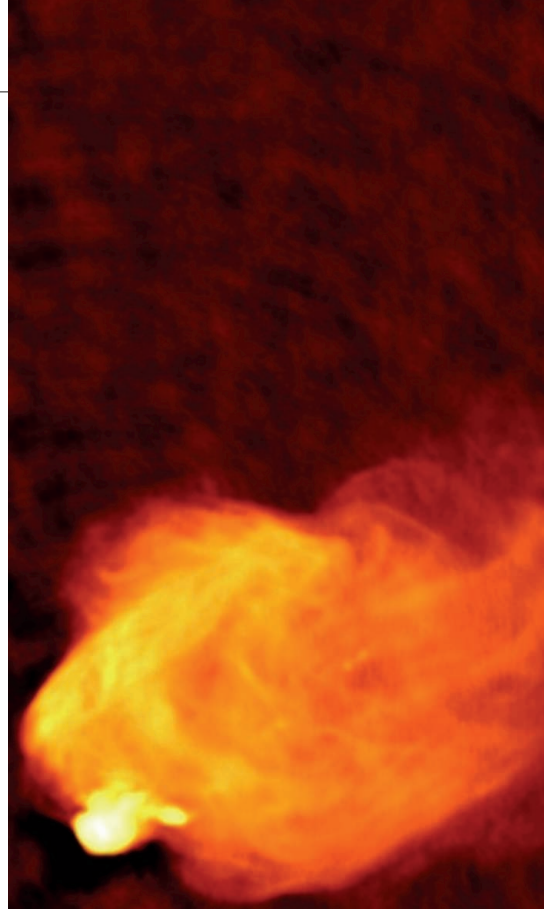

PHOTO: NATIONAL RADIO ASTRONOMY OBSERVATORY

Published by AAAS

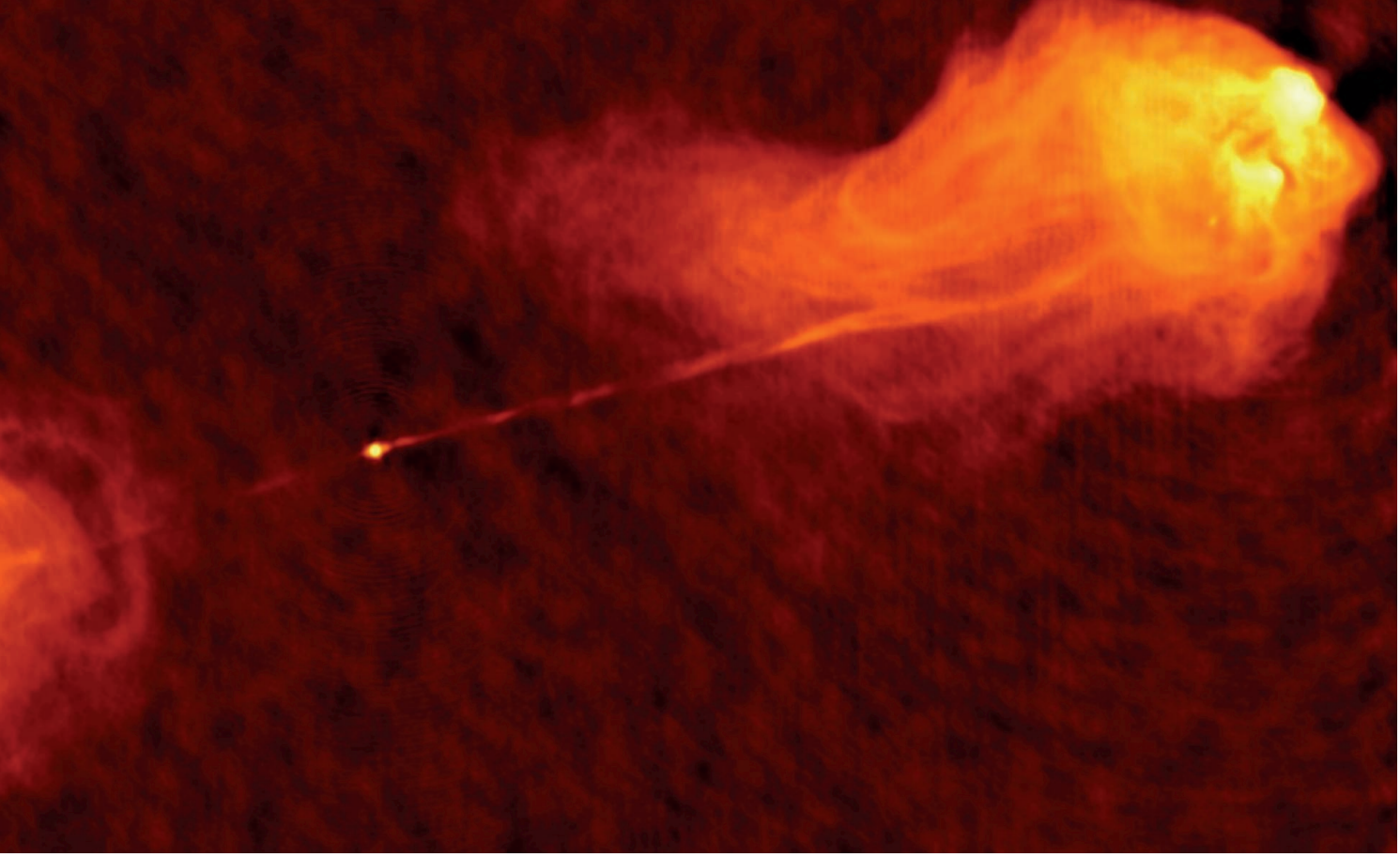

The feast goes on. The powerful radio jet from the quasar Cygnus A is the result of sustained feeding of the black hole. The jets, which emanate from an accretion flow around a massive black hole co-located with the bright spot in the image center and are flowing at velocities close to the speed of light, span a distance far outside the host galaxy and indicate continued activity for at least 0.25 million years. Tidal disruption flares such as the one reported by van Velzen *et al.* (*2*) in ASASSN-14li are the result of a stellar snack that produces similar structures. TDFs, however, evolve on a time scale of days to years, providing a window into the coupled evolution of the accretion flow and relativistic jet. The bright knots at the end of the Cygnus A jets result from a collision with the tenuous gas of the intergalactic medium. In ASASSN-14li, radio emission results from the collision of the jets with denser gas in the nucleus of the host galaxy.

of quasars. These systems are seen to evolve on time scales of hours to days through a set of discrete states in which the nature of the accretion flow determines the presence and activity of a jet (*7*). But such systems are rare and are driven by accretion from a stellar companion, an appreciably distinct environment from that of super massive black hole systems.

Tidal disruption flares (TDFs) exist in a middle ground between quasar and stellar mass black hole evolution. TDFs are events associated with the gravitational disruption of a star making a close passage to a super massive black hole. If a star passes within the tidal radius of a black hole, <100 Schwarzschild radii for a solar-type star, then the differential gravity on the star will rip the star apart (*8*). As the stellar remnant approaches the black hole, its gravitational potential energy is converted into heat through viscous effects. The accretion flow will reach a temperature of 10^5 K and glow brightly at optical, ultraviolet, and x-ray wavelengths for about 100 days.

Van Velzen *et al.* performed sensitive radio telescope observations of a TDF known as ASASSN-14li shortly after its discovery. These observations revealed a luminous and rapidly declining radio source. The radio luminosity cannot be attributed to the accretion flow and so is almost certainly a result of the formation of a relativistic jet flowing out of the system. The rapid and steady decline of the radio luminosity suggests that the jet was created impulsively and then was switched off as the nature of the accretion flow changed. Archival observations indicate that while ASASSN-14li was relatively quiet at optical and x-ray wavelengths, it did harbor a low-power radio source, potentially indicating that the seeds for jet formation existed before the stellar disruption.

Only a handful of other TDFs have shown evidence for jets. Most notably, the source Swift J1644+57 appeared to harbor a jet that was pointed directly toward the Earth, leading to very luminous and highly variable emission (*9*, *10*). The jet in ASASSN-14li is off-axis, that is, beamed away from Earth. As more TDFs with jets are discovered, astronomers can construct a taxonomy of TDFs that resembles the quasar taxonomy and takes into account the many complex variables that couple accretion and outflow: jet orientation, black hole mass and spin, accretion rate, and magnetic field structure.

TDFs are rare, occurring about once every 100,000 years per galaxy (*11*). Typically, they have been found through wide-area optical, ultraviolet, and x-ray surveys that identify bright flashes in the otherwise quiescent nuclei of nearby galaxies (*12*). The results of van Velzen *et al.* suggest that new discoveries may also come from large-area surveys at radio wavelengths. Powerful telescopes such as the Very Large Array, as well as new telescopes optimized for surveys such as the Australian Square Kilometer Array Pathfinder and MeerKAT in South Africa, will have a rich future in searching for TDFs (*13*). ■

REFERENCES

1. M. Livio, *Physics Reports* **311**, 225 (1999).
2. S. van Velzen *et al.*, *Science* **351**, 62 (2016).
3. N. I. Shakura, R. A. Sunyaev, *Astron. Astrophys.* **24**, 337 (1973).
4. F. Yuan, R. Narayan, *Annu. Rev. Astron. Astrophys.* **52**, 529 (2014).
5. R. Genzel *et al.*, *Rev. Mod. Phys.* **82**, 3121 (2010).
6. P. N. Best, T. M. Heckman, *Mon. Not. R. Astron. Soc*, **421**, 1569 (2012).
7. R. P. Fender, T. Belloni, *Annu. Rev. Astron. Astrophys.* **42**, 317 (2004).
8. M. Rees, *Nature* **333**, 523 (1988).
9. A. Zauderer *et al.*, *Nature* **476**, 425 (2011).
10. J. S. Bloom *et al.*, *Science* **333**, 203 (2011).
11. J. Wang, D. Merritt, *Astrophys. J.* **600**, 149 (2004).
12. S. Gezari *et al.*, *Astrophys. J.* **676**, 944 (2008).
13. G. C. Bower, *Astrophys. J. L* **732**, 12 (2011).

10.1126/science.aad5541

Published by AAAS

HUMAN COMPUTATION

The power of crowds

Combining humans and machines can help tackle increasingly hard problems

By **Pietro Michelucci**[1] *and* **Janis L. Dickinson**[2]

Human computation, a term introduced by Luis von Ahn (*1*), refers to distributed systems that combine the strengths of humans and computers to accomplish tasks that neither can do alone (*2*). The seminal example is reCAPTCHA, a Web widget used by 100 million people a day when they transcribe distorted text into a box to prove they are human. This free cognitive labor provides users with access to Web content and keeps websites safe from spam attacks, while feeding into a massive, crowd-powered transcription engine that has digitized 13 million articles from *The New York Times* archives (*3*). But perhaps the best known example of human computation is Wikipedia. Despite initial concerns about accuracy (*4*), it has become the key resource for all kinds of basic information. Information science has begun to build on these early successes, demonstrating the potential to evolve human computation systems that can model and address wicked problems (those that defy traditional problem-solving methods) at the intersection of economic, environmental, and sociopolitical systems.

Like reCAPTCHA, many human computation systems harness the combined efforts of individuals to integrate fast, repetitive work into a single answer. In doing so, they often take advantage of human visual perception, which remains unmatched by machines. Often, small tasks are distributed to many individuals—a method termed microtasking (see the figure, panel A). In one example, 165,000 citizen scientists in 145 countries are using the EyeWire platform to map the three-dimensional structure of retinal neurons. This mapping provides the first glimpse of how the structure and organization of neurons in a mammalian retina function to detect motion (*5*). Visual microtasking is also being used to speed up medical analysis in projects such as MalariaSpot, in which 22 casual gamers count parasites as accurately as a single trained pathologist (*6*).

Microtasking is well suited to problems that can be addressed by repeatedly applying the same simple process to each part of a larger data set (see the figure, panel A), such as stitching together photographs contributed by residents to decide where to drop water during a forest fire. Microtasking alone, however, is inadequate for addressing wicked problems, such as climate change, disease, and geopolitical conflict, which are dynamic, involve multiple, interacting systems, and have nonobvious secondary effects, such as political exploitation of a pandemic crisis. These problems require world knowledge, multistep reasoning, and creative abstraction to illuminate new mitigation strategies. The human computation ecosystems of the future (see the figure, panel C) have huge

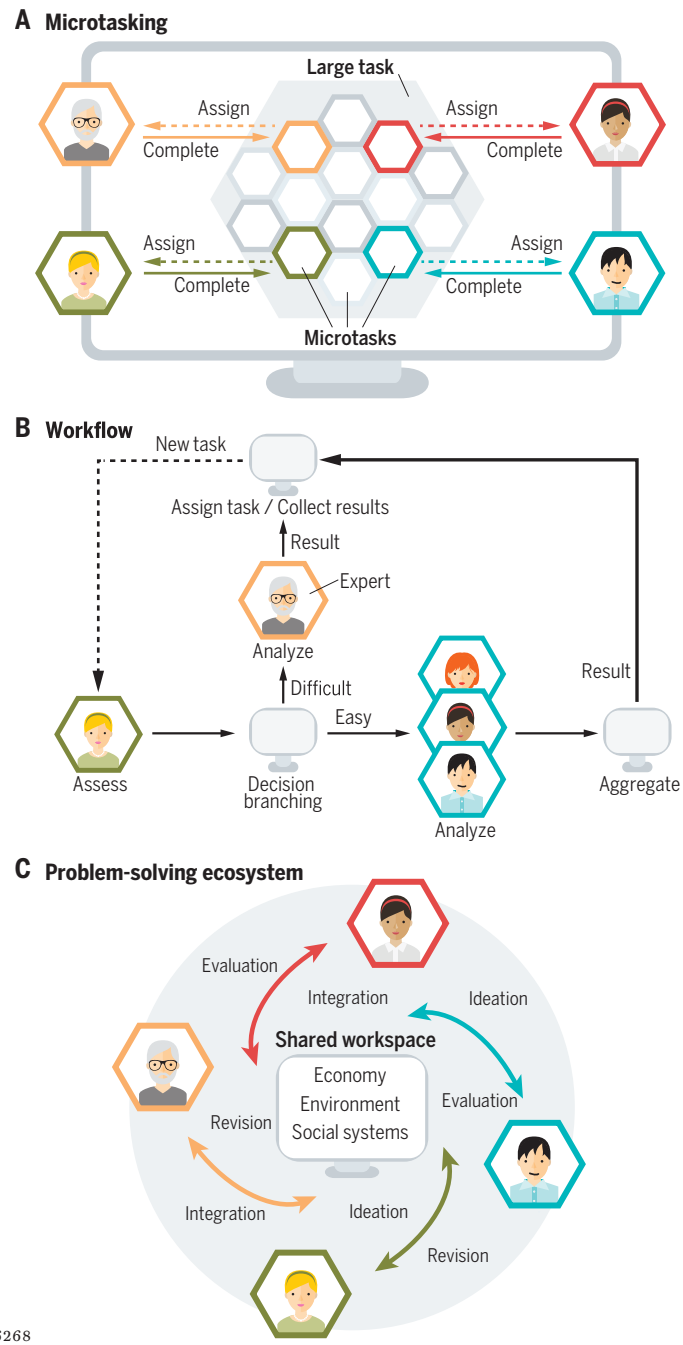

Evolution of human computation systems. (**A**) Crowdsourcing breaks large tasks down into microtasks, which can be things at which humans excel, like classifying images. The microtasks are delivered to a large crowd via a user-friendly interface, and the data are aggregated for further processing. (**B**) Complex workflows funnel crowdworkers into roles such that workers at each step use and augment the information provided by previous workers. (**C**) In creating problem-solving ecosystems, researchers are beginning to explore how to combine the cognitive processing of many human contributors with machine-based computing to build faithful models of the complex, interdependent systems that underlie the world's most challenging problems. Prototypes of these systems provide online workspaces that allow participants to engage in open-ended activities where they contribute, combine, revise, connect, evaluate, and integrate data and concepts within a common analytic framework and, in some cases, prescribe or take actions in the real world. These ecosystems hold promise for responding more effectively to disasters as well as chronic challenges like climate change and geopolitical conflict.

CREDIT: M. GRADY; ADAPTED BY N. CARY/*SCIENCE*

Published by AAAS

potential to help address wicked problems, but are currently being explored in less wicked contexts.

Prototypical examples include the Polymath Project (*7*), which helped prove an 80-year-old mathematical theorem, and ePluribus Problem Solver (*8*), which produced a factually accurate and well-constructed journalistic article based on just a handful of photographs distributed to naïve public participants. In both cases, diverse participants worked in tandem to generate new insights with real-time collective intelligence, rather than first gathering the human-based inputs and then processing them afterwards. This is made possible by enabling participants to work independently, feeding participants novel viewpoints from the community, and allowing for multiple, visible solutions. In the case of the Polymath Project, human contributors adhered to a set of established ground rules, whereas in ePluribus, a computer program and its user interface enforced the ground rules.

Designing increasingly complex systems also requires increased understanding of the human-machine feedback loop. For example, systems can be designed to enhance individual contributions. This is the case for CrowdCrit, which elicits professional-quality critiques of graphics design from the general public. It does this by building domain knowledge into the workflow, so that nonexperts are guided to provide expert-like feedback (*9*).

In CrowdCrit, a computer augments human performance, but the reverse is also possible: Human inputs can be used to guide computers to be more effective, as seen in interactive genetic algorithms, which apply the process of natural selection to evolve new solutions. These algorithms mutate, recombine, and prune candidate solutions to ensure that each successive generation of ideas improves upon the previous one. However, implementing such algorithms for real-world applications often requires contextual knowledge and cognitive capabilities that elude machines. By having humans do the steps that computers cannot do, such as producing, combining, and evaluating ideas, an interactive evolutionary algorithm produced expert-quality solutions for the Gulf of Mexico oil spill (*10*).

Until recently, systems that transcend simple microtasking had to be created from scratch due to a lack of supportive infrastructure. Today, workflow tools have emerged to accelerate development and improve the reliability of human computation systems. The TurKit toolkit, for example, has enabled iterative task delegation (see the figure, panel B) in the generalized crowdsourcing platform Amazon Mechanical Turk, so that contributors can build on each other's work (*11*). Furthermore, QuikTurkit enables real-time crowd responses by prefetching answers before they are needed and queuing multiple jobs at the same time (*12*). These architectural building blocks simplify the development of human computation ecosystems (see the figure, panel C).

"Human computation thus requires a departure from traditional computer science methods..."

In the majority of human computation systems, a small number of participants do most of the work. Given this unusual distribution of effort, we need to improve our understanding of how to maximize recruitment and retention of participants, enhance skill development, and maximize the total effort that participants contribute to projects (*13*). It may be even more challenging to maximize the efficiency with which human inputs, information sharing, and machine-based processing work together. Machines tend to give predictable outputs, such that errors can always be traced to faulty code or design, but humans are less predictable in terms of their availability and the quality of their work.

Human computation thus requires a departure from traditional computer science methods and can benefit from design approaches based on integrated understandings of human cognition, motivation, error rates, and decision theory. Research relating task performance to workflow design and participant experience is sparse; new A-B tests that examine how manipulating such factors can increase performance would increase the predictability of future systems.

Crowdsourcing arose with citizen science as a form of volunteerism, but now spans the gamut from work (paid microtasking) to play (games for good). As more work is done in crowdsourcing environments, we need to consider what this means for the labor force, unemployment rates, and the economy. On the one hand, crowdsourcing provides on-demand labor for companies; however, it is currently outside the purview of labor laws. This must be addressed so that crowdworkers are protected from exploitation.

Some believe that faster computer processing speeds will eventually bridge the gap between machine-based intelligence and human intelligence. However, human computation already affords a tremendous opportunity to combine the respective strengths of humans and machines toward unprecedented capabilities in the short term. It is important that nefarious uses, such as disinformation engineering, in which human computation systems are designed to incite panic, steal information, or manipulate behavior (*14*), are not overlooked. Community-driven guidance concerning transparency, informed consent, and meaningful choice is emerging to address the ethical and social implications of increasingly pervasive and diverse forms of online participation (*15*). Ethical standards can help to ensure that human computation remains humanistic. ■

[1]*Human Computation Institute, Fairfax, VA 22032, USA.*
[2]*Cornell Lab of Ornithology, Cornell University, Ithaca, NY 14850, USA. E-mail: pem@humancomputation.org*

REFERENCES AND NOTES

1. L. von Ahn, thesis, Carnegie Mellon University, Pittsburgh, PA (2005).
2. A. J. Quinn, B. B. Bederson, in *Proceedings of the SIGCHI Conference on Human Factors in Computing Systems* (Association for Computing Machinery, New York, 2011; http://doi.acm.org/10.1145/1978942.1979148), pp. 1403–1412.
3. L. von Ahn, B. Maurer, C. McMillen, D. Abraham, M. Blum, *Science* **321**, 1465 (2008).
4. J. Giles, *Nature* **438**, 900 (2005).
5. J. S. Kim *et al*., *Nature* **509**, 331 (2014).
6. M. A. Luengo-Oroz, A. Arranz, J. Frean, *J. Med. Internet Res*. **14**, e167 (2012).
7. T. Gowers, M. Nielsen, *Nature* **461**, 879 (2009)
8. K. Greene, D. Thomsen, P. Michelucci, *Secur. Inform*. **1**, 12 (2012).
9. K. Luther *et al*., in *Proceedings of the 18th ACM Conference on Computer Supported Cooperative Work; Social Computing* (Association for Computing Machinery, New York, 2015; http://doi.acm.org/10.1145/2675133.2675283), CSCW '15, pp. 473–485.
10. J. V. Nickerson, Y. Sakamoto, L. Yu, in *CHI 2011 Workshop on Crowdsourcing and Human Computation*, M. Bernstein *et al*., Eds. (Association for Computing Machinery, New York, 2011), pp. 1-4.
11. G. Little, L. B. Chilton, M. Goldman, R. C. Miller, in *Proceedings of the ACM SIGKDD Workshop on Human Computation* (Association for Computing Machinery, New York, 2009; http://dl.acm.org/citation.cfm?id=1600159), pp. 29–30.
12. W. S. Lasecki, C. Homan, J. P. Bigham, *Hum. Comput*. 10.15346/hc.v1i1.29 (2014).
13. D. Easley, A. Ghosh, in *Proceedings of the Sixteenth ACM Conference on Economics and Computation* (Association for Computing Machinery, New York, 2015; http://doi.acm.org/10.1145/2764468.2764513), pp. 679–696.
14. D. W. McDonald *et al*., *Interactions* **21**, 72 (2014).
15. A. Bowser, A. Wiggins, *Hum. Comput*. **2**, 19 (2015).

ACKNOWLEDGMENTS

We are grateful to J. P. Bigham, R. J. Crouser, J. Hendler, A. Kittur, W. Lasecki, and T. Malone for insightful comments, and to M. Grady for help with the artwork.

10.1126/science.aad6499

Published by AAAS

CHEMICAL SYNTHESIS

Microbes in a knight's armor

Bacteria studded with nanoparticles produce acetate from carbon dioxide and sunlight

By **Volker Müller**

Demand for bioethanol, biofuels, and other biologically derived commodities is growing worldwide as efforts increase to reduce reliance on fossil fuels and limit climate change (*1*). Most commercial approaches rely on fermentations of organic matter that produce carbon dioxide (CO_2). Microbes that produce such biocommodities from CO_2 and molecular hydrogen (H_2) offer an environmentally friendly alternative. However, the H_2 required for this process is difficult to store and transport and also costs energy to produce. On page 74 of this issue, Sakimoto *et al.* (*2*) report a microbial process that avoids use of H_2. They show how bacteria that normally grow on CO_2 in the dark can be engineered such that they use solar energy to produce a useful chemical product.

The first biofuels were sugar-based and made from renewable carbohydrates; however, this process is in conflict with the production of food for people. Newer biofuels made from lignocellulose do not interfere with the human food chain. However, the production of all these biofuels goes along with the production of CO_2.

These problems are avoided if CO_2 can be used as feedstock (*3*, *4*). Autotrophic organisms such as plants, cyanobacteria, bacteria, and archaea can fix CO_2 and convert it to biomass. Acetate-forming bacteria (acetogens, which live in the dark in the absence of oxygen) can be used in bioreactors to reduce CO_2 with electrons derived from H_2 or carbon monoxide (CO). The resulting products include acetate, ethanol, and larger compounds such as butanol or butyrate (*5*, *6*).

Acetogenic bacteria reduce CO_2 to acetate via the Wood-Ljungdahl pathway (*7*). Among the known pathways for CO_2 fixation, this is the only one that does not consume energy. Instead, it is coupled to the synthesis of cellular energy, thus enabling the organisms to grow. In this pathway, H_2 is oxidized by hydrogenases, electrons are used in CO_2 fixation, and acetate is formed.

The bacteria can also accept electrons from an electrical current on a cathode and grow on the cathode, using anode-derived electrons to reduce CO_2 and form acetate or other products (*8*). These microbial fuel cells can be driven by electrons derived from renewable energies such as wind or solar power. The latter is of particular interest given the essentially limitless availability of solar power. In an integrated bioinorganic photosynthesis approach, a photoanode and photocathode are combined in the same reactor and the CO_2-fixing microbes are grown on the cathode (*9*). A recent publication went a step further by separating the two chambers into an electricity-generating module that feeds electrons into the second module, the microbial fuel cell (*10*, *11*). However, the performance of microbial fuel cells is limited by several factors, such as the ability of microbes to grow on the cathode, electron transfer into the microbial biofilm, and endurance of microbial activity on the cathode. Moreover, the devices are difficult to scale up.

Would it be possible to deliver solar energy to the microbes by a different way in a single reactor? This is what Sakimoto *et al.* describe in their elegant study. They grew the acetogenic bacterium *Moorella thermoacetica* in the presence of cadmium and cysteine, which triggered the production of cadmium sulfide nanoparticles that precipitated on the surface of the bacteria. CdS is a well-suited semiconductor for photosynthesis (*12*). The CdS nanoparticles served as light harvesters; upon illumination, they fed electrons into the bacterial cell, where they were used by the bacteria to reduce CO_2 to acetate. Oxidation of cysteine to cystine replenished the electron pool (see the figure).

Photosynthetic acetate production allowed the bacteria to grow, at least for one doubling of the bacterial population. The product specificity is extremely high, as is the flow of reductants toward the product: Ninety percent of the electrons were directed toward acetate, and acetate was the only product formed. This is a general feature of acetogenic bacteria, making them prime candidates for solar-to-chemical production. Sakimoto *et al.* open up a novel avenue toward this goal.

The report is a proof-of-concept study and, as such, far from the development of applications. For that, production rates have to be improved considerably and the process has to be scaled up. In addition, the range of products made by acetogens is narrow. *M. thermoacetica* only produces acetate; other acetogens capable of electrosynthesis also produce ethanol (*13*, *14*). However, increasing understanding of the biochemistry and bioenergetics of acetogens and the development of genetic tool boxes will allow metabolic engineering of acetogens, increasing the range of products that could be produced from CO_2 and sunlight, a very green method of chemical synthesis. ■

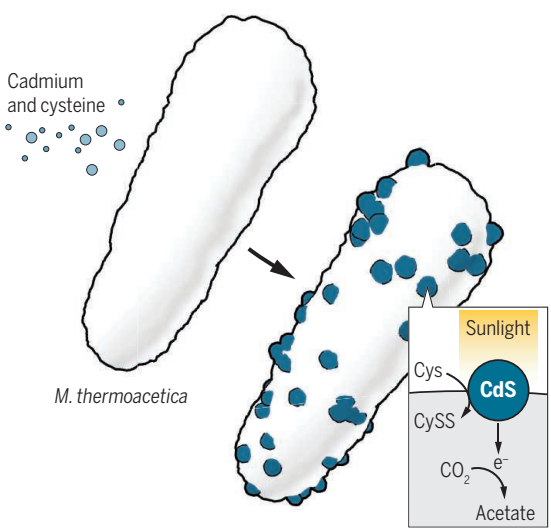

Acetogens see the light. Sakimoto *et al.* show that the anaerobic acetogenic bacterium *M. thermoacetica* can convert cadmium and cysteine to insoluble CdS, which precipitates on the cell surface. Upon illumination, the CdS particles liberate electrons that are fed into the bacteria and are used to reduce CO_2 to acetate. This process is coupled to energy conservation and microbial growth.

Department of Molecular Microbiology and Bioenergetics, Institute of Molecular Biosciences, Goethe University Frankfurt am Main, Frankfurt am Main, Germany. E-mail: vmueller@bio.uni-frankfurt.de

REFERENCES

1. N. Stern, *The Economics of Climate Change* (Cambridge Univ. Press, New York, 2007).
2. K. K. Sakimoto, A. B. Wong, P. Yang, *Science* **351**, 74 (2016).
3. M. Meinshausen *et al.*, *Nature* **458**, 1158 (2009).
4. J. Goldemberg, *Energy Policy* **34**, 2185 (2006).
5. F. R. Bengelsdorf, M. Straub, P. Dürre, *Environ. Technol.* **34**, 1639 (2013).
6. J. Bertsch, V. Müller, *Biotechnol. Biofuels* **8**, 210 (2015).
7. K. Schuchmann, V. Müller, *Nat. Rev. Microbiol.* **12**, 809–821 (2014).
8. K. P. Nevin *et al.*, *mBio.* **1**, e00103-10 (2010).
9. C. Liu *et al.*, *Nano Lett.* **15**, 3634 (2015).
10. E. M. Nichols *et al.*, *Proc. Natl. Acad. Sci. U.S.A.* **112**, 11461 (2015).
11. T. Zhang, *Science* **350**, 738 (2015).
12. R. Vogel, P. Hoyer, H. Weller, *J. Phys. Chem.* **98**, 3183–3188 (1994).
13. K. P. Nevin *et al.*, *Appl. Environ. Microbiol.* **77**, 2882–2886 (2011).
14. R. S. Tanner, L. M. Miller, D. Yang, *Int. J. Syst. Bacteriol.* **43**, 232-236 (1993).

10.1126/science.aad8593

ILLUSTRATION: V. ALTOUNIAN/*SCIENCE*

Published by AAAS

HISTORY OF SCIENCE

Myth busters

Think you know your scientific history? Think again.

By **Jim Endersby**

Newton's Apple and Other Myths About Science
Ronald L. Numbers and Kostas Kampourakis, Eds.
Harvard University Press, 2015. 303 pp.

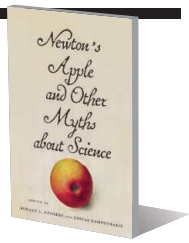

Before Columbus discovered America, people believed that the world was flat. When the apple struck Newton's head, he discovered gravity and replaced God with objective truth. Gregor Mendel was a lone genius who discovered genetics. The launch of Sputnik shook the United States into radically reforming science education.

You will probably have heard at least some of these stories—you may even have believed them—but this delightful collection of short, thought-provoking essays shows that they are all myths. The flat-Earth idea, for example, became popular after Washington Irving (of "Rip Van Winkle" fame) wrote a popular biography of Columbus in 1828, which maintained that Columbus had offered definitive proof that Earth was round. Lesley Cormack notes in her essay that many still equate "rotundity with modernity," readily accusing reactionaries of being flat-Earthers, despite the fact that the spherical nature of Earth has actually been accepted since classical times. In fact, as Cormack notes, there is even evidence that the scholars charged with advising the Spanish monarchy used Earth's spherical shape against Columbus, arguing that its circumference was much larger than he claimed and that the trip would take much longer to complete than he anticipated.

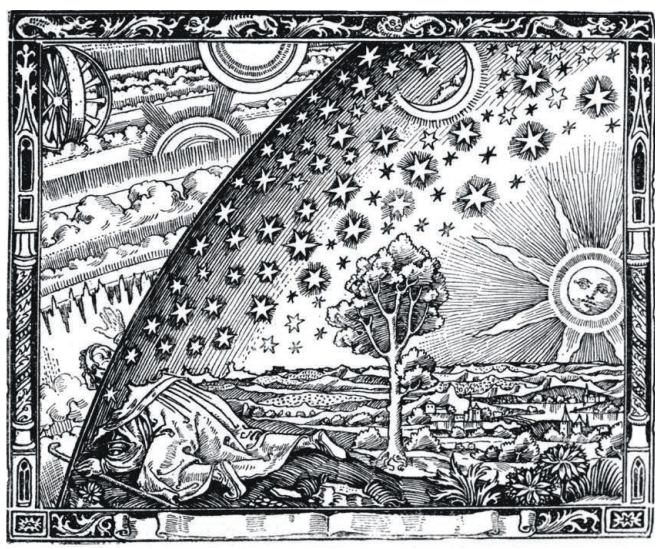

The flat-Earth theory was rejected long before Columbus sailed the ocean blue.

Newton's Apple is full of stories like this. Some will be unexpected, others rather too familiar, but every reader should find something to surprise them. For example, Adam Shapiro shows that modern scholars are mistaken in thinking that Charles Darwin refuted the theological argument for design outlined by William Paley in 1802 in his book *Natural Theology*. Even though this topic is close to my own research (and I already knew it wasn't true), Shapiro managed to surprise me. Paley's celebrated argument proposed that organisms are like artifacts, intelligently planned to achieve specific purposes, such as surviving and reproducing. However, his arguments weren't scientific, they were religious. "Paley didn't invoke God to explain nature," argues Shapiro, "he invoked nature to explain God." What he meant by "design" was that the ways living things were constructed was proof of God's benevolence. As a result, the world was saturated with purpose and thus, from a human perspective, with meaning. Shapiro not only shows this clearly and elegantly but does so in just seven pages!

Inevitably, not every essay is this successful. Some are too short to be persuasive or deal with "myths" that are too diffuse to be debunked in the available space. For example, in one piece, Ron Numbers sets out to demolish the idea that social Darwinism was a major influence on American social theory during the late 19th and early 20th centuries. He offers a lot of interesting evidence, noting, for example, how seldom the phrase "social Darwinism" was actually used by politicians, businessmen, racists, and others during this period. Yet, the chapter doesn't quite persuade, perhaps because when an idea is really widespread, its tenets are taken for granted by many who are unaware of their origins and, therefore, unlikely to reference the original theory. For example, today's genetic determinism includes the popular view that there are "genes for" all manner of specific human traits and that those traits cannot be readily altered. Such ideas have clearly been ubiquitous in recent years, yet if one were to search the works of politicians, journalists, or advertisers for references to Watson and Crick, it's unlikely that such citations would be found.

Few of the chapters reflect explicitly on why myths become myths, but in the superb concluding essay, Michael Gordin does this in the process of debunking the widely accepted belief that science can be easily differentiated from pseudoscience simply by determining whether a particular theory is falsifiable. In addition to the philosophical shortcomings of this approach, he notes that if a negative result is sufficient to falsify a theory, then high-school science students manage to "falsify" most of Western science each week in their lab classes. Gordin goes on to analyze why this particular idea rose to such prominence in the 1980s. When various U.S. states legislated that creationism get equal time in school science classes, it became politically urgent to define why creation "science" was nothing of the kind. Part of the appeal of the falsification axiom (if it could never be disproved, it can't be science) was that it was simple enough for nonscientists to grasp. Yet, when we look at history, falsification simply does not work as a definition of science. As Gordin explains, most historians and scientists accept a sociological definition: Science is what the scientific community says it is (e.g., peer-reviewed work in reputable journals). It's not a perfect definition, nor a stable one, but it has the virtue of being the one by which scientists actually operate. Debunking myths is fun, but it's even more fun when, as Gordin does, the debunker gives you a sense of why some ideas become myths in the first place.

The reviewer is in the School of History, Art History, and Philosophy, University of Sussex, Brighton BN1 9RH, UK. E-mail: j.j.endersby@sussex.ac.uk

10.1126/science.aad2891

PHOTO: CAMILLE FLAMMARION, L'ATMOSPHERE: METEOROLOGIE POPULAIRE

Published by AAAS

CANCER

Winning the war

An insider's guide to the politics and personalities of America's war on cancer

By **Adrian Woolfson**

On 26 December 1971, President Richard Nixon authorized a preemptive strike against a military stockpile in North Vietnam, comprising a 5-day bombing campaign known as Operation Proud Deep Alpha. Only 3 days earlier, he had announced the initiation of another type of war. The conflict this time was not against a foreign ideology or nation but rather against the corrupt and malign processes of human biology that transform healthy cells into unwelcome pathological strangers bent on undermining our existence—an initiative that came to be known as the war on cancer. In this engaging, provocative, and deeply personal book, Vincent DeVita and Elizabeth DeVita-Raeburn provide a compelling insider's guide into the personalities, organizations, and key protagonists that provided the backdrop and impetus for this unprecedented campaign.

Vincent DeVita is well positioned to tell the story of the war on cancer, having served as director of the National Cancer Institute (NCI), physician-in-chief at Memorial Sloan Kettering, and director of the Yale Cancer Center. As a physician, he has devoted his life to caring for cancer patients. As a clinical researcher, he helped develop the concept of combination chemotherapy, which transformed the treatment of human cancers and led to a cure for Hodgkin's lymphoma and diffuse large B-cell lymphoma. He has also experienced malignancy firsthand, having been diagnosed with prostate cancer in 2009.

The book, cowritten with his daughter, Elizabeth, provides a detailed account of the pioneering days of chemotherapy at NCI, including some insightful and, at times, remarkably unflattering accounts of some of the major players in early cancer research. It also includes stories of DeVita's relentless and thoughtful attempts to identify appropriate experimental therapies for his friends, family, and patients, as well as an assorted collection of irreverent and humorous anecdotes.

The Death of Cancer presents a candid and disarming critique of the ways in which medicine, and specifically oncology, is regulated in the United States. DeVita believes that, in some instances, burdensome restrictions have delayed the timely delivery of potentially efficacious medicines to those in desperate need. In his view, the current approval process has also led to an overreliance on randomized clinical trials that may be unnecessary when an experimental agent has already demonstrated overwhelming evidence of efficacy. The insistence on using survival end points in studies on patients with advanced disease may also, he maintains, result in efficacy signals being overlooked.

The book contrasts the bureaucracy associated with contemporary clinical trials with the "war room" days of early chemotherapy, when clinical study protocols could be adjusted in real time according to emerging data. DeVita justifies the need for more flexibility on the basis that individuals facing imminent death have an entirely different relationship to risk. Such individuals, he argues, are more likely to be amenable to the possibility of significant toxicities if there is a potential for prolonged survival.

We are currently in the process of navigating a remarkable new era in which the targeted small molecules and engineered biologics that have enhanced, and in some instances superseded, conventional chemotherapy are being eclipsed by the remarkable results achieved with immunotherapy. Therapeutic advances in the form of checkpoint inhibitors, immune agonists, vaccines, and cellular therapies such as chimeric antibody receptor T and NK cells have been accompanied by next-generation genome-sequencing technologies and biomarker platforms that offer the promise of personalized medicine.

Given the dramatic pace of new discoveries in cancer medicine and the extraordinary results achieved with immunotherapeutic agents, the authors are correct when they assert that we don't need to identify the magic bullet to cure cancer immediately. We simply need to develop treatments, combinations, and schedules capable of keeping patients alive long enough to benefit from the next generation of breakthrough agents.

DeVita's infectious enthusiasm and unshakable belief that cancer will soon become a thing of the past provide both an inspiration and a glimpse into the future, when, like many infectious diseases before them, common cancers are likely to be trivialized. However, the achievement of this goal, he argues, is likely to depend on the development of a more flexible and innovative technical and regulatory framework for clinical trials that facilitates the rapid and adaptive targeting of multiple cancer nodes simultaneously.

10.1126/science.aad3526

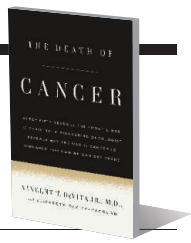

The Death of Cancer
Vincent T. DeVita Jr. and *Elizabeth DeVita-Raeburn*
Sarah Crichton Books, 2015. 349 pp.

MATHEMATICS

Patterns of the Universe
A Coloring Adventure in Math and Beauty
Alex Bellos and Edmund Harriss
The Experiment, 2015. 145 pp.

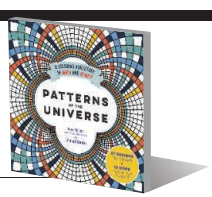

Coloring books, once relegated to the 12-and-under set, have enjoyed a recent surge in popularity among adults. Joining the growing market of coloring products for grown-ups, *Patterns of the Universe* presents 65 striking black-and-white illustrations designed to introduce doodlers to a range of challenging mathematical principles. From the geometry of crystals to the undulating waves created by a Fourier transform to the intricate design of the Mandelbrot set, the elegant patterns are accompanied by brief, accessible explanations of the underlying mathematics.

10.1126/science.aad9853

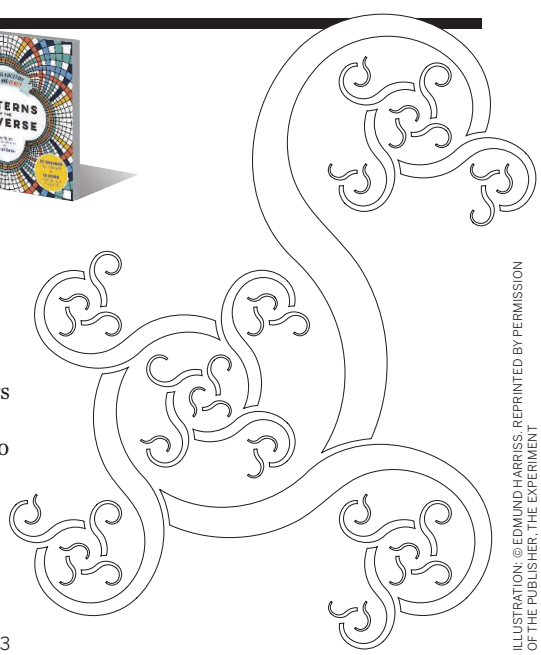

ILLUSTRATION: © EDMUND HARRISS. REPRINTED BY PERMISSION OF THE PUBLISHER, THE EXPERIMENT

The reviewer is the author of The Intelligent Person's Guide to Genetics *(Overlook TP, New York, 2006). E-mail: adrianwoolfson@yahoo.com*

Published by AAAS

RESEARCH

An epigenic switch controls caste behavior in carpenter ants

Simola et al., *p. 42*

IN *SCIENCE* JOURNALS

Edited by **Stella Hurtley**

Polymer-derived ceramic lattices exhibit high thermal shock resistance and low thermal conductivity

THREE-DIMENSIONAL PRINTING

Printing ceramics into complex shapes

Some materials, such as thermoplastics and metals, are naturally suited to being 3D printed because the individual particles can be fused together by applying heat. In contrast, ceramics do not fuse together the same way. Eckel *et al*. developed a way to pattern specific preceramic monomers using either 3D printing or stereolithography into complex, curved, and porous shapes. Upon heating, they observed almost no shrinkage, and the formed parts showed exceptional thermal stability. — MSL

Science, this issue p. 58

VIROLOGY

Coronaviruses in the Middle East

Middle East respiratory syndrome coronavirus (MERS-CoV) causes severe acute respiratory illness and kills about a third of people infected. The virus is common in dromedary camels, which can be a source of human infections. In a survey for MERS-CoV in over 1300 Saudi Arabian camels, Sabir *et al*. found that dromedaries share three coronavirus species with humans. Diverse MERS lineages in camels have caused human infections, which suggests that transfer among host species occurs quite easily. Haagmans *et al*. made a MERS-CoV vaccine for use in camels, using poxvirus as a vehicle. The vaccine significantly reduced virus excretion, which should help reduce the potential for transmission to humans, and conferred cross-immunity to camelpox infections. — CA

Science, this issue p. 81, p. 77

GENOME EDITING

Making the correct cut

The CRISPR/Cas system is a prokaryotic immune system that targets and cuts out foreign DNA in bacteria. It has been adopted for gene editing because it can be designed to recognize and cut specific locations in the genome. A challenge in developing clinical applications is the potential for off-target effects that could result in DNA cleavage at the wrong locations. Slaymaker *et al*. used structure-guided engineering to improve the specificity of *Streptococcus pyogenes* Cas9 (SpCas9). They identified enhanced-specificity variants (eSpCas9) that display reduced off-target cleavage while maintaining robust on-target activity — VV

Science, this issue p. 84

PROTEIN TRANSLOCATION

Seeing the signal sequence in action

Protein translocation across the endoplasmic reticulum (ER) involves the interaction of a signal sequence with the protein translocation channel. Although much work has looked at the details of protein translocation, questions remain. Voorhees and Hegde present a single-particle cryoelectron microscopy study of the mammalian ER translocation apparatus at the point in which the signal sequence is engaging the translocation pore. — SMH

Science, this issue p. 88

ORGANIC CHEMISTRY

A two-for-one twist on Suzuki coupling

The Suzuki-Miyaura coupling reaction is one of the most widely used ways of making carbon-carbon bonds. Essentially,

PHOTO: 2015 HRL LABORATORIES – PHOTO BY DAN LITTLE PHOTOGRAPHY

Published by AAAS

a palladium catalyst activates one carbon fragment and then links it to a second fragment pulled from boron. Zhang *et al*. now demonstrate a twist on the conventional pathway (see the Perspective by Fyfe and Watson). In their system, the palladium initially coaxes together two carbon fragments on one boron center. Then the catalyst stitches a second C-C bond to a third, external fragment. A chiral ligand renders the reaction highly enantioselective. — JSY

Science, this issue p. 70; see also p. 26

PHOTOVOLTAICS

Efficient luminescent solar cells

Shine on! Bi *et al.* fabricated a perovskite-based solar cell that can create extraordinarily high solar-to-electric power conversion and intense electroluminescence. The new-fangled cells should help to produce solar technologies that approach the upper limit for open-circuit voltage. These devices are likely to be competitive with "state-of-the-art" conventional solar technologies and may be used in tandem with more traditional solar cells. — ZHK

Sci. Adv. 10.1126.sciadv.01170 (2016).

CARDIOLOGY

Disruptive technology

Healthy hearts beat synchronously; failing hearts often lose this coordination. Normally, pacemakers are used to reset the heart's rhythm. Kirk *et al.* used pacemakers to restore synchrony by inducing periods of abnormal rhythm—called pacemaker-induced transient asynchrony (PITA). In dogs with heart failure, PITA halted heart chamber dilation and negative remodeling of heart tissue. It also improved cell signaling and force generation, and supported normal muscle fiber structure and function. Some people with pacemakers do not respond to standard resynchronization protocols; PITA could offer them the possibility of restoring rhythm. — MLF

Sci. Transl. Med. **7**, 319ra207 (2015).

BLACK HOLE PHYSICS

Transient radio jet from a black hole

When a star passes too close to a supermassive black hole, it gets ripped apart by the gravitational forces. This causes a tidal disruption flare as the material falls into the black hole. van Velzen *et al*. monitored one such flare with radio telescopes and found evidence for a transient relativistic jet launched by the black hole (see the Perspective by Bower). Larger jets are a feature of active galactic nuclei and have a profound effect on their host galaxy, but are poorly understood. The results will aid our understanding of how black holes "feed" and of the processes governing jet formation. — KTS

Science, this issue p. 62; see also p. 30

MICROBIAL ENGINEERING

Using light in the darkness

Solid-state devices can efficiently capture solar energy to produce chemicals and fuels from carbon dioxide. Yet biology has already developed a high-specificity, low-cost system to do just that through photosynthesis. Sakimoto *et al*. developed a biological-inorganic hybrid that combines the best of both worlds (see the Perspective by Müller). They precipitated semiconductor nanoparticles on the surface of a nonphotosynthetic bacterium to serve as a light harvester. The captured energy sustained cellular metabolism, producing acetic acid: a natural waste product of respiration. — NW

Science, this issue p. 74; see also p. 34

IN OTHER JOURNALS

Edited by **Kristen Mueller** *and* **Jesse Smith**

NEUROSCIENCE

How brains get the full picture

The visual system helps organisms make sense of their world. A network of brain areas called face patches helps monkeys identify other individuals and interpret their behavior. Fisher and Freiwald wanted to determine whether these regions only interpret face information or if they integrate body information, too. They scanned the brains of monkeys that were shown faces, bodies, faces on bodies, or faces on nonbody objects. Posterior face patches and adjacent body patches recognized faces and bodies, respectively. However, these networks could integrate face and body information to represent whole monkeys in the anterior face patches. Thus, the brain combines visual information from distinct but related objects to help organisms understand their social world. — PRS

Proc. Natl. Acad. Sci. U.S.A. **112**, 14717 (2015).

BIOCHEMISTRY

More than one way to target a protein

The primary function of many proteins involves binding to another protein or small molecule. In some cases, however, a second molecule interacting with a distinct site on the protein regulates this primary binding. To identify such functional secondary sites, Ludlow *et al*. used x-ray crystallography to screen a library of molecules to detect binding to 24 protein targets. Two-thirds of the proteins had at least two binding sites. Sequence analysis of secondary sites showed that most were evolutionarily conserved, suggesting biological function. Moreover, their physicochemical properties indicated that secondary sites may be druggable. Targeting these sites could provide a way to increase protein activity in a therapeutically advantageous manner. — VV

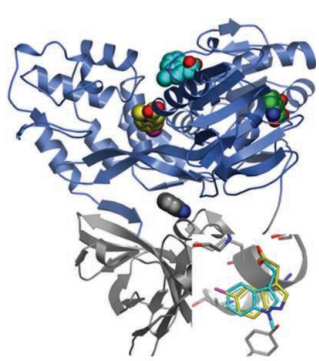

Proteins have multiple binding sites that may contribute to their regulation

CREDIT: LUDLOW *ET AL*., PNAS (9 NOVEMBER 2015) © NATIONAL ACADEMY OF SCIENCES

Proc. Natl. Acad. Sci. U.S.A. 10.1073/pnas.1518946112 (2015).

MITOCHONDRIA

The Drp, Drp, Drp of mitochondrial fission

Mitochondria are very dynamic organelles and undergo regular fusion and fission reactions. Fission involves the dynamin GTPase Drp1, a cytosolic enzyme that is recruited to mitochondria, where it oligomerizes and contracts to cause

Published by AAAS

The brains of monkeys integrate face and body information to interpret social situations

the mitochondrial membrane to constrict. Ji *et al*. studied Drp1 dynamics in live cells. Contrary to current models, fission sites did not directly recruit Drp1 from the cytoplasm. Instead, mitochondria progressively added Drp1 molecules to form oligomers. Most mature Drp1 oligomers did not mediate fission. When the authors experimentally induced mitochondrial fission, actin and Drp1 accumulated sequentially at specific mitochondrial fission sites. Thus, the assembly of fission-productive Drp1 oligomers involves recruitment, maturation, and actin-dependent conversion. — SMH

eLife 10.7554/eLife.11553 (2015).

NEURODEVELOPMENT

Asymmetrical circuits reduce anxiety

Although fish are overall bilaterally symmetrical, the devil is in the details. For instance, in zebrafish, a part of the forebrain called the epithalamus exhibits asymmetry. However, this orientation is reversed in the brains of a small percentage of zebrafish. Facchin *et al*. asked whether this matters to the fish. They found that fish with brains of the minority configuration showed signs of increased anxiety when compared to their majority-configuration siblings. But their brains were not simply flipped. Within the epithalamus, neuronal axons projected in unusual patterns. The results suggest that asymmetries in how the brain processes rewards and aversions may favor neuronal circuits to organize in one way over another. — PJH

J. Neurosci. **35**, 15847 (2015).

Brain asymmetry regulates anxiety in zebrafish

EDUCATION

Peer + peer = increased learning

In math education, the definition of "cooperative learning" is greater than the sum of these two words. Reinholz describes peer-assisted reflection (PAR) in an introductory calculus class, where students work together to attempt to solve a problem, reflect on their work, conference with a peer, and revise and submit a final solution. PAR emphasizes problem-solving processes, including explanation and justification, similar to an inquiry-based science class. The PAR model stresses peer interaction, with students analyzing their peers' work in order to develop analytic skills that they can then apply to their own learning. Student success through PAR was significant and comparable to similar active learning interventions in STEM (science, technology, engineering, and mathematics) courses. Most importantly, PAR resulted in students being less likely to drop introductory calculus. — MM

Int. J. Res. Undergrad. Math. Ed. 10.1007/s40753-015-0005-y (2015).

BIOMATERIALS

Biogenic tools for single-cell surgery

Miniaturization has created a world of new medical tools, from pill-cams that can be swallowed and used to photograph the digestive tract, to tiny robots used for minimally invasive surgery. Srivastava *et al.* pursued this to the level of operating on single cells through the creation of microdaggers. They started with microneedles extracted from plants that are composed of porous calcium oxalate and calcium carbonate. Coating the microneedles with a layer of iron and titanium allowed their manipulation by means of a magnetic field. The tip of the microdagger could drill into a cell, and the porous nature of the needles should make it possible to preload them to deliver drugs to individual cells. — MSL

Adv. Mat. 10.1002/adma.201504327 (2015).

ORGANIC CHEMISTRY

An asymmetric route to amino alcohols

Amines and alcohols are among the most common and versatile functional groups in organic chemistry. The nitroso variant of the Diels-Alder reaction is a convenient means of introducing both to the same molecule. Both ends of the N=O group form a bridge between the outer carbons in a C=C–C=C diene motif, after which the lingering N–O bond can be severed. Maji and Yamamoto present a highly selective asymmetric variant of this reaction, catalyzed by a copper complex bearing a chiral diphosphine ligand. The reaction couples a range of cyclic dienes with nitroso pyrimidines and pyridazines. — JSY

J. Am. Chem. Soc. 10.1021/jacs.5b11273 (2015).

PHOTO: (FROM TOP) © ANUP SHAH/MINDEN PICTURES/CORBIS; MARK SMITH/SCIENCE SOURCE

Published by AAAS

ALSO IN *SCIENCE* JOURNALS

Edited by **Stella Hurtley**

ANTIBIOTIC RESISTANCE

Evolving antibiotic rescue stratagems

Antibiotic resistance threatens to put modern medicine into reverse. But we are not at the end of our options for currently available drugs. Baym *et al*. review what can be done by using combinations of antibiotics to circumvent bacteria's evolutionary strategies. For instance, resistance to one drug may cause sensitivity to another, the effectiveness of two drugs can be synergized by a resistance mutation, and some negative drug interactions may even be beneficial in selecting against resistance. Although not simple to assess, drug combinations still have something to offer for the development of sorely needed anti-infectives. — CA

Science, this issue p. 40

NEURAL CIRCUITS

A way to modulate reward-seeking

Which brain regions are causally involved in reward-related behavior? Ferenczi *et al*. combined focal, cell type–specific, optogenetic manipulations with brain imaging, behavioral testing, and in vivo electrophysiology (see the Perspective by Robbins). Stimulation of midbrain dopamine neurons increased activity in a brain region called the striatum and was correlated with reward-seeking across individual animals. However, elevated excitability of an area called the medial prefrontal cortex reduced both striatal responses to the stimulation of dopamine neurons and the behavioral drive to seek the stimulation of dopamine neurons. Finally, modulating the excitability of medial prefrontal cortex pyramidal neurons drove changes in neural circuit synchrony, as well as corresponding anhedonic behavior. These observations resemble imaging and clinical phenotypes observed in human depression, addiction, and schizophrenia. — PRS

Science, this issue p. 41; see also p. 24

BEHAVIORAL GENETICS

Epigenetic control of caste-specific foraging

In carpenter ants, separate behavioral classes, known as castes, are determined by the epigenetic regulation of genes. Simola *et al*. treated ants of different castes with drugs that affected histone acetylation. Reducing histone acetylation stimulated scouting and foraging behavior. The foraging and scouting behaviors of young ants were permanently changed by directly injecting their brains with histone acetylation inhibitors. — LMZ

Science, this issue p. 42

METABOLISM

From sensing leucine to metabolic control

The mTORC1 protein kinase complex plays central roles in regulating cell growth and metabolism and is implicated in common human diseases such as diabetes and cancer. The level of the amino acid leucine tells an organism a lot about its physiological state, including how much food is available, how much insulin is going to be needed, and whether new muscle mass can be made (see the Perspective by Buel and Blenis). Wolfson *et al*. identified a biochemical sensor of leucine, Sestrin2, which connects the concentration of leucine to the control of organismal metabolism and growth. When leucine bound to Sestrin2, it was released from a complex with the mTORC1 regulatory factor GATOR2, activating the mTORC1 complex. Saxton *et al*. describe the crystal structure of Sestrin2 and show how it specifically detects leucine. Aylett *et al*. determined the structure of human mTORC1 by cryoelectron microscopy and the crystal structure of a regulatory subunit, Raptor. The results reveal the structural basis for the function and intricate regulation of this important enzyme, which is also a strategic drug target. — LBR

Science, this issue p. 43, p. 48, p. 53; see also p. 25

ASTROCHEMISTRY

Water isomers hide their origin

H_2O exists in two spin isomers, ortho and para, in a ratio of 3:1 at room temperature. Some astronomical observations have found water with a ratio of less than 3, thought to be due to water being photodesorbed from ice that had been formed at very low temperatures (≲30 K). Hama *et al*. tested this idea in the laboratory, by forming water ice at low temperature and then photodesorbing it to measure the ortho:para ratio. They found a ratio of 3, even at 10 K. Thus, another explanation for the low ratios in some astronomical objects must be found. — KTS

Science, this issue p. 65

MEMBRANES

Separating H^+ from D^+

In many respects, hydrogen and deuterium show similar properties because they share the same number of protons and electrons and only differ by one neutron. However, when you strip away the electron, a proton ends up having less than half the radius of a deuterion. Lozada-Hidalgo *et al*. used two-dimensional membranes of graphene or hexagonal boron nitride to separate these two charged isotopes, with a separation factor of about 10. — MSL

Science, this issue p. 68

COMPUTER SCIENCE

Computing power of crowds

Every time a person transcribes distorted text to prove that they are human and gain access to a web page, they contribute to a massive effort to digitize books and newspapers. This is just one of many human computation systems that take advantage of the strengths of both humans and computers. In a Perspective, Michelucci and Dickinson chart recent progress in developing sophisticated human computation systems that can address complex economic, medical, and environmental problems. Human visual perception remains unmatched by machines, but humans are less predictable. Human computation developers must therefore take account of research into human cognition and decision-making. — JFU

Science, this issue p. 32

CANCER

Pathway activity as a biomarker

Understanding signaling networks may enable the prediction of disease prognosis. Fey *et al*. constructed a computational model that reproduces the all-or-nothing, switch-like activation of the kinase JNK in neuroblastoma (see also the Focus by Kim and Schoeberl). Switch-like activation of JNK leads to cell death. The authors integrated patient data about the levels of JNK pathway components in neuroblastoma samples into the model, to simulate the activity of the pathway and accurately predict survival based on the dynamic properties of the pathway. Alterations in the network that prevented the switch-like activation of JNK were associated with poor survival of neuroblastoma patients. — NRG

Sci. Signal. **8**, ra130 and fs21 (2015).

Published by AAAS

REVIEW SUMMARY

ANTIBIOTIC RESISTANCE

Multidrug evolutionary strategies to reverse antibiotic resistance

Michael Baym,* Laura K. Stone,* Roy Kishony†

BACKGROUND: Antibiotics are among the most important tools in medicine, but their efficacy is threatened by the evolution of resistance. Since the earliest days of antibiotics, resistance has been observed and recognized as a threat; today, many first-generation drugs are all but ineffective. The paradox of antibiotics is that through their use, they not only inhibit an infection but also select for the emergence and spread of resistance, directly counteracting their long-term efficacy. We have thus far avoided a crisis through the continued modification of existing compounds and the discovery of new antibiotic classes. It has been hoped that restricting the use of particular antibiotics would neutralize the selective advantage of resistance and restore widespread sensitivity over time; however, decades of experience have shown that resistance does not disappear so easily. The same is true for combining antibiotics with compounds that inhibit their specific resistance mechanisms; this approach is effective in potentiating and broadening the spectrum of antibiotics, but it only neutralizes the advantage of resistant bacteria and does not actively select against resistance over time. To prevent the evolution of resistance or turn a resistant population susceptible again, we need ways to fully invert the selective advantage of resistance.

ADVANCES: Recent discoveries have shown that it is possible to invert the selective advantage of resistant bacteria and reverse the evolution of antibiotic resistance. Whereas with single-drug therapy, there is always a selective advantage to resistance, specific combinations of drugs can inhibit bacterial growth while disfavoring resistance to the individual components. To confer a direct disadvantage to resistant mutants, techniques have been developed that exploit the specific physiological and evolutionary interactions between drugs. First, if one drug partially suppresses the effect of another, becoming resistant to the first drug will remove its protection against the second, giving a disadvantage to the resistant mutants. Second, mutations that confer resistance to a drug can be counteracted if they induce synergy between the drug and another compound. Finally, there can be trade-offs between resistances to different compounds such that resistance to one antibiotic causes collateral sensitivity to another antibiotic or to a compound whose toxicity is mediated by the resistance mechanism. These approaches can be used to invert the selective advantage of resistant bacteria competing with their sensitive cousins and can potentially decrease the rate at which resistance evolves, or even drive a resistant bacterial population back toward drug sensitivity.

ON OUR WEB SITE

Read the full article at http://dx.doi.org/10.1126/science.aad3292

OUTLOOK: Substantial barriers remain for the clinical application of selection-inverting treatment strategies. Antibiotic treatment decisions must typically be made within minutes, whereas the isolation and analysis of an infection take between hours and days, even with state-of-the art technology. Further, the optimal choice of these strategies depends on the specific genetics of the pathogen and the resistance mechanism. Thus, practical deployment of selection inversion approaches will require the development of fast, genomic diagnostics that can identify not only the pathogen's current resistance profile but also its future potential for evolution of resistance. Such genomic diagnostics could further be used to inform treatment, channel pathogens toward less resistance-prone genotypes, monitor population-wide and environmental resistance levels, and identify new resistance mechanisms before they enter the clinic.

Additionally, most of the studies on selection inversion have been performed in vitro and need to be validated in animal models and clinical isolates. Strategies relying on coadministration are further complicated by pharmacokinetics, which may vary across compounds. Moreover, the unique drug interactions underlying these approaches may change across different environments and genetic backgrounds or over time as the pathogens evolve. Finally, the deployment of these strategies requires a careful ethical balance between curing the individual and reducing resistance in the community. Ultimately, combating resistance will necessitate a portfolio of strategies that anticipate the evolution of the infection and adapt to both treat and avoid resistance. ■

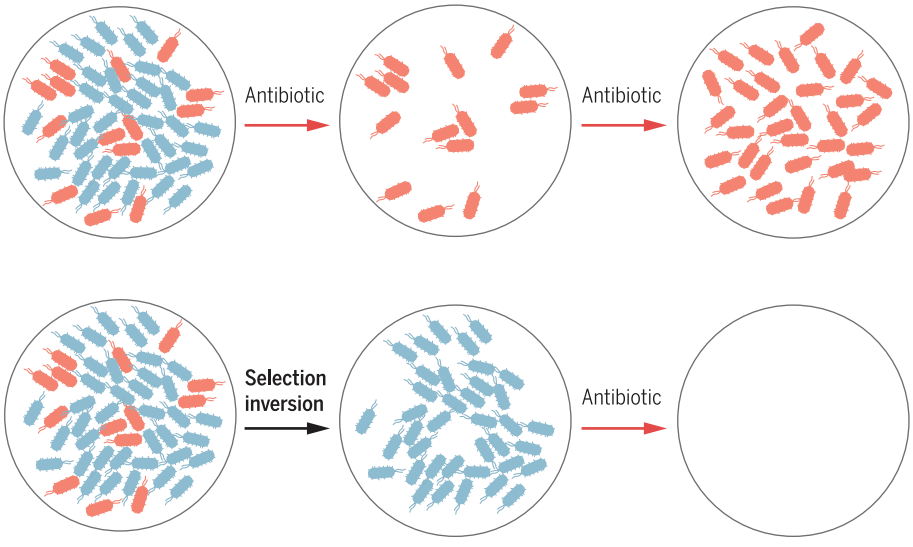

Countering antibiotic resistance through selection inversion. Resistance to antibiotics evolves as a direct consequence of their use to suppress bacterial growth. The present strategy of discovering new antibiotics and waiting for new resistance to evolve is untenable in the long term. However, promising new strategies to manipulate evolution and invert selection against resistance may prolong the utility of existing antibiotics or even restore the activity of old drugs.

The list of author affiliations is available in the full article online.
*These authors contributed equally to this work.
†Corresponding author. E-mail: rkishony@technion.ac.il
Cite this article as M. Baym *et al.*, *Science* **351**, aad3292 (2016). DOI: 10.1126/science.aad3292

REVIEW

ANTIBIOTIC RESISTANCE

Multidrug evolutionary strategies to reverse antibiotic resistance

Michael Baym,[1]* Laura K. Stone,[1]* Roy Kishony[1,2]†

Antibiotic treatment has two conflicting effects: the desired, immediate effect of inhibiting bacterial growth and the undesired, long-term effect of promoting the evolution of resistance. Although these contrasting outcomes seem inextricably linked, recent work has revealed several ways by which antibiotics can be combined to inhibit bacterial growth while, counterintuitively, selecting against resistant mutants. Decoupling treatment efficacy from the risk of resistance can be achieved by exploiting specific interactions between drugs, and the ways in which resistance mutations to a given drug can modulate these interactions or increase the sensitivity of the bacteria to other compounds. Although their practical application requires much further development and validation, and relies on advances in genomic diagnostics, these discoveries suggest novel paradigms that may restrict or even reverse the evolution of resistance.

Antibiotics are among the most important tools in medicine, but their efficacy is threatened by the evolution of resistance. Since the earliest days of antibiotics, resistance has been observed and recognized as a challenge (*1*). Today, many first-generation antibiotics are all but ineffective (*2*). We have thus far avoided a crisis through the continued modification of existing compounds and the discovery of new antibiotic classes. However, while resistance rates continue to rise, the rate of antibiotic discovery has dropped substantially (*3*, *4*). Today, resistance claims over 25,000 lives in the European Union and 23,000 lives in the United States every year (*2*, *5*). In addition to discovering new antibiotics, we must therefore prioritize the development of methods addressing the evolution of resistance (*6*, *7*). In particular, we need to devise new strategies for antimicrobial treatments that could limit, redirect, and perhaps even reverse the course of resistance evolution.

Bacteria evolve resistance to antibiotics by one of two routes: spontaneous mutation and horizontal gene transfer. Spontaneous mutations can confer resistance to an antibiotic by modifying the antibiotic's target or its expression level, or by up-regulating resistance genes, such as those encoding efflux pumps (*8*–*10*). Alternatively, bacteria can acquire dedicated resistance genes through horizontal gene transfer. These genes may encode specialized antibiotic degradation enzymes, efflux pumps, target protection proteins, or bypass pathways (e.g., supply mechanisms for alternative cell wall synthesis pathways) (*8*, *9*). Once they have acquired the resistance gene or mutation, bacteria can continue to grow in the presence of antibiotics, while the growth of sensitive bacteria is halted. Resistant mutants quickly outnumber sensitive bacteria and thus rapidly spread throughout a population, eventually rendering the drug ineffective.

It has been hoped that in the absence of antibiotic pressure, the physiological cost of maintaining resistance would be strong enough to select for loss of the resistance allele, eventually leading to resensitization. In practice, such loss of resistance has not been widely observed for four reasons. First, with few exceptions (*11*), the fitness cost of resistance is often not large enough to be appreciably selected against, and thus resistance genes can remain in the population for years after removal of the drug (*12*–*15*). Second, even when the cost of resistance is large, it can be neutralized by compensatory mutations, or through genetic regulatory mechanisms that activate resistance only in the presence of the drug (*16*, *17*). Third, sustained selection for the presence of a resistance gene with an antibiotic can lead to the accumulation of mutations that not only compensate for the cost of the resistance gene, but make its presence essential for growth even in the absence of the antibiotic (*18*). Finally, antibiotic resistance mutations can, in certain cases, confer increased virulence, giving the resistant mutant a fitness advantage in the absence of antibiotic selection (*19*, *20*).

Thus, as a Sisyphean consequence of their desired short-term inhibition of growth, antibiotics ultimately lead to long-term selection for resistance. Recent theoretical and experimental studies indicate that with particular combinations of compounds, we could decouple the conflicting effects of antibiotic therapy. Thus, it should be possible to develop strategies that use combinations of antibiotics and other compounds to inhibit bacterial growth while minimizing or reversing selection for resistance to the individual components.

Several mechanisms have been studied for minimizing or inverting the selective advantage of antibiotic resistance. The most established approach so far is to administer antibiotics with molecules that inhibit a particular resistance mechanism, thus neutralizing the evolutionary advantage of resistant strains. More recent work has developed strategies that go beyond neutralizing resistance to actively selecting against it using evolutionary and physiological interactions between drugs (see Box 1 and Fig. 1). First, combinations of drugs that physiologically interact to have different effects when coadministered can be used to slow and even invert the evolution of resistance. Second, drug interactions that change as resistance evolves can be exploited to select against resistant mutants. Finally, there has been a resurgence of interest in evolutionary trade-offs between resistances to individual compounds, in which one compound may channel evolution toward increased sensitivity to another compound. Below, we review these strategies and their potential for inhibiting the evolution of resistance. Several complementary strategies for evolutionarily robust bacterial inhibition have been suggested, including suppression of virulence (*21*–*23*), persistence (*24*), and quorum sensing (*25*, *26*), as well as novel targeting strategies to allow higher effective doses (*27*); however, they are outside the scope of this review.

Resistance mechanism inhibitors

Perhaps the most direct way to bypass resistance is to block the resistance mechanism. Resistance is frequently conferred by dedicated efflux pumps or antibiotic-degrading enzymes, which in turn can be countered by compounds that inhibit the resistance machinery (*28*, *29*). To use this strategy therapeutically, an antibiotic is delivered concurrently with resistance-inhibiting compounds; for example, a β-lactam antibiotic paired with an inhibitor of β-lactamase (a resistance enzyme that degrades β-lactams). This allows the antibiotic to kill both resistant and susceptible strains, thereby potentiating the efficacy of the drug and diminishing the selective advantage of the resistance gene (*28*).

Compounds have been discovered that inhibit a large variety of resistance mechanisms (*29*). The most clinically successful examples are the pairings of amoxicillin-clavulanic acid, ampicillin-sulbactam, and pipericillin-tazobactam to block serine β-lactamases (*28*, *30*). Recently, this principle has been expanded to metallo-β-lactamases with the discovery that aspergillomarasmine A inhibits NDM-1 and VIM-2, two clinically important enzymes that degrade β-lactams, including carbapenem antibiotics (*31*). Inhibitors of aminoglycoside-modifying enzymes have also been synthesized (*32*, *33*). Further, high-throughput screening (*34*) and medicinal chemistry efforts (*35*) have yielded leads for inhibitors of ErmC methyltransferase, which confers macrolide resistance. Lastly, several studies have identified inhibitors of different efflux pumps, a major mode of resistance across antibiotic classes (*36*–*41*).

Some of these inhibitors are produced by the same bacterial species that synthesize the antibiotic

[1]Department of Systems Biology, Harvard Medical School, Boston, MA, USA. [2]Department of Biology and Department of Computer Science, Technion - Israel Institute of Technology, Haifa, Israel.
*These authors contributed equally to this work.
†Corresponding author. E-mail: rkishony@technion.ac.il

Box 1. Physiological and evolutionary drug interactions.

Physiological interactions: synergy, antagonism, and suppression

Antibiotics used in combination can interact to synergize, antagonize, or even to suppress each other's effects (Fig. 1A). Antibiotic drug interactions appear when the combined inhibitory effect of two drugs is larger or smaller than expected based on an additive model (*76*, *104*, *105*). A common way to understand drug interactions is to consider the shape of the line in the two-drug concentration space, beyond which the bacteria are fully inhibited (Fig. 1A) (*46*). The null expectation for no interaction is that this isobole appears straight, i.e., the inhibitory power of the combinations depends only on the sum of the two antibiotics' concentrations. Synergistic drug combinations are more inhibitory than this null expectation, whereas antagonistic combinations require higher concentrations to achieve the same degree of inhibition (concave and convex lines, respectively; Fig. 1A). An extreme type of antagonism appears when the combined effect of two drugs is weaker not only compared to the null additive expectation, but also weaker than the effect of one of the drugs alone. These are termed "suppressive" drug interactions and appear as a non-monotonic inhibitory line, where the addition of a drug can in fact relieve growth inhibition (Fig. 1A) (*106*).

Recent technical developments have enabled broad systematic efforts to identify drug interactions and their underlying mechanisms. These studies have revealed synergistic, antagonistic, and suppressive interactions among pairs of antibiotics (*106*–*108*), as well as interactions between antibiotics and compounds with little or no antimicrobial activity (*31*, *109*–*114*). Analysis of pairwise interaction networks between multiple drugs have shown that drugs with the same mode of action have broadly the same interaction profile (*106*), suggesting that drug interactions operate through the core physiology of the cell and not through direct chemical interaction of the compounds. Although for many drug combinations the specific mechanism of interaction is not fully understood, recent work has elucidated the mechanisms behind several interactions: Simultaneous inhibition of different steps in a pathway causes a synergistic interaction between trimethoprim and sulfa drugs (*115*), nonoptimal gene regulation in the face of antibiotic inhibition results in a suppressive interaction between tetracyclines and fluoroquinolones (*116*), and mutations in polysaccharide and adenosine 5′-triphosphate (ATP) synthesis reshape a variety of interactions between antibiotic pairs (*44*).

Evolutionary interactions: cross-resistance and collateral sensitivity

Spontaneous mutations or acquired genes conferring resistance to one antibiotic can increase or decrease the resistance to another antibiotic (Fig. 1B) (*67*, *68*, *117*). These positive and negative evolutionary interactions between antibiotics are termed "cross-resistance" and "collateral sensitivity" (or negative cross-resistance), respectively. For spontaneous resistance mutations, these evolutionary interactions have been mapped systematically, and both positive and negative cross-resistance interactions have been found between many pairs of antibiotics (*56*, *57*). This phenomenon is not unique to bacteria and antibiotics; it has been seen in malaria (*118*, *119*), HIV therapies (*120*), cancer treatments (*121*), and pesticide resistance in plants (*122*, *123*). Importantly, unlike physiological interactions, cross-resistance does not require drugs to be applied in combination, but is a function of the evolutionary response to a single antibiotic.

Recent surveys of cross-resistance interactions found that, as expected, the cross-resistance interactions between drugs in the same class tend to be positive (*56*, *57*), although there are important exceptions (*70*, *71*). Negative cross-resistance is seen frequently with resistance to aminoglycoside antibiotics, resulting from a change in the proton motive force associated with resistance (*56*, *57*). More broad principles of when and in what environments cross-resistance interactions should occur, are not yet known.

whose resistance mechanism they inhibit, suggesting an evolutionary advantage to their use in combination. Clavulanic acid, a β-lactamase inhibitor, is produced by *Streptomyces clavuligerus*, which also produces several β-lactam antibiotics (*42*). Similarly, *Berberis fremontii* makes both the antibiotic berberine and the efflux pump inhibitor, 5′-methoxyhydnocarpin, that blocks berberine export (*40*). It is intriguing to hypothesize that these species evolved not only antibiotic production, but also ways to preserve the activity of those antibiotics by suppressing resistance mechanisms. Hence, known antibiotic producers may be fruitful sources of resistance mechanism inhibitors.

Although inhibitors have been found for several resistance mechanisms, in clinical practice the success of resistance mechanism inhibitors has been limited to serine β-lactamases (*28*, *30*). Several barriers limit the broader application of resistance inhibitors, including drug toxicity, pharmacokinetic differences between the inhibitor and the antibiotic, and an inhibitor's specificity for a particular resistance mechanism. Even when successfully implemented, these approaches are not resilient to the evolutionary process.

While resistance mechanism inhibitors can suppress or bypass specialized bacterial resistance machinery, they are themselves subject to resistance. Most resistance mechanism inhibitors are specific to one class of degradation enzymes or pumps, and therefore their widespread use can select for inhibitor-resistant variants within the class, or for alternate resistance mechanisms (*28*). For example, the β-lactamase inhibitors clavulanic acid, sulbactam, and tazobactam are ineffective against AmpC β-lactamases and metallo-β-lactamases, and over the years have selected for inhibitor-resistant variants of TEM β-lactamases (*28*, *43*).

Critically, resistance mechanism inhibitors, while neutralizing the advantage of resistant bacteria, do not necessarily put them at a competitive disadvantage. Thus, while these inhibitors restore the efficacy of the antibiotic, they do not reduce the relative prevalence of resistance within a patient or in the population. Without negative selective pressure, the resistant strain will remain in the population, even in the absence of the antibiotic (*12*–*15*).

Selection inversion

There are several strategies to combine multiple physiologically or evolutionarily interacting antibiotics, not only to neutralize the selective advantage of resistance but also to impose a direct cost on resistance. The evolution of multidrug resistance often requires the sequential accumulation of resistance to each of the individual drugs. It is therefore important to find out whether single-drug–resistance steps would be selected for or against in a multidrug environment. The result critically depends on the physiological and evolutionary interactions between the drugs (Box 1).

With some notable exceptions, single-drug–resistant mutants maintain the same drug interactions and the same resistances to other drugs as their drug-sensitive parents (Fig. 2A) (*44*). This is because, to a first approximation, bacteria acquiring resistance to one drug (e.g., via a spontaneous target mutation or a horizontally transferred drug efflux pump) behave as if they were exposed to less of that drug. The region of growth for resistant bacteria in a two-drug concentration space would therefore be similar in shape to the region of growth for their drug-sensitive parent, except stretched toward higher concentrations along the drug axis to which the bacteria are resistant (Fig. 2, A and B, horizontal axis). Thus, normally the regime where the resistant bacteria can grow fully encompasses the regime where the sensitive bacteria can grow (Fig. 2A); there is no combination of the two drugs in which the sensitive bacteria outcompete the resistant mutants.

There are, however, three primary ways by which antibiotic combinations can impose a direct cost on resistance and thus select against drug-resistant strains. First, when one drug suppresses another, bacteria becoming resistant to the first drug lose its protective effect and can thus be inhibited more strongly by the second drug than their sensitive ancestors (*45*). In such a suppressive drug pair, the region of concentration allowing growth has a nonmonotonic shape, and therefore stretching this region toward higher drug concentration as a result of resistance to

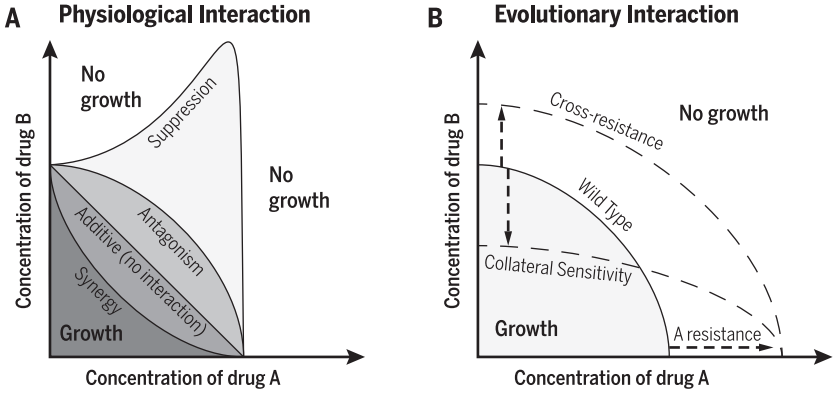

Fig. 1. Physiological interactions and cross-resistance. (**A**) Isoboles of minimum inhibitory concentration (MIC) are shown in the two-drug concentration space for different drug interactions. The MIC of each drug alone occurs where the isobole intersects each drug axis. When the effect of the two drugs is equal to the effect expected when combining two identical drugs, the shape of the MIC line is linear and the drugs are said to be noninteracting (*104*). Synergistic drugs require less-than-expected concentrations, corresponding to a concave MIC line, whereas antagonistic interactions require higher drug concentrations, producing a convex line. Finally, drug interactions are suppressive when their effect in combination is less than that of one of the drugs alone, appearing as a nonmonotonic isobole. (**B**) Cross-resistance and collateral sensitivity: A mutation or acquired gene conferring resistance to drug A can also increase resistance (positive cross-resistance) or decrease resistance (negative cross-resistance or collateral sensitivity) to drug B without otherwise changing the shape of the interaction.

that drug leaves behind a range of concentrations in which the sensitive bacteria can grow and the resistant bacteria cannot (Fig. 2B). Second, if the mutation conferring resistance to one drug also increases the synergy between the two drugs, the mutant can again be inhibited more than its sensitive parent (*46*). This appears as a shape change in the resistant mutant's region of growth, generating a combination of the drugs in which the wild type can grow while the mutant cannot (Fig. 2C). Finally, there may be an evolutionary trade-off, such that resistance to one drug generates sensitivity to the other (Fig. 2D, vertical axis). In this case, sensitivity to the second drug decreases with resistance to the first, allowing selection against resistance with the second drug alone.

Selection inversion using suppressive drug interactions

Suppressive drug interactions can select against single-drug–resistant mutants by creating a concentration regime that inhibits resistant, but not sensitive, bacterial growth. If drug A suppresses drug B, the line of inhibition in the two-drug space becomes nonmonotonic, such that the bacteria grow better at high concentrations of drug B when drug A is present. When the bacteria become resistant to drug A, this inhibitory line is stretched into higher concentrations of drug A (Fig. 2B). This leaves behind a concentration regime where the bacteria sensitive to A can grow, benefiting from the suppression of the effect of drug B by drug A, while the A-resistant ones cannot benefit. Therefore, within certain concentration regimes, suppressive combinations can cause drug-resistant mutants to lose out in competition with their drug-sensitive parental strains (*45*) (Fig. 2B).

Although suppressive interactions can fully invert the selective advantage of resistance, less extreme antagonistic interactions can also reduce, although not invert, the selective advantage of resistant mutants. Such antagonistically interacting drugs can therefore slow the rate of resistance evolution (*47*, *48*). Conversely, synergistic interactions increase the selective advantage of resistant mutants, as becoming resistant to one drug relieves not only its own inhibitory effect but also its synergistic effect on the other drug (*47*, *48*).

The evolutionary benefits of antagonistic or suppressive antibiotic combinations may not always warrant their additional costs. While reducing or inverting selection for resistance, antagonistic and suppressive combinations require higher doses of drugs and longer treatment time. This poses toxicity issues and can increase the potential for accumulating additional resistance mutations (*49*–*53*). Conversely, synergistic combinations increase the selective advantage of resistance mutations, but can also clear infections faster using less drug, reducing toxicity and the time in which resistance can arise (*52*). Thus, there is an optimal level of drug interaction, depending on the context of the infection, that balances clearance and prevention of resistance (*52*).

Deploying combination therapies clinically is likely to be complicated by the need to fine-tune concentrations of the drugs and by potential changes in their interactions. Differential absorption and penetration of the two drugs limit our ability to control their ratio in vivo and can create single-drug compartments that select for resistance (*54*). Further, interactions between the drugs can change within the body or as the target bacteria evolve, and there is no guarantee that interactions will remain suppressive (*55*).

Selection inversion using synergy-inducing drug pairs

Drug combinations can invert the selective pressure to favor sensitivity if their interaction becomes more synergistic in resistant mutants than in the sensitive parental strain. Although, as discussed above, the type of interaction between two drugs typically does not change with the acquisition of resistance (Fig. 2, A and B), in certain cases a resistant allele may not only confer resistance to a given drug but also change its interaction with other drugs (*46*, *55*). If the drug interaction becomes more synergistic, there may exist a concentration regime where the susceptible strain can grow while the resistant strain cannot (Fig. 2C). A comprehensive study examining the pairwise interactions of six antibiotics on a library of nonessential *Escherichia coli* gene deletion mutants showed that the shape of interactions is sometimes modified by inhibition of cellular functions, suggesting that antibiotic interactions can indeed change with the acquisition of particular mutations (*44*). This principle has been established in other contexts—for example, in non–small-cell lung cancer lines, the drugs gefitinib and 17-AAG interact antagonistically in susceptible cells, but interact synergistically when the cells gain gefitinib resistance, and therefore this combination may reduce the emergence of gefitinib-resistant mutants (*46*).

Applying this approach to antimicrobial therapy is currently only hypothetical. Unlike the suppressive drug pairs discussed above, or collaterally sensitive drug pairs discussed below, we currently do not know of a specific drug pair for which resistance to one drug consistently induces synergy to the combination. Further, should we find such pairs of antibiotics, the application of the approach will be challenging because of the need to fine tune the concentrations of two drugs simultaneously.

Selection inversion using collateral sensitivity

Collateral sensitivity, whereby resistance to one drug confers sensitivity to another (Box 1), provides a third mechanism for selection against resistance. Unlike suppression-based selection and synergy-inducing resistance mutations, which require the coadministration of two drugs for inverting the selective advantage of resistance, selection against resistance by collateral sensitivity occurs without coapplication of drugs (Fig. 2D, vertical axis), opening avenues for alternating drugs within the treatment of a single patient, or cycling drugs in a broader population context (*56*). Recent attention has been focused on the use of collateral sensitivity to select against spontaneous resistance mutations (*56*–*59*); its value in countering horizontally transferred resistance has been less explored (*60*–*66*).

Selection against spontaneous resistance

The pioneering work of Szybalski and Bryson in the early 1950s, testing whether spontaneous mutants resistant to different drugs grow in a range of other drugs, showed that cross-resistance and collateral sensitivity between antibiotics are

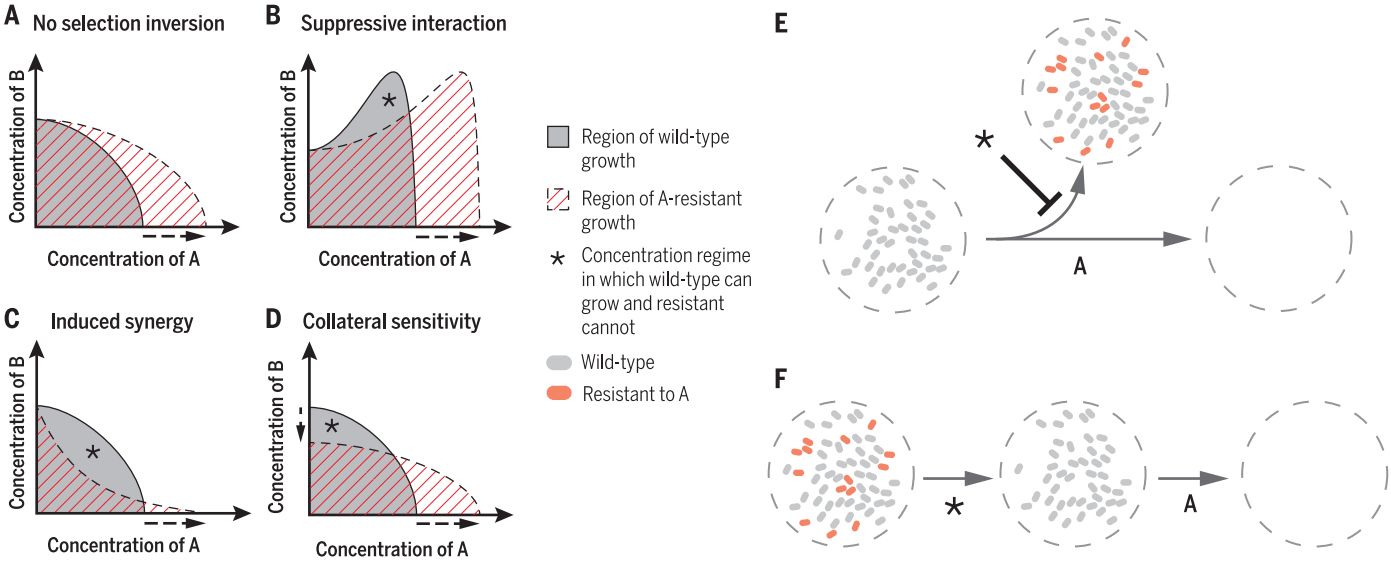

Fig. 2. Selection inversion approaches and potential strategies. (**A**) In typical drug interactions, the region of growth of a single-drug–resistant mutant (e.g., A-resistant, dashed area) completely covers the region of growth of the drug-sensitive wild type (gray area), and the mutant therefore always outcompetes the wild type. (**B** to **D**) There are three principal ways for establishing a concentration regime (*) that selects against resistance: (B) When drug A suppresses drug B, the MIC isobole is nonmonotonic, and so scaling it along the A axis because of resistance leaves a selection-inverting regime. (C) An antagonistic interaction can become synergistic with the acquisition of resistance, making the mutant more sensitive to the combination. (D) Collateral sensitivity, when the MIC of drug B decreases as a result of resistance to drug A, allowing selection against resistance even in the absence of A. (**E**) Using selection inversion approaches on a nonresistant population can decrease the probability of resistance evolution and make long-term therapy more likely to succeed. (**F**) Selection against resistance can also be used as part of a two-phase strategy against a population with resistant mutants. The drug-resistant mutants are selected out of the population in the first phase, allowing a previously ineffective antibiotic to be used in the second.

common (*67*, *68*). More recently, there have been several systematic screens for cross-resistance and collateral sensitivity (*56*–*59*). Some drug pairs show unidirectional collateral sensitivity, where resistance to one drug causes sensitivity to another, but not the other way around (*56*–*59*). In others, reciprocal collateral sensitivity appears, in which selection for resistance to either of the two drugs causes sensitivity to the other (*56*).

Collateral sensitivity can occur directly through mutations in the antibiotic target or indirectly through mutations in other cellular mechanisms (*69*). Drug pairs that target the same protein, such as quinolones and novobiocin (both DNA gyrase inhibitors), often show collateral sensitivity or cross-resistance (*70*, *71*). Here, the interaction occurs directly through the target: The amino acid changes that provide resistance to one drug increase or decrease sensitivity to the other. Collateral sensitivity can also occur through less direct means. Several recent studies have highlighted the prevalent collateral sensitivity between aminoglycosides and other antibiotic classes (*56*, *57*–*59*). Both the import of aminoglycosides and the export of multiple antibiotics through intrinsic efflux pumps require the proton motive force (*72*, *73*). Therefore, when a strain evolves resistance to aminoglycosides by diminishing the proton motive force, it becomes more susceptible to other antibiotics, such as β-lactams, quinolones, and tetracyclines, that are normally exported by the proton-force–dependent pumps (*57*, *59*, *74*). By adapting to the presence of one antibiotic, bacteria effectively specialize and can become less resilient to other antibiotics.

Cross-resistance and collateral sensitivity may affect the potential for and change the rate of evolution of multidrug resistance (*47*, *75*, *76*). Collaterally sensitive drugs can be applied concurrently to reduce the selective advantage of single-drug resistant mutants, or alternatingly to either select for the wild-type over resistance or for de novo mutations that lose resistance (*56*). Concurrent or alternating application of drugs that have unidirectional collateral sensitivity can reduce the evolution of spontaneous resistance, compared with either of the drugs alone (*55*, *77*). Furthermore, coadministration of drugs that have both synergy and collateral sensitivity can restore the activity of defunct antibiotics against resistant strains while preventing the evolution of further resistance (*71*).

Considerable practical challenges stand in the way of exploiting collateral sensitivities between compounds to suppress resistance. All potential methods are likely to fail in the presence of mutations that confer resistance to both drugs (Fig. 3A) (*78*). Further, alternating application of a reciprocally collaterally sensitive pair of drugs suffers from two additional failure modes. First, if collaterally sensitive mutations confer more resistance to one drug than sensitivity to the other drug, such mutations would gradually accumulate resistance to both drugs (Fig. 3B). Second, mutations may not combine additively, and it is possible that the likelihood of collaterally sensitive mutations is reduced following an initial resistance mutation. Translating these methods into effective clinical strategies will require a more comprehensive and precise accounting of the spectrum of resistance mutations and their interactions.

Preliminary attempts to clinically deploy sequential antibiotic therapies have seen mixed results (*78*–*81*). Both theoretical and clinical studies have found that strict regimens of hospital-wide antibiotic cycling do not improve clinical outcomes (*78*, *80*, *81*). Results have been more promising within the context of treating a single patient. An "adjustable cycling" protocol, in which antibiotics are changed based on the patient's condition, can be effective in reducing the evolution of resistance (*79*). Beyond pairs of drugs, more complex regimens, with multiple steps and decisions based on the specific mutations that emerge, will likely be needed to fully invert the selection for antibiotic resistance.

Selection against acquired resistance

Whereas collateral sensitivity mediated through spontaneous mutations has been mapped extensively, there are fewer examples of collateral sensitivity caused by dedicated resistance genes and cassettes spread by horizontal gene transfer (*60*–*66*). A resistance mechanism confers an advantage in the presence of the antibiotic it targets, but may lead to sensitivity to other compounds. Almost all existing examples of such selection-inverting compounds center on the *tet* efflux pumps, which confer tetracycline resistance, but also make bacteria more susceptible to aminoglycosides, salt stress, and fusaric acid (*61*–*65*). A recent screen for selection-inverting compounds, measuring the relative growth of competing resistant and sensitive strains, found

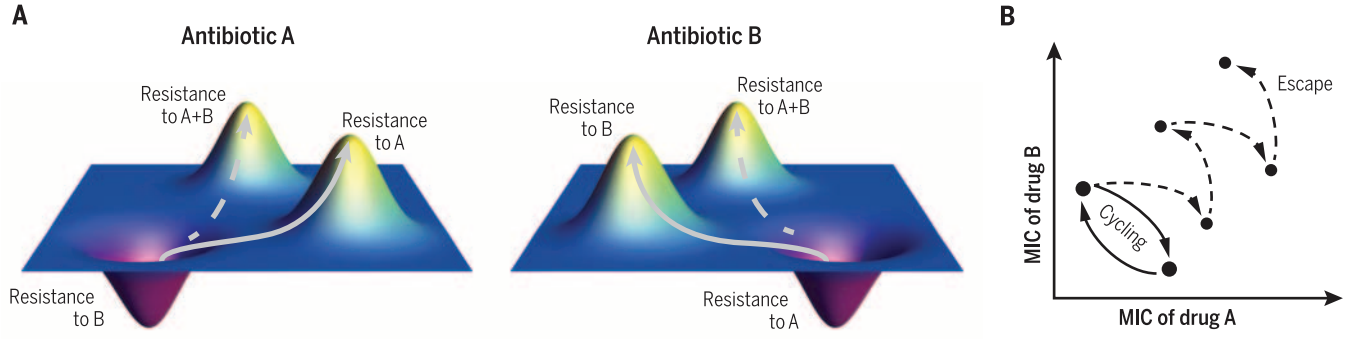

Fig. 3. The efficacy and potential failure of cycling collaterally sensitive antibiotics. (**A**) Fitness landscapes in collaterally sensitive antibiotics. Genotypes that are resistant to drug A or drug B appear as fitness peaks when the environment contains the drug to which they are resistant but as fitness valleys in the other drug treatment. In principle, alternating the drugs can lead to a cycle of evolution switching between these genotypes (solid arrows). However, doubly resistant mutants can evade this trap (dashed arrows). (**B**) Two possible evolutionary trajectories in the MICs of component drugs in antibiotic cycling. Ideally, resistance will alternate between two states (solid arrows). However, repeated accumulation of resistance mutations can also create double-resistance, even in the case where each individual mutation induces collateral sensitivity (dashed arrow).

that some soil microbes produce compounds that select against *tetA* (*60*). The generality of this screening technique will potentially allow systematic identification of compounds that can select against other horizontally transferable antibiotic resistance mechanisms. Furthermore, the same mobility that allows resistance genes to spread rapidly would also accelerate their loss, relative to spontaneous mutations (*73*, *82*, *83*). New selection-inverting compounds would therefore open up possibilities for novel treatment regimens that can convert a population carrying a resistance cassette back to drug sensitivity, potentially increasing sensitivity to other antibiotics whose resistance genes were on the same genetic cassette.

Translation and the need for anticipatory diagnostics

One can envision several different ways in which selection-inverting approaches can be used. For example, since becoming resistant to the combined treatment often requires the stepwise accumulation of mutations providing resistance to each of the individual components, using methods that select against these single-drug resistant mutants can reduce the chance that a doubly resistant mutant appears during treatment (Fig. 2E) (*52*). These approaches can also be used in a "one-two punch" treatment strategy: First select against resistance to eliminate single-drug resistant mutants from a population, and then follow up with the now-effective classical antibiotic (Fig. 2F). It is conceivable that even when a resistant allele is fully fixed in the population, applying a selective pressure against it would select for mutations that delete it or disrupt its function and lead to its long-term loss. However, for selection inversion strategies to be practical, improved diagnostics of resistance mechanisms are needed.

To deploy the correct strategy against a specific mechanism of resistance, we must be able to differentiate at the point of diagnosis what antibiotics an infection is already resistant to and the potential it has to develop resistance. With a few notable exceptions (*84*–*88*), the diagnosis of microbial infections has not changed conceptually over the past several decades: The pathogen is cultured and its growth in the presence of a panel of antibiotics is tested. This culturing-phenotyping approach is not only slow, but only assesses the current abilities of the microbe and not its evolutionary potential. State-of-the-art diagnostic technologies are currently too cumbersome for clinical practice, and substantial technical challenges must be overcome to enable their widespread use. However, with anticipated improvements, technologies for the rapid genomic sequencing of pathogens have the potential to enable faster diagnosis and prediction of antibiotic resistance.

Genomic analysis can potentially detect both the resistance profile of the bug and the specific resistance genes involved (*89*), allowing more targeted use of approaches that inhibit or select against the specific resistance mechanism. As more clinical samples are phenotyped and sequenced, we expect that machine learning techniques will rapidly improve in their ability to predict antibiotic resistance from genomic data. It is possible that by correlating genotypes and phenotypes on a large scale, these approaches will be able to identify resistance conferred not only by known resistance genes, but also to identify novel resistance genotypes. Furthermore, it is possible that such approaches may be able to predict not only what drugs a pathogen is currently capable of resisting, but also its past exposures and future capacity to evolve resistance. As pathogens evolve at the population level, and even within a single patient, the resulting diversity of accumulated mutations allows reconstruction of their phylogeny and can reveal their past history of adaptation to antibiotics and other selective pressures (*90*, *91*). Diagnostics may even be able to predict future evolution and the potential to evolve resistance. For example, if a pathogen's genome is a few mutations away from resistance, we might predict that, while it is not currently resistant, it could become resistant if certain drugs are used. The predictability of the evolutionary process likely varies between drugs, but for some, spontaneous resistance appears to evolve through a limited range of pathways (*91*–*93*). However, higher-order interactions among mutations could make long-term evolution substantially harder to predict (*93*).

Beyond predictive diagnostics at the single-patient level, sequencing-based diagnostics may allow us to predict evolution at a population or epidemic level, ideally before a resistance mechanism even appears in a clinic (*4*). To do this, we must monitor for the emergence and spread of resistance mechanisms (*4*, *94*, *95*). Widespread antibiotic use in agriculture, cosmetics, and medicine can bias the genetic content of the ambient microbiome toward the prevalence of resistance genes, increasing the chance of horizontal gene transfer of resistance to clinical pathogens (*96*–*98*). This can foster low-level resistance, which decreases the additional resistance required to reach clinically significant levels and makes high levels of resistance possible via more evolutionary paths (*99*, *100*). Through sequence-based predictive diagnostic techniques, we should be able to detect the emergence of resistance, its source, and its rate of spread and possibly begin to fight emerging resistance before it enters the clinic.

Challenges and outlook

The practical application of selection-inverting strategies faces major challenges. The majority of multidrug interaction and collateral sensitivity studies have been performed in vitro with *Escherichia coli* and need to be validated in animal models and clinical isolates. The specific uses of these strategies split broadly into two types of clinical case: that of a single patient with a long-term infection (e.g., tuberculosis or methicillin-resistant *Staphylococcus aureus*) or a resistant pathogen circulating in the population (e.g., vancomycin-resistant enterococci or cephalosporin-resistant gonorrhea), each with its own practical and ethical challenges. In a long-term single-patient infection, we must balance the risk of prolonging treatment against the risk of treatment failure from the evolution of resistance. In the case of a pathogen circulating in the population,

the balance is between the efficacy of clearance and the population-level need for long-term suppression of resistance. Thus, even if a treatment strategy can suppress the evolution of resistance, it is unlikely to be widely adopted clinically unless it also provides increased survival on a per-patient basis. It could therefore be advantageous to begin trials of these approaches for suppressing circulating resistance in a veterinary setting, where the health of the herd, rather than of an individual animal, is of primary concern and the ethical concerns are less acute than for human clinical applications. Another difficulty lies in the simultaneous delivery of multicompound treatments; unequal absorption and penetration may lead to pockets of single-drug exposure and thereby promote resistance (*54*). To circumvent this difficulty, hybrid antibiotics linking existing compounds have been proposed, but their in vivo efficacy and evolutionary effects have undergone only limited testing (*101*, *102*). Further, selection against resistance is dependent on the consistency of drug interactions. As microbes face vastly different environments in a host than in vitro, with different nutrient supplies, a range of immune responses, competition with other microbes, phenotypic variability [e.g., persister cells (*24*, *103*)], and their own evolution, there is no immediate guarantee that the interactions observed in vitro are sufficiently stable to reliably direct evolution in vivo.

Ultimately, treating resistance will require a portfolio of strategies including drug discovery, resistance monitoring, and combinations of novel methods to invert the selection for resistance. We are in dire need of techniques to channel pathogens toward less evolvable genotypes. It is no longer sustainable nor sufficient to treat antibiotic-resistant infections simply in response to their current resistance phenotype. Rather, antimicrobial strategies are required that anticipate the evolutionary potential of the infection, and both treat and channel it away from multidrug resistance. We can be certain bacteria will adapt to our treatments, and so our strategies of combatting resistance must also evolve to remain one step ahead.

REFERENCES AND NOTES

1. E. P. Abraham *et al*., Further observations on penicillin. *Lancet* **238**, 177–189 (1941). doi: 10.1016/S0140-6736(00)72122-2
2. Centers for Disease Control and Prevention, *Antibiotic Resistance Threats in the United States, 2013*; www.cdc.gov/drugresistance/pdf/ar-threats-2013-508.pdf (2013).
3. R. Laxminarayan, Antibiotic effectiveness: Balancing conservation against innovation. *Science* **345**, 1299–1301 (2014). doi: 10.1126/science.1254163; pmid: 25214620
4. President's Council of Advisors on Science, Technology, "Report to the President on Combating Antibiotic Resistance" (Executive Office of the President, 2014), pp. 1–78.
5. World Health Organization, "Antimicrobial resistance: Global report on surveillance" (World Health Organization, Geneva, Switzerland, 2014).
6. N. S. McClure, T. Day, A theoretical examination of the relative importance of evolution management and drug development for managing resistance. *Proc. Biol. Sci.* **281**, 20141861–20141861 (2014). doi: 10.1098/rspb.2014.1861; pmid: 25377456
7. K. Bush *et al*., Tackling antibiotic resistance. *Nat. Rev. Microbiol.* **9**, 894–896 (2011). doi: 10.1038/nrmicro2693; pmid: 22048738
8. J. M. A. Blair, M. A. Webber, A. J. Baylay, D. O. Ogbolu, L. J. V. Piddock, Molecular mechanisms of antibiotic resistance. *Nat. Rev. Microbiol.* **13**, 42–51 (2015). doi: 10.1038/nrmicro3380; pmid: 25435309
9. G. D. Wright, Molecular mechanisms of antibiotic resistance. *Chem. Commun. (Camb.)* **47**, 4055–4061 (2011). doi: 10.1039/c0cc05111j; pmid: 21286630
10. A. C. Palmer, R. Kishony, Opposing effects of target overexpression reveal drug mechanisms. *Nat. Commun.* **5**, 4296 (2014). doi: 10.1038/ncomms5296; pmid: 24980690
11. B. M. Vincent, A. K. Lancaster, R. Scherz-Shouval, L. Whitesell, S. Lindquist, Fitness trade-offs restrict the evolution of resistance to amphotericin B. *PLOS Biol.* **11**, e1001692–e17 (2013). doi: 10.1371/journal.pbio.1001692; pmid: 24204207
12. M. Sjölund, K. Wreiber, D. I. Andersson, M. J. Blaser, L. Engstrand, Long-term persistence of resistant *Enterococcus* species after antibiotics to eradicate *Helicobacter pylori*. *Ann. Intern. Med.* **139**, 483–487 (2003). doi: 10.7326/0003-4819-139-6-200309160-00011; pmid: 13679325
13. M. Sjölund, E. Tano, M. J. Blaser, D. I. Andersson, L. Engstrand, Persistence of resistant Staphylococcus epidermidis after single course of clarithromycin. *Emerg. Infect. Dis.* **11**, 1389–1393 (2005). doi: 10.3201/eid1109.050124; pmid: 16229767
14. L. De Gelder *et al*., Combining mathematical models and statistical methods to understand and predict the dynamics of antibiotic-sensitive mutants in a population of resistant bacteria during experimental evolution. *Genetics* **168**, 1131–1144 (2004). doi: 10.1534/genetics.104.033431 pmid: 15579675
15. D. I. Andersson, D. Hughes, Antibiotic resistance and its cost: Is it possible to reverse resistance? *Nat. Rev. Microbiol.* **8**, 260–271 (2010). pmid: 20208551
16. T. N. Nguyen, Q. G. Phan, L. P. Duong, K. P. Bertrand, R. E. Lenski, Effects of carriage and expression of the Tn10 tetracycline-resistance operon on the fitness of Escherichia coli K12. *Mol. Biol. Evol.* **6**, 213–225 (1989). pmid: 2560115
17. M.-L. Foucault, P. Courvalin, C. Grillot-Courvalin, Fitness cost of VanA-type vancomycin resistance in methicillin-resistant Staphylococcus aureus. *Antimicrob. Agents Chemother.* **53**, 2354–2359 (2009). doi: 10.1128/AAC.01702-08; pmid: 19332680
18. R. E. Lenski, S. C. Simpson, T. T. Nguyen, Genetic analysis of a plasmid-encoded, host genotype-specific enhancement of bacterial fitness. *J. Bacteriol.* **176**, 3140–3147 (1994). pmid: 8195066
19. D. Skurnik *et al*., Enhanced in vivo fitness of carbapenem-resistant oprD mutants of Pseudomonas aeruginosa revealed through high-throughput sequencing. *Proc. Natl. Acad. Sci. U.S.A.* **110**, 20747–20752 (2013). doi: 10.1073/pnas.1221552110; pmid: 24248354
20. D. Roux *et al*., Fitness cost of antibiotic susceptibility during bacterial infection. *Sci. Transl. Med.* **7**, 297ra114 (2015). doi: 10.1126/scitranslmed.aab1621; pmid: 26203082
21. R. C. Allen, R. Popat, S. P. Diggle, S. P. Brown, Targeting virulence: Can we make evolution-proof drugs? *Nat. Rev. Microbiol.* **12**, 300–308 (2014). doi: 10.1038/nrmicro3232; pmid: 24625893
22. A. Ross-Gillespie, M. Weigert, S. P. Brown, R. Kümmerli, Gallium-mediated siderophore quenching as an evolutionarily robust antibacterial treatment. *Evol Med Public Health* **2014**, 18–29 (2014). doi: 10.1093/emph/eou003; pmid: 24480613
23. J. G. Swoboda *et al*., Discovery of a small molecule that blocks wall teichoic acid biosynthesis in *Staphylococcus aureus*. *ACS Chem. Biol.* **4**, 875–883 (2009). doi: 10.1021/cb900151k; pmid: 19689117
24. P. A. Smith, F. E. Romesberg, Combating bacteria and drug resistance by inhibiting mechanisms of persistence and adaptation. *Nat. Chem. Biol.* **3**, 549–556 (2007). doi: 10.1038/nchembio.2007.27; pmid: 17710101
25. S. T. Rutherford, B. L. Bassler, Bacterial quorum sensing: Its role in virulence and possibilities for its control. *Cold Spring Harbor Perspect. Med.* **2**, a012427–a012427 (2012). doi: 10.1101/cshperspect.a012427; pmid: 23125205
26. G. Chen *et al*., A strategy for antagonizing quorum sensing. *Mol. Cell* **42**, 199–209 (2011). doi: 10.1016/j.molcel.2011.04.003; pmid: 21504831
27. S. M. Lehar *et al*., Novel antibody-antibiotic conjugate eliminates intracellular *S. aureus*. *Nature* **527**, 323–328 (2015). doi: 10.1038/nature16057; pmid: 26536114
28. S. M. Drawz, R. A. Bonomo, Three decades of beta-lactamase inhibitors. *Clin. Microbiol. Rev.* **23**, 160–201 (2010). doi: 10.1128/CMR.00037-09; pmid: 20065329
29. G. D. Wright, Resisting resistance: New chemical strategies for battling superbugs. *Chem. Biol.* **7**, R127–R132 (2000). doi: 10.1016/S1074-5521(00)00126-5; pmid: 10873842
30. P. Ball, Conclusions: The future of antimicrobial therapy-Augmentin® and beyond. *Int. J. Antimicrob. Agents* **30**, 139–141 (2007). doi: 10.1016/j.ijantimicag.2007.08.016
31. A. M. King *et al*., Aspergillomarasmine A overcomes metallo-β-lactamase antibiotic resistance. *Nature* **510**, 503–506 (2014). doi: 10.1038/nature13445; pmid: 24965651
32. N. E. Allen, W. E. Alborn Jr., J. N. Hobbs Jr., H. A. Kirst, 7-Hydroxytropolone: An inhibitor of aminoglycoside-2″-O-adenylyltransferase. *Antimicrob. Agents Chemother.* **22**, 824–831 (1982). doi: 10.1128/AAC.22.5.824; pmid: 6185088
33. J. Roestamadji, I. Grapsas, S. Mobashery, Mechanism-based inactivation of bacterial aminoglycoside 3′-phosphotransferases. *J. Am. Chem. Soc.* **117**, 80–84 (1995). doi: 10.1021/ja00106a009
34. J. Clancy *et al*., Assays to detect and characterize synthetic agents that inhibit the ErmC methyltransferase. *J Antibiot* **48**, 1273–1279 (1995). doi: 10.7164/antibiotics.48.1273; pmid: 8557568
35. P. J. Hajduk *et al*., Novel inhibitors of Erm methyltransferases from NMR and parallel synthesis. *J. Med. Chem.* **42**, 3852–3859 (1999). doi: 10.1021/jm990293a; pmid: 10508434
36. M. L. Nelson *et al*., Inhibition of the tetracycline efflux antiport protein by 13-thio-substituted 5-hydroxy-6-deoxytetracyclines. *J. Med. Chem.* **36**, 370–377 (1993). doi: 10.1021/jm00055a008; pmid: 8426364
37. T. E. Renau *et al*., Inhibitors of efflux pumps in *Pseudomonas aeruginosa* potentiate the activity of the fluoroquinolone antibacterial levofloxacin. *J. Med. Chem.* **42**, 4928–4931 (1999). doi: 10.1021/jm9904598; pmid: 10585202
38. A. A. Neyfakh, C. M. Borsch, G. W. Kaatz, Fluoroquinolone resistance protein NorA of Staphylococcus aureus is a multidrug efflux transporter. *Antimicrob. Agents Chemother.* **37**, 128–129 (1993). doi: 10.1128/AAC.37.1.128; pmid: 8431010
39. P. N. Markham, A. A. Neyfakh, Inhibition of the multidrug transporter NorA prevents emergence of norfloxacin resistance in *Staphylococcus aureus*. *Antimicrob. Agents Chemother.* **40**, 2673–2674 (1996). pmid: 8913490
40. F. R. Stermitz, P. Lorenz, J. N. Tawara, L. A. Zenewicz, K. Lewis, Synergy in a medicinal plant: Antimicrobial action of berberine potentiated by 5′-methoxyhydnocarpin, a multidrug pump inhibitor. *Proc. Natl. Acad. Sci. U.S.A.* **97**, 1433–1437 (2000). doi: 10.1073/pnas.030540597; pmid: 10677479
41. J.-M. Pagès, L. Amaral, Mechanisms of drug efflux and strategies to combat them: Challenging the efflux pump of Gram-negative bacteria. *Biochim. Biophys. Acta* **1794**, 826–833 (2009). doi: 10.1016/j.bbapap.2008.12.011; pmid: 19150515
42. C. Reading, M. Cole, Clavulanic acid: A beta-lactamase-inhiting beta-lactam from Streptomyces clavuligerus. *Antimicrob. Agents Chemother.* **11**, 852–857 (1977). doi: 10.1128/AAC.11.5.852; pmid: 879738
43. E. B. Chaïbi, D. Sirot, G. Paul, R. Labia, Inhibitor-resistant TEM beta-lactamases: Phenotypic, genetic and biochemical characteristics. *J. Antimicrob. Chemother.* **43**, 447–458 (1999). doi: 10.1093/jac/43.4.447; pmid: 10350372
44. G. Chevereau, T. Bollenbach, Systematic discovery of drug interaction mechanisms. *Mol. Syst. Biol.* **11**, 807 (2015). doi: 10.15252/msb.20156098; pmid: 25924924
45. R. Chait, A. Craney, R. Kishony, Antibiotic interactions that select against resistance. *Nature* **446**, 668–671 (2007). doi: 10.1038/nature05685; pmid: 17410176
46. K. B. Wood, K. C. Wood, S. Nishida, P. Cluzel, Uncovering scaling laws to infer multidrug response of resistant microbes and cancer cells. *Cell Rep.* **6**, 1073–1084 (2014). doi: 10.1016/j.celrep.2014.02.007; pmid: 24613352
47. M. Hegreness, N. Shoresh, D. Damian, D. Hartl, R. Kishony, Accelerated evolution of resistance in multidrug environments. *Proc. Natl. Acad. Sci. U.S.A.* **105**, 13977–13981 (2008). doi: 10.1073/pnas.0805965105; pmid: 18779569
48. J. B. Michel, P. J. Yeh, R. Chait, R. C. Moellering Jr., R. Kishony, Drug interactions modulate the potential for

evolution of resistance. *Proc. Natl. Acad. Sci. U.S.A.* **105**, 14918–14923 (2008). doi: 10.1073/pnas.0800944105; pmid: 18815368
49. J. W. Chow, V. L. Yu, Combination antibiotic therapy versus monotherapy for gram-negative bacteraemia: A commentary. *Int. J. Antimicrob. Agents* **11**, 7–12 (1999). doi: 10.1016/S0924-8579(98)00060-0; pmid: 10075272
50. N. Safdar, J. Handelsman, D. G. Maki, Does combination antimicrobial therapy reduce mortality in Gram-negative bacteraemia? A meta-analysis. *Lancet* **4**, 519–527 (2004). doi: 10.1016/S1473-3099(04)01108-9; pmid: 15288826
51. P. D. Tamma, S. E. Cosgrove, L. L. Maragakis, Combination therapy for treatment of infections with gram-negative bacteria. *Clin. Microbiol. Rev.* **25**, 450–470 (2012). doi: 10.1128/CMR.05041-11; pmid: 22763634
52. J. P. Torella, R. Chait, R. Kishony, Optimal drug synergy in antimicrobial treatments. *PLOS Comput. Biol.* **6**, e1000796 (2010). doi: 10.1371/journal.pcbi.1000796; pmid: 20532210
53. R. Peña-Miller, D. Lähnemann, H. Schulenburg, M. Ackermann, R. Beardmore, The optimal deployment of synergistic antibiotics: A control-theoretic approach. *J. R. Soc. Interface* **9**, 2488–2502 (2012). doi: 10.1098/rsif.2012.0279; pmid: 22628215
54. S. Moreno-Gamez *et al*., Imperfect drug penetration leads to spatial monotherapy and rapid evolution of multidrug resistance. *Proc. Natl. Acad. Sci. U.S.A.* **112**, E2874–E2883 (2015). doi: 10.1073/pnas.1424184112; pmid: 26038564
55. C. Munck, H. K. Gumpert, A. I. N. Wallin, H. H. Wang, M. O. A. Sommer, Prediction of resistance development against drug combinations by collateral responses to component drugs. *Sci. Transl. Med.* **6**, 262ra156 (2014). doi: 10.1126/scitranslmed.3009940; pmid: 25391482
56. L. Imamovic, M. O. A. Sommer, Use of collateral sensitivity networks to design drug cycling protocols that avoid resistance development. *Sci. Transl. Med.* **5**, 204ra132 (2013). doi: 10.1126/scitranslmed.3006609; pmid: 24068739
57. V. Lázár *et al*., Bacterial evolution of antibiotic hypersensitivity. *Mol. Syst. Biol.* **9**, 700 (2013). pmid: 24169403
58. T. Oz *et al*., Strength of selection pressure is an important parameter contributing to the complexity of antibiotic resistance evolution. *Mol. Biol. Evol.* **31**, 2387–2401 (2014). doi: 10.1093/molbev/msu191; pmid: 24962091
59. S. Suzuki, T. Horinouchi, C. Furusawa, Prediction of antibiotic resistance by gene expression profiles. *Nat. Commun.* **5**, 5792 (2014). doi: 10.1038/ncomms6792; pmid: 25517437
60. R. Chait, S. Shrestha, A. K. Shah, J.-B. Michel, R. Kishony, A differential drug screen for compounds that select against antibiotic resistance. *PLOS ONE* **5**, e15179 (2010). doi: 10.1371/journal.pone.0015179; pmid: 21209699
61. B. R. Bochner, H. C. Huang, G. L. Schieven, B. N. Ames, Positive selection for loss of tetracycline resistance. *J. Bacteriol.* **143**, 926–933 (1980). pmid: 6259126
62. T. Podolsky, S. T. Fong, B. T. Lee, Direct selection of tetracycline-sensitive Escherichia coli cells using nickel salts. *Plasmid* **36**, 112–115 (1996). doi: 10.1006/plas.1996.0038; pmid: 8954882
63. T. L. Merlin, G. E. Davis, W. L. Anderson, R. K. Moyzis, J. K. Griffith, Aminoglycoside uptake increased by tet gene expression. *Antimicrob. Agents Chemother.* **33**, 1549–1552 (1989). doi: 10.1128/AAC.33.9.1549; pmid: 2684011
64. T. L. Merlin, D. L. Corvo, J. H. Gill, J. K. Griffith, Enhanced gentamicin killing of Escherichia coli by tet gene expression. *Antimicrob. Agents Chemother.* **33**, 230–232 (1989). doi: 10.1128/AAC.33.2.230; pmid: 2655531
65. J. K. Griffith, T. Kogoma, D. L. Corvo, W. L. Anderson, A. L. Kazim, An N-terminal domain of the tetracycline resistance protein increases susceptibility to aminoglycosides and complements potassium uptake defects in *Escherichia coli*. *J. Bacteriol.* **170**, 598–604 (1988). pmid: 3276661
66. Q. Li *et al*., NB2001, a novel antibacterial agent with broad-spectrum activity and enhanced potency against beta-lactamase-producing strains. *Antimicrob. Agents Chemother.* **46**, 1262–1268 (2002). doi: 10.1128/AAC.46.5.1262-1268.2002; pmid: 11959554
67. W. Szybalski, V. Bryson, Genetic studies on microbial cross resistance to toxic agents. I. Cross resistance of *Escherichia coli* to fifteen antibiotics. *J. Bacteriol.* **64**, 489–499 (1952). pmid: 12999676
68. W. Szybalski, Genetic studies on microbial cross resistance to toxic agents. IV. Cross resistance of Bacillus megaterium to forty-four antimicrobial drugs. *Appl. Microbiol.* **2**, 57–63 (1954). pmid: 13149144
69. V. Lázár *et al*., Genome-wide analysis captures the determinants of the antibiotic cross-resistance interaction network. *Nat. Commun.* **5**, 4352 (2014). doi: 10.1038/ncomms5352; pmid: 25000950
70. L. Chao, An unusual interaction between the target of nalidixic acid and novobiocin. *Nature* **271**, 385–386 (1978). doi: 10.1038/271385a0; pmid: 340962
71. P. R. Gonzales *et al*., Synergistic, collaterally sensitive β-lactam combinations suppress resistance in MRSA. *Nat. Chem. Biol.* **11**, 855–861 (2015). doi: 10.1038/nchembio.1911; pmid: 26368589
72. H. W. Taber, J. P. Mueller, P. F. Miller, A. S. Arrow, Bacterial uptake of aminoglycoside antibiotics. *Microbiol. Rev.* **51**, 439–457 (1987). pmid: 3325794
73. M. N. Alekshun, S. B. Levy, Molecular mechanisms of antibacterial multidrug resistance. *Cell* **128**, 1037–1050 (2007). doi: 10.1016/j.cell.2007.03.004; pmid: 17382878
74. H. Okusu, D. Ma, H. Nikaido, AcrAB efflux pump plays a major role in the antibiotic resistance phenotype of Escherichia coli multiple-antibiotic-resistance (Mar) mutants. *J. Bacteriol.* **178**, 306–308 (1996). pmid: 8550435
75. M. Dragosits, V. Mozhayskiy, S. Quinones-Soto, J. Park, I. Tagkopoulos, Evolutionary potential, cross-stress behavior and the genetic basis of acquired stress resistance in *Escherichia coli*. *Mol. Syst. Biol.* **9**, 643 (2013). doi: 10.1038/msb.2012.76; pmid: 23385483
76. P. J. Yeh, M. J. Hegreness, A. P. Aiden, R. Kishony, Drug interactions and the evolution of antibiotic resistance. *Nat. Rev. Microbiol.* **7**, 460–466 (2009). doi: 10.1038/nrmicro2133; pmid: 19444248
77. S. Kim, T. D. Lieberman, R. Kishony, Alternating antibiotic treatments constrain evolutionary paths to multidrug resistance. *Proc. Natl. Acad. Sci. U.S.A.* **111**, 14494–14499 (2014). doi: 10.1073/pnas.1409800111; pmid: 25246554
78. S. Bonhoeffer, M. Lipsitch, B. R. Levin, Evaluating treatment protocols to prevent antibiotic resistance. *Proc. Natl. Acad. Sci. U.S.A.* **94**, 12106–12111 (1997). doi: 10.1073/pnas.94.22.12106; pmid: 9342370
79. P. Abel zur Wiesch, R. Kouyos, S. Abel, W. Viechtbauer, S. Bonhoeffer, Cycling empirical antibiotic therapy in hospitals: Meta-analysis and models. *PLOS Pathog.* **10**, e1004225–e13 (2014). pmid: 24968123
80. M. H. Kollef, Is antibiotic cycling the answer to preventing the emergence of bacterial resistance in the intensive care unit? *Clin. Infect. Dis.* **43** (Suppl 2), S82–S88 (2006). doi: 10.1086/504484; pmid: 16894520
81. A. L. Pakyz, B. M. Farr, Rates of *Stenotrophomonas maltophilia* colonization and infection in relation to antibiotic cycling protocols. *Epidemiol. Infect.* **137**, 1679–1683 (2009). doi: 10.1017/S0950268809002830; pmid: 19874637
82. Y. Katayama, T. Ito, K. Hiramatsu, A new class of genetic element, staphylococcus cassette chromosome mec, encodes methicillin resistance in Staphylococcus aureus. *Antimicrob. Agents Chemother.* **44**, 1549–1555 (2000). doi: 10.1128/AAC.44.6.1549-1555.2000; pmid: 10817707
83. I. Chopra, M. Roberts, Tetracycline antibiotics: Mode of action, applications, molecular biology, and epidemiology of bacterial resistance. *Microbiol. Mol. Biol. Rev.* **65**, 232–260 (2001). doi: 10.1128/MMBR.65.2.232-260.2001; pmid: 11381101
84. L. Azimi *et al*., Tracing of false negative results in phenotypic methods for identification of carbapenemase by Real-time PCR. *Gene* **576**, 166–170 (2016). doi: 10.1016/j.gene.2015.10.008; pmid: 26456106
85. A. van der Zee *et al*., Multi-centre evaluation of real-time multiplex PCR for detection of carbapenemase genes OXA-48, VIM, IMP, NDM and KPC. *BMC Infect. Dis.* **14**, 27 (2014). doi: 10.1186/1471-2334-14-27; pmid: 24422880
86. H. De Beenhouwer *et al*., Rapid detection of rifampicin resistance in sputum and biopsy specimens from tuberculosis patients by PCR and line probe assay. *Tuber. Lung Dis.* **76**, 425–430 (1995). doi: 10.1016/0962-8479(95)90009-8; pmid: 7496004
87. A. Telenti *et al*., Detection of rifampicin-resistance mutations in *Mycobacterium tuberculosis*. *Lancet* **341**, 647–651 (1993). doi: 10.1016/0140-6736(93)90417-F; pmid: 8095569
88. D. Jonas, M. Speck, F. D. Daschner, H. Grundmann, Rapid PCR-based identification of methicillin-resistant *Staphylococcus aureus* from screening swabs. *J. Clin. Microbiol.* **40**, 1821–1823 (2002). doi: 10.1128/JCM.40.5.1821-1823.2002; pmid: 11980967
89. P. Bradley *et al*., Rapid antibiotic-resistance predictions from genome sequence data for *Staphylococcus aureus* and *Mycobacterium tuberculosis*. *Nat. Commun.* **6**, 10063 (2015). doi: 10.1038/ncomms10063
90. T. D. Lieberman *et al*., Genetic variation of a bacterial pathogen within individuals with cystic fibrosis provides a record of selective pressures. *Nat. Genet.* **46**, 82–87 (2014). doi: 10.1038/ng.2848; pmid: 24316980
91. T. D. Lieberman *et al*., Parallel bacterial evolution within multiple patients identifies candidate pathogenicity genes. *Nat. Genet.* **43**, 1275–1280 (2011). doi: 10.1038/ng.997; pmid: 22081229
92. E. Toprak *et al*., Evolutionary paths to antibiotic resistance under dynamically sustained drug selection. *Nat. Genet.* **44**, 101–105 (2012). doi: 10.1038/ng.1034; pmid: 22179135
93. A. C. Palmer *et al*., Delayed commitment to evolutionary fate in antibiotic resistance fitness landscapes. *Nat. Commun.* **6**, 7385 (2015). doi: 10.1038/ncomms8385; pmid: 26060115
94. T. Nordahl Petersen *et al*., Meta-genomic analysis of toilet waste from long distance flights; a step towards global surveillance of infectious diseases and antimicrobial resistance. *Sci. Rep.* **5**, 11444 (2015). doi: 10.1038/srep11444; pmid: 26161690
95. J. L. Martínez, T. M. Coque, F. Baquero, What is a resistance gene? Ranking risk in resistomes. *Nat. Rev. Microbiol.* **13**, 116–123 (2015). doi: 10.1038/nrmicro3399; pmid: 25534811
96. H. C. Wegener, Antibiotics in animal feed and their role in resistance development. *Curr. Opin. Microbiol.* **6**, 439–445 (2003). doi: 10.1016/j.mib.2003.09.009; pmid: 14572534
97. A. M. Hammerum, O. E. Heuer, Human health hazards from antimicrobial-resistant Escherichia coli of animal origin. *Clin. Infect. Dis.* **48**, 916–921 (2009). doi: 10.1086/597292; pmid: 19231979
98. A. R. Vieira *et al*., Association between antimicrobial resistance in Escherichia coli isolates from food animals and blood stream isolates from humans in Europe: An ecological study. *Foodborne Pathog. Dis.* **8**, 1295–1301 (2011). doi: 10.1089/fpd.2011.0950; pmid: 21883007
99. Q. Chang, W. Wang, G. Regev-Yochay, M. Lipsitch, W. P. Hanage, Antibiotics in agriculture and the risk to human health: How worried should we be? *Evol Appl* **8**, 240–247 (2015). doi: 10.1111/eva.12185; pmid: 25861382
100. R. D. Kouyos *et al*., The path of least resistance: Aggressive or moderate treatment? *Proc. Biol. Sci.* **281**, 20140566–20140566 (2014). doi: 10.1098/rspb.2014.0566; pmid: 25253451
101. V. Pokrovskaya, T. Baasov, Dual-acting hybrid antibiotics: A promising strategy to combat bacterial resistance. *Expert Opin. Drug Discov.* **5**, 883–902 (2010). doi: 10.1517/17460441.2010.508069; pmid: 22823262
102. K. K. Wang *et al*., A hybrid drug limits resistance by evading the action of the multiple antibiotic resistance pathway. *Mol. Biol. Evol.* 10.1093/molbev/msv243 (2015). doi: 10.1093/molbev/msv243; pmid: 26538141
103. O. Fridman, A. Goldberg, I. Ronin, N. Shoresh, N. Q. Balaban, Optimization of lag time underlies antibiotic tolerance in evolved bacterial populations. *Nature* **513**, 418–421 (2014). doi: 10.1038/nature13469; pmid: 25043002
104. S. Loewe, Die quantitation probleme der pharmakologie. *Ergeb. Physiol.* **27**, 47–187 (1928). doi: 10.1007/BF02322290
105. C. T. Keith, A. A. Borisy, B. R. Stockwell, Multicomponent therapeutics for networked systems. *Nat. Rev. Drug Discov.* **4**, 71–78 (2005). doi: 10.1038/nrd1609; pmid: 15688074
106. P. Yeh, A. I. Tschumi, R. Kishony, Functional classification of drugs by properties of their pairwise interactions. *Nat. Genet.* **38**, 489–494 (2006). doi: 10.1038/ng1755; pmid: 16550172
107. M. Cokol *et al*., Large-scale identification and analysis of suppressive drug interactions. *Chem. Biol.* **21**, 541–551 (2014). doi: 10.1016/j.chembiol.2014.02.012; pmid: 24704506
108. M. Cokol *et al*., Systematic exploration of synergistic drug pairs. *Mol. Syst. Biol.* **7**, 544 (2011). doi: 10.1038/msb.2011.71; pmid: 22068327
109. K. R. Allison, M. P. Brynildsen, J. J. Collins, Metabolite-enabled eradication of bacterial persisters by aminoglycosides. *Nature* **473**, 216–220 (2011). doi: 10.1038/nature10069; pmid: 21562562
110. H. H. Lee, M. N. Molla, C. R. Cantor, J. J. Collins, Bacterial charity work leads to population-wide resistance. *Nature* **467**, 82–85 (2010). doi: 10.1038/nature09354; pmid: 20811456
111. N. M. Vega, K. R. Allison, A. N. Samuels, M. S. Klempner, J. J. Collins, Salmonella typhimurium intercepts Escherichia coli signaling to enhance antibiotic tolerance. *Proc. Natl.*

Acad. Sci. U.S.A. **110**, 14420–14425 (2013). doi: 10.1073/pnas.1308085110; pmid: 23946425
112. M. Malik *et al.*, Lethal synergy involving bicyclomycin: An approach for reviving old antibiotics. *J. Antimicrob. Chemother.* **69**, 3227–3235 (2014). doi: 10.1093/jac/dku285; pmid: 25085655
113. L. Ejim *et al.*, Combinations of antibiotics and nonantibiotic drugs enhance antimicrobial efficacy. *Nat. Chem. Biol.* **7**, 348–350 (2011). doi: 10.1038/nchembio.559; pmid: 21516114
114. P. L. Taylor, L. Rossi, G. De Pascale, G. D. Wright, A forward chemical screen identifies antibiotic adjuvants in Escherichia coli. *ACS Chem. Biol.* **7**, 1547–1555 (2012). doi: 10.1021/cb300269g; pmid: 22698393
115. R. J. Nichols *et al.*, Phenotypic landscape of a bacterial cell. *Cell* **144**, 143–156 (2011). pmid: 21185072
116. T. Bollenbach, S. Quan, R. Chait, R. Kishony, Nonoptimal microbial response to antibiotics underlies suppressive drug interactions. *Cell* **139**, 707–718 (2009). doi: 10.1016/j.cell.2009.10.025; pmid: 19914165
117. W. Szybalski, V. Bryson, Genetic studies on microbial cross-resistance to toxic agents. III. Cross-resistance of Mycobacterium ranae to twenty-eight antimycobacterial agents. *Am. Rev. Tuberc.* **69**, 267–279 (1954). pmid: 13114644
118. M. D. Hastings, C. H. Sibley, Pyrimethamine and WR99210 exert opposing selection on dihydrofolate reductase from Plasmodium vivax. *Proc. Natl. Acad. Sci. U.S.A.* **99**, 13137–13141 (2002). doi: 10.1073/pnas.182295999; pmid: 12198181
119. A. K. Lukens *et al.*, Harnessing evolutionary fitness in Plasmodium falciparum for drug discovery and suppressing resistance. *Proc. Natl. Acad. Sci. U.S.A.* **111**, 799–804 (2014). doi: 10.1073/pnas.1320886110; pmid: 24381157
120. S. G. Deeks, Treatment of antiretroviral-drug-resistant HIV-1 infection. *Lancet* **362**, 2002–2011 (2003). doi: 10.1016/S0140-6736(03)15022-2; pmid: 14683662
121. K. M. Pluchino, M. D. Hall, A. S. Goldsborough, R. Callaghan, M. M. Gottesman, Collateral sensitivity as a strategy against cancer multidrug resistance. *Drug Resist. Updat.* **15**, 98–105 (2012). doi: 10.1016/j.drup.2012.03.002; pmid: 22483810
122. J. Gressel, L. A. Segel, Negative cross-resistance; a possible key to atrazine resistance management: A call for whole plant data. *Z. Naturforsch.* **45c**, 470–473 (1990).
123. G. Gadamski, D. Ciarka, J. Gressel, S. W. Gawronski, Negative cross-resistance in triazine-resistant biotypes of *Echinochloa crus-galli* and *Conyza canadensis*. *Weed Sci.* **48**, 176–180 (2000). doi: 10.1614/0043-1745(2000)048[0176:NCRITR]2.0.CO;2

ACKNOWLEDGMENTS

We thank T. Bollenbach, W. P. Hanage, M. Elowitz, J. Jiao, and D. Van Valen for their thoughtful comments and input. This work was supported in part by U.S. National Institutes of Health grant R01-GM081617, European Research Council FP7 ERC Grant 281891, and F. Hoffmann–La Roche Ltd.

10.1126/science.aad3292

RESEARCH ARTICLE SUMMARY

NEURAL CIRCUITS

Prefrontal cortical regulation of brainwide circuit dynamics and reward-related behavior

Emily A. Ferenczi,* Kelly A. Zalocusky,* Conor Liston,* Logan Grosenick, Melissa R. Warden, Debha Amatya, Kiefer Katovich, Hershel Mehta, Brian Patenaude, Charu Ramakrishnan, Paul Kalanithi, Amit Etkin, Brian Knutson, Gary H. Glover, Karl Deisseroth†

INTRODUCTION: The drive to seek and experience reward is conserved across species and, in mammals, involves interactions between subcortical dopaminergic systems and limbic structures such as the striatum. Impairment of this process, observed across a number of psychiatric conditions, is the clinical symptom of anhedonia (loss of enjoyment). The neural mechanisms underlying anhedonia are unknown but could result from abnormal interactions between cortical and subcortical reward circuits. We sought to test the hypothesis that elevated medial prefrontal cortex (mPFC) excitability (a clinical feature associated with anhedonia) exerts suppressive control over the interactions between two distant subcortical regions: the dopaminergic midbrain and the striatum.

RATIONALE: Clinical imaging studies have detected elevated activity in the mPFC in human patients with depression, and treatment is associated with normalization of this overactivity and improvement of anhedonic symptoms. Additionally, human studies have identified areas of the brain that respond to reward anticipation and experience, and this response can be suppressed in psychiatric disease. However, the source of this reward signal and the mechanisms underlying its modulation have not been causally demonstrated. We have integrated a diverse set of chronic and acute optogenetic tools with functional magnetic resonance imaging (fMRI) to provide a bridge between the causal, cellular specificity of rodent optogenetics and the brainwide observations that characterize human neuroimaging, with the goal of locally manipulating and globally visualizing neural activity to understand the regulation of reward-seeking behavior.

ON OUR WEB SITE

Read the full article at http://dx.doi.org/10.1126/science.aac9698

RESULTS: We demonstrate that stimulation of midbrain dopamine neurons drives both striatal fMRI blood oxygen level–dependent (BOLD) activity and reward-seeking behavior, and we show that these are correlated across individuals. We additionally find that silencing of dopamine neurons suppresses activity in the striatum, as well as in other brain regions (such as the hypothalamus), and drives avoidance behavior. Having established this bidirectional control of reward-seeking behavior, we then tested for perturbation of this circuitry via elevation of mPFC excitability. We observed suppression of striatal responses to dopamine, as well as the behavioral drive to seek out dopamine neuron stimulation and other natural rewarding stimuli. Finally, we demonstrate that stably elevated mPFC excitability synchronizes corticolimbic BOLD and electrophysiological activity, which in turn can predict anhedonic behavior in individual animals.

CONCLUSION: Our findings from experiments involving local cell-specific control, simultaneously with global unbiased observation of neural activity, reveal that the mPFC exerts top-down control over midbrain dopaminergic interactions with the striatum and that, when elevated, activity in the mPFC can suppress natural reward-related behavior. Furthermore, we observe that cortical-subcortical neural dynamics work in concert to regulate reward processing. All of these findings have implications for our understanding of natural reward-related physiology and behavior, as well as the pathogenesis of anhedonia. ■

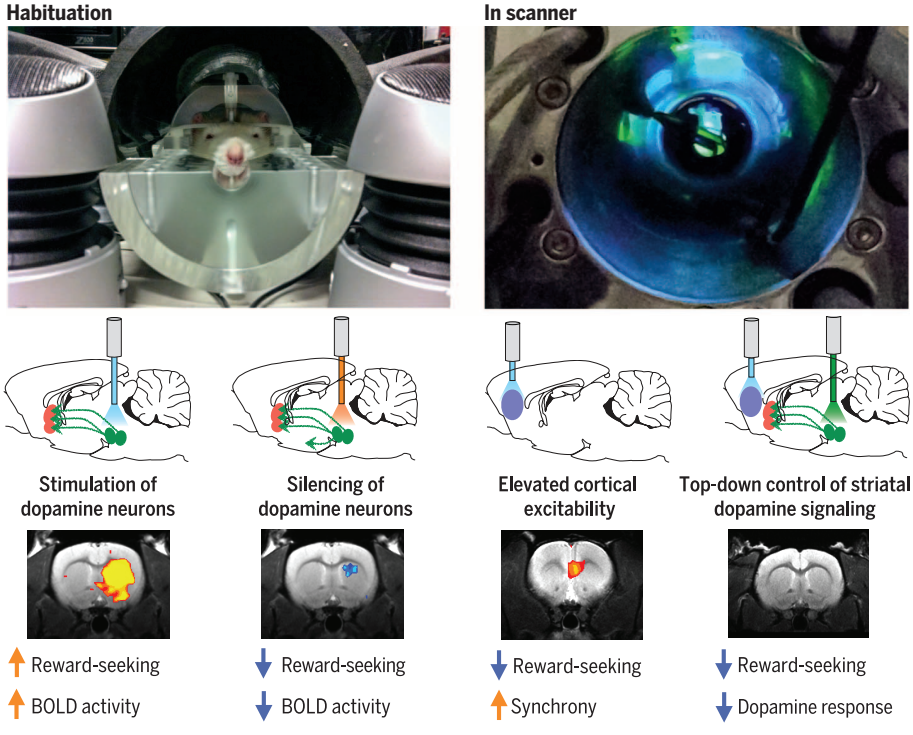

Reward-related signaling between the dopaminergic midbrain and the striatum is under suppressive control by the mPFC. Optogenetic fMRI was used to locally manipulate and globally visualize brainwide neural activity related to reward. Habituated rats were scanned in the awake state (top photographs). We establish that striatal BOLD activity is increased by optogenetic stimulation of dopamine neurons and decreased by optogenetic neural silencing. We demonstrate that focally elevated mPFC excitability suppresses reward-seeking behavior by exerting top-down control over striatal dopamine-induced activity and drives synchrony between specific corticolimbic circuits.

The list of author affiliations is available in the full article online.
***These authors contributed equally to this work.**
†Corresponding author. E-mail: deissero@stanford.edu
Cite this article as E. A. Ferenczi *et al.*, *Science* 351, aac9698 (2016). DOI: 10.1126/science.aac9698

RESEARCH ARTICLE

NEURAL CIRCUITS

Prefrontal cortical regulation of brainwide circuit dynamics and reward-related behavior

Emily A. Ferenczi,[1,2]* Kelly A. Zalocusky,[1,2]* Conor Liston,[3]* Logan Grosenick,[1,2] Melissa R. Warden,[4] Debha Amatya,[1] Kiefer Katovich,[5] Hershel Mehta,[5] Brian Patenaude,[6] Charu Ramakrishnan,[1] Paul Kalanithi,[7] Amit Etkin,[6] Brian Knutson,[5] Gary H. Glover,[8] Karl Deisseroth[1,4,9]†

Motivation for reward drives adaptive behaviors, whereas impairment of reward perception and experience (anhedonia) can contribute to psychiatric diseases, including depression and schizophrenia. We sought to test the hypothesis that the medial prefrontal cortex (mPFC) controls interactions among specific subcortical regions that govern hedonic responses. By using optogenetic functional magnetic resonance imaging to locally manipulate but globally visualize neural activity in rats, we found that dopamine neuron stimulation drives striatal activity, whereas locally increased mPFC excitability reduces this striatal response and inhibits the behavioral drive for dopaminergic stimulation. This chronic mPFC overactivity also stably suppresses natural reward-motivated behaviors and induces specific new brainwide functional interactions, which predict the degree of anhedonia in individuals. These findings describe a mechanism by which mPFC modulates expression of reward-seeking behavior, by regulating the dynamical interactions between specific distant subcortical regions.

The drive to pursue and consume rewards is highly conserved across species (*1*). Subcortical neuromodulatory systems, including midbrain dopaminergic projections, play a central role in predicting and signaling the availability of rewards (*2*–*5*). Anhedonia represents a core symptom of depression but also characterizes other neuropsychiatric disorders, including schizophrenia, suggesting the possibility of shared neural substrates (*6*). Although the underlying cause of anhedonia remains unknown, a number of hypotheses exist, including cortically driven dysregulation of subcortical circuits (*7*–*10*). Imaging studies have detected elevated metabolic activity in the mPFC of human patients suffering from depression (*11*); this type of brain activity is correlated with anhedonic symptoms (*12*–*16*). In particular, the subgenual cingulate gyrus of the medial prefrontal cortex (mPFC) is a therapeutic target for deep brain stimulation in refractory depression, and treatment has been associated with normalization of this localized hyperactivity, alongside patient reports of renewed interest in rewarding aspects of life (*11*, *17*, *18*). By combining optogenetics with functional magnetic resonance imaging (fMRI), we sought to test the hypothesis that the mPFC exerts causal top-down control over the interaction of specific subcortical regions governing dopamine-driven reward behavior, with important implications for anhedonia.

Although human fMRI experiments have resolved activity patterns in distinct subregions of the brain that respond to reward anticipation and experience (*19*, *20*), the causal relationships between neuronal activity in reward-related circuits and brainwide blood oxygen level–dependent (BOLD) patterns have yet to be established. In optogenetic fMRI (ofMRI), light-responsive regulators of transmembrane ion conductance (*21*) are introduced into target cell populations and controlled by focal pulses of light to assess the causal impact of the targeted circuit elements on local and global fMRI responses. We developed and extended this technique to scanning of awake rats and included a number of optogenetic tools specifically suited to our experimental questions.

We began by mapping the brainwide BOLD response to optogenetic stimulation of dopamine neurons in transgenic tyrosine hydroxylase driver (TH-Cre) rats, using an excitatory channelrhodopsin (ChR2 His^{134}→Arg^{134}, hereafter referred to as ChR2). Next, we tested effects of a similarly targeted inhibitory opsin, the enhanced *Natromonas* halorhodopsin (eNpHR3.0) (*22*). We hypothesized that such inhibition of dopamine neurons would reduce BOLD activity in downstream regions, although it is unknown whether tonic dopamine levels would be sufficient to allow detection of a downward modulation in BOLD. Furthermore, the expected direction of the BOLD response is a matter of debate, given the functional heterogeneity of dopamine receptors.

Finally, we assessed the influence of mPFC excitability over this subcortical dopaminergic reward signaling. Altered excitability in the mPFC has been correlated with anhedonic behaviors in human patients and mice (*23*), and there is a growing body of literature characterizing altered resting-state BOLD correlations in patients with psychiatric disease (*24*). Nevertheless, it is still unclear whether and to what extent local changes in prefrontal cortex activity might propagate to distant brain regions to modulate reward-related signals. To address these questions, we used the stabilized step-function opsin (SSFO), a double-mutant excitatory ChR2 (Cys^{128}→Ser^{128}, Asp^{156}→Ala^{156}) engineered to have slow off-kinetics (rate of channel closure τ_{off} ~ 30 min) (*23*). Upon activation by blue light, SSFO causes stable subthreshold depolarization of cell bodies, sensitizing neurons to synaptic input. The resulting elevated excitability of targeted cells (*23*, *25*) outlasts the light pulse, permitting extended-duration shifts in neural excitability and moderate asynchronous increases in neural firing. In milliseconds, SSFO can also be switched off by a pulse of yellow light; this feature is essential for repetitive stimulation in fMRI experiments. Additionally, the transient and minimal light requirements of SSFO decrease the potential for tissue heating (which could cause an artifact in fMRI BOLD studies) (*26*). To directly test the hypothesis that mPFC modulates dopaminergic reward signaling in the striatum, we devised dual-stimulation experiments, combining mPFC SSFO stimulation with dopaminergic midbrain stimulation by using the spectrally shifted excitatory tool $C1V1_{TT}$ [a red-shifted hybrid (*23*, *27*) between *Chlamydomonas* and *Volvox* channelrhodopsins], permitting the assessment of interaction between two distinct cell populations.

Results

Awake ofMRI

Because reward anticipation and experience involve varying states of arousal, and because anesthesia dampens BOLD activity, assessment of the neural activity of awake and alert animals was critical for the collection of behaviorally relevant brainwide signals (*28*). We therefore established protocols for ofMRI in the awake rat, with careful animal habituation and monitoring, permitting the imaging of brain networks uncontaminated by anesthesia or excessive subject movement. Animals were habituated in a mock MRI environment before scanning (Fig. 1A), and respiratory rate and head motion were monitored during scanning (Fig. 1, B to D). Compared with anesthetized protocols, our protocol enhanced the detection of evoked changes in BOLD activity (fig. S1 and table S1). In addition to scanning fluorophore-only (virus-injected, fiber-implanted,

[1]Department of Bioengineering, Stanford University, Stanford, CA 94305, USA. [2]Neurosciences Program, Stanford University, Stanford, CA 94305, USA. [3]Brain Mind Research Institute, Weill Cornell Medical College, New York, NY 10065, USA. [4]Department of Neurobiology and Behavior, Cornell University, Ithaca, NY 14853, USA. [5]Department of Psychology, Stanford University, Stanford, CA 94305, USA. [6]Department of Psychiatry and Behavioral Sciences, Stanford University, Stanford, CA 94305, USA. [7]Department of Neurosurgery, Stanford University, Stanford, CA 94305, USA. [8]Department of Radiology, Stanford University, Stanford, CA, 94305, USA. [9]Howard Hughes Medical Institute, Stanford University, Stanford, CA, 94305, USA.
*These authors contributed equally to this work.
†Corresponding author. E-mail: deissero@stanford.edu

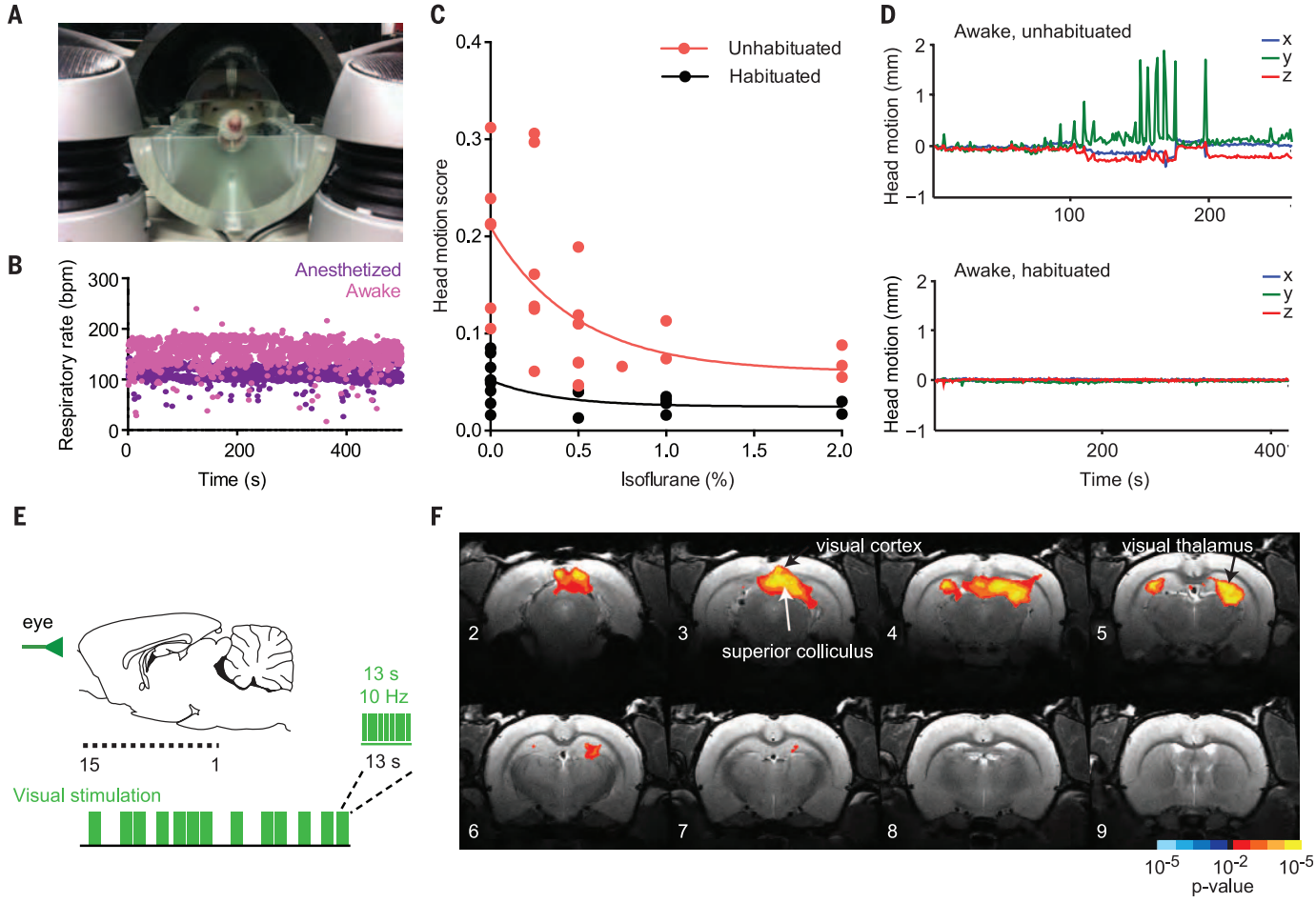

Fig. 1. Optogenetic functional MRI (ofMRI) in awake rats. (**A**) MRI simulation environment for rodent habituation to the scanning procedure. (**B**) Example of respiratory rate monitoring [bpm, breaths per minute; n = 1 rat; eight sequential scans, four anesthetized (1 to 2% isoflurane) and four awake (0% isoflurane)]. (**C**) Effect of habituation on head motion during scanning, as a function of anesthesia depth (n = 2 rats). Head motion score is the root mean square of head translation in three dimensions over the course of a scan. (**D**) Example head motion plots (head translation in three dimensions, calculated as shifts in the center of mass of all voxels in the image over the course of a single scan) for an unhabituated (top) and a habituated (bottom) subject. The unhabituated scan was aborted early. (**E**) Visual stimulation during fMRI. A sagittal view of the brain indicates the location of MRI images from anterior (image 15) to posterior (image 1). The schematic illustrates event-related stimulation design. (**F**) Z-score map of BOLD activity in visual brain regions in response to visual stimulation in control subjects (n = 5 rats, 20 runs). For this figure and all subsequent statistical maps, maps were thresholded at $P < 0.05$ (corrected) [$K > 5$ functional voxels (80 transformed voxels), uncorrected $P < 0.01$]. Gradations in color (e.g., red-orange-yellow) indicate incremental P-value thresholds of one order of magnitude.

no opsin) negative-control subjects [yellow fluorescent protein (YFP) controls], we incorporated a nonoptogenetic visual stimulus as a positive control into our standard fMRI stimulation protocol, in which moderate green light (bursts of 13 s, 10 Hz, 20-ms pulse width, ~0.5 mW) was flashed in front of the eye in a pseudorandomly ordered event-related sequence (Fig. 1E). This stimulus evoked predictable and consistent BOLD activity in subcortical visual regions (superior colliculus, lateral geniculate nucleus) (Fig. 1F).

Brainwide mapping of a dopamine neuron–driven rewarded state

We next investigated how activity in midbrain dopamine neurons affects BOLD activity patterns in dopamine terminal regions (*20*). Because optogenetic control of dopamine neurons has been shown to drive reward-seeking behavior in rodents (*29*, *30*), we predicted that phasic activation of midbrain dopamine neurons would increase striatal BOLD activity by driving synaptic input to the region (*31*), and the response in ventral striatum would be closely correlated with reward-seeking behavior.

We expressed ChR2 fused with YFP in midbrain dopamine neurons by unilaterally injecting a Cre-dependent construct into the right midbrain of tyrosine-hydroxylase TH-Cre transgenic Long-Evans rats (*30*) (Fig. 2A). Specific expression was confirmed by colocalization of YFP with anti-TH staining in confocal images (Fig. 2A). We performed optogenetic stimulation of midbrain dopaminergic neurons in a 7-T small-animal scanner. Blue light pulses were delivered to the midbrain of awake, habituated rats [we used a physiologically relevant in magnitude, event-related stimulation design (phasic 2-s bursts of 20-Hz blue light pulses, 10-ms pulse width, minimum of 11-s recovery time after each stimulation burst) interleaved with the nonoptogenetic visual stimulus described above (Fig. 2B)]. We chose a 2-s burst duration because initial dose-response experiments indicated that this duration was more effective at driving reward-seeking behavior (fig. S2A) and reliable striatal BOLD activity (fig. S2, B and C) compared with shorter burst durations and was also within a previously validated physiological burst-duration range for ventral tegmental area (VTA) neurons (*32*). Unilateral ChR2 stimulation of the midbrain evoked robust, largely ipsilateral increases in BOLD activity in the dorsal and ventral striatum (Fig. 2G), as well as increases in other brain regions, including the retrosplenial cortex and thalamus (Fig. 2C). These widespread changes in BOLD activity were not observed in fluorophore-only (no opsin) YFP-control subjects (Fig. 2, D and H), despite robust activity increases during visual stimulation (Fig. 2, E and F), and the difference in optogenetic response was significant between the ChR2 and YFP-control groups (fig. S3, A and B, and table S2).

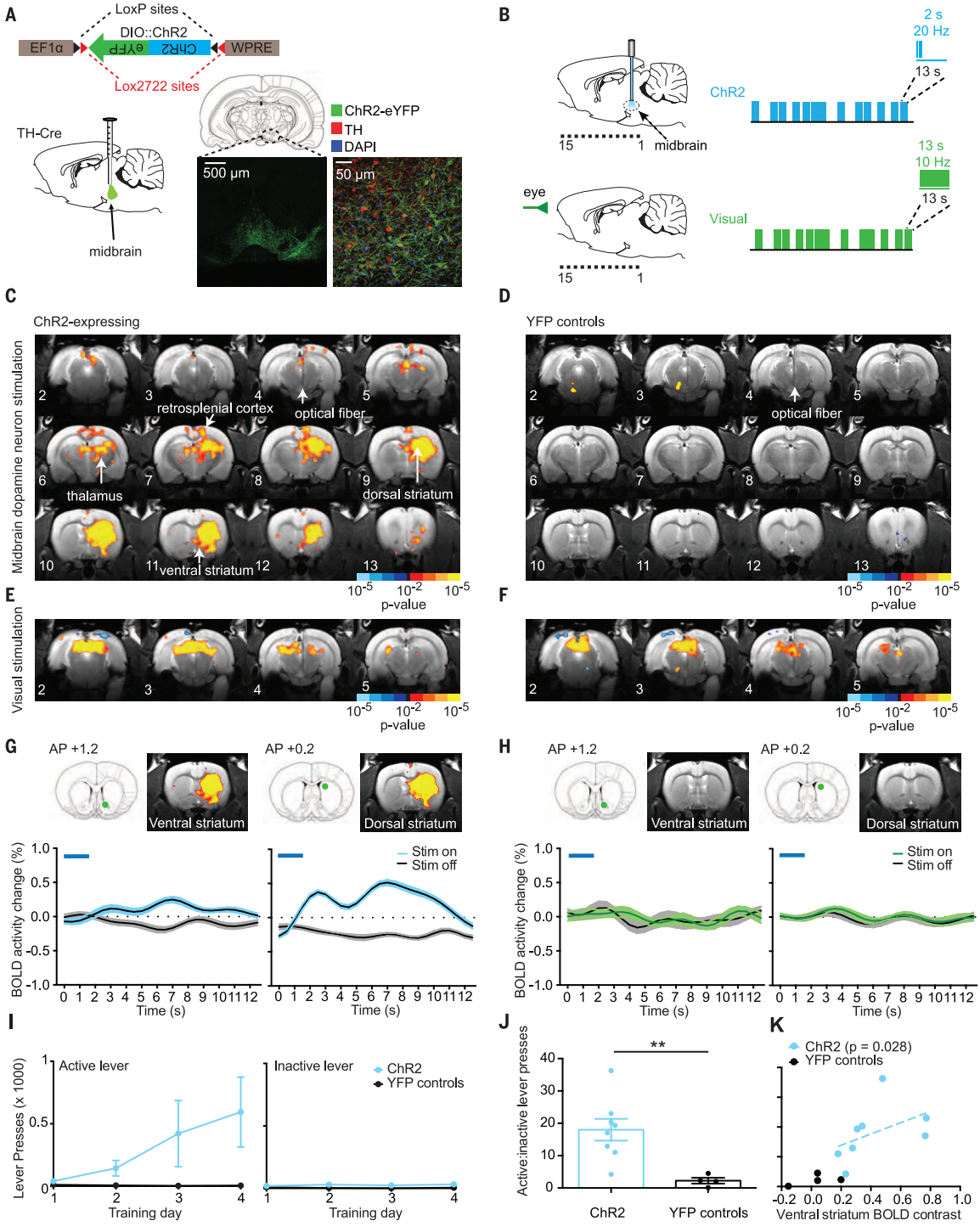

Fig. 2. Influence of midbrain optogenetic dopamine stimulation on brain-wide BOLD activity and behavior. (**A**) Schematic of Cre-dependent ChR2 construct and sagittal view of injection site in the midbrain. Confocal images demonstrate ChR2 expression in dopaminergic neurons in the midbrain. Green, ChR2-YFP; red, tyrosine hydroxylase (TH); blue, 4′,6-diamidino-2-phenylindole (DAPI). (**B**) Schematic of event-related design for midbrain ChR2 stimulation and visual stimulation. (**C**) *Z*-score map of BOLD activity in response to ChR2 stimulation of midbrain dopamine neurons (n = 8 rats, 34 runs). (**D**) *Z*-score map for YFP-control subjects in response to blue light stimulation in the midbrain (n = 4 rats, 21 runs). (**E**) *Z*-score maps for ChR2-expressing subjects (n = 8 rats, 34 runs) and (**F**) YFP-control subjects (n = 4 rats, 21 runs) in response to visual stimulation. (**G**) Average ChR2 stimulation–locked BOLD activity time courses in the ventral and dorsal striatum for ChR2-expressing subjects (n = 8 rats, 34 runs) and (**H**) YFP-control subjects (n = 4 rats, 16 runs). Mean and SEM (n = number of runs) are shown. Timing of light delivery is indicated by the blue lines above the plots. Regions of interest (ROIs) used for time-course extraction are indicated by green dots on atlas images above plots. (**I**) Active and inactive lever presses as a function of training day for ChR2-expressing (n = 8) and YFP-control (n = 4) rats. (**J**) Active-to-inactive lever press ratio on the final day of training for ChR2 and YFP rats (two-tailed Mann-Whitney *U* test: sum of ranks = 68, 11; U = 1; $^{**}P$ = 0.0081). (**K**) Relationship between BOLD activity contrast in the ventral striatum and active-to-inactive lever press ratio for ChR2-expressing subjects (n = 8 rats, Spearman ρ = 0.78, P = 0.028) and YFP-expressing subjects (n = 4 rats).

Visualization of the dynamic influence of optogenetic dopamine stimulation on downstream BOLD activity through stimulation-locked averaged time courses suggested that striatal BOLD activity exhibited a double-peaked profile, particularly in the dorsal striatum (Fig. 2G and fig. S3C). The early response, which peaked 2 to 3 s after the onset of stimulation, with a fast decline, was tightly correlated in magnitude with a second later response (fig. S3D). We suspected that this prompt response resulted directly from vascular inflow to activated regions (providing new, unsaturated spins to blood vessel–containing regions, enhancing signal independently of blood oxygenation level), which we were able to detect because of our fast sampling rate [repetition time (TR) = 0.5 s] (*33*). There was no response to optogenetic stimulation in fluorophore-only YFP-control subjects (Fig. 2H).

Operant chamber behavioral testing confirmed the rewarding nature of optogenetic stimulation of midbrain dopaminergic neurons. ChR2-expressing but not YFP-control rats reliably chose to press a lever to deliver blue light stimulation to the midbrain (active lever), as opposed to a lever that delivered no light (inactive lever) (Fig. 2, I and J). We noted a significant correlation between an individual rat's preference for the active lever over the inactive lever in the operant chamber and the change in BOLD activity in the rat's ventral striatum during ChR2 stimulation in the scanner (Fig. 2K). A similar relation was observed in the dorsal striatum (fig. S3, E and F). Significant correlations were not observed for the total number of lever presses, suggesting that the BOLD activity change was associated with lever selection preference rather than overall motor activity (fig. S3, G and H). Striatal BOLD activity was also influenced by the medial-lateral position of the optical fiber within the VTA (fig. S4), with more lateral positioning associated with stronger BOLD responses in both the dorsal and ventral striatum.

Dopamine neuron–driven BOLD activity patterns require dopamine receptor activation

To better understand the mechanisms underlying BOLD activity patterns driven by activity in dopamine neurons, we next tested whether these BOLD patterns required dopamine receptor activation. In four rats, we performed a series of longitudinal pharmacological experiments consisting of a baseline scan (no pharmacological agents), followed ~24 hours later by a scan in which a cocktail of dopamine D1 receptor and D2 receptor antagonists was administered intraperitoneally immediately before acquisition of functional images, followed by a washout scan (with intraperitoneal injection of saline/dimethyl sulfoxide vehicle control) performed 24 to 48 hours after drug administration to allow sufficient time for drug elimination (*34*, *35*) (Fig. 3, A to C). We observed robust increases in striatal BOLD activity in response to dopamine neuron stimulation at baseline (Fig. 3A). Administration of the dopaminergic antagonists (Fig. 3, B and D to F) significantly reduced these responses. Increases in BOLD activity returned during the washout phase (Fig. 3, C to E; fig. S5; and tables S3 and S4). The ability of the visual stimulus to increase BOLD activity in visual processing circuits remained strong. In fact, it was stronger during D1 and D2 receptor antagonist administration than at baseline and washout, eliminating the possibility that dopamine antagonism abolished all BOLD activity throughout the brain (Fig. 3, A to E) and supporting previous research suggesting that tonic dopamine may play a role in modulating visual processing (*36*–*38*).

These findings were confirmed by a model-free support vector machine classification analysis with recursive feature elimination (SVM-RFE) (*39*) (fig. S6). At baseline, SVM-RFE classified midbrain stimulation versus no stimulation with 82 to 84% accuracy, but accuracy level fell to 63 to 66% for scans acquired after administration of D1 and D2 receptor antagonists and to chance classification rates (~50 to 55%) for YFP-control subjects (fig. S6A). SVM-RFE classified visual stimulation versus no stimulation with 72 to 80% accuracy at baseline and for YFP controls, and the accuracy level increased to 85 to 86% for scans acquired after D1 and D2 receptor antagonist administration (fig. S6B). When features from these optimal classifiers were back-projected onto brain volumes over time, the features were located in the striatum for optogenetic midbrain stimulation and in the visual midbrain and thalamus for visual stimulation, confirming the magnitude and spatial localization of the BOLD activity and its responsiveness to modulation by pharmacological agents during two different types of stimulation.

Optogenetic inhibition of dopamine neurons decreases BOLD activity in divergent brain regions

We wondered whether the silencing of dopamine neurons would also influence BOLD activity. We predicted that because dopamine neurons exhibit tonic activity (*40*), which can be depressed by reward omission (*41*), optogenetic inhibition might decrease BOLD activity in brain regions that are responsive to this tonic input. We expressed the yellow light–activated halorhodopsin eNpHR3.0 (*22*) via a Cre-dependent construct in the midbrain of TH-Cre transgenic rats and histologically confirmed colocalization of TH and eNpHR3.0 expression (fig. S7A). A real-time place preference test revealed that the majority of rats spent significantly less time in the chamber in which they received inhibition of midbrain dopamine neurons (fig. S7B), but midbrain inhibition had little influence on locomotor behavior (fig. S7B). In the MRI scanner, yellow light pulses (590 nm) were delivered to the midbrain with the same event-related design previously used for stimulation, with either 2- or 10-s continuous light pulses (rather than 20-Hz pulses), in parallel with visual stimulation as before (fig. S7, C and F). We observed decreased BOLD activity in the hypothalamus and dorsal striatum in response to the eNpHR3.0 manipulation (fig. S7, D and E), and this result was more pronounced for 10-s inhibition than for 2-s inhibition (fig. S7, G and H, and fig. S2B). Thus, this finding confirms that neural silencing can reduce BOLD activity in a dose-dependent manner (fig. S2, B and C) but in a slightly different spatial pattern from that elicited by phasic activation.

Elevated excitability of the mPFC suppresses natural reward-related behavior

Having characterized brainwide BOLD activity patterns corresponding to a dopamine neuron–driven rewarded state, we next sought to investigate how these signals might be modulated by top-down cortical glutamatergic input, which has been implicated in physiological reward-seeking behaviors (*42*) and pathological anhedonic states (*23*). Neuroimaging studies indicate that elevated metabolic activity in the ventromedial prefrontal cortex is associated with anhedonic symptoms in depression (*11*–*16*), and normalization of prefrontal hyperactivity is associated with renewed interest in rewarding activities (*11*, *17*, *18*). We therefore chose an optogenetic stimulation method (SSFO) that would not drive synchronous elevation in cortical firing but would instead produce an asynchronous enhancement of excitability (*23*) to most accurately re-create the proposed human pathophysiology. We hypothesized that although this manipulation may favor local BOLD activity within the mPFC, the wide-reaching projections of the mPFC would exert a subtler, more modulatory effect through changes in coordination of activity between brain regions (*43*) rather than through directly evoking downstream BOLD activity. Because the cortex is thought to sculpt subcortical activity through feed-forward inhibition via fast-spiking interneurons (*44*), we suspected that elevated cortical excitability might suppress the response of the striatum to dopaminergic signals from the midbrain.

Using the Ca^{2+}/calmodulin kinase IIα (CaMKIIα) promoter, we expressed an optogenetic neural sensitizer (SSFO) to specifically drive asynchronous neural excitability, targeting predominantly excitatory glutamatergic pyramidal neurons in the mPFC of wild-type Sprague-Dawley rats (*45*, *46*) (Fig. 4A). We used in vivo optrode recordings of multiunit activity to confirm the ability of SSFO to increase the excitability of mPFC in response to blue light, as well as the reversibility of this effect with yellow light (Fig. 4B). We also ensured that this excitability increase was asynchronous across neurons as expected, using in vivo multielectrode-array single-unit recordings in awake rats (fig. S8, A to E).

We next performed SSFO optogenetic stimulation experiments in awake rats during fMRI scanning. Rats received stimulation of the mPFC in an event-related design, using a 2-s continuous blue light pulse to activate SSFO (or sham-activate a YFP control) for a total of 10 s. This was followed by deactivation with a 3-s yellow light pulse (Fig. 4C), again interleaved with visual

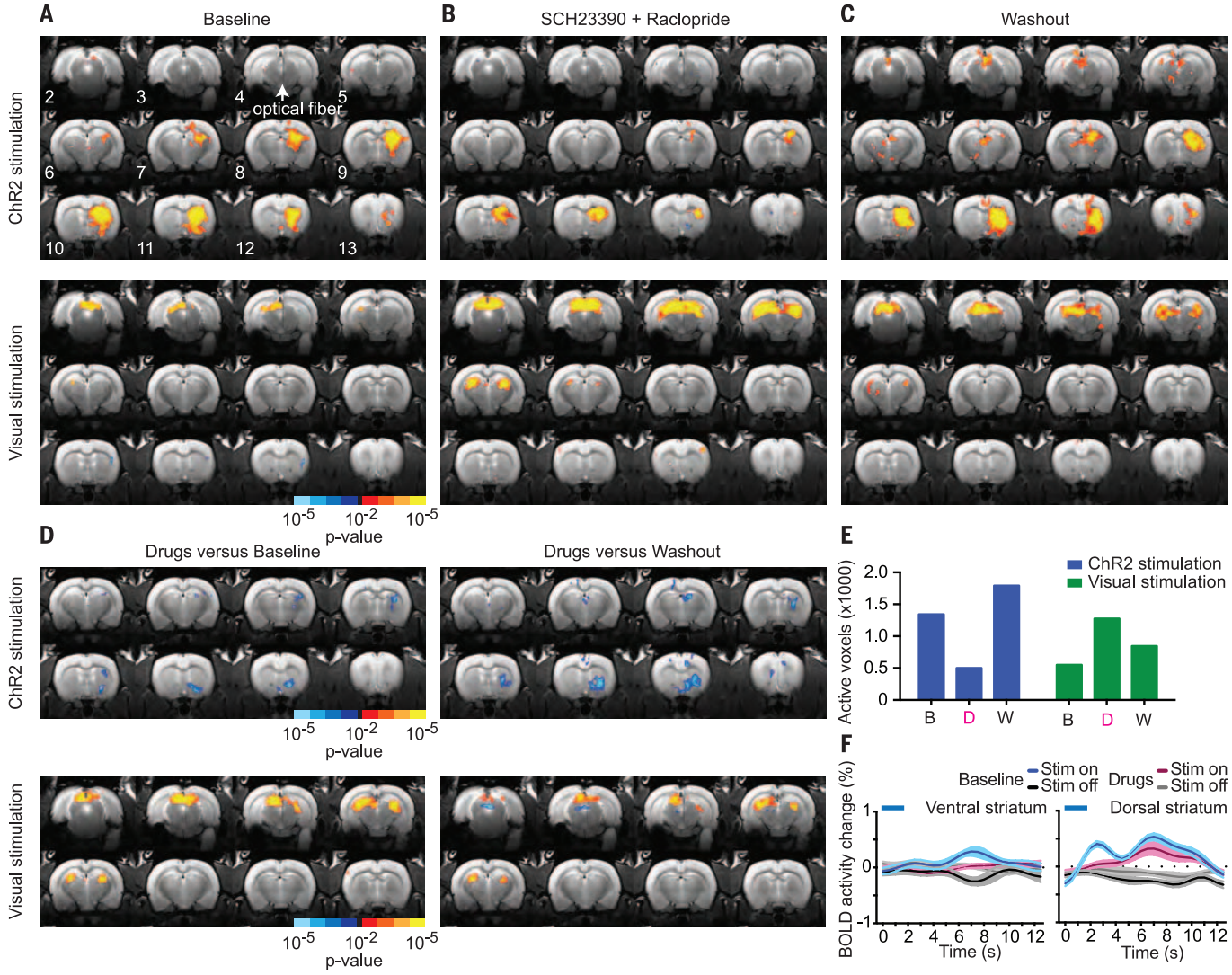

Fig. 3. Sensitivity of brainwide ofMRI BOLD patterns to dopamine receptor pharmacological inhibition. (**A** to **C**) Sequential pharmacological experiments in ChR2-expressing TH-cre rats undergoing ChR2 stimulation of midbrain dopamine neurons (top) and visual stimulation (bottom). (A) Baseline scan (no drugs or vehicle administered, n = 4 rats, 16 runs). (B) Drug scan: systemic (intraperitoneal) administration of D1 (SCH23390, 0.6 mg/kg) and D2 (raclopride, 0.3 mg/kg) dopamine receptor antagonists immediately before acquisition of functional scans (n = 4 rats, 22 runs). (C) Vehicle control washout scan: 48 to 24 hours after drug administration (n = 4 rats, 18 runs). (**D**) Statistical comparison between drug-versus-baseline and drug-versus-washout conditions for ChR2 and visual stimulation. (**E**) Total number of activated voxels in response to ChR2 and visual stimulation under each pharmacological condition. B, baseline; D, drug; W, washout. (**F**) Average stimulation-locked BOLD activity time courses in the ventral and dorsal striatum in response to ChR2 stimulation of midbrain dopamine neurons at baseline (n = 4 rats, 16 runs) in the presence of systemic D1 and D2 receptor antagonists (n = 4 rats, 22 runs). Mean and SEM (n = number of runs) are shown.

stimulation bursts (13 s of 10-Hz green light flashes), to serve as a natural sensory positive control (Fig. 4F). During SSFO stimulation, we observed increased BOLD activity at the optical fiber site [with only limited extension to known nearby projection regions (*47*), consistent with the desired subtle and focal nature of the SSFO-mediated optogenetic manipulation] in SSFO-expressing subjects (Fig. 4D) but not in YFP controls (Fig. 4E), with a significant difference in optogenetic mPFC activation between the two groups (fig. S9A and table S5) despite a similar response to visual stimulation (Fig. 4, G and H, and fig. S9B).

On the basis of human neuroimaging studies, we predicted that this modulation of mPFC excitability would reduce the expression of reward-seeking behavior (*15*, *16*). We employed two well-established appetitive assays: the sucrose preference test (*32*, *48*–*50*) and the social interaction test (*51*). We used a chronic (12-day) sucrose preference test (Fig. 4I) in which rats' preference for a 1% sucrose solution relative to plain water was measured daily. SSFO-expressing rats showed a mild but consistent and reversible reduction in sucrose preference only during days when light-stimulation was delivered. In contrast, YFP-control rats maintained a preference for sucrose (~90%) over the entire testing period (Fig. 4J). Plain water consumption was largely unchanged (Fig. 4K).

In the social interaction test (Fig. 4L), SSFO-expressing rats demonstrated a reversible reduction in social interaction after 3 days of light stimulation, whereas YFP-control rats showed a similar level of interaction across all three tests (Fig. 4M). At the start of the test, SSFO-expressing rats still recognized and explored the juvenile rat to an extent comparable to their YFP-expressing counterparts, but with chronic light stimulation, this engagement diminished more rapidly in SSFO-expressing rats compared with YFP-expressing rats (Fig. 4P). We did not observe any light-mediated effects on novel object exploration, as rats in both groups exhibited initial interest in the novel object, which then abated (Fig. 4N and fig. S10B). We also did not observe any differences in locomotor behavior, consistent with previous studies of mice (Fig. 4O) (*23*).

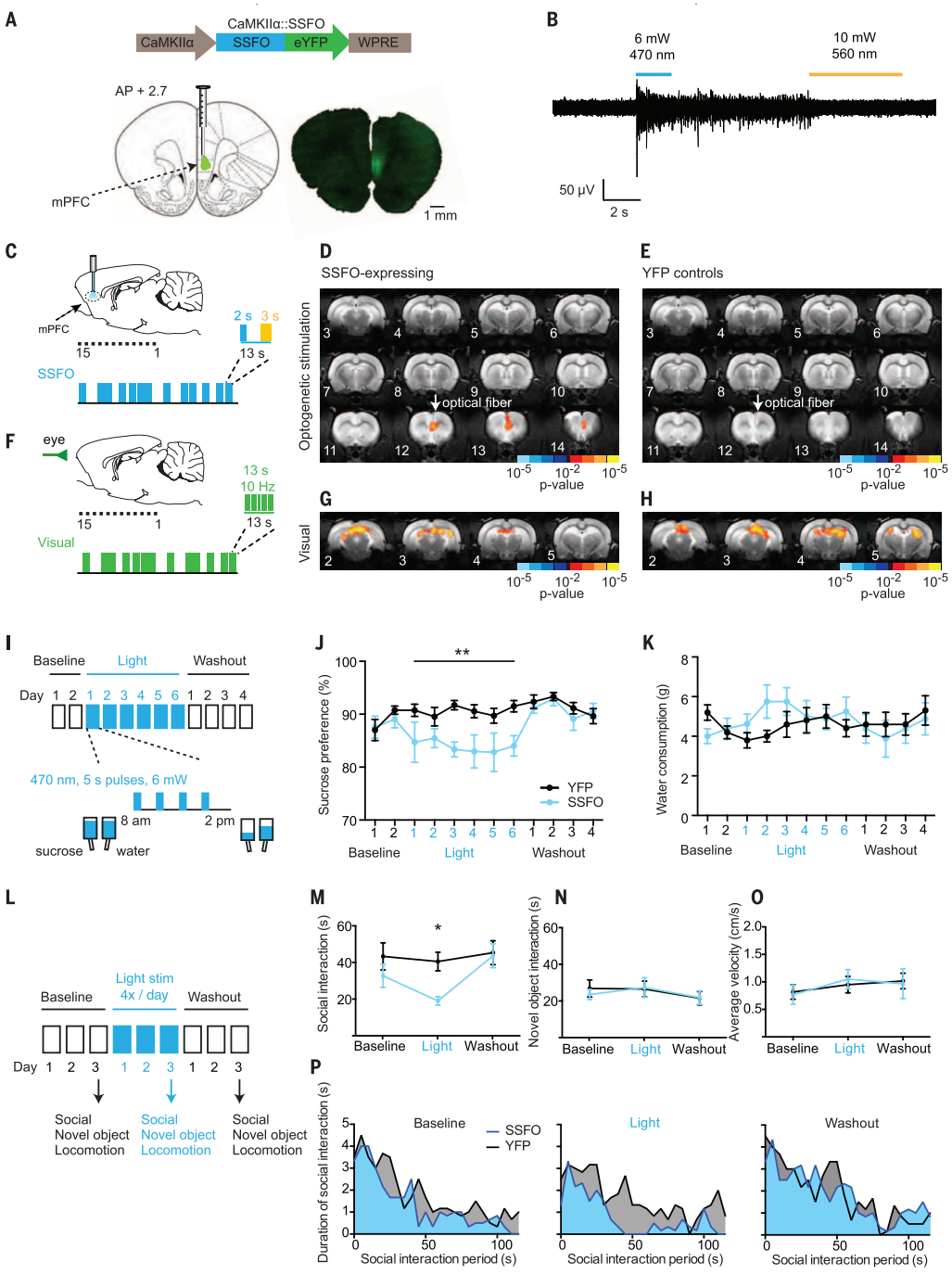

Fig. 4. Prefrontal cortical excitability modulation of multiple natural reward-related behaviors. (**A**) Schematic of the optogenetic construct CKIIα-SSFO-eYFP. Confocal image of SSFO-YFP expression in the mPFC. WPRE, woodchuck hepatitis virus posttranscriptional regulatory element. (**B**) Example of multiunit in vivo anesthetized optrode recording of SSFO stimulation in the mPFC, terminated by yellow light. (**C**) Event-related SSFO stimulation of the mPFC during fMRI scanning (optical fiber positioned in mPFC image 12). (**D**) Brain-wide *Z*-score map of BOLD activity in response to SSFO stimulation of the mPFC in SSFO-expressing subjects (n = 6 rats, 17 runs) and (**E**) YFP-control subjects (n = 5 rats, 20 runs). (**F**) Event-related visual stimulation. (**G**) *Z*-score map in response to visual stimulation in SSFO-expressing subjects (n = 6 rats, 17 runs) and (**H**) YFP-control subjects (n = 5 rats, 20 runs). (**I**) Sucrose preference testing paradigm. (**J**) Sucrose preference across test days for SSFO-expressing subjects (blue, n = 8 rats) and YFP controls (black, n = 10 rats). Mean and SEM are shown. We found a significant interaction between group and test day [$F_{11,176}$ = 2.555, $^{**}P$ = 0.0051, two-way repeated measures analysis of variance (ANOVA)], with significant differences between SSFO and YFP-control groups on days 3, 4, and 6 of light stimulation (P < 0.05, Sidak's multiple comparisons test). (**K**) Plain water consumption across test days for SSFO-expressing subjects (blue, n = 8 rats) and YFP-controls (black, n = 10 rats). Mean and SEM are shown. We found no significant difference between SSFO-expressing and YFP-control groups after multiple comparison testing. (**L**) Social interaction test paradigm. (**M** to **O**) Total duration of social interaction, novel object interaction, and mean velocity are compared across the three test days (n = 6 rats for SSFO social behavior, n = 5 for novel object and velocity, and n = 6 for YFP). We found a significant main effect of light ($F_{2,20}$ = 5.470, $^{*}P$ = 0.0127, two-way repeated measures ANOVA), with a significant difference between SSFO and YFP-control groups only on the light-stimulation day (P < 0.05, Sidak's multiple comparisons test). (**P**) Social investigation (in 5-s bins) over the course of the interaction period. Shaded regions indicate the mean across all rats.

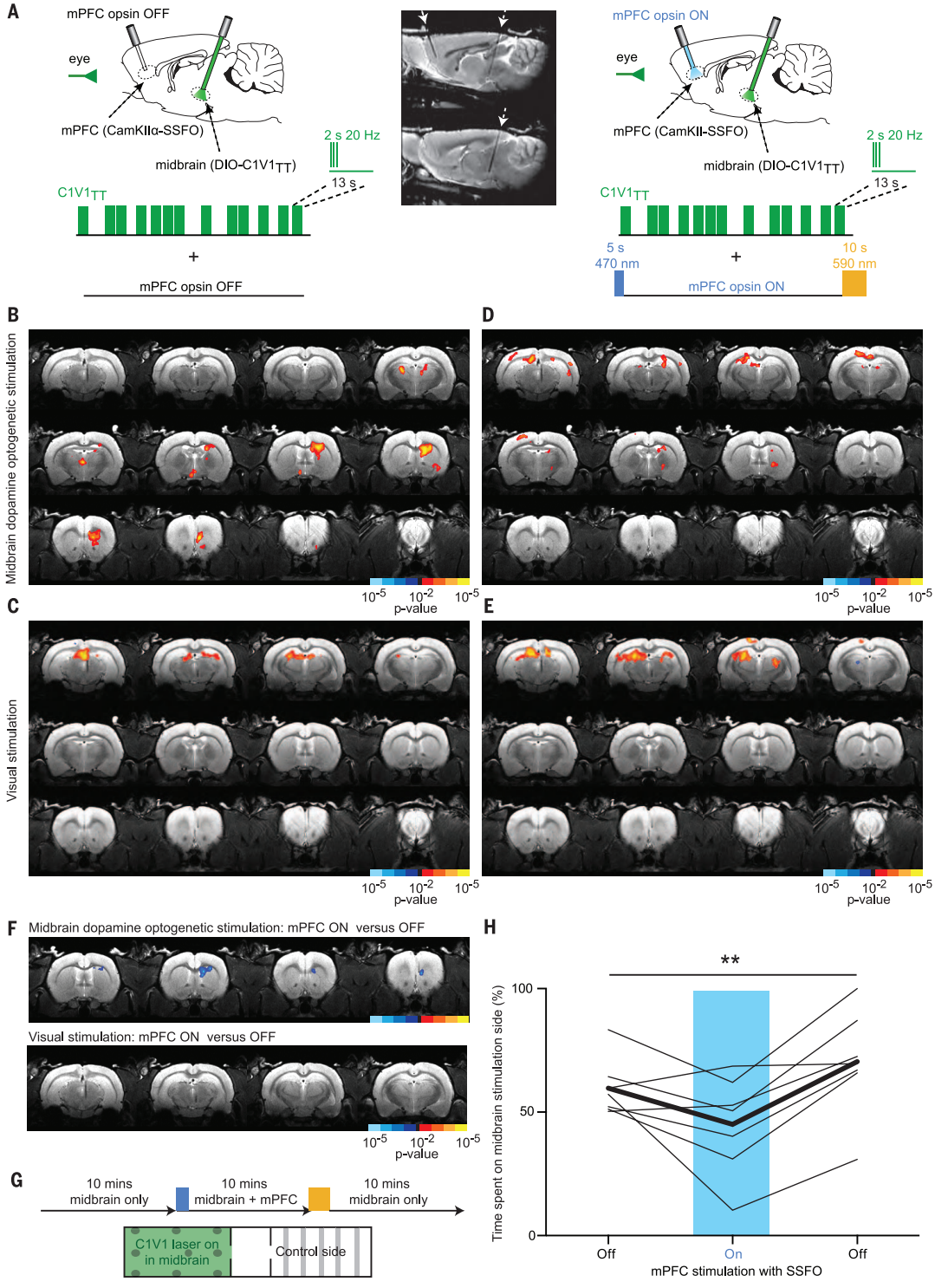

Fig. 5. Cortical suppression of striatal BOLD and behavioral response to midbrain dopaminergic stimulation. (**A**) Schematic illustrating the design of the dual-stimulation experiment. The sagittal T2 anatomy scan (two adjacent sections shown) demonstrates the angled orientation of the two fibers. (**B**) Brain-wide *Z*-score map of BOLD activity in response to C1V1$_{TT}$ stimulation in midbrain dopaminergic neurons and (**C**) visual stimulation alone (n = 6 rats, 32 runs). (**D**) *Z*-score map in response to C1V1$_{TT}$ stimulation and (**E**) visual stimulation in combination with SSFO activation in the mPFC (n = 6 rats, 32 runs). (**F**) Statistical comparison of mPFC-activated versus nonactivated condition for midbrain dopaminergic stimulation and visual stimulation. (**G**) Real-time place preference test for C1V1$_{TT}$ stimulation alone and in combination with mPFC activation with SSFO. The percentage of time spent on the C1V1$_{TT}$ stimulation side was assessed for all three bursts. (**H**) One-way repeated measures ANOVA shows a significant effect of mPFC activation (**P = 0.0047, F = 8.652, number of groups = 3, number of rats = 7), with a significant difference from baseline and washout conditions after Newman-Keuls multiple comparison testing.

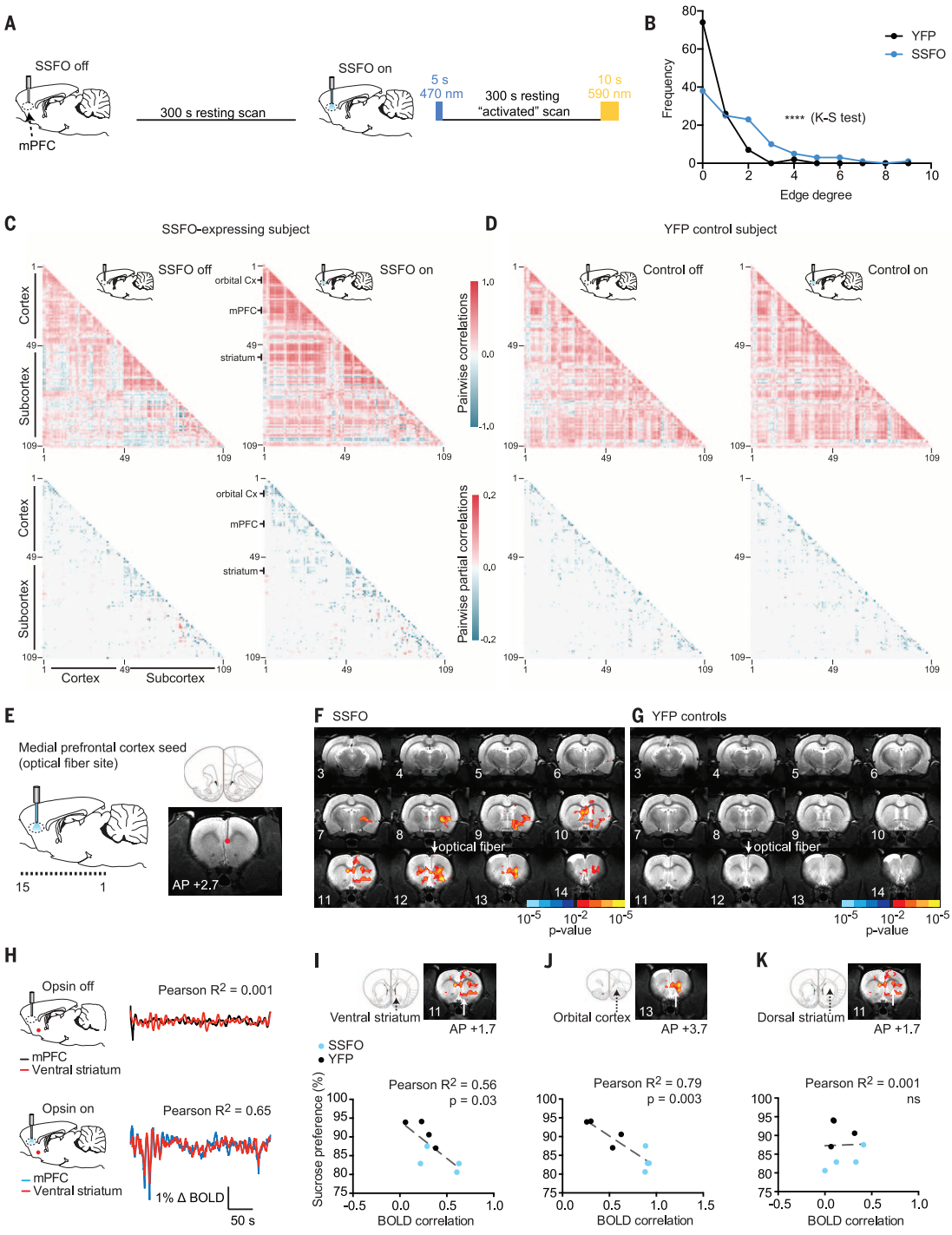

Fig. 6. Evoked changes in brainwide interregional relationships and joint statistics after focal optogenetic modulation of mPFC excitability. (**A**) Brainwide graphical analysis was performed on resting-state fMRI scans for SSFO-expressing and YFP-control subjects to assess changes in BOLD activity partial correlations between mPFC-activated versus nonactivated scans. (**B**) Change in edge degree distribution across SSFO (n = 4 rats, 14 runs) and YFP subjects (n = 4 rats, 15 runs) in response to mPFC activation by light (Kolmogov-Smirnov test for difference in distributions between SSFO and YFP groups: D = 0.3394, ****P < 0.0001). (**C**) Pairwise correlation and sparse partial correlation matrices for 109 brain regions for an example SSFO-expressing subject and (**D**) a YFP-control subject under nonactivated and mPFC-activated conditions. Each matrix represents the data from a single scan. Brain regions (individual ROIs) are labeled by number; the index key is provided in fig. S12. Selected brain regions have been highlighted. (**E**) Seed-based correlation analysis (for mPFC seed). (**F**) Z-score map for changes in correlated BOLD activity with mPFC after SSFO activation for SSFO-expressing subjects (n = 4 rats, 14 runs) and (**G**) YFP-control subjects (n = 4 rats, 15 runs). (**H**) Example BOLD activity time series in two ROIs: mPFC (black or blue) and ventral striatum (red) during opsin-off (Pearson R^2 = 0.001, P = 0.06) and opsin-on (Pearson R^2 = 0.65, P < 0.0001) conditions. (**I** to **K**) Relationship between sucrose preference and mPFC-activated BOLD correlations between the mPFC and three brain regions for SSFO-expressing (blue, n = 4 rats) and YFP-control subjects (black, n = 4 rats). (I) Ventral striatum (Pearson R^2 = 0.56, P = 0.032, n = 8 pairs). (J) Orbital cortex (Pearson R^2 = 0.79, P = 0.0031, n = 8 pairs). (K) Dorsal striatum (Pearson R^2 = 0.001, P = 0.95, n = 8 pairs).

Elevated mPFC excitability suppresses striatal responses to dopamine

We next sought to determine whether this altered behavior might be associated with disrupted recruitment of the striatal response to activation of midbrain dopamine neurons. We performed a dual–optogenetic stimulation experiment in which we expressed a red-shifted channelrhodopsin variant ($C1V1_{TT}$) via a Cre-dependent construct within the midbrain dopamine neurons of TH-Cre transgenic rats, as well as the blue light–activated SSFO in the mPFC under the CaMKIIα promoter in the same rats (Fig. 5A). In the MRI scanner, we used an event-related design (560 nm, 2 s of 20-Hz light pulses, 10-ms pulse width) to stimulate $C1V1_{TT}$, with visual stimulation in parallel as described above. In interleaved, matched scans, we superimposed mPFC activation with SSFO, using a 5-s pulse of blue light (470 nm) to the mPFC before the start of the scan and a 10-s pulse of yellow light (590 nm) to inactivate SSFO at the end of the scan. Although visual responses were similar between the two types of scans (Fig. 5, C, E, and F), we observed significant suppression of the evoked striatal BOLD response to $C1V1_{TT}$-mediated dopaminergic stimulation when the mPFC was activated, compared with when the mPFC was not activated (Fig. 5, B, D, and F; and table S6).

We performed a real-time place preference test in which rats were free to explore two chambers for a total of 30 min, during which time $C1V1_{TT}$ stimulation of dopaminergic cells was continually paired with one chamber. The test began with a 10-min period in which SSFO was not active, then followed by 10 min of superimposed mPFC activation by SSFO (single 5-s pulse of blue light in mPFC at the start, 10-s pulse of yellow light at the end), and finally followed by a final 10 min with SSFO inactive again (Fig. 5G). At baseline, rats tended to preferentially seek out the chamber in which they received midbrain dopamine neuron stimulation, but in the presence of superimposed mPFC activation by SSFO, no such preference was exhibited. Once SSFO was switched off, the sensitivity to midbrain dopamine neuron stimulation returned, as indicated by increased time spent in the $C1V1_{TT}$ stimulation chamber (Fig. 5H).

Elevated mPFC excitability triggers spatiotemporally correlated BOLD activity among distant brain regions and predicts anhedonic behavior

Altered resting-state correlations between the prefrontal cortex and a network of brain regions have been observed in neuroimaging studies of patients with depression (*43*), schizophrenia, and other psychiatric conditions (*24*) for which anhedonia is a prominent symptom. However, causal circuit mechanisms by which these relationships could be altered remain unknown. We hypothesized that stably increasing mPFC excitability would causally modulate resting-state spatiotemporal activity relationships between distant brain structures. We performed resting-state fMRI scans in which rats were either scanned with no optogenetic stimulation at all (nonactivated) or scanned in the mPFC-activated state, in which a 5-s blue light pulse was delivered to activate SSFO before initiation of a 5-min scan. After completion of the activated scan, a 10-s yellow light pulse was delivered to deactivate SSFO (Fig. 6A). No visual stimulation was delivered during these experiments, and nonactivated and activated scans were interleaved over the course of the scanning sessions.

Increased excitability of mPFC CaMKIIα-expressing neurons in awake rats modulated spontaneous BOLD activity fluctuations and resting-state relationships among a number of distinct cortical and subcortical brain regions. To explore these brainwide changes in an unbiased manner, we segmented the brain into 109 anatomical regions defined a priori (fig. S11A), extracted the time course of spontaneous activity during each scan for each brain region, and estimated sparse partial correlations with graphical lasso (*52*, *53*) to identify brain regions (or nodes) with significant changes in connection strength (edge degree) after mPFC activation (Fig. 6, B to D, and fig. S11, B to F). In SSFO-expressing subjects, we found a greater change in the number of significant partial correlations (hereafter referred to as "connection changes") between activated versus nonactivated scans, compared with the YFP-control group (Fig. 6B and figs. S11, C to F, and S12). Many regions—such as the mPFC with the orbital cortex and ventral striatum (Fig. 6C) and the cingulate cortex with the dorsal striatum—became more strongly interconnected after mPFC SSFO activation. The lateral orbital cortex, although not a direct target of the optogenetic excitability change, exhibited the greatest number of connection changes, linking with other areas of the frontal cortex, as well as subcortical regions such as the ventral striatum, claustrum, and septum. Relatively fewer regions became more isolated; these included the auditory and retrosplenial cortices, regions that have been clinically implicated in both depression and schizophrenia (*54*, *55*). Far fewer changes were detected in YFP controls, and these predominantly included lost connections, which could partially reflect alterations in spontaneous BOLD activity due to local metabolic or temperature changes (*26*) or simply temporal drift (figs. S11B and S12).

We next turned to a traditional seed-based analysis (Fig. 6E). Using the time course of spontaneous BOLD activity from a seed at the tip of the optical fiber in mPFC, we confirmed that a number of brain regions—including the orbital cortex, the dorsal and ventral striatum, and the septum—showed significantly increased correlation with fiber site activity after mPFC activation with SSFO (Fig. 6, F and H). No significant changes were observed for YFP-control subjects (Fig. 6G), and the between-group difference (SSFO versus YFP) in correlated activity was significant (fig. S9C and table S7). We considered whether such resting-state BOLD activity correlations could predict the behavioral changes elicited by mPFC activation, in subjects that had participated in behavioral testing as well as fMRI scanning. The strength of BOLD activity correlation between the mPFC and ventral striatum and orbital cortex during SSFO stimulation predicted the degree of anhedonic behavior. This was not true of the dorsal striatum, implying that circuit-specific changes in functional connections can predict behavioral phenotype (Fig. 6, I to K). Moreover, in contrast to these long-range interactions between brain regions, local evoked increases in BOLD activity in the mPFC alone were not sufficient to account for the emergence of the anhedonic behavioral phenotype (fig. S10A), demonstrating the importance of this brainwide analysis.

To explore SSFO-mediated changes in neural signals on a finer time scale, we used dual-site in vivo electrophysiological recordings in the mPFC and the striatum, simultaneously recording local field potentials (LFPs) at each site before and after shifts in mPFC excitability (fig. S13). Coherence in the LFP (in particular, the gamma frequency band, >30 Hz) has been suggested to play a role in mediating functional connectivity across anatomically distributed brain regions (*56*–*59*). Because we have found that elevation in mPFC activity causes increased high-frequency gamma power in the mPFC (*23*) and increased correlated activity between the mPFC and the striatum on longer time scales (Fig. 6), we hypothesized that increased coherence in the gamma frequency range between the mPFC and the striatum might appear after focal elevations in mPFC excitability. Multielectrode arrays were implanted into the mPFC (in addition to an optical fiber) and the striatum (fig. S13A). We recorded the LFP in these two regions at baseline (before light delivery) and after a 2-s pulse of blue light (fig. S13B). After SSFO activation, we observed a reduction in LFP power in the slow gamma frequency range (30 to 40 Hz), with a relative preservation (in the mPFC) or increase (in the striatum) in the fast gamma range (70 to 80 Hz) range (fig. S13, C and D). Across all subjects, this resulted in a significant increase in the ratio of fast to slow gamma power in the striatum (fig. S13E), as well as an increase in LFP coherence between the mPFC and the striatum across the gamma (and even high beta) range of frequencies (fig. S13, F and G). Single-unit recordings of neural spiking in the striatum simultaneous with SSFO activation in the mPFC demonstrated that striatal units showed a mixed pattern of spiking activity in the 500-ms period after a pulse of blue light, with 44% of units exhibiting an increase in spiking and 42% showing a decrease, compared with spiking activity during the 500-ms period preceding the light pulse (fig. S8, F to I). LFP synchrony between brain regions thus represents a complex phenomenon involving both excitatory and inhibitory interactions at the single-cell level (*60*).

Discussion

We have combined focal, cell-type–specific chronic and acute optogenetic manipulations together with fMRI, behavioral testing, and in vivo

electrophysiological recordings to probe interactions between cortical and subcortical brain regions causally involved in reward-related behavior. The major advances of this study are threefold. First, we demonstrate that stimulation of midbrain dopamine neurons is sufficient to increase BOLD activity in the striatum, in a manner correlated with reward-seeking behavior across individual subjects, addressing a long-standing controversy over the potential source of reward-related striatal BOLD activity in human fMRI studies. Second, elevated excitability of the mPFC was found to reduce both striatal BOLD responses to the stimulation of dopamine neurons and the behavioral drive to seek stimulation of dopamine neurons. Thus, the mPFC exerts top-down control over the interaction between the dopaminergic midbrain and the striatum to modulate the expression of reward-related behavior. Finally, stably elevating the excitability of mPFC pyramidal neurons was sufficient to drive changes in corticolimbic BOLD synchrony, as well as corresponding anhedonic behavior, resembling imaging and clinical phenotypes observed in human psychiatric disease. These findings suggest that, rather than acting in parallel, dopaminergic and top-down cortical projections are instead intersecting at the striatum and working in concert to regulate reward processing, with implications for our understanding of the pathogenesis of anhedonia.

The striatum receives midbrain dopaminergic and cortical glutamatergic inputs (*8*, *61*, *62*) and is therefore ideally positioned to both motivate and modulate reward-related behavior (*3*, *42*, *63*). We first observed that specific optogenetic drive of midbrain dopaminergic neurons increased striatal BOLD activity and that rats with greater ventral striatal BOLD activity in the scanner worked harder for optogenetic stimulation of midbrain dopamine neurons in the operant chamber. The observed increases in ventral striatal BOLD activity could be blunted by administration of dopaminergic antagonists and exhibited a similar temporal profile to BOLD activity measured during reward anticipation in humans (*64*). Optogenetic inhibition, on the other hand, reduced BOLD activity in the dorsal striatum, as well as in other unexpected brain regions, such as the hypothalamus, suggesting that the spatial influence of changes in tonic dopamine may differ from that of phasic dopamine. These results alone bridge a gap in our current understanding of dopamine signaling. Previously, researchers have used fast-scan cyclic voltammetry to track dopamine release in selected projection regions (*30*, *65*, *66*) and electrophysiology readouts to investigate the firing of downstream neurons in response to dopamine release (*32*, *51*, *67*). Meanwhile, neuroimaging studies in humans and animals have identified mesolimbic BOLD activity in response to reward-related cues and outcomes (*68*–*71*). However, no causal link had yet been established between defined firing of midbrain dopamine neurons and BOLD activity, but making this connection is crucial for interpretation of BOLD studies in reward-related behavior. Although one might predict that dopamine neuron activation could increase BOLD activity in terminal projection regions, such an association cannot be assumed, because activation of postsynaptic dopamine receptors has diverse modulatory influences through intracellular G protein cascades.

Although we found that reward-seeking behavior increased monotonically with stimulation duration (up to and beyond 2 s), and stimulation of dopamine neurons for 2 s (at 20 Hz, 10-ms pulse width) was more effective than shorter burst durations for eliciting striatal BOLD, in future work it will be interesting to compare further burst and tonic stimulation frequencies in different experimental contexts, which may drive different physiological states and BOLD responses with important consequences for behavior. Additionally, dopamine receptor blockade increased BOLD activity in response to visual stimulation, suggesting that dopamine might modulate aspects of primary sensory processing; this finding prompts many questions about how other neuromodulators (such as serotonin, acetylcholine, and noradrenaline) influence BOLD activity in health or disease. Another area for exploration is the role of co-released neurotransmitters. For example, glutamate exhibits stronger co-release in the ventral compared with the dorsal striatum (*72*). Our pharmacological data show that ventral striatal BOLD was completely suppressed by dopaminergic antagonists, supporting the hypothesis that this signal results from dopamine release. However, analysis of our fiber tip placement in the midbrain (located within the medial-lateral and anterior-posterior spatial extent of the VTA in all animals) suggests that lateral rather than medial VTA fiber placement most effectively increased BOLD activity in the ventral and dorsal striatum (although placement did not significantly influence behavioral responding) (fig. S4). This finding is consistent with recent work showing that the medial VTA projects most strongly to the medial nucleus accumbens (*73*), mapping spatially to sites of vesicular glutamate transporter 2 (VGLUT2)–associated glutamate co-release (*72*), whereas the lateral VTA projects more broadly to the lateral nucleus accumbens and dorsal striatum (*73*). Experiments that establish the role of neurotransmitter co-release in BOLD activity might involve the use of conditional VGLUT2 knockout in dopamine neurons.

Next, we turned to pathophysiological processes that may blunt reward-seeking behavior and contribute to the clinical symptom of anhedonia. Neuroimaging studies in human patients with depression have identified a region of the mPFC (subgenual cingulate gyrus) that exhibits elevated activity (*11*) in correlation with severity of anhedonic symptoms (*15*). The subgenual cingulate becomes increasingly connected within resting-state brain networks in depressed patients, and this network effect is associated with disease refractoriness (*43*). Treatment of depression with the mixed-effect glutamate receptor antagonist ketamine may also improve anhedonic symptoms and increase striatal metabolism (*74*). Imaging studies in patients with schizophrenia have similarly pointed to altered patterns of neural activity associated with anhedonia (*16*, *75*, *76*). These studies led us to hypothesize that dysregulation of long-range neuronal interactions triggered by elevated mPFC excitability could contribute to anhedonia in neuropsychiatric disease (*7*, *8*, *77*). Enhanced mPFC excitability in rats led to specific synchronization of physiological signals (both BOLD and LFP) between the mPFC and connected subcortical regions, and the degree of synchrony between specific brain regions (mPFC, orbital cortex, ventral striatum) correlated with the expression of anhedonic behavior in individual animals. Modulating the excitability of specific cell populations is thus sufficient to drive changes in BOLD activity correlations between brain regions, resembling those observed in human psychiatric disorders. The downstream effect of this phenomenon became most apparent in the context of concurrent dopaminergic stimulation, when mPFC hyperexcitability exerted a top-down suppressive effect on reward-related neural signaling in the striatum and reward-seeking behavior.

The clinical background guiding our work was increased mPFC excitability and fMRI BOLD activity, rather than a specific spiking pattern in a particular cell type. We chose to use SSFO, which does not act via coordinated activation of expressing neurons at a firing frequency chosen by the experimenter, but instead elicits an asynchronous enhancement in excitability by causing subthreshold depolarization (*23*, *25*). Crucially, this manipulation exerted its downstream effects on functional connectivity rather than on the univariate BOLD signal locally or in predicted projection areas. Moreover, this distinct BOLD effect was correlated with a decrease rather than an increase in hedonic behavior. This approach had the additional practical advantages of permitting BOLD signal acquisition without continuous light delivery in the scanner (avoiding the potential for tissue heating) and facilitating chronic manipulations of excitability over days in the appetitive behavioral assays.

Low-frequency electrical stimulation (10 Hz; typical of mPFC neural activity during cognitive tasks) can reduce dopamine release in the striatum, whereas high-frequency electrical stimulation at 60 to 200 Hz can have the opposite effect (*78*). These contrasting observations may relate to the finding that high-frequency (and possibly supraphysiological at ~100 Hz) burst stimulation of the mPFC can exert antidepressant effects in mice (*48*, *79*) and humans (*11*). When mPFC firing rates were mildly and asynchronously elevated within a physiological range by SSFO (fig. S8B), we observed blunting of the striatal response to dopaminergic input and anhedonic effects on behavior. The precise circuit mechanisms of the prefrontal influence on these subcortical interactions could occur via feed-forward inhibition in the striatum, the midbrain, or another intermediary brain region. Alternatively, mPFC activity could increase tonic dopamine release in the striatum, producing a ceiling effect on further dopaminergic signaling and potentially thereby

preventing bursts of dopamine stimulation from evoking phasic BOLD activity in the striatum, as well as diminishing reward-related behavior. As noted in earlier work, in the context of modulation of phasic BOLD activity by dopaminergic drugs (i.e., amphetamine) in humans (*64*), task (or stimulation)–based fMRI cannot readily distinguish a reduction in evoked BOLD activity from a ceiling effect. However, a lack of locomotor stimulation during combined mPFC and dopaminergic stimulation (fig. S14) suggests reduced rather than increased tonic dopamine levels (*80*).

Our large data set (http://clarityresourcecenter.org/ofMRI.html) forms a resource for understanding and modeling dynamic brainwide activity patterns that are causally linked to adaptive and maladaptive reward states. Our ofMRI findings constitute a bridge between the worlds of animal optogenetics and clinical neuroimaging and provide causal evidence for behaviorally meaningful competition between two brain regions for influence over a third region (in this case, between dopaminergic midbrain and glutamatergic prefrontal cortex neurons for influence over the striatum). In a healthy brain, descending projections from the cortex to subcortical limbic regions may be important for guiding behavioral responses to rewarding or salient stimuli (*81*), whereas in clinical anhedonia, increased mPFC excitability may generate a hypersynchronous state between specific cortical (mPFC, orbital cortex) and subcortical (ventral striatum) brain regions, which in turn suppresses the response to neuromodulatory (dopaminergic) signals normally important for reward.

Methods summary

See the supplementary materials for full details of the materials and methods (*82*). A number of key technical refinements allowed us to more readily visualize BOLD responses to a variety of stimuli. First, to scan awake rodents, we constructed a customized MRI-compatible head-fixation apparatus and habituated rats to the scanner environment to minimize stress and motion (as described above). Second, we optimized functional data acquisition using fast single-shot (0.5-s TR; spiral-in/out) image acquisition protocols (*83*–*85*), which minimized motion artifacts from image fusion and reduced susceptibility artifacts from implanted material or airspaces in the skull. Functional images encompassed the cerebral hemispheres (but not the cerebellum), with signal maintained in most brain regions. However, some dropout occurred in posterior ventrolateral regions, including portions of the temporal association cortices, entorhinal cortices, and posteroventral parts of the hippocampus (fig. S1B). Third, we used a pseudorandomly ordered event-related stimulus sequence, which maximized the number of trials per scan while still affording resolution of phasic responses to optogenetic stimulation. Specifically, the maximum length sequence (m-sequence) design (*86*) allowed simultaneous but noncorrelated presentation of two stimuli, such that optogenetic stimulation occurred while a positive-control stimulus (i.e., a visual stimulus) was also applied, to allow verification of BOLD responses to sensory input in experiments in which the BOLD response to optogenetic stimulation might be absent or reduced (e.g., YFP controls, pharmacological manipulations, or dual-stimulation optogenetic experiments). During pilot testing, we noticed that the hemodynamic response function (HRF) to SSFO and visual stimulation differed from that observed in response to ChR2 stimulation of dopamine neurons and from the HRF commonly observed in humans (*87*). We found that for SSFO and visual stimulation, the HRF more closely followed a customized model, with exponential rise and decay (τ = 7 s) (fig. S15). Although modeling with the canonical human HRF replicated our results, the rat-specific model more effectively resolved activity in SSFO and visual experiments. Although the hemodynamic responses of different species might vary for a number of reasons (e.g., differences in the properties of rat capillary networks), they may also vary as a function of brain region (e.g., cortical versus subcortical), neurotransmitter release (dopamine versus glutamate), or the eliciting method of stimulation (e.g., ChR2 versus SSFO). Based on these findings, we recommend that investigators closely inspect raw data acquired in ofMRI experiments before applying models optimized for human data, to ensure that divergent temporal features of the rat HRF are considered.

REFERENCES AND NOTES

1. A. E. Kelley, K. C. Berridge, The neuroscience of natural rewards: Relevance to addictive drugs. *J. Neurosci.* **22**, 3306–3311 (2002). pmid: 11978804
2. W. Schultz, Predictive reward signal of dopamine neurons. *J. Neurophysiol.* **80**, 1–27 (1998). pmid: 9658025
3. S. R. Sesack, A. A. Grace, Cortico-basal ganglia reward network: Microcircuitry. *Neuropsychopharmacology* **35**, 27–47 (2010). doi: 10.1038/npp.2009.93; pmid: 19675534
4. M. W. Howe, P. L. Tierney, S. G. Sandberg, P. E. M. Phillips, A. M. Graybiel, Prolonged dopamine signalling in striatum signals proximity and value of distant rewards. *Nature* **500**, 575–579 (2013). doi: 10.1038/nature12475; pmid: 23913271
5. C. D. Fiorillo, P. N. Tobler, W. Schultz, Discrete coding of reward probability and uncertainty by dopamine neurons. *Science* **299**, 1898–1902 (2003). doi: 10.1126/science.1077349; pmid: 12649484
6. P. Gorwood, Neurobiological mechanisms of anhedonia. *Dialogues Clin. Neurosci.* **10**, 291–299 (2008). pmid: 18979942
7. E. J. Nestler, W. A. Carlezon Jr., The mesolimbic dopamine reward circuit in depression. *Biol. Psychiatry* **59**, 1151–1159 (2006). doi: 10.1016/j.biopsych.2005.09.018; pmid: 16566899
8. S. J. Russo, E. J. Nestler, The brain reward circuitry in mood disorders. *Nat. Rev. Neurosci.* **14**, 609–625 (2013). doi: 10.1038/nrn3381; pmid: 23942470
9. K. Deisseroth, Circuit dynamics of adaptive and maladaptive behaviour. *Nature* **505**, 309–317 (2014). doi: 10.1038/nature12982; pmid: 24429629
10. B. Moghaddam, J. Wood, Teamwork matters: Coordinated neuronal activity in brain systems relevant to psychiatric disorders. *JAMA Psychiatry* **71**, 197–199 (2014). doi: 10.1001/jamapsychiatry.2013.2080; pmid: 24305975
11. H. S. Mayberg *et al*., Deep brain stimulation for treatment-resistant depression. *Neuron* **45**, 651–660 (2005). doi: 10.1016/j.neuron.2005.02.014; pmid: 15748841
12. R. T. Dunn *et al*., Principal components of the Beck Depression Inventory and regional cerebral metabolism in unipolar and bipolar depression. *Biol. Psychiatry* **51**, 387–399 (2002). doi: 10.1016/S0006-3223(01)01244-6; pmid: 11904133
13. M. T. Mitterschiffthaler *et al*., Neural response to pleasant stimuli in anhedonia: An fMRI study. *Neuroreport* **14**, 177–182 (2003). doi: 10.1097/00001756-200302100-00003; pmid: 12598724
14. V. Kumari *et al*., Neural abnormalities during cognitive generation of affect in treatment-resistant depression. *Biol. Psychiatry* **54**, 777–791 (2003). doi: 10.1016/S0006-3223(02)01785-7; pmid: 14550677
15. P. A. Keedwell, C. Andrew, S. C. R. Williams, M. J. Brammer, M. L. Phillips, The neural correlates of anhedonia in major depressive disorder. *Biol. Psychiatry* **58**, 843–853 (2005). doi: 10.1016/j.biopsych.2005.05.019; pmid: 16043128
16. P.-O. Harvey, J. Pruessner, Y. Czechowska, M. Lepage, Individual differences in trait anhedonia: A structural and functional magnetic resonance imaging study in non-clinical subjects. *Mol. Psychiatry* **12**, 767–775 (2007).doi: 10.1038/sj.mp.4002045; pmid: 17505465
17. K. J. Ressler, H. S. Mayberg, Targeting abnormal neural circuits in mood and anxiety disorders: From the laboratory to the clinic. *Nat. Neurosci.* **10**, 1116–1124 (2007). doi: 10.1038/nn1944; pmid: 17726478
18. M. T. Berlim, A. McGirr, F. Van den Eynde, M. P. A. Fleck, P. Giacobbe, Effectiveness and acceptability of deep brain stimulation (DBS) of the subgenual cingulate cortex for treatment-resistant depression: A systematic review and exploratory meta-analysis. *J. Affect. Disord.* **159**, 31–38 (2014). doi: 10.1016/j.jad.2014.02.016; pmid: 24679386
19. J. P. O'Doherty, Reward representations and reward-related learning in the human brain: Insights from neuroimaging. *Curr. Opin. Neurobiol.* **14**, 769–776 (2004). doi: 10.1016/j.conb.2004.10.016; pmid: 15582382
20. B. Knutson, J. C. Cooper, Functional magnetic resonance imaging of reward prediction. *Curr. Opin. Neurol.* **18**, 411–417 (2005). doi: 10.1097/01.wco.0000173463.24758.f6; pmid: 16003117
21. E. S. Boyden, F. Zhang, E. Bamberg, G. Nagel, K. Deisseroth, Millisecond-timescale, genetically targeted optical control of neural activity. *Nat. Neurosci.* **8**, 1263–1268 (2005). doi: 10.1038/nn1525; pmid: 16116447
22. V. Gradinaru, K. R. Thompson, K. Deisseroth, eNpHR: A *Natronomonas* halorhodopsin enhanced for optogenetic applications. *Brain Cell Biol.* **36**, 129–139 (2008). doi: 10.1007/s11068-008-9027-6; pmid: 18677566
23. O. Yizhar *et al*., Neocortical excitation/inhibition balance in information processing and social dysfunction. *Nature* **477**, 171–178 (2011). doi: 10.1038/nature10360; pmid: 21796121
24. N. D. Woodward, C. J. Cascio, Resting-state functional connectivity in psychiatric disorders. *JAMA Psychiatry* **72**, 743–744 (2015). doi: 10.1001/jamapsychiatry.2015.0484; pmid: 26061674
25. A. Berndt, O. Yizhar, L. A. Gunaydin, P. Hegemann, K. Deisseroth, Bi-stable neural state switches. *Nat. Neurosci.* **12**, 229–234 (2009). doi: 10.1038/nn.2247; pmid: 19079251
26. I. N. Christie *et al*., fMRI response to blue light delivery in the naïve brain: Implications for combined optogenetic fMRI studies. *Neuroimage* **66**, 634–641 (2013). doi: 10.1016/j.neuroimage.2012.10.074; pmid: 23128081
27. F. Zhang *et al*., Red-shifted optogenetic excitation: A tool for fast neural control derived from *Volvox carteri*. *Nat. Neurosci.* **11**, 631–633 (2008). doi: 10.1038/nn.2120; pmid: 18432196
28. M. A. Pisauro, N. T. Dhruv, M. Carandini, A. Benucci, Fast hemodynamic responses in the visual cortex of the awake mouse. *J. Neurosci.* **33**, 18343–18351 (2013). doi: 10.1523/JNEUROSCI.2130-13.2013; pmid: 24227743
29. H.-C. Tsai *et al*., Phasic firing in dopaminergic neurons is sufficient for behavioral conditioning. *Science* **324**, 1080–1084 (2009). doi: 10.1126/science.1168878; pmid: 19389999
30. I. B. Witten *et al*., Recombinase-driver rat lines: Tools, techniques, and optogenetic application to dopamine-mediated reinforcement. *Neuron* **72**, 721–733 (2011). doi: 10.1016/j.neuron.2011.10.028; pmid: 22153370
31. N. K. Logothetis, J. Pauls, M. Augath, T. Trinath, A. Oeltermann, Neurophysiological investigation of the basis of the fMRI signal. *Nature* **412**, 150–157 (2001). doi: 10.1038/35084005; pmid: 11449264
32. K. M. Tye *et al*., Dopamine neurons modulate neural encoding and expression of depression-related behaviour. *Nature* **493**, 537–541 (2013). doi: 10.1038/nature11740; pmid: 23235822
33. G. H. Glover, S. K. Lemieux, M. Drangova, J. M. Pauly, Decomposition of inflow and blood oxygen level-dependent (BOLD) effects with dual-echo spiral gradient-recalled echo (GRE) fMRI. *Magn. Reson. Med.* **35**, 299–308 (1996). doi: 10.1002/mrm.1910350306; pmid: 8699940
34. J. A. Bourne, SCH 23390: The first selective dopamine D_1-like receptor antagonist. *CNS Drug Rev.* **7**, 399–414 (2001). doi: 10.1111/j.1527-3458.2001.tb00207.x; pmid: 11830757

35. S. P. S *et al*., A highly sensitive LC-MS/MS method for the determination of *S*-raclopride in rat plasma: Application to a pharmacokinetic study in rats. *Biomed. Chromatogr.* **25**, 930–937 (2011). doi: 10.1002/bmc.1547; pmid: 21154642
36. B. Noudoost, T. Moore, Control of visual cortical signals by prefrontal dopamine. *Nature* **474**, 372–375 (2011). doi: 10.1038/nature09995; pmid: 21572439
37. J. T. Arsenault, K. Nelissen, B. Jarraya, W. Vanduffel, Dopaminergic reward signals selectively decrease fMRI activity in primate visual cortex. *Neuron* **77**, 1174–1186 (2013). doi: 10.1016/j.neuron.2013.01.008; pmid: 23522051
38. D. Zaldivar, A. Rauch, K. Whittingstall, N. K. Logothetis, J. Goense, Dopamine-induced dissociation of BOLD and neural activity in macaque visual cortex. *Curr. Biol.* **24**, 2805–2811 (2014). doi: 10.1016/j.cub.2014.10.006; pmid: 25456449
39. F. De Martino *et al*., Combining multivariate voxel selection and support vector machines for mapping and classification of fMRI spatial patterns. *Neuroimage* **43**, 44–58 (2008). doi: 10.1016/j.neuroimage.2008.06.037; pmid: 18672070
40. A. A. Grace, Phasic versus tonic dopamine release and the modulation of dopamine system responsivity: A hypothesis for the etiology of schizophrenia. *Neuroscience* **41**, 1–24 (1991). doi: 10.1016/0306-4522(91)90196-U; pmid: 1676137
41. P. N. Tobler, A. Dickinson, W. Schultz, Coding of predicted reward omission by dopamine neurons in a conditioned inhibition paradigm. *J. Neurosci.* **23**, 10402–10410 (2003). pmid: 14614099
42. A. Ghazizadeh, F. Ambroggi, N. Odean, H. L. Fields, Prefrontal cortex mediates extinction of responding by two distinct neural mechanisms in accumbens shell. *J. Neurosci.* **32**, 726–737 (2012). doi: 10.1523/JNEUROSCI.3891-11.2012; pmid: 22238108
43. M. D. Greicius *et al*., Resting-state functional connectivity in major depression: Abnormally increased contributions from subgenual cingulate cortex and thalamus. *Biol. Psychiatry* **62**, 429–437 (2007). doi: 10.1016/j.biopsych.2006.09.020; pmid: 17210143
44. J. D. Berke, Functional properties of striatal fast-spiking interneurons. *Front. Syst. Neurosci.* **5**, 45 (2011). doi: 10.3389/fnsys.2011.00045; pmid: 21743805
45. J. H. Lee *et al*., Global and local fMRI signals driven by neurons defined optogenetically by type and wiring. *Nature* **465**, 788–792 (2010). doi: 10.1038/nature09108; pmid: 20473285
46. A. M. Aravanis *et al*., An optical neural interface: In vivo control of rodent motor cortex with integrated fiberoptic and optogenetic technology. *J. Neural Eng.* **4**, S143–S156 (2007). doi: 10.1088/1741-2560/4/3/S02; pmid: 17873414
47. H. W. Berendse, Y. Galis-de Graaf, H. J. Groenewegen, Topographical organization and relationship with ventral striatal compartments of prefrontal corticostriatal projections in the rat. *J. Comp. Neurol.* **316**, 314–347 (1992). doi: 10.1002/cne.903160305; pmid: 1577988
48. C. Hamani *et al*., Antidepressant-like effects of medial prefrontal cortex deep brain stimulation in rats. *Biol. Psychiatry* **67**, 117–124 (2010). doi: 10.1016/j.biopsych.2009.08.025; pmid: 19819426
49. D. Chaudhury *et al*., Rapid regulation of depression-related behaviours by control of midbrain dopamine neurons. *Nature* **493**, 532–536 (2013). doi: 10.1038/nature11713; pmid: 23235832
50. B. K. Lim, K. W. Huang, B. A. Grueter, P. E. Rothwell, R. C. Malenka, Anhedonia requires MC4R-mediated synaptic adaptations in nucleus accumbens. *Nature* **487**, 183–189 (2012). doi: 10.1038/nature11160; pmid: 22785313
51. L. A. Gunaydin *et al*., Natural neural projection dynamics underlying social behavior. *Cell* **157**, 1535–1551 (2014). doi: 10.1016/j.cell.2014.05.017; pmid: 24949967
52. J. Friedman, T. Hastie, R. Tibshirani, Sparse inverse covariance estimation with the graphical lasso. *Biostatistics* **9**, 432–441 (2008). doi: 10.1093/biostatistics/kxm045; pmid: 18079126
53. T. Zhao, H. Liu, K. Roeder, J. Lafferty, L. Wasserman, The huge package for high-dimensional undirected graph estimation in R. *J. Mach. Learn. Res.* **13**, 1059–1062 (2012).
54. R. L. Bluhm *et al*., Retrosplenial cortex connectivity in schizophrenia. *Psychiatry Res. Neuroimaging* **174**, 17–23 (2009). doi: 10.1016/j.pscychresns.2009.03.010; pmid: 19783410
55. M. de la Iglesia-Vaya *et al*., Abnormal synchrony and effective connectivity in patients with schizophrenia and auditory hallucinations. *NeuroImage Clin.* **6**, 171–179 (2014). doi: 10.1016/j.nicl.2014.08.027; pmid: 25379429
56. G. G. Gregoriou, S. J. Gotts, H. Zhou, R. Desimone, High-frequency, long-range coupling between prefrontal and visual cortex during attention. *Science* **324**, 1207–1210 (2009). doi: 10.1126/science.1171402; pmid: 19478185
57. M. Siegel, T. H. Donner, A. K. Engel, Spectral fingerprints of large-scale neuronal interactions. *Nat. Rev. Neurosci.* **13**, 121–134 (2012). pmid: 22233726
58. K. M. Igarashi, L. Lu, L. L. Colgin, M.-B. Moser, E. I. Moser, Coordination of entorhinal-hippocampal ensemble activity during associative learning. *Nature* **510**, 143–147 (2014). doi: 10.1038/nature13162; pmid: 24739966
59. G. Buzsáki, X.-J. Wang, Mechanisms of gamma oscillations. *Annu. Rev. Neurosci.* **35**, 203–225 (2012). doi: 10.1146/annurev-neuro-062111-150444; pmid: 22443509
60. G. Buzsáki, C. A. Anastassiou, C. Koch, The origin of extracellular fields and currents—EEG, ECoG, LFP and spikes. *Nat. Rev. Neurosci.* **13**, 407–420 (2012). doi: 10.1038/nrn3241; pmid: 22595786
61. S. Ikemoto, Dopamine reward circuitry: Two projection systems from the ventral midbrain to the nucleus accumbens-olfactory tubercle complex. *Brain Res. Rev.* **56**, 27–78 (2007). doi: 10.1016/j.brainresrev.2007.05.004; pmid: 17574681
62. S. N. Haber, B. Knutson, The reward circuit: Linking primate anatomy and human imaging. *Neuropsychopharmacology* **35**, 4–26 (2010). doi: 10.1038/npp.2009.129; pmid: 19812543
63. T. W. Robbins, B. J. Everitt, Neurobehavioural mechanisms of reward and motivation. *Curr. Opin. Neurobiol.* **6**, 228–236 (1996). doi: 10.1016/S0959-4388(96)80077-8; pmid: 8725965
64. B. Knutson *et al*., Amphetamine modulates human incentive processing. *Neuron* **43**, 261–269 (2004). doi: 10.1016/j.neuron.2004.06.030; pmid: 15260961
65. D. L. Robinson, B. J. Venton, M. L. Heien, R. M. Wightman, Detecting subsecond dopamine release with fast-scan cyclic voltammetry in vivo. *Clin. Chem.* **49**, 1763–1773 (2003). doi: 10.1373/49.10.1763; pmid: 14500617
66. P. E. Phillips, D. L. Robinson, G. D. Stuber, R. M. Carelli, R. M. Wightman, "Real-time measurements of phasic changes in extracellular dopamine concentration in freely moving rats by fast-scan cyclic voltammetry," in *Drugs of Abuse: Neurological Reviews and Protocols*, J. Q. Wang, Ed. (Methods in Molecular Medicine Series, Humana Press, Totowa, NJ, 2003), pp. 443–464.
67. S. M. Nicola, J. Surmeier, R. C. Malenka, Dopaminergic modulation of neuronal excitability in the striatum and nucleus accumbens. *Annu. Rev. Neurosci.* **23**, 185–215 (2000). doi: 10.1146/annurev.neuro.23.1.185; pmid: 10845063
68. B. Knutson, C. M. Adams, G. W. Fong, D. Hommer, Anticipation of increasing monetary reward selectively recruits nucleus accumbens. *J. Neurosci.* **21**, RC159 (2001). pmid: 11459880
69. B. H. Schott *et al*., Mesolimbic functional magnetic resonance imaging activations during reward anticipation correlate with reward-related ventral striatal dopamine release. *J. Neurosci.* **28**, 14311–14319 (2008). doi: 10.1523/JNEUROSCI.2058-08.2008; pmid: 19109512
70. B. Knutson, S. E. B. Gibbs, Linking nucleus accumbens dopamine and blood oxygenation. *Psychopharmacology* **191**, 813–822 (2007). doi: 10.1007/s00213-006-0686-7; pmid: 17279377
71. H.-S. Liu *et al*., Dorsolateral caudate nucleus differentiates cocaine from natural reward-associated contextual cues. *Proc. Natl. Acad. Sci. U.S.A.* **110**, 4093–4098 (2013). doi: 10.1073/pnas.1207531110; pmid: 23431137
72. G. D. Stuber, T. S. Hnasko, J. P. Britt, R. H. Edwards, A. Bonci, Dopaminergic terminals in the nucleus accumbens but not the dorsal striatum corelease glutamate. *J. Neurosci.* **30**, 8229–8233 (2010). doi: 10.1523/JNEUROSCI.1754-10.2010; pmid: 20554874
73. K. T. Beier *et al*., Circuit architecture of VTA dopamine neurons revealed by systematic input-output mapping. *Cell* **162**, 622–634 (2015). doi: 10.1016/j.cell.2015.07.015; pmid: 26232228
74. N. Lally *et al*., Anti-anhedonic effect of ketamine and its neural correlates in treatment-resistant bipolar depression. *Transl. Psychiatry* **4**, e469 (2014). doi: 10.1038/tp.2014.105; pmid: 25313512
75. G. Juckel *et al*., Dysfunction of ventral striatal reward prediction in schizophrenia. *Neuroimage* **29**, 409–416 (2006). doi: 10.1016/j.neuroimage.2005.07.051; pmid: 16139525
76. E. C. Dowd, D. M. Barch, Anhedonia and emotional experience in schizophrenia: Neural and behavioral indicators. *Biol. Psychiatry* **67**, 902–911 (2010). doi: 10.1016/j.biopsych.2009.10.020; pmid: 20004364
77. A. Lüthi, C. Lüscher, Pathological circuit function underlying addiction and anxiety disorders. *Nat. Neurosci.* **17**, 1635–1643 (2014). doi: 10.1038/nn.3849; pmid: 25402855
78. M. E. Jackson, A. S. Frost, B. Moghaddam, Stimulation of prefrontal cortex at physiologically relevant frequencies inhibits dopamine release in the nucleus accumbens. *J. Neurochem.* **78**, 920–923 (2001). doi: 10.1046/j.1471-4159.2001.00499.x; pmid: 11520912
79. H. E. Covington III *et al*., Antidepressant effect of optogenetic stimulation of the medial prefrontal cortex. *J. Neurosci.* **30**, 16082–16090 (2010). doi: 10.1523/JNEUROSCI.1731-10.2010; pmid: 21123555
80. B. Giros, M. Jaber, S. R. Jones, R. M. Wightman, M. G. Caron, Hyperlocomotion and indifference to cocaine and amphetamine in mice lacking the dopamine transporter. *Nature* **379**, 606–612 (1996). doi: 10.1038/379606a0; pmid: 8628395
81. L. K. Krugel, G. Biele, P. N. Mohr, S.-C. Li, H. R. Heekeren, Genetic variation in dopaminergic neuromodulation influences the ability to rapidly and flexibly adapt decisions. *Proc. Natl. Acad. Sci. U.S.A.* **106**, 17951–17956 (2009). doi: 10.1073/pnas.0905191106; pmid: 19822738
82. Full details of the materials and methods are available as supplementary materials on *Science* Online.
83. G. H. Glover, C. S. Law, Spiral-in/out BOLD fMRI for increased SNR and reduced susceptibility artifacts. *Magn. Reson. Med.* **46**, 515–522 (2001). doi: 10.1002/mrm.1222; pmid: 11550244
84. C. S. Law, G. H. Glover, Interleaved spiral-in/out with application to functional MRI (fMRI). *Magn. Reson. Med.* **62**, 829–834 (2009). doi: 10.1002/mrm.22056; pmid: 19449373
85. C. Chang, G. H. Glover, Variable-density spiral-in/out functional magnetic resonance imaging. *Magn. Reson. Med.* **65**, 1287–1296 (2011). doi: 10.1002/mrm.22722; pmid: 21500257
86. G. T. Buračas, G. M. Boynton, Efficient design of event-related fMRI experiments using M-sequences. *Neuroimage* **16**, 801–813 (2002). doi: 10.1006/nimg.2002.1116; pmid: 12169264
87. G. H. Glover, Deconvolution of impulse response in event-related BOLD fMRI. *Neuroimage* **9**, 416–429 (1999). doi: 10.1006/nimg.1998.0419; pmid: 10191170

ACKNOWLEDGMENTS

We declare no conflicts of interest. K.D. is supported by the Defense Advanced Research Projects Agency Neuro-FAST program; the National Institute of Mental Health; the National Institute on Drug Abuse (NIDA); the NSF; the Simons Foundation; the Gatsby Foundation; the Wiegers Family Fund; and the Grosfeld, Reeves, Snyder, Woo, and Albert Yu and Mary Bechman Foundations. G.H.G. is supported by NIH grant P41 EB015891. This research was also supported in part by a Bio-X Seed grant and a Stanford Neuroscience Institute grant to B.K. and K.D. E.A.F. was supported by a Fulbright International Science and Technology Fellowship, a Stanford Graduate Fellowship, and a Gerald J. Lieberman Fellowship. K.A.Z. was supported by the NSF Graduate Research Fellowship Program, the Stanford Neurosciences Program NIH Training Grant, and a National Research Service Award Predoctoral Fellowship from NIDA (1F31MH105151_01). C.L. was supported by NARSAD and NIH grant R00 MH097822. We thank Z. J. Malchano, T. Davidson, L. J. Pisani, and R. Watkins for advice and technical support and the entire Deisseroth laboratory for guidance. Data displayed in Fig. 6 are available as a full online resource data set at http://clarityresourcecenter.org/ofMRI.html.

SUPPLEMENTARY MATERIALS

www.sciencemag.org/content/351/6268/aac9698/suppl/DC1
Materials and Methods
Figs. S1 to S16
Tables S1 to S7
Caption for Data S1
References (*88*–*95*)

9 July 2015; accepted 17 November 2015
10.1126/science.aac9698

RESEARCH ARTICLE SUMMARY

BEHAVIORAL GENETICS

Epigenetic (re)programming of caste-specific behavior in the ant *Camponotus floridanus*

Daniel F. Simola,*† Riley J. Graham,† Cristina M. Brady, Brittany L. Enzmann, Claude Desplan, Anandasankar Ray, Laurence J. Zwiebel, Roberto Bonasio, Danny Reinberg,* Jürgen Liebig,* Shelley L. Berger*

INTRODUCTION: Eusocial insects, such as ants, live a communal lifestyle within colonies of close genetic relatives. Colony members are organized into castes defined by behavioral and, in some species, morphological traits. This caste system allows for colonial division of labor and is a key adaptation of eusocial insects. However, there is limited understanding of the molecular regulation of caste-specific behavior and the principles underlying division of labor. In the carpenter ant *Camponotus floridanus*, morphologically distinct worker castes called minors and majors exhibit unique patterns of histone posttranslational modifications, including lysine acetylation regulated by CBP [cyclic adenosine monophosphate response element–binding protein (CREB) binding protein], a conserved histone acetyltransferase (HAT).

RATIONALE: Because chromatin regulators such as CBP have been associated with caste-specific traits, we tested whether caste-specific behavioral states in eusocial insects are functionally regulated via epigenetic mechanisms. We assessed innate differences in foraging and scouting (by the lead forager), classic altruistic behaviors of eusocial systems, between minor and major worker castes in *C. floridanus*. We examined whether CBP and histone deacetylases (HDACs) functionally regulate caste-specific foraging and scouting behaviors. Further, we tested whether caste-specific behavioral states may be reprogrammed through epigenomic manipulations.

RESULTS: *C. floridanus* minors and majors exhibited innate differences in foraging and scouting behaviors, with minors performing the bulk of both activities. Treatments with small-molecule inhibitors of class I and II HDAC activity (HDACi) enhanced foraging and scouting. This gain of function was suppressed by treatment with a small-molecule HAT inhibitor of CBP (HATi). Transcriptome and chromatin analyses in the brains of minors treated with HATi and HDACi revealed changes in genes linked to regions of hyperacetylated histone H3 Lys^{27} (a lysine targeted by CBP) near CBP binding sites. Although untreated majors rarely foraged, suppression of histone deacetylation by injection of HDACi or small interfering RNAs (siRNAs) against the HDAC-encoding gene *Rpd3* into young major brains was sufficient to induce and sustain minor-like foraging and scouting for up to 50 days. Strikingly, coinjection of CBP HATi suppressed HDACi-induced foraging and scouting in majors.

ON OUR WEB SITE

Read the full article at http://dx.doi.org/10.1126/science.aac6633

CONCLUSION: Caste-specific foraging and scouting behaviors are tightly linked to morphology and are likely regulated epigenetically by the balance between CBP-mediated acetylation and HDAC-mediated deacetylation of histones in the ant central brain. Thus, behavioral plasticity can be manipulated in the ant *C. floridanus* by pharmacological and genetic tools that target chromatin regulatory enzymes to stimulate, inhibit, and reprogram behavior. These findings reveal the epigenome as a likely substrate underlying caste-based division of labor in eusocial insects. Furthermore, in light of the conserved role of CBP in learning and memory in both invertebrates and mammals, these data suggest that CBP-mediated histone acetylation may similarly facilitate the complex social interactions found in vertebrate species. ■

The list of author affiliations is available in the full article online.
*Corresponding author. E-mail: simola@upenn.edu (D.F.S.); danny.reinberg@nyumc.org (D.R.); juergen.liebig@asu.edu (J.L.); bergers@upenn.edu (S.L.B.)
†These authors contributed equally to this work.
Cite this paper as D. F. Simola *et al.*, *Science* **351**, aac6633 (2016). DOI: 10.1126/science.aac6633

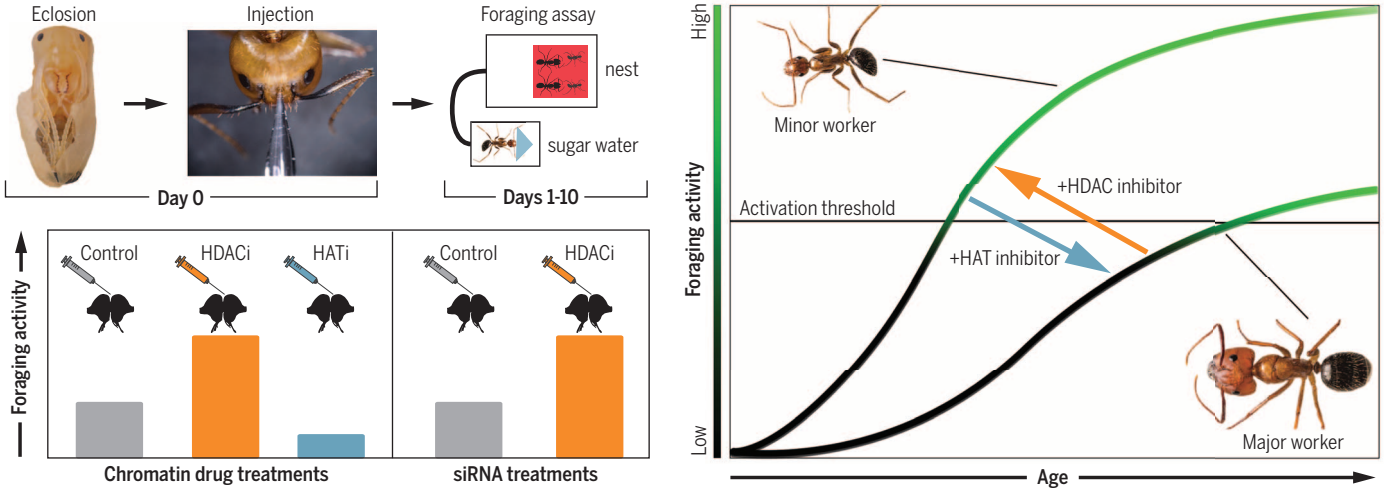

An epigenetic model for division of labor. Left: Workers were injected at eclosion and tested for foraging activity. HDAC inhibition (HDACi) with chromatin drugs or siRNA enhanced foraging; HATi suppressed foraging. Right: Minor and major workers express distinct behavioral ontogenies. Minors forage earlier in life and with greater intensity than majors. HDACi in majors stimulated minor-like foraging behavior, a gain of function suppressed by HATi treatment.

RESEARCH ARTICLE

BEHAVIORAL GENETICS

Epigenetic (re)programming of caste-specific behavior in the ant *Camponotus floridanus*

Daniel F. Simola,[1,2]*† Riley J. Graham,[2,3]† Cristina M. Brady,[1,2] Brittany L. Enzmann,[4] Claude Desplan,[5] Anandasankar Ray,[6] Laurence J. Zwiebel,[7] Roberto Bonasio,[1,2] Danny Reinberg,[8]* Jürgen Liebig,[4]* Shelley L. Berger[1,2,3,9]*

Eusocial insects organize themselves into behavioral castes whose regulation has been proposed to involve epigenetic processes, including histone modification. In the carpenter ant *Camponotus floridanus*, morphologically distinct worker castes called minors and majors exhibit pronounced differences in foraging and scouting behaviors. We found that these behaviors are regulated by histone acetylation likely catalyzed by the conserved acetyltransferase CBP. Transcriptome and chromatin analysis in brains of scouting minors fed pharmacological inhibitors of CBP and histone deacetylases (HDACs) revealed hundreds of genes linked to hyperacetylated regions targeted by CBP. Majors rarely forage, but injection of a HDAC inhibitor or small interfering RNAs against the HDAC *Rpd3* into young major brains induced and sustained foraging in a CBP-dependent manner. Our results suggest that behavioral plasticity in animals may be regulated in an epigenetic manner via histone modification.

Colonies of eusocial insects organize themselves into castes comprising individuals that exhibit specific behaviors over extended periods of time. This colonial division of labor is a key adaptation responsible for the ecological and evolutionary success of eusocial insects (*1*–*4*). Different eusocial species have evolved unique strategies for regulating the expression of behavioral castes on the basis of age, morphology, and social context. The most fundamental examples of division of labor involve the differentiation of individuals into sterile (worker) and reproductive (queen) castes. In addition, workers often express a variety of specialized behaviors depending on age [e.g., the honey bee *Apis mellifera* (*2*)], body size [e.g., the fire ant *Solenopsis invicta* (*5*)], or both [e.g., formicid ants (*1*–*4*, *6*)].

The principles underlying the social control of behavior and the corresponding molecular mechanisms that regulate individual behavioral plasticity have been studied primarily in solitary species, such as the fly *Drosophila* (*7*). Recently, obligately social insects, including the eusocial honey bee *A. mellifera* and carpenter ant *Camponotus floridanus*, have emerged as models of more complex behavior (*8*–*10*). Findings in these species suggest that epigenetic processes, including DNA methylation (*11*–*15*) and histone posttranslational modifications (hPTMs) (*16*), may play key roles in regulating caste-based behavioral plasticity.

C. floridanus workers exhibit caste-specific behaviors

To investigate the role of hPTMs in regulating ant behavioral castes, we studied *C. floridanus* (*12*), which expresses two distinct female worker caste morphologies, called minors and majors (Fig. 1A, right). These morphs are distinguished by head width and length of scape (basal antennal segment; a proxy for body size) (fig. S1, A and B) and are produced in a 2:1 ratio in mature colonies (fig. S1C). Although genetic factors may contribute to the quantitative variation in worker morphology (fig. S1D), the production of minor and major castes per se is likely not caused by allelic variation. Rather, workers are genetically related supersisters (r = 0.75) resulting from a single diploid mother mating with a single haploid father (*17*). Further, treatment of undifferentiated larvae with the DNA methylation inhibitor 5-aza-2′-deoxycytidine (5-aza-dC) increases head width and scape length in the resulting adults (*15*).

A survey of hPTMs in *C. floridanus* indicated that several hPTMs, especially the acetylation of Lys^{27} on histone H3 (H3K27ac), have distinct genome-wide patterns in the bodies and brains of minors and majors (*16*). These differences can be attributed to differential localization of the conserved acetyltransferase and transcriptional coactivator CBP [cyclic adenosine monophosphate response element–binding protein (CREB) binding protein] in each caste, and they correspond to differences in gene expression (*16*). In addition, a functional histone deacetylase inhibitor (HDACi), the fatty acid 10-HDA, is a major component of royal jelly, an environmental regulator of queen production in honey bees (*18*). Taken together, these findings suggest that hPTMs influence the generation of distinct castes in eusocial insects and that histone acetylation might regulate caste-based behavioral plasticity.

To examine caste-based behavioral plasticity in *C. floridanus*, we fitted the nest of a 7-year-old queen-right (i.e., containing a queen) colony with a foraging arena and counted the number and caste of each ant that foraged out to feed on water or 20% sugar water over 24-hour periods (see Materials and Methods) (*19*). Minors performed the vast majority of foraging, with a distinct circadian pattern and preference for sugar water (Fig. 1A). To control for effects of social interactions, we isolated 1-day-old ants and monitored their foraging behavior either in isolation for 10 days (fig. S1, E and F) or when mixed with older, mature workers for 4 months (fig. S1, G and H). In both cases, minors were the predominant foragers.

To determine whether caste-based foraging may be a generic feature of *Camponotus* ants, we also assayed the sympatric species *C. tortuganus*. In both species, minors foraged but majors did not (fig. S1I), indicating that minor and major *Camponotus* workers display natural differences in foraging behavior (*20*–*22*).

Age correlates with behavioral plasticity in eusocial insects, including other *Camponotus* species (*22*). We therefore marked 1-day-old callows on a weekly basis in several queen-right colonies. We analyzed equal-sized cohorts of workers with identical colony background, caste morphology, and age (±48 hours) in an assay where either minors or majors were isolated from their natal nest and were water-starved (i.e., by withholding sugar) for 24 hours before foraging. Under these stringent conditions, minors showed significantly greater foraging activity than age-matched majors, although majors did forage at a low rate (Fig. 1B and fig. S2A). Moreover, mixed cohorts of age-matched minors and majors displayed lower foraging activity than minors alone, yet only 28% of foraging was attributed to majors (Fig. 1B).

Additionally, we analyzed foraging behavior as a function of starvation time, because majors are physically larger and may have twice the food storage capacity of minors. Majors required more than 9 days of starvation to match the foraging activity of minors starved for only 24 hours (Mann-Whitney U test, P < 0.01; fig. S2B). Thus, minors

[1]Department of Cell and Developmental Biology, University of Pennsylvania Perelman School of Medicine, Philadelphia, PA 19104, USA. [2]Program in Epigenetics, University of Pennsylvania, Philadelphia, PA 19104, USA. [3]Department of Biology, University of Pennsylvania, Philadelphia, PA 19104, USA. [4]School of Life Sciences, Arizona State University, Tempe, AZ 85287, USA. [5]Department of Biology, New York University, New York, NY 10003, USA. [6]Department of Entomology, University of California, Riverside, CA 92521, USA. [7]Department of Biological Sciences, Vanderbilt University, Nashville, TN 37232, USA. [8]Department of Molecular Pharmacology and Biochemistry, New York University School of Medicine, New York, NY 10016, USA. [9]Department of Genetics, University of Pennsylvania Perelman School of Medicine, Philadelphia, PA 19104, USA. ***Corresponding author. E-mail: simola@upenn.edu (D.F.S.); danny.reinberg@nyumc.org (D.R.); juergen.liebig@asu.edu (J.L.); bergers@upenn.edu (S.L.B.)** †These authors contributed equally to this work.

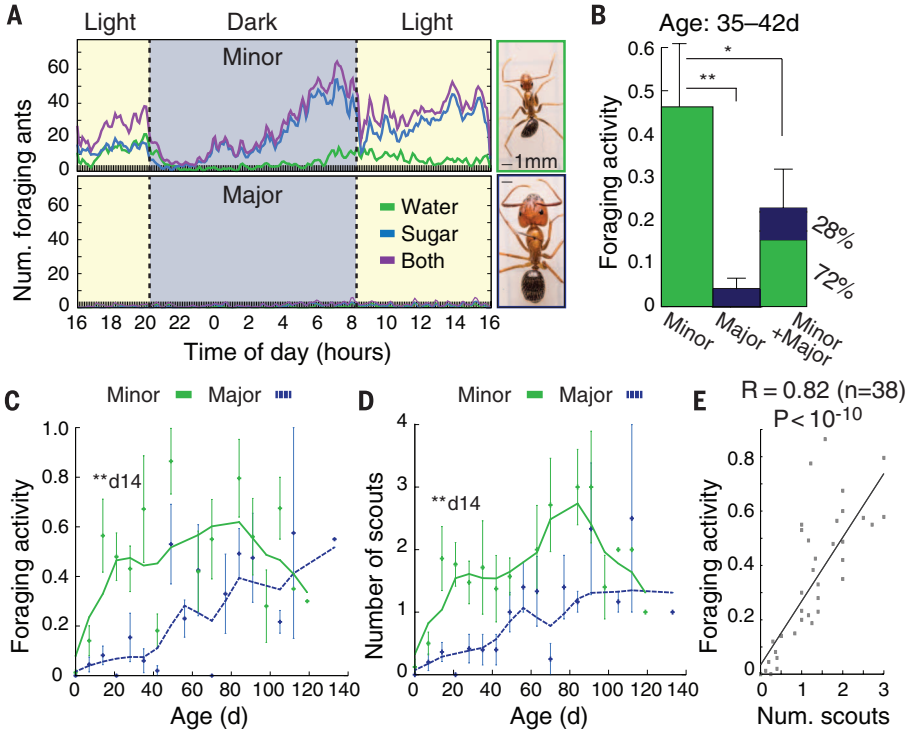

Fig. 1. Foraging and scouting behaviors depend on worker caste and age. (**A**) Circadian foraging activity for minor (top) and major (bottom) workers in a single monogamous colony. Photographs show representative minor and major workers (fig. S1, A and B). (**B**) Average foraging activity (defined in fig. S2A) ± SE for 35- to 42-day-old minors and majors isolated and sugar-starved for 24 hours; rightmost column shows foraging activity for mixed cohorts of 10 majors and 10 minors of the same age. (**C** and **D**) Foraging activity (C) and number of scouts (D) for minors and majors isolated and sugar-starved for 24 hours, as a function of adult age after eclosion. Error bars denote SE over at least five independent replicates from six colonies. The earliest age of significant caste-differential behavior (day 14) is noted. Asterisks in (B) to (D) denote significance by Mann-Whitney U test: $*P < 0.05$, $**P < 0.01$. (**E**) Number of scouts versus foraging activity for data in (C) and (D). Pearson correlation coefficient is shown.

appear to be the predominant foragers in queen-right colonies (Fig. 1A) as well as in young (fig. S1, F and H) and mature (Fig. 1B) worker cohorts.

We also examined how caste and age affect the lead foragers, called scouts, which have been reported to constitute a distinct behavioral caste in a few eusocial species (*1*, *20*, *21*, *23*) (see below). Scouts are the first ants to leave a nest, discover a food source, and return to the nest with this food, before recruiting additional ants to forage (movie S1 and table S1). Analysis of the number of scouts and foraging activity over 4 months revealed both caste- and age-based differences (Fig. 1, C and D). Minors exhibited significantly more foraging and scouting activity than did majors by 14 days of age (Fig. 1, C and D). Also, the foraging speed of 60-day-old scouts was greater than that of 7-day-old scouts by as much as a factor of 6 (fig. S2C). We exclusively assayed ants that were naïve to a foraging arena, so these effects are not due to learning. Finally, the number of scouts in a cohort correlated strongly with the cohort's foraging activity (Fig. 1E); this finding suggests that scouts, which are predominantly minors, determine a cohort's overall foraging activity (*24*).

These results indicate that foraging and scouting behaviors in *C. floridanus* depend on caste morphology, age, and social context, consistent with observations in other ant species (*1*–*3*, *20*–*23*). They also support the view that eusocial species that express polymorphic worker castes have the potential for greater colony-level behavioral complexity than species with a monomorphic worker caste, as caste morphology apparently provides an additional dimension of behavioral variation that can be controlled by colonies to optimize division of labor (*1*–*4*, *22*).

Histone deacetylases inhibit foraging and scouting behaviors

Minors always foraged and scouted more than majors, regardless of age and social context; this observation is consistent with the idea that minors and majors harbor innate, molecularly determined differences that influence behavior. Given results suggesting a functional role for histone acetylation in determining caste-specific traits (*16*), we examined whether foraging behavior might be regulated by histone acetylation dynamics controlling gene transcription.

We first measured mRNA abundance in brains of young, age-matched minors and majors from the same colony for the five class I and II HDACs encoded in the *C. floridanus* genome. Orthologs of these genes have established roles in neuronal and behavioral plasticity in other insects and mammals (*25*–*27*). Both *Rpd3/Hdac1a* (a putative H3K27ac deacetylase) and *Hdac6* showed caste-specific expression patterns (Student's *t* test, $P < 0.003$; fig. S3).

We confirmed that both *Rpd3* and *Hdac6* transcripts also increased with age in minors and majors, using 25 brains evenly sampled from five colonies for each caste and age point ($n = 100$ brains total; Fig. 2A). These observations are consistent with specific HDACs influencing foraging behavior, either via age-dependent decreases in histone acetylation or via increased histone acetylation dynamics, as has been observed for *Rpd3* in *Drosophila* (*25*).

We then examined foraging and scouting behaviors after inhibiting the activity of class I and II HDACs by feeding workers a small-molecule HDACi, valproic acid (VPA) (*28*). As expected (*28*, *29*), VPA treatments increased global levels of H3K27ac when fed to larvae and minors (Student's *t* test, $P < 0.02$; fig. S4A). We fed non-lethal concentrations of 10 mM VPA (*28*, *29*) to mixed cohorts of 25- to 30-day-old minors and majors for 30 days. Foraging was assessed after pooling a treated cohort with a corresponding untreated cohort of colony- and age-matched minors and majors (Fig. 2B). Both VPA-treated minors and majors exhibited significantly more foraging than did controls (Fig. 2C). VPA-treated minors were also the first to act as scouts by finding food in 73% of trials (Fig. 2D and fig. S4B), whereas majors never scouted (Fig. 2D). These results indicate that increasing histone acetylation shifts the behavior of both minors and majors toward increased foraging and feeding, although minors remain the predominant foragers and scouts.

To confirm that increases in foraging activity elicited by VPA were due to HDAC inhibition, we used a second HDACi, trichostatin A (TSA), which has greater potency (i.e., inhibitory concentration, IC_{50}) than VPA, as well as greater specificity toward histone substrates for inhibiting the removal of acetyl groups (*28*, *29*). As with VPA treatments, we assayed foraging using 25- to 30-day-old workers. However, we repeatedly assayed foraging over 42 days (rather than once after 30 days), and we assayed treated and untreated cohorts of minors separately (rather than mixed) to avoid any potential confounding effects due to social interactions (Fig. 2E).

In this assay, relative to controls, minors fed TSA displayed significantly greater foraging activity in a dose-dependent manner (Fig. 2F). TSA also increased the number of scouts (Fig. 2G). Because only a minority of ants fed during a foraging trial, TSA does not appear to cause general locomotor hyperactivity. Furthermore, pharmacological treatment did not affect the correlation between foraging activity and the number of scouts ($R = 0.80$; fig. S4C) relative to controls ($R = 0.82$; Fig. 1E), nor did it affect the duration of a scout's return to the nest after feeding (expedition time) [Mann-Whitney U test, $P < 0.9$ for TSA versus dimethyl sulfoxide (DMSO); fig. S4D]. Also,

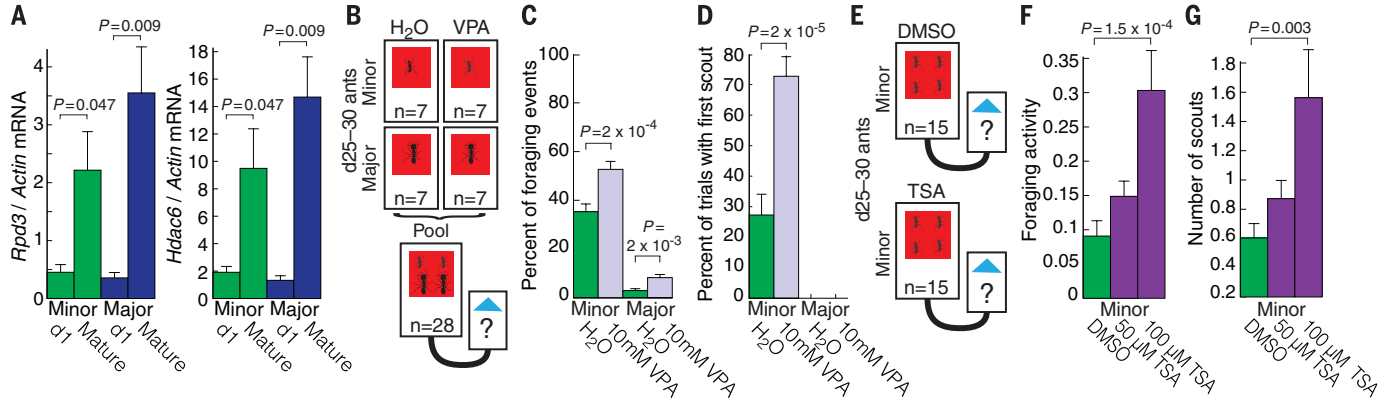

Fig. 2. HDAC inhibition stimulates foraging and scouting behaviors. (**A**) RT-qPCR analysis of mRNA abundance for *Rpd3* (*Hdac1a*) and *Hdac6* in young (1 day old) and mature (>30 days old) major and minor brains. Each bar indicates the mean ± SE over five colonies, where each measurement represents a pooled sample of five individual brains (n = 100 brains total). mRNA abundance was normalized against actin mRNA. P values were computed by Mann-Whitney U test. Primers are reported in table S2. (**B**) Schematic of foraging assay for VPA-treated ants. Cohorts of 28 minors and majors, age 25 to 30 days, were fed 20% sugar water with or without 10 mM VPA for 30 days (seven ants in four treatment groups). Ants were then pooled, sugar-starved for 24 hours, and assayed for foraging after attaching a foraging arena. Blue triangle denotes sugar water food source. (**C**) Average percent of all foraging events performed by untreated or VPA-treated minors or majors when pooled as in (B). (**D**) Average percent of trials in which the first scout that foraged and fed on sugar water had been provided sugar water alone or with VPA. Error bars in (C) and (D) denote SE over 46 trials from 12 colonies. (**E**) Schematic of foraging assay for TSA-treated ants. Cohorts of 15 minors, age 25 to 30 days, were fed 20% sugar water containing DMSO with or without 50 μM or 100 μM TSA for 42 days. Unlike in (B) to (D), treatment groups were assayed for foraging separately, without pooling, after 24 hours of sugar starvation. (**F** and **G**) Average foraging activity (F) and number of scouts (G) for DMSO- or TSA-treated minor cohorts in foraging assay shown in (E). Cohorts were tested weekly over 42 days. Error bars denote SE over six measurements per cohort for 14 (DMSO) or 18 (TSA) independent cohorts from six colonies. P values were computed by Mann-Whitney U test.

TSA-treated minors showed low mortality over the 42-day treatment course (fig. S4E), which suggests that sickness and/or hunger are unlikely explanations for increased foraging and feeding. Hence, we conclude that HDAC activity normally inhibits foraging behavior in workers.

CBP-dependent histone acetylation regulates foraging and scouting behaviors

Because of the reported correspondence between genomic regions of caste-specific hPTMs and CBP binding (*16*), we tested whether the stimulation of foraging behavior by HDAC inhibition depends on stabilization or enhancement of hPTMs acetylated by CBP, such as H3K27ac. We thus used the small molecule C646, a specific inhibitor of CBP's histone acetyltransferase (HAT) activity (HATi) in mammals and insects (*30*, *31*). CBP's mammalian paralog p300 is also targeted by C646, but it is not encoded in the *C. floridanus* genome.

Feeding 25 μM C646 to larvae significantly decreased H3K27ac throughout the genome after global between-sample normalization (Wilcoxon signed-rank test, $P < 10^{-20}$; fig. S5A). In particular, C646 treatment significantly altered H3K27ac levels for more than 800 genes [χ^2 test, false discovery rate (FDR) < 0.05; fig. S5B]. Genes affected most by C646 showed significant loss of H3K27ac (Mann-Whitney U test, $P < 4 \times 10^{-4}$; fig. S5C). These genes are enriched for a variety of functional terms pertaining to the structure, development, differentiation, and communication of neurons (Fisher's exact test, FDR < 0.05; fig. S5D). This suggests that C646 treatment, despite interfering with a pleiotropic pathway of gene regulation, preferentially inhibits genes with neuronal functions.

To test whether the increased foraging activity of HDACi-treated workers depends on the HAT activity of CBP, we fed 25- to 30-day-old minors a cocktail of 50 μM TSA together with either 50 μM or 100 μM C646 and assayed foraging behavior as above with TSA alone (Fig. 2E). Treatment with 50 μM C646 did not significantly affect foraging or scouting, either alone or in combination with TSA (Fig. 3, A and B, and fig. S4F, red and blue versus green). In contrast, treatment with 100 μM C646 essentially blocked all foraging and scouting, despite the presence of TSA at a dosage that stimulated foraging alone (Fig. 3, A and B, and fig. S4F, blue versus purple). Indeed, delivering 100 μM C646 alone was sufficient to inhibit scouting within 14 days of treatment (Mann-Whitney U test, $P < 0.05$; fig. S4G). Moreover, C646 had minimal, nonsignificant effects on scout expedition time (fig. S4D) and mortality (fig. S4E), which suggests that it did not affect locomotion or induce severe toxicity. These results imply that HDACi-induced foraging is mediated by histone residues that are acetylated by CBP, such as H3K27ac (*32*, *33*).

Because foraging activity correlates strongly with the number of scouts, and because scouting is inhibited by C646, we reasoned that CBP may be required to induce workers to become scouts. To examine this, we assayed individually marked 25- to 30-day-old minors in isolated cohorts. We found that the median duration of individual scouting behavior was 20 days, with some ants consistently scouting for the 49-day duration of the assay (Fig. 3C). Moreover, most of the workers that scouted (66%) emerged in the first 15 days (i.e., were 40 to 45 days old), rather than uniformly over time (Fig. 3D). Therefore, scouts likely represent a persistent behavioral caste expressed by select individuals in *C. floridanus*.

We tested whether the addition of C646 after 14 days of TSA treatment, after most scouts have already emerged (Fig. 3D), affected TSA-dependent increases in scouting and foraging. Indeed, addition of 100 μM C646 after 2 weeks of 50 μM TSA treatment by feeding failed to reverse increases in foraging and scouting (Fig. 3E, orange versus purple), in contrast to parallel treatment of 50 μM TSA together with 100 μM C646 (Fig. 3E, orange versus blue). These results suggest that CBP, via its histone acetylation activity, may serve as a licensing factor to enable the transition of a worker into the scout behavioral caste. Moreover, the fact that the timing of C646 delivery appears to be critical to elicit the behavioral response suggests that loss of foraging is not due to the toxicity of C646 or its nonspecific effects on general locomotion (fig. S4, D and E).

We then examined how the observed changes in behavior after treatment with TSA and C646 are associated with molecular changes. We analyzed genome-wide mRNA expression in individual brains dissected from 21 minors sampled while feeding on sugar water during a scouting run (Fig. 4A and figs. S6 and S7) (*19*). Hierarchical clustering analysis of the 250 genes exhibiting greatest differential expression among treatments yielded two clusters of brain samples, a TSA-treated group and a DMSO-treated or TSA + C646–treated group, consistent with our behavioral analyses (Fig. 4B). In contrast, random gene subsampling and analysis of internal spike-in control transcripts failed to partition samples by treatment group, as expected (fig. S8).

Most of the top 250 differentially expressed genes (72%) were up-regulated with TSA (Fig. 4B, left), consistent with an overall increase in histone acetylation due to TSA and overall decrease

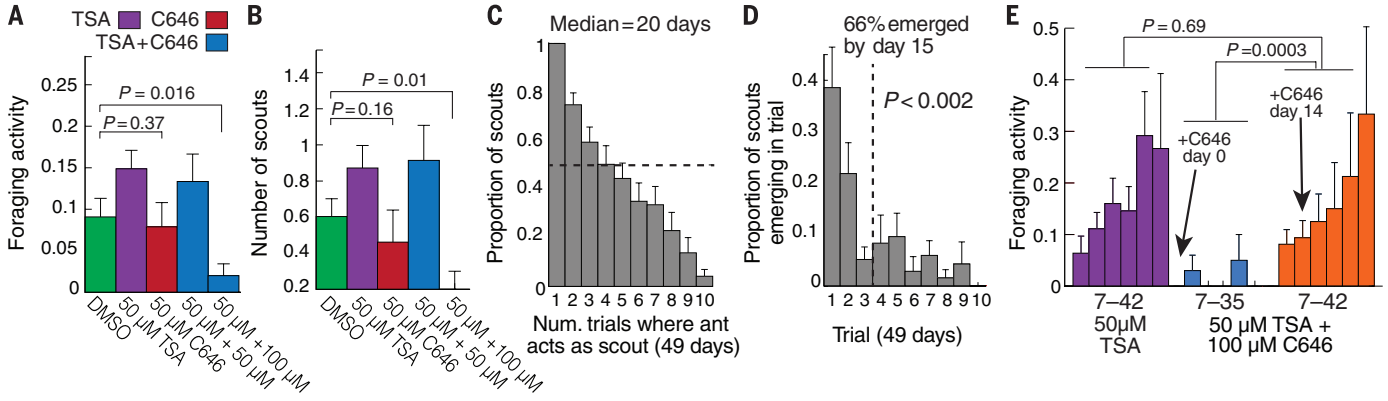

Fig. 3. CBP-dependent acetylation regulates foraging via production of scouts. (**A** and **B**) Average foraging activity ± SE (A) and number of scouts ± SE (B) for cohorts of 15 minors isolated at age 25 to 30 days and continuously fed DMSO, 50 µM TSA, 50 µM C646, 50 µM TSA + 50 µM C646, or 50 µM TSA + 100 µM C646 ad libitum in 20% sugar water (Fig. 2E). (**C**) Proportion of minors that scouted for 1 to 10 consecutive foraging trials over a span of 49 days; an ant that scouted once acted as a scout for a median of 20 days (four trials, indicated by dashed line). (**D**) Distribution of the number of trials after isolation until an individual first scouted; dashed line indicates 15 days after isolation (three trials). Error bars in (C) and (D) denote SE over seven replicate cohorts of 15 minors, age 30 to 35 days, from four colonies. *P* value in (D) is from a χ^2 test. (**E**) Average foraging activity ± SE for individual trials per treatment group over 42 days. Orange bars represent trials in which C646 was provided starting 14 days after isolation and first administration of TSA; for blue bars, C646 was provided starting immediately upon isolation in parallel with TSA. Cohorts were tested weekly over 42 days. Error bars in (A) and (E) denote SE over six measurements per cohort and 14 (green), 6 (red), 18 (purple), 11 (blue), or 8 (orange) independent cohorts sampled from six colonies. *P* values in (A), (B), and (E) were estimated by Mann-Whitney U test.

in CBP-mediated acetylation due to C646. Gene ontology analysis of the 101 genes with significant differential expression (Bonferroni $P < 0.05$; table S3) (*19*) revealed enrichment for hormone signaling, dendrite morphogenesis, synaptic transmission, and sphingolipid biosynthesis (Fisher's exact test, $P < 0.01$; fig. S7C) as processes responsive to chromatin regulation (*25*, *33*, *34*). These results argue that inhibition of HATs and HDACs by chronic feeding of small-molecule inhibitors may affect the expression of specific genes in the ant central brain.

To assess whether TSA and C646 affect brain gene expression via alterations in chromatin structure, we performed chromatin immunoprecipitation sequencing (ChIP-seq) for H3K27ac and H3K9ac, two hPTMs implicated in neuronal and behavioral plasticity (*27*, *35*), using tissue from nine of the scout brains also used for RNA-seq (Fig. 4A). We normalized these data using input lysate as well as internal spike-in lysate (ChIP-Rx) from the evolutionarily divergent ant *H. saltator* (*12*, *19*, *36*).

We identified regions of interest (ROIs) that were differentially marked by H3K9ac or H3K27ac between DMSO and TSA treatments (dmROIs) (Fig. 4C). These dmROIs covered 0.33% (H3K9ac) and 1.5% (H3K27ac) of the genome, respectively, and predominantly occurred in noncoding regions (~90%; fig. S9A). Notably, dmROIs exhibited both gains and losses in histone acetylation in TSA-treated samples (Fig. 4C), possibly from acclimation to chronic treatment.

We then assessed whether dmROIs occur near differentially expressed genes. Indeed, dmROIs for H3K27ac were significantly enriched among the top 500 differentially expressed genes, with the greatest significance for the top 100 genes (Fig. 4D and fig. S9, B and C), whereas dmROIs for H3K9ac showed no significant enrichment near these genes (Fig. 4D). Furthermore, we found a mild but significant correlation between the magnitude of a gene's differential expression and the differential enrichment of the nearest H3K27ac dmROI, with correlation coefficients increasing with differential expression ($0.11 < R < 0.31$; Fig. 4E). These results are consistent with a chromatin-based model of gene regulation underpinning foraging behavior.

If CBP mediates the observed, drug-dependent changes in chromatin and gene expression, dmROIs should also cluster near binding sites for CBP (*16*, *35*). Using a genome-wide annotation of CBP binding sites (*16*), we identified 3173 putatively active CBP sites with H3K27ac enrichment (fig. S9D). Like dmROIs, these binding sites were also enriched near the top differentially expressed genes (Mann-Whitney U test, $P < 0.001$ for the top 1000 genes; fig. S9E). Furthermore, dmROIs for H3K27ac, but not H3K9ac, were proximal to H3K27ac-positive CBP binding sites (median distance of 0.6 kb versus 8.7 kb from center of CBP site; Fig. 4F). Lastly, 475 H3K27ac dmROIs showed overlap with CBP sites by at least 50%. These data suggest that chronic drug treatment may induce both direct and indirect effects involving multiple histone residues and multiple regulatory factors (*30*–*33*). Taken together, these results are consistent with our prior observation of differential H3K27ac in the brains of minors and majors (*16*) and suggest that CBP may modulate foraging behavior in workers in part by regulating histone acetylation levels at specific genomic loci in the brain.

HDAC inhibition induces and sustains minor-like behavior in majors

We next sought to discern why minors and majors are differentially predisposed to forage (Fig. 1) and why majors treated with HDAC inhibitors forage and scout less than minors (Fig. 2, C and D, and fig. S10A). Given that CBP regulates the production of scouts (an age-based caste), we reasoned that differential activity of CBP and HDACs in the brains of young minors and majors might likewise establish behavioral states tied to morphological caste.

To evaluate this model, we first identified 160 genes that exhibited significant differential expression by caste in brains of 1-day-old workers from the same colony (Bonferroni $P < 0.01$; Fig. 5A and table S4) (*19*). These caste-differential genes pertain to synaptic transmission, synapse structure, and neurotransmitter release (Fisher's exact test, FDR < 0.25; fig. S11C). Furthermore, these genes were particularly responsive to TSA and C646 treatments in mature minor scout brains (Student's *t* test, $R = 0.43$, $P < 10^{-7}$; Fig. 5B)—a trend also seen for the entire transcriptome ($R = 0.10$, $P < 10^{-15}$) but not for random gene subsets (99.9%; Fig. 5B, inset).

Among these jointly caste- and drug-responsive genes were those encoding D12, a component of the ATAC HAT complex (*37*); Rho guanosine triphosphate exchange factor Trio, which regulates dendrite morphogenesis (*38*); and *N*-methyl-D-aspartate receptor (NMDAR) 1, which regulates olfactory learning and memory (*39*) (Fig. 5C). These observations are consistent with a classic response threshold model (*10*) whereby caste-specific behavioral states are established with chromatin regulatory factors, which suppress behavioral plasticity by regulating genes that modulate the brain's sensitivity to environmental cues, in turn contributing to stable neuroanatomical differences between behavioral castes (*40*, *41*).

Because caste-specific foraging appears to become more pronounced with age (and correspondingly with social experience) (Fig. 5E, gray bars, and fig. S1, F and H), we further hypothesized that majors may be most sensitive to TSA immediately after eclosion, prior to the establishment of molecular barriers that restrict behavioral

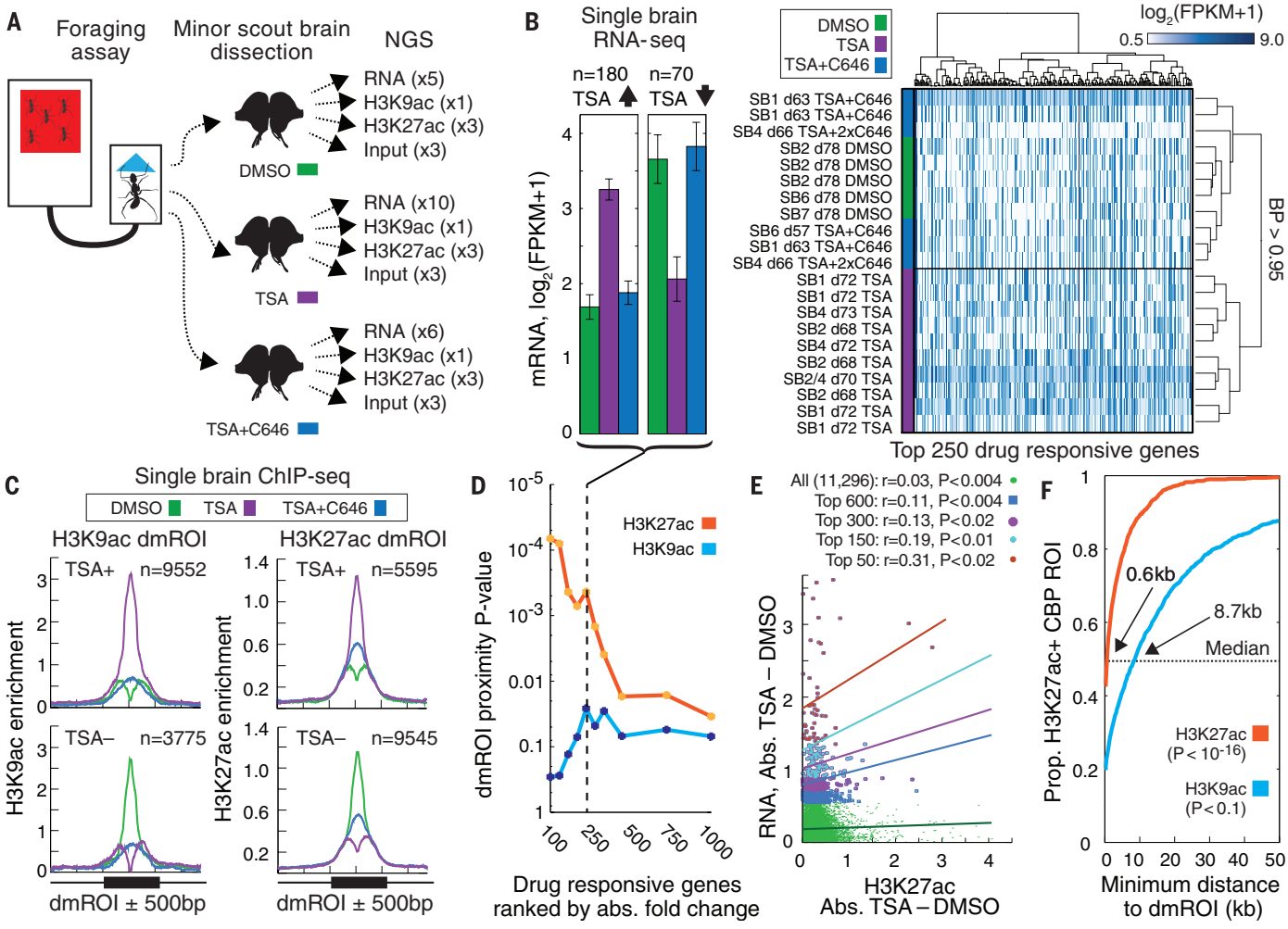

Fig. 4. HAT and HDAC inhibitors alter gene expression and histone acetylation in scout brains. (**A**) Schematic for genomics analysis. Minor scouts were sampled at the time of feeding in a foraging arena, and their central brains were dissected, homogenized, and analyzed by next-generation sequencing, with replication as indicated. (**B**) mRNA expression in brains of ~70-day-old minor scouts for the 250 genes with the greatest alteration between TSA treatment and DMSO or TSA + C646 treatment (n = 21 samples). FPKM denotes fragments per kilobase of transcript per million mapped reads. Left: Average (±SE) mRNA expression of these 250 genes. Right: Hierarchical clustering of samples for the 250 genes, using Mahalanobis distance and Ward's agglomeration criterion. P values were computed by bootstrap (*19*); BP, bootstrap probability. (**C**) Normalized ChIP-seq enrichment plots for H3K9ac and H3K27ac over significant dmROIs (±500 base pairs) that gain (top) or lose (bottom) enrichment with TSA treatment [$P < 0.001$ compared to an empirical null distribution (*19*)]. (**D**) P values for H3K27ac and H3K9ac dmROIs reflect proximity to gene transcription start sites (TSSs) ranked by absolute differential expression compared to randomly selected genes; P values were computed by Mann-Whitney U test (*19*). (**E**) Absolute change in a gene's TSS-proximal H3K27ac dmROI versus absolute change in mRNA level between TSA and DMSO samples, binned by magnitude of differential expression (top 50, 150, 300, and 600 genes). Lines denote linear regression trendlines for each group. Pearson correlation coefficients are shown; P values were computed by Student's t test. (**F**) Distributions of minimum distance from a dmROI to an H3K27ac-positive CBP binding site for H3K27ac and H3K9ac dmROIs. P values were computed by Mann-Whitney U test with randomly sampled ROI coordinates (n = 250 trials).

plasticity. Unfortunately, 1-day-old workers did not scout after starvation (fig. S10B) and hence could not receive TSA by feeding. We therefore developed a technique to deliver controlled treatment doses directly to ant brains by microinjection (Fig. 5E, inset, table S5, and movie S2). Remarkably, injecting 1 μl of 50 μM TSA onto newly eclosed major brains robustly stimulated foraging activity despite the presence of untreated age-, colony-, and group size–matched minor nestmates (Fig. 5, D and E, and fig. S12).

Over 10 days, majors injected with TSA upon eclosion consistently foraged more than did majors injected with DMSO (Mann-Whitney U test, $P < 6 \times 10^{-6}$)—and at levels similar to untreated minor nestmates ($P < 0.13$; Fig. 5E). These results suggest that inhibiting HDAC activity in young majors is sufficient to mitigate chromatin-based barriers that restrict caste-based behavioral plasticity.

In contrast, majors injected with 50 μM TSA and 100 μM C646 largely failed to forage (Fig. 5E, blue), consistent with the observed effects of these drugs when fed to mature minors (Fig. 3A, blue). To confirm that suppression of foraging by C646 was not due to off-target effects, we applied a second HAT inhibitor of CBP, EML425, which functions by a different mechanism than C646 (*42*); again, majors injected with 50 μM TSA and 100 μM EML425 exhibited little foraging (Fig. 5E, light blue).

We also examined the long-term effects of these brain injections within our starvation-based foraging assay (Fig. 2E). Remarkably, 30 to 50 days after the single-injection treatments, TSA-injected majors still displayed significantly increased foraging activity, and with more scouts, than did age- and colony-matched majors injected with DMSO (Mann-Whitney U test, $P < 0.05$) or TSA + C646 ($P < 0.01$; Fig. 5F). In contrast, untreated minor nestmates showed no significant differences in foraging among treatment groups (Fig. 5F). Taken together, these findings indicate that CBP is a likely epigenetic factor involved in establishing and maintaining morphological and age-dependent behavioral castes.

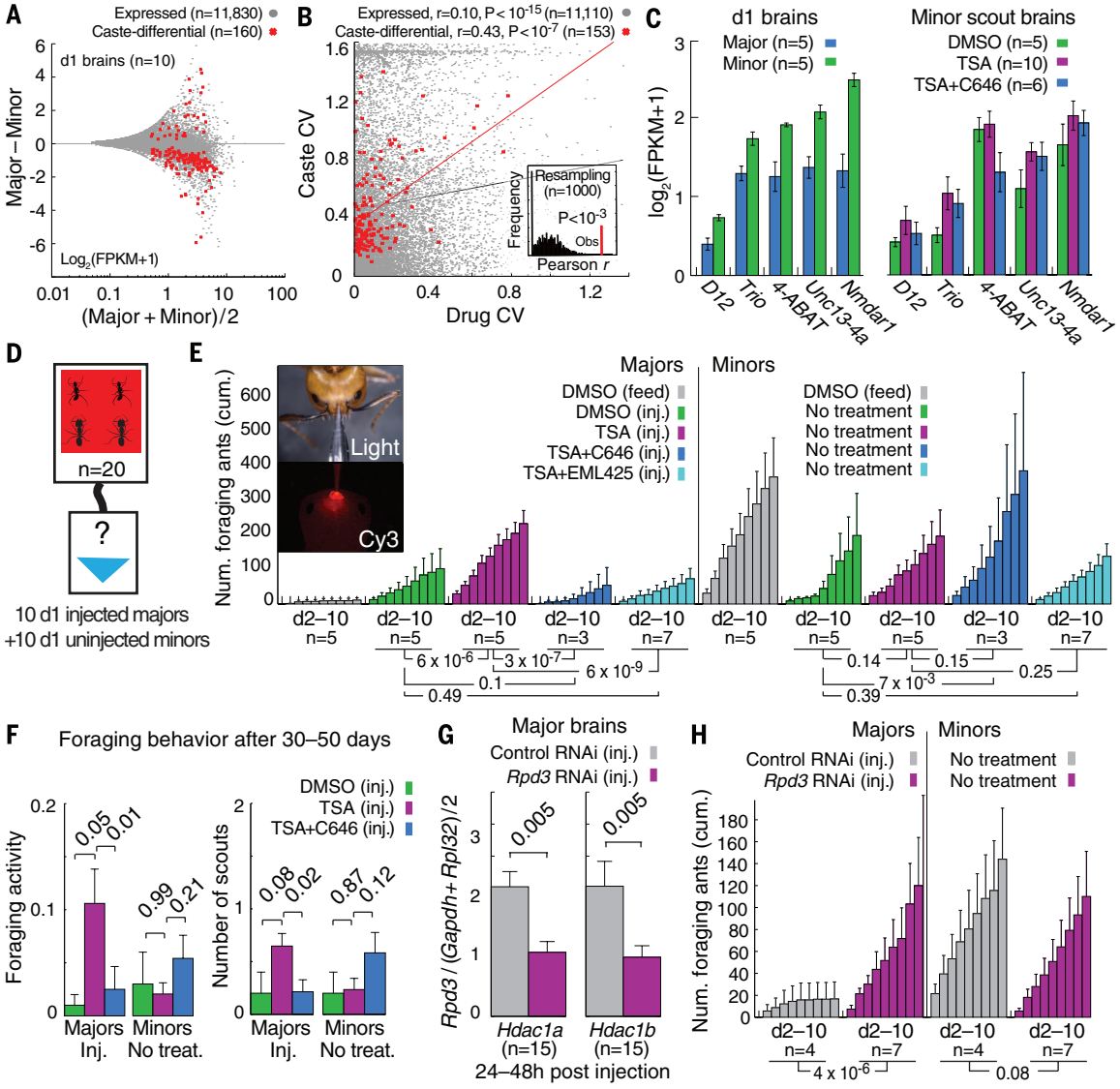

Fig. 5. RPD3 and CBP mediate epigenetic reprogramming of major workers. (**A**) Differential versus average scatterplot comparing mRNA levels for brains dissected from individual 1-day-old majors and minors ($n = 5$ per caste) from one colony. Caste-differential genes were identified by Mann-Whitney U test ($P < 0.05$) and gene-specific SE (Bonferroni $P < 0.01$). (**B**) Scatterplot comparing coefficients of variation (CVs) in gene expression between drug treatments and caste. Pearson correlation coefficients are shown. Inset shows correlation coefficients for 1000 random sets of 153 genes sampled from 11,110 expressed genes. (**C**) mRNA levels for select caste-differential genes in 1-day-old worker brains (left) and minor scout brains (right). Error bars denote SE among biological replicates. 4-ABAT, 4-aminobutyrate aminotransferase; Unc13-4a, mammalian uncoordinated homology 13, 4a ortholog. (**D**) Schematic of piggyback foraging assay. Majors and minors received no injection (gray) or 0.5% DMSO, 50 μM TSA, 50 μM TSA + 100 μM C646, or 50 μM TSA + 100 μM EML425 and were placed in a nest box attached to a foraging arena with 20% sugar water (blue triangle) (fig. S1E). (**E**) Cumulative foraging over the course of 9 days for pooled cohorts of minor and major nestmates, measured by time-lapse photography every 6 min. Uninjected cohorts were fed 20% sugar water containing 0.5% DMSO. Error bars denote SE over replicate cohorts. See table S5 for colony background and mortality information. Photographs (and movie S2) depict brain injection procedure. *P* values were estimated by Mann-Whitney U test using counts of daily foraging events. (**F**) Long-term assessment of foraging activity (left) and number of scouts (right) for the same injected majors and control minors from (E). (**G**) RT-qPCR analysis of mRNA abundance for *Rpd3* (*Hdac1a* and *Hdac1b*) in major brains 24 to 48 hours after injection with nontargeting (control) RNAi or *Rpd3* RNAi. Each bar indicates the mean ± SE over measurements from 15 brains. Abundance was normalized against *Gapdh1* and *Rpl32*. (**H**) Cumulative foraging over the course of 9 days for pooled cohorts of minors and majors, as in (D). *P* values in (E) to (H) were computed by Mann-Whitney U test.

Finally, we developed and applied a transient RNA interference (RNAi) technique (*19*) to examine whether minor-like foraging may be induced in majors by specifically inhibiting *Rpd3/Hdac1* mRNA. *Rpd3* was selected because it encodes a class I HDAC putatively targeted by TSA and because its mRNA abundance increased with age in *C. floridanus* (Fig. 2A). RPD3 also deacetylates residues acetylated by CBP, such as H3K27ac (*32*). Injection of 27-nucleotide double-stranded small interfering RNA (siRNA) oligos against the *Rpd3* and *Rpd3*-like transcripts into 1-day-old major brains led to a factor of 2 reduction in their mRNA levels in the central brain after 24 to 48 hours, relative to injection of nontargeting control double-stranded siRNAs (Fig. 5G). Moreover, *Rpd3* RNAi induced minor-like foraging in injected majors (Fig. 5H). This result suggests that RPD3 normally acts to repress foraging in *C. floridanus* workers by removing acetyl groups from histones catalyzed by CBP.

Discussion

Our examination of foraging behavior as a caste-specific trait in the ant *C. floridanus* sheds light on a fundamental question in sociobiology regarding molecular determinants of division of labor in

eusocial insects (*1*). Whereas recent studies have brought increasing attention to the role of genetic variation in caste specification (*2*, *8*, *9*, *43*), our findings implicate the histone-modifying enzymes RPD3/HDAC1 and CBP as licensing and reprogramming factors underlying morphology and age-dependent social behaviors, hence revealing a key role for chromatin-based regulation of behavioral castes. *C. floridanus* colonies express two distinct morphological worker castes, minors and majors, and our results show that minors perform the majority of foraging and scouting for a colony (Fig. 1). HDACi-induced changes in CBP-dependent histone acetylation in the brains of mature minors reinforce and accentuate foraging and scouting (Figs. 2 and 3). In scouting ants, these behavioral changes correspond to altered transcript abundance of select neuronal genes with specific roles in synaptic transmission and olfactory learning, and to changes in histone acetylation that occur near CBP binding sites proximal to these genes (Fig. 4).

Remarkably, the delivery of a single dose of HDACi or RNAi against *Rpd3* in major brains immediately after pupal eclosion is sufficient to overcome the intrinsic molecular barriers that normally inhibit major foraging and scouting (Fig. 5). Hence, regulation of caste-specific social behaviors involves an epigenomic landscape that remains plastic for a period of time after eclosion. This malleability appears to permit drug- and RNAi-mediated up-regulation of genes that are inherently expressed at lower levels in majors, resulting in "transdifferentiation" between behavioral castes.

Epigenetic control over behavioral castes, and thus division of labor, may allow colonies to adapt dynamically to drastic ecological changes within their lifetime—for example, in response to prolonged famine or colony predation, which can alter caste ratios (*13*). Hence, our findings may be broadly relevant to other eusocial insects that display age-based or caste-based division of labor. Further, our results suggest that CBP and HDACs might help to establish complex social interactions for other invertebrate, vertebrate, and mammalian species, in which these conserved enzymes are known to play critical roles in the regulation of behavioral plasticity as well as in learning and memory (*27*–*29*, *44*, *45*). Finally, our ability to alter a canonical altruistic behavior in a truly social organism by experimental perturbation of a single gene suggests that the application of increasingly versatile reverse genetic approaches in eusocial insects will allow us to expose the general organizational principles underlying complex social systems (*10*).

Materials and methods

Ant colonies and husbandry

Mature, queen-right colonies of *C. floridanus* and *C. tortuganus* were used in this study, collected as foundresses from Long Key and Sugar Loaf Key in the Florida Keys, USA, in 2007 and 2011. Colonies were maintained in a sealed environmental growth chamber at constant temperature (25°C) and humidity (50%) under a 12:12 light:dark cycle. Colonies were fed twice weekly with excess supplies of water, 20% sugar water (sucrose cane sugar), and Bhatkar-Whitcomb diet (*46*).

Caste and age identification

Adult morphological caste was identified by body size and head width. For calibration, head width and scape (basal antennal segment) length (a proxy for body size) were measured using a digital micrometer (Fisher Scientific FB70252) and stereomicroscope (Nikon SMZ-1500) for 377 workers. A worker was considered a major if her head width exceeded 2.25 mm and a minor if under 1.75 mm. Age was determined by marking gasters of 1-day-old callows with enamel paint (Testors). One-day-old ants were identified by their location among brood in the nest, their general behavior, and their light cuticle coloration (compared to a reference panel of ants aged from pupation through 30 days).

Foraging assays and analysis

Three assays were used for analysis of foraging behavior. In the whole-colony foraging assay, a foraging arena (fig. S1G) was attached to a mature (7.5-year-old) queen-right colony containing more than 4000 workers. Petri dishes containing 15 ml each of pure water (×2) or 20% sugar water (×2) were placed in the arena. The arena was photographed every 3 min continuously for periods of 24 hours. For each photograph, the time of day and number of majors and minors feeding from water and sugar water dishes were recorded.

In the piggyback foraging assay, worker cohorts were isolated from single colonies (with specified caste, age, and number) and placed into a "piggyback" nest box (fig. S1E). A 1.5-ml Eppendorf tube containing 20% sugar water was placed in the arena on the wall opposite the arena entrance. The arena was photographed every 6 min continuously for periods of 24 hours over the course of 10 days. The time and caste of each ant that fully entered into the foraging arena was recorded and analyzed blindly. Idle ants that spent more than 30 min in the arena without feeding on sugar or departing from the foraging arena were not counted.

In the starvation-induced foraging assay, worker cohorts were isolated from single colonies as above and placed into "standard" 195c nest boxes (fig. S1G). Seven larvae (instar 2 to 4) were included to facilitate acclimation to the new nest. A 1.5-ml Eppendorf microcentrifuge tube containing 20% sugar water was provided and replaced weekly. Twenty-four hours prior to assay, the tube of sugar water was replaced with a 1.5-ml tube containing ultrapure water filtered by Milli-Q (EMD Millipore). At assay time (14:00 to 17:00 hours), a foraging arena was attached to the 195c nest box, and a half weigh boat containing 500 μl of 20% sugar water was placed within the arena at the far side relative to the tube leading to the nest. Video recordings were made for each foraging trial lasting 70 to 75 min and were analyzed blindly.

Time and caste of each ant that entered the foraging arena from the nest and fed on (i.e., contacted and consumed) sugar water for at least 10 s (one feeding event) were recorded. An ant must have returned to the nest, then reentered the foraging arena and refed to be counted again. Also, the time that the first feeding ant (a scout) returned to the nest (by descending beneath a piece of red acetate film covering a nest cavity) was recorded, as well as the number of scouts, defined as the number of individual ants feeding before the first scout returned to the nest. Scout expedition time was computed as the difference between the time the first scout returned to the nest and the time that she began to feed on sugar water. Quantitation of each foraging trial video recording was used to estimate a foraging activity statistic that summarized the foraging plus feeding rate of a worker cohort. This statistic (fig. S2A) was computed as the number of scouts plus the number of additional feeding events occurring within the first 20 min after the first scout's return to the nest.

Reverse transcription quantitative polymerase chain reaction (RT-qPCR) sample preparation and analysis

Individual brains dissected from 1-day-old ants were rinsed in sterile phosphate-buffered saline solution (PBS) and transferred to 1.5-ml microcentrifuge tubes containing 500 μl of ice-cooled PBS. Brain tissue was dissociated by sonication using a Diagenode Bioruptor Standard device for 30 s on low power. Total RNA was purified from individual brains by phenol:chloroform extraction and purification using RNase-free Agencourt AMPure XP beads (Beckman Coulter). cDNA was produced from total RNA using SuperScript III Reverse Transcriptase (Invitrogen). Abundance of specific mRNA transcripts was estimated using Power SYBR Green PCR Master Mix (Life Technologies) on a Real Time qPCR machine (Applied Biosystems 7900HT). Relative transcript abundance was estimated using the delta Ct method (*19*).

Chromatin immunoprecipitation

Chromatin lysate and subsequent immunoprecipitated double-stranded DNA (dsDNA) were prepared using antibodies recognizing H3K9ac (Active Motif 39137, Lot 102), H3K27ac (Abcam ab4729, Lot GR132150-4), and total H3 (Abcam ab1791, Lot GR135488-1) by processing larvae or adult ants as described (*16*, *19*).

Foraging assays for pharmacologically treated ants

Analysis of VPA (Calbiochem) was performed using the starvation-induced foraging assay. For a single foraging trial, four groups of seven minor or major 25- to 30-day-old ants (age-matched within 72 hours) were isolated from a queen-right colony and placed into 28c nest boxes (seven ants in each of four boxes). Ants were paint-marked to distinguish each individual. VPA was dissolved in liquid Bhatkar (or no VPA as control) to final desired concentration and replaced daily for 32 to 42 days (depending on number of starvation days). After 32 days of treatment, all 28 ants were pooled into a common 195c nest box (fig. S1G) containing seven larvae (instar 2 to 4). The ants

were starved with water for 24 hours, then assayed for foraging by attaching a 79c foraging arena (fig. S1G) and recording the time of every foraging and feeding event for each individual ant. If a cohort failed to exhibit a single feeding event within an hour of assay, the foraging arena was detached and the ants were starved for another 24 hours, for a maximum of 10 days. In the rare case of multiple feeding events by the same individual ant, only the first feeding event was recorded.

For TSA and C646 treatments, foraging assays were conducted using cohorts of 15 workers of the same age (within 48 hours) and colony. No larvae were provided, as the isolated ants were kept in the same 195c nest box for the duration of the trial. Pharmacological small molecules TSA (Sigma-Aldrich) and C646 (Calbiochem) were dissolved in DMSO and then in 20% sugar water to the desired final concentration. Ants were permitted to drink this solution ad libitum. Fresh aliquots were prepared from stock every 48 hours. During 24-hour starvation periods, fresh aliquots were prepared by dissolving a compound into water; otherwise, aliquots were dissolved in 20% sugar water. Each cohort was assayed for foraging activity 7, 14, 21, 28, 35, and 42 days after isolation, unless indicated otherwise. Foraging activity, number of scouts, and expedition time were computed as described above.

Preparation of RNA-seq libraries

Whole brains were dissected from individual mature minor scouts fed DMSO, 50 μM TSA, or 50 μM TSA with either 50 μM or 100 μM C646 for 45 days. Scouts were identified, sampled, and frozen on dry ice while feeding on sugar water after foraging, during a starvation-induced foraging assay. Each dissected brain was rinsed in PBS and transferred to a 1.5-ml microcentrifuge tube containing 100 μl of prechilled PBS (on ice). Brain tissue was dissociated using a Diagenode Bioruptor Standard device for 30 s on low power. A 15-μl aliquot representing 15% of cells in a single brain [estimated to be 20,000 to 25,000 cells (*47*)] was taken for RNA-seq; this represents a sufficient sampling of cells to recapitulate whole-brain transcriptome patterns (fig. S6) and allows remaining cells to be processed for ChIP-seq.

Total RNA was purified by phenol:chloroform extraction and purification using RNase-free Agencourt AMPure XP beads (Beckman Coulter). 1 μl of ERCC RNA Spike-In Mix (Ambion) was added to each 15-μl aliquot of total RNA to facilitate transcript-level normalization relative to cell number and to control for technical variation during library preparation. The mRNA fraction of RNA was purified by selection for polyadenylated transcripts using oligo(dT)25 Dynabeads (Invitrogen) as described (*48*), and RNA fragmentation was performed for 8 min at 94°C. cDNA was produced from total RNA using SuperScript III Reverse Transcriptase (Invitrogen), and second-strand synthesis was performed using deoxyuridine triphosphate (dUTP) to preserve strand specificity (*48*). Strand-specific RNA-seq libraries were produced for these dUTP-incorporated dsDNA libraries after one round of linear amplification (*19*).

RNA-seq libraries from individual 1-day-old minor and major brains were processed as above, except that whole brains were dissected from 10 1-day-old minors and majors sampled from the same colony at the same time and the same location in the nest. All 10 brains were dissected in a single session; all RNA-seq libraries were prepared from the entire brain samples as a single batch; all libraries were bar-coded and sequenced on the same flowcell.

All dsDNA libraries were prepared using the NEB NextUltra DNA Library Prep Kit for Illumina (New England BioLabs) and were amplified by PCR for 15 cycles, purified using Agencourt Ampure XP beads, and quantified by Qubit 2.0 Fluorometer (Invitrogen) and Kapa qPCR (Kapa Biosystems). Libraries were sequenced on an Illumina NextSeq 500 Desktop Sequencer.

Preparation of ChIP-seq libraries

ChIP was performed on individual scout brains using 45 μl of remaining cell material (60,000 to 75,000 cells) for a subset of the same brains used for RNA-seq (above). Chromatin was prepared as described (*16*), except that brain tissue was cross-linked with formaldehyde for 5 min. Before immunoprecipitation, cross-linked chromatin prepared from pools of heads and thoraces from 1-day-old workers of the evolutionarily divergent ant *Harpegnathos saltator* was added to a final concentration of 2.5% by volume based on Qubit protein quantitation [ChIP-Rx (*36*)]. After mixing *C. floridanus* (75 μg/IP) and *H. saltator* (1.88 μg/IP) chromatin, immunoprecipitation was performed as described (*16*) using 1 μg of antibody for H3K27ac or H3K9ac. dsDNA was purified from ChIP material as described (*16*), and ChIP-seq libraries were prepared using the NEB NextUltra DNA Library Prep Kit for Illumina. Libraries were amplified by PCR for 15 cycles, purified using Agencourt Ampure XP beads, quantified by Qubit and Kapa qPCR, and sequenced on an Illumina NextSeq 500 Desktop Sequencer.

Analysis of RNA-seq and ChIP-seq data

Sequenced reads were aligned to a diploid version of the *C. floridanus* reference genome v3.0 (*12*) after incorporating single-nucleotide polymorphisms (SNPs) (table S9). This diploid reference was first split into two pseudo-haplotypes by randomly partitioning the two alleles at each SNP into two haploid genome sequences. Mapping was performed against each reference haplotype using Glimmr (*16*), with calls to Bowtie2 (*49*) with options (–end-to-end–very-sensitive) and allowing each read to display valid alignment for up to 10 distinct genomic locations (-k 10). Mapped reads were merged into a single alignment file by retaining the alignments for a given read that contained fewer mismatches to the particular reference haplotype. For RNA-seq, remaining unmapped reads were also aligned to a reference transcriptome containing full-length transcripts for annotated genes. Remaining unmapped reads were trimmed in an iterative manner from full-length 75-nt reads to 55-nt reads to 35-nt reads, where the 10 outer bases on either end of the read were removed at each step. Quantitation, normalization, and analysis of RNA-seq and ChIP-seq data are described in (*19*).

Brain injection procedure

Before eclosion, major and minor pupae were removed from their natal colony and reared in smaller nests by 15 adult minors. In 24-hour intervals, newly eclosed callows were removed from rearing nests and organized into age-matched treatment groups containing 10 majors and 10 minors. Individuals were isolated in 1.5-ml microcentrifuge tubes and cooled on ice for up to 5 min until sedated. Major workers were moved to an ice-cooled silicone platform, and their cuticles were superficially perforated at the target injection site using a sterilized steel pin (Minutae, Sphinx). Immediately after perforation, a borosilicate glass needle filled with injection material was directed to the injection site using a robotic arm (Patchman N2, Eppendorf) and the needle tip was placed just beneath the surface of the cuticle to avoid damage to underlying tissue. A Femtojet microinjector (Eppendorf) delivered 1 μl of injection material to the injection site. After injection, individuals were given 1 hour to recover before being assessed for morbidity and mortality. Successful injections were pooled in groups of 10 with age-matched minors and placed into the test arena for behavioral analysis.

RNAi-mediated mRNA knockdown and analysis

Individual major brains were injected with a 1-μl pool of 1 μM each of two different 27-nt double-stranded siRNAs targeting *Rpd3* (Cflo_10463) and *Rpd3-like* (Cflo_10465) (*Rpd3* RNAi) or a 1-μl pool of 1 μM each of two different nontargeting control double-stranded siRNAs (Control RNAi) (*19*). Individuals were killed 24 or 48 hours after injection. cDNA libraries were prepared from individual dissected brains as described above. RT-qPCR was performed as described above, using primers specific to Cflo_10463 and Cflo_10465 and to *Gapdh1* and *Rpl32* mRNAs (table S2). Quantitation was performed using the median quantity estimated based on fivefold dilution series of each primer. *Rpd3* quantities were normalized to the average of *Gapdh1* and *Rpl32* quantities as controls. *P* values were calculated by Mann-Whitney U test.

Brain injection piggyback foraging assay

Cohorts of 10 majors and 10 minors, all 1 day old, were sampled from a single queen-right colony. Only majors received brain injections with a fixed delivery volume of 1 μl, containing 0.5% DMSO, 50 μM TSA, or 50 μM TSA with 100 μM C646. For RNAi, majors were injected with pools of 1 μM 27-nt duplex RNA oligos (RPD3 or nontargeting controls) (table S6). All injections were performed between 15:00 and 17:00 hours. After injection, majors were placed with their minor nestmates into a piggyback nest box with foraging arena containing a microcentrifuge tube with 1 ml of 20% sugar water. The arena was photographed

every 6 min for 10 days; recorded photographs were analyzed blindly as described above.

REFERENCES AND NOTES

1. B. Hölldobler, E. O. Wilson, *The Ants* (Belknap/Harvard Univ. Press, Cambridge, MA, 1990).
2. G. E. Robinson, Regulation of division of labor in insect societies. *Annu. Rev. Entomol.* **37**, 637–665 (1992). doi: 10.1146/annurev.en.37.010192.003225; pmid: 1539941
3. E. O. Wilson, Behavioral discretization and the number of castes in an ant species. *Behav. Ecol. Sociobiol.* **1**, 141–154 (1976). doi: 10.1007/BF00299195
4. E. J. Fjerdingstad, R. H. Crozier, The evolution of worker caste diversity in social insects. *Am. Nat.* **167**, 390–400 (2006). doi: 10.1086/499545; pmid: 16673347
5. W. R. Tschinkel, *The Fire Ants* (Belknap/Harvard Univ. Press, Cambridge, MA, 2013).
6. C. Lucas, M. B. Sokolowski, Molecular basis for changes in behavioral state in ant social behaviors. *Proc. Natl. Acad. Sci. U.S.A.* **106**, 6351–6356 (2009). doi: 10.1073/pnas.0809463106; pmid: 19332792
7. C. Dulac, Brain function and chromatin plasticity. *Nature* **465**, 728–735 (2010). doi: 10.1038/nature09231; pmid: 20535202
8. G. E. Robinson, C. M. Grozinger, C. W. Whitfield, Sociogenomics: Social life in molecular terms. *Nat. Rev. Genet.* **6**, 257–270 (2005). doi: 10.1038/nrg1575; pmid: 15761469
9. C. R. Smith, A. L. Toth, A. V. Suarez, G. E. Robinson, Genetic and genomic analyses of the division of labour in insect societies. *Nat. Rev. Genet.* **9**, 735–748 (2008). doi: 10.1038/nrg2429; pmid: 18802413
10. H. Yan *et al*., Eusocial insects as emerging models for behavioural epigenetics. *Nat. Rev. Genet.* **15**, 677–688 (2014). doi: 10.1038/nrg3787; pmid: 25200663
11. R. Kucharski, J. Maleszka, S. Foret, R. Maleszka, Nutritional control of reproductive status in honeybees via DNA methylation. *Science* **319**, 1827–1830 (2008). doi: 10.1126/science.1153069; pmid: 18339900
12. R. Bonasio *et al*., Genomic comparison of the ants *Camponotus floridanus* and *Harpegnathos saltator*. *Science* **329**, 1068–1071 (2010). doi: 10.1126/science.1192428; pmid: 20798317
13. B. R. Herb *et al*., Reversible switching between epigenetic states in honeybee behavioral subcastes. *Nat. Neurosci.* **15**, 1371–1373 (2012). doi: 10.1038/nn.3218; pmid: 22983211
14. R. Bonasio *et al*., Genome-wide and caste-specific DNA methylomes of the ants *Camponotus floridanus* and *Harpegnathos saltator*. *Curr. Biol.* **22**, 1755–1764 (2012). doi: 10.1016/j.cub.2012.07.042; pmid: 22885060
15. S. Alvarado, R. Rajakumar, E. Abouheif, M. Szyf, Epigenetic variation in the *Egfr* gene generates quantitative variation in a complex trait in ants. *Nat. Commun.* **6**, 6513 (2015). doi: 10.1038/ncomms7513; pmid: 25758336
16. D. F. Simola *et al*., A chromatin link to caste identity in the carpenter ant *Camponotus floridanus*. *Genome Res.* **23**, 486–496 (2013). doi: 10.1101/gr.148361.112; pmid: 23212948
17. J. Gadau, J. Heinze, B. Hölldobler, M. Schmid, Population and colony structure of the carpenter ant *Camponotus floridanus*. *Mol. Ecol.* **5**, 785–792 (1996). doi: 10.1111/j.1365-294X.1996.tb00374.x; pmid: 8981768
18. A. Spannhoff *et al*., Histone deacetylase inhibitor activity in royal jelly might facilitate caste switching in bees. *EMBO Rep.* **12**, 238–243 (2011). doi: 10.1038/embor.2011.9; pmid: 21331099
19. See supplementary materials on *Science* Online.
20. P. Calabi, J. F. A. Traniello, Behavioral flexibility in age castes of the ant *Pheidole dentata*. *J. Insect Behav.* **2**, 663–677 (1989). doi: 10.1007/BF01065785
21. Z. S. Liang *et al*., Molecular determinants of scouting behavior in honey bees. *Science* **335**, 1225–1228 (2012). doi: 10.1126/science.1213962; pmid: 22403390
22. D. P. Mersch, A. Crespi, L. Keller, Tracking individuals shows spatial fidelity is a key regulator of ant social organization. *Science* **340**, 1090–1093 (2013). pmid: 23599264
23. B. Hölldobler, Recruitment behavior in *Camponotus socius* (Hym. Formicidae). *Z. Vgl. Physiol.* **75**, 123–142 (1971).
24. N. Stroeymeyt, N. R. Franks, M. Giurfa, Knowledgeable individuals lead collective decisions in ants. *J. Exp. Biol.* **214**, 3046–3054 (2011). doi: 10.1242/jeb.059188; pmid: 21865517
25. H. L. Fitzsimons, M. J. Scott, Genetic modulation of Rpd3 expression impairs long-term courtship memory in *Drosophila*. *PLOS ONE* **6**, e29171 (2011). doi: 10.1371/journal.pone.0029171; pmid: 22195015
26. A. Fischer, F. Sananbenesi, X. Wang, M. Dobbin, L.-H. Tsai, Recovery of learning and memory is associated with chromatin remodelling. *Nature* **447**, 178–182 (2007). doi: 10.1038/nature05772; pmid: 17468743
27. C. G. Vecsey *et al*., Histone deacetylase inhibitors enhance memory and synaptic plasticity via CREB:CBP-dependent transcriptional activation. *J. Neurosci.* **27**, 6128–6140 (2007). doi: 10.1523/JNEUROSCI.0296-07.2007; pmid: 17553985
28. M. Göttlicher *et al*., Valproic acid defines a novel class of HDAC inhibitors inducing differentiation of transformed cells. *EMBO J.* **20**, 6969–6978 (2001). doi: 10.1093/emboj/20.24.6969; pmid: 11742974
29. Y. Cho, A. Griswold, C. Campbell, K.-T. Min, Individual histone deacetylases in *Drosophila* modulate transcription of distinct genes. *Genomics* **86**, 606–617 (2005). doi: 10.1016/j.ygeno.2005.07.007; pmid: 16137856
30. E. M. Bowers *et al*., Virtual ligand screening of the p300/CBP histone acetyltransferase: Identification of a selective small molecule inhibitor. *Chem. Biol.* **17**, 471–482 (2010). doi: 10.1016/j.chembiol.2010.03.006; pmid: 20534345
31. N. T. Crump *et al*., Dynamic acetylation of all lysine-4 trimethylated histone H3 is evolutionarily conserved and mediated by p300/CBP. *Proc. Natl. Acad. Sci. U.S.A.* **108**, 7814–7819 (2011). doi: 10.1073/pnas.1100099108; pmid: 21518915
32. F. Tie *et al*., CBP-mediated acetylation of histone H3 lysine 27 antagonizes *Drosophila* Polycomb silencing. *Development* **136**, 3131–3141 (2009). doi: 10.1242/dev.037127; pmid: 19700617
33. Q. Jin *et al*., Distinct roles of GCN5/PCAF-mediated H3K9ac and CBP/p300-mediated H3K18/27ac in nuclear receptor transactivation. *EMBO J.* **30**, 249–262 (2011). doi: 10.1038/emboj.2010.318; pmid: 21131905
34. L. Schrader, D. F. Simola, J. Heinze, J. Oettler, Sphingolipids, transcription factors, and conserved toolkit genes: Developmental plasticity in the ant *Cardiocondyla obscurior*. *Mol. Biol. Evol.* **32**, 1474–1486 (2015). doi: 10.1093/molbev/msv039; pmid: 25725431
35. A. N. Malik *et al*., Genome-wide identification and characterization of functional neuronal activity-dependent enhancers. *Nat. Neurosci.* **17**, 1330–1339 (2014). doi: 10.1038/nn.3808; pmid: 25195102
36. D. A. Orlando *et al*., Quantitative ChIP-Seq normalization reveals global modulation of the epigenome. *Cell Rep.* **9**, 1163–1170 (2014).pmid: 25437568
37. T. Suganuma *et al*., ATAC is a double histone acetyltransferase complex that stimulates nucleosome sliding. *Nat. Struct. Mol. Biol.* **15**, 364–372 (2008). doi: 10.1038/nsmb.1397; pmid: 18327268
38. S. C. Iyer *et al*., The RhoGEF trio functions in sculpting class specific dendrite morphogenesis in *Drosophila* sensory neurons. *PLOS ONE* **7**, e33634 (2012). doi: 10.1371/journal.pone.0033634; pmid: 22442703
39. S. Xia *et al*., NMDA receptors mediate olfactory learning and memory in *Drosophila*. *Curr. Biol.* **15**, 603–615 (2005). doi: 10.1016/j.cub.2005.02.059; pmid: 15823532
40. W. Gronenberg, S. Heeren, B. Hölldobler, Age-dependent and task-related morphological changes in the brain and the mushroom bodies of the ant *Camponotus floridanus*. *J. Exp. Biol.* **199**, 2011–2019 (1996).pmid: 9319922
41. G. S. Withers, S. E. Fahrbach, G. E. Robinson, Selective neuroanatomical plasticity and division of labour in the honeybee. *Nature* **364**, 238–240 (1993). doi: 10.1038/364238a0; pmid: 8321320
42. C. Milite *et al*., A novel cell-permeable, selective, and noncompetitive inhibitor of KAT3 histone acetyltransferases from a combined molecular pruning/classical isosterism approach. *J. Med. Chem.* **58**, 2779–2798 (2015). doi: 10.1021/jm5019687; pmid: 25730130
43. J. Wang *et al*., A Y-like social chromosome causes alternative colony organization in fire ants. *Nature* **493**, 664–668 (2013). doi: 10.1038/nature11832; pmid: 23334415
44. E. Korzus, M. G. Rosenfeld, M. Mayford, CBP histone acetyltransferase activity is a critical component of memory consolidation. *Neuron* **42**, 961–972 (2004). doi: 10.1016/j.neuron.2004.06.002; pmid: 15207240
45. J. M. Alarcón *et al*., Chromatin acetylation, memory, and LTP are impaired in $CBP^{+/-}$ mice: A model for the cognitive deficit in Rubinstein-Taybi syndrome and its amelioration. *Neuron* **42**, 947–959 (2004). doi: 10.1016/j.neuron.2004.05.021; pmid: 15207239
46. A. Bhatkar, W. H. Whitcomb, Artificial diet for rearing various species of ants. *Fla. Entomol.* **53**, 229–232 (1970). doi: 10.2307/3493193
47. B. Ehmer, W. Gronenberg, Mushroom body volumes and visual interneurons in ants: Comparison between sexes and castes. *J. Comp. Neurol.* **469**, 198–213 (2004). doi: 10.1002/cne.11014; pmid: 14694534
48. S. Zhong, J.-G. Joung, Y. Zheng, Y.-r. Chen, B. Liu, Y. Shao, J. Z. Xiang, Z. Fei, J. J. Giovannoni, High-throughput Illumina strand-specific RNA sequencing library preparation. *Cold Spring Harb. Protoc.* 10.1101/pdb.prot5652 (2011).
49. B. Langmead, S. L. Salzberg, Fast gapped-read alignment with Bowtie 2. *Nat. Methods* **9**, 357–359 (2012). doi: 10.1038/nmeth.1923; pmid: 22388286

ACKNOWLEDGMENTS

We thank D. Kronauer and I. Fetter-Pruneda for advice on brain injections, and P. Cole, D. Meyers, M. Sammons, P. Shah, and H. Yan for intellectual contributions. Supported by Howard Hughes Medical Institute Collaborative Innovation Award 2009005 (S.L.B., C.D., J.L., A.R., D.R., and L.J.Z.), NIH training grant T32HD083185 in developmental biology from the University of Pennsylvania (D.F.S.), and NIH New Innovator Award DP2MH107055 (R.B.). Sequencing data have been deposited in the National Center for Biotechnology Information Gene Expression Omnibus (www.ncbi.nlm.nih.gov/geo) under accession number GSE69553. Behavioral data are available in tables S7 and S8. *C. floridanus* SNPs are available in table S9, and gene annotations are available in table S10. Software used for high-throughput sequencing and gene ontology analyses is available on GitHub (https://github.com/dfsimola/glimmr).

SUPPLEMENTARY MATERIALS

www.sciencemag.org/content/351/6268/aac6633/suppl/DC1
Materials and Methods
Figs. S1 to S12
Tables S1 to S10
Movies S1 and S2
References (*50*–*54*)

27 May 2015; accepted 20 November 2015
10.1126/science.aac6633

RESEARCH ARTICLES

METABOLISM

Sestrin2 is a leucine sensor for the mTORC1 pathway

Rachel L. Wolfson,[1,2,3,4]* Lynne Chantranupong,[1,2,3,4]* Robert A. Saxton,[1,2,3,4] Kuang Shen,[1,2,3,4] Sonia M. Scaria,[1,2] Jason R. Cantor,[1,2,3,4] David M. Sabatini[1,2,3,4]†

Leucine is a proteogenic amino acid that also regulates many aspects of mammalian physiology, in large part by activating the mTOR complex 1 (mTORC1) protein kinase, a master growth controller. Amino acids signal to mTORC1 through the Rag guanosine triphosphatases (GTPases). Several factors regulate the Rags, including GATOR1, a GTPase-activating protein; GATOR2, a positive regulator of unknown function; and Sestrin2, a GATOR2-interacting protein that inhibits mTORC1 signaling. We find that leucine, but not arginine, disrupts the Sestrin2-GATOR2 interaction by binding to Sestrin2 with a dissociation constant of 20 micromolar, which is the leucine concentration that half-maximally activates mTORC1. The leucine-binding capacity of Sestrin2 is required for leucine to activate mTORC1 in cells. These results indicate that Sestrin2 is a leucine sensor for the mTORC1 pathway.

It has long been appreciated that in addition to being a proteogenic amino acid, leucine is also a signaling molecule that directly regulates aspects of animal physiology, including satiety (*1*), insulin secretion (*2*), and skeletal muscle anabolism (*3*, *4*). Because the liver has a low capacity to metabolize leucine, its concentrations in the blood fluctuate according to its consumption, so that dietary leucine can directly affect physiology (*5*–*7*). A key mediator of the effects of leucine is the mTOR complex 1 (mTORC1) protein kinase (*8*, *9*), which regulates growth by controlling processes such as protein and lipid synthesis, as well as autophagy.

In addition to leucine, many environmental signals regulate the mTORC1 pathway, including other amino acids such as arginine, as well as glucose and various growth factors and forms of stress (*10*, *11*). How mTORC1 senses and integrates these diverse inputs is not well understood, but it is clear that the Rheb and Rag guanosine triphosphatases (GTPases) have necessary but distinct roles. Rheb is a monomeric GTP-binding protein, and the Rags function as obligate heterodimers of RagA or RagB bound to RagC or RagD (*12*–*14*). Both the Rheb and Rag GTPases localize, at least in part, to the lysosomal surface (*15*–*18*), which is an important site of mTORC1 regulation (*19*). In a Rag-dependent manner, amino acids promote the translocation of mTORC1 to the lysosome, where Rheb, if bound to GTP, stimulates its kinase activity. Growth factors trigger the GTP-loading of Rheb by driving its GTPase activating protein (GAP), the tuberous sclerosis complex, off the lysosomal surface (*18*).

Regulation of the Rag GTPases by amino acids is complex, and many distinct factors have important roles (*20*). A lysosome-associated supercomplex containing Ragulator, SLC38A9, and the vacuolar adenosine triphosphatase (v-ATPase) interacts with the Rag GTPases and is necessary for the activation of mTORC1 by amino acids (*21*–*24*). Ragulator anchors the Rag heterodimers to the lysosome and has nucleotide exchange activity for RagA and RagB (*21*, *25*). SLC38A9 is an amino acid transporter and a potential lysosomal arginine sensor (*23*), but the function of the v-ATPase in mTORC1 activation is unclear. Two GAP complexes stimulate GTP hydrolysis by the Rag GTPases, with GATOR1 acting on RagA and RagB (*26*), and folliculin–folliculin interacting protein 2 (FLCN-FNIP2) acting on RagC and RagD (*27*). The separate GATOR2 complex negatively regulates GATOR1 through an unknown mechanism and is necessary for mTORC1 activation (*26*). Last, the Sestrins are GATOR2-interacting proteins whose molecular function is not known (*28*, *29*). Previous reports argue that the Sestrins inhibit mTORC1 signaling through AMPK and TSC (*30*), but recent studies question this mechanism (*28*, *31*).

The amino acid sensors upstream of mTORC1 have eluded researchers for many years. Whereas SLC38A9 is a strong candidate for sensing arginine at lysosomes (*23*), the long-sought sensor of leucine has thus far been unknown. Here, we present evidence that Sestrin2 is a leucine sensor for the mTORC1 pathway.

Leucine directly regulates the Sestrin2-GATOR2 interaction

Activation of mTORC1 by amino acids requires the pentameric GATOR2 complex (*26*). Although its molecular function is unknown, epistasis-like experiments suggest that GATOR2 suppresses GATOR1, the GAP for and inhibitor of RagA and RagB (*26*). Within cells, Sestrin2 binds to GATOR2 in an amino acid–sensitive manner (*28*, *29*); removal of all amino acids from the culture media induces the interaction, and readdition of the amino acids reverses it (*28*). Although several amino acids can regulate mTORC1 signaling, arginine and leucine are the best-established, and deprivation of either strongly inhibits mTORC1 in various cell types (*8*, *32*, *33*).

In human embryonic kidney–293T (HEK-293T) cells, removal of either leucine or arginine from the cell medium inhibited mTORC1 signaling to similar extents, as indicated by ribosomal protein S6 kinase 1 (S6K1) phosphorylation. However, only leucine depletion caused Sestrin2 to bind to GATOR2, inducing the interaction as effectively as complete amino acid starvation did (Fig. 1A). Leucine readdition rapidly reversed the binding, and amino acids did not affect the interaction between WD repeat–containing protein 24 (WDR24) and Mios, two core components of GATOR2 (Fig. 1A and fig. S1A).

Sestrin2 is homologous to two other proteins, Sestrin1 and Sestrin3 (*34*–*36*); when overexpressed, all three can interact with GATOR2 (*28*). As with Sestrin2, leucine starvation and stimulation strongly regulated the interaction of endogenous Sestrin1 with GATOR2 (fig. S1B). In contrast, endogenous Sestrin3 bound to GATOR2 irrespective of leucine concentrations (fig. S1B), suggesting that this interaction is constitutive or regulated by signals that remain to be defined.

Although enzymatic events triggered by leucine may mediate the effects of leucine on the Sestrin2-GATOR2 interaction, it was tempting to consider the possibility that leucine might act directly on the complex. Consistent with this possibility, the addition of leucine, but not arginine, to ice-cold detergent lysates of cells deprived of all amino acids abrogated the interaction to the same extent as leucine stimulation of live cells did (Fig. 1B). Leucine also disrupted the interaction when added directly to immunopurified Sestrin2-GATOR2 complexes that were isolated from amino acid–deprived cells. Of the 18 amino acids tested at 300 μM each, only those most similar to leucine—methionine, isoleucine, and valine—had any effect on the Sestrin2-GATOR2 interaction in vitro (Fig. 1C).

When added to the purified complexes, leucine dose-dependently disrupted the Sestrin2-GATOR2 complex, with the half-maximal effect at about 1 μM (Fig. 1D). Methionine and isoleucine were considerably less potent, acting at concentrations about 10- and 25-fold greater than leucine, respectively (Fig. 1E). These values reflect only the relative potencies of these amino acids, owing to the fact that equilibrium conditions were not attained because the large assay volume precluded Sestrin2 from rebinding to GATOR2 once it had dissociated.

Sestrin2 binds leucine with a dissociation constant (K_d) of 20 μM

Given that leucine disrupts the purified complex, we reasoned that leucine might bind directly to

[1]Whitehead Institute for Biomedical Research and Massachusetts Institute of Technology, Department of Biology, 9 Cambridge Center, Cambridge, MA 02142, USA. [2]Howard Hughes Medical Institute, Department of Biology, Massachusetts Institute of Technology, Cambridge, MA 02139, USA. [3]Koch Institute for Integrative Cancer Research, 77 Massachusetts Avenue, Cambridge, MA 02139, USA. [4]Broad Institute of Harvard and Massachusetts Institute of Technology, 7 Cambridge Center, Cambridge, MA 02142, USA. *These authors contributed equally to this work. †**Corresponding author. E-mail: sabatini@wi.mit.edu**

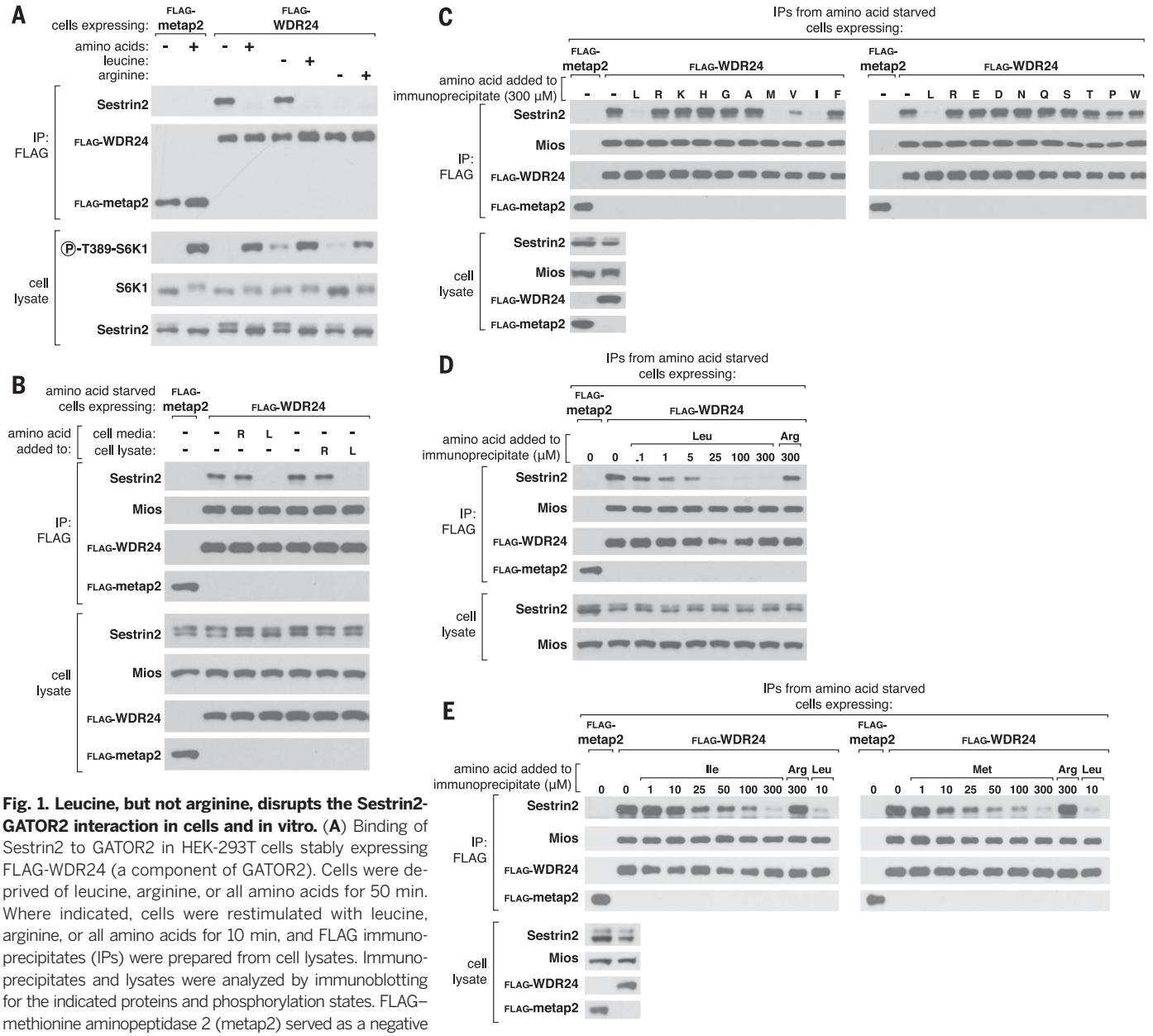

Fig. 1. Leucine, but not arginine, disrupts the Sestrin2-GATOR2 interaction in cells and in vitro. (**A**) Binding of Sestrin2 to GATOR2 in HEK-293T cells stably expressing FLAG-WDR24 (a component of GATOR2). Cells were deprived of leucine, arginine, or all amino acids for 50 min. Where indicated, cells were restimulated with leucine, arginine, or all amino acids for 10 min, and FLAG immunoprecipitates (IPs) were prepared from cell lysates. Immunoprecipitates and lysates were analyzed by immunoblotting for the indicated proteins and phosphorylation states. FLAG–methionine aminopeptidase 2 (metap2) served as a negative control. (**B**) Effects of leucine and arginine on the Sestrin2-GATOR2 interaction in ice-cold detergent lysates of amino acid–starved cells. HEK-293T cells stably expressing FLAG-metap2 or FLAG-WDR24 were deprived of all amino acids for 50 min. Leucine or arginine was added to the culture media or to cell lysates, and FLAG immunoprecipitates were prepared and analyzed as in (A). (**C**) Effects of individual amino acids on the purified Sestrin2-GATOR2 complex. FLAG immunoprecipitates were prepared from HEK-293T cells stably expressing FLAG-metap2 or FLAG-WDR24 and deprived of all amino acids for 50 min. Indicated amino acids (300 μM) were added directly to the immunoprecipitates, which, after re-washing, were analyzed as in (A). (**D**) Disruption of the purified Sestrin2-GATOR2 complex by leucine. The experiment was performed and analyzed as in (C), except that indicated concentrations of leucine (Leu) or arginine (Arg) were used. (**E**) Disruption of the Sestrin2-GATOR2 interaction by isoleucine (Ile) and methionine (Met). The experiment was performed and analyzed as in (C), except that the indicated concentrations of isoleucine, methionine, leucine, or arginine were used.

Sestrin2 or GATOR2. To test this, we developed an equilibrium binding assay in which purified proteins immobilized on agarose beads were incubated with radioactive amino acids, and the bound amino acids were quantified after washing. Radiolabeled leucine bound to Sestrin2 but not to WDR24, the GATOR2 complex, or the control protein Rap2A, in a manner that was fully competed by excess nonradiolabeled leucine (Fig. 2A). In contrast, arginine did not bind to either Sestrin2 or Rap2A (fig. S2A). Consistent with the differential sensitivities to leucine of the Sestrin1- and Sestrin3-GATOR2 complexes, Sestrin1 bound leucine to a similar extent as did Sestrin2, whereas Sestrin3 bound leucine very weakly (Fig. 2B and fig. S2A). *Drosophila* dSestrin (CG11299-PD) also bound leucine, albeit at lower amounts than the human protein did (fig. S2, B and C).

Because all of these proteins were expressed in and purified from HEK-293T cells, the above results did not rule out the possibility that an unidentified protein that copurifies with Sestrin2 (and Sestrin1) is the actual receptor for leucine. To address this possibility, we prepared human Sestrin2 in bacteria, which is a heterologous system that does not encode a Sestrin homolog or even a TOR pathway. Consistent with the results obtained with Sestrin2 prepared in human cells, radiolabeled leucine bound to bacterially produced Sestrin2 but not to the RagA-RagC heterodimer, which was used as a control (Fig. 2C). Furthermore, in a thermal shift assay, leucine, but not arginine, shifted the melting temperature

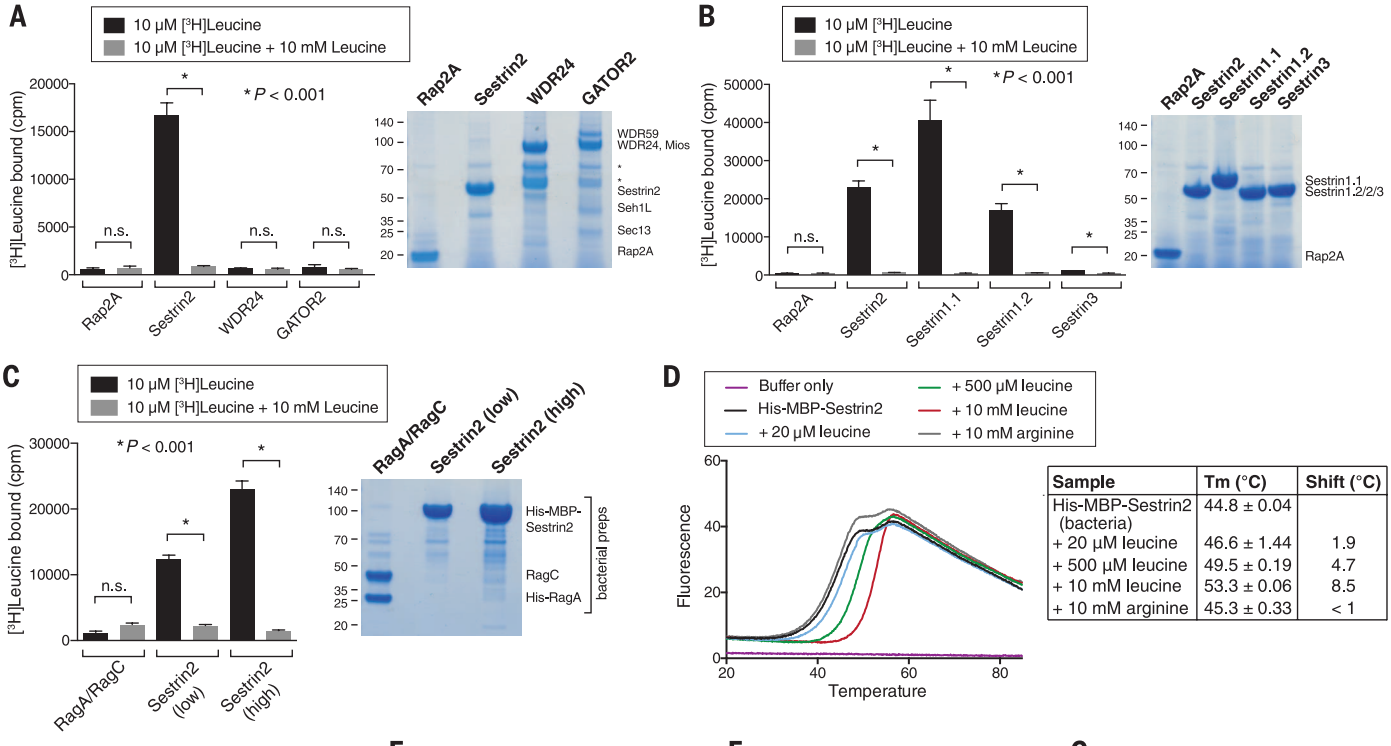

Sample	Tm (°C)	Shift (°C)
His-MBP-Sestrin2 (bacteria)	44.8 ± 0.04	
+ 20 μM leucine	46.6 ± 1.44	1.9
+ 500 μM leucine	49.5 ± 0.19	4.7
+ 10 mM leucine	53.3 ± 0.06	8.5
+ 10 mM arginine	45.3 ± 0.33	< 1

Fig. 2. Sestrin2 binds leucine with a K_d of 20 μM. (**A**) Binding of radiolabeled leucine to Sestrin2 but not to WDR24, GATOR2, or the control protein Rap2A. FLAG immunoprecipitates prepared from HEK-293T cells transiently expressing the indicated proteins or complexes were used in binding assays with [^{3}H]leucine, as described in the supplementary materials. Unlabeled leucine was added where indicated. Values are means ± SD for three technical replicates from one representative experiment (n.s., not significant). SDS–polyacrylamide gel electrophoresis, followed by Coomassie Blue staining, was used to analyze immunoprecipitates that were prepared in parallel to those included in the binding assays. Asterisks in the right panel indicate breakdown products in the WDR24 and GATOR2 purifications. (**B**) Leucine-binding capacities of Sestrin1 (two isoforms), Sestrin2, and Sestrin3. FLAG immunoprecipitates were prepared and binding assays were performed and analyzed as in (A). (**C**) Leucine binds to bacterially produced Sestrin2 but not to the RagA/RagC heterodimer. Leucine binding assays were performed as described in the supplementary materials and analyzed as in (A) with polyhistidine (His)–mannose binding protein (MBP)–Sestrin2 or His–RagA/RagC bound to the Ni–NTA (nitrilotriacetic acid) resin. (**D**) Effects of leucine and arginine on the melting temperature of bacterially produced Sestrin2 in a thermal shift assay. His-MBP-Sestrin2 was incubated with Sypro Orange dye, with or without leucine or arginine. When the sample was heated, the change in fluorescence was captured and used to calculate melting temperatures (Tm) under the indicated conditions. Values are means ± SD for three replicates. (**E**) Sestrin2 binds leucine with a K_d of 20 μM. FLAG-Sestrin2 immunoprecipitates, prepared as in (A), were used in binding assays with 10 or 20 μM [^{3}H]leucine and indicated concentrations of unlabeled leucine. In the representative graph, each point represents the normalized mean ± SD for n = 3 experiments in an assay with 10 μM [^{3}H]leucine. K_d was calculated from the results of six experiments (three with 10 μM and three with 20 μM [^{3}H]leucine). (**F**) Methionine can compete with the binding of leucine to Sestrin2. (**G**) Isoleucine can compete in the binding of leucine to Sestrin2. In (F) and (G), FLAG-Sestrin2 immunoprecipitates, prepared as in (A), were used in binding assays with 10 μM [^{3}H]leucine and indicated concentrations of unlabeled methionine and isoleucine, respectively. In the graphs, each point represents the normalized mean ± SD for n = 3 experiments K_i values were calculated using data from the three experiments.

of bacterially produced Sestrin2, but not of two control proteins, by up to 8.5° C (Fig. 2D and fig. S2, E and F). Collectively, these data strongly suggest that leucine binds directly to Sestrin2.

Although the thermal shift assay is valuable for assessing the capacity of a protein to bind a ligand, this method is not suitable for obtaining an accurate K_d (*37*). Therefore, we used a competition binding assay with increasing amounts of unlabeled leucine to determine that leucine has a K_d for Sestrin2 of 20 ± 5 μM (Fig. 2E). In comparison, methionine and isoleucine competed with leucine binding with inhibitory constants (K_i) of 354 ± 118 μM and 616 ± 273 μM, respectively (Fig. 2, F and G). These values are respectively about one-eighteenth and one-thirtieth the affinity of leucine for Sestrin2, and they correlate well with the relative potencies of leucine, methionine, and isoleucine in disrupting the Sestrin2-GATOR2 interaction in vitro (Fig. 1, D and E).

Sestrin2 regulates mTORC1 through GATOR2

Consistent with leucine regulating mTORC1 by modulating the binding of Sestrin2 to GATOR2, 20 to 40 μM leucine had half-maximal effects on both the Sestrin2-GATOR2 interaction and mTORC1 activity in HEK-293T cells (Fig. 3, A and B). This concentration range encompasses the K_d of leucine for Sestrin2, indicating that the affinity of Sestrin2 for leucine is physiologically relevant.

To formally test whether Sestrin2 regulates mTORC1 by interacting with GATOR2, we identified a Sestrin2 mutant (S190W) that binds leucine but has a severely decreased capacity to bind GATOR2 (Fig. 3, C and D). In Sestrin1, -2, and -3 triple-null HEK-293T cells, mTORC1 signaling was active and unaffected by leucine deprivation

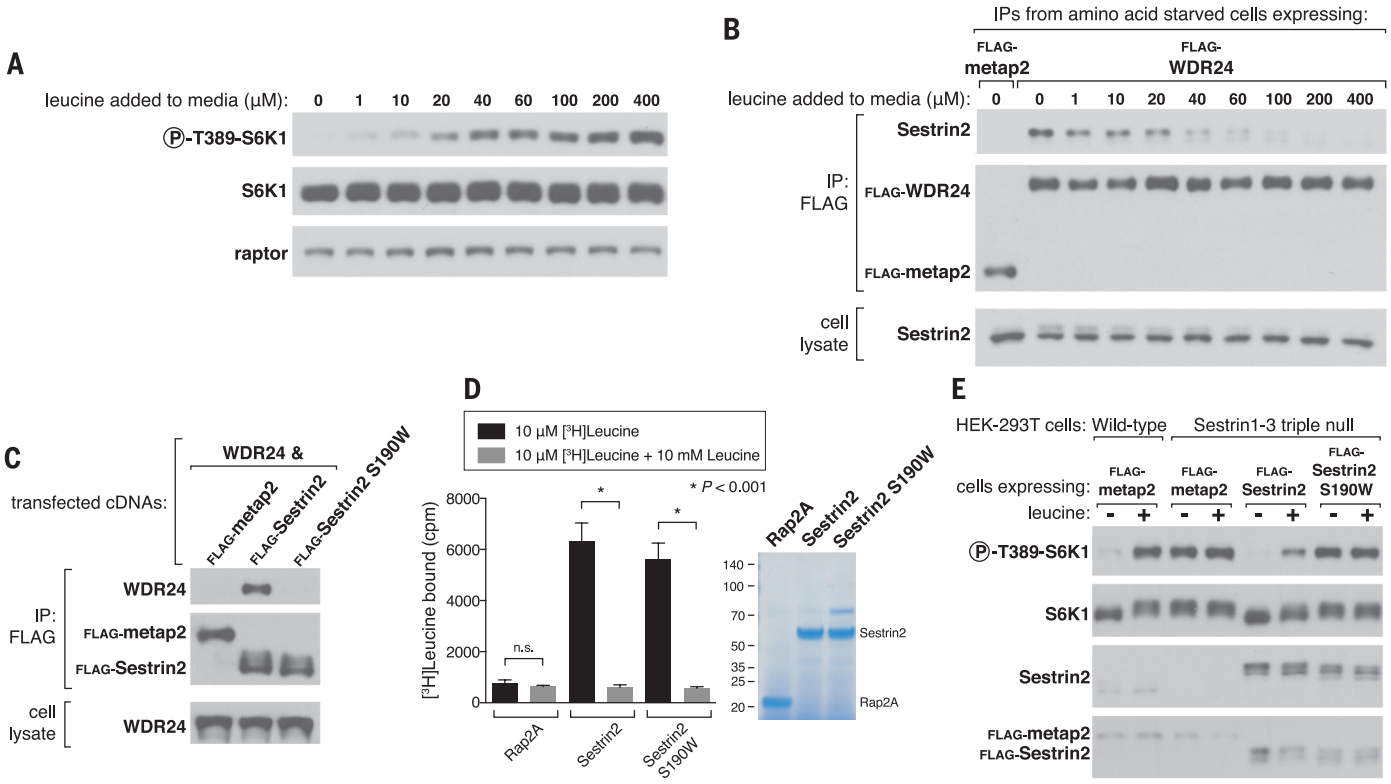

Fig. 3. Sestrin2 regulates mTORC1 through GATOR2. (**A**) Effects of varying leucine concentrations on mTORC1 activity, as measured by the phosphorylation of S6K1. HEK-293T cells were deprived of leucine for 50 min and restimulated with leucine at the indicated concentrations for 10 min. Cell lysates were analyzed via immunoblotting for the indicated proteins and phosphorylation states. (**B**) Effects of varying leucine concentrations on the Sestrin2-GATOR2 interaction. HEK-293T cells stably expressing the indicated proteins were starved as in (A) and FLAG immunoprecipitates were collected. The immunopurified complexes were treated with the indicated concentrations of leucine and then analyzed as in Fig. 1C. (**C**) Decreased GATOR2-binding capacity of the Sestrin2 S190W mutant. FLAG immunoprecipitates were prepared from HEK-293T cells transiently expressing the indicated proteins and were analyzed by immunoblotting for the indicated proteins. (**D**) Determination of the leucine-binding capacity of Sestrin2 S190W. Assays were performed and immunoprecipitates were analyzed as in Fig. 2A. (**E**) In Sestrin1, -2, and -3 triple-null cells expressing Sestrin2 S190W, the mTORC1 pathway cannot sense the absence of leucine. Wild-type HEK-293T cells and Sestrin1, -2, and -3 triple-null HEK-293T cells, generated with the CRISPR/Cas9 (clustered regularly interspaced short palindromic repeat/CRISPR-associated nuclease 9) system, were used to express the indicated FLAG-tagged proteins. Cells were starved of leucine for 50 min and, where indicated, stimulated with leucine for 10 min; lysates were analyzed via immunoblotting.

(Fig. 3E). In these cells, expression of wild-type Sestrin2 restored the leucine sensitivity of the mTORC1 pathway, but expression of Sestrin2 S190W had no effect (Fig. 3E). Thus, Sestrin2 must be able to interact with GATOR2 for the mTORC1 pathway to sense the absence of leucine.

For leucine to activate mTORC1, Sestrin2 must be able to bind leucine

To test whether the leucine-binding capacity of Sestrin2 is necessary for mTORC1 to sense the presence of leucine, we identified two Sestrin2 mutants, L261A and E451A, which do not bind leucine to an appreciable degree (Fig. 4A). Leucine did not meaningfully affect the interaction of the mutants with GATOR2 in vitro, consistent with the role of Sestrin2 in mediating the effects of leucine on the Sestrin2-GATOR2 complex (Fig. 4B). Expression of wild-type Sestrin2 in the Sestrin1, -2, and -3 triple-null cells restored the leucine sensitivity of the mTORC1 pathway in these cells, but expression of either mutant inhibited signaling and rendered the mTORC1 pathway insensitive to leucine (Fig. 4C and fig. S3A). Furthermore, in Sestrin1, -2, and -3 triple-null cells that expressed the mutants, the localization of mTOR to lysosomes in the presence of leucine was decreased, whereas that of RagC was not affected (fig. S4, A to D). Thus, activation of mTORC1 by leucine requires the binding of leucine to Sestrin2.

Conclusions

Sestrin2 has several properties that are consistent with its being a leucine sensor for the mTORC1 pathway: (i) it binds leucine at affinities consistent with the concentrations at which leucine is sensed; (ii) Sestrin2 mutants that do not bind leucine cannot signal the presence of leucine to mTORC1; and (iii) loss of Sestrin2 and its homologs renders the mTORC1 pathway insensitive to the absence of leucine. Although we have not investigated Sestrin1 as thoroughly, it appears to behave similarly to Sestrin2, so we propose that Sestrin1 and Sestrin2 are leucine sensors upstream of mTORC1.

Given that Sestrin2 has appreciable affinity for methionine, it would not be surprising if, in contexts where leucine concentrations are low and methionine concentrations are high, Sestrin2 serves as a methionine sensor for the mTORC1 pathway.

Sestrin2 binds to and likely inhibits GATOR2, but how this leads to suppression of mTORC1 cannot be determined until the molecular function of GATOR2 has been clarified. In addition, structural studies are needed to understand how the binding of leucine to Sestrin2 disrupts its interaction with GATOR2, and why leucine binds very poorly to Sestrin3.

Because Sestrin1 and Sestrin2 are soluble proteins, it is likely that they sense free leucine in the cytosol. Although these concentrations are unknown, the Michaelis constant of the human leucyl–transfer RNA synthetase (LRS) for leucine has been reported to be 45 μM (*38*). This value is similar to the affinity of Sestrin2 for leucine, suggesting that cytosolic free leucine concentrations are within this range. Like Sestrin2, LRS binds isoleucine and methionine at lower affinities than it binds leucine (about 30-fold less in the case of LRS) (*38*). The similarities between

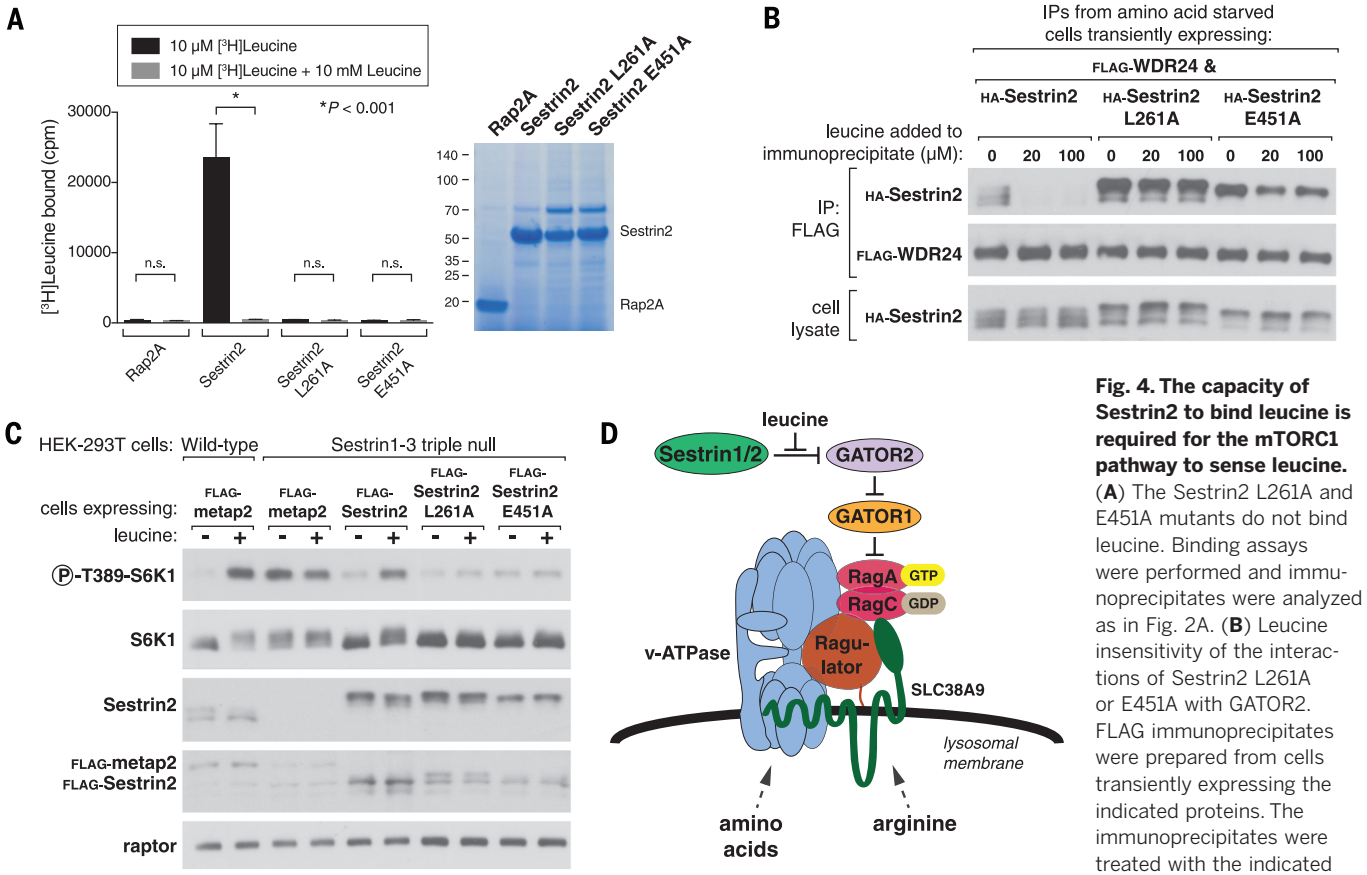

Fig. 4. The capacity of Sestrin2 to bind leucine is required for the mTORC1 pathway to sense leucine. (**A**) The Sestrin2 L261A and E451A mutants do not bind leucine. Binding assays were performed and immunoprecipitates were analyzed as in Fig. 2A. (**B**) Leucine insensitivity of the interactions of Sestrin2 L261A or E451A with GATOR2. FLAG immunoprecipitates were prepared from cells transiently expressing the indicated proteins. The immunoprecipitates were treated with the indicated concentrations of leucine and analyzed as in Fig. 1C (HA, hemagglutinin epitope). (**C**) In Sestrin1, -2, and -3 triple-null cells expressing Sestrin2 L261A or E451A, the mTORC1 pathway cannot sense the presence of leucine. Cells were generated and analyzed as in Fig. 3E. (**D**) Model showing how amino acid inputs from multiple sensors in distinct compartments impinge on the Rag GTPases to control mTORC1 activity.

the amino acid–binding characteristics of Sestrin2 and LRS support the notion that the affinity and specificity of Sestrin2 for leucine are sufficient for it to serve as a leucine sensor.

Our work suggests a model in which signals emerging from distinct amino acid sensors in different cellular compartments converge on the Rag GTPases at the lysosomal surface to regulate mTORC1 activity (Fig. 4D). The putative arginine sensor SLC38A9 probably monitors lysosomal contents, and Sestrin2 is almost certainly a cytosolic sensor. There must also be an amino acid sensor upstream of the FLCN-FNIP2 complex (the GAP for RagC and RagD), but its identity and cellular localization are unknown. A future challenge is to determine how the Rag GTPases integrate the inputs from the different sensors; this will likely require a much better understanding of the function of each Rag in the heterodimer. Moreover, in vivo characterization of the different sensors will be needed to comprehend how specific tissues adapt the amino acid sensing pathway to their particular needs.

Given that Sestrin2 (and Sestrin1) are likely to have leucine-binding pockets, these proteins may be targets for the development of small-molecule modulators of the mTORC1 pathway. Leucine attenuates the decrease in skeletal-muscle protein synthesis that occurs in the elderly and stimulates satiety (*1*, *39*). Thus, small molecules that potently mimic the effects of leucine on Sestrin2 could have therapeutic value. Furthermore, caloric restriction inhibits mTORC1 signaling (*40*, *41*) and is associated with increased health span and life span in multiple organisms (*42*, *43*). Thus, small molecules that antagonize the effects of leucine on Sestrin2 might have caloric restriction–mimicking properties.

REFERENCES AND NOTES

1. M. Potier, N. Darcel, D. Tomé, *Curr. Opin. Clin. Nutr. Metab. Care* **12**, 54–58 (2009).
2. U. Panten, J. Christians, E. von Kriegstein, W. Poser, A. Hasselblatt, *Diabetologia* **10**, 149–154 (1974).
3. J. S. Greiwe, G. Kwon, M. L. McDaniel, C. F. Semenkovich, *Am. J. Physiol. Endocrinol. Metab.* **281**, E466–E471 (2001).
4. K. S. Nair, R. G. Schwartz, S. Welle, *Am. J. Physiol.* **263**, E928–E934 (1992).
5. D. K. Layman, D. A. Walker, *J. Nutr.* **136**, 319S–323S (2006).
6. E. G. Frame, *J. Clin. Invest.* **37**, 1710–1723 (1958).
7. A. E. Harper, R. H. Miller, K. P. Block, *Annu. Rev. Nutr.* **4**, 409–454 (1984).
8. H. L. Fox *et al.*, *Am. J. Physiol.* **275**, C1232–C1238 (1998).
9. C. J. Lynch *et al.*, *J. Cell. Biochem.* **77**, 234–251 (2000).
10. C. C. Dibble, B. D. Manning, *Nat. Cell Biol.* **15**, 555–564 (2013).
11. A. Efeyan, D. M. Sabatini, *Biochem. Soc. Trans.* **41**, 902–905 (2013).
12. E. Hirose, N. Nakashima, T. Sekiguchi, T. Nishimoto, *J. Cell Sci.* **111**, 11–21 (1998).
13. A. Schürmann, A. Brauers, S. Massmann, W. Becker, H.-G. Joost, *J. Biol. Chem.* **270**, 28982–28988 (1995).
14. T. Sekiguchi *et al.*, *J. Biol. Chem.* **276**, 7246–7257 (2001).
15. C. Buerger, B. DeVries, V. Stambolic, *Biochem. Biophys. Res. Commun.* **344**, 869–880 (2006).
16. K. Saito *et al.*, *J. Biochem.* **137**, 423–430 (2005).
17. Y. Sancak *et al.*, *Science* **320**, 1496–1501 (2008).
18. S. Menon *et al.*, *Cell* **156**, 771–785 (2014).
19. A. Efeyan, R. Zoncu, D. M. Sabatini, *Trends Mol. Med.* **18**, 524–533 (2012).
20. L. Chantranupong, R. L. Wolfson, D. M. Sabatini, *Cell* **161**, 67–83 (2015).
21. Y. Sancak *et al.*, *Cell* **141**, 290–303 (2010).
22. R. Zoncu *et al.*, *Sci. Signal.* **334**, 678–683 (2011).
23. S. Wang *et al.*, *Science* **347**, 188–194 (2015).
24. M. Rebsamen *et al.*, *Nature* **519**, 477–481 (2015).
25. L. Bar-Peled *et al.*, *Cell* **150**, 1196–1208 (2012).
26. L. Bar-Peled *et al.*, *Science* **340**, 1100–1106 (2013).
27. Z.-Y. Tsun *et al.*, *Mol. Cell* **52**, 495–505 (2013).
28. L. Chantranupong *et al.*, *Cell Rep.* **9**, 1–8 (2014).
29. A. Parmigiani *et al.*, *Cell Rep.* **9**, 1281–1291 (2014).
30. A. V. Budanov, M. Karin, *Cell* **134**, 451–460 (2008).
31. M. Peng, N. Yin, M. O. Li, *Cell* **159**, 122–133 (2014).
32. E. F. Blommaart, J. J. Luiken, P. J. Blommaart, G. M. van Woerkom, A. J. Meijer, *J. Biol. Chem.* **270**, 2320–2326 (1995).
33. K. Hara *et al.*, *J. Biol. Chem.* **273**, 14484–14494 (1998).
34. H. Peeters *et al.*, *Hum. Genet.* **112**, 573–580 (2003).
35. L. Buckbinder, R. Talbott, B. R. Seizinger, N. Kley, *Proc. Natl. Acad. Sci. U.S.A.* **91**, 10640–10644 (1994).
36. A. V. Budanov *et al.*, *Oncogene* **21**, 6017–6031 (2002).
37. T. Rogez-Florent *et al.*, *J. Mol. Recognit.* **27**, 46–56 (2014).
38. X. Chen *et al.*, *Nucleic Acids Res.* **39**, 235–247 (2011).
39. C. S. Katsanos *et al.*, *Am. J. Physiol. Endocrinol. Metab.* **291**, E381–E387 (2006).
40. M. N. Stanfel *et al.*, *Biochim. Biophys. Acta* **1790**, 1067–1074 (2009).

41. J. Gallinetti, E. Harputlugil, J. R. Mitchell, *Biochem. J.* **449**, 1–10 (2013).
42. C. M. McCay, M. F. Crowell, L. A. Maynard, *Nutrition* **5**, 155–171, discussion 172 (1989).
43. B. K. Kennedy, K. K. Steffen, M. Kaeberlein, *Cell. Mol. Life Sci.* **64**, 1323–1328 (2007).

ACKNOWLEDGMENTS

D.M.S. is a founder, a member of the Scientific Advisory Board, a paid consultant, and a shareholder of Navitor Pharmaceuticals, which is targeting for therapeutic benefit the amino acid sensing pathway upstream of mTORC1. The His-MBP-Sestrin2 pMAL6H-C5XT plasmid is available from Navitor Pharmaceuticals under a materials transfer agreement with Navitor Pharmaceuticals. R.L.W., L.C., R.A.S., D.M.S., and the Whitehead Institute have filed two provisional patents that relate to the Sestrin2-GATOR2 interaction. We thank all members of the Sabatini Lab for helpful insights, in particular S. Wang for experimental advice; O. Levsh, from the laboratory of J.-K. Weng, for generously providing the control proteins used in the thermal shift assays; Navitor Pharmaceuticals for providing the His-MBP-Sestrin2 pMAL6H-C5XT plasmid; and Cell Signaling Technology for providing many antibodies. This work was supported by grants from NIH (R01 CA103866 and AI47389) and the Department of Defense (W81XWH-07-0448) to D.M.S.; fellowship support from NIH to R.L.W. (T32 GM007753 and F30 CA189333) and L.C. (F31 CA180271); and a grant from the Paul Gray Undergraduate Research Opportunities Program Fund to S.M.S. (3143900). K.S. is a Pfizer Fellow of the Life Sciences Research Foundation. D.M.S. is an investigator of the Howard Hughes Medical Institute.

SUPPLEMENTARY MATERIALS

www.sciencemag.org/content/351/6268/43/suppl/DC1
Materials and Methods
Figs. S1 to S4
References (*44*, *45*)

1 April 2015; accepted 11 September 2015
10.1126/science.aab2674

STRUCTURAL BIOLOGY

Architecture of human mTOR complex 1

Christopher H. S. Aylett,[1]* Evelyn Sauer,[2]* Stefan Imseng,[2]* Daniel Boehringer,[1] Michael N. Hall,[2]† Nenad Ban,[1]† Timm Maier[2]†

Target of rapamycin (TOR), a conserved protein kinase and central controller of cell growth, functions in two structurally and functionally distinct complexes: TORC1 and TORC2. Dysregulation of mammalian TOR (mTOR) signaling is implicated in pathologies that include diabetes, cancer, and neurodegeneration. We resolved the architecture of human mTORC1 (mTOR with subunits Raptor and mLST8) bound to FK506 binding protein (FKBP)–rapamycin, by combining cryo–electron microscopy at 5.9 angstrom resolution with crystallographic studies of *Chaetomium thermophilum* Raptor at 4.3 angstrom resolution. The structure explains how FKBP-rapamycin and architectural elements of mTORC1 limit access to the recessed active site. Consistent with a role in substrate recognition and delivery, the conserved amino-terminal domain of Raptor is juxtaposed to the kinase active site.

Since its discovery in 1991 as the target of the immunosuppressant rapamycin, TOR has emerged as a central regulator of cell growth and metabolism. TOR was identified in yeast (*1*, *2*); the mammalian ortholog is mTOR (*3*, *4*). The serine and threonine kinase activity of TOR is tightly regulated in response to physiological conditions, and aberrant mTOR signaling occurs in multiple pathologies, including diabetes, cancer, and neurodegeneration (*5*, *6*).

TOR is the core component of two, functionally distinct signaling complexes, TOR complex 1 (TORC1) and TORC2 (*7*–*13*). TORC1 is sensitive to rapamycin and regulates cell growth by activating protein, lipid, and nucleotide synthesis and by inhibiting autophagy. TORC2 is less well characterized but is rapamycin insensitive and controls diverse cellular processes through phosphorylation of several targets. Mammalian TORC1 (mTORC1) contains, in addition to mTOR, Raptor (regulatory-associated protein of mTOR) (*8*, *9*), mammalian homolog of protein Lethal with Sec Thirteen (mLST8) (*7*, *14*), and possibly several noncore subunits. Whereas mTOR and mLST8 are also found in mTORC2, Raptor is absent. Instead, Rictor (rapamycin-insensitive companion of mTOR) (*7*, *10*, *11*) and additional subunits (*15*–*17*) are required for mTORC2 activity.

[1]Institute of Molecular Biology and Biophysics, ETH Zürich, Zürich, Switzerland. [2]Biozentrum, University of Basel, Basel, Switzerland.
*These authors contributed equally to this work. †**Corresponding author. E-mail: ban@mol.biol.ethz.ch (N.B.); m.hall@unibas.ch (M.N.H.); timm.maier@unibas.ch (T.M.)**

The regulation of mTORC1 signaling involves interactions with several binding partners and translocation of mTORC1 within the cell (*12*, *13*). mTORC1 is activated in response to nutrients (amino acids) through the Rag guanosine triphosphatase (GTPase) signaling pathway (*18*, *19*), by growth factors through inhibition of the tuberous sclerosis complex 1 and 2 (TSC1 and TSC2) heterodimer and thereby activation of the small GTPase Rheb (*20*, *21*), and by cellular energy status through adenosine monophosphate–activated protein kinase (AMPK) phosphorylation of TSC2 and Raptor (*22*, *23*).

TOR is the founding member of the phosphatidylinositol-kinase–related kinase (PIKK) family (*24*), members of which share an elaborate domain organization. The kinase domain is situated at the C terminus, following long arrays of first HEAT (Huntingtin, EF3A, ATM, TOR), and then tetratricopeptide (TPR), repeats (*25*, *26*). The crystal structure of a compact C-terminal fragment of human mTOR containing the FAT (Frap, ATM, TRRAP) domain and the kinase domain has been resolved in complex with its obligate accessory protein, mLST8 (*27*).

Inhibition of mTOR by rapamycin is dependent on the formation of a complex with an intracellular receptor, FK506-binding protein (FKBP) (*28*, *29*), which then binds mTOR in mTORC1. FKBP interacts with mTOR through the hydrophobic rapamycin molecule, which binds pockets in each protein (*1*, *30*, *31*). The N terminus of the kinase domain forms the FKBP-rapamycin complex binding (FRB) domain, which juts outward from the N-lobe (*27*). Binding of the FKBP-rapamycin complex to the FRB domain has been predicted to narrow the active-site cleft (*27*), suggesting that rapamycin inhibition is due to steric hindrance (*32*). The FRB domain also binds cognate mTOR targets, and the mutation of key residues in the FRB domain impairs phosphorylation of model substrates (*27*).

The catalytic activity and substrate specificity of mTORC1 are regulated by Raptor. Raptor is a multidomain protein, predicted by sequence similarity to consist of an RNC (Raptor N-terminal Conserved) domain, a central set of armadillo repeats, and a C-terminal β propeller (*8*, *9*). Raptor functions in substrate binding, being required for phosphorylation of many mTORC1 substrates, the best characterized of which are the translational regulators ribosomal protein S6 kinase (S6K1) and eukaryotic translation initiation factor 4E-binding protein (4EBP). Phosphorylation of these substrates is dependent on their TOR signaling (TOS) motif, which binds Raptor directly (*33*, *34*).

Biochemical investigation of the oligomeric state and composition of TORCs demonstrated that TOR and mTOR complexes are dimeric, and allowed assignment of core components. Owing to difficulties in working with intact mTORC1, however, information on the three-dimensional arrangement of proteins and domains within the complex was limited to crystal structures of fragments (*27*, *31*), and a low-resolution (26 Å) reconstruction through cryo–electron microscopy (cryo-EM) (*35*) revealing twofold-symmetric, dimeric particles roughly 300 Å by 200 Å by 100 Å in size. In that study, however, the handedness of the reconstruction and the position of individual subunits could not be reliably assigned.

We resolved the structures of human mTORC1 and *Chaetomium thermophilum* Raptor (CtRaptor) at 5.9 and 4.3 Å resolution by cryo-EM and x-ray crystallography, respectively. We provide a description of the architecture of mTORC1 at a secondary structural level, placing the folded domains of all three mTORC1 subunits and revealing their relative arrangement within the complex.

Results and discussion

Determination of the cryo-EM structure of mTORC1

We coexpressed and copurified human mTOR, Raptor, and mLST8 from insect cells, obtaining a homogeneous mTORC1 complex with a molecular size of ~1.0 MD (fig. S1, A and B). Purified

material phosphorylated the mTORC1 substrate 4EBP1 and was inhibited by torin1 or FKBP-rapamycin, as expected for native mTORC1 (fig. S1C). For structural studies, a stable mTORC1 sample was generated by expression in the presence of rapamycin followed by mild glutaraldehyde gradient fixation (*36*). Single-particle analysis of cryo–electron micrographs from this mTORC1 sample yielded a reconstruction with an overall resolution of 5.9 Å (gold-standard Fourier shell correlation = 0.143 cut-off), within which only a few peripheral regions were ordered to lower resolution (figs. S2 and S3). Secondary structural elements were clearly resolved throughout most remaining regions of the complex, allowing all folded domains predicted within mTORC1 to be assigned. The reconstruction presented here is complemented by the crystal structure of *C. thermophilum* Raptor that fits the EM density of human mTORC1 and confirms the segregation of the Raptor and mTOR repeat regions. Both the crystal structure of the C-terminal fragment of mTOR (*27*) and the Raptor structure fit our density, allowing us to determine the handedness of the reconstruction (Fig. 1 and fig. S4). The overall shape of our reconstruction agrees with that of the published reconstruction; however, it appears that the handedness of the previous reconstruction was assigned incorrectly (*35*).

mTORC1 forms a hollow dimer with minimal subunit contacts

mTORC1 adopts a cage-like, dimeric architecture in which the C_2 symmetry axis passes through a large cavity (>60 Å across in places), leading to its characteristic hollow lozenge shape (Fig. 1, A and B). The kinase domains of mTOR are located near the center of the assembly and come close to each other but do not make contact. Raptor and mLST8 contribute peripheral parts of the complex, making up the pinnacles of the longer and shorter axes of the lozenge, respectively. When viewed from an angle perpendicular to the symmetry axis, one face of mTORC1 is characterized by the mTOR kinase domains and mLST8 subunits, with both active-site clefts opening outward from this side of the complex (Fig. 1, A and C). The opposite face comprises the N-terminal HEAT repeat domains of mTOR, which form superhelical α solenoids (Fig. 1, B and D). Raptor binds within the well-ordered juncture of two HEAT repeat domains. The RNC domain abuts the FRB region of the mTOR kinase domain, and the more C-terminal armadillo repeat and β-propeller domains extend outward, becoming less well resolved (Fig. 1, B and C).

The mTOR HEAT repeats contain two α-helical solenoids

The N-terminal portion of mTOR has a bipartite structure consisting largely of α-solenoid helical repeats. The extended, N-terminal region merges directly into the more compact, C-terminal fragment, which wraps around the kinase domain. The repetitive N terminus of mTOR, a prototypical HEAT repeat (*25*, *26*), forms two α solenoids (Fig. 2). The larger section is a highly curved superhelix, which we have dubbed the "horn," seven repeats of which can be placed at the individual-helix level. The remaining repeats are less clearly resolved, indicating local flexibility. The smaller region adopts a relatively linear arrangement consisting of seven HEAT repeats and a helical linkage to the compact fragment, which we refer to as the "bridge" (Fig. 2). The horn and bridge HEAT domains pack against one another. Nevertheless both sections are

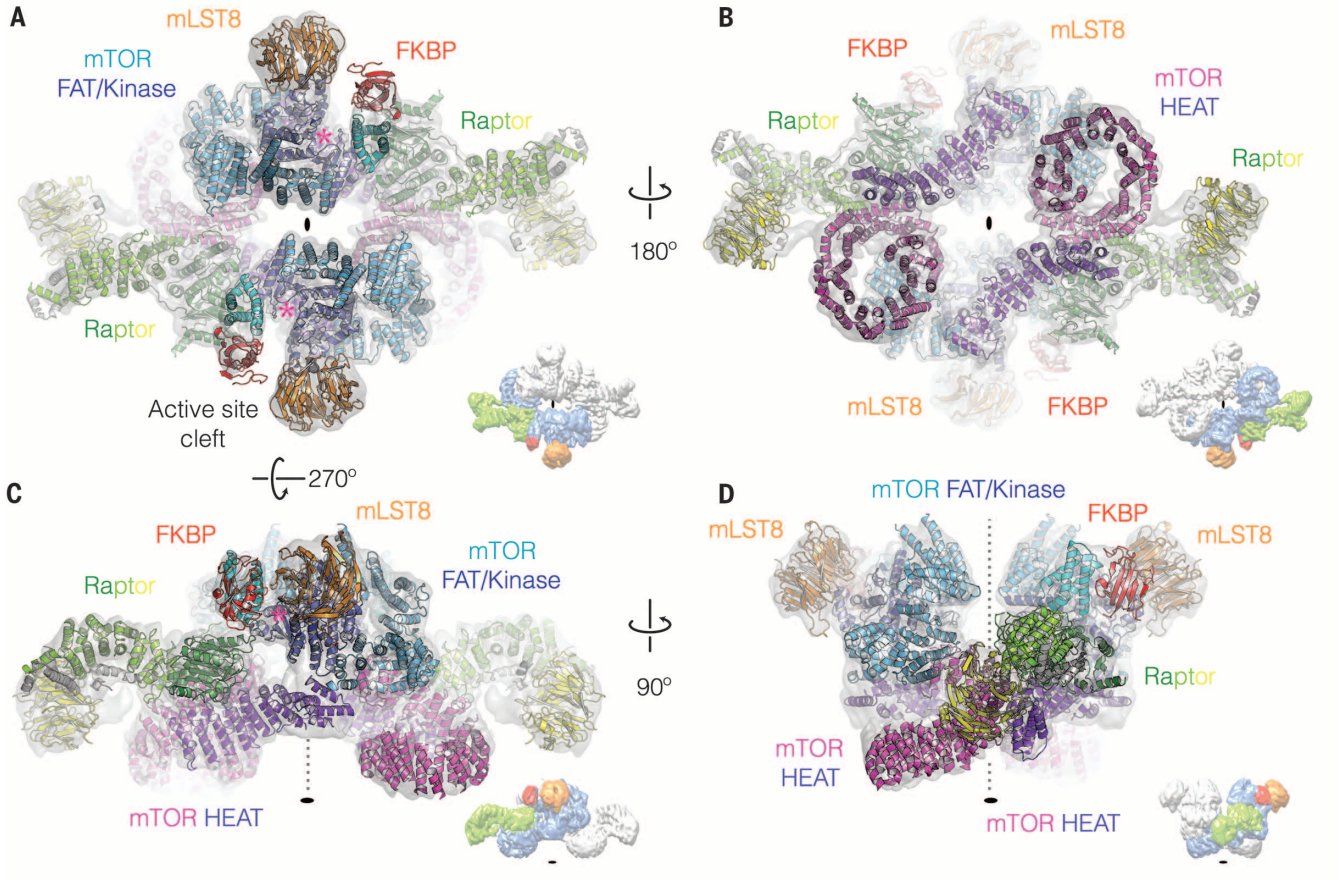

Fig. 1. mTORC1 adopts a dimeric, lozenge-shaped architecture. The reconstructed density obtained without masking peripheral regions, filtered to its global resolution (6.1 Å) and contoured at 3 σ, is shown as a translucent surface, and the corresponding model in cartoon representation. Each successive panel (**A** to **D**) is rotated as indicated. Raptor is in shades of green, mTOR in purples (N-terminal HEAT repeats) and blues (C-terminal FAT and kinase domains), mLST8 in orange, and FKBP in red. The active site, at the base of a restrictive cleft, is indicated by a magenta asterisk. A tinted surface representation showing the surface corresponding to one of each of the subunits within the proposed model of mTORC1 is inset.

predominantly exposed to the environment, supporting a purported role in binding mTOR regulators. The bridge region merges directly into the TPR repeats of the FAT domain (Fig. 2), and the prior crystal structure of this region fits our density with only minor adjustments (*27*) (Fig. 1 and fig. S4).

While no linkage between the two HEAT domains is visualized, their termini are in close proximity to one another. Although we cannot definitively assign sequence to regions of density at this resolution, the available evidence from studies of homologs (*37*) supports an interpretation in which the domains are continuous and contiguous, with the horn representing the N-terminal section and the bridge the more C-terminal part (see Materials and Methods). This suggested topology is shown in Fig. 2.

mTOR HEAT repeats bridge the kinase domains

Although Raptor is proposed to mediate mTOR dimerization by binding between the mTOR subunits (*35*), our structure reveals that mTOR itself forms a complete dimer (Fig. 2). The horn and bridge HEAT domains pack against one another, and the first HEAT repeat of the mTOR horn region is buried against the base of the adjacent mTOR FAT domain, completing an interlocking interaction between the two subunits (Fig. 3A). Dimerization changes the conformation of the FAT domain of mTOR relative to that in the monomeric crystal structure (fig. S4) (*27*). TPR helices 4 to 12 rotate to accommodate the interaction, presenting the interface and stacking neatly across the first repeat of the horn (Fig. 3B). Notably, the conformation of the kinase domain appears unaffected by dimerization. This is not unexpected, as the kinase domain can maintain an active state even in the absence of Rheb (*27*). Thus regulation is probably mediated largely by controlling substrate access to the active site.

Structure of Raptor

Raptor determines substrate specificity of mTORC1, by mediating recruitment (*18*, *19*) and recognition (*8*, *9*). Density corresponding to the RNC domain and the proximal part of the armadillo repeat of human Raptor is well defined in our reconstruction, whereas the distal portion of the armadillo repeat and the C-terminal β-propeller domain are flexible (Fig. 1). To resolve the entire Raptor structure, we purified insect cell-expressed Raptor from *C. thermophilum* (CtRaptor), which exhibits 44% sequence identity to human Raptor (fig. S5). To facilitate crystallization, CtRaptor was subjected to limited proteolysis, which removed a large N-terminal extension absent in human Raptor (fig. S6). Several smaller proteolytic fragments remained associated with the Raptor core (fig. S6). Experimental phases for CtRaptor crystals were determined with a mercury derivative, and a backbone model was traced at a resolution of 4.3 Å (fig. S7). CtRaptor adopts an extended Z shape with the RNC and β-propeller domains arranged at opposite ends of the armadillo domain (Fig. 4).

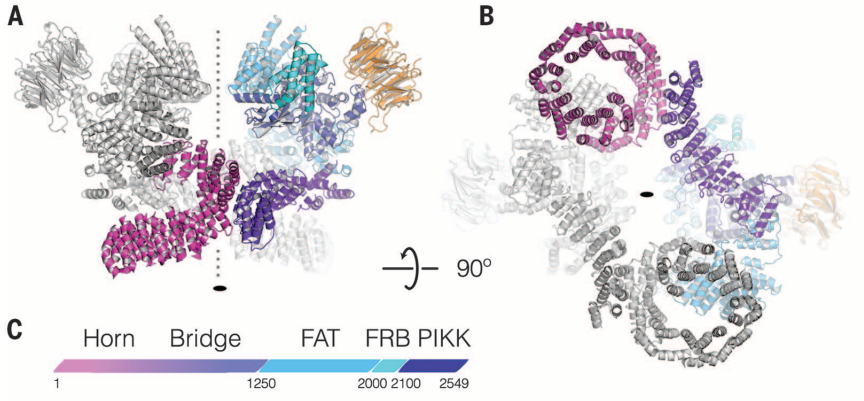

Fig. 2. Model showing the suggested domain organization of the mTOR dimer. (**A** and **B**) The C-terminal kinase and FAT domains of mTOR form a compact unit, and the N-terminal HEAT domains adopt an elongated structure with two separate α-solenoids: the "horn" and "bridge." The proposed model is shown in cartoon representation, rotated as indicated. Symmetry-related mTOR domains are shown in gray. (**C**) Linear representation of the domain organization of mTOR. The residue numbers indicate the domain boundaries; domain lengths are consistent in residues.

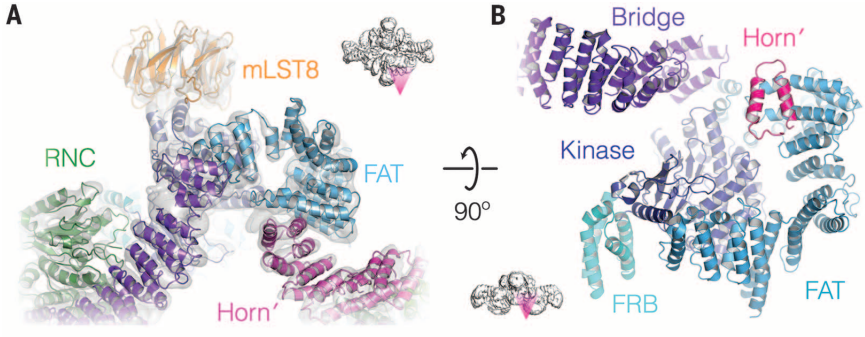

Fig. 3. The horn and bridge of mTOR complete a full dimeric interaction, linking the two FAT-PIKK units. (**A**) The complete interaction is shown intact, and the reconstruction, filtered to its global resolution (5.9 Å) and contoured at 6 σ, is indicated as a translucent surface; the corresponding model is shown as a secondary structural cartoon. (**B**) The interaction surface is shown with the point of view rotated as indicated. The symmetry-related horn domain is denoted horn′.

The N-terminal RNC domain exhibits an α-β-α sandwich fold that is structurally related to that found in CASPases (fig. S8A), consistent with conserved motifs in both families (*38*). The RNC domain is connected to the armadillo domain through four helices, three of which originate from a large insertion (relative to the CASPase fold) between strand one and a shortened helix four, and the fourth from the C terminus of the RNC domain. Two of the active-site residues of CASPases are conserved in the RNC domain (*38*). Our model of CtRaptor reveals that there is also structural conservation of the corresponding regions. However, the N terminus of helix 1, which contributes a key arginine residue to the CASPase active site, is displaced by more than 13 Å in CtRaptor.

The Raptor armadillo domain comprises seven helical hairpins, five of which are canonical armadillo repeats (fig. S8B). The β-propeller domain of Raptor associates with the armadillo repeats through the interaction of blades two and three with repeats five, six, and seven. The interaction takes place at the rim of the β propeller, leaving the face accessible for putative interacting proteins (Fig. 4 and fig. S8B). Three additional stretches of extended CtRaptor peptide are visible in the electron density (Fig. 4 and fig. S7). Stretch 1, belonging to the N terminus, originates at the β propeller, spans the entire armadillo domain, and joins the N terminus of the RNC domain. Stretch 2 forms a V-shaped helical segment at the C terminus of the repeat domain beneath the β propeller. Stretch 3 runs along the concave face of the armadillo domain. Stretches 2 and 3 likely represent the linker region between the armadillo and β-propeller domains, corresponding to the fragments observed by mass spectrometry (fig. S6). The corresponding linker region of human Raptor (residues 700 to 900) is frequently phosphorylated (*39*); based on our structural data, such posttranslational modification could affect interactions with the Raptor core in vivo.

The conformation of CtRaptor in crystals is close to that of human Raptor in the mTORC1 EM reconstruction, allowing us to fit the crystal

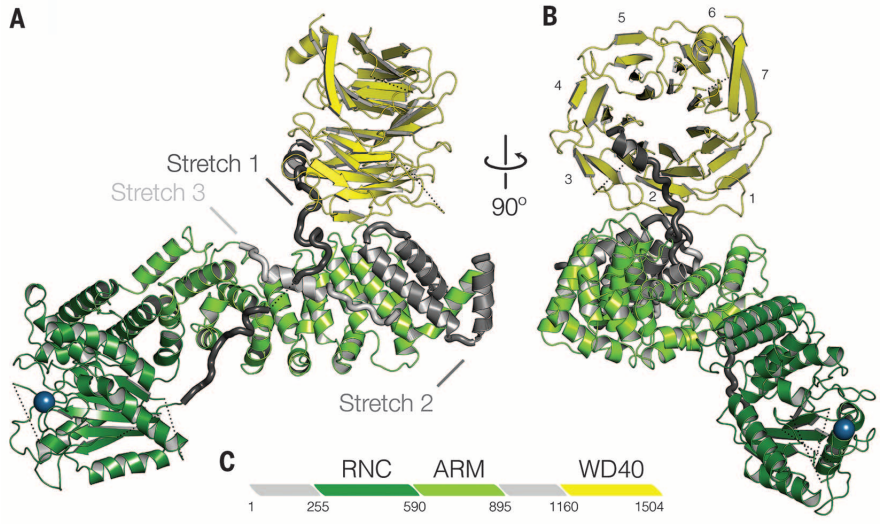

Fig. 4. CtRaptor adopts a Z shape with the RNC domain and the β propeller at opposing ends of the armadillo domain. (**A** and **B**) CtRaptor is shown in cartoon representation, and domain borders are indicated in a sequence schematic. The putative substrate-binding site, inferred from homology to CASPases, is indicated by a blue sphere. Polypeptide linkers are shown in gray; stretch 1 (dark gray) originates from the N terminus of the RNC domain and spans the armadillo (ARM) domain to the β propeller; stretch 2 (medium gray) is associated with the C-terminal region of the armadillo domain; stretch 3 (light gray) is bound along the concave surface of the armadillo domain. (**C**) Linear representation of the domain organization of Raptor. The residue numbers indicate the domain boundaries; domain lengths are consistent in residues.

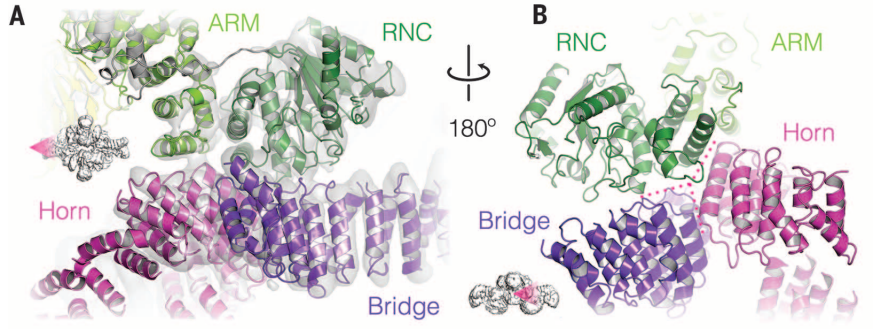

Fig. 5. Raptor binds to and organizes the N terminus of mTOR through a horn-bridge-armadillo α-solenoid stack. (**A**) The complete interaction is shown with the reconstructed density, filtered to its global resolution (5.9 Å) and contoured at 6 σ, indicated as a translucent surface; the corresponding model is shown as a secondary structural cartoon. (**B**) The antiparallel α-solenoid stack is shown as a secondary structural cartoon; the image generated with the point of view rotated as indicated and the threefold interaction surface are shown with dotted magenta lines.

structure as a rigid body into the EM density. The projection of the β-propeller domain of Raptor away from the core of mTORC1 is consistent with a role for this domain in the recruitment of regulatory proteins (Figs. 1 and 4) (*18*, *19*). The Raptor RNC domain is positioned directly at the mTOR active-site cleft, implying its involvement in Raptor-mediated substrate recognition (Figs. 1 and 4) (*33*, *34*).

Raptor stabilizes the mTOR HEAT domains

Raptor is necessary for formation of the mTORC1 complex. The principal interaction between Raptor and mTOR consists of an α-solenoid stack formed between the horn and bridge domains of mTOR and the Raptor armadillo domain (Fig. 5A). The horn and bridge domains run antiparallel to each other, forming a contact offset by half their depth (Fig. 5B). The N-terminal helices of the Raptor armadillo repeat and the base of the RNC domain occupy this "step," making up the remaining interaction surface with the loops of the HEAT repeats within the bridge and helices of those in the horn (Fig. 5B). Given that Raptor provides roughly two-thirds of the interaction surface stabilizing the HEAT domains, the stability of the N-terminal regions of mTOR would be weakened in its absence. The formation of the mTORC1 dimer is also dependent on the interaction between the (flexible) horn N-terminal HEAT domain of mTOR and the C-terminal FAT domain. Without stabilization of the mTOR N-terminal HEAT repeats in a single conformation, dimers could not be readily formed. Raptor binding thus may favor the dimerization of mTOR molecules without directly engaging in dimer formation (*7*, *35*).

Implications of mTORC1 architecture for substrate selectivity and delivery

The structure of the C-terminal mTOR fragment revealed that the kinase domain is held in a catalytically active conformation by the surrounding FAT domain and segments inserted within the kinase domain itself (*27*). The FRB domain and mLST8 limit access to the adenosine 5′-triphosphate (ATP)–binding cleft, preventing activity toward noncognate substrates, which would otherwise be problematic for a constitutively active enzyme. In our assembled complex, access to the active site is further restricted by Raptor. Whereas the FRB domain and mLST8 narrow the active-site cleft from the N- and C-lobe sites, respectively, the RNC domain additionally restricts access from the solvent-exposed surface below the FRB domain. This results in the enclosure of the active-site cleft from all directions, reducing its width to ~20 Å (Fig. 6A).

Raptor directly interacts with substrate proteins through their TOS motifs, FDIDL in S6K1 (*34*) and FEMDI in 4EBP1 (*33*), which include a conserved aspartate at position four. Given the structural similarity between the RNC domain and CASPases, which recognize four-residue sequences with an aspartate at position four, equivalent residues in CASPase and Raptor may function in substrate recognition (Fig. 6, C and D). The corresponding site is located directly within the mTORC1 active-site cleft, ~50 Å from the kinase center and optimally positioned for recruitment and delivery of subtrate to the active site (Fig. 6). Considering that the peripheral Raptor β propeller has been proposed to bind proteins involved in regulating mTORC1, it is possible that this regulation occurs via the peptide stretch connecting the β propeller to the RNC domain of Raptor.

Our cryo-EM maps of mTORC1 reveal additional density next to the FRB domain (Fig. 6). This density represents a copurified complex of *Spodoptera frugiperda* FKBP (SfFKBP) and rapamycin, which was used to enhance mTORC1 expression. SfFKBP shares 78% identity to human FKBP12, and its presence in purified mTORC1 was confirmed by mass spectrometry. The FKBP-rapamycin density further reduces the active-site cleft to ~10 Å. It also lies between the RNC domain and the active site, supporting steric hindrance as the mechanism by which rapamycin may inhibit mTOR toward certain substrates, but not others (*32*) (Fig. 6B). Although it has been proposed that FKBP-rapamycin binding compromises mTORC1 stability, possibly by displacing Raptor (*35*), we do not observe this effect.

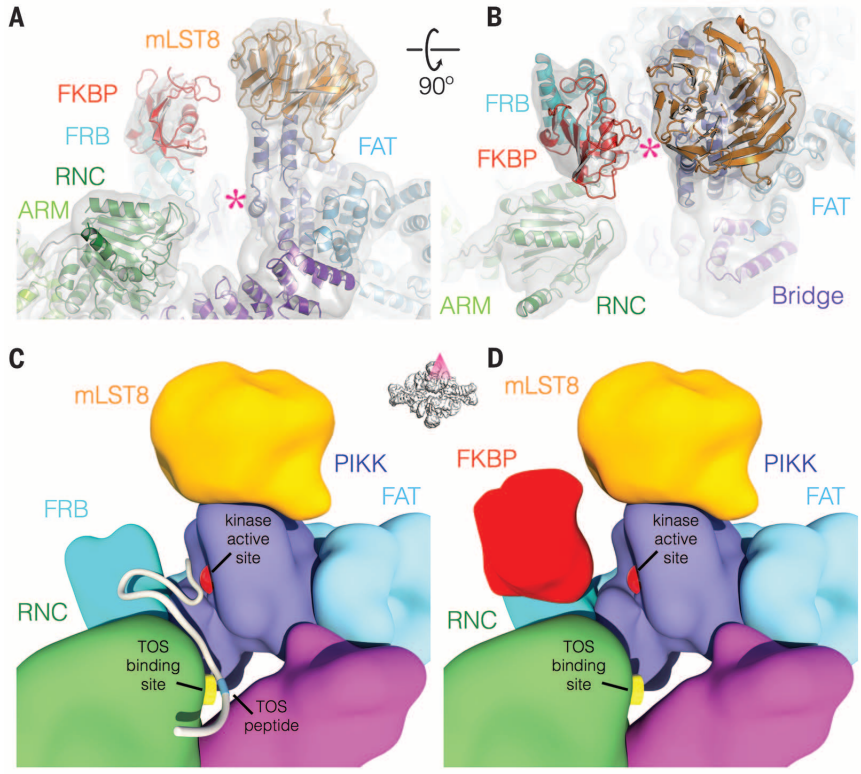

Fig. 6. The RNC domain of Raptor is positioned adjacent to the FRB domain of mTOR, complementing the active-site cleft of the kinase domain. (**A** and **B**) View into the active-site cleft of one half of an mTORC1 dimer. The reconstructed density, filtered to its global resolution (5.9 Å) and contoured at 3 σ, is indicated as a translucent surface, and the corresponding model is shown in cartoon representation. The active site is indicated with a magenta asterisk. Panel (B) is shown with the perspective rotated, as indicated. (**C** and **D**) Schematic illustrating the proposed mode of substrate (gray) binding and delivery to the mTOR active site.

Furthermore, the FRB domain that binds FKBP-rapamycin (*30*, *31*) is not near the dimerization interface; nor does it contact the RNC domain, making it unlikely that the binding of FKBP-rapamycin would destabilize mTORC1 by steric hindrance (Fig. 6B).

Implications for mTORC2 and other kinases

The architecture of mTORC1 provides a structural basis for studying mTORC1 function. Given the similar overall appearance of our structure and that of TORC2 (*37*, *40*), we anticipate that the architecture of mTORC1 might be conserved in parts of mTORC2. In particular, we anticipate that the mode of dimerization, in which a complete dimer is formed through mTOR-mTOR contacts alone, will be conserved. An interaction of Rictor in mTORC2 with the bridge and horn HEAT domains, similar to that of Raptor in mTORC1, could stabilize the N terminus of mTOR and facilitate mTORC2 dimerization. Raptor forms this interaction through its armadillo repeat domain; a large domain of Rictor is also predicted to form an α-helical solenoid. Other members of the PIKK kinase family, including ATM, require accessory proteins that interact with HEAT repeats and are thought to dimerize in vivo. Although the N-terminal HEAT-repeat domains of the family are their least conserved parts, it appears possible, given the residual sequence similarity, that PIKK family members may have common modes of interaction (*24*).

REFERENCES AND NOTES

1. J. Heitman, N. R. Movva, M. N. Hall, *Science* **253**, 905–909 (1991).
2. J. Kunz *et al.*, *Cell* **73**, 585–596 (1993).
3. E. J. Brown *et al.*, *Nature* **369**, 756–758 (1994).
4. D. M. Sabatini, H. Erdjument-Bromage, M. Lui, P. Tempst, S. H. Snyder, *Cell* **78**, 35–43 (1994).
5. E. Dazert, M. N. Hall, *Curr. Opin. Cell Biol.* **23**, 744–755 (2011).
6. S. Menon, B. D. Manning, *Oncogene* **27** (suppl. 2), S43–S51 (2008).
7. R. Loewith *et al.*, *Mol. Cell* **10**, 457–468 (2002).
8. D.-H. Kim *et al.*, *Cell* **110**, 163–175 (2002).
9. K. Hara *et al.*, *Cell* **110**, 177–189 (2002).
10. E. Jacinto *et al.*, *Nat. Cell Biol.* **6**, 1122–1128 (2004).
11. D. D. Sarbassov *et al.*, *Curr. Biol.* **14**, 1296–1302 (2004).
12. M. Laplante, D. M. Sabatini, *Cell* **149**, 274–293 (2012).
13. M. Shimobayashi, M. N. Hall, *Nat. Rev. Mol. Cell Biol.* **15**, 155–162 (2014).
14. D.-H. Kim *et al.*, *Mol. Cell* **11**, 895–904 (2003).
15. M. A. Frias *et al.*, *Curr. Biol.* **16**, 1865–1870 (2006).
16. E. Jacinto *et al.*, *Cell* **127**, 125–137 (2006).
17. Q. Yang, K. Inoki, T. Ikenoue, K.-L. Guan, *Genes Dev.* **20**, 2820–2832 (2006).
18. Y. Sancak *et al.*, *Science* **320**, 1496–1501 (2008).
19. E. Kim, P. Goraksha-Hicks, L. Li, T. P. Neufeld, K.-L. Guan, *Nat. Cell Biol.* **10**, 935–945 (2008).
20. Y. Zhang *et al.*, *Nat. Cell Biol.* **5**, 578–581 (2003).
21. K. Inoki, Y. Li, T. Xu, K. L. Guan, *Genes Dev.* **17**, 1829–1834 (2003).
22. K. Inoki, T. Zhu, K. L. Guan, *Cell* **115**, 577–590 (2003).
23. D. M. Gwinn *et al.*, *Mol. Cell* **30**, 214–226 (2008).
24. C. T. Keith, S. L. Schreiber, *Science* **270**, 50–51 (1995).
25. M. A. Andrade, P. Bork, *Nat. Genet.* **11**, 115–116 (1995).
26. B. A. Knutson, *J. Struct. Biol.* **170**, 354–363 (2010).
27. H. Yang *et al.*, *Nature* **497**, 217–223 (2013).
28. J. J. Siekierka, S. H. Hung, M. Poe, C. S. Lin, N. H. Sigal, *Nature* **341**, 755–757 (1989).
29. M. W. Harding, A. Galat, D. E. Uehling, S. L. Schreiber, *Nature* **341**, 758–760 (1989).
30. J. Chen, X. F. Zheng, E. J. Brown, S. L. Schreiber, *Proc. Natl. Acad. Sci. U.S.A.* **92**, 4947–4951 (1995).
31. J. Choi, J. Chen, S. L. Schreiber, J. Clardy, *Science* **273**, 239–242 (1996).
32. A. Y. Choo, J. Blenis, *Cell Cycle* **8**, 567–572 (2009).
33. S. S. Schalm, D. C. Fingar, D. M. Sabatini, J. Blenis, *Curr. Biol.* **13**, 797–806 (2003).
34. H. Nojima *et al.*, *J. Biol. Chem.* **278**, 15461–15464 (2003).
35. C. K. Yip, K. Murata, T. Walz, D. M. Sabatini, S. A. Kang, *Mol. Cell* **38**, 768–774 (2010).
36. B. Kastner *et al.*, *Nat. Methods* **5**, 53–55 (2008).
37. C. Gaubitz *et al.*, *Mol. Cell* **58**, 977–988 (2015).
38. K. Ginalski, H. Zhang, N. V. Grishin, *Trends Biochem. Sci.* **29**, 522–524 (2004).
39. K. G. Foster *et al.*, *J. Biol. Chem.* **285**, 80–94 (2010).
40. S. Wullschleger, R. Loewith, W. Oppliger, M. N. Hall, *J. Biol. Chem.* **280**, 30697–30704 (2005).

ACKNOWLEDGMENTS

We thank the ETH Zürich Scientific Center for Optical and Electron Microscopy (ScopeM) for access to EM facilities, P. Tittmann for technical support, T. Sharpe for size exclusion chromatography multi-angle laser light scattering analysis, the Biozentrum Proteomics Core Facility for mass spectrometric protein identification, the beamline staff at Swiss Light Source beamlines X06SA and X06DA for crystallographic support, and H. S. T. Bukhari for 3D modelling in Maya. C.H.S.A. was supported by an ETH Zürich postdoctoral fellowship and a European Molecular Biology Organization long-term fellowship. E.S. was supported by a fellowship from the People Program (Marie Curie Actions; REA grant agreement number 328159). This work was supported by the European Research Council funding to M.N.H. and N.B., and by the Swiss National Science Foundation via the National Centre of Excellence in RNA and Disease, project funding 138262 and R'Equip 145023. The cryo-EM density maps representing mTORC1 have been deposited in the EM Databank as EMD-3212 and EMD-3213 and the corresponding model in the Protein Data Bank as PDB ID 5FLC. The crystal structure of CtRaptor has been deposited in the Protein Data Bank as PDB ID 5EF5.

SUPPLEMENTARY MATERIALS

www.sciencemag.org/content/351/6268/48/suppl/DC1
Materials and Methods
Figs. S1 to S8
Table S1
References (*41*–*56*)

23 July 2015; accepted 10 November 2015
10.1126/science.aaa3870

METABOLISM

Structural basis for leucine sensing by the Sestrin2-mTORC1 pathway

Robert A. Saxton,[1,2,3,4,5] Kevin E. Knockenhauer,[1] Rachel L. Wolfson,[1,2,3,4,5] Lynne Chantranupong,[1,2,3,4,5] Michael E. Pacold,[1,2,3,4,5] Tim Wang,[1,2,3,4,5] Thomas U. Schwartz,[1] David M. Sabatini[1,2,3,4,5]*

Eukaryotic cells coordinate growth with the availability of nutrients through the mechanistic target of rapamycin complex 1 (mTORC1), a master growth regulator. Leucine is of particular importance and activates mTORC1 via the Rag guanosine triphosphatases and their regulators GATOR1 and GATOR2. Sestrin2 interacts with GATOR2 and is a leucine sensor. Here we present the 2.7 angstrom crystal structure of Sestrin2 in complex with leucine. Leucine binds through a single pocket that coordinates its charged functional groups and confers specificity for the hydrophobic side chain. A loop encloses leucine and forms a lid-latch mechanism required for binding. A structure-guided mutation in Sestrin2 that decreases its affinity for leucine leads to a concomitant increase in the leucine concentration required for mTORC1 activation in cells. These results provide a structural mechanism of amino acid sensing by the mTORC1 pathway.

The mechanistic target of rapamycin complex 1 (mTORC1) protein kinase is a major growth regulator that coordinates cell anabolism and catabolism with the availability of key nutrients such as amino acids (*1*–*3*). Among the amino acids, leucine is of particular interest because of its ability to promote important physiological phenomena, including muscle growth and satiety (*4*–*6*), in large part through the activation of mTORC1 (*7*, *8*). However, the biochemical mechanism of leucine sensing by the mTORC1 pathway has remained elusive.

Whereas growth factors, energy, and other inputs signal to mTORC1 primarily through the tuberous sclerosis complex–Rheb axis (*9*–*11*), amino acids act by regulating the nucleotide state of the heterodimeric Rag guanosine triphosphatases (GTPases) and promoting the localization of mTORC1 to the lysosome, its site of activation (*12*–*14*). Lysosomal amino acids including arginine are thought to signal to the Rags through a lysosomal membrane–associated complex consisting of the v-ATPase (vacuolar-type H^+-dependent adenosine triphosphatase) (*15*), the Ragulator complex (*16*), and the putative arginine sensor SLC38A9 (*17*, *18*). Cytosolic leucine, however, signals to the Rags through a distinct pathway consisting of GATOR1, which is the GTPase-activating protein for RagA and RagB, and a pentameric protein complex of unknown function called GATOR2 (*19*, *20*).

[1]Department of Biology, Massachusetts Institute of Technology (MIT), Cambridge, MA 02139, USA. [2]Whitehead Institute for Biomedical Research, 9 Cambridge Center, Cambridge, MA 02142, USA. [3]Howard Hughes Medical Institute, Department of Biology, MIT, Cambridge, MA 02139, USA. [4]Koch Institute for Integrative Cancer Research, 77 Massachusetts Avenue, Cambridge, MA 02139, USA. [5]Broad Institute of Harvard and MIT, 7 Cambridge Center, Cambridge, MA 02142, USA.
***Corresponding author. E-mail: sabatini@wi.mit.edu**

Proteomic studies have identified the Sestrins as GATOR2-interacting proteins that inhibit mTORC1 only in the absence of amino acids (*21*, *22*). Subsequent in vitro studies demonstrated that the Sestrin2-GATOR2 interaction is sensitive specifically to leucine, which binds Sestrin2 with a dissociation constant of ~20 μM. Human embryonic kidney (HEK)–293T cells expressing a Sestrin2 mutant that cannot bind leucine fail to activate mTORC1 in response to leucine, suggesting that Sestrin2 is the primary leucine sensor for the mTORC1 pathway in these cells (*20*). However, Sestrin2 shares no sequence similarity with known amino acid–binding domains, raising the question of how this protein can detect leucine and signal its presence to mTORC1.

Here we present the structure of human Sestrin2 in complex with leucine, revealing in atomic detail the mechanism of leucine sensing by the mTORC1 pathway.

Structure of leucine-bound Sestrin2

To understand how Sestrin2 detects leucine, we expressed and purified full-length human Sestrin2 from *Escherichia coli* and verified binding to leucine in vitro by differential scanning fluorimetry (fig. S1) (*23*). Although we were unable to obtain crystals of Sestrin2 alone, incubation of the protein with leucine allowed the formation of crystals containing leucine-bound Sestrin2 that diffracted to 2.7 Å resolution. We solved the structure using single-wavelength anomalous dispersion with selenomethionine-derivatized protein and refined the model against the native data to final working and free residuals, R_{work} and R_{free}, of 19.6% and 22.3%, respectively (table S1). Sestrin2 crystallized in a cubic space group containing five copies per asymmetric unit.

Sestrin2 is a 55-kD, monomeric, all α-helical, globular protein that contains distinct N-terminal (NTD, residues 66 to 220) and C-terminal (CTD, residues 339 to 480) domains connected by a partially disordered, partially helical linker domain (residues 221 to 338) (Fig. 1A). The N-terminal 65 residues of the protein appear disordered and were not observed in our structure. Electron density map analysis revealed the presence of a single leucine molecule bound to Sestrin2 in the CTD (Fig. 2A).

The NTD and CTD of Sestrin2 appear to be structurally similar and superpose well, with a root mean square deviation (RMSD) of ~3.0 Å over 55 aligned Cα positions, despite a low sequence identity of 10.9% (Fig. 1B). Furthermore, the two domains make extensive contacts with each other, primarily through the two core hydrophobic helices N9 and C7, burying 1872 $Å^2$ of surface area (Fig. 1A).

A small region in the N terminus of Sestrin2 has weak sequence similarity to the bacterial alkylhydroperoxidase AhpD (*24*). Analysis of our structure with the National Center for Biotechnology Information's Vector Alignment Search Tool [VAST (*25*)] showed that Sestrin2 shares a common fold with the carboxymucolactone decarboxylase (CMD) protein family, consisting of bacterial γ-CMD as well as AhpD (Pfam database identification number: PF02627). Despite low sequence similarity, Sestrin2 strongly resembles an AhpD homodimer, with each half of Sestrin2 matching a single AhpD molecule (Fig. 1C and fig. S2A). The NTD and CTD both superpose well with *Ralstonia eutropha* AhpD, with RMSDs of ~2.0 Å over 129 and 101 Cα positions, respectively. Thus, Sestrin2 structurally resembles an intramolecular homodimer of two CMD-like domains, despite extensive divergence in the primary sequence.

To test the importance of the intramolecular contacts between the two domains of Sestrin2, we expressed the FLAG-tagged N- and C-terminal halves either alone or together as separate polypeptides and performed coimmunoprecipitation analysis. Although neither domain alone bound GATOR2, the separated halves, when expressed together, bound strongly both to each other and to GATOR2 (Fig. 1D). Similarly, although neither half of Sestrin2 alone bound to leucine, the coexpressed halves did bind leucine (Fig. 1E). Therefore, the NTD and CTD of Sestrin2 interact stably with each other and are both required for the interactions with GATOR2, as well as with leucine.

In addition to its role as a leucine sensor and GATOR2 inhibitor, Sestrin2 has been reported to have peroxiredoxin reductase activity, based in large part on its weak sequence similarity to bacterial AhpD, which does have this activity (*24*). However, other groups have failed to reproduce this finding (*26*). The active site of AhpD contains two cysteines, both of which are required for its catalytic activity (*26*, *27*). Superposing our Sestrin2 structure with AhpD confirms previous reports (*24*, *26*) that only one of these active site residues is present in the N-terminal half of Sestrin2 (Cys^{125}), whereas both are absent from the C-terminal half (fig. S2B). This suggests that Sestrin2 either does not reduce peroxiredoxins or does so through an entirely different mechanism than does AhpD.

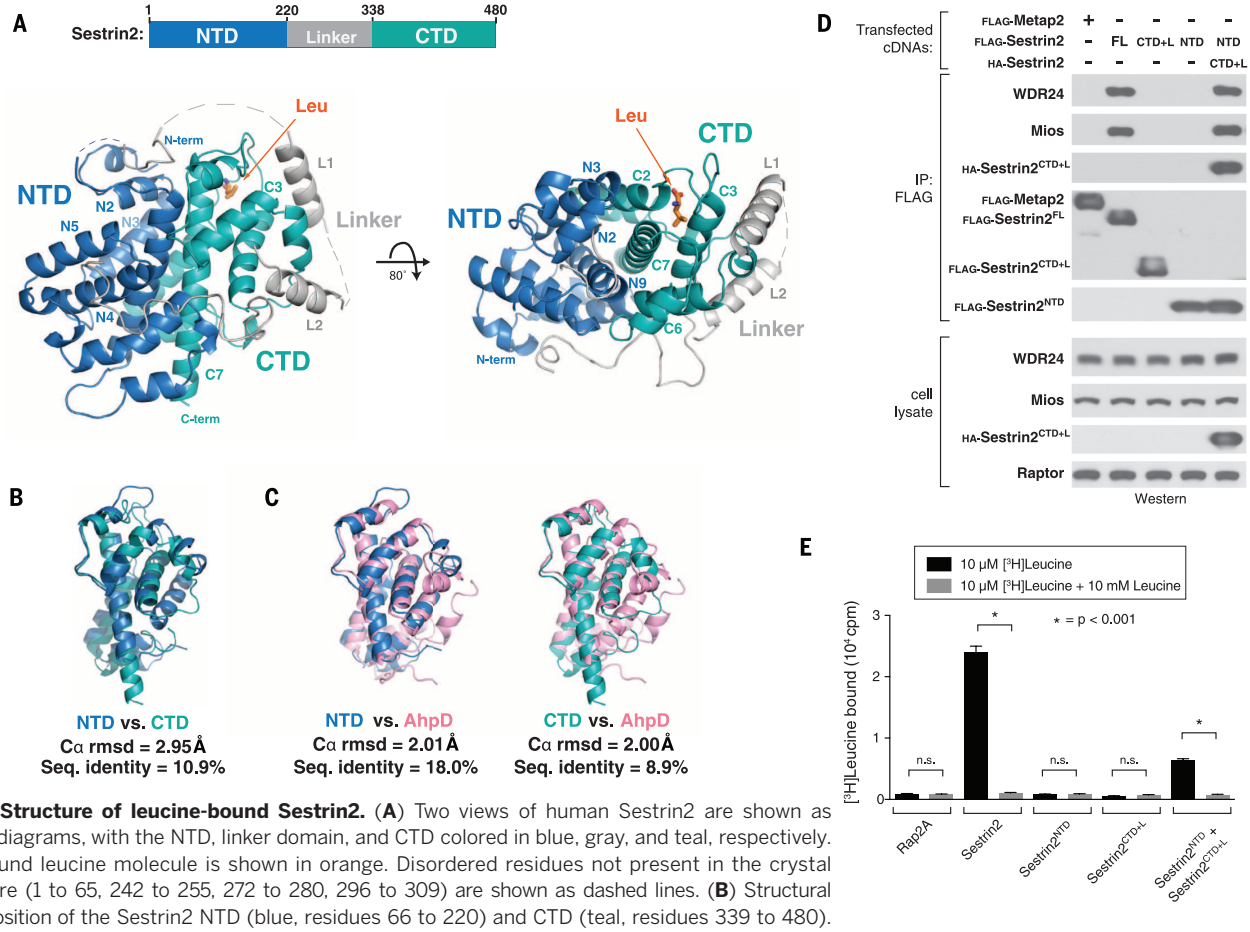

Fig. 1. Structure of leucine-bound Sestrin2. (**A**) Two views of human Sestrin2 are shown as ribbon diagrams, with the NTD, linker domain, and CTD colored in blue, gray, and teal, respectively. The bound leucine molecule is shown in orange. Disordered residues not present in the crystal structure (1 to 65, 242 to 255, 272 to 280, 296 to 309) are shown as dashed lines. (**B**) Structural superposition of the Sestrin2 NTD (blue, residues 66 to 220) and CTD (teal, residues 339 to 480). (**C**) Structural superposition of the Sestrin2 NTD (blue) and CTD (teal) with a *R. eutropha* AhpD dimer (pink; PDB accession code: 2PRR). (**D**) Immunoprecipitation of N- and C-terminal fragments of Sestrin2. HEK-293T cells transiently transfected with FLAG-metap2, FLAG-Sestrin2 full length (FL), FLAG-Sestrin2-NTD (1 to 220), FLAG-Sestrin2-CTD+L (CTD plus linker, 220 to 480), or both Flag-Sestrin2-NTD and HA-Sestrin2-CTD+L (HA, hemagglutinin epitope) were starved for amino acids for 50 min. FLAG immunoprecipitates were prepared from cell lysates. Immunoprecipitates and lysates from one representative experiment were analyzed by immunoblotting for the indicated proteins. WDR24 and Mios were used as representative GATOR2 components. (**E**) [^{3}H]leucine binding assay using N- and C-terminal fragments of Sestrin2. FLAG immunoprecipitates prepared from HEK-293T cells transiently expressing the indicated proteins were used as described in the methods (supplementary materials). Unlabeled leucine was used as a competitor where indicated. Values are means ± SDs for three technical replicates from one representative experiment. Two-tailed *t* tests were used for comparisons between two groups.

Sestrin2 is also reported to inhibit the mTORC1 pathway by directly acting as a guanine nucleotide dissociation inhibitor (GDI) for RagA and RagB through a motif consisting of Arg^{419}, Lys^{422}, and Lys^{426} (*28*). However, in our structure, two of these three residues are buried (Lys^{422} and Lys^{426}; fig. S2C), and Sestrin2 shows no structural similarity to known GDI proteins.

Recognition of leucine by Sestrin2

Sestrin2 binds leucine through a single pocket formed at the intersection of helices C2, C3, and C7 in the CTD. Charged residues Glu^{451} and Arg^{390} form two sides of the pocket and anchor leucine in place through salt bridges with the free amine and carboxyl groups, respectively (Fig. 2, A and B). In addition, helix L1 in the linker domain packs against the side of the pocket via residue Leu^{261} (fig. S3A). This is consistent with mutagenesis studies that identified Glu^{451} and Leu^{261} as critical for leucine binding (*20*). Meanwhile, the isopropyl side chain of the bound leucine points down toward the hydrophobic base of the pocket, forming extensive van der Waals contacts with residues Leu^{389}, Trp^{444}, and Phe^{447} (Fig. 2, A and B). The depth and overall hydrophobicity of this pocket floor make it well suited to accommodate leucine (Fig. 2B).

To test the importance of these protein-ligand interactions, we generated a series of Sestrin2 leucine-pocket mutants. Disrupting the electrostatic coordination of the free amine by switching a single oxygen atom in Glu^{451} to nitrogen [Glu^{451}→Gln^{451}(E451Q)] resulted in a complete loss of leucine binding, as did eliminating the interaction between Arg^{390} and the free carboxyl (R390A; Fig. 2C). In addition, although leucine readily triggered dissociation of the wild-type Sestrin2-GATOR2 complex, both the E451Q and R390A mutants remained constitutively bound to GATOR2, even in the presence of leucine (Fig. 2D). The hydrophobic integrity of the pocket floor is also critical: The insertion of a single charged residue (W444E) was sufficient to abolish any detectable interaction with leucine (Fig. 2, C and D). Consistent with an essential role for these residues in leucine sensing, a multiple sequence alignment of Sestrin homologs showed that both Glu^{451} and Arg^{390} are strictly conserved in Sestrin proteins across phylogenetically diverse organisms, as is the hydrophobic nature of the pocket floor (Fig. 2E).

These results provide a molecular explanation for how the Sestrin2-mTORC1 pathway specifically detects leucine and not other amino acids. Although Glu^{451} and Arg^{390} probably interact with any amino acid containing free amine and carboxyl groups, the hydrophobic base of the pocket excludes all charged and polar amino acids. Furthermore, large hydrophobic residues such as phenylalanine will clash with Trp^{444} in the pocket floor, whereas small aliphatic amino acids such as alanine or valine will fail to make favorable van der Waals contacts. Thus, only leucine and the structurally similar amino acids isoleucine and methionine interact appreciably. This is consistent with the finding that only leucine and, to a much

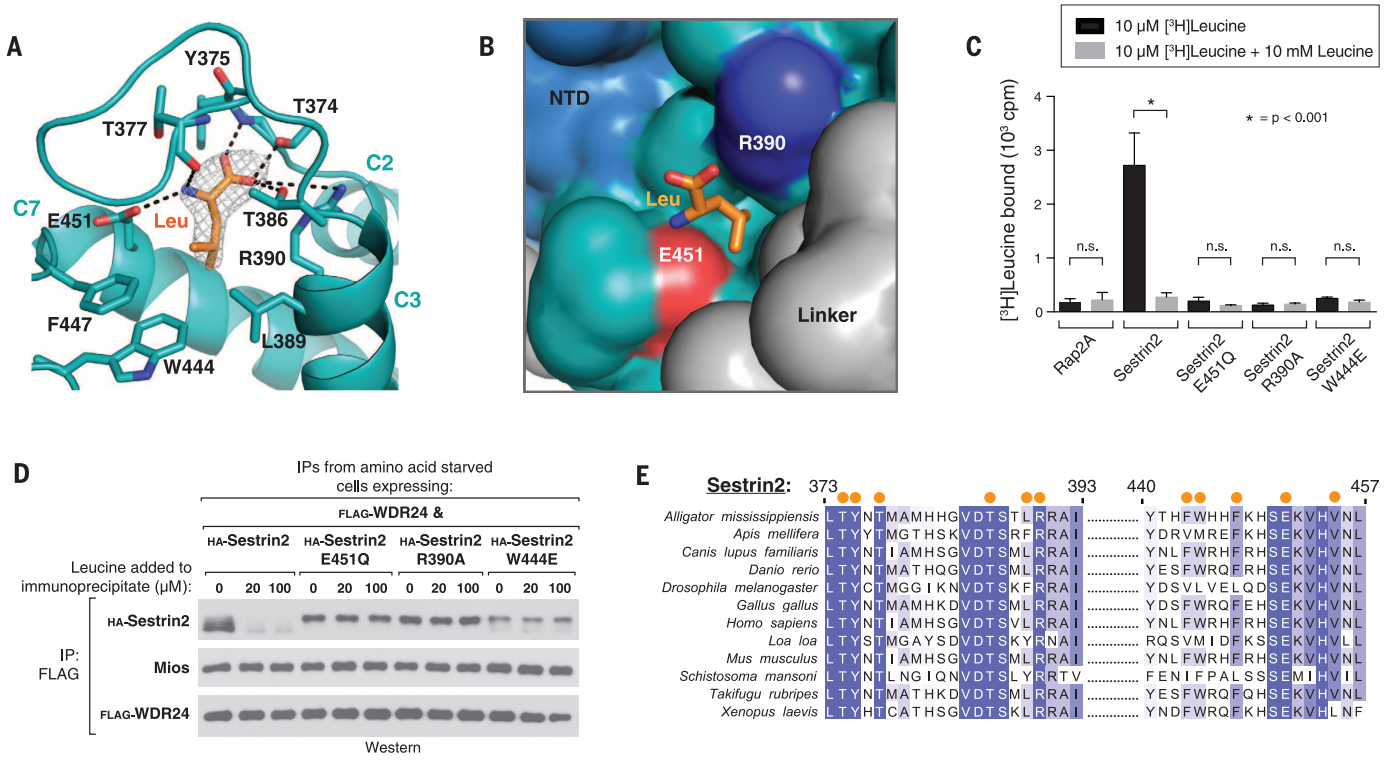

Fig. 2. Recognition of leucine by Sestrin2. (**A**) Close-up view of the leucine-binding pocket in Sestrin2, focusing on the bound leucine (shown in orange) together with its $2F_o–F_c$ electron density map, which was calculated and contoured at 1.5σ from an omit map lacking leucine and all pocket residues. Predicted hydrogen bonds or salt bridges are shown as black dashed lines. Helix numbers are labeled as in Fig. 1A. (**B**) Surface representation of leucine-bound Sestrin2, focusing on the leucine-binding pocket. The bound leucine is represented as a stick model (orange). Residues 373 to 387 are omitted to allow visibility of the pocket. Residue Glu^{451}, which contacts the amine of leucine, is shown in red; Arg^{390}, which contacts the carboxyl of leucine, is shown in blue. The domains of Sestrin2 are colored as in Fig. 1A. (**C**) Binding of the E451Q, R390A, and W444E mutants of Sestrin2 to leucine. HA immunoprecipitates prepared from HEK-293T cells transiently expressing the indicated HA-tagged proteins were used in binding assays with [^{3}H]leucine. Binding was analyzed as in Fig. 1E. (**D**) Effect of leucine on the interactions of Sestrin2 E451Q, R390A, or W444L with GATOR2. FLAG immunoprecipitates were prepared from cells stably expressing FLAG-WDR24 and transiently expressing the indicated HA-tagged Sestrin2 constructs. The immunoprecipitates were treated with the indicated concentrations of leucine and analyzed by immunoblotting for the indicated proteins. (**E**) Multiple sequence alignment of Sestrin2 homologs from various organisms. The positions of residues contacting leucine are indicated with orange dots. Positions are colored white to blue according to increasing sequence identity.

lesser extent, isoleucine and methionine disrupt the Sestrin2-GATOR2 interaction in vitro (*20*).

The corresponding region in the NTD of Sestrin2 is filled by protein side chains and cannot accommodate leucine (fig. S3B). However, the positions of key residues including Trp^{444} and Glu^{451} are conserved in the NTD pocket (Trp^{189} and Glu^{193}), and a leucine side chain contributed by Leu^{107} occupies the same position as the bound leucine in the CTD (fig S3B).

A lid-latch mechanism is required for leucine binding by Sestrin2

In addition to contacting the charged sides and hydrophobic base of the pocket, a "lid" formed by a loop connecting helices C2 and C3 encloses the top of the leucine, so that it is completely buried within the structure (Fig. 2A). Three highly conserved threonine residues (Thr^{374}, Thr^{377}, and Thr^{386}) are positioned directly above the leucine and help coordinate the free amine and carboxyl groups, locking the ligand in place (Figs. 2E and 3A). The side chain hydroxyl groups of Thr^{374} and Thr^{386} make hydrogen bond contacts with the carboxyl group of leucine, whereas the free amine donates a hydrogen bond to the backbone carbonyl of Thr^{377} (Figs. 2A and 3A).

To analyze the importance of these lid interactions for leucine detection by Sestrin2, we generated mutants that we predicted would eliminate the critical contacts between the lid and leucine. Mutation of either Thr^{374} or Thr^{386} (T374A or T386A) abolished the interaction with leucine and resulted in a constitutive interaction with GATOR2 (Fig. 3, C and D), demonstrating a crucial role for the lid in leucine binding.

Although our in vitro binding data demonstrated a requirement for both the N- and C-terminal halves of Sestrin2 (Fig. 1D), the structural model shows that the bound leucine only makes direct contacts with residues in the CTD (Fig. 2A). Further structural analysis, however, revealed that the lid residue Tyr^{375} forms a tight hydrogen bond with the N-terminal residue His^{86}, located in a loop between helices N2 and N3 adjacent to the leucine-binding pocket (Fig. 3B). This interaction appears to form a "latch," which locks the lid in place over the bound leucine. This interdomain contact appears to be critical for the Sestrin2-leucine interaction, given that specifically eliminating this hydrogen-bonded latch with either a Y375F or H86A mutation abolished leucine binding (Fig. 3, C and D). Both Tyr^{375} and His^{86} are also highly conserved in Sestrin proteins across organisms (Fig. 2E and fig. S4). The requirement for His^{86} to maintain the latch interaction probably explains why the NTD of the protein is also essential for the interaction with leucine.

Altering the leucine sensitivity of the mTORC1 pathway in cells

One prediction for a bona fide cellular leucine sensor is that its affinity for leucine should in part determine the sensitivity of the mTORC1 pathway to leucine. We tested this hypothesis directly by generating a mutant of Sestrin2 with a lower affinity for leucine. We predicted that deepening the hydrophobic base of the pocket by mutating Trp^{444} to Leu (W444L) would reduce the van der Waals contacts with the bound leucine side chain, thereby weakening but not eliminating the interaction (Fig. 4A).

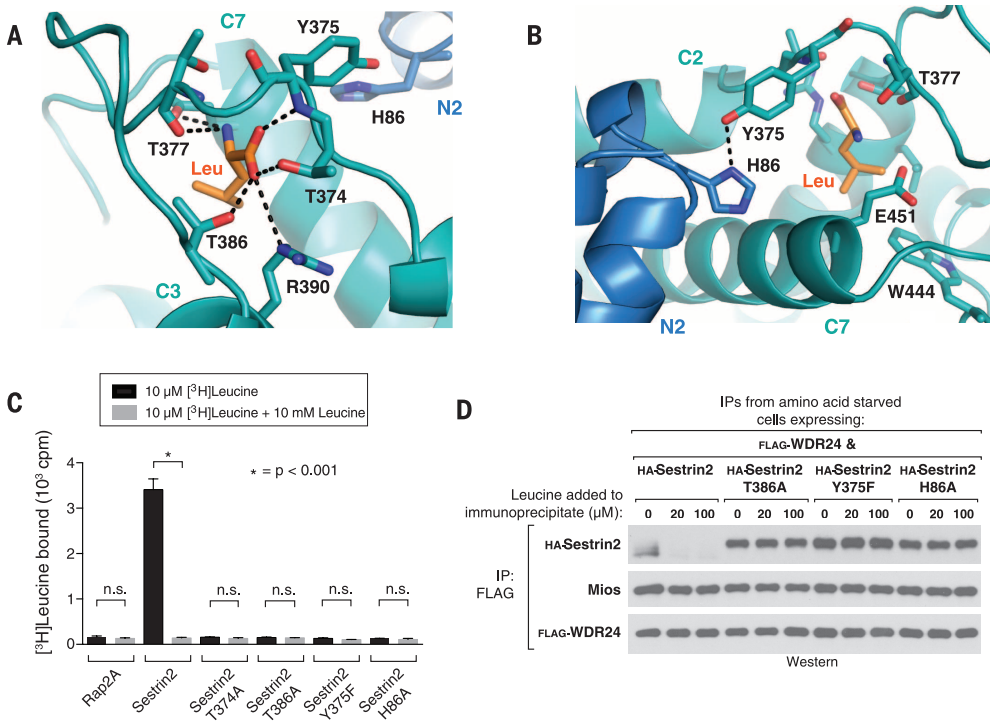

Fig. 3. A lid-latch mechanism is required for leucine binding by Sestrin2. (**A**) Top-down view of the leucine-bound pocket, focusing on the lid residues Thr[374], Thr[377], and Thr[386], which form hydrogen bonds with the amine and carboxyl groups of leucine (indicated by black dashed lines). Leucine is represented as a stick model (orange). Helix numbers are labeled as in Fig. 1A. (**B**) Orthogonal view of the leucine-binding pocket, focusing on the latch formed by the predicted hydrogen bond between Tyr[375] and His86, which locks the lid in place over the bound leucine (orange). Helix numbers are labeled as in Fig. 1A. (**C**) Binding of Sestrin2 T374A, T386A, Y375F, and H86A mutants to leucine. Binding assays were performed and immunoprecipitates analyzed as in Fig. 2C. (**D**) Effect of leucine on the interactions of Sestrin2 T386A, Y375F, or H86A with GATOR2 in vitro. FLAG immunoprecipitates were prepared from cells stably expressing FLAG-WDR24 and transiently expressing the indicated HA-tagged Sestrin2 constructs and were analyzed as in Fig. 2D.

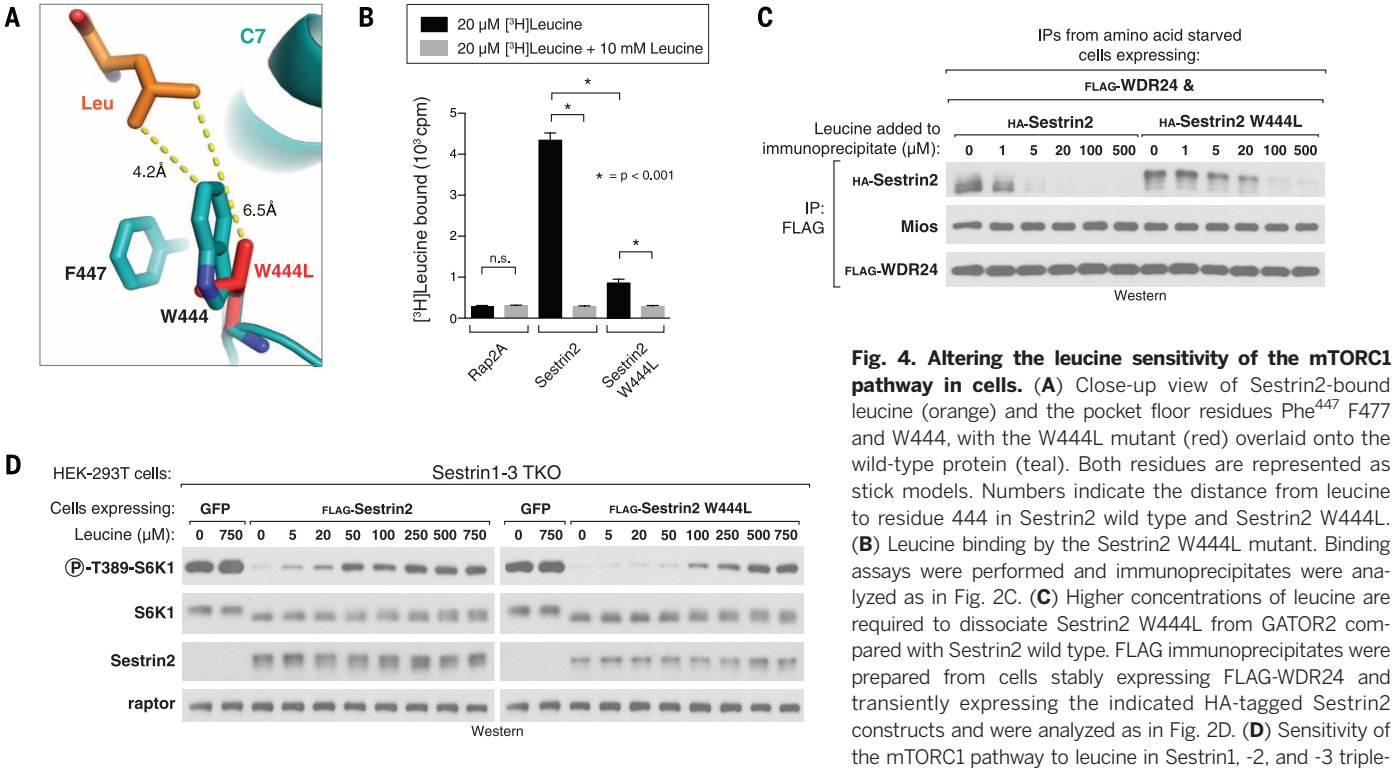

Fig. 4. Altering the leucine sensitivity of the mTORC1 pathway in cells. (**A**) Close-up view of Sestrin2-bound leucine (orange) and the pocket floor residues Phe[447] F477 and W444, with the W444L mutant (red) overlaid onto the wild-type protein (teal). Both residues are represented as stick models. Numbers indicate the distance from leucine to residue 444 in Sestrin2 wild type and Sestrin2 W444L. (**B**) Leucine binding by the Sestrin2 W444L mutant. Binding assays were performed and immunoprecipitates were analyzed as in Fig. 2C. (**C**) Higher concentrations of leucine are required to dissociate Sestrin2 W444L from GATOR2 compared with Sestrin2 wild type. FLAG immunoprecipitates were prepared from cells stably expressing FLAG-WDR24 and transiently expressing the indicated HA-tagged Sestrin2 constructs and were analyzed as in Fig. 2D. (**D**) Sensitivity of the mTORC1 pathway to leucine in Sestrin1, -2, and -3 triple-knockout (TKO) cells expressing Sestrin2 wild type or W444L. HEK-293T cells generated with the CRISPR/Cas9 system expressing the indicated proteins via lentiviral transduction. Cells were starved of leucine for 50 min and then restimulated with the indicated amount of leucine for 10 min. Cell lysates from one representative experiment were prepared and analyzed via immunoblotting.

Consistent with this, the Sestrin2 W444L mutant bound one-sixth to one-eighth the amount of leucine that bound to wild-type Sestrin2 (Fig. 4B). Furthermore, the addition of ~10 to 15 times more leucine was required to fully dissociate the W444L mutant from GATOR2, as compared with wild-type Sestrin2 (Fig. 4C).

To test the effect of this mutation on mTORC1 signaling in cells, we used a HEK-293T cell line in which Sestrin1, -2, and -3 were knocked out by the CRISPR-Cas9 system (Sestrin TKO cells). The mTORC1 signaling in these cells is fully resistant to leucine deprivation, and reintroduction of wild-type Sestrin2 restores normal signaling, with half-maximal mTORC1 activity occurring on addition of ~20 to 50 μM leucine (Fig. 4D) (*20*). Expression of Sestrin2 W444L in the Sestrin TKO lines, however, shifted the dose response of mTORC1 to leucine, so that addition of ~250 to 500 μM was required to achieve half-maximal activation of the pathway (Fig. 4D). Thus, the affinity of Sestrin2 for leucine is a major determinant of the sensitivity of the mTORC1 pathway to leucine in human cells.

Although the overall hydrophobicity of the pocket floor is well conserved, the specific residues present at the W444 and F447 positions vary across organisms, and some organisms, including *Drosophila*, carry the corresponding W444L mutation (Fig. 2E). These differences may alter the shape and depth of the leucine-binding pocket, leading to different affinities or specificities for leucine in different organisms. This may represent an evolutionary adaptation to enable efficient sensing of leucine concentrations that are physiologically relevant in these organisms.

Characterizing the GATOR2 binding site on Sestrin2

To better understand how leucine binding triggers dissociation of Sestrin2 from GATOR2, we sought to structurally characterize the GATOR2 binding interface of Sestrin2. Mutagenesis studies identified residue S190 in the NTD as required for GATOR2 binding (*20*); however, this site is distal to the leucine-binding pocket. Mapping electrostatic potential onto the solvent-exposed surface of Sestrin2 revealed a region in close proximity to the leucine-binding site that contains the highly conserved charged residues Asp^{406} and Asp^{407} (Fig. 5A and fig. S5, A and B). Mutating these residues to alanine (DD406-7AA) completely eliminated GATOR2 binding without affecting leucine binding (Fig. 5B and fig. S5C), suggesting that this region is required for the Sestrin2-GATOR2 interaction. Therefore, Sestrin2 may make multiple contacts with GATOR2 through both the NTD and CTD (Figs. 5C and 1B), consistent with both halves of Sestrin2 being required for GATOR2 binding (Fig. 1D).

Conclusions

Our results provide a structural model of leucine sensing by the Sestrin2-mTORC1 pathway and shed light on the mechanism through which mTORC1 couples cell growth to leucine availability. The structure shows that Sestrin2 contains an evolutionarily unique leucine-binding pocket consisting of a hydrophobic floor that determines specificity for the side chain of leucine, with adjacent glutamate and arginine residues that coordinate the free amine and carboxyl groups, respectively. An additional lid-latch mechanism helps lock the ligand in place and is required for binding.

Our structure also reveals a highly conserved GATOR2 binding site in close proximity to the leucine-binding pocket, suggesting possible mechanisms for how leucine binding can cause dissociation of Sestrin2 from GATOR2. The key residues for the GATOR2 interaction, Asp^{406} and Asp^{407}, are located on a loop separated from the lid of the pocket by the 15-residue helix C3 (Fig. 5A). It is therefore conceivable that a conformational change in the lid, corresponding to leucine binding or release, could transmit a conformational

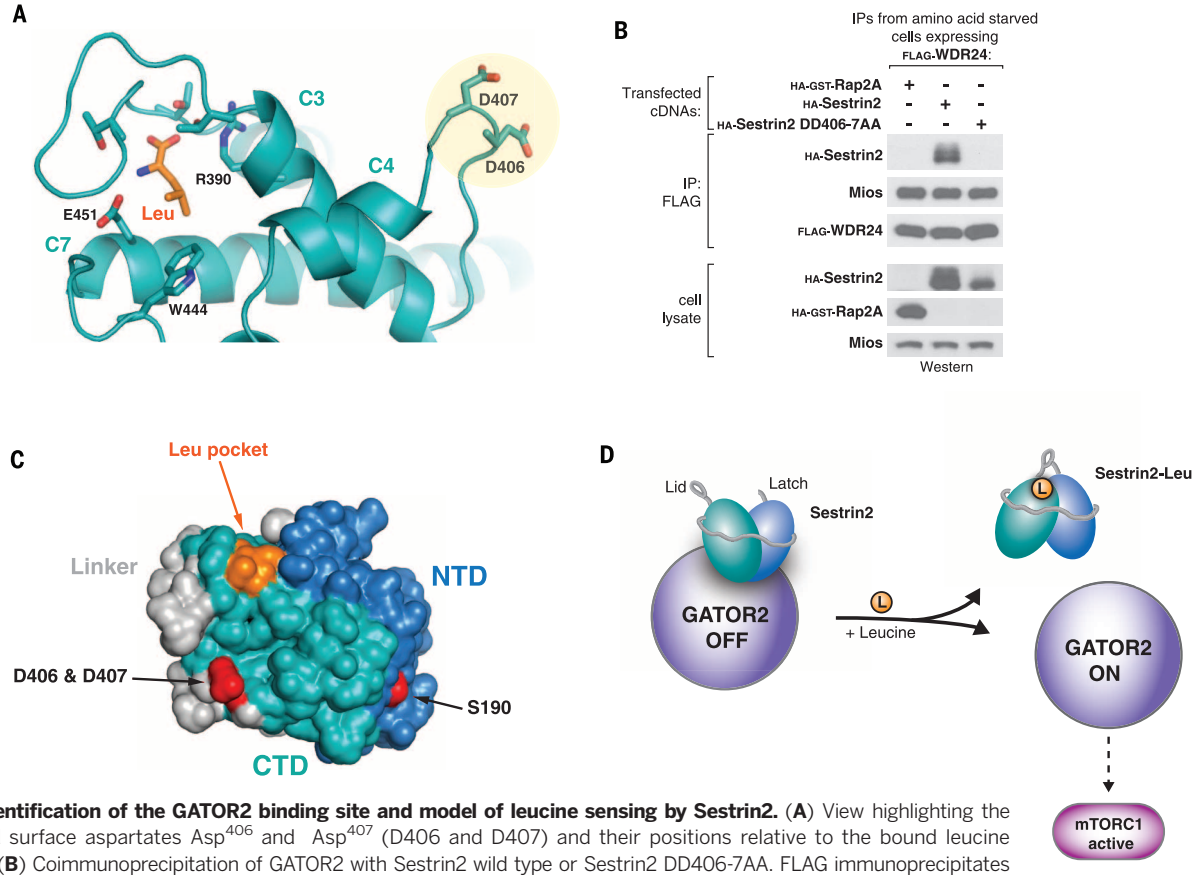

Fig. 5. Identification of the GATOR2 binding site and model of leucine sensing by Sestrin2. (**A**) View highlighting the conserved surface aspartates Asp^{406} and Asp^{407} (D406 and D407) and their positions relative to the bound leucine (orange). (**B**) Coimmunoprecipitation of GATOR2 with Sestrin2 wild type or Sestrin2 DD406-7AA. FLAG immunoprecipitates were prepared from cells stably expressing FLAG-WDR24 and transiently expressing the indicated HA-tagged Sestrin2 constructs and were analyzed as in Fig. 2D. (**C**) Surface view of Sestrin2, highlighting the GATOR2 binding sites (red) and their positions relative to the leucine-binding pocket (orange). Domains are colored as in Fig. 1A. (**D**) Model of leucine sensing by Sestrin2. Binding of leucine (orange) causes closing of the lid-latch, resulting in a conformational change that alters the position of the GATOR2 binding site in the CTD. This leads to dissociation of Sestrin2 from GATOR2, enabling GATOR2 to activate the mTORC1 pathway.

change to the GATOR2 binding site via movement of helix C3 (Fig. 5D). Alternatively, a segment of the partially disordered linker domain, which contacts the leucine-binding pocket via Leu261 in helix L1 (fig. S3A), is also in close proximity to the GATOR2 binding site in our structure (Fig. 5C). Therefore, changes in the leucine-binding state of Sestrin2 could potentially alter the position of the linker domain, thereby affecting the availability of the GATOR2 binding site.

Despite these insights, several important questions remain. Fully understanding how leucine binding causes dissociation of Sestrin2 from GATOR2 will probably require ascertaining the structure of either apo-Sestrin2 or the Sestrin2-GATOR2 complex. Furthermore, understanding the exact mechanism by which Sestrin2 inhibits the mTORC1 pathway awaits the elucidation of the molecular function of GATOR2.

Finally, as a critical regulator of cell growth, mTORC1 is misregulated in various human diseases, including cancer and diabetes, as well as in aging (*1*, *29*). By revealing the mechanism through which a natural small molecule regulates this pathway, our results may enable the identification of compounds to pharmacologically target the nutrient-sensing pathway upstream of mTORC1 in vivo.

REFERENCES AND NOTES

1. R. Zoncu, A. Efeyan, D. M. Sabatini, *Nat. Rev. Mol. Cell Biol.* **12**, 21–35 (2011).
2. C. C. Dibble, B. D. Manning, *Nat. Cell Biol.* **15**, 555–564 (2013).
3. J. L. Jewell, R. C. Russell, K. L. Guan, *Nat. Rev. Mol. Cell Biol.* **14**, 133–139 (2013).
4. M. Potier, N. Darcel, D. Tomé, *Curr. Opin. Clin. Nutr. Metab. Care* **12**, 54–58 (2009).
5. J. S. Greiwe, G. Kwon, M. L. McDaniel, C. F. Semenkovich, *Am. J. Physiol. Endocrinol. Metab.* **281**, E466–E471 (2001).
6. K. S. Nair, R. G. Schwartz, S. Welle, *Am. J. Physiol.* **263**, E928–E934 (1992).
7. H. L. Fox, P. T. Pham, S. R. Kimball, L. S. Jefferson, C. J. Lynch, *Am. J. Physiol.* **275**, C1232–C1238 (1998).
8. C. J. Lynch, H. L. Fox, T. C. Vary, L. S. Jefferson, S. R. Kimball, *J. Cell. Biochem.* **77**, 234–251 (2000).
9. A. Efeyan, D. M. Sabatini, *Biochem. Soc. Trans.* **41**, 902–905 (2013).
10. C. Buerger, B. DeVries, V. Stambolic, *Biochem. Biophys. Res. Commun.* **344**, 869–880 (2006).
11. K. Saito, Y. Araki, K. Kontani, H. Nishina, T. Katada, *J. Biochem.* **137**, 423–430 (2005).
12. L. Bar-Peled, L. D. Schweitzer, R. Zoncu, D. M. Sabatini, *Cell* **150**, 1196–1208 (2012).
13. Y. Sancak *et al.*, *Science* **320**, 1496–1501 (2008).
14. Y. Sancak *et al.*, *Cell* **141**, 290–303 (2010).
15. R. V. Durán, M. N. Hall, *EMBO Rep.* **13**, 121–128 (2012).
16. R. Zoncu *et al.*, *Science* **334**, 678–683 (2011).
17. S. Wang *et al.*, *Science* **347**, 188–194 (2015).
18. M. Rebsamen *et al.*, *Nature* **519**, 477–481 (2015).
19. L. Bar-Peled *et al.*, *Science* **340**, 1100–1106 (2013).
20. R. L. Wolfson *et al.*, *Science* **351**, 43–48 (2016).
21. L. Chantranupong *et al.*, *Cell Rep.* **9**, 1–8 (2014).
22. A. Parmigiani *et al.*, *Cell Rep.* **9**, 1281–1291 (2014).
23. F. H. Niesen, H. Berglund, M. Vedadi, *Nat. Protoc.* **2**, 2212–2221 (2007).
24. A. V. Budanov, A. A. Sablina, E. Feinstein, E. V. Koonin, P. M. Chumakov, *Science* **304**, 596–600 (2004).
25. J. F. Gibrat, T. Madej, S. H. Bryant, *Curr. Opin. Struct. Biol.* **6**, 377–385 (1996).
26. H. A. Woo, S. H. Bae, S. Park, S. G. Rhee, *Antioxid. Redox Signal.* **11**, 739–745 (2009).
27. A. Koshkin, C. M. Nunn, S. Djordjevic, P. R. Ortiz de Montellano, *J. Biol. Chem.* **278**, 29502–29508 (2003).
28. M. Peng, N. Yin, M. O. Li, *Cell* **159**, 122–133 (2014).
29. M. Laplante, D. M. Sabatini, *Cell* **149**, 274–293 (2012).

ACKNOWLEDGMENTS

D.M.S. is a founder, a member of the Scientific Advisory Board, a paid consultant, and a shareholder of Navitor Pharmaceuticals, which is targeting for therapeutic benefit the amino acid sensing pathway upstream of mTORC1. We thank all members of the Sabatini and Schwartz laboratories for helpful insights. We also thank Cell Signaling Technologies for providing many antibodies. This work is based on research conducted at the Northeastern Collaborative Access Team beamlines, which are funded by the National Institute of General Medical Sciences from the National Institutes of Health (P41 GM103403). The Pilatus 6M detector on 24-ID-C beam line is funded by a NIH-ORIP HEI grant (S10 RR029205). This research used resources of the Advanced Photon Source, a U.S. Department of Energy (DOE) Office of Science User Facility operated for the DOE Office of Science by Argonne National Laboratory under contract no. DE-AC02-06CH11357. This work was supported in part by the NIH Predoctoral Training Grant T32GM007287. This work has also been supported by grants from NIH (R01CA103866 and AI47389) and the U.S. Department of Defense (W81XWH-07- 0448) to D.M.S. Fellowship support was provided by NIH to R.L.W. (awards T32 GM007753 and F30 CA189333), L.C. (F31 CA180271), and T.W. (F31 CA189437). T.W. is also supported by an award from the MIT Whitaker Health Sciences Fund. M.E.P. is supported by the Sally Gordon Fellowship of the Damon Runyon Cancer Research Foundation (award DRG-112-12) and a Department of Defense Breast Cancer Research Program Postdoctoral Fellowship (award BC120208). D.M.S. is an investigator of the Howard Hughes Medical Institute. Coordinates and structure factors for the x-ray crystal structures of Sestrin2 have been deposited in the Protein Data Bank (PDB) with accession code 5DJ4.

SUPPLEMENTARY MATERIALS

www.sciencemag.org/content/351/6268/53/suppl/DC1
Materials and Methods
Figs. S1 to S6
Table S1
References (*30*–*44*)

11 August 2015; accepted 5 November 2015
Published online 19 November 2015
10.1126/science.aad2087

REPORTS

3D PRINTING

Additive manufacturing of polymer-derived ceramics

Zak C. Eckel, Chaoyin Zhou, John H. Martin, Alan J. Jacobsen, William B. Carter, Tobias A. Schaedler*

The extremely high melting point of many ceramics adds challenges to additive manufacturing as compared with metals and polymers. Because ceramics cannot be cast or machined easily, three-dimensional (3D) printing enables a big leap in geometrical flexibility. We report preceramic monomers that are cured with ultraviolet light in a stereolithography 3D printer or through a patterned mask, forming 3D polymer structures that can have complex shape and cellular architecture. These polymer structures can be pyrolyzed to a ceramic with uniform shrinkage and virtually no porosity. Silicon oxycarbide microlattice and honeycomb cellular materials fabricated with this approach exhibit higher strength than ceramic foams of similar density. Additive manufacturing of such materials is of interest for propulsion components, thermal protection systems, porous burners, microelectromechanical systems, and electronic device packaging.

In comparison with metals and polymers, ceramics are difficult to process, particularly into complex shapes. Because they cannot be cast or machined easily, ceramics are typically consolidated from powders by sintering or deposited in thin films. Flaws, such as porosity and inhomogeneity introduced during processing, govern the strength because they initiate cracks, and—in contrast to metals—brittle ceramics have little ability to resist fracture. This processing challenge has limited our ability to take advantage of ceramics' impressive properties, including high-temperature capability, environmental resistance, and high strength. Recent advances in additive manufacturing have led to a multitude of different techniques, but all additive manufacturing techniques developed for ceramic materials are powder-based layer-by-layer processes that are restricted to a small number of compositions (*1*, *2*). Only a few of the commercially available three-dimensional (3D) printing systems offer printing of ceramics, either by selective curing of a photosensitive resin that contains ceramic particles, selective deposition of a liquid binder agent onto ceramic particles (binder jetting), or selective fusion of a powder bed with a laser (*3*, *4*). All these techniques are limited by slow fabrication rates, and in many cases, a time-consuming binder removal process. By starting with powders, consolidation to a dense part is an almost insurmountable challenge, and residual porosity is typically unavoidable. Furthermore, many additive processes introduce large thermal gradients that tend to cause cracks in ceramics. Pores, cracks, and inhomogeneities are responsible for the low strength and poor reliability of additively manufactured ceramic parts.

Polymer-derived ceramics were discovered in the 1960s (*5*). Upon heat treatment (typically under inert atmosphere), they pyrolyze into SiC, Si_3N_4,

HRL Laboratories, LLC, 3011 Malibu Canyon Road, Malibu, CA 90265, USA.
*Corresponding author. E-mail: taschaedler@hrl.com

BN, AlN, SiOC, SiCN, BCN, or other compositions, whereas volatile species (CH_4, H_2, CO_2, H_2O, and hydrocarbons) leave the material. Preceramic polymers are currently used to synthesize ceramic fibers and to densify ceramic matrix composites by infiltration. Two-dimensional photolithography and soft lithography have been demonstrated (*6*, *7*). The absence of a sintering step enables lower synthesis temperatures without the need for pressure, as compared with classical ceramic powder processing, and the absence of sintering additives results in improved thermomechanical properties (*8*).

By attaching thiol, vinyl, acrylate, methacrylate, or epoxy groups to an inorganic backbone such as a siloxane, silazane, or carbosilane, ultraviolet (UV)–active preceramic monomers can be obtained (*7*, *9*). Two different additive manufacturing techniques based on photopolymerization can be used to achieve spatial control. For conventional stereolithography (SLA), sufficient polymerization inhibitor and UV absorber are added to the resin formulation to confine the polymerization to the laser exposure point and to minimize scatter to maintain fidelity in the features of the printed part. UV light is then scanned across the resin surface to expose a cross section and build up a thin slice (30 to 100 μm) of the part to be manufactured. Although almost any geometry can be fabricated with this approach, the process is slow, because every 30- to 100-μm thin layer has to be exposed separately. Structures with linear features extending from the exposure surface, such as lattices and honeycombs, can be formed 100 to 1000 times as rapidly with the self-propagating photopolymer waveguide technology (SPPW) (*10*, *11*). Monomers are selected to promote a change in the index of refraction upon polymerization, which causes internal reflection of the UV light, trapping it in the already-formed polymer. This exploits a self-focusing effect that forms a polymer waveguide, tunneling the light toward the tip of the waveguide and causing it to polymerize further. This reduces the need for additives that control scatter and UV absorption. The architecture of the material or structure can then be defined by a patterned mask that defines the areas exposed to a collimated UV light source (*10*).

Both methods produce parts consisting of cross-linked polymer (Fig. 1), where the cross-link density depends on exposure parameters and can be increased by thermal treatments or additional UV exposure. Unpolymerized resin can be recycled and reused.

The configuration and microstructure of the preceramic polymer determine the composition, microstructure, and yield of ceramic after pyrolysis. A high cross-link density is necessary to prevent the loss of low–molecular mass species and fragmentation during pyrolysis. Siloxane-based polymers with their Si-O-Si backbone result in silicon oxycarbides, whereas silazanes introduce nitrogen due to their Si-N-Si backbone. Combining siloxanes with silazanes results in a SiOCN ceramic after pyrolysis. The addition of silane compounds typically reduces the amount of oxygen and pushes the ceramic composition toward SiC (*8*). The ratio of carbon in the final ceramic can be tailored by adding phenyl groups on the side chain of the polymer or using a carbon-based cross-linking agent such as divinyl benzene. The precursor chemistry can also be changed to incorporate other elements—for example, B or Zr to enhance temperature capability (*12*); Fe, Co, or Ni to introduce magnetic properties; or Cu, Pd, or Pt for catalytic properties (*13*). To fabricate the structures shown in Fig. 1 a UV-curable siloxane resin system was formulated by mixing (mercaptopropyl) methylsiloxane with vinylmethoxysiloxane and adding UV free-radical photo initiator, free-radical inhibitor, and UV absorber. The resulting liquid resin was used in a benchtop stereolithography 3D printer (Formlabs Form 1+). To fabricate the larger microlattice and honeycomb structures via SPPW for mechanical testing, the resin was reformulated without UV absorber, poured into a DELRIN reservoir, and exposed with UV light through a patterned mask (see the supplementary materials for details).

Pyrolysis at 1000°C in argon was accompanied by 42% mass loss and 30% linear shrinkage. The resultant ceramic is amorphous, as ascertained by x-ray diffraction (XRD) and transmission electron microscopy (TEM), and has a composition of 26.7 atomic percent (at %) Si, 33.4 at % C, 4.1 at % S, and 35.8 at % O, or $SiO_{1.34}C_{1.25}S_{0.15}$, as measured by inductively coupled plasma mass spectrometry. The ceramic structures fabricated are fully dense, with no porosity or surface cracks observed by scanning electron microscopy and TEM (Fig. 2). Ceramic parts fabricated with the self-propagating photopolymer waveguide process exhibit a very smooth surface (Fig. 2A), whereas parts fabricated by stereolithography show the typical steps at the surface from the layer-by-layer printing process (Fig. 2C). As the undulations could act as stress concentrators and negatively affect the mechanical properties, all mechanical tests were performed on parts fabricated by SPPW. The SiOC ceramic fractures in a conchoidal manner typical for brittle amorphous materials, with curved breakage surfaces and ripples (Fig. 2B). To avoid shattering on pyrolysis, the printed polymer structure is typically limited to features with less than ~3 mm in thickness in one dimension and the heating rate to less than 20°C/min, so that evolving gases can escape. By selecting appropriate cellular architectures, large

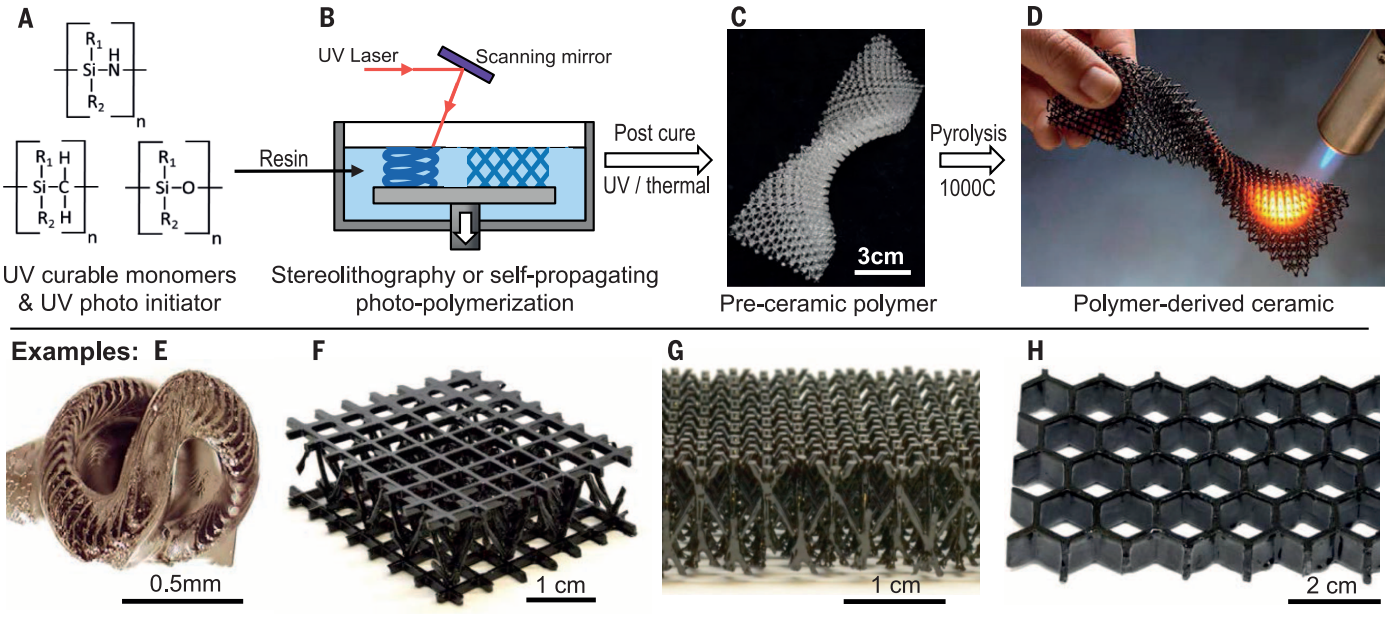

Fig. 1. Additive manufacturing of polymer-derived ceramics. (**A**) UV-curable preceramic monomers are mixed with photoinitiator. (**B**) The resin is exposed with UV light in a SLA 3D printer or through a patterned mask. (**C**) A preceramic polymer part is obtained. (**D**) Pyrolysis converts the polymer into a ceramic. Examples: (**E**) SLA 3D printed cork screw. (**F** and **G**) SPPW formed microlattices. (**H**) Honeycomb.

ceramic structures can be fabricated, with the size only limited by the equipment. This fabrication process introduces no noticeable gradients in composition, and temperature gradients can be mitigated by the cellular architecture, resulting in remarkably uniform shrinkage during pyrolysis. The shape of the polymer structure is therefore maintained well and the shrinkage can be predicted, as long as any surfaces in contact with the structure during pyrolysis are lubricated to prevent sticking. Various cellular architectures have been demonstrated with the self-propagating photopolymer waveguide process, including microlattices with densities of 0.22 to 0.35 g/cm^3 (Fig. 1G), honeycombs with densities of 0.3 to 0.8 g/cm^3 (Fig. 1H), and pyramidal truss cores with graded density (fig. S4C).

Compression and shear testing was performed on as-pyrolyzed silicon oxycarbide structures, and the results are summarized in Fig. 3 and table S1. A compressive failure strength of 163 MPa was measured on a honeycomb structure with a density of 0.8 g/cm^3 using a prescribed displacement rate of 10 μm/s. Shear testing was performed on four microlattices with densities of 0.22 to 0.35 g/cm^3 according to ASTM C273, using a single lap shear test fixture, and resulted in ultimate shear strengths in the range of 3.7 to 4.9 MPa and modulus values of 830 to 1570 MPa. Failure in compression was catastrophic by sudden brittle fracture, whereas failure in shear was gradual by successive brittle fracture of single struts. The mechanical properties of silicon oxycarbide microlattice structures are compared to those of ceramic foams of similar density (Fig. 3). Noteworthy is the ~10 times higher compressive strength as compared with commercially available SiC foams (Duocel) and aluminosilicate foam (ceramic insulation) (table S2), as well as silicon oxycarbide foams (*14*). The improvement in shear strength does not appear as large in Fig. 3B because the values reported for SiC and aluminosilicate foams are flexural strength, which is measured by a bending test and is generally higher. Even in comparison to state-of-the-art cellular sandwich core materials, aluminum alloy honeycomb (HexWeb) and closed-cell polymer foam (Divinycell), the polymer-derived ceramic cellular materials look favorable. Sample details and measurement results are summarized in table S1.

The mechanical properties of a cellular material depend on the mechanical properties of the solid constituent material, the relative density of the cellular material, and the cellular architecture (i.e., the spatial configuration of voids and solid). Two factors contribute to the observed high strength. First, the ordered, periodic architectures are inherently more mechanically efficient than a random foam architecture. Gibson and Ashby (*15*) have described the general relationships for the elastic modulus (E) and failure strength (σ) of a cellular material as

$$E \approx C_1 (E_s) (\rho/\rho_s)^{n1} \quad (1)$$
$$\sigma \approx C_2 (\sigma_s) (\rho/\rho_s)^{n2} \quad (2)$$

The terms E_s and σ_s are the elastic modulus and representative failure strength of the solid material, respectively. The term ρ/ρ_s is the relative density of the cellular material, which is defined as its density (ρ) divided by the density of the solid constituent material (ρ_s). ρ_s of SiOC is 2.05 g/cm^3. The proportionality constants C_1 and C_2 are related to the geometric configuration of the cellular material with respect to the loading direction. The exponents n1 and n2 are 2 and 1.5, respectively, for foams, where the cell struts exhibit bending-dominated deformation during elastic loading (*15*). Conversely, a lattice material can exhibit stretching-dominated deformation, when the lattice members are configured so that they are loaded either in tension or compression, which results in much-improved mechanical properties that decrease linearly with density (n1 = 1 and n2 = 1). The ceramic microlattices exhibit a scaling n2 = 1.06 (R^2 = 0.88), and the honeycombs show n2 = 1.18 (R^2 = 0.92), demonstrating stretching-dominated mechanical performance. The difference in compressive strength arising from the different scaling of stretch-dominated versus bending-dominated architecture should be a factor of 3.2 at a relative density of 10% and increases to 5.8 at 3%. The proportionality constant C_2 for a brittle foam is ~0.2 (*15*), whereas the constant is estimated to be

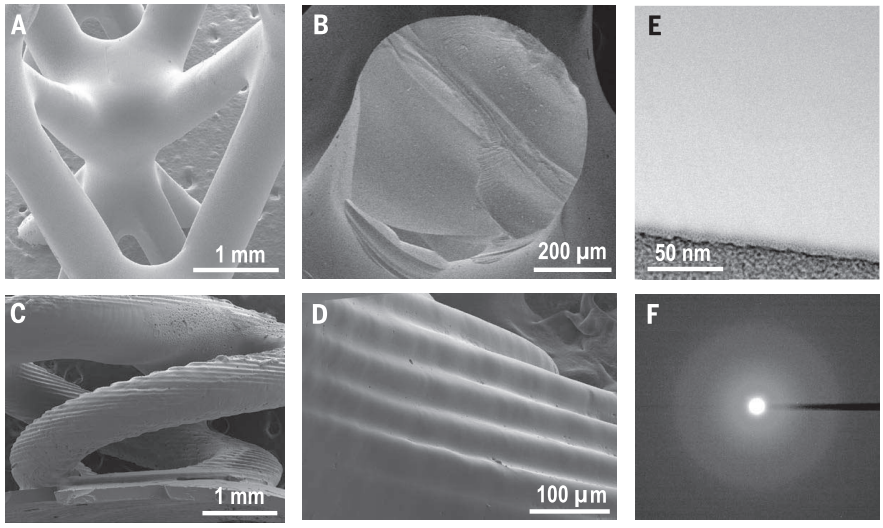

Fig. 2. Electron microscopy characterization of SiOC microlattice and cork screw. (**A**) SPPW-formed lattice node showing smooth surface. (**B**) Fracture surface of a strut. (**C**) SLA printed corkscrew showing undulations on the surface. (**D**) 3D printing step size is 50 μm. (**E**) Bright-field TEM image showing no porosity. (**F**) TEM diffraction indicating amorphous structure.

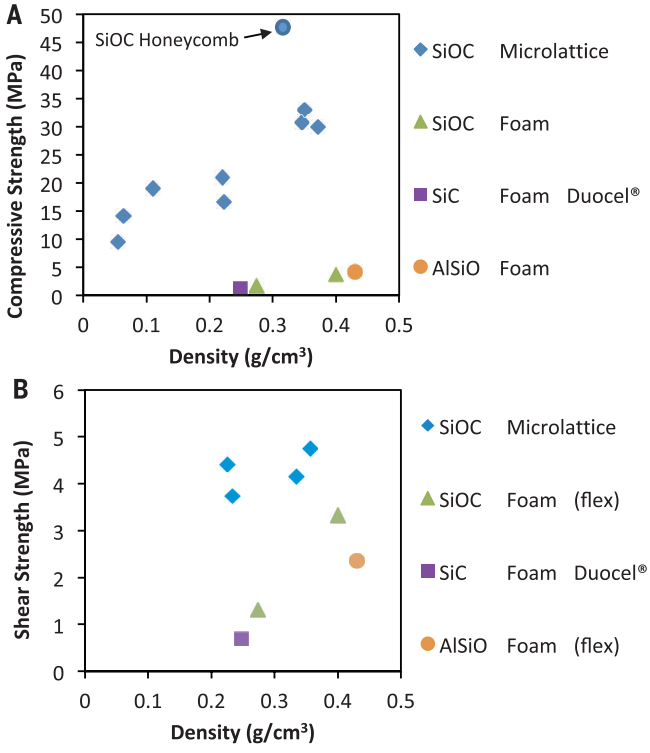

Fig. 3. Strength of polymer-derived SiOC materials compared to ceramic foams. (**A**) Compressive strength. (**B**) Shear strength.

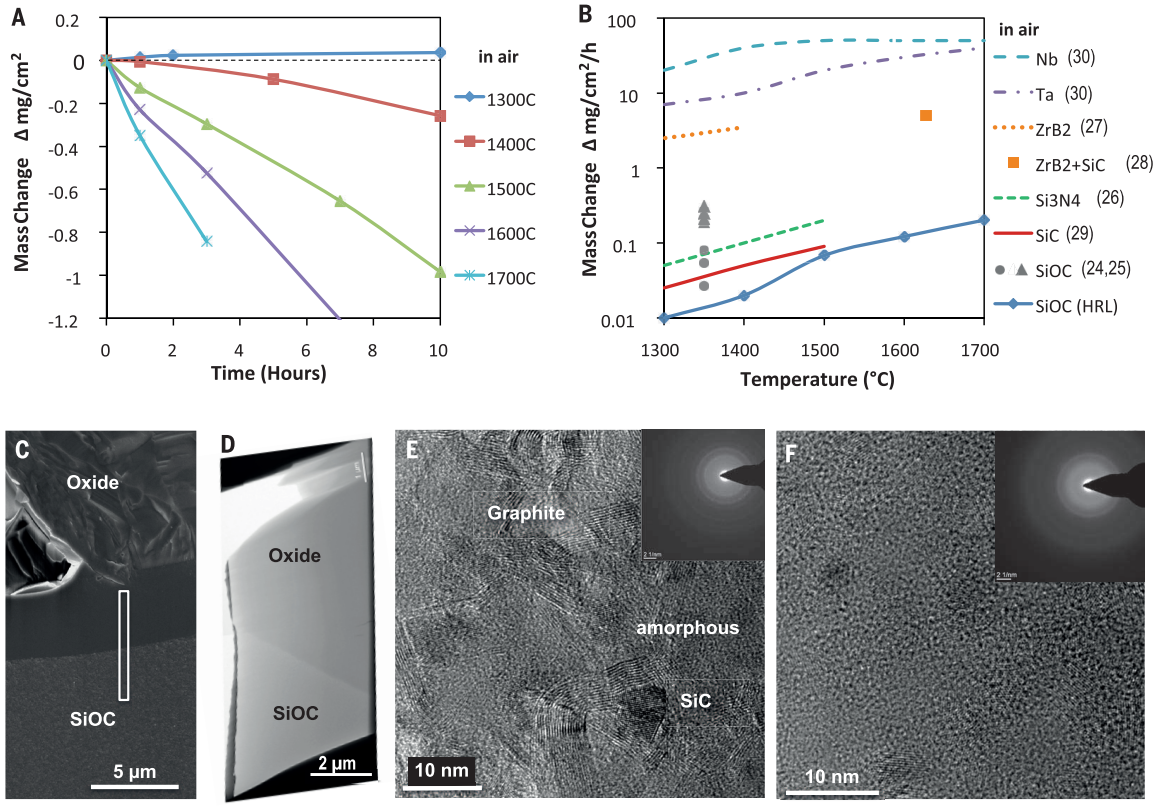

Fig. 4. High-temperature oxidation of silicon oxycarbide microlattice. (**A**) Mass change measured after consecutive heat treatments at different temperatures normalized by surface area. (**B**) Mass change compared with other materials. [Data from (*24*–*30*)] (**C**) Fracture surface of a SiOC microlattice heat-treated 1300°C/10 hours + 1500°C/10 hours selected for extraction of (**D**) Focused ion beam lamella. (**E**) TEM image of the SiOC region. (**F**) TEM image of the SiO_2 region.

1/3 for microlattices (*16*), 0.87 for pyramidal truss structures (*16*), and 1 for honeycombs, accounting for additional increases in strength.

This high intrinsic strength is the second factor besides the architecture contributing to the much higher strength of these cellular materials as compared with previously reported ceramic foams. The high intrinsic strength of polymer-derived silicon oxycarbide is attributed to a low distribution of flaws in the material, as ascertained by the absence of porosity and cracks in electron microscopy. The fracture strength of brittle materials is given by

$$\sigma_{\text{fracture}} = \sqrt{\frac{E\gamma r}{4ad_0}} \qquad (3)$$

where γ is the surface energy and d_0 is the equilibrium distance between atomic centers, which together with E determine the theoretical strength, whereas cracks with half-length a and crack-tip radius r introduce stress concentrations that reduce the fracture strength. Because the flaw population in the polymer-derived ceramic material can be controlled well through the high purity of the starting resin and the development of smooth and pore-free surfaces, higher fracture-strength values with a tighter distribution are measured as compared with other ceramic materials, especially when derived from conventional powder routes. Ultimate strength values are reported, but due to the brittle nature of the material, they coincide with the yield and fracture strength.

To calculate the modulus of the solid constitutive SiOC material, the equation for shear modulus of microlattices (*17*) is used

$$G = \frac{E}{8}\sin^2(2\theta)\frac{\rho}{\rho_s} \qquad (4)$$

Because accurate modulus measurements could only be performed in shear testing. An average Young's modulus of 102 ± 26 GPa is obtained, which is in the range reported for similar compositions (*5*).

The silicon oxycarbide family of polymer-derived ceramics has demonstrated excellent high-temperature properties, including remarkable resistance to crystallization, oxidation, and creep (*8*, *18*). These properties have been ascribed to the amorphous material exhibiting nanodomains of silica tetrahedra that are encased in a network of graphene (*19*). The heart of the 1- to 3-nm domains is formed by silicon-oxygen tetrahedra, and the interdomain boundaries consist of layers of sp^2 carbons. Silicon atoms bonded to one or two carbons substituted for oxygen make up the interface between silica domains and graphene walls (*19*).

The silicon oxycarbide microlattice structures showed excellent stability at high temperatures in air. At 1300°C, the structures gained ~0.15% mass over 10 hours, and most of this mass gain occurred within the first 2 hours. It is hypothesized that this is associated with a replacement reaction at the SiOC surface, creating an amorphous SiO_2 oxide layer and releasing CO or CO_2. This oxide growth was qualitatively observed as a shift in interference coloration at the microlattice surface. After each subsequent heat treatment, there was a shift in iridescent coloration associated with increased thickness of the clear and thin (100 to 1000 nm) oxide scale, consistent with thin-film interference coloration. At 1400°C, the samples showed a slow but steady mass decline of ~1% after 10 hours. This mass loss was attributed to the "burn off" of free carbon in the SiOC structure (*20*). After 10 hours at 1400°C, a hazy surface oxide was observed. This oxidation product was characterized to be cristobalite by XRD. A similar behavior was observed at 1500°C, 1600°C, and 1700°C, albeit with an increasing mass loss rate and more pronounced cristobalite oxidation products (Fig. 4C). The highest temperature to which SiOC samples were exposed was 1700°C, and no degradation other than surface oxidation was observed. The mass loss is normalized by the surface area (Fig. 4A). The change in oxide structure is attributed to the oxidation product being amorphous at or below 1300°C, whereas above 1400°C it crystalizes to cristobalite. O_2 diffusion into the bulk oxidizes available free carbon, and at even higher temperatures, carbothermal reduction of SiO_2 from free carbon in the structure begins (*20*). The oxide shell on the surface appears to slow these reactions by limiting diffusion

of the O_2 into the structure and CO_X products out of the bulk. Upon cooling, there is a phase change with 7% volume change in the cristobalite (*21*), as well as a large shift in coefficient of thermal expansion (*22*), which leads to a cracked surface oxide. Upon reheating, the oxidation appears to restart underneath the cracked oxide layer, leading to a multilayer oxide scale after several heat treatments. X-ray diffraction did not detect phases other than cristobalite, indicating that bulk crystallization products, specifically β-SiC, were not present or were below the detection limit due to their small size and volume fraction (fig. S3). TEM of a sample heat-treated for 10 hours at 1300°C followed by 10 hours at 1500°C revealed the onset of bulk crystallization with scattered β-SiC crystals <10 nm inside the amorphous matrix. A lamella was milled out of a fractured surface of a microlattice strut, as indicated by the rectangle in Fig. 4C, so that oxide and SiOC base material could be analyzed (Fig. 4D). Bright-field images showed small crystallites of a few nanometers in size in both the oxide and SiOC region. High-resolution imaging could identify the crystallites as graphite and β-SiC, based on the lattice spacing and diffraction pattern (Fig. 4E). The small size of 5 to 10 nm of the crystals and the high fraction of remaining amorphous matrix indicate that crystallization had just started. The crystallites in the silicon oxide region are even smaller (Fig. 4F), consistent with the recent formation of this oxide region. Larger crystals are probably present in older oxide layers further from the interface, contributing to the cristobalite diffraction pattern recorded by XRD below. Noteworthy were small pores in the SiOC region that were not observed before the heat treatments and presumably developed due to carbon leaving as CO or CO_2 gas.

This indicates that the amorphous $SiO_{1.34}C_{1.25}S_{0.15}$ is more stable than other silicon oxycarbide compositions, which crystallize sooner (*23*). The high-temperature stability with respect to mass change in air is compared with other materials in Fig. 4B (mass change was extrapolated from reported mass versus time curves after 1 hour exposure in air). The silicon-oxycarbide structures show better oxidation performance than silicon oxycarbide materials from previous studies, which used different starting precursors, compositions, and pyrolysis temperatures (*20*, *24*, *25*). Silicon oxycarbide is more resistant to oxidation than SiC and Si_3N_4 and has been investigated as oxidation protection coating for these materials (*8*).

Various ceramic compositions can be processed with our approach, including materials that are difficult to form via sintering of powders, such as SiOC, Si_3N_4, and SiC ceramics. In this demonstration, we focused on structures out of silicon oxycarbide, and our cellular SiOC materials exhibit strength 10 times as high as commercially available ceramic foams of similar density and survive temperatures of 1700°C in air with surface oxidation. Such cellular ceramic materials are of interest for the core of lightweight, load-bearing ceramic sandwich panels for high-temperature applications—for example, in hypersonic vehicles and jet engines. Stereolithography of ceramics will open opportunities for complex-shaped, temperature- and environment-resistant ceramic structures from the microscale—e.g., in microelectromechanical systems (MEMS) or device packaging—to the macro scale—e.g., in propulsion or thermal protection systems.

REFERENCES AND NOTES

1. J. Deckers, J. Vleugels, J.-P. Kruth, *J. Ceram. Sci. Technol.* **5**, 245–260 (2014).
2. N. Travitzky *et al.*, *Adv. Eng. Mater.* **16**, 729–754 (2014).
3. A. Zocca, P. Colombo, C. M. Gomes, J. Günster, *J. Am. Ceram. Soc.* **98**, 1983–2001 (2015).
4. T. T. Wohlers, T. Caffrey, *Wohlers Report* (Wohlers Associates, Fort Collins, CO, 2013).
5. P. Colombo, G. Mera, R. Riedel, G. D. Sorarù, *J. Am. Ceram. Soc.* **93**, 1805–1837 (2010).
6. S. Martínez-Crespiera *et al.*, *Sens. Actuators A Phys.* **169**, 242–249 (2011).
7. L.-A. Liew *et al.*, *Sens. Act. A* **95**, 120–134 (2002).
8. P. Colombo, R. Riedel, G. D. Sorarù, H. J. Kleebe, Eds., *Polymer Derived Ceramics* (DEStech Publications, Lancaster, PA, 2010).
9. M. Schulz *et al.*, *Adv. Eng. Mater.* **6**, 676–680 (2004).
10. A. J. Jacobsen, W. Barvosa-Carter, S. Nutt, *Adv. Mater.* **19**, 3892–3896 (2007).
11. T. A. Schaedler *et al.*, *Science* **334**, 962–965 (2011).
12. R. Riedel *et al.*, *Nature* **382**, 796–798 (1996).
13. M. Zaheer, T. Schmalz, G. Motz, R. Kempe, *Chem. Soc. Rev.* **41**, 5102–5116 (2012).
14. P. Colombo, J. R. Hellmann, D. L. Shelleman, *J. Am. Ceram. Soc.* **84**, 2245–2251 (2001).
15. L. J. Gibson, M. F. Ashby, *Cellular Solids: Structure and Properties* (Cambridge Univ. Press, Cambridge, 1997).
16. A. J. Jacobsen, W. Barvosa-Carter, S. Nutt, *Acta Mater.* **55**, 6724–6733 (2007).
17. A. J. Jacobsen, W. Barvosa-Carter, S. Nutt, *Acta Mater.* **56**, 2540–2548 (2008).
18. T. Varga *et al.*, *J. Am. Ceram. Soc.* **90**, 3213–3219 (2007).
19. A. Saha, R. Raj, D. L. Williamson, *J. Am. Ceram. Soc.* **89**, 2188–2195 (2006).
20. T. Xu, Q. Ma, Z. Chen, *Ceram. Int.* **37**, 2555–2559 (2011).
21. M. D. Beals, S. Zerfoss, *J. Am. Ceram. Soc.* **27**, 285–292 (1944).
22. L. Huang, J. Kieffer, *J. Chem. Phys.* **118**, 1487–1498 (2003).
23. A. Saha, R. Raj, *J. Am. Ceram. Soc.* **90**, 578–583 (2007).
24. S. Modena, G. D. Soraru, Y. Blum, R. Raj, *J. Am. Ceram. Soc.* **88**, 339–345 (2005).
25. G. Chollon, *J. Eur. Ceram. Soc.* **20**, 1959–1974 (2000).
26. W. C. Tripp, H. C. Graham, *J. Am. Ceram. Soc.* **59**, 399–403 (1976).
27. E. Opila, S. Levine, J. Lorincz, *J. Mater. Sci.* **39**, 5969–5977 (2004).
28. W. C. Tripp, H. C. Graham, *J. Electrochem. Soc.* **118**, 1195–1199 (1971).
29. J. A. Coppala, M. Srinivasan, K. T. Faber, R. H. Smoak (The Carborundum Company, USA)., in Proceedings of International Symposium on Factors in Densification and Sintering of Oxide and Non-oxide Ceramics, October 3 to 5, 1978, Hakone, Japan (Gakujutsu Bunken Fukyu-kai, Tokyo, 1979), pp. 400–417.
30. N. M. Geyer, Aeronautical Systems Division Technical Report 61-322, from the published Proceedings for the Materials Symposium, 13 to 15 September 1961, Phoenix, AZ.

ACKNOWLEDGMENTS

The authors gratefully acknowledge financial support by HRL Laboratories, LLC, and the Defense Advanced Research Projects Agency under the Materials with Controlled Microstructural Architecture program managed by J. Goldwasser (contract no. W91CRB-10-0305) and thank N. Verma (University of California, Santa Barbara) for TEM analysis and C. G. Levi and C. S. Roper for useful discussions. Patent applications have been filed under serial numbers 62/183580, 62/128410, and 62/092733 with the U.S. Patent and Trademark office.

SUPPLEMENTARY MATERIALS

www.sciencemag.org/content/351/6268/58/suppl/DC1
Materials and Methods
Figs. S1 to S4
Tables S1 to S3
References

18 August 2015; accepted 13 November 2015
10.1126/science.aad2688

BLACK HOLE PHYSICS

A radio jet from the optical and x-ray bright stellar tidal disruption flare ASASSN-14li

S. van Velzen,[1]* G. E. Anderson,[2,3] N. C. Stone,[4] M. Fraser,[5] T. Wevers,[6] B. D. Metzger,[4] P. G. Jonker,[6,7] A. J. van der Horst,[8] T. D. Staley,[2] A. J. Mendez,[1] J. C. A. Miller-Jones,[3] S. T. Hodgkin,[5] H. C. Campbell,[5] R. P. Fender[2]

The tidal disruption of a star by a supermassive black hole leads to a short-lived thermal flare. Despite extensive searches, radio follow-up observations of known thermal stellar tidal disruption flares (TDFs) have not yet produced a conclusive detection. We present a detection of variable radio emission from a thermal TDF, which we interpret as originating from a newly launched jet. The multiwavelength properties of the source present a natural analogy with accretion-state changes of stellar mass black holes, which suggests that all TDFs could be accompanied by a jet. In the rest frame of the TDF, our radio observations are an order of magnitude more sensitive than nearly all previous upper limits, explaining how these jets, if common, could thus far have escaped detection.

Although radio jets are a ubiquitous and well-studied feature of accreting compact objects, it remains unclear why only a subset of active galactic nuclei (AGNs) are radio-loud. A stellar tidal disruption flare (TDF) presents a novel method with which to study jet production in accreting supermassive black holes. These flares occur after perturbations to a star's orbit have brought it to within a few tens of Schwarzschild radii of the central supermassive black hole and the star gets torn apart by the black hole's tidal force. A large amount of gas is suddenly

injected close to the black hole event horizon, and we therefore anticipate the launch of a relativistic jet as this stellar debris gets accreted (*1*, *2*). About two dozen TDFs have so far been discovered at soft x-ray, ultraviolet (UV), and optical wavelengths (*3*–*5*). All of these flares can be described by black body emission, hence their description as thermal TDFs. Hard x-ray emission from a relativistic jet launched after a stellar disruption has been observed in three cases (*6*–*10*). These so-called relativistic TDFs are readily detected at radio frequencies [the best-studied source, Swift J1644+57, reached a peak flux of 30 millijansky (mJy) at 22 GHz (*11*, *12*)]. Surprisingly, radio observations of thermal TDFs show no signs of equally powerful jets (*13*, *14*), bringing into question the universality of jet production triggered by large changes in the accretion rate (*15*).

On 2 December 2014, the All-Sky Automated Survey for Supernovae (ASAS-SN) reported the discovery of ASASSN-14li (*16*), an optical transient with a blue continuum in Swift UV/Optical Telescope (UVOT) follow-up observations, located in the nucleus of a galaxy at redshift $z = 0.021$. These properties prompted this transient to be classified as a potential stellar tidal disruption flare. The source was also detected in Swift X-ray Telescope (XRT) observations, but only at soft x-ray energies (0.3 to 1 keV) (Fig. 1). We began a radio monitoring campaign with the Arcminute Microkelvin Imager (AMI) at 15.7 GHz 22 days after the first Swift observation and obtained two observations with the Westerbork Synthesis Radio Telescope (WSRT) at 1.4 GHz (supplementary text and table S1). The 15.7-GHz light curve shows a monotonic decay (factor 5 decrease in 140 days) (Fig. 2), suggesting that we observed the fading of a relativistic outflow that was produced by the impulsive accretion event onto the supermassive black hole.

The host galaxy is detected at 3 mJy in archival radio images at 1.4 GHz. The expected radio flux due to star formation is at most 10^{-3} mJy (supplementary text), and we therefore conclude that the preflare radio flux is due to an AGN. The only other property of the host that suggests ongoing accretion before the flare in 2014 is narrow [OIII] line emission with a luminosity of $L_{[OIII]} = 8 \times 10^{38}$ erg s^{-1}. This low luminosity implies that the AGN was in the radiatively inefficient, jet-dominated mode (*17*).

On the basis of the detection of an AGN before the optical flare, one might infer ASASSN-14li to be a brief period of enhanced activity of the pre-existing accretion disk, but this is inconsistent with nearly all of the observed properties of the flare. First, the very low x-ray black body temperature ($T \approx 0.06$ keV), including substantial absorption features, is unlike the x-ray properties of any known AGN (*18*). Second, the large x-ray flux increase with respect to the archival upper limit (Fig. 1) is seen for less than 0.5% of sources in a blind all-sky search for x-ray variability (*19*). Third, the factor of 100 increase with respect to the baseline UV flux seen in ASASSN-14li is more than an order of magnitude larger than observed in a 3-year monitoring campaign of 663 AGN (*20*). And last, we found no significant variability in 8 years of optical observations of the host galaxy of ASASSN-14li by the Catalina Real-Time Transient Survey. A stellar tidal disruption is therefore the best interpretation for ASASSN-14li.

The x-ray temperature and luminosity of ASASSN-14li are similar to thermal TDFs discovered with x-ray surveys (*3*) and can be explained by a newly formed, radiatively efficient accretion disk with an inner radius at a few Schwarzschild radii from the black hole (*21*). Its optical/UV properties are also very similar to previous optically discovered TDFs, which are characterized by a large and constant black body temperature [$T = (2 - 3) \times 10^4$ K] (table S5 and fig. S2).

Thermal TDFs are typically detected at optical/UV or soft x-ray frequencies, but not both (table S3). This could be explained by the existence of a region at 1000 Schwarzschild radii from the black hole that produces the optical emission via reprocessing of the x-ray photons that originate from the inner accretion disk (*22*). If the product of the optical depth for x-ray ionization and the covering factor of this region is $\gg 1$, luminous optical emission would be produced while x-rays from the inner disk are obscured. In this model, ASASSN-14li can be explained if the evolution of the reprocessing layer gradually allows the escape of more x-ray photons toward our line of sight. This would explain why the x-ray light curve tracks the theoretical $t^{-5/3}$ fallback rate only after about 100 days into the monitoring campaign (Fig. 2) and why the optical light curve of x-ray dim TDFs show less variability than that of ASASSN-14li [for example, the x-ray dim TDF PS1-10jh (*23*) showed only 0.03 magnitude (mag) root-mean-square variability, compared with 0.2 mag for ASASSN-14li]. An alternative explanation for the initially constant x-ray flux is inefficient circularization of the tidal debris streams (*24*), which slows down the formation of the inner accretion disk.

The key property of ASASSN-14li is the detection of variable radio emission. Adopting the standard flat or slightly inverted radio spectrum (*17*) for emission of the original AGN jet, we found that our 15.7 GHz observations were always below the 3 mJy baseline level of this jet. The decaying 15.7 GHz light curve of ASASSN-14li therefore indicates that we have observed the termination of an AGN jet because of an increased accretion rate. If the AGN jet had not been terminated, we would have expected an increase with respect to this baseline level. Without an engine to drive particle acceleration in the AGN jet, the synchrotron luminosity will decrease on a time scale of ~10 days at 10 GHz. Inverse Compton cooling of the electrons on TDF photons can speed up this decrease by a factor ~10 (supplementary text). Hence, the radio flux of the original AGN jet is unlikely to be a dominant component to our post-flare radio observations.

The combined optical and x-ray luminosity during the first month of observations of ASASSN-14li

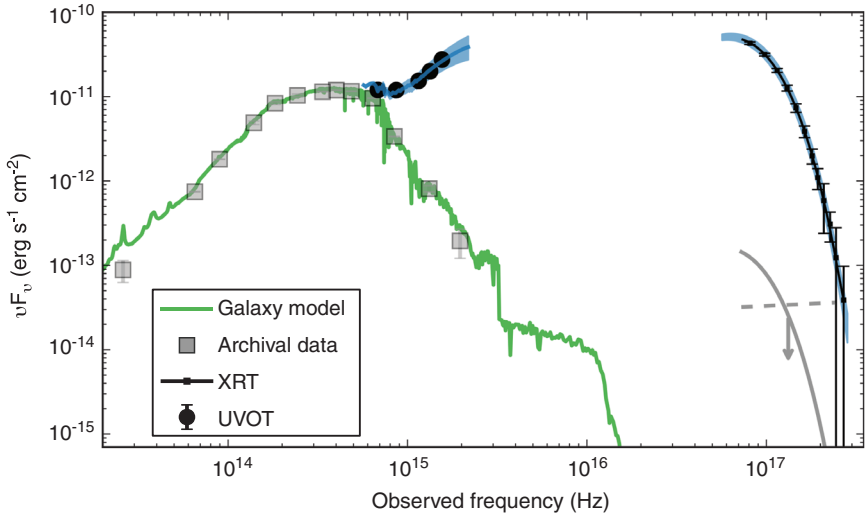

Fig. 1. Flare and host spectral energy distribution (SED). Shown is the first epoch of the series of Swift x-ray (unfolded spectrum) and broadband optical/UV observations of ASASSN-14li. These observations can each be described by a single black body with $T = 7.7 \times 10^5$ K and $T = 3.5 \times 10^4$ K, respectively (blue lines; width reflects uncertainty on the temperature). The SED of the host galaxy based on archival data (gray squares) shows no sign of star formation or an AGN as demonstrated by our best-fit synthetic galaxy spectrum (green line). The pre-flare x-ray limit is shown for both a black body spectrum of similar temperature as the current x-ray spectrum (gray solid line) and a standard power-law AGN spectrum ($\Gamma = 1.9$; gray dashed line).

[1]Department of Physics and Astronomy, The Johns Hopkins University, Baltimore, MD 21218, USA. [2]Department of Physics, University of Oxford, Denys Wilkinson Building, Keble Road, Oxford OX1 3RH, UK. [3]International Centre for Radio Astronomy Research, Curtin University, GPO Box U1987, Perth WA 6845, Australia. [4]Columbia Astrophysics Laboratory, Columbia University, New York, NY 10027, USA. [5]Institute of Astronomy, University of Cambridge, Madingley Road, Cambridge CB3 0HA, UK. [6]Department of Astrophysics, Radboud University Nijmegen, Heyendaalseweg 135, 6525 AJ Nijmegen, Netherlands. [7]SRON, Netherlands Institute for Space Research, Sorbonnelaan 2, 3584 CA Utrecht, Netherlands. [8]Department of Physics, The George Washington University, 725 21st Street NW, Washington, DC 20052, USA.
***Corresponding author. E-mail: sjoert@jhu.edu**

amounts to a few tens of percent of the Eddington luminosity [adopting a central black hole mass of $10^{6.5}$ solar mass ($M_\odot$)] (supplementary text), compared with <1% of the Eddington limit before the flare. ASASSN-14li shares several properties with the flares produced by stellar mass black holes upon being subjected to similarly large changes in their accretion rates. Accretion onto stellar mass black holes in x-ray binaries (XRBs) occurs in two distinct spectral modes, which are separated by a state change that occurs at a few percent of the Eddington luminosity (*25*). Radio observations of XRBs consistently show the disappearance of a steady compact jet and the launch of transient ejecta during the change from the nonthermal (hard) state to the thermal (soft) state (*15*). In direct analogy with XRBs, the steady jet that existed before the infall of material from the tidal disruption has been quenched or suppressed, and the accretion disk spectrum is now dominated by thermal emission. The co-added Swift XRT data of the TDF shows no evidence for a nonthermal (2 to 10 keV) component at the level needed to power the preflare [OIII] line luminosity (supplementary text), suggesting that the geometrically thick accretion flow that powered the previous steady jet has collapsed.

The maximum radio luminosity of ASASSN-14li is three orders of magnitude lower than that of Swift J1644+57 (*11*) and evolves on a much shorter time scale. This immediately implies a large difference in jet power between these two events. The radio light curve of ASASSN-14li can be reproduced by using a model similar to that applied to Swift J1644+57 (*1*), in which synchrotron shock emission is produced as the transient ejecta decelerate upon interacting with dense gas in the nuclear region surrounding the black hole. Assuming the ejecta were launched ~20 days before the first Swift observation of ASASSN-14li and applying a simple blast wave model yields a total jet energy of $E_j \sim 10^{48}$ erg, under the common assumption that 20 and 1% of the energy dissipated by the shocks is placed into relativistic electrons and magnetic fields, respectively (*1*). This energy is four orders of magnitude lower than the total jet energy of Swift J1644+57 (*26*).

By the time of our radio observations, the newly launched jet would have swept up enough matter to slow to mildly relativistic velocities (bulk Lorentz factor $\Gamma_j \approx 2$), causing each lobe to spread laterally in a quasispherical manner (similar to a mushroom cloud). The approximately isotropic nature of the radio emission at the time of the observations also implies that a finely tuned viewing angle with respect to the jet axis is not required. The gas density of ~10^3 cm^{-3} that is required to decelerate the jet at a characteristic radius of 0.1 pc can be explained by the Bondi accretion flow needed to supply the radiatively inefficient flow that existed before the flare (supplementary text). The deceleration of the new jet implies it cannot be launched into the funnel cleared by the previous jet, which occurs naturally if the new jet orientation is determined by the angular momentum of the new accretion disk rather than the black hole spin vector.

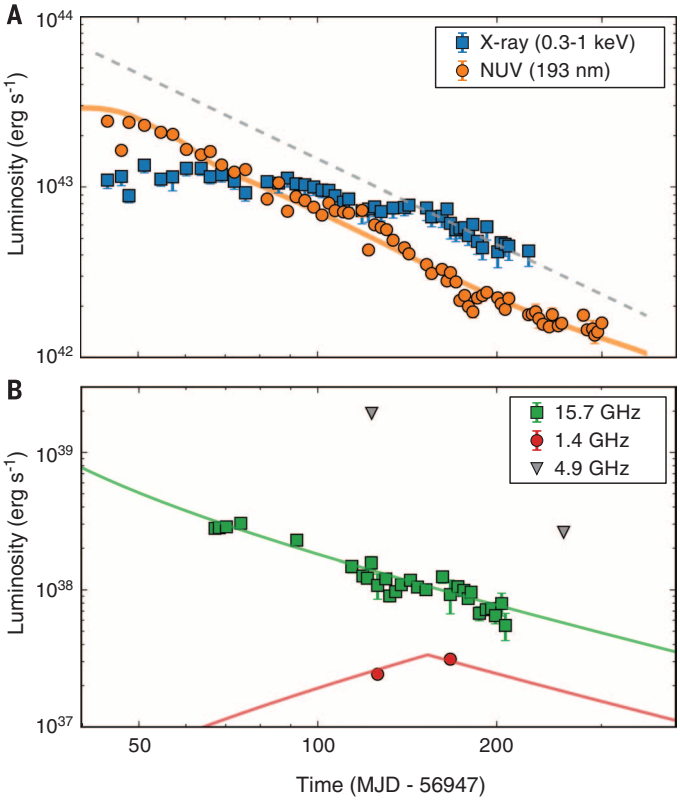

Fig. 2. Multi-wavelength light curves of the tidal disruption flare ASASSN-14li. (**A**) Integrated soft x-ray (0.3 to 1 keV) luminosity and monochromatic (νL_ν) near-UV (UVW2-band) luminosity. A spline fit to the observed *g*-band light curve of the known tidal flare PS1-10jh (*23*), corrected for cosmological time dilation and scaled up by 15%, is shown for reference (solid line). The dashed gray line indicates a $(t - t_0)^{-5/3}$ power law, the approximate theoretically expected fallback rate of the stellar debris for a disruption at t_0. The normalization of the time axis [in Modified Julian Day (MJD)] is chosen to highlight that the (late-time) light curves are consistent with this power law (t_0 = 56947 ± 2 MJD) (fig. S1). Error bars show the 1σ statistical uncertainty, often smaller than the marker size. (**B**) Monochromatic radio luminosity at 15.7 GHz (AMI) and 1.4 GHz (WSRT) of ASASSN-14li and our jet model (solid lines). The spectral indices during the two epochs of dual radio frequency coverage are −0.4 ± 0.1 and −0.6 ± 0.1 (first and second epoch, respectively). The two most stringent upper limits on the early-time 5-GHz emission of previous thermal TDFs (gray triangles) (table S4) were not sensitive enough to detect transient radio emission similar to ASASSN-14li.

Adopting the analogy of tidal disruption events as laboratories for studying accretion physics, we have thus far obtained two well-sampled multi-wavelength experiments with very different outcomes: One yielded a powerful jet (Swift J1644+57), whereas the second event—promptly followed up at radio frequencies (ASASSN-14li)—revealed a much weaker jet. A common explanation for the wide range of black hole jet efficiency is black hole spin—powerful jets require higher spin. This model, however, cannot readily explain the radio light curve of ASASSN-14li because it would predict that the radio luminosity should increase after the disruption (because the spin remains unchanged, whereas the gas supply is greatly enhanced with respect to the predisruption accretion rate). Besides spin, powerful jets may require a large magnetic flux near the black hole horizon (*27*). Our observations could suggest that the magnetic flux stored in a preexisting accretion flow is not tapped efficiently upon the disruption and accretion of a star, contrary to simulation predictions (*28*).

The majority of radio follow-up observations of thermal TDFs were obtained many years after the peak of the flare. Our observations are the first to sample the light curve within 30 days of the peak. Combined with the low redshift of ASASSN-14li, this explains why similar jets in previous thermal TDFs have eluded detection (table S4). In analogy with the consistent production of transient jets during accretion flow state changes of stellar mass black holes, our observations suggest that radio-emitting outflows could be a common feature of all TDFs. Adopting a 5σ detection threshold of 90 μJy for a monthly all-sky survey with the Square Kilometer Array at 1.4 GHz (*29*), a galaxy density of 5×10^{-3} Mpc^{-3} and a jet production rate equal to the observed thermal TDF rate [3×10^{-5} galaxy^{-1} year^{-1} (*30*)] yields a detection rate of ~10^2 thermal TDF jets per year. Although the nonthermal tidal disruption jets selected by Swift are much more powerful, they are a smaller subpopulation of all stellar disruptions. In blind radio transients surveys, both types of TDF jets could be detected at roughly similar rates.

REFERENCES AND NOTES

1. D. Giannios, B. D. Metzger, *Mon. Not. R. Astron. Soc.* **416**, 2102–2107 (2011).
2. S. van Velzen, E. Körding, H. Falcke, *Mon. Not. R. Astron. Soc.* **417**, L51–L55 (2011).
3. N. Bade, S. Komossa, M. Dahlem, *Astron. Astrophys.* **309**, L35 (1996).
4. S. Gezari *et al.*, *Astrophys. J.* **698**, 1367–1379 (2009).
5. S. van Velzen *et al.*, *Astrophys. J.* **741**, 73 (2011).
6. J. S. Bloom *et al.*, *Science* **333**, 203–206 (2011).
7. A. J. Levan *et al.*, *Science* **333**, 199–202 (2011).
8. D. N. Burrows *et al.*, *Nature* **476**, 421–424 (2011).
9. S. B. Cenko *et al.*, *Astrophys. J.* **753**, 77 (2012).
10. G. C. Brown *et al.*, *Mon. Not. R. Astron. Soc.* **452**, 4297–4306 (2015).
11. B. A. Zauderer *et al.*, *Nature* **476**, 425–428 (2011).
12. E. Berger *et al.*, *Astrophys. J.* **748**, 36 (2012).
13. G. C. Bower, B. D. Metzger, S. B. Cenko, J. M. Silverman, J. S. Bloom, *Astrophys. J.* **763**, 84 (2013).
14. S. van Velzen, D. A. Frail, E. Körding, H. Falcke, *Astron. Astrophys.* **552**, A5 (2013).
15. R. P. Fender, T. M. Belloni, E. Gallo, *Mon. Not. R. Astron. Soc.* **355**, 1105–1118 (2004).
16. T. W.-S. Holoien *et al.*, *Mon. Not. R. Astron. Soc.*; http://arxiv.org/abs/1507.01598 (2015).
17. H. Falcke, E. Körding, S. Markoff, *Astron. Astrophys.* **414**, 895 (2004).
18. J. M. Miller *et al.*, *Nature* **526**, 542–545 (2015).
19. J. Kanner *et al.*, *Astrophys. J.* **774**, 63 (2013).
20. S. Gezari *et al.*, *Astrophys. J.* **766**, 60 (2013).
21. A. Ulmer, *Astrophys. J.* **514**, 180–187 (1999).
22. J. Guillochon, H. Manukian, E. Ramirez-Ruiz, *Astrophys. J.* **783**, 23 (2014).
23. S. Gezari *et al.*, *Nature* **485**, 217–220 (2012).
24. H. Shiokawa, J. H. Krolik, R. M. Cheng, T. Piran, S. C. Noble, *Astrophys. J.* **804**, 85 (2015).
25. T. J. Maccarone, *Astron. Astrophys.* **409**, 697–706 (2003).
26. P. Mimica, D. Giannios, B. D. Metzger, M. A. Aloy, *Mon. Not. R. Astron. Soc.* **450**, 2824–2841 (2015).
27. J. C. McKinney, A. Tchekhovskoy, R. D. Blandford, *Science* **339**, 49–52 (2013).
28. L. Z. Kelley, A. Tchekhovskoy, R. Narayan, *Mon. Not. R. Astron. Soc.* **445**, 3919–3938 (2014).
29. R. Fender *et al.*, in *Advancing Astrophysics with the Square Kilometre Array*, T. L. Bourke *et al.*, Eds. (Proceedings of Science, 2014), chap. 51.
30. S. van Velzen, G. R. Farrar, *Astrophys. J.* **792**, 53 (2014).

ACKNOWLEDGMENTS

We are grateful to the ASAS-SN team for making their newly identified optical transient public. We thank J. Krolik for useful discussions. We thank the staff of the Mullard Radio Astronomy Observatory for their invaluable assistance in the operation of AMI. We thank the WSRT director for granting the observations in Director's Discretionary Time and the WSRT staff for obtaining these observations. The WSRT is operated by ASTRON (Netherlands Institute for Radio Astronomy) with support from the Netherlands foundation for Scientific Research. S.v.V. is supported by NASA through a Hubble Fellowship (HST-HF2-51350.001). G.E.A., T.D.S., and R.P.F. acknowledge support from the European Research Council via Advanced Investigator Grant 267697. G.E.A. also acknowledges the support of the International Centre for Radio Astronomy Research (ICRAR), a Joint Venture of Curtin University and The University of Western Australia, funded by the Western Australian State government. M.F. and H.C.C. acknowledge support from the European Union FP7 program through European Research Council grant 320360. B.D.M. and N.C.S. acknowledge support from NASA grant NNX14AQ68G, NSF grant AST-1410950, and the Alfred P. Sloan Foundation. N.C.S. is also supported by NASA through an Einstein Fellowship. J.C.A.M.-J. is supported by an Australian Research Council Future Fellowship (FT140101082). The data presented here can be found in the supplementary materials; raw optical/UV/x-ray observations are available in the NASA/Swift archive (http://heasarc.nasa.gov/docs/swift/archive, Target Name: BRUTUS6984_2); raw radio observations (WSRT and AMI) are maintained by the observatories and available upon request.

SUPPLEMENTARY MATERIALS

www.sciencemag.org/content/351/6268/62/suppl/DC1
Supplementary Text
Figs. S1 and S2
Tables S1 to S5
References (*31*–*106*)

31 July 2015; accepted 13 November 2015
Published online 26 November 2015
10.1126/science.aad1182

ASTROCHEMISTRY

Statistical ortho-to-para ratio of water desorbed from ice at 10 kelvin

Tetsuya Hama,* Akira Kouchi, Naoki Watanabe

The anomalously low ortho-to-para ratios (OPRs) exhibited by gaseous water in space have been used to determine the formation temperature (< 50 kelvin) of ice on cold interstellar dust. This approach assumes that the OPR of water desorbed from ice is related to the ice formation temperature on the dust. However, we report that water desorbed from ice at 10 kelvin shows a statistical high-temperature OPR of 3, even when the ice is produced in situ by hydrogenation of O_2, a known formation process of interstellar water. This invalidates the assumed relation between OPR and temperature. The necessary reinterpretation of the low OPRs will help elucidate the chemical history of interstellar water from molecular clouds and processes in the early solar system, including comet formation.

Astronomical observations have revealed water (H_2O) to be ubiquitous in space. Gaseous H_2O has been discovered in star- and planet-forming regions and in the atmospheres of planets both in and beyond our solar system. H_2O ice is also abundant in cold interstellar clouds and solar-system bodies such as comets. Studying the chemistry of the H_2O in these sources can provide information about their physical conditions and eventually may help us to understand the evolution of stars and planetary systems, including our solar system (*1*–*3*). Spectroscopy can reveal the abundance ratio of nuclear spin isomers of H_2O, namely the ortho-to-para ratio (OPR). Because a proton is a fermion with a nuclear spin angular momentum of $I = {}^1/_2$, two nuclear spin isomers exist for H_2O: ortho (I = 1, triplet) and para (I = 0, singlet). Conversion between the nuclear spin isomers by radiation or nonreactive collisions is extremely slow in the gas phase (*4*, *5*). The different nuclear spin isomers are thus treated as almost entirely separate species, making the OPR a valuable tracer for the physical and chemical history experienced by molecules, including their formation (*1*). The OPR is related to the spin temperature (T_{spin}) by Eq. 1, which is defined at thermodynamic equilibrium (*6*)

$$\mathrm{OPR} = \frac{3\sum(2J+1)\exp\left[\frac{-E_o(J_{K_a,K_c})}{k_B T_{spin}}\right]}{\sum(2J+1)\exp\left[\frac{-E_p(J_{K_a,K_c})}{k_B T_{spin}}\right]} \quad (1)$$

where $E_o(J_{K_a,K_c})$ and $E_p(J_{K_a,K_c})$ are the energy of a rotational level in ortho- and para-H_2O, respectively, and k_B is the Boltzmann constant. J is the

Institute of Low Temperature Science, Hokkaido University, Sapporo 060–0819, Japan.
*Corresponding author. E-mail: hama@lowtem.hokudai.ac.jp

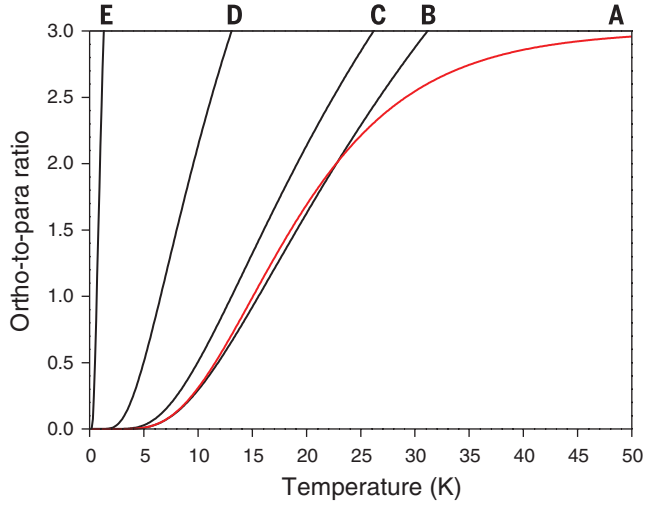

Fig. 1. OPR of H_2O as function of temperature. Curve A is calculated from Eq. 1 with the gas-phase constants (*7*). Approximated curves B to E are calculated from Eq. 9 with ΔE values of (B) 23.8 cm^{-1} (gas-phase), (C) 20 cm^{-1} (H_2O in Ar matrix) (*22*), (D) 10 cm^{-1}, and (E) 1.0 cm^{-1}. Approximated curves B to E tend toward 9, not the statistical OPR value of 3, because only the lowest ortho- and para-rotational states are considered in Eq. 9, and thus the contribution of the rotational degeneracy is not cancelled as in curve A from Eq. 1.

total angular momentum quantum number, and K_a and K_c are the projections of J onto the principal a and c axes, respectively (*3*). In the electronic and vibrational ground state, the Pauli principle leads ortho-H_2O to exist in rotational states with odd $K_a + K_c$, and para-H_2O to exist in rotational states with even $K_a + K_c$ (*1*, *3*). As shown with Fig. 1, curve A, T_{spin} may be used as a probe for low-temperature regions because para-H_2O ($J_{K_a,K_c} = 0_{00}$) is more stable than ortho-H_2O ($J_{K_a,K_c} = 1_{01}$) in the gas phase owing to the 23.8 cm^{-1} (34.2 K) rotational energy difference between them (*7*).

The OPRs of gaseous H_2O have been observed in cometary comae since the 1980s (*6*, *8*) and are in the range of 2.0 to 3.0, with a typical value of 2.5, which corresponds to a T_{spin} of ~30 K (*9*, *10*). This temperature has been interpreted as an indicator of the temperature at which these comets formed some 4.6 billion years ago (*6*). The OPR of H_2O has also recently been measured in star- and planet-forming regions. It is generally close to the statistical value of 3 (*1*, *3*), but lower values have also been reported for some star-forming regions (0.1 to 2.4, T_{spin} = 8 to 27 K) and a proto-planetary disk (0.8, T_{spin} = 14 K) (*1*, *3*, *11*, *12*). Given that these values are much lower than those observed in cometary comae (*10*), it has been suggested that cometary ice is a heterogeneous mixture of different icy dust grains from throughout the entire solar nebula, with some formed in warm regions at >50 K (OPR = 3) and others in cold regions at 10 to 20 K (OPR < 1) (*12*). Ice-covered dust in low-temperature interstellar regions (<50 K) is too cold to allow the thermal desorption of H_2O; instead, photodesorption has been proposed as a plausible explanation for the observed abundance and low OPR of interstellar gaseous H_2O (*1*). However, the nuclear-spin state of H_2O desorbed from ice remains poorly understood, especially at low temperatures, and the proposal that the OPR is linked to the formation temperature has not been validated. Consequently, the meaning of the observed OPRs in cometary comae and star- and planet-forming regions is still unknown, despite the accumulation of observational studies (*1*–*3*, *9*, *10*).

In this study, we measured the OPR of photodesorbed H_2O from water ice at 10 K experimentally. To test the proposal that T_{spin} is related to the condensation or formation temperature, two types of water ice samples were prepared at 10 K: vapor-deposited amorphous H_2O ice and amorphous H_2O ice produced in situ through the nonenergetic hydrogenation of solid O_2 through the successive reactions 2 to 6 (*13*):

$$O_2 + H \rightarrow HO_2 \quad (2)$$
$$HO_2 + H \rightarrow H_2O_2 \quad (3)$$
$$H_2O_2 + H \rightarrow H_2O + OH \quad (4)$$
$$OH + H \rightarrow H_2O \quad (5)$$
$$OH + H_2 \rightarrow H_2O + H \quad (6)$$

Interstellar amorphous H_2O ice on dust also forms via reactions 4 to 6 (*1*–*3*, *14*). In most interstellar regions, the hydrogenation of atomic O (O + H → OH) followed by reaction 5 is assumed to be the dominant reaction for H_2O ice formation (*1*). H_2O was photodesorbed from the ice by excitation with ultraviolet 157 nm radiation in a vacuum at 10 K; its OPR was then measured by means of rotationally resolved resonance-enhanced multiphoton ionization (REMPI) spectroscopy (*13*, *15*–*19*). Shown in Fig. 2 are the REMPI spectra of photodesorbed H_2O in the ground $\tilde{X}\,^1A_1(v = 0)$ state from vapor-deposited H_2O ice and H_2O ice produced in situ. Both spectra appear identical and show stronger ortho-H_2O lines than para-H_2O lines. The rotational temperature (T_{rot}) and T_{spin} were evaluated from the H_2O REMPI spectra by using the program PGOPHER (*13*, *20*). Spectral simulations at T_{rot} = 200 K for T_{spin} = 200 K (OPR = 3) and T_{spin} = 10 K (OPR = 0.3) are shown in Fig. 2. Comparing the experimental and simulated spectra indicates that the OPRs of H_2O desorbed from both ices show a statistical value of 3. Our spectral simulation shows little change in the REMPI spectra of H_2O for $T_{spin} \geq 30$ K (*13*, *18*), which agrees with the energy gap for H_2O between the lowest ortho ($J_{K_a,K_c} = 1_{01}$) and para ($J_{K_a,K_c} = 0_{00}$) rotational levels (ΔE = 34.2 K) (*7*). We also measured the OPR of H_2O thermally desorbed from the two ices by heating at 150 K (*13*). Both REMPI spectra were reproduced by the simulation by using $T_{rot} = T_{spin}$ = 150 K (OPR = 3), a value that is neither the condensation nor the formation temperature (10 K).

Molecular dynamics calculations (*21*) and experimental studies (*15*) have identified a "kick-out" photodesorption mechanism after the absorption of a single vacuum ultraviolet photon (*13*). In this mechanism (reactions 7 and 8), an H_2O molecule is desorbed from the ice without

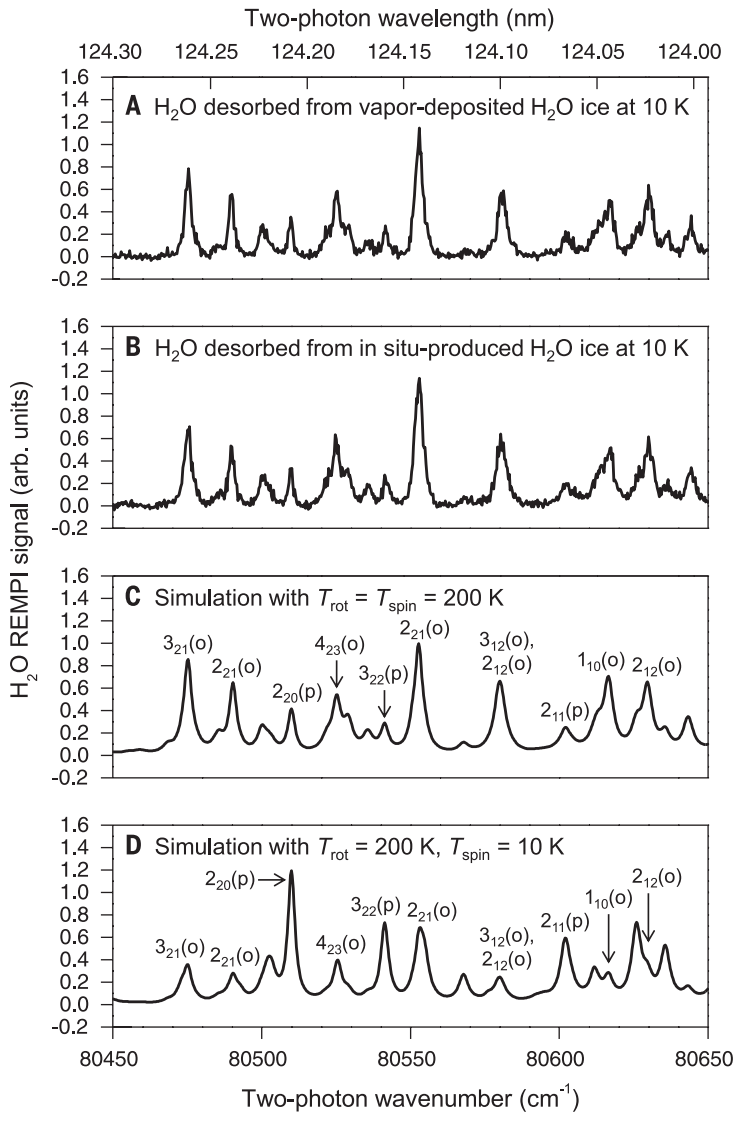

Fig. 2. REMPI spectra of photodesorbed H_2O after 157 nm photoirradiation of water ice at 10 K. (**A**) Vapor-deposited H_2O ice. (**B**) H_2O ice produced in situ by means of hydrogenation of O_2. (**C** and **D**) Simulated spectra with T_{rot} = 200 K and (C) T_{spin} = 200 K and (D) T_{spin} = 10 K. Indications (J_{K_a,K_c}) are rotational assignments, where "o" and "p" denote ortho and para, respectively.

intramolecular bond dissociation by the momentum transfer from an energetic H atom released by the photodissociation of a neighboring H_2O molecule:

$$H_2O(ice) + h\nu \rightarrow hot\ H + OH \quad (7)$$
$$hot\ H + H_2O(ice) \rightarrow H + H_2O \quad (8)$$

This suggests that the desorbed H_2O can preserve the original OPR of the ice, and thus, the low OPR of interstellar H_2O has been assumed to reflect its formation temperature (*1*, *11*, *12*). The chosen T_{rot} value of 200 K in Fig. 2 is comparable with previous experimental and calculated values for the kick-out mechanism of H_2O (T_{rot} = 300 ± 50 K) (*15*). However, the present results clearly rule out the proposal that the low OPR reflects the temperature of ice formation. This previous proposal implicitly assumes that para-H_2O is more stable than ortho-H_2O in ice—as it is in the gas phase—because of the energy difference of the rotational levels. However, this thermodynamic stability only appears when the molecules are free to rotate in the gas phase; thus, the T_{spin} curve A in Fig. 1 only applies to H_2O in the gas phase. The temperature dependence of the OPR should behave differently in rotationally hindered systems. For example, although H_2O can rotate almost freely in a solid argon (Ar) matrix, there is weak rotational hindrance because of van der Waals interactions between H_2O and Ar. As a result, the energy difference between the lowest ortho and para rotational levels (ΔE) is reduced to ~20 cm^{-1} (*22*). Below 25 K, ortho-H_2O and para-H_2O mainly exists in the $J_{K_a,K_c} = 1_{01}$ and 0_{00} rotational states, respectively, and Eq. 1 can be approximated by Eq. 9 (*1*)

$$OPR = \frac{3\sum(2J+1)\exp\left[\frac{-E_o(J_{K_a,K_c})}{k_B T_{spin}}\right]}{\sum(2J+1)\exp\left[\frac{-E_p(J_{K_a,K_c})}{k_B T_{spin}}\right]}$$
$$\approx 9\exp\left(\frac{-\Delta E}{k_B T_{spin}}\right) \quad (9)$$

The approximate OPRs of H_2O when in Eq. 9 ΔE = 23.8 and 20 cm^{-1} are shown in Fig. 1, curves B and C, respectively. Arbitrary curves assuming ΔE = 10 and 1.0 cm^{-1} are also shown for reference. The curves show that the OPR can reach the statistical value of 3 at low temperature and low ΔE.

In ice, H_2O has a high barrier (4700 cm^{-1}, 6700 K) to rotation because of its hydrogen bonds (*23*). Both ortho- and para-H_2O are no longer free rotors at 10 K, and the quenched ΔE value in ice is 3×10^{-13} cm^{-1} (5×10^{-13} K) (*24*), which indicates quasidegeneracy. Because the nuclear spin-spin interaction energy is sufficiently small (typically less than 10^{-6} cm^{-1}) (*24*–*26*), this suggests that the thermodynamic stability of ortho- and para-H_2O molecules should be comparable in ice at 10 K. Moreover, as a result of this rotational quenching, fast nuclear-spin conversion (NSC) of H_2O can occur in ice by the ortho-para state mixing through intermolecular proton–proton magnetic dipolar interactions (10^{-7} to 10^{-6} cm^{-1}, 10^4 to 10^5 Hz) between neighboring H_2O molecules (*3*, *24*, *25*, *27*). The estimated time scale for NSC is on the order of the inverse of the magnetic dipolar interactions of 10^{-5} to 10^{-4} s (10 to 100 μs) (*24*, *25*). These values are eight to nine orders of magnitude longer than the time scale for photodesorption (5×10^{-13} s, 500 fs) (*21*), indicating that NSC through magnetic interactions is negligible during photodesorption (*13*). Therefore, our results suggest that the OPR of H_2O in ice is practically in dynamic equilibrium at the statistical value of 3 regardless of the formation process of the ice (reactions 4 to 6). This is due to the comparable thermodynamic stability of ortho- and para-H_2O and the fast continuous ortho–para interconversion in ice. The OPR of nascent H_2O formed on ice, the nuclear-spin state of H_2O in ice at 10 K, and the NSC time on and in ice could not be measured in our study, although the NSC time could be measured by using recent ortho- or para-H_2O separation techniques (*27*–*30*).

The present study shows that the OPR of H_2O desorbed from ice at 10 K has the statistical value of 3. This value thus cannot be used to deduce the surface temperature of interstellar dust at H_2O formation or condensation. The origin of the anomalous OPRs observed for interstellar H_2O is still an open question because the role of gas-phase processes is poorly understood. The NSC of H_2O may occur via its chemical reaction with ions such as H^+ or H_3O^+. However, accurate state-to-state rate coefficients at low temperature are unknown. Other reactions involving the formation and destruction of H_2O and its precursors [such as H_2, H_2O^+, and H_3O^+ (*1*)] must also be treated as nuclear spin-state–dependent. Quantitative estimation of these gas-phase processes requires careful consideration of nuclear-spin and dynamical restrictions in the ortho/para branching ratio of the products, which may prevent the OPR from reaching a simple thermodynamic equilibrium (*31*, *32*). Thus, careful attention should be paid to the conversion of OPR to T_{spin}. Nevertheless, the OPR can still be used as a physicochemical tracer because of its quantum mechanical properties. Reinterpretation of its importance by considering gas-phase processes may clarify new or missed roles of interstellar H_2O in star and planet formation. The OPR of H_2O in a comet also does not indicate the past formation temperature of the ice nucleus. The value should be statistical at desorption from the comet nucleus, and the NSC of H_2O in a coma is predicted to be inefficient (*6*). This can explain why nearly all of the observed OPRs lie within 1 or 2σ of the statistical value (*10*).

REFERENCES AND NOTES

1. E. F. van Dishoeck, E. Herbst, D. A. Neufeld, *Chem. Rev.* **113**, 9043–9085 (2013).
2. A. G. G. M. Tielens, *Rev. Mod. Phys.* **85**, 1021–1081 (2013).
3. T. Hama, N. Watanabe, *Chem. Rev.* **113**, 8783–8839 (2013).
4. A. Miani, J. Tennyson, *J. Chem. Phys.* **120**, 2732–2739 (2004).
5. P. Cacciani, J. Cosléou, M. Khelkhal, *Phys. Rev. A* **85**, 012521 (2012).
6. M. J. Mumma, H. A. Weaver, H. P. Larson, *Astron. Astrophys.* **187**, 419–424 (1987).
7. J. Tennyson, N. F. Zobov, R. Williamson, O. L. Polyansky, *J. Phys. Chem. Ref. Data* **30**, 735–831 (2001).
8. M. J. Mumma, H. A. Weaver, H. P. Larson, D. S. Davis, M. Williams, *Science* **232**, 1523–1528 (1986).
9. J. Crovisier, *Faraday Discuss.* **133**, 375–385, discussion 427–452 (2006).
10. K. Willacy *et al.*, *Space Sci. Rev.* **197**, 151–190 (2015).
11. Y. Choi, F. F. S. van der Tak, E. A. Bergin, R. Plume, *Astron. Astrophys.* **572**, L10 (2014).
12. M. R. Hogerheijde *et al.*, *Science* **334**, 338–340 (2011).
13. Materials and methods are available as supplementary materials on *Science* Online.
14. Y. Oba *et al.*, *Astrophys. J.* **701**, 464–470 (2009).
15. T. Hama *et al.*, *J. Chem. Phys.* **132**, 164508 (2010).
16. G. Meijer, J. J. ter Meulen, P. Andresen, A. Bath, *J. Chem. Phys.* **85**, 6914–6922 (1986).
17. C.-H. Yang, G. Sarma, J. J. ter Meulen, D. H. Parker, C. M. Western, *Phys. Chem. Chem. Phys.* **12**, 13983–13991 (2010).
18. T. Hama, N. Watanabe, A. Kouchi, M. Yokoyama, *Astrophys. J.* **738**, L15 (2011).
19. A. Yabushita *et al.*, *Astrophys. J.* **699**, L80–L83 (2009).
20. C. M. Western, PGOPHER, a program for simulating rotational structure, University of Bristol; available at http://pgopher.chm.bris.ac.uk. We used the H2OCX.pgo file (http://pgopher.chm.bris.ac.uk/Help/h20cx.htm) to simulate the measured REMPI spectra.
21. S. Andersson, E. F. van Dishoeck, *Astron. Astrophys.* **491**, 907–916 (2008).
22. L. Abouaf-Marguin, A.-M. Vasserot, C. Pardanaud, X. Michaut, *Chem. Phys. Lett.* **447**, 232–235 (2007).
23. R. J. Wittebort, M. G. Usha, D. J. Ruben, D. E. Wemmer, A. Pines, *J. Am. Chem. Soc.* **110**, 5668–5671 (1988).
24. G. Buntkowsky *et al.*, *Z. Phys. Chem.* **222**, 1049–1063 (2008).
25. H.-H. Limbach *et al.*, *ChemPhysChem* **7**, 551–554 (2006).
26. M. Goldman, *Spin Temperature and Nuclear Magnetic Resonance in Solids* (Clarendon Press, Oxford, 1970).
27. R. Sliter, M. Gish, A. F. Vilesov,*J. Phys. Chem. A* **115**, 9682–9688 (2011).
28. T. Kravchuk *et al.*, *Science* **331**, 319–321 (2011).
29. D. A. Horke, Y.-P. Chang, K. Długołęcki, J. Küpper, *Angew. Chem. Int. Ed.* **53**, 11965–11968 (2014).
30. C. Manca Tanner, M. Quack, D. Schmidiger, *J. Phys. Chem. A* **117**, 10105–10118 (2013).
31. D. Gerlich, F. Windisch, P. Hlavenka, R. Plašil, J. Glosik, *Phil. Trans. R. Soc. London A* **364**, 3007–3034 (2006).
32. E. Herbst, *EPJ Web Conf.* **84**, 06002 (2015).

ACKNOWLEDGMENTS

We thank Y. Kimura, H. Hidaka, Y. Oba, H. Ueta, Y. Kunisada, T. Sugimoto, and A. Yabushita for helpful comments and discussions. This work was supported by Japan Society for the Promotion of Science KAKENHI grant 24224012 and Ministry of Education, Culture, Sports, Science and Technology KAKENHI grant 25108002. The authors declare no conflicts of interest. All the data reported in this manuscript are presented in the main paper and in the supplementary materials. The REMPI spectrum data used to create the figures are available as additional supplementary data files.

SUPPLEMENTARY MATERIALS

www.sciencemag.org/content/351/6268/65/suppl/DC1
Materials and Methods
Figs. S1 to S5
References (*33*–*41*)
Supplementary Data Files

9 September 2015; accepted 24 November 2015
10.1126/science.aad4026

MEMBRANES

Sieving hydrogen isotopes through two-dimensional crystals

M. Lozada-Hidalgo,[1]*† S. Hu,[1]† O. Marshall,[1] A. Mishchenko,[1] A. N. Grigorenko,[1] R. A. W. Dryfe,[2] B. Radha,[1] I. V. Grigorieva,[1] A. K. Geim[1]*

One-atom-thick crystals are impermeable to atoms and molecules, but hydrogen ions (thermal protons) penetrate through them. We show that monolayers of graphene and boron nitride can be used to separate hydrogen ion isotopes. Using electrical measurements and mass spectrometry, we found that deuterons permeate through these crystals much slower than protons, resulting in a separation factor of ≈10 at room temperature. The isotope effect is attributed to a difference of ≈60 milli–electron volts between zero-point energies of incident protons and deuterons, which translates into the equivalent difference in the activation barriers posed by two-dimensional crystals. In addition to providing insight into the proton transport mechanism, the demonstrated approach offers a competitive and scalable way for hydrogen isotope enrichment.

Unlike conventional membranes used for sieving atomic and molecular species, monolayers of graphene and hexagonal boron nitride (hBN) exhibit subatomic selectivity (*1*–*5*). They are permeable to thermal protons (*5*)—and electrons (*6*)—but in the absence of structural defects, are completely impermeable to larger, atomic species (*1*–*5*, *7*–*10*). Proton transport through these two-dimensional (2D) crystals is a thermally activated process, with energy barriers E of ≈0.3 and 0.8 eV for monolayers of hBN and graphene, respectively, that were attributed to different densities of their electron clouds that must be pierced by incident protons (*5*). Investigating whether deuterons—nuclei of the heavier hydrogen isotope, deuterium (D)—can pass through atomically thin crystals is of interest for elucidating the proton transport mechanism (*11*–*14*). If the 2D membranes can distinguish between the two nuclei (hydrons), this would also be of interest for applications, as hydrogen isotopes are important for various analytical and tracing technologies, and heavy water is used in huge quantities by nuclear fission plants. The existing H/D separation techniques, such as water–hydrogen sulfide exchange and cryogenic distillation (*15*, *16*), are extremely energy intensive and show low separation factors (<2.5), which stimulates continuous search for alternative technologies (*15*–*21*) [see supplementary materials (*22*)].

We investigated whether deuterons (D^+) permeate through 2D crystals differently from protons (H^+) studied previously (*5*). Two complementary approaches, electrical conductivity measurements and gas flow detection by mass spectrometry (*22*), were explored. In the first approach, graphene and hBN monocrystals were mechanically exfoliated and suspended over micrometer-sized holes etched in silicon wafers (fig. S1). To measure 2D crystals' hydron conductivity σ, both sides of the resulting membranes were coated with a proton-conducting polymer—Nafion (*23*)—and electrically contacted with Pd electrodes that converted electron into hydron flow (Fig. 1A, inset). The measurements were performed in an atmosphere of either H_2-Ar/H_2O or D_2-Ar/D_2O in 100% humidity at room temperature. The different atmospheres turned Nafion into a proton (H-Nafion) or deuteron (D-Nafion) (*24*) conductor with little presence of the other isotope (fig. S2). For reference, similar devices but without 2D membranes were fabricated. The latter exhibited similar conductance, whether H- or D-Nafion was used, and it was typically 100 times higher than that found for devices incorporating 2D crystals. This shows that the series contribution to our device resistances from Nafion and Pd contacts could be neglected (*5*, *22*).

For both H- and D-Nafion devices, the measured current I varied linearly with applied bias voltage V (Fig. 1A), but different 2D crystals showed widely different areal conductivities, $\sigma = I/SV$, where S is the membrane area (Fig. 1B). Monolayer hBN exhibited the highest proton conductivity, σ_H, followed by bilayer hBN and monolayer graphene (Fig. 1B), in agreement with the previous work (*5*). σ was markedly smaller (by a factor of 10) for D-Nafion devices compared to their H-Nafion counterparts, independent of the tested 2D crystal (Fig. 1B). Furthermore, we carried out similar measurements for Pt-activated membranes (hBN and graphene monolayers covered with a discontinuous layer of Pt to enhance hydron transport) (*22*) and, again, the conductivity for deuterons, σ_D, was always about $1/10$ of that for protons (fig. S3). This pronounced isotope effect is unexpected, and its independence of 2D barrier height is particularly puzzling. These observations do not follow from either previous experiments (*5*, *10*) or existing theories (*7*–*9*) in which the calculated barriers arise from the interaction of a positive point charge with the 2D crystals' electron clouds, and the hydron mass is assumed to be irrelevant.

In our second series of experiments, graphene membranes were used to separate a liquid cell and a vacuum chamber (Fig. 2A). On the liquid side (input), graphene was coated with a thin Nafion layer that faced a reservoir containing a proton-deuteron electrolyte (HCl in H_2O mixed with DCl in D_2O). The atomic fractions of H^+ and D^+ in this mixture could be changed as required. The other side of graphene, decorated with Pt nanoparticles, faced the vacuum chamber equipped with a mass spectrometer (*5*, *22*). A bias—typically, ≲2 V to avoid damage to our devices (fig. S6)—was applied directly between graphene and the electrolyte (Fig. 2A and fig. S1). This setup effectively represents an electrochemical pump (*25*, *26*) in which the graphene membrane serves simultaneously as a semitransparent hydron barrier and a drain electrode for protons and deuterons. The gas and liquid impermeability was checked for each experimental device with a He leak detector. The key advantage of mass spectrometry with respect to our electrical measurements is that it can distinguish between different hydron species. This allowed us to determine directly the composition of output gas flows for different input electrolytes. Unfortunately, mass spectrometry is also much less sensitive than electrical measurements and, therefore, large hydron fluxes were necessary to probe the current-induced gas flows in the presence of a fluctuating background in the spectrometer (*22*). To compensate for the lower sensitivity, we used high I and graphene crystals as large as possible, fabricating membranes up to 50 μm in diameter. This allowed flows >>10^{10} molecules/s for all three possible gases—H_2, D_2, and protium deuteride (HD)—which appeared on the vacuum side (Fig. 2B and fig. S4).

We found that the flow of each of the gases varied linearly with I, as expected, but depended strongly on the relative concentrations ($[H^+]$:$[D^+]$) of hydrons in the input electrolyte ($[H^+] + [D^+] = 100\%$). This is illustrated in Fig. 2B for the case of D_2 and further in figs. S4 to S6. By measuring such flow-current dependences for different $[H^+]$:$[D^+]$ inputs, we determined the percentage of H_2, D_2, and HD in output flows (Fig. 2C). These data are easily converted into the percentage of H and D atoms at the output of our electrochemical pump as a function of $[H^+]$ or $[D^+]$ at its input. We find that the output fraction of atomic hydrogen is disproportionally high with respect to the input fraction of protons (Fig. 2D). For example, for equal amounts of protons and deuterons at the input, H accounted for ≈95% of the atoms in the output flow—that is, graphene membranes efficiently sieved out deuterium. As a control experiment, we repeated the same measurements substituting graphene with porous carbon and found no preferential flow of protons or deuterons, as expected (fig. S5). To quantify the observed sieving efficiencies, we calculated the separation factor α. The data in Fig. 2D yield α ≈ 10, in good

[1]School of Physics and Astronomy, University of Manchester, Manchester M13 9PL, UK. [2]School of Chemistry, University of Manchester, Manchester M13 9PL, UK.
*Corresponding author. E-mail: marcelo.lozadahidalgo@manchester.ac.uk (M.L.-H.); geim@manchester.ac.uk (A.K.G.)
†These authors contributed equally to this work.

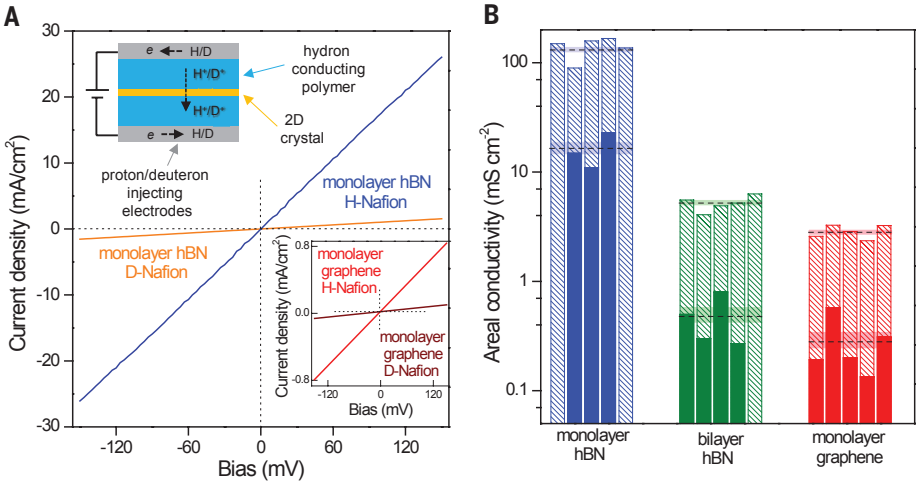

Fig. 1. Proton versus deuteron conductivities of 2D crystals. (**A**) Examples of *I*-*V* characteristics for hydron transport through monolayers of hBN (main panel) and graphene (lower inset). Top inset: Schematics of the experimental setup. Pd electrodes supply protons or deuterons into H- or D-Nafion; 2D crystals serve as barriers for hydrons. (**B**) Proton and deuteron conductivities (shaded and solid bars, respectively) for the most hydron-conductive 2D crystals. Each bar (solid or shaded) corresponds to a different device (nearly 30 are shown). The dashed lines mark the average conductivities for the six sets of devices, and the shaded areas around them show the standard errors.

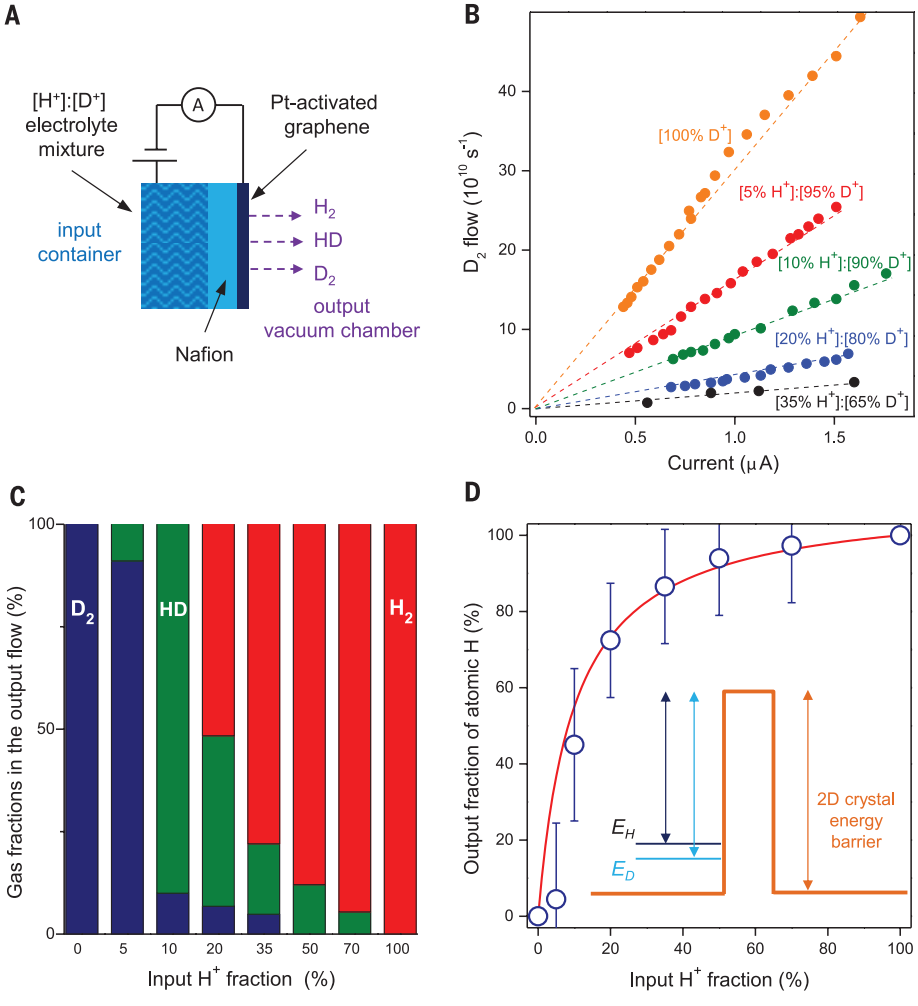

Fig. 2. Isotope separation by electrochemical pumping of hydrons through graphene. (**A**) Schematic of our mass spectrometry setup. (**B**) D_2 flow versus applied current for various proton-deuteron fractions in the input electrolyte. The dashed lines are linear fits. (**C**) Relative fractions of H_2, HD, and D_2 in the output flow for eight different compositions of the input electrolyte. (**D**) Fraction of H atoms at the output for different $[H^+]$ inputs. Inset: Schematic of the energy barrier presented by a 2D crystal for proton and deuteron transfer. The black and blue horizontal lines indicate zero-point states of protons and deuterons, respectively, in Nafion and water. The solid red curve shows the separation dependence expected for the known difference $E_D - E_H = 60$ meV, with no fitting parameters.

agreement with the value found from the ratio σ_H/σ_D in our conductivity measurements (*22*).

To explain the observed isotope effect, we first recall that proton permeation through 2D crystals is a thermally activated process (*5*, *9*). Therefore, if we neglect—to a first approximation (*22*)—the pre-exponential factor in the Arrhenius equation, our results can equivalently be described in terms of the energy barriers E_H and E_D presented by 2D crystals to proton and deuteron transport, respectively. Accordingly, we can write $\sigma_H/\sigma_D \approx \exp(\Delta E/k_BT)$, where $\Delta E = E_D - E_H$ and k_B is Boltzmann's constant. Although E_H and E_D obviously determine the hydron permeability of 2D crystals (*5*, *7*–*9*), their selectivity depends only on ΔE. Statistical analysis of the data in Fig. 1B yields $\sigma_H/\sigma_D \approx 10 \pm 0.8$, which translates into $\Delta E \approx 60 \pm 2$ meV for all the tested 2D membranes. Furthermore, the same value of ΔE allows us to describe quantitatively the selectivity found by the mass spectrometry measurements. As shown in supplementary materials, the protium output is given by $[H] = [H^+]/\{[H^+]+\exp(-\Delta E/k_BT)[D^+]\}$. This dependence is plotted in Fig. 2D using $\Delta E = 60$ meV and shows excellent agreement with the experiment.

Where does the difference between E_H and E_D come from, and why is it the same for all the tested 2D membranes despite their hydron conductivities being different by many orders of magnitude? The protons and deuterons in our experiments move not in vacuum but along hydrogen-bonded networks provided by sulfonate groups (SO_3^-) and water in Nafion (*23*). It is reasonable to expect that, before jumping through 2D crystals, hydrons remain transiently bonded to sulfonate and water groups and, accordingly, this presents the initial state in the transfer process (Fig. 2D, inset). The zero-point energies of these hydrogen-oxygen bonds are ≈0.2 eV for protons and ≈0.14 eV for deuterons (*11*, *22*). As illustrated in Fig. 2D, zero-point oscillations effectively reduce the activation barrier with respect to vacuum by 0.2 eV for protons, whereas for deuterons the reduction is smaller by 60 meV. This explanation is

consistent with all the experimental evidence. We expect the same-strength isotope effect if the 2D crystals are combined with other proton conductors based on oxides (*13*, *25*–*28*), and the separation factor should be even larger for proton-conducting media with stronger hydrogen bonds; for example, in fluorides (*28*).

The above explanation allows for several observations about proton transport through 2D crystals. First, it partially explains the disagreement between the experiment (*5*) and theory (*5*, *8*–*10*) in the absolute value of E_H for graphene: Zero-point oscillations reduce the activation barrier by ≈0.2 eV compared to theoretical values. We speculate that the remaining differences [<20% in the case of (*8*)] may be accounted for by considering other effects of the surrounding media (for example, two-body processes involving a distortion of the electron clouds by protons residing at the Nafion-graphene interface). Second, the experiments confirm that hydrogen chemisorption to 2D crystals is not the limiting step in the transfer process because, otherwise, the isotope effect would be different for hBN and graphene. Third, the described sieving mechanism implies $\alpha \approx 30$ for tritium-hydrogen separation. Fourth, it is quite remarkable that zero-point oscillations, a purely quantum effect, can still dominate room-temperature transport properties of particles 4000 times heavier than electrons.

The observed large α compares favorably with sieving efficiencies of the existing methods for hydrogen isotope separation (*15*–*20*). The high proton conductivity exhibited by graphene and boron nitride monolayers, comparable to that of commercial Nafion films (*5*, *22*), makes them potentially interesting for such applications. In this respect, the increasing availability of graphene grown by chemical vapor deposition (CVD) (*29*, *30*) provides a realistic prospect of scaling up the described devices from micrometer sizes to those required for industrial uses. Indeed, although micromechanical cleavage allows 2D membranes of highest quality, the approach is not scalable. As a proof of concept, we repeated the mass spectrometry measurements using centimeter-sized membranes made from CVD graphene and achieved the same $\alpha \approx 10$ (fig. S7). Notably, this shows that macroscopic cracks and pinholes present in CVD graphene do not affect the efficiency, because hydrons are electrochemically pumped only through the graphene areas that are electrically contacted (*22*). Furthermore, we estimate the energy costs associated with this isotope separation method as ≈0.3 kWh per kilogram of feed water (*22*), appreciably lower than costs of the existing enrichment processes (*15*, *16*). All this comes on top of the fundamentally simple and robust sieving mechanism, potentially straightforward setups, and the need for only water at the input without the use of chemical compounds (*16*).

REFERENCES AND NOTES

1. J. S. Bunch *et al.*, *Nano Lett.* **8**, 2458–2462 (2008).
2. S. P. Koenig, L. Wang, J. Pellegrino, J. S. Bunch, *Nat. Nanotechnol.* **7**, 728–732 (2012).
3. O. Leenaerts, B. Partoens, F. M. Peeters, *Appl. Phys. Lett.* **93**, 193107 (2008).
4. V. Berry, *Carbon* **62**, 1–10 (2013).
5. S. Hu *et al.*, *Nature* **516**, 227–230 (2014).
6. L. Britnell *et al.*, *Nano Lett.* **12**, 1707–1710 (2012).
7. L. Tsetseris, S. T. Pantelides, *Carbon* **67**, 58–63 (2014).
8. W. L. Wang, E. Kaxiras, *New J. Phys.* **12**, 125012 (2010).
9. M. Miao, M. B. Nardelli, Q. Wang, Y. Liu, *Phys. Chem. Chem. Phys.* **15**, 16132–16137 (2013).
10. J. L. Achtyl *et al.*, *Nat. Commun.* **6**, 6539 (2015).
11. K. B. Wiberg, *Chem. Rev.* **55**, 713–743 (1955).
12. B. E. Conway, *Proc. R. Soc. A Math. Phys. Eng. Sci.* **256,** 128–144 (1960).
13. K. D. Kreuer, A. Fuchs, J. Maier, *Solid State Ion.* **77**, 157–162 (1995).
14. A. Paris *et al.*, *Adv. Funct. Mater.* **23**, 1628–1635 (2013).
15. H. K. Rae, Ed., *Separation of Hydrogen Isotopes* (ACS Symposium Series, Washington, DC, 1978).
16. A. I. Miller, *Can. Nucl. Soc. Bull.* **22**, 1–14 (2001).
17. J. J. M. Beenakker, V. D. Borman, S. Y. Krylov, *Chem. Phys. Lett.* **232**, 379–382 (1995).
18. X. Zhao, S. Villar-Rodil, A. J. Fletcher, K. M. Thomas, *J. Phys. Chem. B* **110**, 9947–9955 (2006).
19. B. E. Conway, *Proc. R. Soc. London Ser. A* **247**, 400–419 (1958).
20. J. H. Rolston, J. Den Hartog, J. P. Butler, *J. Phys. Chem.* **80**, 1064–1067 (1976).
21. J. B. Marling, I. P. Herman, S. J. Thomas, *J. Chem. Phys.* **72**, 5603–5634 (1980).
22. See supplementary materials on *Science* Online.
23. K. A. Mauritz, R. B. Moore, *Chem. Rev.* **104**, 4535–4586 (2004).
24. K. W. Feindel, S. H. Bergens, R. E. Wasylishen, *J. Power Sources* **173**, 86–95 (2007).
25. T. Hibino, K. Mizutani, H. Iwahara, *J. Electrochem. Soc.* **140**, 2588 (1993).
26. K. D. Kreuer, *Chem. Mater.* **8**, 610–641 (1996).
27. D. Marx, M. E. Tuckerman, J. Hutter, M. Parrinello, *Nature* **397**, 601–604 (1999).
28. D. Marx, *ChemPhysChem* **7**, 1848–1870 (2006).
29. A. Reina *et al.*, *Nano Lett.* **9**, 30–35 (2009).
30. K. S. Kim *et al.*, *Nature* **457**, 706–710 (2009).

ACKNOWLEDGMENTS

This work was supported by the European Research Council, Lloyd's Register Foundation, the Graphene Flagship, the Royal Society, the Air Force Office of Scientific Research, and the Office of Naval Research. M.L.-H. acknowledges a Ph.D. studentship provided by the Consejo Nacional de Ciencia y Tecnología (Mexico). The reported results are included in a patent application "Graphene-Proton Transport," which is mostly based on (*5*).

SUPPLEMENTARY MATERIALS

www.sciencemag.org/content/351/6268/68/suppl/DC1
Materials and Methods
Figs. S1 to S7
References (*31*–*49*)

8 July 2015; accepted 18 November 2015
10.1126/science.aac9726

ORGANIC CHEMISTRY

Catalytic conjunctive cross-coupling enabled by metal-induced metallate rearrangement

Liang Zhang, Gabriel J. Lovinger, Emma K. Edelstein, Adam A. Szymaniak, Matteo P. Chierchia, James P. Morken*

Transition metal catalysis plays a central role in contemporary organic synthesis. Considering the tremendously broad array of transition metal–catalyzed transformations, it is remarkable that the underlying elementary reaction steps are relatively few in number. Here, we describe an alternative to the organometallic transmetallation step that is common in many metal-catalyzed reactions, such as Suzuki-Miyaura coupling. Specifically, we demonstrate that vinyl boronic ester ate complexes, prepared by combining organoboronates and organolithium reagents, engage in palladium-induced metallate rearrangement wherein 1,2-migration of an alkyl or aryl group from boron to the vinyl α-carbon occurs concomitantly with C–Pd σ-bond formation. This elementary reaction enables a powerful cross-coupling reaction in which a chiral Pd catalyst merges three simple starting materials—an organolithium, an organoboronic ester, and an organotriflate—into chiral organoboronic esters with high enantioselectivity.

Organoboronic acids and their derivatives are widely available and broadly useful starting materials for organic synthesis (*1*). In addition to being environmentally benign and generally inexpensive, these reagents exhibit a near-ideal balance of stability and reactivity. Although chemically and configurationally stable, organoboronic esters engage in a broad array of carbon-carbon and carbon-heteroatom bond-forming processes upon activation. The most commonly practiced such reaction is the transition metal–catalyzed Suzuki-Miyaura cross-coupling reaction between organic electrophiles and organoboron compounds (*2*). In broad strokes, the mechanism of the Suzuki-Miyaura reaction involves a sequence of (i) oxidative addition between a metal catalyst and the electrophile, (ii) transmetallation with the organoboron reagent, and (iii) reductive elimination of the C-C bonded product (*3*). Here, we used an alternative pathway to the organoboron transmetallation step. The overall putative catalytic cycle enables a class of organoboron cross-coupling that we term "conjunctive cross-coupling" (Fig. 1A) because it merges

Department of Chemistry, Boston College, Chestnut Hill, MA 02467, USA.
***Corresponding author. E-mail: morken@bc.edu**

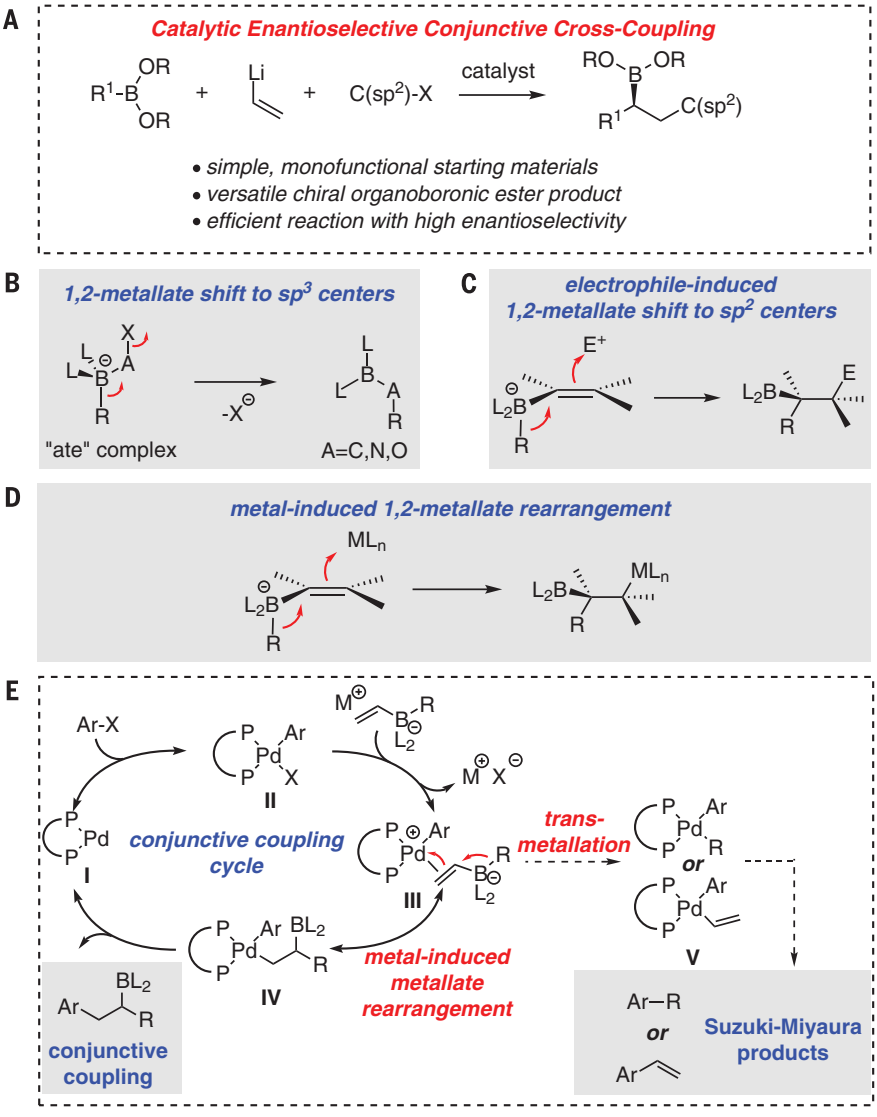

Fig. 1. Metal-induced metallate shift as a strategy for catalytic reaction design. (**A**) The catalytic conjunctive cross-coupling process. (**B**) Common metallate shift to saturated carbon centers requires a leaving group. L, ligand. (**C**) Metallate shift to unsaturated carbons is often activated by addition of an external electrophile. M, metal; E, electrophile. (**D**) A metallate shift promoted by a metal complex can serve as an alternative to a transmetallation process. (**E**) Proposed catalytic cycle for conjunctive cross-coupling. Ar, aryl group.

two nucleophilic reagents into one during the course of the reaction. Overall, the conjunctive cross-coupling constructs chiral products by merging three simple starting materials: an organolithium reagent, an organoboronic ester, and an organic electrophile. The reaction, which adds to recent catalytic alkene carboboration reactions (*4*, *5*), establishes two new carbon-carbon bonds and forms a stereogenic center bearing a useful organoboronic ester with high enantioselectivity.

Organoboronic esters are known to participate in a wide range of reactions that occur by stereospecific 1,2-metallate rearrangements (*6*, *7*). The preponderance of these reactions occur with a four-coordinate anionic boron-centered "ate" complex (Fig. 1B) that rearranges by a 1,2-carbon shift from boron to an adjacent sp^3-hybridized electrophilic center (designated "A") bearing an attached leaving group (X). The stereoelectronic requirements of the metallate shift dictate an anti-periplanar arrangement of the migrating carbon atom (R) and the leaving group such that the overall process is stereoretentive at R but stereoinvertive at A (*8*). These processes are common (*9*) for transformations where the "A" group is a carbon, nitrogen, or oxygen atom and less common but still established for sulfur and phosphorus (*10*, *11*). Because of the stereospecific nature of the above-described processes, stereoselectivity in metallate shifts is generally subject to substrate control (*12*), although Jadhav and Man reported an example with selectivity dictated by a chiral catalyst (*13*). Metallate rearrangement from boron to sp (*14*) and sp^2 (*15*) hybridized carbons often require the addition of an external electrophilic activator (Fig. 1C), and generally the 1,2-metallate shift is followed by elimination to reestablish unsaturation (*16*). In this context, we considered that in place of stoichiometric electrophilic activating agents, π-acidic late transition metals might similarly promote the 1,2-metallate shift of alkenyl boronates (Fig. 1D) and that the resulting chiral organometallic intermediate might be used in subsequent bond-forming processes.

In one embodiment of catalysis based on metal-induced 1,2-metallate rearrangements, we considered that an electrophilic palladium complex (**II**, Fig. 1E), generated by oxidative addition of **I** with an organic electrophile, might induce 1,2-migration in a vinyl boronate-derived ate complex (**III**→**IV**) and establish a new C–C bond and a boron-substituted stereogenic center. Subsequent reductive elimination (**IV**→**I**) would serve to establish a second C–C bond, release the product, and concomitantly furnish a reduced Pd complex that might continue a catalytic cycle. The net reaction, in this cycle, is aligned with important work from Murakami, who studied reactions of alkynyl boron ate complexes (*17*). Although π-acidic late transition metal complexes are well known to activate alkenes for nucleophilic attack, nucleopalladation with Pd(II) complexes generated by oxidative addition reactions are less common (*18*, *19*). For the envisioned process to be successful, several key questions emerged: Would the Pd(II) aryl complexes be sufficiently π-acidic to facilitate metallate rearrangement (**III**→**IV**)? Would common direct transmetallation (**III**→**V**) dominate the reaction and furnish Suzuki-Miyaura products?

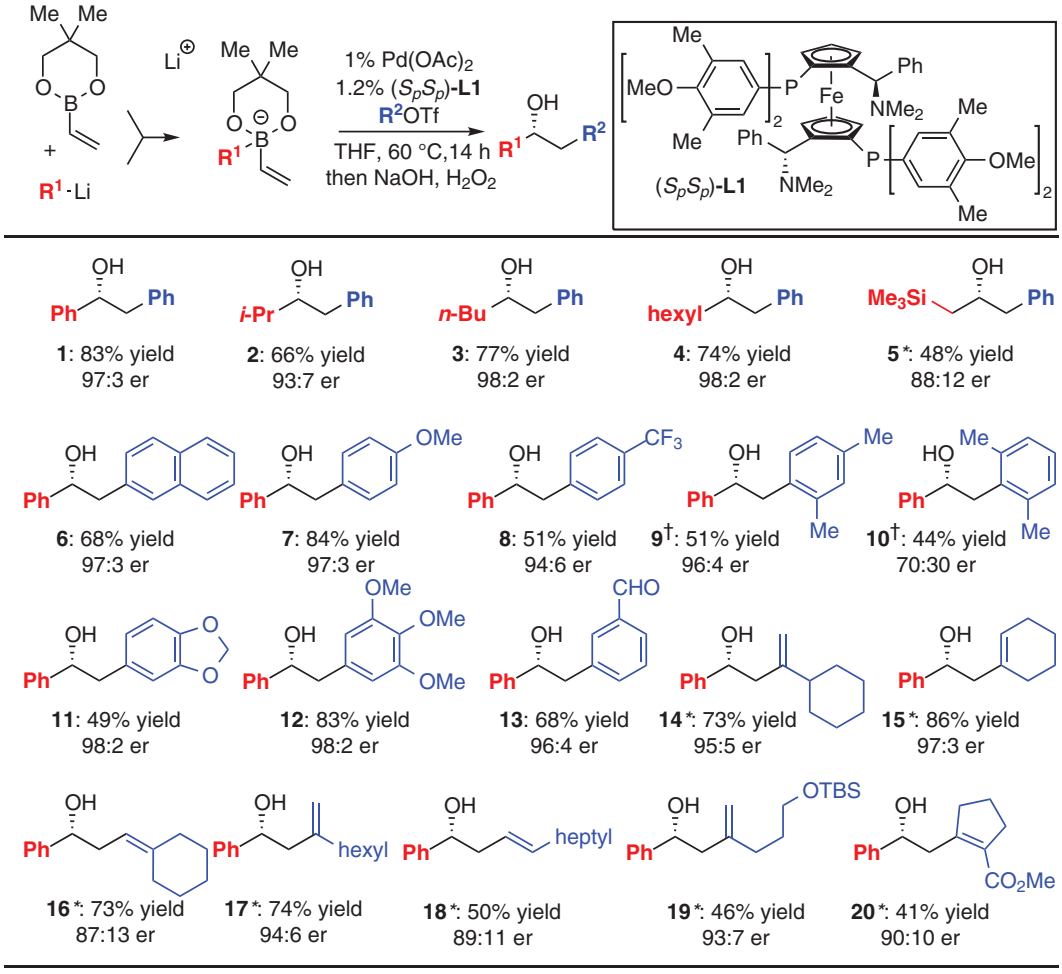

Fig. 2. Scope of the catalytic conjunctive cross-coupling reaction starting from vinyl boronic esters. Yields represent isolated yield of purified material and are an average of two experiments. The absolute configuration was determined by anomalous dispersion x-ray and by chromatographic comparison to known compounds. *VinylB(neo) was replaced with vinylB(pin); †reaction conducted at 80°C. er was determined by chiral supercritical fluid chromatography. OAc, acetate; Me, methyl group; Ph, phenyl group; OTf, trifluoromethanesulfonate; OTBS, tert-butyldimethylsiloxy.

Could facial selectivity in olefin binding render the migration (**III**→**IV**) enantioselective? Last, would β-hydrogen elimination in intermediates such as **IV** compete with reductive elimination?

To begin our studies of the conjunctive cross-coupling reaction, we selected phenyl triflate as the electrophile, anticipating that the outer-sphere triflate anion would leave open a coordination site on Pd for alkene binding (Fig. 1E, **III**). In an effort to minimize steric penalties that might inhibit metallate shift, we opted for an unsubstituted vinyl group in construction of the boron ate complex. Similarly, on the basis of recent studies from Mayr and Aggarwal (*20*, *21*), we selected a *neo*-pentylglycolato ligand for boron because the ate complexes derived from this ligand (versus others readily available) were determined to be the most nucleophilic. Last, in an effort to favor reductive elimination relative to β-hydrogen elimination in putative intermediate **IV**, we selected ligands with large bite angles for the palladium complex. Initial experiments with achiral bidentate ferrocenyl 1,1′-diphosphines were promising and suggested that the conjunctive cross-coupling could indeed operate. A survey of a number of chiral diphosphine structures revealed that Josiphos (*22*) and MandyPhos (Solvias AG, Kaiseraugst, Switzerland) (*23*) are particularly effective ligand classes, with the MandyPhos ligand **L1** providing an outstanding level of enantioselectivity and very good catalyst efficiency in the reaction.

In optimizing the reaction conditions, we found tetrahydrofuran (THF) to be the most effective solvent. Therefore, when the migratory R group was appended to boron by addition of hydrocarbon solutions of organolithium reagents to the neopentyl glycol–derived vinyl boronic ester vinylB(neo) (Fig. 2), the resulting ate complexes were evaporated to dryness and redissolved in THF before reaction. The efficiency of the reaction was also greatly diminished by chloride, bromide, or iodide ions, an obstacle easily overcome by the continued use of aryl and alkenyl triflates as the electrophile. For coupling of alkenyl triflate electrophiles, the reaction selectivity was markedly enhanced with boron ate complexes derived from pinacolato ligands in place of the *neo*-pentylglycol derivative [e.g., product **15** is formed in 53% yield and 82:18 enantiomeric ratio (er) when using the *neo*-pentylglycol ligand], whereas for aryl triflates, the *neo*-pentylglycol ligand furnished higher selectivity [**1** formed in 94% yield, 93:7 er using B(pin) group]. With these features optimized, the scope of the conjunctive coupling was explored with an array of ate complexes and electrophiles. During these experiments, it was most convenient to oxidize the product organoboronic ester to the derived alcohol by treatment with NaOH and H_2O_2; however, isolation of the organoboron product itself is also possible (the organoboron precursor to alcohol **1** was isolated in 76% yield by silica gel chromatography). As shown in Fig. 2, both aryl and alkyl groups proved competent migrating elements in conjunctive coupling reactions. In cases where the yield of product is low, analysis of the reaction mixture before oxidation showed that by-products generally consist of recovered organoboronic ester (likely generated during workup by protonolysis of one carbon ligand from the ate complex) and direct Suzuki-Miyaura products. Primary and secondary alkyl groups migrate, as do functionalized alkyl appendages [e.g., (trimethylsilyl)methyl]. Conjunctive couplings were also effective for both electron-rich and electron-poor electrophiles. Moderately encumbered electrophiles, such as ortho-substituted arenes, can engage in the reaction, although the more highly substituted 2,6-dimethylphenyl derivative suffered from lower selectivity. With respect to preparation of chiral hydrocarbon frameworks, a range of substituted alkenyl triflates participate, and the configuration of the product alkene directly reflects that of the precursor electrophile.

The ate complex could be generated either by addition of an organolithium reagent to vinylB(neo) (Fig. 2) or by addition of vinyllithium to organoboronic esters (Fig. 3). Considering the broad

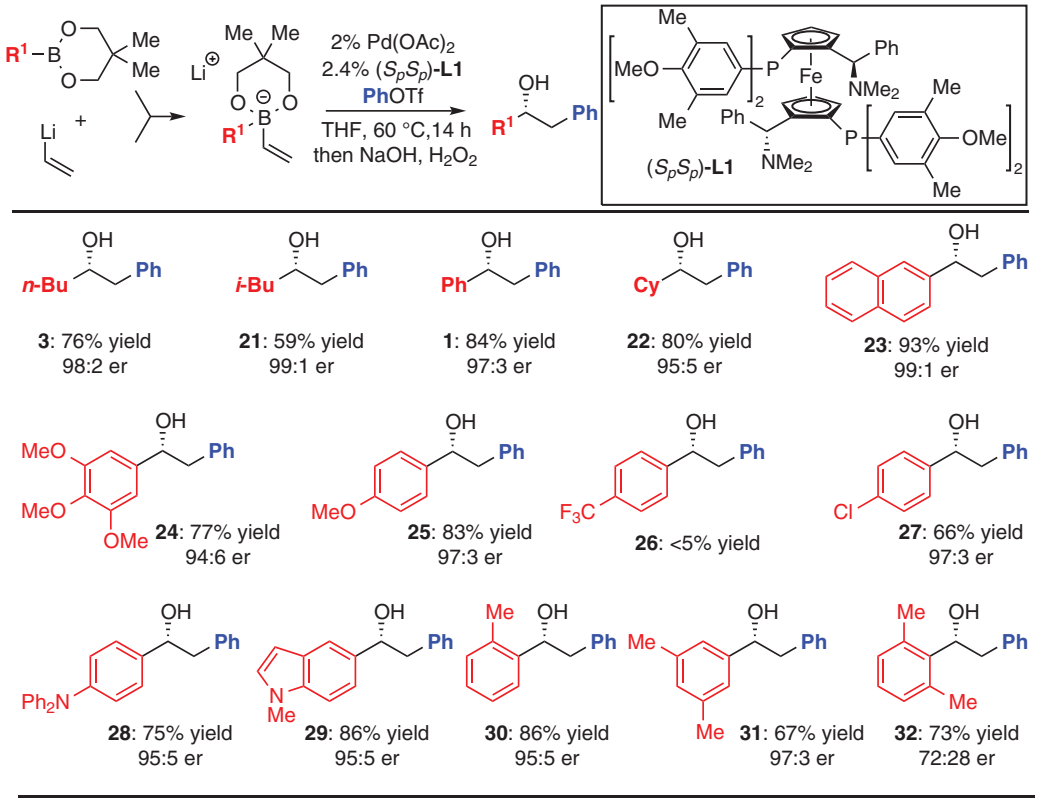

Fig. 3. Scope of the catalytic conjunctive cross-coupling reaction starting from alkyl or aryl boronic esters. Yields represent isolated yield of purified material and are an average of two experiments. Cy, cyclohexyl group.

array of organoboronic esters that are already available for use in common cross-coupling processes, the latter strategy is particularly enabling. In this context, we found that the presence of lithium halide salts, even at 1 to 2 mole percent (mol %) loading, markedly erodes conjunctive coupling efficiency. Thus, to perform the reaction with highest efficiency with 2 mol % catalyst loading, it is critical that halide-free vinyllithium be used. To prepare this reagent, we developed a procedure that involved lithium-halogen exchange with *n*-BuLi (Bu, butyl group) in hexane, followed by low-temperature recrystallization of pure vinyllithium. When these precautions are taken, conducting the reaction as in Fig. 3 allowed the scope of the migrating group to be surveyed more completely and revealed that, although reactions requiring migration of very electron-deficient groups are still a challenge, electron-neutral and electron-rich arenes can engage in the migration, as can those that are more highly substituted (i.e., 2,6-disubstituted arenes). We also found that, with 5 mol % catalyst loading, vinyllithium prepared as above but without recrystallization was effective (e.g., **3** formed in 69% yield, 98:2 er) and that vinyllithium prepared by lithium-tin exchange (*24*) could be used directly (2 mol % catalyst, **1** formed in 83% yield, 97:3 er).

To probe the utility of conjunctive cross-coupling to practical organic synthesis, we were attracted to the natural product (–)-combretastatin (*25*), a member of a family of cytotoxic stilbene-derived natural products that bind β-tubulin (Fig. 4A). Although many synthetic methods have facilitated the construction of combretastatins (*26*),

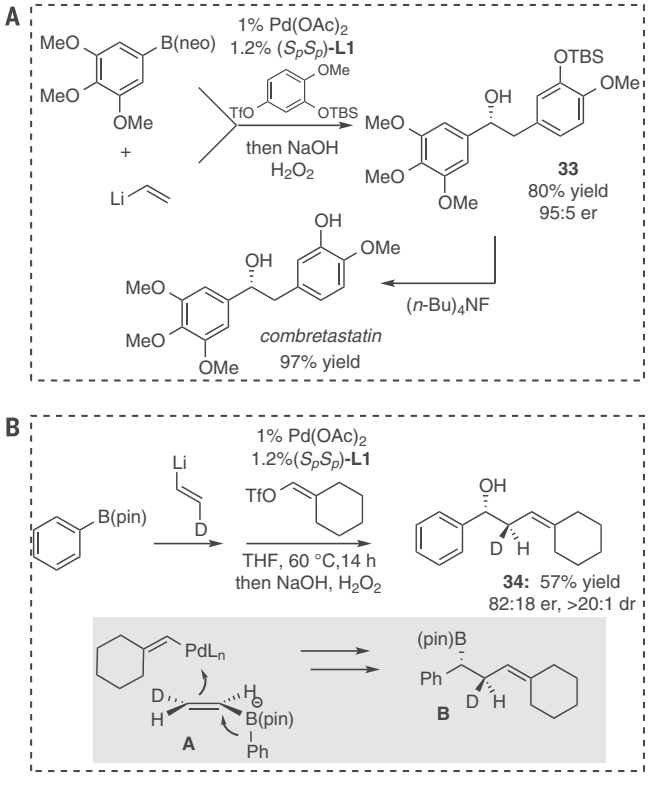

Fig. 4. Synthesis and mechanistic studies. (**A**) Synthesis of combretastatin by conjunctive cross-coupling. (**B**) The stereochemical course of metal-induced metallate rearrangement. dr, diastereomeric ratio.

alternative processes may engage different starting materials and thereby provide access to distinct analogs. In the case of conjunctive cross-coupling, the requisite boronic ester and electrophile are readily available and, as depicted in Fig. 4A, are readily converted to the coupled product in an efficient and highly selective fashion. Removal of the silicon protecting group furnished the target

structure, spectra of which were fully consistent with the natural isolate.

The mechanism of the conjunctive coupling reaction is the subject of ongoing investigations, although the substrate scope (Figs. 2 and 3) gives clues about the process. The observation that electron-deficient arenes are less prone to migration is consistent with the mechanistic hypothesis put forward in Fig. 1E. According to this hypothesis, formation of **IV** would likely be stereochemistry determining, and, in line with this prediction, the selectivity of the reaction depends not only on the ligand framework but also on the organoboronic ester ligand (pinacol versus *neo*-pentylglycol), the migrating group, and the electrophile. In addition to these observations, one preliminary experiment sheds important light on the nature of the metal-induced metallate rearrangement that appears to underlie the conjunctive coupling process. As depicted in Fig. 4B, when the reacting ate complex was constructed from stereochemically defined deuterium-labeled vinyllithium (*27*) and phenylB(pin), the (1*R*,2*R*) stereoisomer of the conjunctive coupling product was formed in >20:1 diastereoselection (82:18 er). Although other interpretations are possible, should the mechanism be in line with that proposed in Fig. 1E and reductive elimination occur with retention of configuration at carbon (a reasonable assumption), the observed stereochemical outcome in Fig. 4B is consistent with anti-migration of the arene group to a Pd-olefin complex (Fig. 1D). Such an outcome is reminiscent of nucleometallation reactions that do not involve preassociation of the migrating group and the metal center (*28*).

We anticipate that many other transition metal–catalyzed reactions might also be reengineered to incorporate metal-induced metallate rearrangements, thereby providing distinct strategies for catalytic enantioselective synthesis.

REFERENCES AND NOTES

1. D. G. Hall, Ed., *Boronic Acids* (Wiley-VHC, Weinheim, Germany, 2011).
2. N. Miyaura, K. Yamada, A. Suzuki, *Tetrahedron Lett.* **20**, 3437–3440 (1979).
3. N. Miyaura, A. Suzuki, *Chem. Rev.* **95**, 2457–2483 (1995).
4. T. Jia *et al.*, *J. Am. Chem. Soc.* **137**, 13760–13763 (2015).
5. W. Su *et al.*, *Angew. Chem. Int. Ed.* **54**, 12957–12961 (2015).
6. E.-I. Negishi, *Org. React.* **33**, 1–246 (1985).
7. V. K. Aggarwal, G. Y. Fang, X. Ginesta, D. M. Howells, M. Zaja, *Pure Appl. Chem.* **78**, 215–229 (2006).
8. M. M. Midland, A. R. Zolopa, R. L. Halterman, *J. Am. Chem. Soc.* **101**, 248–249 (1979).
9. A. Suzuki, *Top. Curr. Chem.* **112**, 67–115 (1983).
10. P. M. Draper, T. H. Chan, D. N. Harpp, *Tetrahedron Lett.* **11**, 1687–1688 (1970).
11. S. P. Thomas, R. M. French, V. Jheengut, V. K. Aggarwal, *Chem. Rec.* **9**, 24–39 (2009).
12. D. Leonori, V. K. Aggarwal, *Top. Organomet. Chem.* **49**, 271–295 (2015).
13. P. K. Jadhav, H.-W. Man, *J. Am. Chem. Soc.* **119**, 846–847 (1997).
14. A. Suzuki *et al.*, *J. Am. Chem. Soc.* **95**, 3080–3081 (1973).
15. For lead references, see (*29*).
16. G. Zweifel, H. Arzoumanian, C. C. Whitney, *J. Am. Chem. Soc.* **89**, 3652–3653 (1967).
17. N. Ishida, Y. Shimamoto, M. Murakami, *Org. Lett.* **11**, 5434–5437 (2009).
18. J. S. Nakhla, J. W. Kampf, J. P. Wolfe, *J. Am. Chem. Soc.* **128**, 2893–2901 (2006).
19. D. Bruyère, D. Bouyssi, G. Balme, *Tetrahedron* **60**, 4007–4017 (2004).
20. G. Berionni, A. I. Leonov, P. Mayer, A. R. Ofial, H. Mayr, *Angew. Chem. Int. Ed.* **54**, 2780–2783 (2015).
21. K. Feeney, G. Berionni, H. Mayr, V. K. Aggarwal, *Org. Lett.* **17**, 2614–2617 (2015).
22. A. Togni *et al.*, *J. Am. Chem. Soc.* **116**, 4062–4066 (1994).
23. J. J. Almena Perea, M. Lotz, P. Knochel, *Tetrahedron Asymmetry* **10**, 375–384 (1999).
24. D. Seyferth, M. A. Weiner, *J. Am. Chem. Soc.* **83**, 3583–3586 (1961).
25. G. R. Pettit, G. M. Cragg, D. L. Herald, J. M. Schmidt, P. Lohavanijaya, *Can. J. Chem.* **60**, 1374–1376 (1982).
26. R. Singh, H. Kaur, *Synthesis* **2009**, 2471–2491 (2009).
27. R. P. Hughes, H. A. Trujillo, J. W. Egan Jr., A. L. Rheingold, *J. Am. Chem. Soc.* **122**, 2261–2271 (2000).
28. R. I. McDonald, G. Liu, S. S. Stahl, *Chem. Rev.* **111**, 2981–3019 (2011).
29. A. Bottoni, M. Lombardo, A. Neri, C. Trombini, *J. Org. Chem.* **68**, 3397–3405 (2003).

ACKNOWLEDGMENTS

Experimental data are available in the associated Supplementary Materials. This research was supported in part by the NIH, National Institute of General Medical Sciences (GM 64451), and by Boston College. Metrical parameters for the crystal structure of compound **1** are available free of charge from the Cambridge Crystallographic Data Centre under accession number CCDC 1437520.

SUPPLEMENTARY MATERIALS

www.sciencemag.org/content/351/6268/70/suppl/DC1
Materials and Methods
Tables S1 to S7
References (*30*–*57*)

12 October 2015; accepted 18 November 2015
10.1126/science.aad6080

MICROBIAL ENGINEERING

Self-photosensitization of nonphotosynthetic bacteria for solar-to-chemical production

Kelsey K. Sakimoto,[1,2] Andrew Barnabas Wong,[1,2] Peidong Yang[1,2,3,4]*

Improving natural photosynthesis can enable the sustainable production of chemicals. However, neither purely artificial nor purely biological approaches seem poised to realize the potential of solar-to-chemical synthesis. We developed a hybrid approach, whereby we combined the highly efficient light harvesting of inorganic semiconductors with the high specificity, low cost, and self-replication and -repair of biocatalysts. We induced the self-photosensitization of a nonphotosynthetic bacterium, *Moorella thermoacetica*, with cadmium sulfide nanoparticles, enabling the photosynthesis of acetic acid from carbon dioxide. Biologically precipitated cadmium sulfide nanoparticles served as the light harvester to sustain cellular metabolism. This self-augmented biological system selectively produced acetic acid continuously over several days of light-dark cycles at relatively high quantum yields, demonstrating a self-replicating route toward solar-to-chemical carbon dioxide reduction.

The necessity of improving the natural mechanisms of solar energy capture for sustainable chemical production (*1*) has motivated the development of photoelectrochemical devices based on inorganic solid-state materials (*2*). Although solid-state semiconductor light absorbers often exceed biological light harvesting in efficiency (*3*), the transduction of photoexcited electrons into chemical bonds (particularly toward multicarbon compounds from CO_2) remains challenging with abiotic catalysts (*4*, *5*). Such catalysts struggle to compete with the high-specificity, low-cost material requirements and the self-replicating, self-repairing properties of biological CO_2 fixation (*6*). Thus, a viable solution must combine the best of both worlds: the light-harvesting capabilities of semiconductors with the catalytic power of biology.

[1]Department of Chemistry, University of California–Berkeley, Berkeley, CA 94720, USA. [2]Materials Sciences Division, Lawrence Berkeley National Laboratory, Berkeley, CA 94720, USA. [3]Department of Materials Science and Engineering, University of California–Berkeley, Berkeley, CA 94720, USA. [4]Kavli Energy NanoSciences Institute, Berkeley, CA 94720, USA.
***Corresponding author. E-mail: p_yang@berkeley.edu**

Several inorganic-biological hybrid systems have been devised: semiconductor nanoparticles with hydrogenases to produce biohydrogen (*7*), long wavelength–absorbing nanomaterials to improve the photosynthetic efficiency of plants (*8*), and whole cells with photoelectrodes for CO_2 fixation (*9*, *10*). Whole-cell microorganisms are favored to facilitate the multistep process of CO_2 fixation and can self-replicate and self-repair (*11*). Furthermore, bacteria termed "electrotrophs" can undergo direct electron transfer from an electrode (*12*). However, traditional chemical synthesis of the semiconductor component often requires high-purity reagents, high temperatures, and complex microfabrication techniques. Additionally, the integration of such foreign materials with biotic systems is nontrivial (*13*). Many reports have shown that some microorganisms induce the precipitation of nanoparticles (*14*), producing an inherently biocompatible nanomaterial under mild conditions.

Although photosynthetic organisms can precipitate semiconductor nanoparticles, their metabolic pathways are arguably less desirable than those of their nonphotosynthetic counterparts. Although gene modification of phototrophs has

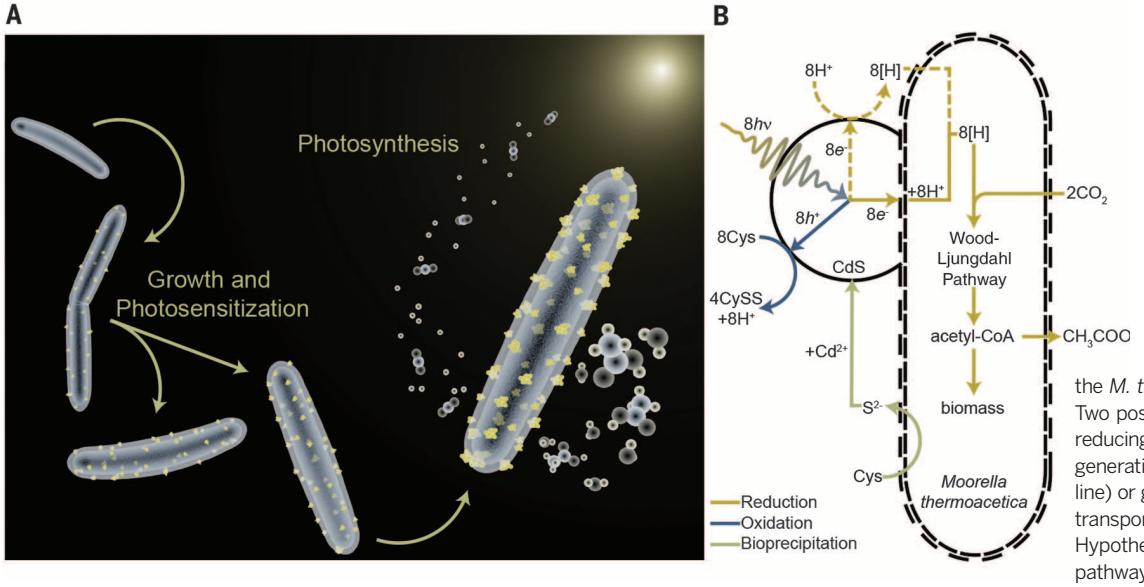

Fig. 1. *M. thermoacetica*–CdS reaction schematics. (**A**) Depiction of the *M. thermoacetica*–CdS hybrid system, proceeding from the growth of the cells and bioprecipitation (loading) of the CdS nanoparticles (shown in yellow) through photosynthetic conversion of CO_2 (center right) to acetic acid (right). (**B**) Pathway diagram for the *M. thermoacetica*–CdS system. Two possible routes to generate reducing equivalents, [H], exist: generation outside the cell (dashed line) or generation by direct electron transport to the cell (solid line). Hypothesized electron transfer pathways are presented in fig. S1.

progressed (*15*), nonphotosynthetic bacteria remain the workhorse of synthetic biology, offering a facile way to tailor the product diversity from CO_2 reduction (*16*). Additionally, thermodynamic comparisons reveal substantial energetic advantages to photosensitizing nonphotosynthetic CO_2 reduction (*17*). Of particular interest is the Wood-Ljungdahl pathway, through which CO_2 is reduced to acetyl coenzyme A (acetyl-CoA), a common biosynthetic intermediate, and eventually to acetic acid, both of which can be further upgraded to high-value products by wild-type and genetically engineered organisms (*10*, *18*). This pathway is also used by CO_2-fixing electrotrophs, enabling the use of semiconductor photoelectrons in this energetically efficient biosynthetic route.

We developed a hybrid system containing the nonphotosynthetic CO_2-reducing bacterium *Moorella thermoacetica* (ATCC 39073) and its biologically precipitated CdS nanoparticles (*19*). CdS is a well-studied semiconductor with an appropriate band structure and is suitable for photosynthesis (*20*). As an acetogen and an electrotroph, *M. thermoacetica* serves as an ideal model organism to explore the capabilities of a hybrid system (*21*).

The photosynthesis of acetic acid by *M. thermoacetica* and CdS is a two-step, one-pot synthesis (Fig. 1). First, the precipitation of CdS by *M. thermoacetica* is triggered by the addition of Cd^{2+} and cysteine (Cys) as the sulfur source (*19*, *22*). *M. thermoacetica* uses photogenerated electrons from illuminated CdS nanoparticles to carry out photosynthesis (Fig. 1B). The absorption of a photon, $h\nu$, by CdS produces an electron and hole pair, e^- and h^+. The electron generates a reducing equivalent, [H] (see supplementary text and fig. S1 for elaboration of this process), that is passed on to the Wood-Ljungdahl pathway to synthesize acetic acid from CO_2. Cysteine quenches the h^+, leading to the oxidized disulfide form, cystine (CySS) (see supplementary text for the full set of reaction equations). The overall photosynthetic reaction is

$$2\ CO_2 + 8\ Cys + 8\ h\nu \xrightarrow{M.\ thermoacetica\text{–}CdS} CH_3COOH + 2H_2O + 4\ CySS \quad (1)$$

The precipitation of CdS by *M. thermoacetica* was initiated by the addition of $Cd(NO_3)_2$ to an early exponential growth culture of glucose-grown cells supplemented with Cys (fig. S2) (*19*). Scanning electron microscopy (SEM), scanning transmission electron microscopy (STEM), and energy-dispersive x-ray spectroscopy (EDS) mapping revealed clusters of smaller nanoparticles (<10 nm; Fig. 2, A and B) composed of cadmium and sulfur on the cells (Fig. 2, C to E, and fig. S3). Absorption spectra and Tauc plots yielded a measured direct band gap of 2.51 ± 0.05 eV (fig. S4A). The slightly larger measured band gap relative to bulk CdS (2.42 eV) suggests the quantum confinement expected of <10-nm particles (*20*). Powder x-ray diffraction showed broad peaks consistent with small particles of the wurtzite phase (fig. S4B).

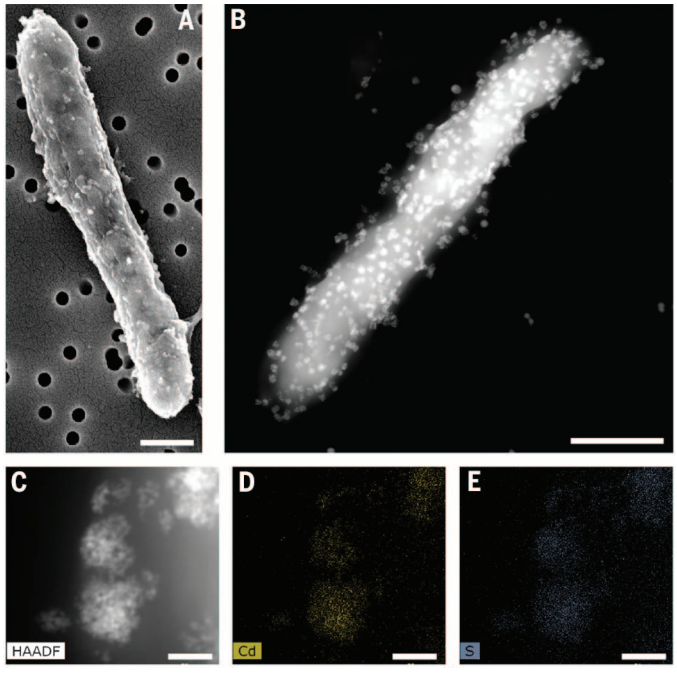

Fig. 2. Electron microscopy of *M. thermoacetica*–CdS hybrids. (**A**) SEM image of CdS nanoparticles on *M. thermoacetica*. (**B**) High-angle annular dark field (HAADF) STEM image of a single cell, showing clusters across the entire cell surface. (**C**) HAADF image and EDS mapping showing clusters mainly composed of (**D**) cadmium and (**E**) sulfur. Further elemental mapping is provided in fig. S3. Scale bars in (A) and (B), 500 nm; in (C) and (D), 50 nm.

To confirm photosynthesis, a series of deletional control experiments was carried out in which *M. thermoacetica*, CdS, and light were systematically removed (Fig. 3, A and B). In the absence of light (405 ± 5 nm), acetic acid concentrations decreased [from ~2 mM accumulated under initial

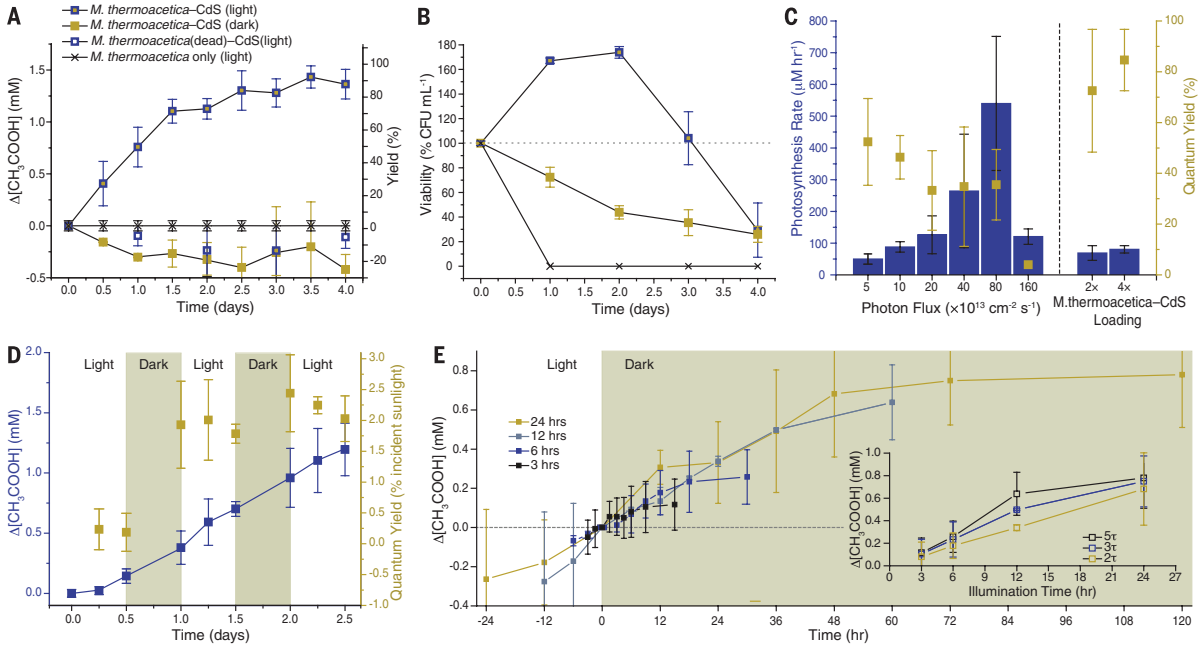

Fig. 3. Photosynthesis behavior of *M. thermoacetica*–CdS hybrids. (**A**) Photosynthetic production of acetic acid by *M. thermoacetica*–CdS hybrids and deletional controls. The key applies to (A) and (B) only. (**B**) CFU viability assays for *M. thermoacetica*–CdS hybrids and deletional controls. (**C**) Rates of acetic acid production and quantum yields for increasing illumination intensities and *M. thermoacetica*–CdS concentrations. (**D**) Photosynthetic acetic acid production under low-intensity simulated sunlight with light-dark cycles. (**E**) Acetic acid production under dark conditions for varying illumination times. The inset shows the relation between illumination time, τ, and acetic acid yield under dark conditions at increasing multiples of τ. All points and error bars show the mean and error-propagated SD, respectively, of triplicate experiments.

H_2:CO_2 acclimation, as measured by quantitative proton nuclear magnetic resonance (^{1}H-qNMR) spectroscopy], potentially as the result of a dark catabolic process. The viability determined by colony-forming units (CFU) assays slowly declined to ~25% after 4 days (from the initial 5.9 ± 0.4 × 10^4 CFU ml^{-1} and 1.7 ± 0.4 × 10^9 cells ml^{-1}), indicating that the *M. thermoacetica*–CdS system requires light to maintain viability. The viability of bare *M. thermoacetica* without CdS dropped to 0% within the first day under light, consistent with previous observations of semiconducting and/or insulating precipitates having a photoprotective role toward bacteria (*23*). Only *M. thermoacetica*–CdS hybrids exposed to light produced acetic acid. The ^{1}H-qNMR spectrum revealed acetic acid to be the only product of CO_2 reduction, confirming the high selectivity expected of biological catalysts (fig. S5). After the first 1.5 days, the rate of production began to plateau because of the limiting amounts of the sacrificial reductant, Cys.

We calculated a maximum yield of ~90% acetic acid (based on the initial Cys concentration), which is consistent with previous observations that in the Wood-Ljungdahl pathway, ~10% of reduced CO_2 is directed toward cell biomass (*24*). During photosynthesis, both the viability and the cell counts of the *M. thermoacetica*–CdS system nearly doubled after the first day (fig. S6), on par with the doubling time of autotrophic growth (~25 hours). Although the growth was not vigorous and perhaps was limited by the total amount of CdS and other nutrients, these results suggest the possibility of a completely self-reproducing hybrid organism sustained purely through solar energy. After the third and fourth days, viability decreased in coincidence with the depletion of Cys, leading to oxidative photodamage (fig. S7).

Under increasing blue light flux (435 to 485 nm), the rate of acetic acid production increased (Fig. 3C). At 5 × 10^{13} photons cm^{-2} s^{-1}, a quantum yield of 52 ± 17% was observed. The rate of photosynthesis increased up to 160 × 10^{13} photons cm^{-2} s^{-1}, after which the rate dramatically decreased and the quantum yield dropped to 4 ± 1%, possibly due to photooxidative degradation under high light intensities (*25*). At high light fluxes, large holes formed in the cell surface and, in some cases, resulted in the complete destruction of the cell membrane (fig. S7). The high quantum yield of the *M. thermoacetica*–CdS system is notable, given that previous analogous systems often have had reported quantum efficiencies of ~20% (*7*). This result is rationalized by the low light flux of these measurements, which reduces losses from recombination (*26*). With four times the normal loading of *M. thermoacetica*–CdS hybrids, we measured a quantum yield of 85 ± 12% (Fig. 3C). Under higher concentrations, the average flux per bacterium decreased, correlating with increased quantum yield.

To further characterize their photosynthetic behavior, we illuminated *M. thermoacetica*–CdS hybrids under low-intensity simulated sunlight (air mass 1.5 global spectrum, 2 W m^{-2}) with a light-dark cycle of 12 hours each to mimic day-night cycles (Fig. 3D). Unexpectedly, acetic acid concentrations not only increased under illumination but continued to increase in the dark at the same rate, through several light-dark cycles. A potential explanation lies in the accumulation of biosynthetic intermediates during the light cycle, which are then used during the dark cycle. These may include a number of reductive species [e.g., NADH (reduced nicotinamide adenine dinucleotide), NADPH (reduced NAD phosphate), or ferredoxin)] or intermediates in the Wood-Ljungdahl pathway such as acetyl-CoA (*27*). A proton gradient may also be storing energy for adenosine triphosphate synthesis in the dark. Further experiments that varied the duration of the light cycle (Fig. 3E) revealed a proportionality between the length of illumination, τ, and the acetic acid yield under dark conditions. Although the initial rate during and just after illumination appears to be relatively constant, consistent with a zero-order catalytic reaction, the yield begins to plateau after 2τ, exhibiting a linearity between illumination time and acetic acid yield (Fig. 3E, inset). However, at 5τ, samples that were illuminated for 24 hours break this trend. These observations suggest that during up to 12 hours of illumination, some intermediate accumulates, enabling a proportional acetic acid yield during the dark cycle. Beyond this, the intermediate may saturate, with longer illumination times yielding no further acetic acid. We measured a peak quantum yield of 2.44 ± 0.62% of total incident low-intensity simulated sunlight (Fig. 3D). These quantum yields are order-of-magnitude comparable to the year-long averages determined for plants and algae, which range from ~0.2 to 1.6% (*1*).

Biological routes to solid-state materials have often struggled to compete with high-quality traditionally synthesized materials. This work

demonstrates not only that biomaterials can be of sufficient quality to carry out useful photochemistry, but that in some ways they may be more advantageous in biological applications. Most traditional nanoparticle syntheses require organic capping ligands to control the particle shape. These ligands present a barrier to charge transfer between the semiconductor and the catalyst, often requiring electron tunneling (*13*). The ligand-free approach taken here may help to establish a favorable interface between the bacteria and the semiconductor, resulting in improved efficiencies. Additionally, metal chalcogenides such as CdS have had limited application because of oxidative photodegradation; the ability of bacteria to precipitate metal chalcogenides from the products of photodissolution (Cd^{2+} and oxidized sulfur complex ions) suggests a potential regenerative pathway to circumvent the debilitating photoinstability through a precipitative self-regeneration.

The *M. thermoacetica*–CdS system displays behavior that may help it to exceed the utility of natural photosynthesis. First, the quantum yield increased with higher *M. thermoacetica*–CdS concentrations. The ability to tune the effective light flux per bacterium by changing the concentration of the suspension is a considerable advantage over similar light management practices in natural photosynthesis that are achieved through genetic engineering of chloroplast expression (*28*). Second, the catabolic energy loss observed during dark cycles in natural photosynthesis was absent in our hybrid system, which may be an innate feature of the Wood-Ljungdahl pathway, in which acetic acid is a waste product of normal respiration. Additionally, many plants and algae tend to store a large portion of their photosynthetic products as biomass, which requires extensive processing to produce useful chemicals. In contrast, the *M. thermoacetica*–CdS system directs ~90% of photosynthetic products toward acetic acid, reducing the cost of diversifying to other chemical products.

This system could be improved by substituting Cys oxidation with a more beneficial oxidation reaction, such as oxygen evolution, wastewater oxidation for water purification, or oxidative biomass conversion (*29*, *30*). Expanding the material library available through biologically induced precipitation will increase the capacity for light absorption and raise the upper limit on semiconductor-bacteria photosynthetic efficiency. The availability of genetic engineering tools for *M. thermoacetica* (*31*), as well as the introduction of electrotrophic and nanoparticle precipitation behavior in model bacteria such as *Escherichia coli* (*32*, *33*), suggests a potential role for synthetic biology in rationally designing such hybrid organisms.

Beyond the development of advanced solar- to-chemical synthesis platforms, this hybrid organism also has potential as a tool to study biological systems. The native integration of semiconductor nanoparticles with bacterial metabolic processes provides a distinctive optical tag for the study of microbial behavior, such as semiconductor-bacteria electron transfer (*34*, *35*), by providing a sensitive, noninvasive, nonchemical probe.

REFERENCES AND NOTES

1. A. W. D. Larkum, *Curr. Opin. Biotechnol.* **21**, 271–276 (2010).
2. D. Gust, T. A. Moore, A. L. Moore, *Acc. Chem. Res.* **42**, 1890–1898 (2009).
3. R. E. Blankenship *et al.*, *Science* **332**, 805–809 (2011).
4. T. J. Meyer, *Acc. Chem. Res.* **22**, 163–170 (1989).
5. A. M. Appel *et al.*, *Chem. Rev.* **113**, 6621–6658 (2013).
6. A. S. Hawkins, P. M. McTernan, H. Lian, R. M. Kelly, M. W. W. Adams, *Curr. Opin. Biotechnol.* **24**, 376–384 (2013).
7. K. A. Brown, M. B. Wilker, M. Boehm, G. Dukovic, P. W. King, *J. Am. Chem. Soc.* **134**, 5627–5636 (2012).
8. J. P. Giraldo *et al.*, *Nat. Mater.* **13**, 400–408 (2014).
9. J. P. Torella *et al.*, *Proc. Natl. Acad. Sci. U.S.A.* **112**, 2337–2342 (2015).
10. C. Liu *et al.*, *Nano Lett.* **15**, 3634–3639 (2015).
11. L. Lapinsonnière, M. Picot, F. Barrière, *ChemSusChem* **5**, 995–1005 (2012).
12. K. P. Nevin *et al.*, *Appl. Environ. Microbiol.* **77**, 2882–2886 (2011).
13. P. W. King, *Biochim. Biophys. Acta* **1827**, 949–957 (2013).
14. W. J. Crookes-Goodson, J. M. Slocik, R. R. Naik, *Chem. Soc. Rev.* **37**, 2403–2412 (2008).
15. D. C. Ducat, P. A. Silver, *Curr. Opin. Chem. Biol.* **16**, 337–344 (2012).
16. L. S. Gronenberg, R. J. Marcheschi, J. C. Liao, *Curr. Opin. Chem. Biol.* **17**, 462–471 (2013).
17. A. G. Fast, E. T. Papoutsakis, *Curr. Opin. Chem. Eng.* **1**, 380–395 (2012).
18. M. C. A. A. Van Eerten-Jansen *et al.*, *ACS Sustainable Chem. Eng.* **1**, 513–518 (2013).
19. Materials and methods are available as supplementary materials on *Science* Online.
20. R. Vogel, P. Hoyer, H. Weller, *J. Phys. Chem.* **98**, 3183–3188 (1994).
21. H. L. Drake, S. L. Daniel, *Res. Microbiol.* **155**, 869–883 (2004).
22. D. P. Cunningham, L. L. Lundie Jr., *Appl. Environ. Microbiol.* **59**, 7–14 (1993).
23. J. D. Holmes *et al.*, *Photochem. Photobiol.* **62**, 1022–1026 (1995).
24. S. L. Daniel, T. Hsu, S. I. Dean, H. L. Drake, *J. Bacteriol.* **172**, 4464–4471 (1990).
25. E. Dumas *et al.*, *Environ. Sci. Technol.* **44**, 1464–1470 (2010).
26. B. Liu, X. Zhao, C. Terashima, A. Fujishima, K. Nakata, *Phys. Chem. Chem. Phys.* **16**, 8751–8760 (2014).
27. K. Schuchmann, V. Müller, *Nat. Rev. Microbiol.* **12**, 809–821 (2014).
28. B. Hankamer *et al.*, *Physiol. Plant.* **131**, 10–21 (2007).
29. H. G. Cha, K.-S. Choi, *Nat. Chem.* **7**, 328–333 (2015).
30. B. E. Logan, K. Rabaey, *Science* **337**, 686–690 (2012).
31. A. Kita *et al.*, *J. Biosci. Bioeng.* **115**, 347–352 (2013).
32. H. M. Jensen *et al.*, *Proc. Natl. Acad. Sci. U.S.A.* **107**, 19213–19218 (2010).
33. C. L. Wang, A. M. Lum, S. C. Ozuna, D. S. Clark, J. D. Keasling, *Appl. Microbiol. Biotechnol.* **56**, 425–430 (2001).
34. M. Rosenbaum, F. Aulenta, M. Villano, L. T. Angenent, *Bioresour. Technol.* **102**, 324–333 (2011).
35. J. S. Deutzmann, M. Sahin, A. M. Spormann, *mBio* **6**, e00496-15 (2015).

ACKNOWLEDGMENTS

The interface design part of this work was supported by the U.S. Department of Energy under contract no. DE-AC02-05CH11231 (PChem). Work at the Molecular Foundry was supported by the Office of Science, Office of Basic Energy Sciences, of the U.S. Department of Energy under contract no. DE-AC02-05CH11231. Solar-to-chemical production experiments were supported by NSF (grant DMR-1507914). The authors thank J. J. Gallagher and M. C. Y. Chang for the original inoculum of *M. thermoacetica* ATCC 39073. K.K.S acknowledges support from the NSF Graduate Research Fellowship Program under grant DGE-1106400. The authors thank the National Center for Electron Microscopy. All data are available in the body of the paper or in the supplementary materials.

SUPPLEMENTARY MATERIALS

www.sciencemag.org/content/351/6268/74/suppl/DC1
Materials and Methods
Supplementary Text
Figs. S1 to S9

28 August 2015; accepted 19 November 2015
10.1126/science.aad3317

VIROLOGY

An orthopoxvirus-based vaccine reduces virus excretion after MERS-CoV infection in dromedary camels

Bart L. Haagmans,[1]* Judith M. A. van den Brand,[1] V. Stalin Raj,[1] Asisa Volz,[2] Peter Wohlsein,[3] Saskia L. Smits,[1] Debby Schipper,[1] Theo M. Bestebroer,[1] Nisreen Okba,[1] Robert Fux,[2] Albert Bensaid,[4] David Solanes Foz,[4] Thijs Kuiken,[1] Wolfgang Baumgärtner,[3] Joaquim Segalés,[5,6] Gerd Sutter,[2]* Albert D. M. E. Osterhaus[1,7,8]*

Middle East respiratory syndrome coronavirus (MERS-CoV) infections have led to an ongoing outbreak in humans, which was fueled by multiple zoonotic MERS-CoV introductions from dromedary camels. In addition to the implementation of hygiene measures to limit further camel-to-human and human-to-human transmissions, vaccine-mediated reduction of MERS-CoV spread from the animal reservoir may be envisaged. Here we show that a modified vaccinia virus Ankara (MVA) vaccine expressing the MERS-CoV spike protein confers mucosal immunity in dromedary camels. Compared with results for control animals, we observed a significant reduction of excreted infectious virus and viral RNA transcripts in vaccinated animals upon MERS-CoV challenge. Protection correlated with the presence of serum neutralizing antibodies to MERS-CoV. Induction of MVA-specific antibodies that cross-neutralize camelpox virus would also provide protection against camelpox.

Coronaviruses (CoVs) cause common colds in humans, but zoonotic transmissions occasionally introduce more pathogenic viruses into the human population. For example, the SARS-CoV caused the 2003 outbreak of severe acute respiratory syndrome (SARS). In 2012, a previously unknown virus, now named Middle East respiratory syndrome CoV (MERS-CoV), was isolated from the sputum of a 60-year-old Saudi Arabian man who suffered from acute pneumonia and subsequently died (*1*, *2*). Several infection clusters have been reported over the past

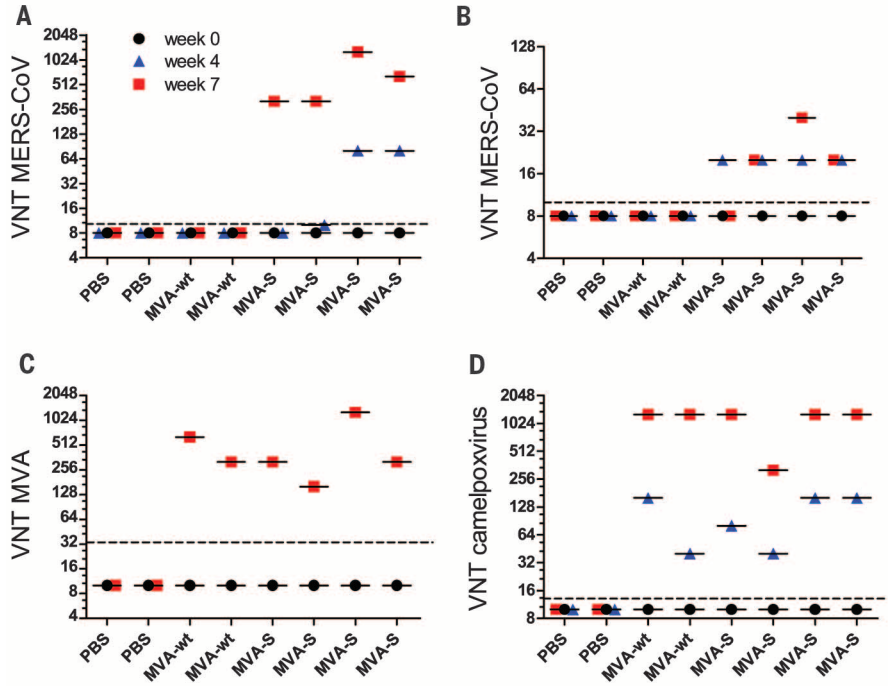

Fig. 1. Virus-neutralizing antibody responses to MERS-CoV, MVA, and camelpox virus in vaccinated dromedary camels. (**A** to **D**) Individual virus neutralization titers (VNT) from dromedary camels vaccinated with PBS, MVA-wt, or MVA-S against MERS-CoV [(A) and (B)], MVA (C), and camelpox virus (D), as determined from sera [(A), (C), and (D)] and nasal swabs (B). Here, VNT is expressed as the ratio denominator only [i.e., 32 on the *y* axis of (A) represents 1:32]. Different symbols indicate time points after immunization sera were analyzed: week 0 (black circles), week 4 (blue triangles), and week 7 (red squares). Dashed lines depict the detection limit of the assays.

3 years in the Middle East and also in South Korea, with ~35% of the reported human cases being fatal (*3*, *4*). Dromedary camels (*Camelus dromedarius*) were suspected to be the reservoir host after neutralizing antibodies to MERS-CoV were detected in these animals (*5*–*8*). Subsequently, the virus detected in nasal swabs from these animals was found to be similar to that in human MERS cases associated with farms where the dromedaries were kept (*9*, *10*). In addition, Chan *et al.* determined that MERS-CoV from dromedary camels replicates in human lung sections cultured ex vivo (*11*). More recent studies also provide serological evidence for camel-to-human transmission (*12*, *13*). Because of its widespread presence in dromedary camels (*14*–*16*), zoonotic infections of MERS-CoV in humans will continue to occur. Therefore, strict implementation of quarantine and isolation measures, as well as the development of candidate vaccines and antivirals, is urgently needed.

The spike protein is considered to be a key component for vaccines against CoV infections. The identification of dipeptidyl peptidase 4 (DPP4) as the MERS-CoV receptor (*17*) has facilitated the subsequent characterization of the receptor binding domain in the S1 region of the MERS-CoV spike protein (*18*, *19*). When tested as a vaccine in mice, full-length spike protein of MERS-CoV expressed by modified vaccinia virus Ankara (MVA-S) induced high levels of circulating antibodies that neutralize MERS-CoV and limited lower respiratory tract replication in animals transduced with the human receptor DPP4 and inoculated with MERS-CoV (*20*, *21*). MVA, a highly attenuated strain of vaccinia virus, serves as one of the most advanced recombinant poxvirus vectors in preclinical and clinical trials for vaccines against infectious diseases and cancer. As a proof of principle, we tested the protective efficacy of a MVA–MERS-CoV candidate vaccine in dromedary camels.

In dromedary camels, MERS-CoV replication is mainly restricted to the upper respiratory tract (*22*). Therefore, we inoculated four dromedary camels twice at a 4-week interval, with 2×10^8 plaque-forming units (PFU) MVA-S administered in both nostrils via a mucosal atomization device, to disperse the vaccine on the nasal epithelium, and 10^8 PFU MVA-S delivered intramuscularly in the neck of each animal (*23*). Similarly, four control animals received nonrecombinant wild-type MVA (MVA-wt) (n = 2) or phosphate-buffered saline (PBS) (n = 2). All animals vaccinated with the MVA-S vaccine developed detectable serum neutralizing MERS-CoV–specific antibody titers (Fig. 1A). No MERS-CoV–specific antibodies were detected in sera of the PBS- or MVA-wt–immunized control animals. The specificity of the antibody response was confirmed by enzyme-linked immunosorbent assay, using recombinant S1 protein (fig. S1). In addition, low levels of MERS-CoV–neutralizing antibodies (virus neutralization titer of 1:20 to 1:40) were detected 3 weeks after the boost immunization in the nasal swabs of three animals (Fig. 1B). Because a MVA-vectored vaccine was used, antibodies neutralizing MVA were also detected (Fig. 1C); these antibodies cross-neutralized camelpox virus (Fig. 1D). Camelpox virus infections occur frequently in dromedaries and cause severe disease that can be prevented by vaccines based on attenuated camelpox viruses (*24*).

Three weeks after the boost immunization, all dromedary camels were inoculated with 10^7 median tissue culture infectious dose ($TCID_{50}$) of MERS-CoV via the intranasal route, using a mucosal atomization device. Upon challenge, the animals showed only mild clinical signs, which were mainly limited to a relatively small rise in body temperature in control-vaccinated animals 1 day after challenge (fig. S2). In addition, some dry mucus was observed in one of the nostrils of most animals after day 4, but from days 8 to 10 onward, all control-vaccinated animals exhibited a runny nose that was not observed in MVA-S–vaccinated animals (Fig. 2, A and B). Previous studies have shown that both experimentally and naturally infected dromedary camels may show nasal discharge after MERS-CoV infection (*15*, *22*). We next tested nasal respiratory tract samples for the presence of infectious virus. Whereas MERS-CoV was found at high titers in all four control-vaccinated animals, mean viral titers in the animals that received the MVA-S vaccine were significantly reduced (Fig. 2C). At 4 days post-inoculation (dpi), an increase in MERS-CoV RNA level was noted in the MVA-S–vaccinated animals (Fig. 2D). At 6 dpi, one of the MVA-S–vaccinated animals excreted low levels of infectious virus (10^3 $TCID_{50}$/ml) (Fig. 2C). Sequencing of the spike gene of this virus showed no amino acid changes in the receptor binding domain (fig. S3), which suggests that this virus did not emerge as

[1]Department of Viroscience, Erasmus Medical Center, Rotterdam, Netherlands. [2]German Centre for Infection Research (DZIF), Institute for Infectious Diseases and Zoonoses, Ludwig-Maximilians-Universität München, Munich, Germany. [3]Department of Pathology, University of Veterinary Medicine, Hannover, Germany. [4]Institut de Recerca i Tecnologia Agroalimentàries (IRTA), Centre de Recerca en Sanitat Animal [CReSA, IRTA–Universitat Autònoma de Barcelona (UAB)], Campus de la UAB, 08193 Bellaterra, Spain [5]UAB, CReSA, (IRTA-UAB), Campus de la UAB, 08193 Bellaterra, Spain. [6]Departament de Sanitat i Anatomia Animals, Facultat de Veterinària, UAB, 08193 Bellaterra, Spain. [7]Artemis One Health, Utrecht, Netherlands. [8]Research Center for Emerging Infections and Zoonoses (RIZ), University of Veterinary Medicine, Hannover, Germany.
***Corresponding author. E-mail: b.haagmans@erasmusmc.nl (B.L.H.); gerd.sutter@lmu.de (G.S.); albert.osterhaus@tiho-hannover.de (A.D.M.E.O.)**

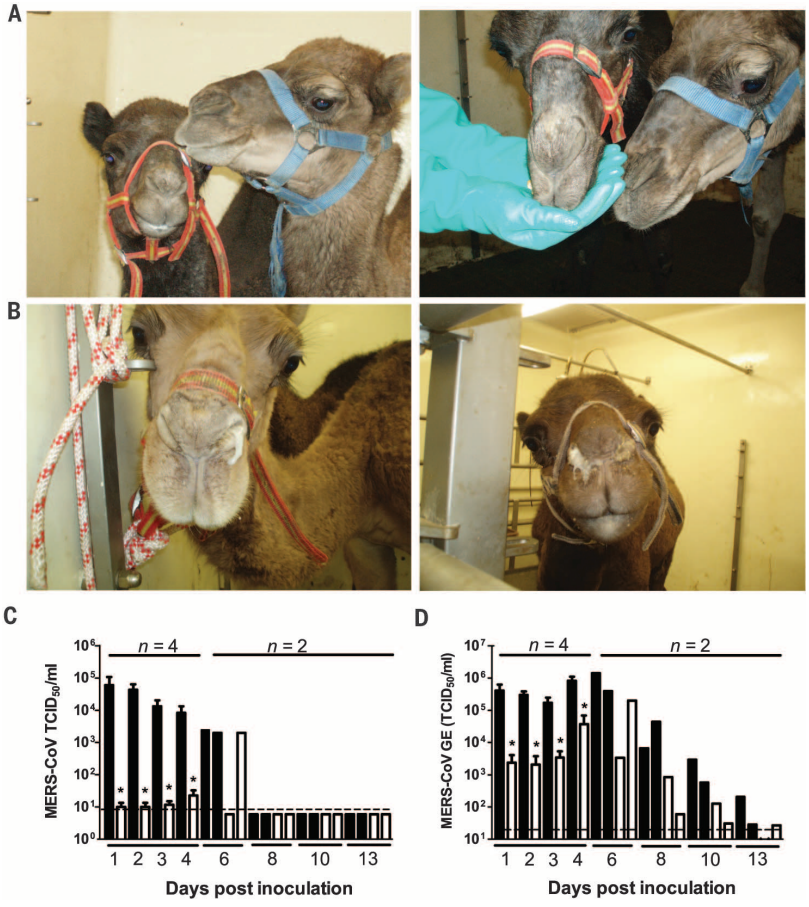

Fig. 2. Clinical signs and MERS-CoV excretion in nasal swabs of dromedary camels vaccinated with MVA-S vaccine. (**A** and **B**) Two MVA-S–vaccinated (A) and two control-vaccinated dromedary camels (B) were analyzed for the presence of mucus excretion 8 to 10 days after MERS-CoV challenge. (**C** and **D**) Detection of infectious MERS-CoV (C) and MERS-CoV RNA (D) at different time points after challenge in nasal swabs of dromedary camels vaccinated with MVA-S (white bars) or MVA-wt or PBS (black bars). Dashed lines depict the detection limit of the assays. Error bars represent mean values ± SEM; *$P < 0.05$; $n = 4$ animals per group. GE, genome equivalents.

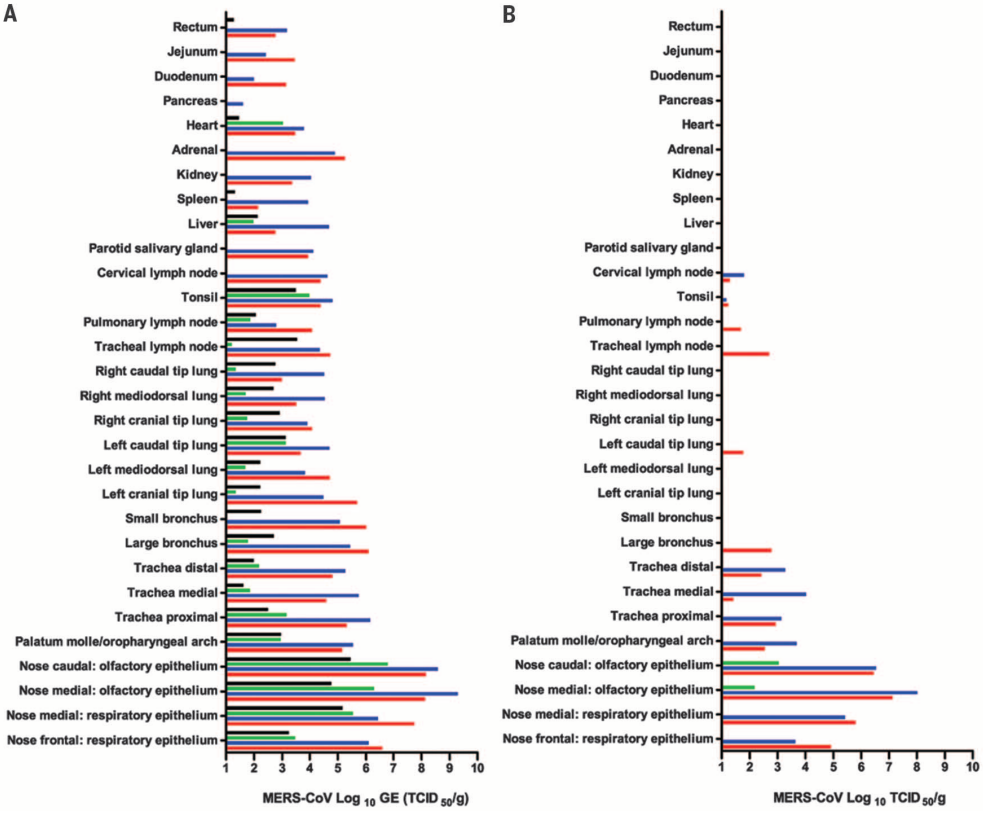

Fig. 3. Detection of MERS-CoV in tissues of vaccinated dromedary camels. (**A** and **B**) Levels of MERS-CoV viral RNA (A) and infectious virus (B) were determined in tissue homogenates from MVA-S–vaccinated (green and black bars) or control-vaccinated (red and blue bars) camels 4 days after challenge.

a result of escape from vaccine-induced antibodies (Fig. 2C). Rather, the observation that this animal had no detectable MERS-CoV antibody response in the nasal swab at time of challenge may indicate that, for unknown reasons, priming with the MVA-S vaccine was less effective in this animal compared with the other vaccinated animals. Antibodies to MERS-CoV rapidly increased 8 dpi in control-vaccinated animals (fig. S4), consistent with the absence of infectious virus in the nasal swabs at that time (Fig. 2C). Low levels of viral RNA, but no infectious virus, were detected in rectal swabs after MERS-CoV challenge (fig. S5), but not in any of the sera tested.

To analyze pathological changes and viral replication in organs of the animals, we euthanized two animals per group and performed necropsies at 4 and 14 dpi. Gross pathology showed no substantial changes in the organs of any of the animals. However, at 4 dpi MERS-CoV RNA transcripts were detected in several organs of the control-vaccinated animals (Fig. 3A), although infectious virus particles were restricted to noses and tracheas (Fig. 3B). In the absence of infectious MERS-CoV, relatively high levels of viral RNA have also been observed in tissues of experimentally infected rhesus macaques and rabbits (*25*, *26*). In contrast, infectious MERS-CoV particles were found at low levels in the noses of animals that had received the MVA-S vaccine (Fig. 3B). At 14 dpi, only viral RNA was detected, mainly in control-vaccinated animals (fig. S6).

Differences in upper respiratory tract viral replication between vaccinated groups were confirmed by MERS-CoV in situ hybridization (ISH) and immunohistochemistry (IHC). At 4 dpi, only a few cells in the nasal epithelium of MVA-S–vaccinated dromedaries stained positive for MERS-CoV RNA by ISH, as compared with cells from control-vaccinated animals (Fig. 4, A and B). Viral replication in the control-vaccinated animals was consistent with histopathological analyses showing multifocal moderate rhinitis with multifocal epithelial necrosis, as well as lymphocytic and neutrophilic exocytosis (Fig. 4C). In the nasal submucosa, we observed edema and infiltrates with lymphocytes, neutrophils, plasma cells, and macrophages. In the trachea and bronchi, we noted infiltration in the lamina propria, as well as a multifocal mild tracheitis and bronchitis with epithelial necrosis and lymphocytic and neutrophilic exocytosis. In the lymph nodes and the tonsils, we detected follicular hyperplasia. Marked MERS-CoV antigen expression in the nasal epithelium was associated with the nasal lesions (Fig. 4C). Through the use of ISH, the presence of MERS-CoV RNA in the nasal cavity was confirmed in cells similar to those that scored positive by IHC (Fig. 4C). Furthermore, a few epithelial cells in the trachea and bronchus and those covering the palatum molle—as well as large stellate cells (consistent with dendritic cells) in the lymphoid tissue of the palatum molle, tonsils, and tracheal and cervical lymph nodes—were found to be positive for viral antigen by IHC (fig. S7). In contrast, in MVA-S–vaccinated animals the rhinitis was accompanied by less submucosal edema with antigen expression in some nasal cells (Fig. 4C). Eosinophilic granulocytes were not observed in the lungs of MVA-S–vaccinated animals challenged with MERS-CoV. In one MVA-S–vaccinated animal, viral antigen expression was found in a few dendritic-like cells in the lymphoid tissue of the palatum molle, tonsils, and tracheal and cervical lymph nodes, as well as in the gut-associated lymphoid tissue of the duodenum (table S1). At 14 dpi, we observed multifocal mild rhinitis, tracheitis, and bronchitis and follicular hyperplasia in the lymphoid tissue of control- and MVA-S–vaccinated animals. In the lungs of almost all animals, we detected multifocal mild infiltration of neutrophils, histiocytes, and lymphocytes that was not associated with viral antigen expression. In the other extrarespiratory tissues examined, we found no substantial morphological changes or viral antigen expression. Overall, these results indicate that vaccination of dromedary camels with MVA-S induces protective immunity resulting in reduction of excreted infectious MERS-CoV, without evidence for antibody-dependent enhancement of viral replication, as seen in feline CoV infection (*27*). Given the potential transient nature of mucosal immune responses, follow-up studies are needed to determine the longevity of the responses induced by the MVA-S vaccine, with respect to protection as well as antibody-dependent enhancement of viral replication when antibody levels are waning. In addition, dosing of the vaccine and alternative methods of administration must be explored in more detail before this candidate vaccine will be useful in the field.

Protective immunity to CoVs is orchestrated by antibody and cellular immune responses. Investigations in mice have already provided evidence that inoculation with MERS-CoV spike protein–based candidate vaccines, monoclonal antibodies directed against the spike protein, or dromedary immune serum induces protective immunity against lower respiratory tract MERS-CoV infection (*28*–*30*). In dromedary camels, a DNA vaccine encoding the spike protein induced MERS-CoV neutralizing antibody responses that were similar to antibody levels in animals inoculated with the MVA-S vaccine, but no challenge experiments were performed (*31*). However, studies in the field also indicated that MERS-CoV–seropositive dromedaries may carry MERS-CoV viral RNA in their nasal excretions (*8*, *15*, *16*). Thus, sterilizing immunity

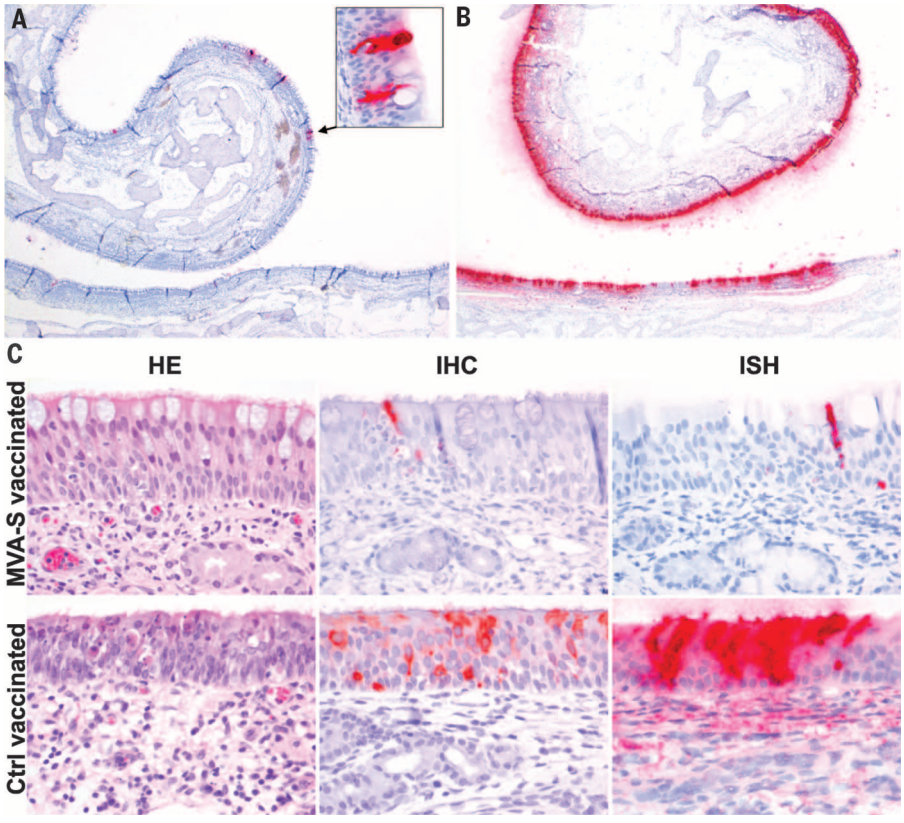

Fig. 4. Histopathology and expression of viral antigen and viral RNA in the nasal respiratory epithelium of MVA-S–vaccinated and control-vaccinated dromedaries 4 days after challenge with MERS-CoV. (**A** to **C**) Detection of MERS-CoV viral RNA by ISH in the noses of MVA-S–vaccinated (A) or control-vaccinated (B) dromedary camels. Nasal respiratory tissue of a representative MVA-S–vaccinated dromedary exhibited no prominent lesions (C), as revealed by staining with hematoxylin and eosin (HE). IHC and ISH results revealed a few viral antigen–positive cells and the presence of viral RNA, respectively. Nasal respiratory tissue of a control (Ctrl)–vaccinated dromedary exhibited multifocal necrosis of epithelial cells and infiltration of neutrophils, lymphocytes, and a few macrophages in the epithelium and lamina propria, with viral antigens and viral RNA present in abundance at the same location (C).

may not be possible to achieve, as virus replicates in the upper respiratory tract even in the presence of specific antibodies, similarly to other respiratory viruses. Because dromedary camels do not show severe clinical signs upon MERS-CoV infection, vaccination of dromedaries should primarily aim to reduce virus excretion to prevent virus spreading. Young dromedaries excrete more infectious MERS-CoV than adults (*8*, *15*, *16*), so young animals should be vaccinated first. Our results reveal that MVA-S vaccination of young dromedary camels may significantly reduce infectious MERS-CoV excreted from the nose. Two major advantages of the orthopoxvirus-based vector used in our study include its capacity to induce protective immunity in the presence of preexisting (e.g., maternal) antibodies (*32*) and the observation that MVA-specific antibodies cross-neutralize camelpox virus, revealing the potential dual use of this candidate MERS-CoV vaccine in dromedaries. Dromedary camels vaccinated with conventional vaccinia virus showed no clinical signs upon challenge with camelpox virus, whereas control animals developed typical symptoms of generalized camelpox (*33*). The MVA-S vectored vaccine may also be tested for protection of humans at risk, such as health care workers and people in regular contact with camels.

REFERENCES AND NOTES

1. A. M. Zaki, S. van Boheemen, T. M. Bestebroer, A. D. Osterhaus, R. A. Fouchier, *N. Engl. J. Med.* **367**, 1814–1820 (2012).
2. S. van Boheemen *et al.*, *mBio* **3**, e00473-12 (2012).
3. A. Assiri *et al.*, *N. Engl. J. Med.* **369**, 407–416 (2013).
4. A. Zumla, D. S. Hui, S. Perlman, *Lancet* **386**, 995–1007 (2015).
5. C. B. E. M. Reusken *et al.*, *Lancet Infect. Dis.* **13**, 859–866 (2013).
6. M. A. Müller *et al.*, *Emerg. Infect. Dis.* **20**, 2093–2095 (2014).
7. M. G. Hemida *et al.*, *Euro Surveill.* **19**, 20828 (2014).
8. A. N. Alagaili *et al.*, *mBio* **5**, e00884-14 (2014).
9. B. L. Haagmans *et al.*, *Lancet Infect. Dis.* **14**, 140–145 (2014).
10. Z. A. Memish *et al.*, *Emerg. Infect. Dis.* **20**, 1012–1015 (2014).
11. R. W. Chan *et al.*, *Lancet Respir. Med.* **2**, 813–822 (2014).
12. M. A. Müller *et al.*, *Lancet Infect. Dis.* **15**, 559–564 (2015).
13. C. B. Reusken *et al.*, *Emerg. Infect. Dis.* **21**, 1422–1425 (2015).
14. C. B. Reusken *et al.*, *Emerg. Infect. Dis.* **20**, 1370–1374 (2014).
15. A. I. Khalafalla *et al.*, *Emerg. Infect. Dis.* **21**, 1153–1158 (2015).
16. M. G. Hemida *et al.*, *Emerg. Infect. Dis.* **20**, 1231–1234 (2014).
17. V. S. Raj *et al.*, *Nature* **495**, 251–254 (2013).
18. H. Mou *et al.*, *J. Virol.* **87**, 9379–9383 (2013).
19. L. Du *et al.*, *J. Virol.* **87**, 9939–9942 (2013).
20. F. Song *et al.*, *J. Virol.* **87**, 11950–11954 (2013).
21. A. Volz *et al.*, *J. Virol.* **89**, 8651–8656 (2015).
22. D. R. Adney *et al.*, *Emerg. Infect. Dis.* **20**, 1999–2005 (2014).
23. Materials and methods are available as supplementary materials on *Science* Online.
24. S. Duraffour, H. Meyer, G. Andrei, R. Snoeck, *Antiviral Res.* **92**, 167–186 (2011).
25. E. de Wit *et al.*, *Proc. Natl. Acad. Sci. U.S.A.* **110**, 16598–16603 (2013).
26. B. L. Haagmans *et al.*, *J. Virol.* **89**, 6131–6135 (2015).
27. H. Vennema *et al.*, *J. Virol.* **64**, 1407–1409 (1990).
28. J. Zhao *et al.*, *Proc. Natl. Acad. Sci. U.S.A.* **111**, 4970–4975 (2014).
29. K. E. Pascal *et al.*, *Proc. Natl. Acad. Sci. U.S.A.* **112**, 8738–8743 (2015).
30. J. Zhao *et al.*, *J. Virol.* **89**, 6117–6120 (2015).
31. K. Muthumani *et al.*, *Sci. Transl. Med.* **7**, 301ra132 (2015).
32. K. J. Stittelaar *et al.*, *J. Virol.* **74**, 4236–4243 (2000).
33. S. M. Hafez *et al.*, *Vaccine* **10**, 533–539 (1992).

ACKNOWLEDGMENTS

We thank F. van der Panne for figure preparation and P. van Run, S. Jany, X. Abad, I. Cordón, M. Jesús Navas, M. Mora, and all animal caretakers from the CReSA biosecurity level 3 laboratories and animal facilities for technical assistance. This study was funded by Nederlandse Organisatie voor Wetenschappelijk Onderzoek (grant 91213066) and was supported in part by the Niedersachsen-Research Network on Neuroinfectiology (N-RENNT) of the Ministry of Science and Culture of Lower Saxony, Germany. Animal model development was performed as part of the Zoonotic Anticipation and Preparedness Initiative (ZAPI project) [Innovative Medicines Initiative (IMI) grant 115760], with assistance and financial support from IMI and the European Commission and contributions from the EFPIA partners. B.L.H., V.S.R., T.M.B., G.S., and A.D.M.E.O. have applied for patents on MERS-CoV. A.D.M.E.O. is chief scientific officer of Viroclinics Biosciences. A.D.M.E.O and T.K. hold certificates of shares in Viroclinics Biosciences. Nucleotide sequence data are available in GenBank under accession numbers KT966879 and KT966880.

SUPPLEMENTARY MATERIALS

www.sciencemag.org/content/351/6268/77/suppl/DC1
Materials and Methods
Figs. S1 to S7
Table S1
References (*34*, *35*)

31 July 2015; accepted 12 November 2015
Published online 17 December 2015
10.1126/science.aad1283

VIROLOGY

Co-circulation of three camel coronavirus species and recombination of MERS-CoVs in Saudi Arabia

Jamal S. M. Sabir,[1]* Tommy T.-Y. Lam,[2,3,4]* Mohamed M. M. Ahmed,[1,6]* Lifeng Li,[3,4]* Yongyi Shen,[3,4] Salah E. M. Abo-Aba,[1,7] Muhammad I. Qureshi,[1] Mohamed Abu-Zeid,[1,7] Yu Zhang,[2,3,4] Mohammad A. Khiyami,[8] Njud S. Alharbi,[1] Nahid H. Hajrah,[1] Meshaal J. Sabir,[1] Mohammed H. Z. Mutwakil,[1] Saleh A. Kabli,[1] Faten A. S. Alsulaimany,[1] Abdullah Y. Obaid,[9] Boping Zhou,[2] David K. Smith,[4] Edward C. Holmes,[5] Huachen Zhu,[2,3,4]† Yi Guan[1,2,3,4]†

Outbreaks of Middle East respiratory syndrome (MERS) raise questions about the prevalence and evolution of the MERS coronavirus (CoV) in its animal reservoir. Our surveillance in Saudi Arabia in 2014 and 2015 showed that viruses of the MERS-CoV species and a human CoV 229E–related lineage co-circulated at high prevalence, with frequent co-infections in the upper respiratory tract of dromedary camels. Including a betacoronavirus 1 species, we found that dromedary camels share three CoV species with humans. Several MERS-CoV lineages were present in camels, including a recombinant lineage that has been dominant since December 2014 and that subsequently led to the human outbreaks in 2015. Camels therefore serve as an important reservoir for the maintenance and diversification of the MERS-CoVs and are the source of human infections with this virus.

Major outbreaks of Middle East respiratory syndrome (MERS) have been repeatedly reported in the Arabian Peninsula since 2012 and recently in South Korea (*1*–*3*), renewing concerns about potential changes in the mode of MERS coronavirus (CoV) transmission. Although increasing evidence suggests that dromedary camels are the most likely source of human infections (*4*–*14*), the prevalence and evolution of the MERS-CoV in this animal and the route of virus transmission to humans are not well defined, and little is known of other CoV species that may circulate in camels and how they might influence CoV ecology.

We conducted surveillance for CoVs in dromedary camels in Saudi Arabia, the country most affected by MERS, from May 2014 to April 2015. Initially, paired nasal and rectal swabs were collected from camels at slaughterhouses, farms, and wholesale markets in Jeddah and Riyadh. Because rectal swabs were negative for MERS-CoVs (tables S1 and S2), only nasal swabs were subsequently collected at these sites and in Taif (*15*). Of the 1309 camels tested, 25.3% were positive for CoV, as established by reverse transcription polymerase chain reaction (RT-PCR) and confirmed by Sanger sequencing. The majority of the CoV-positive camels

[1]Biotechnology Research Group, Department of Biological Sciences, Faculty of Science, King Abdulaziz University, Jeddah 21589, Saudi Arabia. [2]State Key Laboratory of Emerging Infectious Diseases (The University of Hong Kong–Shenzhen Branch), Shenzhen Third People's Hospital, Shenzhen, China. [3]Shantou University–The University of Hong Kong Joint Institute of Virology, Shantou University, Shantou, China. [4]Centre of Influenza Research and State Key Laboratory of Emerging Infectious Diseases, School of Public Health, The University of Hong Kong, Hong Kong Special Administrative Region, China. [5]Marie Bashir Institute for Infectious Diseases and Biosecurity, Charles Perkins Centre, School of Biological Sciences and Sydney Medical School, The University of Sydney, Sydney, New South Wales 2006, Australia. [6]Department of Nucleic Acids Research, Genetic Engineering and Biotechnology Research Institute, City for Scientific Research and Technology Applications, Borg El-Arab, Post Office Box 21934, Alexandria, Egypt. [7]Microbial Genetics Department, Genetic Engineering and Biotechnology Division, National Research Center, Dokki, Giza, Egypt. [8]King Abdulaziz City for Science and Technology, Riyadh 11442, Saudi Arabia. [9]Department of Chemistry, Faculty of Science, King Abdulaziz University, Jeddah 21589, Saudi Arabia.
*These authors contributed equally to this work. **†Corresponding author. E-mail: zhuhch@hku.hk (H.Z.); yguan@hku.hk (Y.G.)**

came from wholesale markets (tables S1 and S2), where indigenous camels mixed with camels imported from Sudan and Somalia. Local camels had significantly higher positive rates for MERS-CoVs and other CoVs than did imported camels (Pearson's χ^2 test, $P < 0.05$; tables S1 and S2).

Three CoV species were detected in dromedary camels: MERS-CoV (betacoronavirus, group C); betacoronavirus 1 (betacoronavirus, group A); and human CoV 229E (alphacoronavirus) (fig. S1). Viruses from the latter two species are designated as camel β1-HKU23-CoVs and camelid α-CoVs, respectively. Although CoVs were detected almost year-round in these animals, a relatively higher prevalence of both MERS-CoV and camelid α-CoV was observed from December 2014 to April 2015 (tables S1 and S2). Juvenile camels (0.5 to 1 year old) had the highest levels of respiratory

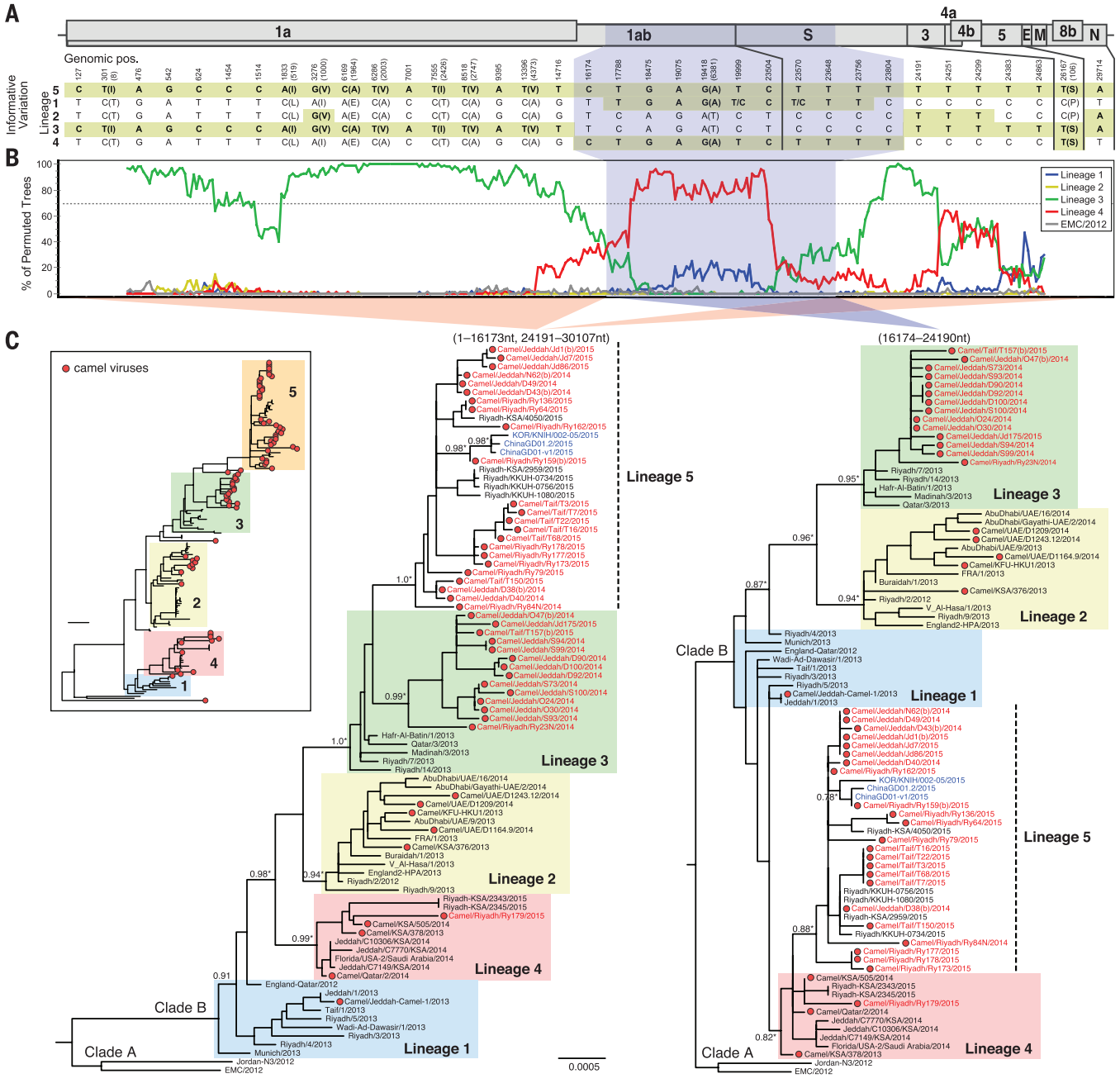

Fig. 1. Genomic recombination in MERS-CoVs. Only the variable sites (variants shared by more than two sequences; see the supplementary materials) were used for (A) and (B). (**A**) A rescaled structure of the MERS-CoV genome (top) with consensus nucleotides, and any corresponding amino acid substitutions, that are phylogenetically informative in defining the lineages (bottom) (*15*). Nucleotides common with lineage 5 are highlighted (nucleotide substitution C26167T results in amino acid substitution P106S in ORF4b). The likely exchanged region is shaded blue. (**B**) Bootscanning recombination analysis based on the variable genomic sites. The dashed line indicates 70% bootstrap support. (**C**) Maximum-likelihood phylogenetic trees inferred for the outer (left) and inner (right) nonrecombinant regions, indicating that lineage 5 is a recombinant of lineages 3 and 4. A subset of sequences from each lineage was used. Camel viruses are indicated by red circles; those sequenced in this study are shown in red text. Shimodaira-Hasegawa–like branch test values and Bayesian inference clade probabilities >0.9 (indicated by asterisks) are shown at selected lineages. Branch lengths reflect the number of nucleotide substitutions per site, and the trees were rooted by Camel/Egypt/NRCE-HKU205/2013. The inset tree was inferred using all available MERS-CoV genomic sequences ($n = 164$; fig. S2).

infections with both the MERS-CoV and camelid α-CoV, followed by calves under 6 months, both at about twice the rate observed in camels aged 1 to 2 years (table S2). Younger camels seem to play a more important epidemiological role in maintaining both viruses, which is consistent with previous findings (*10*, *11*, *16*, *17*).

The overall positive rates for MERS-CoV and camelid α-CoV from nasal swabs were 12.1 and 19.8%, respectively (tables S1 and S2). However, only 3 of 304 camel rectal swabs were CoV-positive for either camelid α- or camel β1-HKU23-CoVs (tables S1 and S2). Thus, a major mode of virus shedding of the MERS- and camelid α-CoVs is from the respiratory tract of dromedary camels. Over half of MERS-CoV–positive nasal swabs (56.6%) were also positive for camelid α-CoVs, indicating frequent co-infections of these viruses (tables S1 and S2). Nasal swabs from two animals contained all three species of CoVs detected in our survey. The high prevalence of these viruses suggests that they are enzootic in dromedary camels.

To examine the genetic diversity and evolution of the camel CoVs, metagenomic sequencing was carried out using the original swab materials that were positive in the initial RT-PCR screening. A total of 93 full-length viral genomes (67 MERS-CoVs, 25 camelid α-CoVs, and one camel β1-HKU23-CoV) were obtained from 79 nasal swab samples. Thirty-eight of these samples presented co-infections of MERS-CoV with one or both of the two other CoV species, but only 14 samples yielded two complete genomes.

β1-HKU23-CoVs have been detected in camels in Dubai (*18*), and the camelid α-CoVs are closely related to a virus isolated from alpacas in California in 2007 (fig. S1) (*19*, *20*). The camelid α-CoVs clustered with the human CoV 229E (fig. S1), a causal agent of common colds in humans. The high prevalence of asymptomatic infections with camelid α-CoVs in Saudi Arabian camels emphasizes the important role that this species plays in CoV ecology.

Recombination has been reported in the MERS-CoV species (*21*, *22*). Phylogenetic analysis of the MERS-CoV full-genome sequences obtained in this study (n = 67), together with those available in public databases (n = 106), revealed recombination signatures that defined five major phylogenetically stable lineages, all of which contained human and camel MERS-CoV sequences (Fig. 1 and figs. S2 and S3). A few viruses that showed inconsistent topologies in subgenomic trees, suggesting that they have a more varied history of recombination, were not classified within the five main lineages (fig. S2). MERS-CoVs from Saudi Arabian camels were found within each of the five lineages; the viruses sequenced in this study fell into lineages 3, 4, and 5, with the exception of some minor recombinants (Figs. 1 and 2 and figs. S2 and S3). Thus, the evolution of MERS-CoVs within camels has led to diverse lineages that have all caused human infections, indicating that there is a low barrier for interspecies transmission.

MERS-CoVs obtained between July and December 2014 mainly fell into lineages 3 and 5, whereas those from 2015 were principally from lineage 5

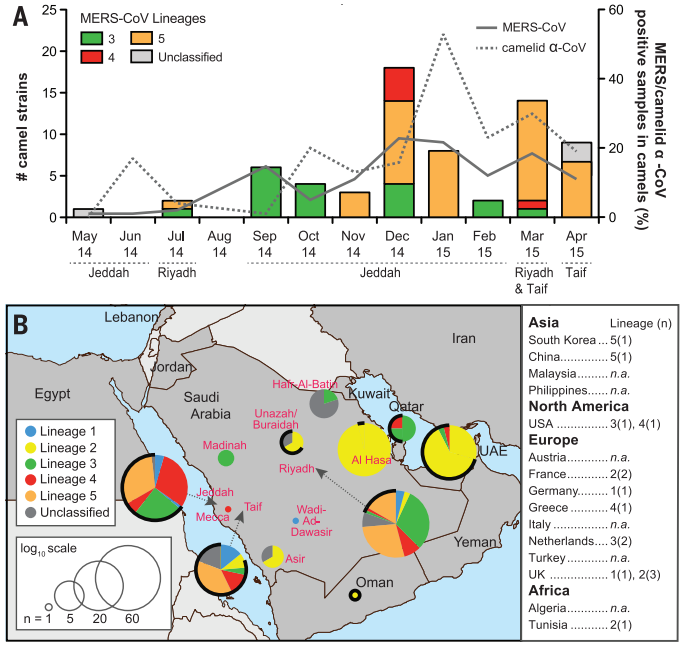

Fig. 2. Lineage distribution of MERS-CoV. Genetic lineages within MERS-CoVs were determined by phylogenetic analysis (fig. S3). (**A**) The bar chart shows the number of camel MERS-CoV sequences obtained, by lineage and month of sampling. Monthly percentages of samples positive for MERS or camelid α-CoVs (determined by RT-PCR) are indicated by solid and dashed lines, respectively (right axis). Sampling sites are indicated below the sampling months. (**B**) Lineage distribution of all available MERS-CoV complete or partial genome sequences from countries that have reported MERS-CoV infections (n.a., sequence not available). For Saudi Arabia, counts are shown by city. In the pie charts, colors represent the lineages, and thick black edges indicate camel sequences.

(Fig. 2 and figs. S2 and S3). Four viruses sampled during December 2014, which showed evidence of a small recombinant region, and a virus from March 2015 belonged to lineage 4 (Fig. 2 and figs. S2 to S4). Viruses from lineage 5, which are associated with the Korean outbreak and the recent human infections in Riyadh (Fig. 1) (*3*), were first identified in our surveillance in July 2014 and have been predominant in Saudi Arabian camels since November 2014. However, all of the human viruses of this lineage were reported from February 2015 onward. The MERS-CoV variants associated with the recent outbreak of human infections in South Korea [e.g., ChinaGD01-v1/2015 and KOR/KNIH/002-05/2015 (*23*, *24*)] show the highest similarity (99.96 to 99.98%, full genome) to a camel virus (Camel/Riyadh/Ry159/2015) sampled in March 2015 (Fig. 1 and figs. S2 and S3).

A statistically significant signal for phylogenetic incongruence in lineage 5 defined two recombinant sources of the MERS-CoV genome: (i) positions 1 to 16,173 and 24,191 to end, and (ii) positions 16,174 to 24,190 (Fig. 1). The phylogeny indicates that lineage 5 viruses evolved from a recombinant virus that acquired the 5' part of ORF1ab and the 3' part of the S (spike) gene from lineage 4 and the remaining genomic regions from lineage 3 (Fig. 1C). In both subgenomic phylogenies, lineage 5 viruses were closely related to lineage 3 and 4 viruses from Saudi Arabian camels, suggesting that they hosted this recombination event. Ten synonymous nucleotide changes and a Thr6381Ala amino acid substitution in the nsp14-exonuclease of the ORF1ab polyprotein, relative to lineage 3, were due to the recombination in lineage 5 (Fig. 1A). The possible function of these substitutions requires further investigation. A molecular clock dating analysis indicates that the recombination event probably occurred between December 2013 and June 2014 (fig. S5). Nine other putative MERS-CoV recombinant strains (fig. S4) were seemingly generated by sporadic events and have not persisted in the population, or may represent mixed infections of MERS-CoV strains from different lineages. Although frequent co-infections of MERS- and camelid α-CoVs were observed (tables S1 and S2), no evidence of recombination among them was identified.

Four CoV species circulate widely in humans, and two others have caused severe sporadic infections with limited human-to-human transmission (*1*, *25*). The wide species range of CoVs and their propensity to cross species boundaries suggest that more will emerge in the future. Since the first report of MERS in 2012 (*1*, *2*), the causative virus has been transmitted to over 25 countries, mostly by international travelers that have been to the Middle East (*3*). Even though a high prevalence of MERS-CoVs has been detected in this work and in previous studies of dromedary camels (*4*–*14*), limited quarantine and biosecurity measures are in place to reduce the exposure of humans to the virus, and more cases must be expected in the future. The recent outbreak of MERS in Korea (*3*) shows that MERS-CoVs have the ability to cause large outbreaks in environments

that are different from Middle East. Although changes in human population density, climate conditions, and social factors may contribute to the spread of MERS-CoVs in other regions, the prevention of transmission at the animal/human interface is likely to be the most efficient measure to contain the threat from this virus.

REFERENCES AND NOTES

1. A. M. Zaki, S. van Boheemen, T. M. Bestebroer, A. D. Osterhaus, R. A. Fouchier, *N. Engl. J. Med.* **367**, 1814–1820 (2012).
2. A. Bermingham *et al.*, *Euro Surveill.* **17**, 20290 (2012).
3. World Health Organization, *Middle East Respiratory Syndrome Coronavirus (MERS-CoV)* (2015); www.who.int/emergencies/mers-cov/en/.
4. C. B. E. M. Reusken *et al.*, *Lancet Infect. Dis.* **13**, 859–866 (2013).
5. A. N. Alagaili *et al.*, *MBio* **5**, e00884-14 (2014).
6. E. I. Azhar *et al.*, *N. Engl. J. Med.* **370**, 2499–2505 (2014).
7. M. G. Hemida *et al.*, *Euro Surveill.* **18**, 20659 (2013).
8. B. Meyer *et al.*, *Emerg. Infect. Dis.* **20**, 552–559 (2014).
9. B. L. Haagmans *et al.*, *Lancet Infect. Dis.* **14**, 140–145 (2014).
10. U. Wernery *et al.*, *Emerg. Infect. Dis.* **21**, 1019–1022 (2015).
11. A. I. Khalafalla *et al.*, *Emerg. Infect. Dis.* **21**, 1153–1158 (2015).
12. D. R. Adney *et al.*, *Emerg. Infect. Dis.* **20**, 1999–2005 (2014).
13. M. A. Müller *et al.*, *Lancet Infect. Dis.* **15**, 559–564 (2015).
14. R. A. Perera *et al.*, *Euro Surveill.* **18**, 20574 (2013).
15. Materials and methods are available as supplementary materials on *Science* Online.
16. E. A. Farag *et al.*, *Infect. Ecol. Epidemiol.* **5**, 28305 (2015).
17. V. M. Corman *et al.*, *Emerg. Infect. Dis.* **20**, 1319–1322 (2014).
18. P. C. Woo *et al.*, *Emerg. Infect. Dis.* **20**, 560–572 (2014).
19. B. M. Crossley, R. E. Mock, S. A. Callison, S. K. Hietala, *Viruses* **4**, 3689–3700 (2012).
20. B. M. Crossley *et al.*, *J. Vet. Diagn. Invest.* **22**, 94–97 (2010).
21. G. Dudas, A. Rambaut, http://biorxiv.org/content/early/2015/06/12/020834 (2015).
22. V. M. Corman *et al.*, *J. Virol.* **88**, 11297–11303 (2014).
23. Q. Xie *et al.*, *Sci. China Life Sci.* **58**, 818–820 (2015).
24. Y. J. Kim *et al.*, *Genome Announc.* **3**, e00787–e15 (2015).
25. R. J. de Groot *et al.*, *J. Virol.* **87**, 7790–7792 (2013).

ACKNOWLEDGMENTS

We thank C.-H. Yip, C.-L. Cheung, Y. Chai, C. Ma, T. Gan, Z. Jin, Z. Ou, P. Huang, J. Zhou, and G. Yu for technical assistance and P. Kellam, A. Bin Saeed, M. Cotten, M. A. Barry, and A. M. Somily for making sequences available before their formal publication. This study was supported by the Deanship of Scientific Research (DSR 46-130-35-HiCi) of King Abdulaziz University; the Vice President for Educational Affairs A. O. Alyoubi under the umbrella of the Development Committee of Basic Sciences at King Abdulaziz University; the Shenzhen Peacock Plan High-End Talents Program (award KQTD201203); and the Li Ka Shing Foundation and Theme-based Research Scheme (award T11-705/14-N). E.C.H. is supported by an Australia Fellowship from the National Health and Medical Research Council of Australia (award AF30). All authors declare no competing financial interests. The sequences generated by this study were deposited in GenBank under accession numbers KT368824 to KT368916; additional data can be found in the supplementary materials.

SUPPLEMENTARY MATERIALS

www.sciencemag.org/content/351/6268/81/suppl/DC1
Materials and Methods
Figs. S1 to S5
Tables S1 and S2
References (*26*–*47*)

24 June 2015; accepted 12 November 2015
Published online 17 December 2015
10.1126/science.aac8608

GENOME EDITING

Rationally engineered Cas9 nucleases with improved specificity

Ian M. Slaymaker,[1,2,3,4]* Linyi Gao,[1,4]* Bernd Zetsche,[1,2,3,4] David A. Scott,[1,2,3,4] Winston X. Yan,[1,5,6] Feng Zhang[1,2,3,4]†

The RNA-guided endonuclease Cas9 is a versatile genome-editing tool with a broad range of applications from therapeutics to functional annotation of genes. Cas9 creates double-strand breaks (DSBs) at targeted genomic loci complementary to a short RNA guide. However, Cas9 can cleave off-target sites that are not fully complementary to the guide, which poses a major challenge for genome editing. Here, we use structure-guided protein engineering to improve the specificity of *Streptococcus pyogenes* Cas9 (SpCas9). Using targeted deep sequencing and unbiased whole-genome off-target analysis to assess Cas9-mediated DNA cleavage in human cells, we demonstrate that "enhanced specificity" SpCas9 (eSpCas9) variants reduce off-target effects and maintain robust on-target cleavage. Thus, eSpCas9 could be broadly useful for genome-editing applications requiring a high level of specificity.

The RNA-guided endonuclease Cas9 from microbial clustered regularly interspaced short palindromic repeat (CRISPR)–Cas adaptive immune systems is a powerful tool for genome editing in eukaryotic cells (*1*, *2*). However, the nuclease activity of Cas9 can be triggered even when there is imperfect complementarity between the RNA guide sequence and an off-target genomic site, particularly if mismatches are distal to the protospacer adjacent motif (PAM), a short stretch of nucleotides required for target selection (*3*, *4*). These off-target effects pose a challenge for genome-editing applications. Here, we report the structure-guided engineering of *Streptococcus pyogenes* Cas9 (SpCas9) to improve its DNA targeting specificity.

Several strategies to enhance Cas9 specificity have been reported, including reducing the amount of active Cas9 in the cell (*3*, *5*, *6*), using Cas9 nickase mutants to create a pair of juxtaposed single-stranded DNA nicks (*7*, *8*), truncating the guide sequence at the 5′ end (*9*), and using a pair of catalytically inactive Cas9 nucleases, each fused to a FokI nuclease domain (*10*, *11*). Although each of these approaches reduces off-target mutagenesis, they have a number of limitations: Reducing the amount of Cas9 can decrease on-target cleavage efficiency, double nicking requires the concurrent delivery of two single-guide RNAs (sgRNAs), and truncated guides can increase indel formation at some off-target loci and reduce the number of target sites in the genome (*12*, *13*).

[1]Broad Institute of MIT and Harvard, Cambridge, MA 02142, USA. [2]McGovern Institute for Brain Research, Massachusetts Institute of Technology, Cambridge, MA 02139, USA. [3]Department of Brain and Cognitive Sciences, Massachusetts Institute of Technology, Cambridge, MA 02139, USA. [4]Department of Biological Engineering, Massachusetts Institute of Technology, Cambridge, MA 02139, USA. [5]Graduate Program in Biophysics, Harvard Medical School, Boston, MA 02115, USA. [6]Harvard-MIT Division of Health Sciences and Technology, Harvard Medical School, Boston, MA 02115, USA.
*These authors contributed equally to this work. †Corresponding author. E-mail: zhang@broadinstitute.org

Cas9-mediated DNA cleavage is dependent on DNA strand separation (*14*, *15*). Mismatches between the sgRNA and its DNA target in the first 8 to 12 PAM-proximal nucleotides can eliminate nuclease activity; however, this nuclease activity can be restored by introducing a DNA:DNA mismatch at that location (*3*, *16*–*19*). We hypothesized that nuclease activity is activated by strand separation and reasoned that by attenuating the helicase activity of Cas9, mismatches between the sgRNA and target DNA are less energetically favorable, resulting in reduced cleavage activity at off-target sites (fig. S1).

The crystal structure of SpCas9 in complex with guide RNA and target DNA (*14*, *15*) provides a basis to improve specificity through rational engineering. The structure reveals a positively charged groove, positioned between the HNH, RuvC, and PAM-interacting domains in SpCas9, that is likely to be involved in stabilizing the nontarget strand of the target DNA (Fig. 1, A and B, and fig. S2). We hypothesized that neutralization of positively charged residues within this nontarget strand groove (nt-groove) could weaken nontarget strand binding and encourage rehybridization between the target and nontarget DNA strands, thereby requiring more stringent Watson-Crick base pairing between the RNA guide and the target DNA strand.

To test this hypothesis, we generated SpCas9 mutants consisting of individual alanine substitutions at 31 positively charged residues within the nt-groove and assessed changes to genome-editing specificity (Fig. 2A; fig. S3, A and B; and fig. S4). Single amino acid mutants were tested for specificity by targeting them to the *EMX1*(1) target site in human embryonic kidney (HEK) cells using a previously validated guide sequence; indel formation was assessed at the on-target site and three known genomic off-target (OT) sites (*3*, *4*). Five of the 31 single amino acid mutants reduced activity at all three off-target sites by a factor of at least 10 compared with wild-type (WT) SpCas9 while maintaining on-target cleavage

efficiency, and six others improved specificity by a factor of 2 to 5. These mutants also exhibited improved specificity when tested on a second locus, *VEGFA*(1) (Fig. 2B).

Although some single amino acid mutants were more specific than WT SpCas9 when targeting *EMX1*(1) and *VEGFA*(1), off-target indels were still detectable (~0.5%) (Fig. 2B). To further improve specificity, we performed combinatorial mutagenesis using the top single amino acid mutants identified in the initial screen. Eight out of 34 combination mutants retained wild-type on-target activity and displayed undetectable off-target indel levels at *EMX1*(1) OT1, *VEGFA*(1) OT1, and *VEGFA*(1) OT2 (Fig. 2C and fig. S3, C and D).

To ensure that the observed decrease in off-target activity was not accompanied by reduced on-target activity, we measured on-target indel formation at 10 target sites in three genomic loci using the top 14 mutants (fig. S5) and ranked these based on a combination of preserved on-target activity and decreased off-target activity. We identified three mutants with both high efficiency (WT levels of on-target indel formation) and specificity SpCas9 (K855A), SpCas9 (K810A/K1003A/R1060A) [also referred to as eSpCas9 (1.0)], and SpCas9 (K848A/K1003A/R1060A) [also referred to as eSpCas9(1.1)]. These three variants were selected for further analysis.

We expanded this assay to assess whether SpCas9(K855A), eSpCas9(1.0), and eSpCas9(1.1) broadly retained efficient nuclease activity, measuring on-target indel generation at 24 target sites spanning 10 genomic loci (Fig. 3A). All three mutants generated similar indel levels as WT SpCas9 with the majority of target sites (Fig. 3B). Mutants were expressed equivalently or at higher levels than WT SpCas9 based on a Western blot (Fig. 3C),

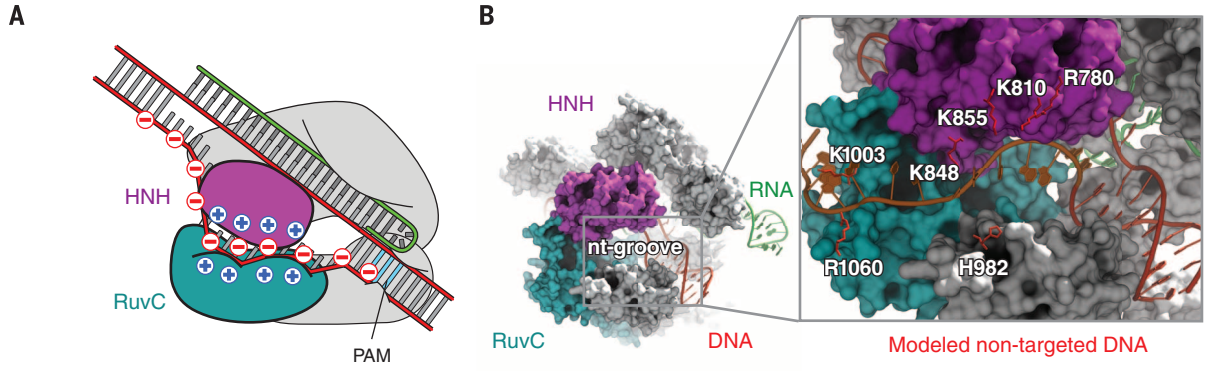

Fig. 1. Structure-guided mutagenesis improves specificity of SpCas9. (**A**) A model of Cas9 unwinding highlighting locations of charge on DNA and the nt-groove. The nt-groove between the RuvC (teal) and HNH (magenta) domains stabilizes DNA unwinding through nonspecific DNA interactions with the noncomplementary strand. RNA:cDNA and Cas9:ncDNA interactions drive DNA unwinding in competition against cDNA:ncDNA rehybridization. (**B**) A crystal structure of SpCas9 (Protein Data Bank ID 4UN3) showing the nt-groove situated between the HNH (magenta) and RuvC (teal) domains. The nontarget DNA strand (red) was manually modeled into the nt-groove (inset).

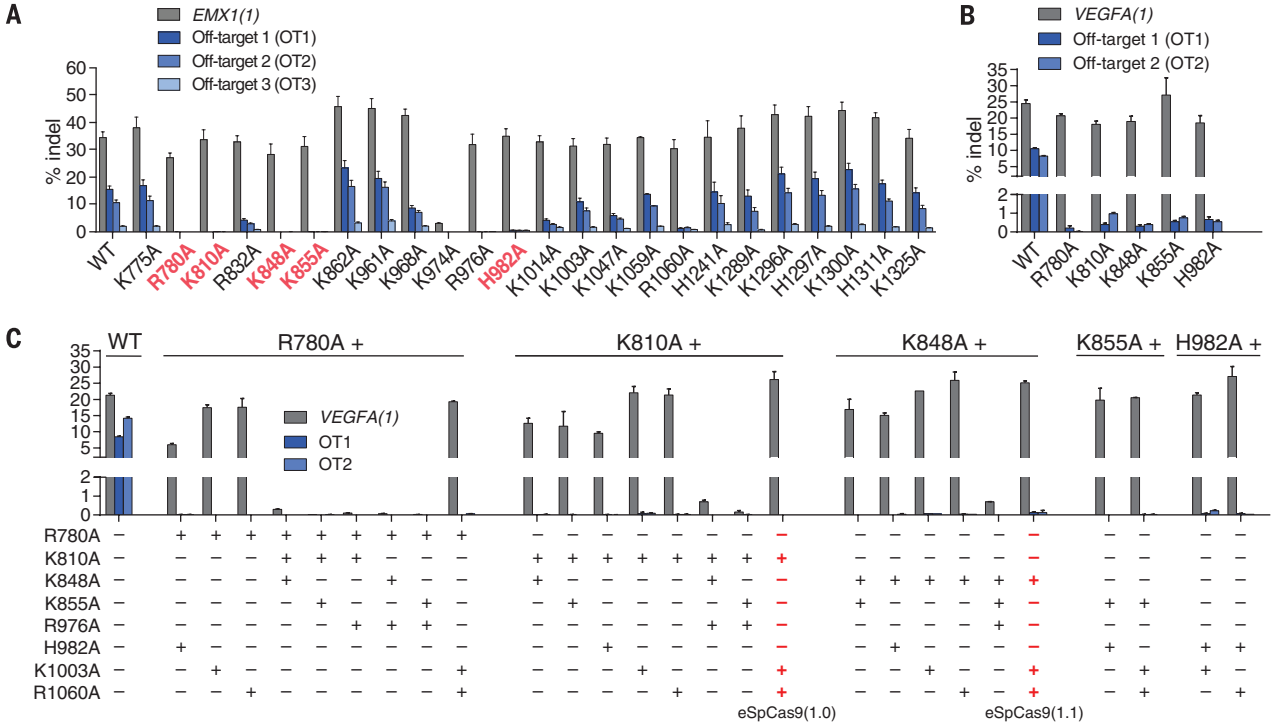

Fig. 2 Point mutations in Cas9 improve targeting specificity. (**A**) Screen of alanine single mutants for improvement in specificity. The top five specificity-conferring mutants are highlighted in red. (**B**) Assessment of top single mutants at additional off-target loci. (**C**) Combination mutants improve specificity compared with single mutants. eSpCas9(1.0) and eSpCas9(1.1) are highlighted in red.

Fig. 3. SpCas9 mutants maintain on-target efficiency. (**A**) Assessment of mutants for efficient on-target cutting with 24 sgRNAs targeted to 10 genomic loci. (**B**) Box-and-whisker plot of normalized on-target indel formation for mutants. (**C**) Western blot of SpCas9 using antibody to SpCas9.

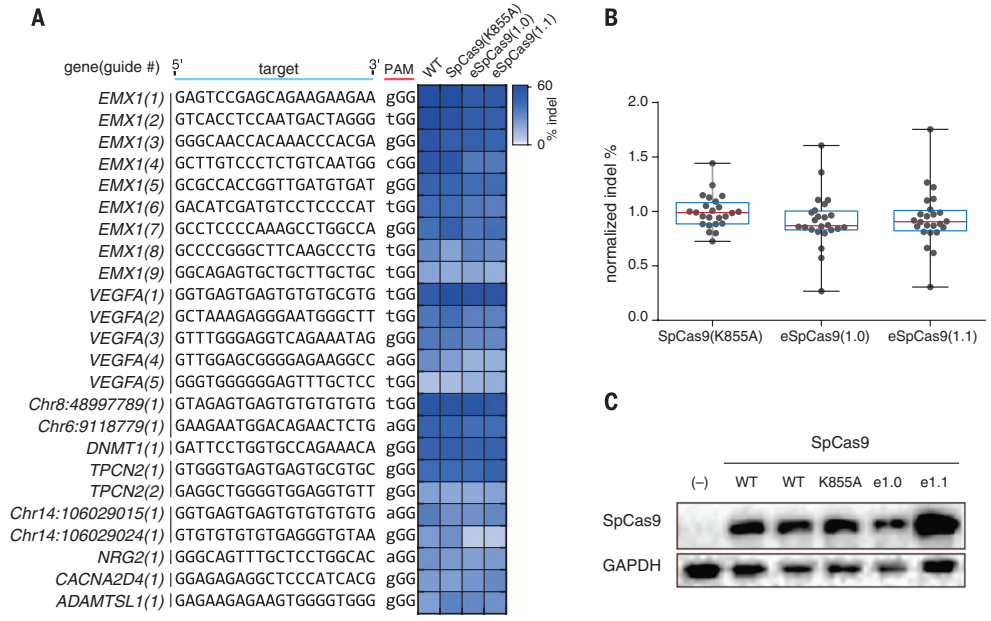

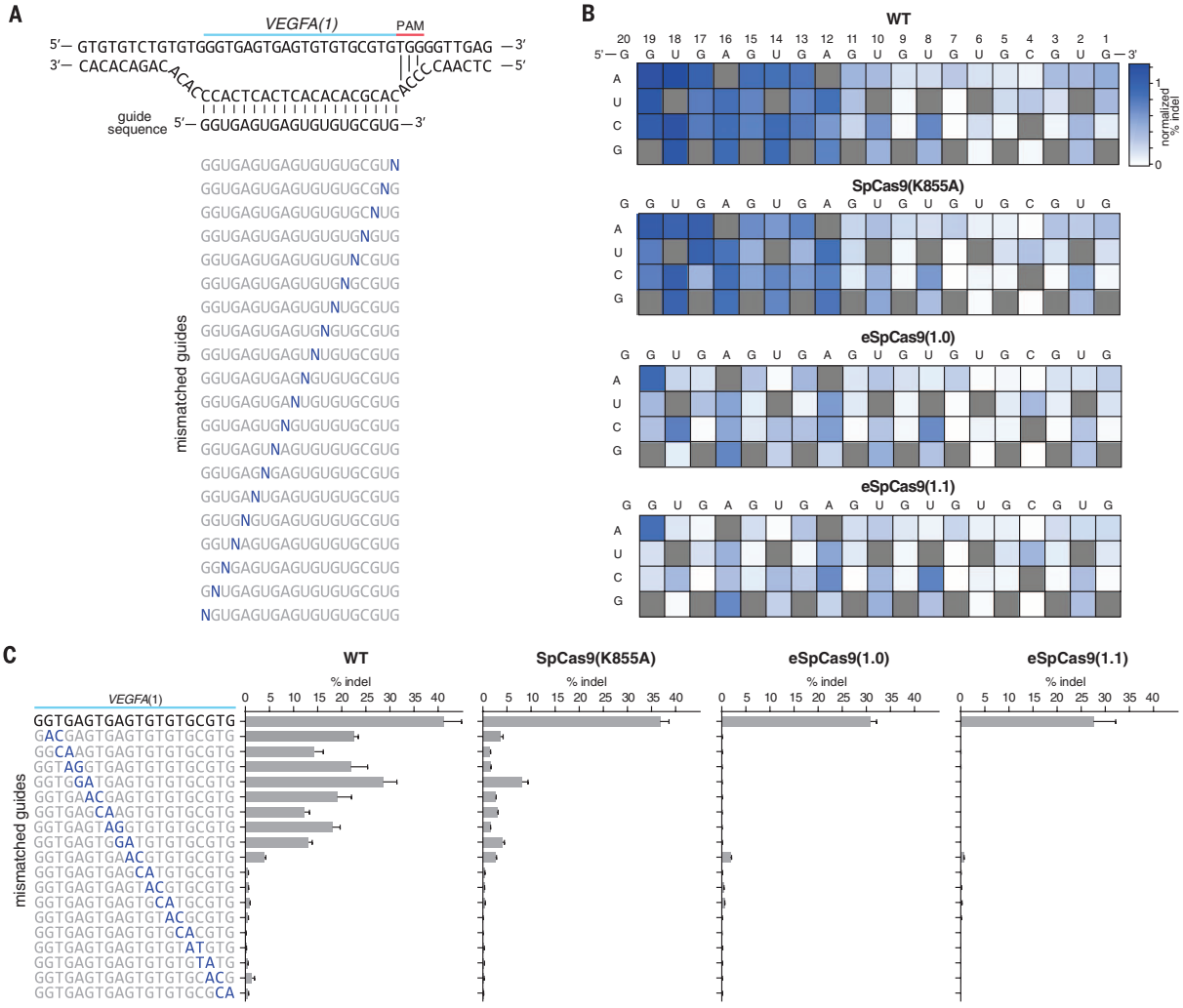

Fig. 4. SpCas9 mutants exhibited increased sensitivity to single- and double-base mismatches between the guide RNA and target DNA. (**A**) Schematic showing design of mismatched guide sequences against *VEGFA*(1). (**B**) Heat maps showing indel percentage of guide sequences with a single-base mismatch. (**C**) Indel formation with guide sequences containing consecutive transversion mismatches.

indicating that improvements in specificity were not due to decreased protein expression levels.

We compared the specificity of the three mutants to WT SpCas9 with truncated guide sequences [18 nucleotides for *EMX1*(1) and 17 nucleotides for *VEGFA*(1)], which have been shown to reduce off-target indel formation (*12*) (fig. S6). When using full-length (20 nucleotides) guides, all three mutants reduced cleavage at all off-target sites assessed compared with WT spCas9. Specifically, eSpCas9(1.0) and eSpCas9(1.1) with 20-nucleotide RNA guides eliminated cleavage at 22 out of 24 off-target sites (<0.2% indel). In contrast, WT SpCas9 with truncated guides eliminated 14 out of 24 sites but also increased off-target activity at five sites compared with WT SpCas9 with 20-nucleotide guides.

To further understand the tolerance SpCas9 (K855A), eSpCas9(1.0), and eSpCas9(1.1) for mismatched target sites, we systematically mutated the *VEGFA*(1) guide sequence to introduce single- and double-base mismatches at different positions (Fig. 4, A to C). Compared with WT SpCas9, all three mutants induced lower levels of indels with mismatched guides. Of note, eSpCas9(1.0) and eSpCas9(1.1) induced lower indel levels even with single-base mismatches located outside of the 7- to 12–base pair seed sequence. Given that we did not observe any difference between eSpCas9(1.0) and eSpCas9(1.1) in terms of specificity, we selected SpCas9(K855A) and eSpCas9(1.1) for further analysis based on on-target efficiency.

We assessed the genome-wide editing specificity of SpCas9(K855A) and eSpCas9(1.1) using BLESS (direct in situ breaks labeling, enrichment on streptavidin and next-generation sequencing) (*20*, *21*), which quantifies DNA double-stranded breaks (DSBs) across the genome (fig. S7A), for both the *EMX1*(1) and *VEGFA*(1) targets for both mutants and compared these results to WT SpCas9. We used a previously established computational pipeline for distinguishing Cas9-induced DSBs from background DSBs (*21*) (fig. S7B). Both SpCas9 (K855A) and eSpCas9(1.1) exhibited a genome-wide reduction in off-target cleavage and did not generate any new off-target sites (Fig. 5, A to D).

These findings also provide insight into the mechanism of Cas9 targeting and nuclease activity. We propose that off-target cutting occurs when the strength of Cas9 binding to the nontarget DNA strand exceeds forces of DNA rehybridization. Consistent with this model, mutations designed to weaken interactions between Cas9 and the noncomplementary DNA (ncDNA) strand led to a substantial improvement in specificity. The model also suggests that, conversely, specificity can be decreased by strengthening the interactions between Cas9 and the nontarget strand. Consistent with this hypothesis, we generated two mutants, S845K and L847R, each of which exhibited decreased specificity (fig. S8). Similar strategies described in this study can also be successfully applied to other Cas9 family proteins, such as *Staphylococcus aureus* Cas9 (SaCas9) (fig. S9), to engineer nucleases with improved specificity.

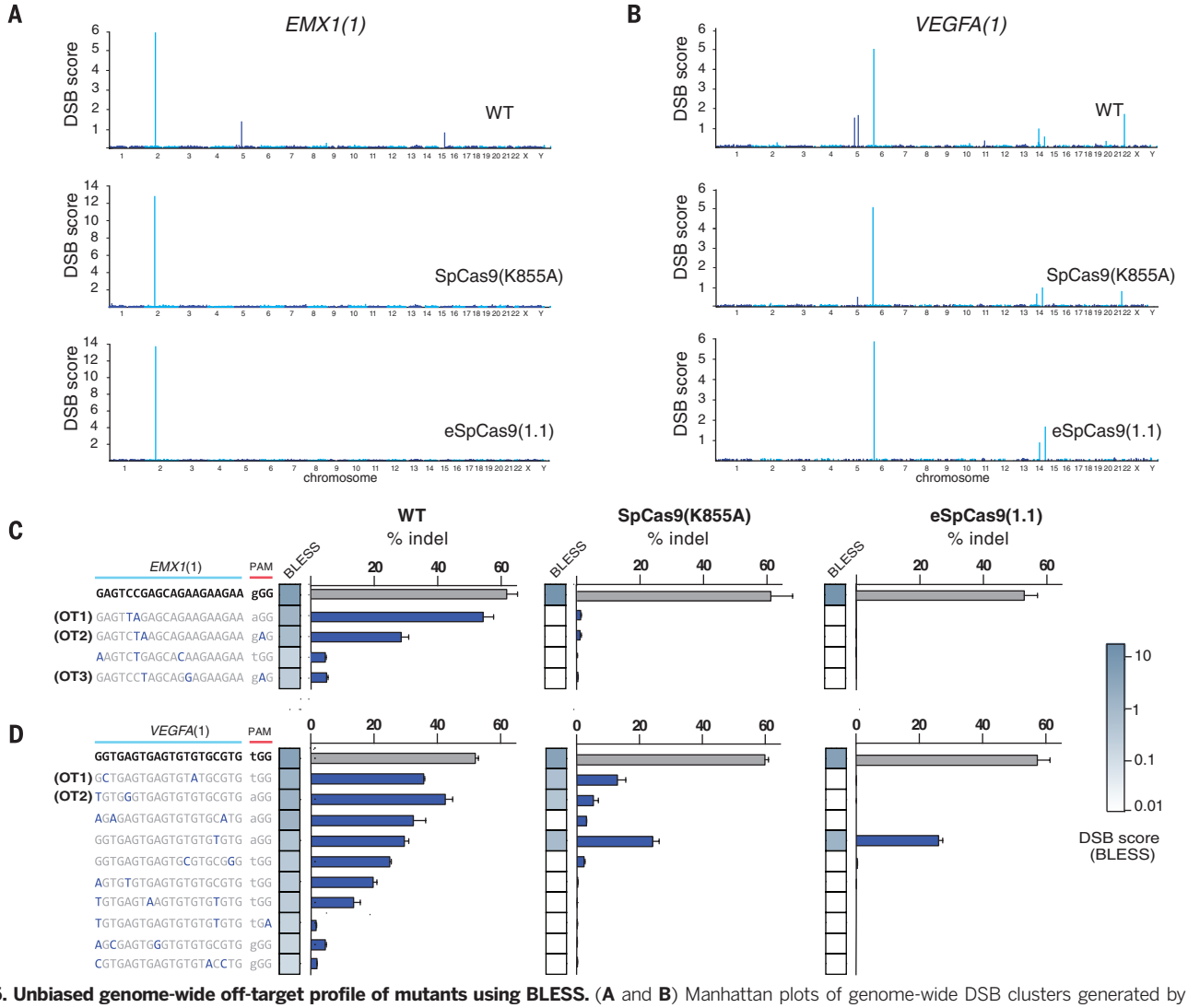

Fig. 5. Unbiased genome-wide off-target profile of mutants using BLESS. (**A** and **B**) Manhattan plots of genome-wide DSB clusters generated by each SpCas9 mutant using the *EMX1*(1) and *VEGFA*(1) targeting guides. (**C** and **D**) Targeted deep-sequencing validation of off-target sites identified in BLESS. Off-target sites are ordered by DSB score (blue heat map).

We have demonstrated through structure-guided design that neutralization of positive charges in the nt-groove can dramatically decrease off-target indel formation while preserving on-target activity. These data show that eSpCas9(1.1) can be used to increase the specificity of genome-editing applications. Future structure-guided interrogation of Cas9 binding and cleavage mechanism will likely enable further optimization of the CRISPR-Cas9 genome-editing toolbox.

REFERENCES AND NOTES

1. L. Cong *et al.*, *Science* **339**, 819–823 (2013).
2. P. Mali *et al.*, *Science* **339**, 823–826 (2013).
3. P. D. Hsu *et al.*, *Nat. Biotechnol.* **31**, 827–832 (2013).
4. Y. Fu *et al.*, *Nat. Biotechnol.* **31**, 822–826 (2013).
5. B. Zetsche, S. E. Volz, F. Zhang, *Nat. Biotechnol.* **33**, 139–142 (2015).
6. K. M. Davis, V. Pattanayak, D. B. Thompson, J. A. Zuris, D. R. Liu, *Nat. Chem. Biol.* **11**, 316–318 (2015).
7. F. A. Ran *et al.*, *Cell* **154**, 1380–1389 (2013).
8. P. Mali *et al.*, *Nat. Biotechnol.* **31**, 833–838 (2013).
9. Y. Fu, J. D. Sander, D. Reyon, V. M. Cascio, J. K. Joung, *Nat. Biotechnol.* **32**, 279–284 (2014).
10. S. Q. Tsai *et al.*, *Nat. Biotechnol.* **32**, 569–576 (2014).
11. J. P. Guilinger, D. B. Thompson, D. R. Liu, *Nat. Biotechnol.* **32**, 577–582 (2014).
12. Y. Fu, J. D. Sander, D. Reyon, V. M. Cascio, J. K. Joung, *Nat. Biotechnol.* **32**, 279–284 (2014).
13. S. Q. Tsai *et al.*, *Nat. Biotechnol.* **33**, 187–197 (2015).
14. H. Nishimasu *et al.*, *Cell* **156**, 935–949 (2014).
15. C. Anders, O. Niewoehner, A. Duerst, M. Jinek, *Nature* **513**, 569–573 (2014).
16. E. Semenova *et al.*, *Proc. Natl. Acad. Sci. U.S.A.* **108**, 10098–10103 (2011).
17. B. Wiedenheft *et al.*, *Proc. Natl. Acad. Sci. U.S.A.* **108**, 10092–10097 (2011).
18. W. Jiang, D. Bikard, D. Cox, F. Zhang, L. A. Marraffini, *Nat. Biotechnol.* **31**, 233–239 (2013).
19. S. H. Sternberg, S. Redding, M. Jinek, E. C. Greene, J. A. Doudna, *Nature* **507**, 62–67 (2014).
20. N. Crosetto *et al.*, *Nat. Methods* **10**, 361–365 (2013).
21. F. A. Ran *et al.*, *Nature* **520**, 186–191 (2015).

ACKNOWLEDGMENTS

We thank J. Dahlman for helpful discussions and a critical review of the manuscript; F. A. Ran, R. J. Platt, and J. Joung for experimental assistance; and the entire Zhang laboratory for support and advice. I.S. is supported by the Simons Center for the Social Brain. W.X.Y. is supported by T32GM007753 from the National Institute of General Medical Sciences and a Paul and Daisy Soros Fellowship. F.Z. is supported by the National Institutes of Health through NIMH (5DP1-MH100706 and 1R01MH110049) and NIDDK (5R01DK097768-03), a Waterman Award from the National Science Foundation, the Keck, New York Stem Cell, Damon Runyon, Searle Scholars, Merkin, and Vallee Foundations, and B. Metcalfe. F.Z. is a New York Stem Cell Foundation Robertson Investigator. I.S., L.G., B.Z., and F.Z. are inventors on provisional patent application 62/181,453 applied for by the Broad Institute and MIT that covers the engineered CRISPR proteins described in this manuscript. Plasmid DNA encoding eSpCas9(1.0) and eSpCas9(1.1) are available from Addgene under a Universal Biological Material Transfer Agreement with the Broad Institute and MIT. F.Z. is a founder and scientific advisor for Editas Medicine and a scientific advisor for Horizon Discovery. Further information about the protocols, plasmids, and reagents can be found at the Zhang laboratory website (www.genome-engineering.org).

SUPPLEMENTARY MATERIALS

www.sciencemag.org/content/351/6268/84/suppl/DC1
Materials and Methods
Figs. S1 to S12
Tables S1 to S3
Supplementary DNA Sequences
References

24 September 2015; accepted 18 November 2015
Published online 1 December 2015
10.1126/science.aad5227

PROTEIN TRANSLOCATION

Structure of the Sec61 channel opened by a signal sequence

Rebecca M. Voorhees and Ramanujan S. Hegde*

Secreted and integral membrane proteins compose up to one-third of the biological proteome. These proteins contain hydrophobic signals that direct their translocation across or insertion into the lipid bilayer by the Sec61 protein–conducting channel. The molecular basis of how hydrophobic signals within a nascent polypeptide trigger channel opening is not understood. Here, we used cryo–electron microscopy to determine the structure of an active Sec61 channel that has been opened by a signal sequence. The signal supplants helix 2 of Sec61α, which triggers a rotation that opens the central pore both axially across the membrane and laterally toward the lipid bilayer. Comparisons with structures of Sec61 in other states suggest a pathway for how hydrophobic signals engage the channel to gain access to the lipid bilayer.

The universally conserved Sec complex forms a gated protein translocation channel at the eukaryotic endoplasmic reticulum (ER) and bacterial plasma membrane (*1*). The central component of this channel, SecY in bacteria and Sec61α in eukaryotes, contains 10 transmembrane (TM) helices arranged around a central pore (*2*). Two single-TM subunits in eukaryotes, Sec61β and Sec61γ, are peripheral to Sec61α. The central pore in the inactive Sec complex is occluded by a short "plug" helix that must be displaced to allow translocation. The interface where TM helices 2 and 3 contact helices 7 and 8 defines a "lateral gate" for membrane access of polypeptides (*1–3*).

Crystal structures of the Sec complex (*2*, *4–6*) lack a translocating polypeptide and likely represent a range of inactive states. Depending on crystal contacts or translocation partners, the lateral gate and plug are in various states of opening and displacement. However, the biological relevance of these channel conformations has been difficult to interpret without a well-resolved and matched active structure. Previous structures of translocation or insertion intermediates of the ribosome-Sec complex determined by cryo–electron microscopy (cryo-EM) were of moderate resolution (*7–9*), contained heterogeneous substrates (*9*), required artificial stabilization (*8*), or were at an uncertain stage of insertion (*7*). Although these earlier structures provided the first views of substrate-induced structural changes consistent with lateral gate opening, the data could not clearly resolve individual Sec61 TM helices or the nature of their interactions with the signal. Thus, a molecular understanding of how substrates open the channel for translocation or insertion is incomplete.

We devised a strategy to tag and purify the canine ribosome-Sec61 complex engaged by the first 86 residues of the secretory protein prepro-lactin (fig. S1). Translocation, protease-protection, and photo–cross-linking experiments verified that, like the well-characterized native 86-residue intermediate (*10–15*), our tagged complex represents a functional translocation intermediate engaged by Sec61 (figs. S2 to S4). The nascent polypeptide remains engaged with Sec61 during and after purification (fig. S4), which makes it suitable for structure determination by single-particle cryo-EM.

The structure of this engaged ribosome-Sec61 complex was reconstructed from 101,339 particles to an overall resolution of 3.6 Å (figs. S5 and S6 and table S1). The local resolution of the Sec61 channel ranged from ~ 3.5 Å near the ribosome to ~7.0 Å at the lumenal loops. Most TM helices were at ~4.5 to 5.5 Å resolution (fig. S6), which revealed clear helical pitch and many bulky side chains in sharpened maps (fig. S7). All 12 TM helices of the Sec61 complex could be unambiguously assigned, leaving a single helix we ascribed to the signal sequence (Fig. 1, A and B, and fig. S8). Density visible throughout the ribosomal exit tunnel and in parts of the Sec61 channel (Fig. 1C) suggests a looped configuration for the nascent chain, consistent with earlier cross-linking studies (*11*).

The well-resolved structure of a biochemically validated early translocation intermediate permitted detailed comparisons with other Sec61 states to gain insights into the conformational changes accompanying channel opening. A previous cryo-EM structure of the porcine ribosome-Sec61 complex lacking a nascent polypeptide (*9*) represents a "primed" state preceding nascent chain insertion. Relative to this primed structure, the engaged channel is open laterally toward the lipid bilayer and axially across the membrane (Fig. 2). The ribosome-Sec61 interaction remains fixed, with only minor movements of the associated Sec61γ and TM helices 6, 7, 8, and 9 of Sec61α. The other seven TM helices of the Sec61 complex rotate as a rigid body by ~22° (Fig. 2A and movies S1 and S2), which creates space between helices 2 and 7 for intercalation of the signal peptide (Fig. 2B). Notably, cryo-tomography

MRC Laboratory of Molecular Biology, Medical Research Council, Francis Crick Avenue, Cambridge CB2 0QH, UK.
***Corresponding author. E-mail: rhegde@mrc-lmb.cam.ac.uk**

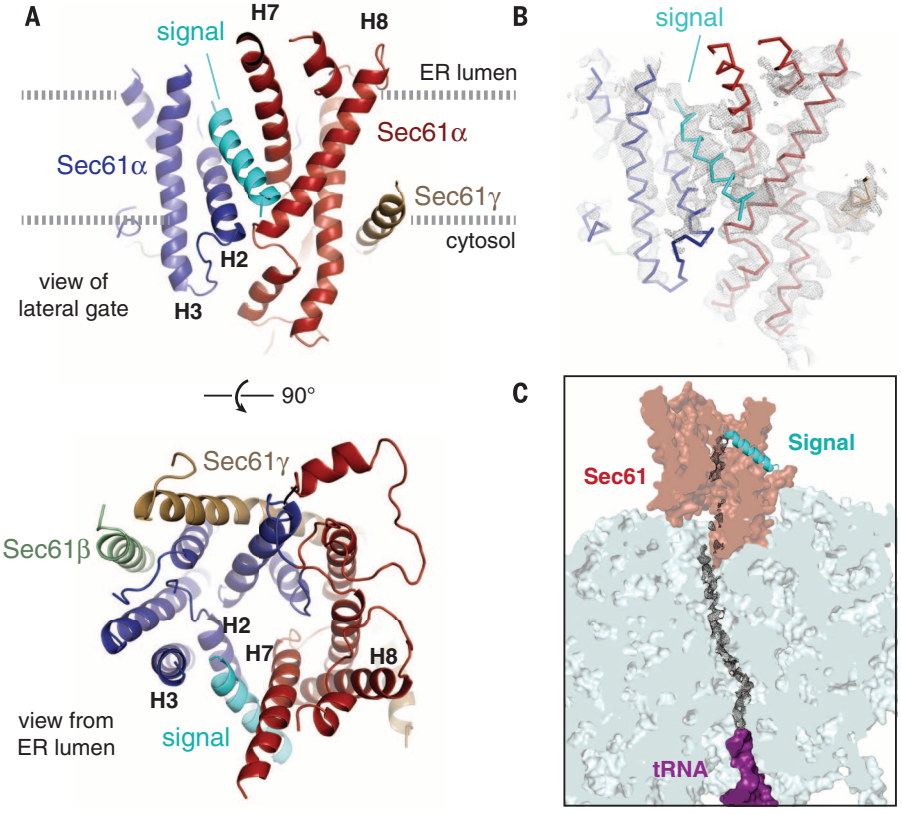

Fig. 1. Structure of the signal peptide-engaged Sec61 complex. (**A**) View of the lateral gate (top) or from the ER lumen of the Sec61 complex bound to the preprolactin signal peptide (cyan). The mobile regions of Sec61α are blue; the comparatively immobile regions are red. The β and γ subunits are pale green and tan, respectively. Helices that compose the lateral gate are labeled. (**B**) Experimental density for the structure (mesh, filtered to 4.5 Å resolution) superimposed on the backbone trace of the structural model. (**C**) Density observed for the nascent polypeptide through the ribosomal tunnel and parts of the Sec61 channel.

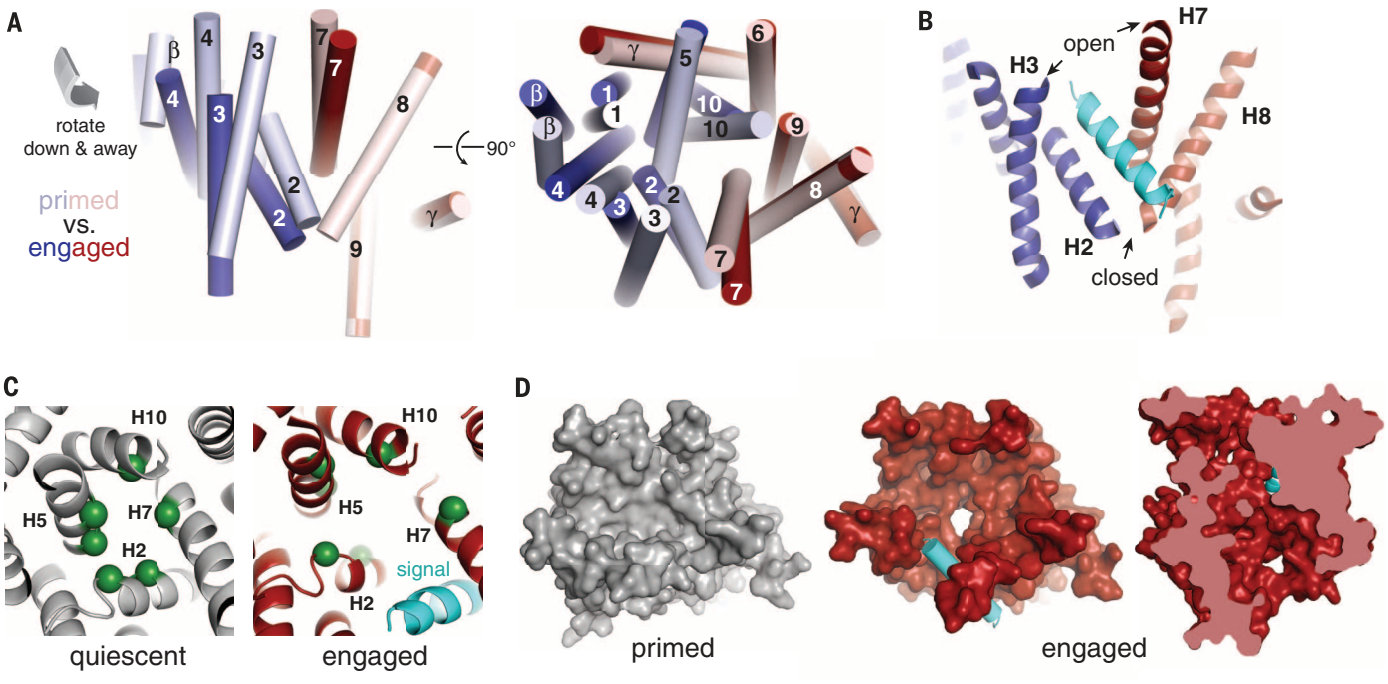

Fig. 2. Conformational changes to Sec61 upon engagement by a signal peptide. (**A**) Positions of the transmembrane helices of the Sec61 complex in the ribosome-primed (pale colors, PDB 3J7Q) and signal-engaged (bright colors) states. The mobile regions of Sec61α are blue; the comparatively immobile regions are red. Individual helices are labeled; the signal has been omitted for clarity. (**B**) View of the asymmetrically opened lateral gate. (**C**) View of the pore ring residue positions (green spheres) in the quiescent SecY crystal structure (gray, PDB 1RH5) and engaged Sec61 complex (red). The signal is cyan. (**D**) (Left and middle) Surface view of the primed (gray, PDB 3J7Q) and engaged (red) states of the Sec61 complex viewed from the ER lumen. The lumenal loops have been removed for clarity. The signal peptide is cyan. (Right) cutaway view perpendicular to the membrane of the engaged Sec61 complex showing an open channel.

of the Sec61 complex in native ER microsomes shows a similar configuration (*16*). Although the heterogeneous and uncertain functional state of the cryo-tomography structure complicates its placement within the translocation cycle (*17*), it does illustrate that our engaged structure is likely to be compatible with a membrane environment.

Because the 22° rotation is oblique relative to the plane of the membrane, lateral gate opening is asymmetric: the lumenal end of the gate parts by ~15 Å, whereas the cytosolic side remains closed (Fig. 2B). Oblique rotation of helices 2, 5, and 10 away from helix 7 displaces a set of six conserved "pore ring" residues (table S2) from their normally planar configuration (Fig. 2C). The plug is apparently destabilized by separation of the pore ring, atop which it ordinarily sits (*2*), which leads to an unobstructed conduit across the membrane (Fig. 2D). Thus, opening of the Sec61 channel is directly coupled to successful signal sequence recognition via its intercalation in the lateral gate.

To understand how the signal sequence reaches this position, we asked whether Sec61 priming by the ribosome might favor subsequent signal sequence engagement. For comparison, we used the *M. jannaschii* x-ray structure of an isolated Sec complex in its "quiescent" state (*2*), whose overall architecture, TM helix interactions, and key functional motifs (table S2) are well conserved in mammals. Relative to the quiescent channel, the ribosome-primed Sec61 complex is partially destabilized in two ways. First, a "polar cluster" of three residues on helices 2 and 7 that form stabilizing hydrogen bonds is separated in the primed state (Fig. 3A). Hence, the lateral gate is partially cracked in the precise region eventually occupied by the signal peptide. Second, the external surface of the primed Sec61 complex (Fig. 3B) contains a hydrophilic seam that is energetically disfavored by its exposure to the hydrophobic interior of the lipid bilayer. A similar conformational change is seen in the bacterial SecY complex bound to SecA (*6*). Thus, two diverse translocation partners from different translocation pathways, the ribosome and SecA, induce similar priming events by binding to the cytosolic loops of the Sec61 and SecY complex, respectively.

When viewed from the ribosomal exit tunnel, nearly all of the surfaces on the primed Sec61 complex available to a nascent signal peptide are hydrophilic. The only substantive hydrophobic patch, deep within the channel pore, might serve as the initial interaction site for a hydrophobic signal (Fig. 4A). This hydrophobic patch is composed of residues from the lateral gate and pore ring (table S2) and is positioned adjacent to the region of the lateral gate weakened by ribosome priming (Fig. 4B). Packing of the hydrophobic signal at this destabilized region may facilitate its intercalation into the lateral gate, driven by the energetically favorable exposure of the signal to lipid, so that it eventually adopts the conformation seen in our structure.

The position of the engaged signal perfectly supplants helix 2 and replaces its interactions with helices 7 and 8 to stabilize the open channel conformation (Fig. 4, C and D). Hydrophilic segments of polypeptide would not be energetically favored in this position, which explains why they cannot open the channel. The conserved hydrophobicity and length of helix 2 suggests that the biophysical properties of helix 2 may dictate what constitutes a functional signal for translocation, a property that is similar, but not identical across species. The concept of a hydrophobicity threshold set by an intramolecular "placeholder" is also used by the signal recognition particle at an earlier step of this pathway (*18*) and may be a general mechanism for increasing recognition fidelity of widely divergent sequences.

Our structure of the signal-engaged Sec61 translocon, together with earlier quiescent and primed structural states, leads to a molecular model for selective gating of the translocon by hydrophobic signals. Ribosome binding constrains the cytosolic loops of Sec61 to enforce a conformation in which key lateral gate contacts, including the conserved polar cluster, are weakened. A hydrophobic patch close to this site attracts hydrophobic signals to their point of initial engagement. If the signal is sufficiently hydrophobic, it can proceed further to displace the comparably hydrophobic helix 2 and access the lipid bilayer while simultaneously widening the central pore to destabilize the plug. Thus, polypeptides initially sample the cytosolic vestibule of Sec61 and gain access to the lipid bilayer via the channel interior, contingent on both a suitably hydrophobic signal and an appropriately primed translocation channel.

This stepwise model for translocon opening is consistent with fluorescence and cross-linking studies showing that signals are initially in an aqueous environment (*19*) near Sec61α (*10*–*13*) and only access lipid after further elongation (*13*, *15*). Furthermore, mutants of the lateral gate, plug, and pore ring residues in the hydrophobic patch

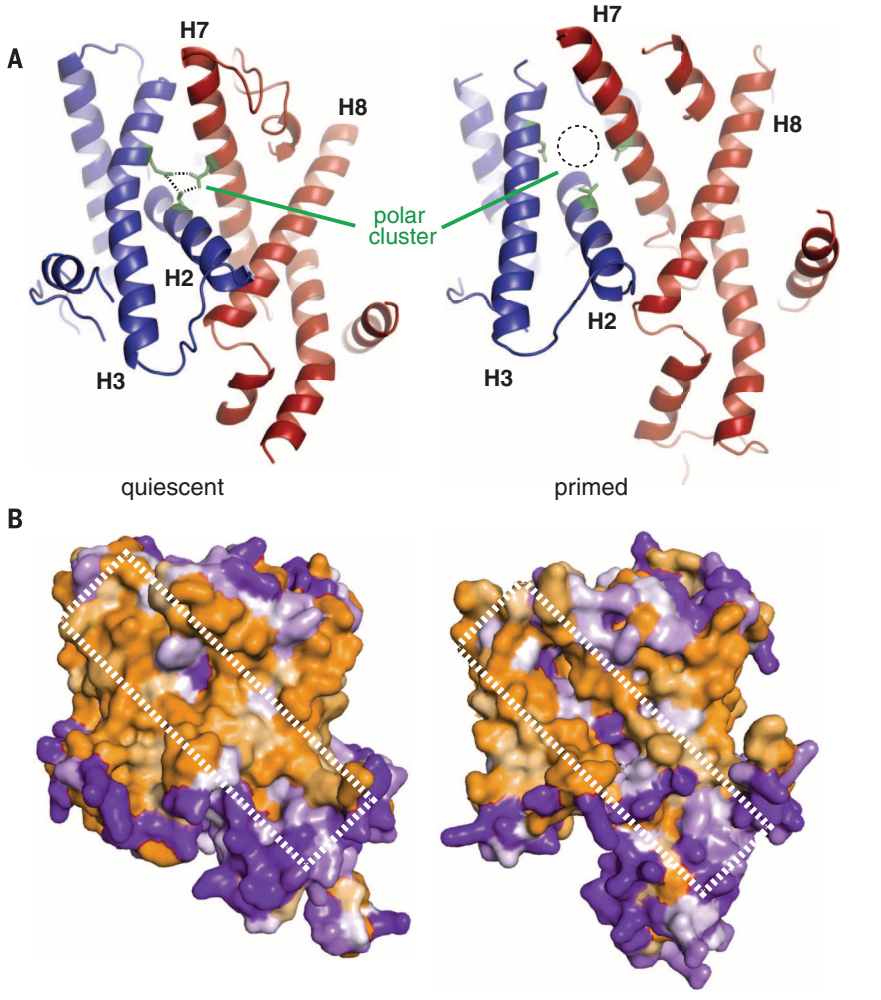

Fig. 3. The lateral gate is destabilized in the ribosome-primed Sec61 complex. (**A**) Comparison of the quiescent SecY (left, PDB 1RH5) and primed Sec61 (right, PDB 3J7Q) complexes. Ribosome binding results in partial destabilization of the lateral gate by shifting helices 2 and 3 away from the midline, which disrupts the polar cluster (green). (**B**) Space-filling model viewing the lateral gate of the quiescent (left) and primed (right) structures colored by hydrophobicity, in which orange is hydrophobic and purple is hydrophilic. The hydrophilic seam produced by ribosome binding is indicated.

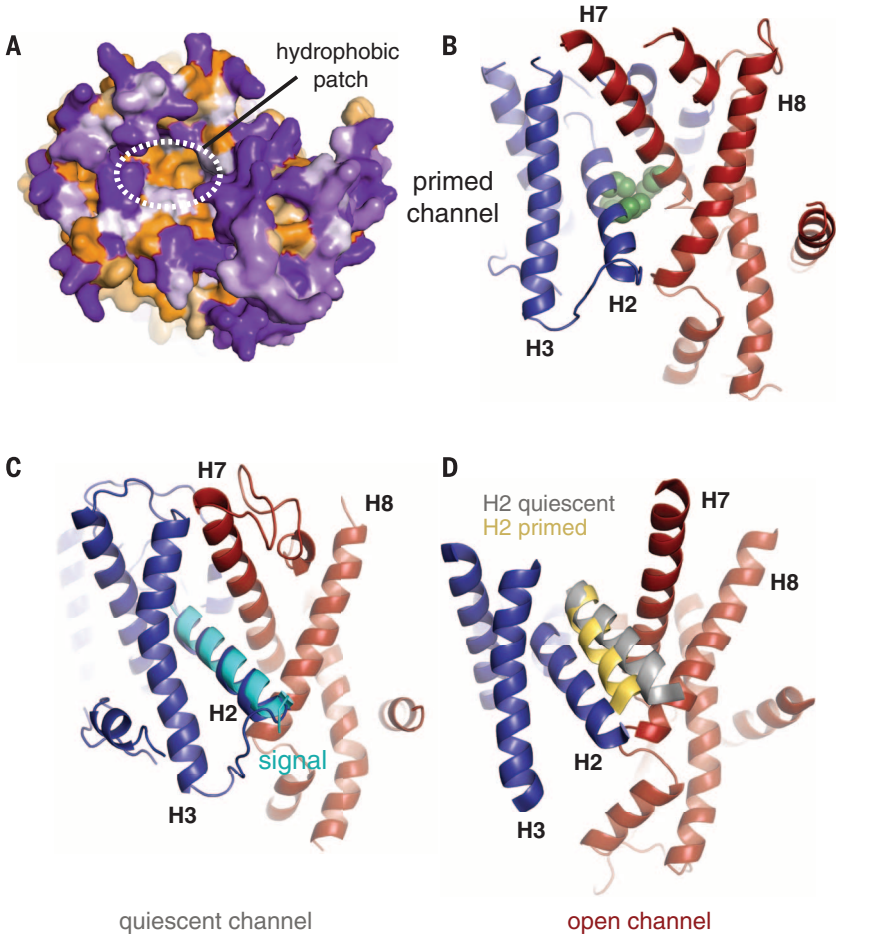

Fig. 4. Putative path of the signal peptide into the Sec61 lateral gate. (**A**) Space-filling model of the cytosolic vestibule of Sec61 viewed from the ribosome, colored by hydrophobicity as in Fig. 3B. (**B**) Residues comprising the hydrophobic patch are at the lateral gate. (**C**) The eventual position of the signal peptide (cyan), relative to the stationary ribosome-bound regions of Sec61, is essentially identical to the position of helix 2 in the quiescent state. (**D**) Positions of helix 2 in the quiescent (gray) and primed (yellow) states superimposed on the engaged Sec61 structure (red and blue). The signal peptide is omitted for clarity but would reside precisely in the position of the quiescent helix 2.

or polar cluster region allow crippled signal sequences to mediate translocation (*20*–*25*). It is possible that such mutants lead to a more dynamic Sec61 channel that can open without signal sequence intercalation into the lateral gate. This would bypass the signal recognition step captured by our structure and permit promiscuous translocation. Conversely, stabilization of lateral gate contacts increases the hydrophobic threshold for signal sequence–mediated translocation (*24*, *25*). Similarly, inhibitors that impede Sec61 opening are thought to bind at the plug and lateral gate junction (*26*, *27*). Thus, defining the location of a signal in the process of initiating translocation permits molecular interpretations of earlier functional data and provides a basis for future studies of other stages in protein translocation. Analysis of signals and TM domains of different biophysical properties in both defined and native translocon complexes will be crucial for understanding how the Sec61 translocon is able to handle the remarkably diverse substrates transiting the membrane.

REFERENCES AND NOTES

1. E. Park, T. A. Rapoport, *Annu. Rev. Biophys.* **41**, 21–40 (2012).
2. B. Van den Berg *et al.*, *Nature* **427**, 36–44 (2004).
3. K. Plath, W. Mothes, B. M. Wilkinson, C. J. Stirling, T. A. Rapoport, *Cell* **94**, 795–807 (1998).
4. P. F. Egea, R. M. Stroud, *Proc. Natl. Acad. Sci. U.S.A.* **107**, 17182–17187 (2010).
5. T. Tsukazaki *et al.*, *Nature* **455**, 988–991 (2008).
6. J. Zimmer, Y. Nam, T. A. Rapoport, *Nature* **455**, 936–943 (2008).
7. M. Gogala *et al.*, *Nature* **506**, 107–110 (2014).
8. E. Park *et al.*, *Nature* **506**, 102–106 (2014).
9. R. M. Voorhees, I. S. Fernández, S. H. W. Scheres, R. S. Hegde, *Cell* **157**, 1632–1643 (2014).
10. S. High *et al.*, *J. Biol. Chem.* **268**, 26745–26751 (1993).
11. W. Mothes, S. Prehn, T. A. Rapoport, *EMBO J.* **13**, 3973–3982 (1994).
12. B. Jungnickel, T. A. Rapoport, *Cell* **82**, 261–270 (1995).
13. W. Mothes, B. Jungnickel, J. Brunner, T. A. Rapoport, *J. Cell Biol.* **142**, 355–364 (1998).
14. K. S. Crowley, S. Liao, V. E. Worrell, G. D. Reinhart, A. E. Johnson, *Cell* **78**, 461–471 (1994).
15. B. Martoglio, M. W. Hofmann, J. Brunner, B. Dobberstein, *Cell* **81**, 207–214 (1995).
16. S. Pfeffer *et al.*, *Nat. Commun.* **6**, 8403 (2015).
17. Although P-site transfer RNA was absent from the majority of ribosomes used for the cryo-tomography structure (*16*), the presence or absence of heterogeneous endogenous nascent polypeptides within Sec61 could not be determined conclusively. Thus, the conclusion that the Sec61 complex is constitutively open upon ribosome binding, independent of substrate or functional state, may be premature. Indeed, biochemical studies in native microsomes show substrate-induced Sec61 opening (*14*), no translocation of Sec61-docked polypeptides with a mutant signal (*12*), and no lipid access to early translocation intermediates (*13*). Genetic studies show that modulation of lateral gate interactions influences translocation (*20*–*27*). Thus, multiple independent findings argue that substrates induce structural changes to the Sec61 complex that open it laterally.
18. R. M. Voorhees, R. S. Hegde, *eLife* **4**, e07975 (2015).
19. K. S. Crowley, G. D. Reinhart, A. E. Johnson, *Cell* **73**, 1101–1115 (1993).
20. T. Junne, T. Schwede, V. Goder, M. Spiess, *J. Biol. Chem.* **282**, 33201–33209 (2007).
21. M. A. Smith, W. M. J. Clemons Jr., C. J. DeMars, A. M. Flower, *J. Bacteriol.* **187**, 6454–6465 (2005).
22. A. I. Derman, J. W. Puziss, P. J. J. Bassford Jr., J. Beckwith, *EMBO J.* **12**, 879–888 (1993).
23. R. S. Osborne, T. J. Silhavy, *EMBO J.* **12**, 3391–3398 (1993).
24. A. P. Maillard, S. Lalani, F. Silva, D. Belin, F. Duong, *J. Biol. Chem.* **282**, 1281–1287 (2007).
25. S. F. Trueman, E. C. Mandon, R. Gilmore, *J. Cell Biol.* **199**, 907–918 (2012).
26. A. L. Mackinnon, V. O. Paavilainen, A. Sharma, R. S. Hegde, J. Taunton, *eLife* **3**, e01483 (2014).
27. T. Junne *et al.*, *J. Cell Sci.* **128**, 1217–1229 (2015).

ACKNOWLEDGMENTS

We thank F. de Haas, V. Ragunath, and C. Savva for help with data collection; S. Chen, G. McMullan, J. Grimmett, and T. Darling for technical support; S. Shao for helpful discussions. This work was supported by the UK Medical Research Council (MC_UP_A022_1007 to RSH) and a Wellcome Trust postdoctoral fellowship (R.M.V.). The Cryo-EM map for the engaged ribosome-Sec61 complex has been deposited with the EMDataBank (EMDB-3245). The Protein Data Bank accession number for the engaged Sec61 complex is 3JC2.

SUPPLEMENTARY MATERIALS

www.sciencemag.org/content/351/6268/88/suppl/DC1
Materials and Methods
Figs. S1 to S8
Tables S1 and S2
Captions for Movies S1 and S2
References (*28*–*46*)
Movies S1 and S2

21 September 2015; accepted 20 November 2015
10.1126/science.aad4992

want new technologies?

antibodies
apoptosis
biomarkers
cancer
cytometry
data
diseases
DNA
epigenetics
genomics
immunotherapies
medicine
microbiomics
microfluidics
microscopy
neuroscience
proteomics
sequencing
toxicology
transcriptomics

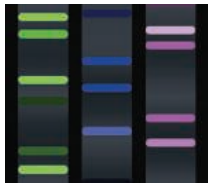

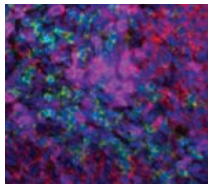

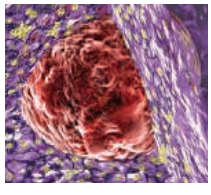

watch our webinars

Learn about the latest breakthroughs, new technologies, and ground-breaking research in a variety of fields. Our expert speakers explain their quality research to you and answer questions submitted by live viewers.

VIEW NOW!
webinar.sciencemag.org

Science
AAAS

Brought to you by the *Science*/AAAS Custom Publishing Office

@SciMagWebinars

Join the Conversation!

Twitter is a great way to connect with AAAS members and staff about the issues that matter to you most. Be a part of the discussion while staying up-to-date on the latest news and information about your personal member benefits.

Follow us @AAASmember and join the conversation with #AAAS

AAAS MemberCentral

MemberCentral.aaas.org

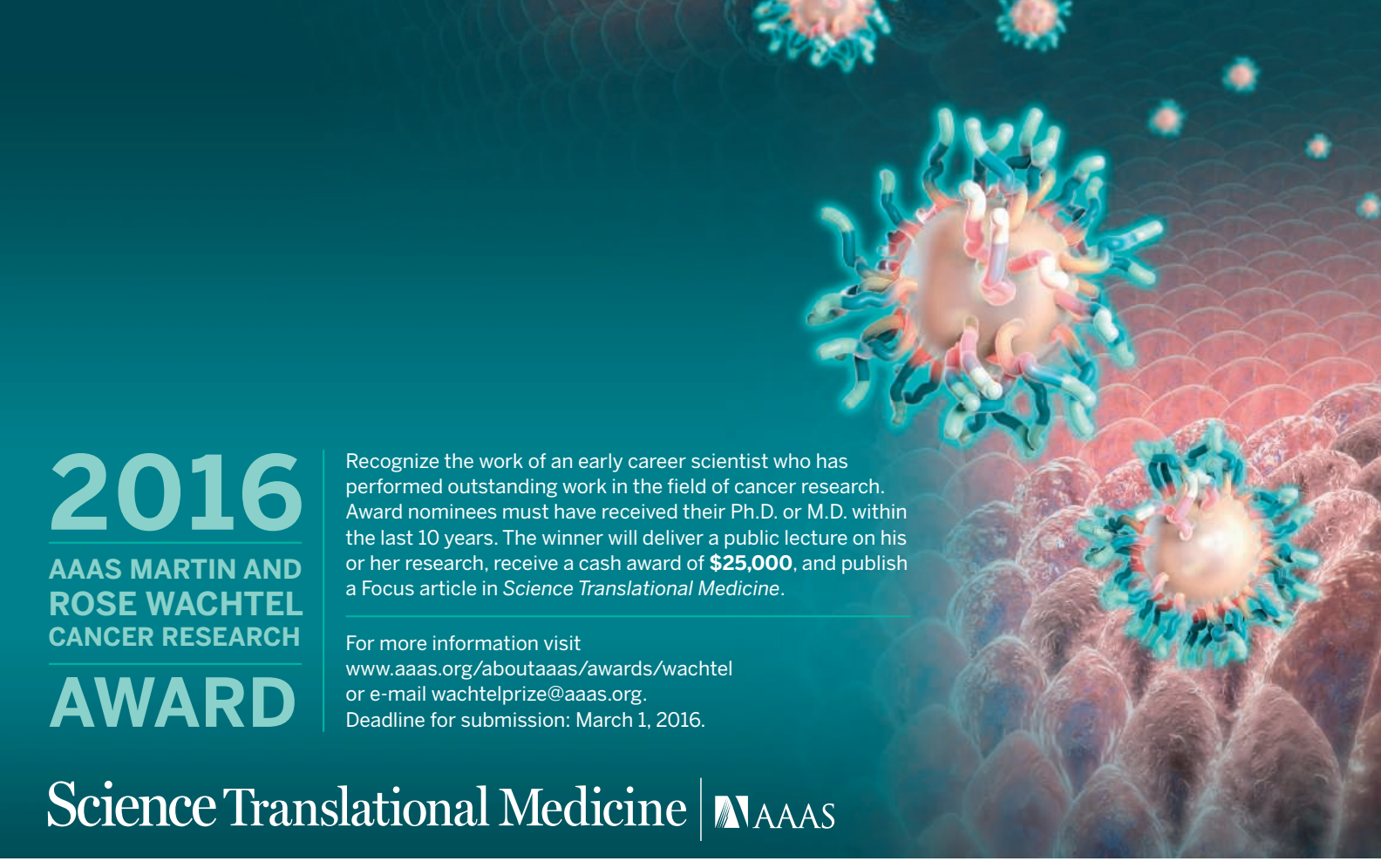

2016
AAAS MARTIN AND ROSE WACHTEL CANCER RESEARCH AWARD

Recognize the work of an early career scientist who has performed outstanding work in the field of cancer research. Award nominees must have received their Ph.D. or M.D. within the last 10 years. The winner will deliver a public lecture on his or her research, receive a cash award of **$25,000**, and publish a Focus article in *Science Translational Medicine*.

For more information visit
www.aaas.org/aboutaaas/awards/wachtel
or e-mail wachtelprize@aaas.org.
Deadline for submission: March 1, 2016.

Science Translational Medicine | AAAS

myIDP:
A career plan customized for you, by you.

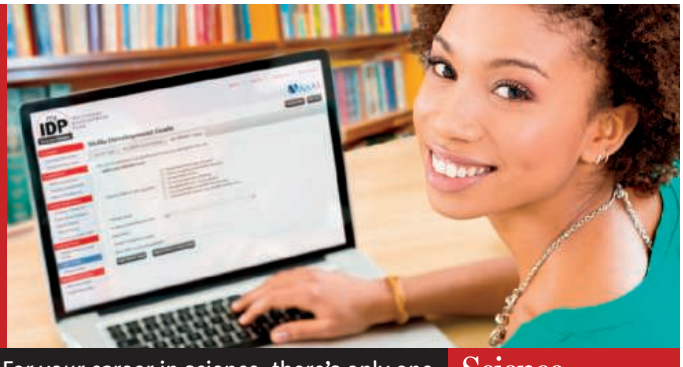

For your career in science, there's only one Science

my IDP
ScienceCareers

Recommended by leading professional societies and the NIH

Features in myIDP include:

- Exercises to help you examine your skills, interests, and values
- A list of 20 scientific career paths with a prediction of which ones best fit your skills and interests
- A tool for setting strategic goals for the coming year, with optional reminders to keep you on track
- Articles and resources to guide you through the process
- Options to save materials online and print them for further review and discussion
- Ability to select which portion of your IDP you wish to share with advisors, mentors, or others
- A certificate of completion for users that finish myIDP.

Visit the website and start planning today!
myIDP.sciencecareers.org

ScienceCareers In partnership with:

FASEB · UCSF University of California San Francisco · Medical College of Wisconsin · Burroughs Wellcome Fund

Mass Spectrometer

Scientists performing advanced research in proteomics, biopharma, and metabolism/metabolomics can now test new limits of detection, characterization, and quantitation with the latest Tribrid mass spectrometer (MS). As the newest addition to the pioneering line of Thermo Scientific Orbitrap Tribrid MSs, the Orbitrap Fusion Lumos Tribrid MS is designed to expand performance in advanced proteomics, biopharma, and metabolomics applications, including quantitation using isobaric tags, low level posttranslational modification (PTM) analysis, data independent acquisition (DIA), and top-down proteomics. The new instrument features enhanced sensitivity resulting in improved analyte detection, characterization, and quantitation, enabling scientists to perform more comprehensive sample analyses faster and with better accuracy than ever before. To achieve proteome-wide coverage, the Orbitrap Fusion Lumos MS combines the versatility of a Tribrid system with the selectivity of Orbitrap technology, its sensitivity and speed rivaling that of a triple quadrupole instrument.

Thermo Fisher Scientific
For info: 800-424-6723
www.thermoscientific.com/lumos

Isolating Feet

For those looking for the flexibility of being able to use a reflective collimator on different experiments around their laboratory, Optical Surfaces has developed self-aligning isolating feet. The isolating feet allow a ±10 mm height adjustment and enable easy relocation of the reflective collimator without any loss of performance. The isolating feet clamp onto standard optical tables and operate in two modes. When the unit is static, the isolating feet are set in "no floating mode." However, to ensure smooth and safe transfer from one place to another, the isolating feet may be set in "floating mode." High stability and performance on the reflective collimators is achieved using a zero expansion off-axis parabola, manufactured to better than lambda/10 peak-valley (P-V) surface accuracy. The optics within each unit are secured by the use of stress-free mounts and come prealigned in our laboratories for optimum performance. The off-axis design produces no central obscuration, ensuring highly efficient transmission.

Optical Surfaces
For info: +44-208-668-6126
www.optisurf.com

Transfection Platform

The new CHOgro Expression System addresses the low transient gene expression levels in early stage drug development by providing researchers a system that achieves high titers in suspension Chinese hamster ovary (CHO) cells, allowing them to quickly obtain sufficient quantities of relevant candidate proteins. The CHOgro Expression System is a robust and simple CHO transient protein expression system enabled by critical media attributes such as high-density cell growth, quick adaptation, and minimization of cell clumping posttransfection. By optimizing the components of the system, antibody titers increase 2–10 fold over existing technologies with higher amounts of antibody secreted per cell. Six different representative antibody constructs have been tested using this system, and even CHO cells maintained in other commercially available media formulations can be easily adapted with a full media exchange to the CHOgro Expression Medium 24 hours prior to transfection, and yield multifold increases in transient expression levels.

Mirus Bio
For info: 888-530-0801
www.mirusbio.com/chogro

NIR/SWIR Camera

The NIRvana: 640LN is the highest performance scientific-grade camera available for near-infrared and short-wavelength infrared (NIR/SWIR) applications. This new addition to the popular NIRvana line features a specially designed indium gallium arsenide (InGaAs) focal plane array (FPA) with extremely low readout, and thermal noise that is ideal for ultra-low-light imaging and spectroscopy. The NIRvana: 640LN delivers a combination of >75% quantum efficiency in the critical NIR/SWIR window, along with the deepest liquid nitrogen cooling (83° Kelvin) currently achievable for an advanced InGaAs FPA, permitting exposure times in excess of 60 minutes. The camera's unprecedented performance facilitates challenging applications in the NIR/SWIR wavelength region. The NIRvana: 640LN is fully compatible with Princeton Instruments' LightField 64-bit application software, an optional package that provides complete control of camera features via a cutting-edge graphical user interface. For researchers requiring a custom interface, toolkits for National Instruments' LabVIEW and MathWorks' MATLAB are available, as are free software development kits (SDKs).

Princeton Instruments
For info: 609-587-9797
www.princetoninstruments.com

Micromanipulator

Eppendorf has served as an expert partner to in vitro fertilization (IVF) labs for more than 20 years. It is our ambition to provide our customers with premium products that live up to the highest standards of quality and performance. The new TransferMan 4m continues this tradition of technical excellence and user friendliness. With its innovative and intuitive operation concept, the TransferMan 4m allows for unprecedented movement control. Advanced features including its unique DualSpeed joystick and smart functions help to speed up and facilitate the handling of sensitive samples. The TransferMan 4m therefore helps minimize exposure of sensitive cells to trauma or adverse conditions like room temperature or removal from a CO_2 atmosphere. The TransferMan 4m is an excellent tool for applications, such as intracytoplasmic sperm injection (ICSI), preimplantation genetic diagnosis (PGD), and related techniques. In conjunction with the manual microinjectors of the CellTram family, it forms an ideal system for demanding cell manipulation procedures.

Eppendorf
For info: 800-645-3050
www.eppendorf.com/cellmanipulation

Electronically submit your new product description or product literature information! Go to www.sciencemag.org/products/newproducts.dtl for more information.

Newly offered instrumentation, apparatus, and laboratory materials of interest to researchers in all disciplines in academic, industrial, and governmental organizations are featured in this space. Emphasis is given to purpose, chief characteristics, and availability of products and materials. Endorsement by *Science* or AAAS of any products or materials mentioned is not implied. Additional information may be obtained from the manufacturer or supplier.

Join AAAS. Get instant access to *Science*. Support all of the sciences.

When you subscribe to *Science*, you become part of the American Association for the Advancement of Science (AAAS), a nonprofit community of more than 100,000 members worldwide who believe in the power of science to make the world a better place. AAAS is hard at work promoting science in government, schools, and in the public commons around the globe.

AAAS's award-winning journal *Science* offers the top peer-reviewed research across multiple disciplines. With your subscription, you'll get:

- 51 weeks of home delivery of *Science*
- Instant online retrieval of every *Science* article ever published, dating back to 1880
- Full access to the *Science* mobile site and apps
- Career advice, webinars, blogs and fascinating features exclusively for AAAS members
- Members-only newsletters, and much more

With increasing public skepticism about science–and public funding for research more uncertain than ever–our work has never been more important. Join hands with us today!

Visit promo.aaas.org/joinaaas. Together, we can make a difference.

Science
AAAS

18,000 IHC VALIDATED ANTIBODIES IN YOUR HANDS

Triple A Polyclonals, the antibodies developed by the prestigious Human Protein Atlas project, are made available to fellow researchers by Atlas Antibodies. This gives you access to 18,000 extensively validated antibodies targeting all human proteins, each supplied with more than 500 annotated IHC images. All Triple A Polyclonals are produced by us at Atlas Antibodies.

Welcome to Atlas Antibodies. The world leading provider of antibodies for immunohistochemistry.

Charlotta, Product Manager Triple A Polyclonals

MADE IN SWEDEN

ATLAS ANTIBODIES

Learn more today at atlasantibodies.com

Science Careers Advertising

For full advertising details, go to ScienceCareers.org and click For Employers, or call one of our representatives.

Tracy Holmes
Worldwide Associate Director
Science Careers
Phone: +44 (0) 1223 326525

THE AMERICAS

E-mail: advertise@sciencecareers.org

Fax: +1 (202) 289 6742

Tina Burks
Phone: +1 (202) 326 6577

Nancy Toema
Phone: +1 (202) 326 6578

Online Job Posting Questions
Phone: +1 (202) 312 6375

EUROPE / INDIA / AUSTRALIA / NEW ZEALAND / REST OF WORLD

E-mail: ads@science-int.co.uk

Fax: +44 (0) 1223 326532

Sarah Lelarge
Phone: +44 (0) 1223 326527

Kelly Grace
Phone: +44 (0) 1223 326528

Online Job Posting Questions
Phone: +44 (0) 1223 326528

JAPAN

Katsuyoshi Fukamizu (Tokyo)
E-mail: kfukamizu@aaas.org
Phone: +81 3 3219 5777

Hiroyuki Mashiki (Kyoto)
E-mail: hmashiki@aaas.org
Phone: +81 75 823 1109

CHINA / KOREA / SINGAPORE / TAIWAN / THAILAND

Ruolei Wu
Phone: +86 186 0082 9345
E-mail: rwu@aaas.org

All ads submitted for publication must comply with applicable U.S. and non-U.S. laws. *Science* reserves the right to refuse any advertisement at its sole discretion for any reason, including without limitation for offensive language or inappropriate content, and all advertising is subject to publisher approval. *Science* encourages our readers to alert us to any ads that they feel may be discriminatory or offensive.

ScienceCareers
FROM THE JOURNAL SCIENCE AAAS

ScienceCareers.org

UNIVERSITY OF CALIFORNIA
UC RIVERSIDE

Cluster Hire in Healthy Aging
Assistant, Associate or Full Professor

The University of California Riverside is embarking on a major new hiring initiative that will add 300 tenured and tenure-track positions in 33 cross-disciplinary areas selected through a peer-reviewed competition (clusterhiring.ucr.edu). Over the next three years, we will hire multiple faculty members in each area and invest in research infrastructure to support their work. This initiative will build critical mass in vital and emerging fields of scholarship, foster truly cross-disciplinary work and further diversify the faculty at one of America's most diverse research universities. We encourage applications from scholars committed to excellence and seeking to help redefine the research university for the next generation.

In an initiative to establish a comprehensive program addressing health and wellbeing of aging populations, we seek to hire up to three tenure-track or tenured faculty whose research addresses the public policy, social, behavioral, and/or biological determinants of health as they relate to the needs of older adults. Candidates whose research addresses mechanisms of aging at the cellular, individual and/or community level, characterizes predictors of aging outcome, and leads to develop/test interventions to improve the quality of life and care of seniors are encouraged to apply. We seek researchers that collectively span multi-disciplinary levels of investigation (from molecular mechanisms of inflammation and cellular senescence to complex behaviors such as cognitive and decision making processes, and social policies especially as they relate to minority aging) using state of the art techniques (molecular, behavioral, computational, imaging, genetic and clinical research) applied to experimental model systems of aging or human populations.

All candidates must have a doctorate in a relevant field (e.g. Biology, psychology, sociology, public policy, public health, or medicine) and be strongly committed to both undergraduate and graduate teaching. Preference will be given to applicants who have demonstrated a strong commitment to interdisciplinary research and whose research interests complement those of existing faculty and strengthen our initiative to develop an extramurally funded Center for Research on Aging. Successful candidates may be placed within the College of Natural and Agricultural Sciences, the College of Humanities, Arts and Social Sciences, the School of Public Policy or the School of Medicine depending on the preferences of the candidate and the host departments. Junior candidates are expected to develop an internationally recognized and externally funded research program, while senior candidates must have a demonstrated record of success in these areas. Successful candidates must also have a clear potential or demonstrated ability to successfully work with and benefit a diverse student body.

The University of California, Riverside is centrally located within the Southern California area and situated in an historic citrus growing area surrounded by mountain ranges. Riverside is an hour away from ski slopes, surfing, or hiking in mountain wilderness or desert environments, and housing in the area is very affordable. The campus is located in close proximity to a host of high profile universities, research institutes, and biotech industries in Southern California. Applicants must hold a Ph.D., M.D., Pharm D., or equivalent degree and qualify for a tenure track or tenured faculty appointment at the University of California. Applications will be reviewed beginning February 4th and the positions will remain open until filled.

The University of California is an Equal Opportunity / Affirmative Action Employer with a strong institutional commitment to the achievement of excellence and diversity among its faculty and staff. All qualified applicants will receive consideration for employment without regard to race, color, religion, sex, sexual orientation, gender identity, national origin, age, disability, protected veteran status, or any other characteristic protected by law.

UCR is a world-class research university with an exceptionally diverse undergraduate student body. Its mission is explicitly linked to providing routes to educational success for underrepresented and first-generation college students. A commitment to this mission is a preferred qualification.

Advancement through the faculty ranks at the University of California is through a series of structured, merit-based evaluations, occurring every 2-3 years, each of which includes substantial peer input.

To Apply: Please submit the following items electronically through the APRecruit system: Cover Letter, Curriculum Vitae, statement of research accomplishments and goals, statement of teaching expertise and diversity statement. For full consideration applications should be received by **February 4th, 2016**. Applications will be accepted until the positions are filled.

http://medschool.ucr.edu/employment/faculty/healthy_aging.html

University of Pittsburgh

Director, Center for Vaccine Research

The University of Pittsburgh is seeking applications for the position of director, Center for Vaccine Research (CVR). This interdepartmental center is dedicated to high-quality research on novel vaccines and highly pathogenic/select agents. The center includes the 15,000-square-foot Vaccine Research Laboratory (VRL) and the Regional Biocontainment Laboratory (RBL), with 10 fully equipped BSL-3 laboratories and four fully equipped ABSL-3 facilities, a necropsy suite, a Clinical Imaging Core (including coupled micro-PET and CT, IVIS Spectrum imaging, and live-cell microscopy), and an Aerobiology Core for computerized quantitative aerosol exposure in animal models. The CVR research portfolio totals more than $30 million in multiyear grants and contracts from NIH, industry, and DoD. Learn more about the important work taking place at the CVR by visiting: www.cvr.pitt.edu.

Competitive candidates must have a track record of exceptional research in vaccine development or infectious disease pathogenesis and must meet the requirements of the academic rank of full professor with tenure. Other key characteristics include a broad vision for new vaccine research, ability to foster collaborations, and significant administrative and leadership experience.

With more than $400 million of NIH funding, the University of Pittsburgh ranks fifth among more than 3,000 entities that receive NIH support. The University's Schools of the Health Sciences include the Schools of Medicine, Nursing, Dental Medicine, Pharmacy, Health and Rehabilitation Sciences, and the Graduate School of Public Health. The schools serve as the academic partner of UPMC (University of Pittsburgh Medical Center), a global health system with 23 hospitals, more than 60,000 employees, and close to $11 billion of annual revenue.

Please send curriculum vitae and a letter outlining interest and qualifications to: **Chair, CVR Search Committee, Res Pav 1.9, Hillman Cancer Center, 5117 Centre Avenue, Pittsburgh, PA 15213** or email: **DIRofCVR@pitt.edu**. To ensure full consideration, materials must be received by **February 15, 2016**.

The University of Pittsburgh is an Affirmative Action, Equal Opportunity Employer.

SIGMA XI
THE SCIENTIFIC RESEARCH SOCIETY

EXECUTIVE DIRECTOR

The Board of Directors of Sigma Xi, The Scientific Research Society, invites nominations and applications for the position of Executive Director and Chief Executive Officer. The Executive Director will be located at the Society's Headquarters in the Research Triangle Park in North Carolina.

With the membership of approximately 100,000 individuals and more than 520 chapters worldwide, Sigma Xi, a highly respected voice of science, occupies a unique position as the principal honor society of science in North America and elsewhere. The multifaceted purpose of the Society is to honor scientific achievement, improve the quality of research and access to science, enhance overall scientific literacy, encourage interdisciplinary research, and inform policy makers and the public decision-makers about science, while fostering worldwide interaction among researchers.

The Executive Director is the Society's chief executive officer and, in association with the Board of Directors of the Society, manages the Society's membership and chapter programs and scholarly activities, as well as administrative operations. The successful candidate will be a leader with commitment to executing the goals and growth of Sigma Xi and leading the planning and implementation of the Society into the future.

The Executive Director must be effective at communication on the national and international stage, be a consensus builder with the ability to motivate and lead volunteers, peers, and staff, and possess demonstrated skills in management. She or he must possess proven fundraising ability and experience with management of program activities. Standing and recognition in the scientific and technical community are essential; familiarity with Sigma Xi and its programs and research experience are important criteria. Experience in public- and private-sector venues, as well as academia is highly desirable, as is having attained a Ph.D. in a STEM discipline.

Applications and nominations should include current curriculum vitae, the names and addresses of three references, and a statement of reasons why the position is of interest. This material will be kept in confidence and should be directed to: **Dr. John C. Nemeth, Interim Executive Director and CEO, Chair, Search Committee, Sigma Xi, The Scientific Research Society, P. O. Box 13975, Research Triangle Park, NC 27709.**

Screening of applications will begin on **January 15, 2016**, and will continue until a candidate is selected. It is hoped that a selection will have been made by April 1, 2016, with the effective date of the appointment as soon as feasible.

Sigma Xi is an Equal Opportunity Employer.

POSITIONS OPEN

KANSAS STATE UNIVERSITY | College of Veterinary Medicine

HEAD AND PROFESSOR, DEPARTMENT OF ANATOMY AND PHYSIOLOGY

The College of Veterinary Medicine at Kansas State University invites applications and letters of nomination for the Head of the Department of Anatomy and Physiology. The successful candidate will have a Ph.D. or other earned doctoral degree in biomedical sciences or related, an outstanding history of scholarly achievement and continuing success in extramurally funded research, exceptional leadership, strong commitment to professional and graduate student education and the professional development of faculty, staff and students. Applicants should submit a single PDF that includes a letter of application addressing leadership philosophy and vision; curriculum vitae; and contact information for three individuals from whom letters of reference may be requested. Application and nomination materials should be sent to website: **geyestone@vet.k-state.edu.** For further information, please refer to website: **www.vet.k-state.edu/about/employment /opportunities.html**. Review of applications will begin immediately and continue until the position is filled. Applications should be submitted prior to **February 12, 2016**.

Kansas State University is an Equal Opportunity Employer of individuals with disabilities and protected veterans and actively seeks diversity among its employees. Background check required.

AAAS is here –
helping scientists achieve career sucess.

Every month, over 400,000 students and scientists visit ScienceCareers.org in search of the information, advice, and opportunities they need to take the next step in their careers.

A complete career resource, free to the public, *Science* Careers offers hundreds of career development articles, webinars and downloadable booklets filled with practical advice, a community forum providing answers to career questions, and thousands of job listings in academia, government, and industry. As a AAAS member, your dues help AAAS make this service available to the scientific community. If you're not a member, join us. Together we can make a difference.

To learn more, visit
aaas.org/plusyou/sciencecareers

AAAS + U = Δ

Post Your Jobs
1 million candidates*
151,000 job applications*
Reach Scientists. Fill Positions.
ScienceCareers
employers.sciencecareers.org
*Jan–Dec 2014

Advance your career with expert advice from *Science* Careers.

Download Free Career Advice Booklets!

ScienceCareers.org/booklets

Featured Topics:

- Networking
- Industry or Academia
- Job Searching
- Non-Bench Careers
- And More

ScienceCareers

FROM THE JOURNAL SCIENCE AAAS

FRED HUTCH
CURES START HERE™

Senior Faculty Position in Immunology

The Vaccine and Infectious Disease Division (VIDD) of the Fred Hutchinson Cancer Research Center seeks exceptional applicants for a full-time faculty position at the Full Member rank (comparable to Professor). The primary responsibility of this position is to develop a strong research agenda within the Division's Immunology and Vaccine Development Program with emphasis on mechanisms of memory/effector T-cell generation and immune dysfunction in the context of cancer or chronic infections. The candidate will be expected to help develop and lead a comprehensive, cross-disciplinary program involving multiple investigators that will include a focus on pathogen-induced cancers. VIDD scientists integrate clinical care, computational methods, and basic science research in immunology, virology, and vaccine design to reduce the global burden of infectious disease.

Candidates for this position must have a well-established, robust, funded program that is nationally and internationally recognized for excellence in immunology, immunotherapeutic design, or viral oncogenesis.

Applicants must have an MD (or foreign equivalent) or PhD (or foreign equivalent). Selection criteria include excellence in scholarship, creativity in research, and demonstrated leadership in the profession.

The Fred Hutchinson offers a vibrant intellectual environment within a beautiful, lakeside campus in Seattle's South Lake Union biotech hub. VIDD occupies a new building that is connected by walking trails to Seattle Cancer Care Alliance and the other four Divisions of the Fred Hutch and by trolley to major research partners such as the University of Washington School of Medicine, Seattle Children's Research Institute, Center for Infectious Disease Research (formerly Seattle Biomedical Research Institute), and the Infectious Disease Research Institute.

Salary DOE + excellent benefits.

Interested candidates should submit a CV, a concise research plan statement, and the names and contact information for three (3) references to **fredhutch.org/job/6653**. Specific inquiries can be directed to **Dr. Julie McElrath** at **206-667-1858**. Applications should be received by **February 1, 2016** to assure consideration, and will be evaluated as received.

The Fred Hutchinson Cancer Research Center is an Affirmative Action, Equal Opportunity Employer. All qualified applicants will receive consideration for employment without regard to, among other things, race, religion, color, national origin, sex, age, status as protected veterans, or status as qualified individuals with disabilities. We strongly encourage applications from women, minorities, individuals with disabilities and covered veterans.

Faculty Position
X-ray Lasers in Biology and Materials Science

The University at Buffalo seeks applications and nominations to fill a newly created, Full Professor position in the area, broadly defined, of the use of X-ray lasers in biology and materials science. Appointment will be made in an appropriate School and Department, depending on the background of the candidate. The successful candidate will also be a key leader in the BioXFEL Center (**https://www.bioxfel.org/**). This NSF-funded Science and Technology Center is spearheading the effort to revolutionize how structural biology is done by developing the use of X-ray lasers to capture biological molecules in atomic detail, view their functional motions by making molecular movies, and observe interactions in their native environments. The University at Buffalo seeks to use this Center award as leverage to develop a strong research and academic presence in X-ray laser science.

The successful candidate will:

- Be an acknowledged leader in their field and demonstrate strengths in one or more important research areas important to the mission of BioXFEL. These may include topics in the current BioXFEL portfolio, or new fields such as detector development and expanding into areas at the intersection of structural biology and materials science that would expand BioXFEL's horizons.
- Have a strong track record of published, highly visible scientific achievements and a strong history of external, peer-reviewed research funding.
- Have experience with large-scale collaborations and management skills to establish future cross discipline research approaches.

The successful applicant will have the opportunity to interact with a diverse interdisciplinary group that includes interaction with the new Department of Materials Design and Innovation at UB which has a unique focus on data intensive imaging and spectroscopy as well as the multiple institutions participating in BioXFEL. Applicants should write a vision statement no longer than two pages that develops frontier ideas for XFEL research both at a personal and institutional level.

Applications, including the vision statement, curriculum vitae, three reprints and contact information for three references should be submitted to: **www.ubjobs.buffalo.edu/applicants/Central?quickFind=58503**. Screening of applicants will begin immediately and continue until the position is filled.

The University at Buffalo is an Equal Opportunity/Affirmative Action Employer/Recruiter.

University at Buffalo
The State University of New York

DUKE NUS
GRADUATE MEDICAL SCHOOL SINGAPORE

Director

Programme in Neuroscience and Behavioural Disorders
Duke-NUS Medical School

Duke-National University of Singapore Medical School (Duke-NUS) seeks an outstanding neuroscientist (MD, PhD, or MD/PhD) with strong leadership skills to be the new Director of the Programme in Neuroscience and Behavioural Disorders. Duke-NUS is a joint venture between two leading universities: the National University of Singapore and Duke University. The Programme in Neuroscience and Behavioural Disorders has an outstanding faculty with expertise in areas including cognitive neuroscience, developmental neuroscience and the study of synaptic circuitry, with strong translational programmes in psychiatric disorders and neurodegeneration. The Programme has its home in a modern facility adjacent to Singapore General Hospital, and maintains strong basic, translational and clinical research partnerships throughout Singapore, particularly with the National Neuroscience Institute and the Institute of Mental Health.

The Programme Director will provide leadership, including engagement with the broader neuroscience community in Singapore and with Duke University; strategic hiring and programme development; medical school and graduate education; faculty mentoring; and budgetary and space planning. The School will provide the Director with the resources to support the highest level of research. More information on the Programme can be found at **http://research.duke-nus.edu.sg/nbd/index.php**

Duke-NUS has retained the executive search firm RSA Group to assist the search committee in its work. Confidential inquiries, nominations, referrals, and curricula vitae should be sent electronically and in confidence to:
danni.swain@thersagroup.com
Quoting reference **S15145**

THAYER SCHOOL OF ENGINEERING AT DARTMOUTH

Tenure Track Faculty Position at the Intersection of Energy and Design

The Thayer School of Engineering at Dartmouth seeks to add to an existing group of faculty active in energy-related research as part of a major expansion of faculty and programs. We are looking for a candidate with research interests involving the application of creative design methodology to energy use and conservation in the built environment. The successful applicant will have a Ph.D. in engineering or a closely-related discipline, show evidence of being a motivated teacher, and show promise of leading an externally-funded research program. The specific field of academic preparation is open, although we have an interest in persons who can teach in thermodynamics, fluids, or transport. A hire at the Assistant Professor level is anticipated.

Review of applications will begin **February 1st, 2016**. A complete CV, statement of research and teaching interests, and contact information for three references should be sent as a PDF via email to **Thayer.Energy.Design.Search@dartmouth.edu**.

Dartmouth is a member of the Ivy League and consistently ranks among the world's greatest academic institutions. Home to a celebrated liberal arts curriculum and pioneering professional schools, Dartmouth has shaped the education landscape and prepared leaders through its inspirational learning experience. The College has forged a singular identity, combining its deep commitment to outstanding undergraduate liberal arts and graduate education with distinguished research and scholarship in the Arts and Sciences and its three leading professional schools — Geisel School of Medicine, Thayer School of Engineering, and Tuck School of Business. For more information see http://engineering.dartmouth.edu. Home to Dartmouth College, the Upper Connecticut Valley is a vibrant, academic and professional community offering excellent schools, lively arts, and an unmatched quality of life in a beautiful setting. Amenities associated with urban areas in Boston MA, Burlington VT, and Montreal QC are all within a few hours drive.

Dartmouth College is an Equal Opportunity/Affirmative Action Employer with a strong commitment to diversity. In that spirit, we are particularly interested in receiving applications from a broad spectrum of people, including women, minorities, individuals with disabilities, veterans or any other legally protected group.

Two Fantastic Recruiting Opportunities!

FACULTY CAREERS | January 29, 2016

Gear up to recruit for the faculty positions at your university with this much anticipated issue that reaches thousands of Ph.D. scientists looking for positions in academia.

Reserve ads by Jan 12 to guarantee space.

POSTDOC CAREERS | March 25, 2016

Be sure to promote your openings to the thousands of scientists who will be reading *Science* to find out about the latest postdoc opportunities.

Reserve ads by March 8 to guarantee space.

Produced by the *Science*/AAAS Custom Publishing Office.

SCIENCECAREERS.ORG

To book your ad: **advertise@sciencecareers.org**
The Americas: 202-326-6582 **Europe/RoW:** +44-0-1223-326500
Japan: +81-3-3219-5777 **China/Korea/Singapore/Taiwan:** +86-186-0082 9345

PURDUE
UNIVERSITY

Faculty Positions in Structural Biology
Markey Center for Structural Biology
Department of Biological Sciences

The Department of Biological Sciences, Purdue University, is initiating a major effort to expand its investment in Structural Biology and invites applicants at all academic professorial levels to fill multiple new tenure-track faculty positions in this accelerating area. The Structural Biology Group at Purdue is recognized worldwide for its leadership in structural biology of viruses, membrane proteins, and technical approaches to crystallographic and electron microscopy challenges. Creative investigators in a variety of research approaches, X-ray crystallography, NMR spectroscopy and electron microscopy, are sought to enhance these current structural investigations. Potential areas of research interest include but are not limited to studies of viruses and other pathogens, membrane proteins, cancer biology, target molecules for structure-based drug discovery and development of new technologies in structural biology. This position is aligned with major campus-wide investments in the life sciences including the Center for Drug Discovery (https://www.purdue.edu/research/pcdd/), the Center for Integrative Neurosciences and the Institute for Inflammation, Immunology and Infectious Disease (https://www.purdue.edu/research/life-sciences/).

Applicants for senior positions in Structural Biology must have a Ph.D. or equivalent in an appropriate discipline and currently hold a position equivalent to an Associate or Full Professor. Structural biologists with a clear cancer focus in their research will also be considered by the Purdue Center for Cancer Research as a Walther Cancer Professor (https://www.cancerresearch.purdue.edu). Applicants at the junior rank in Structural Biology must have a Ph.D. or equivalent in an appropriate discipline and at least 2 years of postdoctoral experience. There is particular interest in researchers trained in single particle cryo-electron microscopy or whole cell electron tomography.

Successful applicants for these positions are expected to direct a dynamic and collaborative research program in structural biology to address fundamental questions in the area of human disease, to excel at teaching at the undergraduate and/or graduate level and participate in ongoing programs at Purdue.

Extensive opportunities for collaboration exist within the Department, which has over 50 faculty members conducting research in neurobiology, virology, microbiology, molecular and cell biology, bioinformatics, evolutionary biology and ecology (http://www.bio.purdue.edu/). These opportunities are enhanced by a highly interactive community of scientists within the Colleges of Science, Pharmacy, Veterinary Medicine and Engineering and existing and emerging interdisciplinary centers in the life sciences. Abundant infrastructure support for structural biology exists, including advanced imaging analysis and biophysical instrumentation available in established core facilities at the Bindley Bioscience Center and the Birck Nanotechnology Center in Discovery Park (http://www.purdue.edu/discoverypark/).

Applications should be submitted electronically to **https://hiring.science.purdue.edu/** as a single PDF file containing a letter of interest, a detailed curriculum vitae, contact information for three references, a two to three page summary of research interests, and a one-page teaching statement. The Department of Biological Sciences is committed to advancing diversity in all areas of faculty effort – scholarship, instruction and engagement. Candidates should address at least one of these areas in their cover letter, including past experience, current activity and/or future goals to promote a climate that values diversity and inclusion. As an ADVANCE institution, Purdue University is dedicated to the recruitment, retention and advancement of women in the STEM disciplines. Inquiries should be directed to **Cynthia Stauffacher, Chair, Structural Biology Search Committee** at **StructureSearch@bio.purdue.edu** or **Structural Biology Search Committee, Department of Biological Sciences, Purdue University, 915 W. State St., West Lafayette, IN 47907-2054**. Review of applications will begin **December 15, 2015** and continue until these positions are filled. A background check is required for employment in this position.

Purdue University is an EOE/Affirmative Action Employer. All qualified applicants, including minorities, women, individuals with disabilities and veterans are encouraged to apply.

ETH zürich

Professor of Soil Resources

→ The Department of Environmental Systems Science (www.usys.ethz.ch) of ETH Zurich invites applications for a professorial faculty position focusing on (1) the role of soil as a key natural resource, supporting a wide range of forest and other terrestrial ecosystem functions and services and (2) quantifying the effects of changes of land use and climate on various soil functions at local to global scales. The appointment will be at full professor level. Candidates should be interested in system-oriented multidisciplinary research and are expected to develop an innovative and internationally recognized research program, making an important contribution to linking the assessment and modelling of soil function to land-use and climate change.

→ The successful candidate will have a strong background in soil sciences as well as an international track record in research and will be a motivated and capable university teacher. Additionally, skills in mathematical modelling and/or spatial information systems are a great plus. Teaching duties will include introductory and advanced-level courses on the assessment, modelling and management of soil resources as part of the environment. The new professor will be expected to teach undergraduate level courses (German or English) and graduate level courses (English).

→ **Please apply online at www.facultyaffairs.ethz.ch**

→ Applications should include a curriculum vitae, a list of publications, and a statement of future research and teaching interests. The letter of application should be addressed **to the President of ETH Zurich, Prof. Dr. Lino Guzzella. The closing date for applications is 15 March 2016.** ETH Zurich is an equal opportunity and family friendly employer and is further responsive to the needs of dual career couples. We specifically encourage women to apply.

ScienceCareers online @sciencecareers.org

By **Artaza Gilani**

Beyond the tick boxes

There are many great schools in England, where I grew up, but the one where I did the first part of my secondary education wasn't one of them. Most of the students there did not go on to university, and fights and verbal abuse were common. Now that I am a physician, people ask me how I made it out of there, and sometimes they even seem to feel sorry for me, but I am proud of my past. Attending this school taught me unique and valuable skills. I learned the importance of standing up for myself and for what I believe in. I also learned how to interact with people with challenging behaviors and defuse emotionally charged situations through a diplomatic approach. Above all, my experience at this school prepared me to question things and push back against practices I disagree with, in my personal and professional lives.

As I pursue a career combining clinical practice, research, and teaching, I have noticed a number of cultural norms that trouble me. For instance, in the medical community, it is all too common to see students neglected or humiliated during their training. I am also uneasy with some of the trends and practices in the research community. Recently, for example, I received an email—and it wasn't the first one—offering an "easy" opportunity to build up my research CV. The selling point was that, without much work, I would gain a publication that would help me tick a box on future job applications.

Such messages reflect a worrisome status quo in our research environment. They typify the publish-or-perish paradigm and shed light on a questionable approach to career advancement: Through fear of not progressing, researchers sometimes pursue activities not for the opportunity to explore, learn, and grow, but just so they may add more items to their CVs.

Throughout my career, I have tried to avoid doing things halfheartedly. A couple of years ago, I declined an invitation to take part in a large and well-funded research project that probably would have looked great on my CV. It was just so remote from any of my areas of interest that—even though it offered a chance to gain research experience and develop transferable skills, both of which are certainly important—I would have struggled to justify my involvement. I remain grateful for the opportunity, but I don't regret my decision. I am glad it went to somebody who wanted it more than I did, and meanwhile I have been able to learn from other research projects in medical education that lie closer to my heart.

"Throughout my career, I have tried to avoid doing things halfheartedly."

Some would argue that, by taking this approach, I exclude myself from opportunities and appear to be lazy or detached. I do recognize that there is a pragmatic rationale behind ticking boxes, and I am aware of the risks of not following suit. I would like to do a research doctorate, and I know that I may struggle to compete with others in academia who have played the game better than I have. My counterargument is that it is a simple matter of quality versus quantity. It is true that, by choosing my ventures carefully, I may have been involved in fewer projects. But I like to think that the work I have done, I have done right, and this takes a lot of effort, passion, and commitment.

My career strategy is to look for interesting niches where a few high-quality pieces of work will be held in higher regard than dozens of lesser quality. Colleagues and supervisors have told me that my standout quality is the passion I have for the work I do. My hope is that, when applying for a job, grant, or whatever else may come along, I will have enough on paper to make it to a stage where I can present myself in person, display that passion, and speak for the value of the approach I have taken. In the long run, I hope that the current academic paradigm will shift so that we can look beyond the tick boxes: Perhaps this will improve scholarship and help develop a more creative research community. ■

Artaza Gilani is a medical doctor at Whipps Cross University Hospital of Barts Health NHS Trust in the United Kingdom. *For more on life and careers, visit sciencecareers.org. Send your story to SciCareerEditor@aaas.org.*

ILLUSTRATION: ROBERT NEUBECKER

Published by AAAS